HARVARD UNIVERSITY
Graduate School of Arts and Sciences



DISSERTATION ACCEPTANCE CERTIFICATE

The undersigned, appointed by the

Department of Physics

have examined a dissertation entitled

NV centers as local probes of two-dimensional materials

presented by Bo Loren Dwyer

candidate for the degree of Doctor of Philosophy and hereby certify that it is worthy of acceptance.

Signature _____

Typed name: Professor Mikhail Lukin, Chair

Signature _____

Typed name: Professor Philip Kim

Signature _____

Typed name: Professor Amir Yacoby

Date: April 29, 2021

NV centers as local probes of two-dimensional materials

A DISSERTATION PRESENTED
BY
Bo Loren Dwyer
TO
The Department of Physics

IN PARTIAL FULFILLMENT OF THE REQUIREMENTS
FOR THE DEGREE OF
Doctor of Philosophy
IN THE SUBJECT OF
Physics

Harvard University
Cambridge, Massachusetts

April 2021

©2021 – Bo Loren Dwyer
all rights reserved.

Dissertation Advisor: Professor Mikhail D. Lukin Bo Loren Dwyer

NV centers as local probes of two-dimensional materials

Abstract

Over the past decade, Nitrogen Vacancy (NV) color centers in diamond have emerged as powerful tools for quantum simulation and metrology. These atom-like defects, while confined to the diamond lattice, exhibit many properties of trapped atoms including optical transitions and high sensitivity to magnetic fields. These properties, combined with their small scale, has led to many applications for NV centers as sensors biology, chemistry, and condensed matter physics. In this thesis, we use NV centers to study a number of two dimensional systems, including Van der Waals heterostructures and the surface of the diamond itself. First, we correlate NV center measurements with various surface sensitive spectroscopy techniques to identify and mitigate deleterious sources of noise at the surface. We use this information to develop a surface treatment that extends the coherence time of shallow NV centers, which is necessary for most sensing applications. We then investigate a particular system of defects hosted at the diamond surface, the g=2 "dark" surface spins, and determine their properties through coherence measurements of shallow NV centers. We find that the characteristic shape of the coherence decay can itself be used as a sensor, as it encodes information about the dynamical nature of the sensing target as well as the distance between the NV center sensor and the two dimensional surface. We then turn to measuring electronic properties of 2D heterostructures composed of graphene and hexagonal boron nitride. By mapping out the spatial dependence of magnetic noise due to phonon scattering in a highly biased graphene field effect transistor, we discover a previously undescribed electron-phonon instability in graphene that is analogous to amplified spontaneous emission in a laser. Finally, we use NV centers to measure the gate dependent orbital magnetic response of a single sheet of graphene through a gate modulation lock-in technique. The ability to measure local magnetic properties of 2D materials with NV centers will likely find many uses in future experiments, as they are compatible with traditional transport techniques and provide spatially resolved information even in devices with inhomogenous properties.

Contents

Title page i
Copyright page ii
Abstract iii
Listing of figures vii
Dedication page xxviii
Acknowledgements xxix

1 Introduction and Background **1**
1.1 Prologue 2
1.2 Overview of this thesis 3
1.3 NV centers in diamond 5
1.4 Graphene 83

2 Origins of diamond surface noise **102**
2.1 Introduction 103
2.2 Origins of diamond surface noise probed by correlating single spin measurements with surface spectroscopy 125
2.3 Discussion 139

3 Dynamics of surface defects **143**
3.1 Background 144
3.2 Measurement techniques 150
3.3 Probing spin dynamics on diamond surfaces using a single quantum sensor 151
3.4 Discussion 166

4 Global and local probes of an electron-phonon Cerenkov instability in graphene **171**
4.1 Background 173
4.2 Electron-phonon instability in graphene revealed by global and local noise probes . 185
4.3 Discussion 196

5 Local probe of magnetic susceptibility in 2D materials 199
5.1 Introduction . . . 200
5.2 NV centers as local probes of orbital magnetism in 2D materials . . . 203
5.3 Experimental results . . . 205
5.4 Methods . . . 215
5.5 Discussion . . . 219

6 Conclusion 222

Appendix A Supporting material for Chapter 2 225
A1 Methods . . . 225
A2 Process Calibration for Oxygen Annealing . . . 229
A3 Effects of Sample Contamination . . . 233
A4 sp^2 Carbon Formation During High Temperature Annealing to Remove Etch Damage Layer . . . 238
A5 Process Calibration for Oxygen Annealing . . . 239
A6 Surface Damage from Oxygen Processing and Reactive Ion Etching . . . 244
A7 Shallow NV Spin Coherence in Rough Samples . . . 248
A8 Dynamical Decoupling Data . . . 249
A9 Noise Spectral Density Extracted from NV Center Measurements . . . 250
A10 Electron Affinity Measurement . . . 259
A11 LEED Pattern of Oxygen-annealed Surface . . . 260
A12 Comparison of XPS Spectra for Triacid-cleaned and Oxygen-annealed Surfaces . . . 262

Appendix B Supporting material for Chapter 3 265
B1 Measurement setup . . . 265
B2 Sample processing . . . 267
B3 Fitting procedures . . . 269
B4 Removal of surface spins through annealing . . . 271
B5 Additional surface spin measurements . . . 279
B6 Derivation of DEER signal for static and hopping surface spins . . . 284
B7 Effects of finite surface spin T_1 time . . . 293
B8 Exponent transition for additional NV centers . . . 300
B9 Additional model analysis . . . 302
B10 Fraction of spins that are hopping . . . 306

Appendix C Supporting material for Chapter 4 308
C1 Device fabrication . . . 308
C2 AC conductivity and noise measurements . . . 314
C3 Local noise measurements with diamond NV magnetometry . . . 322
C4 Basic device transport characterization . . . 325

C5 Additional noise and conductivity measurements 326
C6 Additional NV center measurements 332
C7 Theory 338
C8 Alternative mechanisms 358

Appendix D Supporting material for Chapter 5 **362**
D1 Theoretical treatment 362

References **401**

Listing of figures

1.1 Depiction of the positioning of the NV center defect (green and clear spheres) in the carbon (black spheres) lattice of diamond. The quantization axis is the bond connecting the nitrogen and vacancy. 5

1.2 **NV center formation.** Nitrogen ions are implanted with a chosen density and energy (depth), leaving vacancies as they tear through the lattice. Annealing makes the vacancies mobile, and some will naturally find a nitrogen to partner with, forming the NV center complex. 9

1.3 **The NV level structure.** Single electron orbitals are determined by symmetry considerations and filled with the six electrons that make up the NV^- color center. Labels on the left indicate the IR of the single electron orbitals and labels on the right indicate the linear combination of dangling bonds. 14

1.4 **Eigenstates and transitions of the NV^- center.** (A) Symmetries of the wavefunctions of the NV center as described by two holes. The left hand column indicates the orbitals of the two holes, with the singlet (S) or triplet (T) character in parentheses. The center column lists the spin and orbital parts of the wavefunction, and the right column the overall symmetry. α, β refer to spin up and spin down, respectively. $E_\pm = |a_1 E_\pm - e_\pm a_1\rangle$, with $e_\pm = \mp(e_x \pm i e_y)$. $|X\rangle = \frac{1}{2}(|E_-\rangle - |E_+\rangle)$ and $|Y\rangle = \frac{i}{2}(|E_-\rangle + |E_+\rangle)$. (B) Energy level diagram for the electronic states of the NV center. States on the left are triplets while those on the right are singlets. Red arrows indicate allowed transitions, while dashed arrows are spin orbit induced transitions. J is the exchange energy of the Coulomb interaction. Figures taken with permission from Ref.[239]. . 17

1.5 **Rabi oscillations of an NV center under a microwave drive.** (A) Pulse sequence, consisting of an intitalization step that pumps the NV center spin into $m_s = 0$, a microwave drive of variable duration, and optical readout of the NV center spin state. (B) Rabi oscillations from an NV center (red points) with a sinusoidal fit (blue line). The curve does not start exactly at zero due to effects of the microwave switch. . . 23

1.6 **State representation on the Bloch sphere.** (A) A rotation of θ about the y axis and (B) a rotation of φ about the z axis. 24

1.7 **π pulse detuning.** Detuning dependence for a π pulse applied to a two level system with initial condition $c(t = 0) = 0$ 26

1.8 **NV center ODMR.** Optically detected magnetic resonance of an NV center, showing the two spin transitions split by an external magnetic field. 27
1.9 **Bloch sphere depiction of a Ramsey pulse sequence.** A $\pi/2$ pulse sends the spin vector to the equator, where it precesses under the influence of the Hamiltonian to acquire a phase. Following this, another $\pi/2$ pulse around the same axis converts the phase into a spin population that can then be read out.. 28
1.10 **Spin dephasing and sensitivity.** (A) Simulated NV center fluorescence signals in a DC field of $\gamma_e B_z$ = 1 MHz, but with differing decay envelopes characterized by the exponential decay constant $\frac{1}{T_2^*}$ (B) Fourier transforms of simulated signals in (A), showing increased broadening for shorter values of T_2^*. 30
1.11 **Bloch sphere representation of the spin echo.** As in the Ramsey sequence, the spin state is tilted onto the equator of the Bloch sphere and allowed to precess, but midway through the free precession interval a π pulse reverses the dynamics. The precession is refocused, except for parts of the Hamiltonian that give different (preferably opposite) phase accumulations in the first and second half of the sequence. 31
1.12 **Coherence oscillations and revivals.** (A) Simulated NV center spin signal for a periodic magnetic field with random phase. (B) Spin Echo signal from an NV center in a diamond with a natural abundance of 13C, displaying oscillations in the coherence at $\gamma_N B_{app}$ due to a nearby 13C atom. 34
1.13 **Filter function plots for different pulse numbers.** Filter functions (divided by ω^2) for CPMG sequences with increasing pulse number n. For a fixed total time, increasing n pushes the filter function to higher frequencies and it becomes more sharply peaked. 38
1.14 **Pulse sequence frequency filtering.** Intuitive explanation of filtering in CMPG sequences. A signal with a frequency commensurate with the pulse sequence (blue curve) contributes phase of the same sign for the entire sequence (light blue shading). A signal with a different frequency (red curve) contributes positive (light red) and negative (dark red) phases, and so contributes less to the phase accumulation of the NV center. Central pulse sequence is symmetric XY8. 40
1.15 **NMR signal from protons.** Typical NMR signal for a shallow (5 nm) deep NV center. τ is the time between π pulses in a 43 pulse XY-8 sequence. Red points are data, blue is a fit from Ref.[279]. 41
1.16 **NV center electric field sensitivity.** (A)-(C): Simulated electric field induced frequency shift for $m_s = -1$, plotted in polar coordinates as a function of φ_B. $E_\perp = 500$ kV/cm, $B_z = 10$ Gauss. $|B_\perp|$ has values of 0 Gauss (A), 50 Gauss (B), and 100 Gauss (C). Radial scale is in MHz. (D) Relative frequency change for $E_\perp = 500$ kV/cm for different strengths of $|B_\perp|$. $B_z = 10$ Gauss. 48

1.17 **Response of $m_s = \pm 1$ splittings under electric fields.** A field can be applied parallel ($E_\parallel$, (A)) or perpendicular ($E_\perp$, (B)) to the NV quantization axis. B_z = 1 Gauss to avoid overlap of the two frequencies in (A). Note the different scales of the y axes. 50
1.18 **Resonant readout of NV centers.** (A) SEM of nanostructured solid immersion lens used to increase collection efficiency in resonant readout experiment. (B) Simplified level structure showing the E_x and A_1 transitions used for spin pumping and readout. (C) Photoluminescence spectrum of an NV center taken while scanning the excitation laser frequency, relative to 470.443 THz. (D) Count rates from the E_x transition and A_1 transition (inset) as a function of readout duration. The decay is due to mixing between the excited states that results in non-cyclicity of the transitions. Figure taken with permission from Ref.[295]. 56
1.19 **Off resonant readout** 60
1.19 (continued) 61
1.20 **Emission spectra of the two charge states of the NV center.** Since NV^0 has a higher energy zero phonon line than NV^-, it is possible to selectively excite NV^-. Figure taken with permission from Ref.[299]. 62
1.21 **Spin to charge mapping.** (A) Pulse sequence for a T_1 measurement using spin to charge conversion with resonant charge state readout. (B) Photon count distribution for readouts with the resonant 637 nm laser without any charge state initialization, showing a Poisson mixture distribution. The Poisson parameters for NV^0 and NV^- are given by λ^0 and λ^-, respectively. (C) Separated photon count distributions for NV^0 and NV^- under resonant excitation, separated using optimal thresholding during the initial charge state check readout. 64
1.22 **Multicolor charge state initialization.** NV^- population with multicolor initialization. 66
1.23 **Nuclear spin repetitive readout.** (A) Illustration of the concept behind repetitive readout of a nuclear spin memory, where the electronic spin state is mapped to the nuclear spin and the nuclear spin state is read out repeatedly. (B) Pulse sequence for sensing with nuclear spin enhanced readout. (C) Readout fidelity of the nuclear spin as a function of repetitions. Figures (B) and (C) taken with permission from from Ref.[226]. 70
1.24 **Hyperfine ESR** 74
1.24 (continued) 75
1.25 **Hyperfine oscillations in a Ramsey measurement.** (A) Ramsey dataset from a ^{14}N NV center, displaying modulation from the nuclear spin. (B) Fourier transform of (A), in which the three distinct frequencies are visible. 77
1.26 **ESEEM oscillations.** (A) Spin echo experiment performed on a ^{15}N NV center with a slight external field misalignment, displaying ESEEM. (B) Fourier transform of (A). 82
1.27 The honeycomb lattice of graphene. 83

1.28 **The graphene lattice.** (A) Hexagonal lattice of graphene, composed of two triangular Bravais lattices (blue and red points). (B) Brillouin zone of the hexagonal lattice. For graphene, the K and K' points are equivalent because of sublattice symmetry. . 85
1.29 **Graphene band structure.** (A) Band structure of graphene, plotted from Eq. (1.134). (B) Low energy band structure projection near one of the equivalent K points, showing the linear, gapless dispersion of low energy excitations. 88
1.30 **Control of the charge density of graphene through the field effect.** (A) When a small voltage is applied between the plates of a capacitor made of graphene and a gate, only a few excess electrons are present in the graphene. (B) When a larger voltage is applied, the capacitor equation necessitates that more charge be present on each plate, which increases the charge density and hence the Fermi level of the graphene. (C) Transport through a graphene field effect transistor as the gate voltage is tuned through the Dirac point, showing an increase in resistance there. 91
1.31 **Anomalous quantum hall effect in graphene.** (A) Hall resistance (black) and magnetoresistance (red) of electrons in graphene as the magnetic field is varied, showing pronounced hall plateaus. Numbers are filling factors. The inset shows the same experiment repeated for hole doped graphene. (B) Hall resistance (black) and magnetoresistance (orange) at 9 T as a function of gate voltage. Unlike in conventional materials, the quantum hall effect can be observed in graphene by varying the Fermi level through electrostatic gating. Inset is zoomed in to the high filling factor region. (C) Diagram showing the Landau level density of states and hall resistance as a function of Fermi energy. Graphene uniquely has a Landau level at $E_F = 0$. Figure taken with permission from Ref.[396]. 95
1.32 **Fabrication of 2D heterostructures.** Contruction of a 2D material heterostructure. (A) Flakes of different materials are selected by inspection under an optical microscope. (B) A polymer stamp is used to repeatedly pick up and set flakes on top of each other, building a stack from the top down. (C) A finished stack is etched and contacted with standard photolithography techniques. 98
1.33 **Stacking of 2D materials.** (A) With the wide variety of different Van der Waals materials available, devices with desirable properties can be constructed layer by layer. Figure taken with permission from Ref.[121]. (B) Relative twist angle is a parameter available in Van der Waals materials that is unique. Rotating two layers with respect to each other results in a long wavelength Moiré potential that can produce interesting effects. 100

2.1 Depiction of surface X-ray spectroscopy, where X-rays excite electrons from the atoms of the diamond surface. 103

2.2 **Band bending near the diamond surface.** (A) Energy levels of diamond before charge redistribution. The presence of acceptor states on the surface alters the charge distribution as electrons move to occupy these low energy states. (B) After charge redistribution, holes accumulate at the surface to balance the electrons that now occupy the surface traps. This has the effect of bending the energy bands upwards on approach to the surface, while the Fermi level remains constant. LUMO: lowest unoccupied molecular orbital, HOMO: highest occupied molecular orbital. Figure taken with permission from Ref.[63]. 106
2.3 **Energy levels of defects in the diamond band gap.** Energy levels of various defects in diamond relative to the valence (E_V) and conduction E_C bands. Since NV^0 is lower in energy than NV^-, local variations in the Fermi level from nearby defects can make NV^- unstable. Band bending can likewise shift the positions of the defect states so that NV^- lies above the Fermi energy. Figure taken with permission from Ref.[84]. . 107
2.4 **Surface reconstruction of diamond.** 109
2.4 (continued) 110
2.5 **Surface electron affinities for different diamond surface terminations.** The clean surface has a slightly positive electron affinity, but hydrogen termination makes this negative due to the low electronegativity of hydrogen. Oxygen termination, by contrast, results in a very high electron affinity due to its high electronegativity, surpassed only by Fluorine for common elements. Figure taken with permission from Ref.[293]. 112
2.6 **sp^2 defects on the diamond surface.** (A) first two layers of carbon on (100) diamond, showing an sp^2 defect formed by removal of a terminal carbon atom. (B) NEXAFS spectra near the C1s edge, showing regions associated with sp^2 carbon in three diamond samples (gray box). Graphene was used as a uniform coverage sp^2 reference in this experiment. Figure taken with permission from Ref.[338]. 114
2.7 **As grown and polished surfaces.** (A) An as-grown diamond surface displays facets in an optical image (left) but the surface is very smooth on these facets (right). (B) A polished diamond shows scaife marks from the polishing procedure, but these can be smoothed (and the strain removed) by isotropic $ArCl_2$ ion etching. 115
2.8 **XPS schematic.** 118
2.8 (continued) 119
2.9 **Depiction of LEED.** 123
2.9 (continued) 124

2.10 **Creation of shallow NV centers with long coherence times** (a) Schematic showing an NV center near the diamond surface. The surface can host defects that produce electric and magnetic field noise. (b) Hahn echo coherence time, $T_{2,\mathrm{Echo}}$, as a function of NV depth, measured across six samples with different surface conditions. Although the triacid-cleaned surfaces have different origins and processing histories (see Appendix A1), the relationship between $T_{2,\mathrm{Echo}}$ and depth is similar across all samples, and the high-temperature and oxygen-annealed sample exhibits significantly improved coherence times at the same depths. (c) Surface processing steps before implantation to remove surface polish damage and subsurface RIE damage, and after implantation to form NV centers and create a well-ordered oxygen surface termination. The high-temperature annealing step can be performed at 800 °C or 1200 °C. (d) AFM images of initial scaife-polished diamond (top) and the final surface after oxygen annealing (middle). Scale bar is 100 nm. (bottom) Confocal image showing individually resolvable NV centers. Scale bar is 1 μm. 128

2.11 **Comparison of NV centers under the triacid-cleaned (red squares) and oxygen-annealed (blue diamonds) surfaces** (a) Hahn echo decay curves from the same NV center. The Hahn echo coherence time, $T_{2,\mathrm{Echo}}$, is improved after oxygen annealing. (b) Coherence time, T_2, as a function of number of the dynamical decoupling pulses, N. Dashed lines depict the scaling expected for slowly fluctuating noise, $T_2 \propto N^{2/3}$. (c) Measured $T_{2,\mathrm{Echo}}$ ($N = 1$, opaque) and $T_{2,\mathrm{XY8}}$, ($N = 8$, transparent) for six NV centers through four steps of surface termination and reset (inset), showing that the oxygen annealing is reversible and reproducible. (d,e) Single- and double-quantum spin relaxation times, $T_{1,\mathrm{SQ}}$ and $T_{1,\mathrm{DQ}}$, as a function of NV depth (transitions indicated in insets). $T_{1,\mathrm{SQ}}$ shows a more pronounced improvement with oxygen annealing compared to $T_{1,\mathrm{DQ}}$, indicating that magnetic noise is more strongly suppressed than electric field noise. 131

2.11 (continued) 132

2.12 **Surface spectroscopy comparison between triacid-cleaned (blue) and oxygen-annealed (red) surfaces** (a) Schematic showing surface-sensitive spectroscopy techniques used to probe the diamond surface. (b,c) Polarization dependence of NEXAFS spectra at the oxygen K-edge. The polarization angle is defined relative to the surface normal. The y-axis for all NEXAFS spectra is the partial electron yield (PEY), normalized and baseline subtracted (see Appendix A2.2). The oxygen-annealed surface spectrum exhibits strong polarization dependence, indicating that oxygen groups at the surface are well-ordered. (d) NEXAFS spectra at the carbon K-edge from three triacid-cleaned samples (blue curves) and two oxygen-annealed samples (red curves). Triacid-cleaned surfaces show a higher density of unoccupied states (shaded regions). The full energy range is shown in the inset. (e) UPS spectra with excitation energy $h\nu = 21.2$ eV of the triacid-cleaned (blue) and oxygen-annealed (red) surfaces. The spectral width, ω, is indicated by the shaded regions. The oxygen-annealed surface exhibits a higher positive electron affinity, E_A, (+2.14 eV) than the triacid-cleaned surface (+0.92 eV). 135

2.12 (continued) 136
2.13 **Detailed characterization of the oxygen-annealed surface** (a) XPS survey scan showing dominant carbon and oxygen peaks. Peaks marked with (∗) are Auger peaks associated with carbon and oxygen. (left inset) High-resolution XPS carbon 1*s* spectrum showing a dominant diamond sp^3 peak with three side peaks assigned to sp^2 carbon, and carbon singly- and doubly-bonded to oxygen. (right inset) High-resolution XPS oxygen 1*s* spectrum showing a dominant ether (C-O-C) peak and two satellite peaks assigned to alcohol (C-O-H) and ketone (C=O). (b) LEED pattern showing a 1×1 reconstruction of the oxygen-annealed surface, consistent with ether termination. (c) Ball and stick diagrams illustrating the surface termination before and after oxygen annealing. The disordered, acid-cleaned surface hosts a mixture of groups, which transform into a highly-ordered, predominantly ether-terminated surface upon oxygen annealing. 138
2.14 T_1 **for different implantation energies.** Measurements of NV center T_1 relaxation times at 70 K as a function of implantation energy. Straggle is introduced along the x axis to separate points from the same sample, so the energy of each point is approximate. 141

3.1 Artistic rendition of surface spins temprarily occupying traps on the diamond surface. 144
3.2 **Double electron-electron resonance.** (A) Pulse sequence for DEER, where a π pulse is applied to a target spin speices concurrent with the NV center π pulse in a spin echo. All off resonant phase precession is refocused, but the target spins are flipped and so phase accumulation continues. (B) For a single nearby target spin, coherent oscillations are observed at the coupling freuqency between the NV center and the surface spin. (C) For a few nearby spins, multiple couplings are resolvable in the DEER signal. (D) For a dense bath of spins, all traces of oscilaltion are eliminated and instead an incoherent, Gaussian decay is expected. Note that the time axis in (D) is reduced by a factor of 10. 147
3.3 **Double electron-electron resonance of diamond surface spins. a**, Cartoon of experiment, depicting a near surface NV center (dark red arrow) with nearby traps (black wells) that are transiently occupied by spin 1/2 defects (black arrows). A 532 nm laser is used to polarize and readout the NV center. **b**, Pulse sequence for DEER, where simultaneous microwave π pulses are applied to the NV center (blue block) and surface spins (red block) midway through the free precession interval τ. Green blocks indicate NV center spin initialization and readout. **c**, Spin echo, $C(\tau)$ (blue) and DEER, $D(\tau)$ (red) curves for a representative NV center with coherence oscillations caused by slight magnetic field misalignment (left panel). In order to investigate the DEER signal, $S(\tau)$ (orange) without the influence of decoherence from other sources, $D(\tau)$ is divided by the coherence curve $C(\tau)$ (right panel). Error bars in **c** are the standard error of the mean due to photon shot noise, propagated point-by-point for the right panel. 154

3.4 **DEER coupling rates and stretching factors. a**, Fitted DEER couplings as a function of depth for numerous NV centers. All samples in the left plot have nominally identical surface preparations (activated or reset surface, SI), while samples in the right plot represent different surface preparations described in Appendix B. Shaded region indicates expected couplings for surface spin densities of $0.001-0.05$ nm^{-2}, according to Eq. (3.4). **b**, DEER coupling vs depth for the same NV centers in before (blue) and after (orange) annealing at 650 ° C. **c**, Fitted exponent as a function of depth for samples in **a**. Filled markers are samples with similar surfaces. Shaded region indicates exponents between 1 and 2. Inset: example DEER coupling curve from (orange points) fit with a fixed $n = 2$ (red) and with n as a free parameter (purple). $n = 0.7$ is a better fit. **d**, Fits of exponent vs depth for simulated data. Colors indicate different simulation spin densities of 0.008 nm^{-2} (light blue), 0.006 nm^{-2} (dark blue), 0.004 nm^{-2} (light purple), and 0.002 nm^{-2} (dark purple). Shaded regions are confidence intervals for fits of simulated data. Dashed lines indicate limiting values of $n = 2$ and $n = 2/3$. (Inset) Simulation of representative spin configurations (dots) relative to an NV center that is 5 nm deep (red diamond). Simulation radius is 25 nm. DEER signals for the representative configurations are shown in the last panel. Dashed line is an average of 10, 000 iterations. All error bars are 68% confidence intervals of the fits. . 157

3.5 **Temporal transition of the stretching factor. a**, DEER echo signal from shallow NV centers in with three different depths extracted from the proton NMR signal. Error bars are the standard error of the mean due to photon shot noise. The purple line is a fit with the analytical result for configurational averaging (SI). Dashed line is $n = 2$, dotted line is $n = \frac{2}{3}$. Curves are offset for clarity. **b**, Diagram depicting the expanding strong dipolar coupling volume of the NV center as the duration of the echo sequence increases. The form of the signal detected by the NV center changes as the volume intersects with the 2D plane of the surface spins. **c**, Simulations of the DEER echo signal detected from a 5 nm deep NV center near a surface with a logarithmically spaced density of 10^{-4} nm^{-2} (blue) to 10^{-2} nm^{-2} (purple) where surface spins undergo configurational averaging. The dashed lines correspond to $n = 2$, and the dotted lines correspond to $n = \frac{2}{3}$. **d**, Simulation of the DEER echo signal detected from NV centers with log spaced depths from 1 nm (blue) to 10 nm (purple) with configurational averaging of the surface spins. The density of simulated surface spins is 0.005 nm^{-2}. The solid black line is the analytic solution for a 1 nm deep NV center (SI). 160

3.6 **Transient strong coupling of surface spins. a**, Coherence (blue), coherently coupled DEER signal (red), and incoherent bath signal (orange) from the same NV center measured at different times. **b**, Time series for NV center in **a**, with a fixed free precession interval of 2 μs. The DEER signal drops below 0 for short intervals, indicating transient coherent coupling to a nearby dark spin (black arrows). Error bars are the standard error of the mean due to photon shot noise. 163

3.7 **Mid sequence scrambling of surface spins.**(A) Simulated DEER decay curves for the case of fixed positions for each free precession interval (blue) and for different positions for the two free precession intervals (green), as could be the case for a mid sequence scrambling pulse. (B) Same simulation as in (A), but with $\ln S(\tau)^{-1}$ plotted on a log-log plot so that the stretching factor is given by the slope. 166

3.8 **Simulation of 3D to 2D crossover behavior in the case of a central spin sensing a spin bath in a slab of finite thickness.** (A) Schematic of a central spin (yellow and red arrow) in a slab of bath spins (red). Once the sphere of strong coupling breaks out of the slab, counting proceeds as a 3D volume intersecting a surface. (B) Calcualted DEER signals for the slab geometry. (C) Same simulation as in (B), but with $\ln S(\tau)^{-1}$ plotted on a log-log plot so that the stretching factor is given by the slope. The initial slope is for 3D spin counting ($n = 1$) but when the dipolar coupling volume breeches the slab it continues as 2D ($n = 2/3$). In principle at the very earliest times, no spins are counted and $n = 2$, which is the regime explored in the previous section. . . . 169

4.1 Artistic rendition of the electron-phonon Cerenkov effect in graphene. 172

4.2 **Acoustic phonon scattering in graphene.** (A) If the Fermi surface of graphene is large enough, it is easy for an electron to scatter to an unoccupied state along the Fermi surface through absorption or emission of a phonon in the available phonon space. (B) Once the Fermi surface shrinks such that $2k_F < q_{\max}$, only a small fraction of the available phonon space can contribute to scattering. (C) A "supercollision" scattering event permits an electron to scatter with a long wavelength phonon since the defect absorbs some momentum. T_{BG} = Bloch-Gr̈uniesen temperature, $2\hbar v_s k_F/k_B$, where v_s is the speed of sound. Figure taken with permission from Ref.[33]. 176

4.3 **Origins of 1/f noise.** (A) Traps in the substrate or gate dielectric can cause conductance fluctuations with a distribution of time constants. (B) For a logaraithmically spaced distribution of trapping times, the total noise exhibits a 1/f spectral dependence. (C) Typical noise spectrum in electronic devices, which is dominated at low frequencies by 1/f noise but which transitions to thermal or shot noise once the 1/f noise decreases below the noise floor. Some devices may exhibit an additional G-R "bump" at a characteristic frequency. (D) 1/f noise only occurs at low frequencies, but it upconverts to higher frequencies in real world systems due to nonlinearities and so makes up a significant portion of the noise in modern communications systems. Figure taken with permission from Ref.[19]. 177

4.4 **Noise in graphene devices.** (A) 1/f noise in several graphene devices on SiO_2. Figure taken with permission from Ref.[19]. (B) Crossover from thermal noise to shot noise in a short graphene device. Inset: conductivity of graphene device as a function of gate voltage showing the Dirac peak. Fit is to the expression in Eq. (4.8). (C) Fitted Fano factor of $\approx 1/3$ at different gate voltages. (B) and (C) taken with permission from Ref.[88]. 181

4.5 **Power dependence of noise in graphene.** (A) Temperature of electrons in a graphene device as a function of heating power, as measured by Johnson noise thermometry. The fit is to a 1/3 power scaling. (B) NV center relaxation rate as a function of heating power, showing a similar scaling. The power scaling is in agreement with a dominant defect assisted cooling mechanism[33]. 182
4.6 **Global and local conductivity measurement of graphene.** (A) Global conductance of a graphene field effect transistor as a function of gate voltage, measured in transport. (B) Corresponding relaxation rate of a NV center located under the device. A small, constant Joule heating current of 2.7 mW is applied to increase the electron temperature and make the noise signal larger. 183
4.7 **Relaxation of NV centers near conductors.** (A) The NV center relaxation rate is sensitive to the transverse conductivity of a material, since longitudinal charge fluctuations are suppressed. (B) Fluctuations with a short wavelength (large k) create a magnetic field that averages out at the location of the NV center, while (C) $k \sim 1/d_{NV}$ has the largest contribution to the decay. 184
4.8 **Non-equilibrium dynamics in graphene probed both globally and locally.** (**A**) Device schematic: hBN-encapsulated graphene device on diamond substrate containing NV centers for nano-magnetometry. Inset: optical image of clean hBN-encapsulated device A1 ($6 \times 5.4\,\mu\text{m}^2$). (**B**) Condition for Cerenkov emission of phonons: when $v_\text{D} > v_\text{s}$, stimulated phonon emission dominates over absorption (right). (**C**) 2-probe resistance versus carrier density of device A1 ($T = 10$ K). (**D**) Current density as a function of applied electric field ($T = 80$ K) in clean device A1 (blue) and disordered device B1 ($7 \times 18\,\mu\text{m}^2$, black). The gray dashed line indicates where $v_\text{D} = v_\text{s}$ for the LA mode. (**E**) Global electronic noise PSD (averaged over $100-300$ MHz) as a function of bias power in devices A1 (blue) and B1 (black). Blue curve satisfies $v_\text{D} > v_\text{s}$ for $P > 0.12\,\mu\text{W}/\mu\text{m}^2$. (**F**) Local magnetic noise (measured by NV nano-magnetometry) versus applied bias power in clean device C1 on diamond substrate. 187
4.9 **Spatially-resolved local noise measurements with NV magnetometry.** (**A**) Fluorescence image of NV centers underneath device C2, with false colored contacts and boarders added. (**B**) NV spin relaxation from polarized to thermal state (dashed lines), when DC currents $j = 0$ (dark) and $j = 0.19$ mA/μm (light) are passed through the device. Solid lines are fits. (**C**) Local magnetic noise near drain contact as a function of graphene current density (device C1), in electron- and hole-doped regime (blue and red, respectively). (**D**) Spatial map of the local magnetic noise (device C2) at $j = 0.18$ mA/μm and $n = 0.92 \times 10^{12}$ cm^{-2}. The spatial profile is consistent with the exponential growth of phonons due to Cerenkov amplification (cartoon, top). Dashed black curve shows the theoretically predicted excess phonon population (offset to account for background noise). (**E**) The growth direction is reversed by changing the current direction (left) or the charge carrier sign (right). 190

4.10 **Slow dynamics in global electronic measurements.** (**A**) Global noise spectra at $n = 2\times10^{12}$ cm^{-2}. Colored curves: Clean device A2 ($9.5\times11\,\mu$m^2) at bias ranging from 0 to 0.8 V (bottom to top). Black: Disordered device B1 at maximum power applied to device A2 (scaled 7x). (**B**) AC differential conductivity spectra (excitation -20dBm) (Ch. C) with biases 0 to 0.8 V (top to bottom, colors same as A). The real component is suppressed at low frequencies. Grey curve: imaginary component at 0.8 V. Black lines are fits. (**C**-**D**) Features in noise and conductivity spectra shift to higher frequencies in a shorter (6 μm) device (device A1), under similar electric field as maximum in (A) and (B). (**E**-**F**) Extracted traversal time from (B) and (D) as a function of drift velocity and device length. Dashed curves correspond to speed of sound in graphene (light gray: TA, dark gray: LA). (**G**) Cartoon of important rates in the driven electron-phonon system. During Cerenkov amplification, the correlation time observed in electronic measurements is limited by the phonon traversal time, $T = L/v_s$. 191

4.11 **Dependence on bath temperature and charge density**. (**A**) Global noise PSD as a function of bath temperature at constant drift velocities and carrier density $n = 2\times10^{12}$ cm^{-2}. (**B**) Calculated peak phonon emission frequency, which can be tuned via the graphene carrier density. (Blue: $T_e = 0$ K, red: $T_e = 320$ K). (**C**) Normalized global current noise as a function of carrier density for different device lengths ($j = 0.6$ mA/μm). Solid curves show predicted total phonon emission. (**D**) The charge density at which the noise peaks (n_{peak}) for a wider variety of samples than in (C), with fit (turquoise). Error bars represent sampling spacing of carrier densities. 195

5.1 Artistic rendition of orbital diamagnetism detection in graphene. 200

5.2 **Sensitivity and resolution of magnetometers.** Sensitivity vs. sample separation for several different magenetometers, including NV centers. Figure taken with permission from Ref.[39]. 201

5.3 **Levitation of graphite.** Bulk graphite can be levitated over a permanent magnet under ambient conditions. HOPG = higyly oriented pyrolitic graphite, which is a form of graphite where the individual graphite crystals are well aligned with each other. . 204

5.4 **Graphene device on diamond.** (A) Image taken under 532 nm illumination, which produces background fluorescence that overwhelms the NV center fluorescence. Inset: optical image of the device on diamond. (B) Same as (A) but taken with a low powered laser tuned to the NV center zero phonon line (ZPL), which permits imaging through the device and selectively addressing NV centers that are close together due to the inhomogeneous distribution of ZPLs. 205

5.5 **NV center decohrence at low temperatures.** (A) Representative T_2^* measurement for NV centers in a ^{12}C enriched diamond at 60K. (B) Representative T_2 measurement for NV ceters in the same diamond sample. The longer decoherence time translates to increased sensitivity in an AC sensing scheme. 206

5.6 **Global and local transport of graphene.** (A) Quantum lock in sequence for AC sensing graphene currents. V_{SD} is sinusoidally varied (amplitude = 5 mV) in phase with a concurrent spin echo on the NV center. (B) Each gate voltage produces a different current density (blue), which the NV center sense as a change in magnetic field (red). Blue curve is determined from a global transport measurement. 208
5.7 **Gate dependent diamagnetism in graphene.** (A) Pulse sequence used to detect diamagnetic sheilding from graphene. A square wave of amplitude 40 mV is applied at different offset values while a sine magnetometry pulse sequence is applied to the NV center. The signal detected by the NV center is the derivative of the magnetic field with respect to the gate voltage, which we integrate in (C) to find the change in magnetic field as the gate is swept through the Dirac point. 211
5.7 (continued) 212
5.8 **Magnetization signal at different locations.** Each color curve is taken from an NV center at the corresponding location in the inset. 213
5.9 **Discriminating between electric and magnetic fields.** (A) Applying amagnetic field results in opposite freqeuency shifts for the m_s = +1 and m_s = -1 states. (B) By chaning the measurement qubit basis, we find that the signal inverts, which implies that it is magnetic in nature. (C) Electric fields cause the qubit states to move in the same direction. (D) For an NV center very close to the device edge, we find that the measured signal does not invert upon switching qubit bases, implying that this signal is due to the fringing electric fields of the FET. 214
5.10 **Temperature dependence of magnetization peak.** NV center measurement taken at different temperatures, showing an increase in the measured field difference and broadening of the signal. 215
5.11 **High temperature annealing effect on T_1.** For samples implanted at high densities, an additional anneal at 1200° C improves spin relaxation time because divacancies are annealed out. 216
5.12 **Cryostat used for NV center measurements.** A magnet is attached to the translation stage inside of the bellows to introduce a magnetic field to the sample. 217
5.13 **Minimizing photodoping.** (A) Device structure, with a back gate between the dielectric interface between the bottom hBN and diamond to prevent charge accumulation during photoexcitation. (B) As an additional precaution, the device gate was connected to an analog switch so that it could be grounded whenever a laser was switched on for readout. (C) As a result of these precautions, photodoping was significantly reduced. Global transport measurements during initial cool down (blue) and taken after one month of measurements (green). 218

A.1 **Sample contamination.** (a) XPS spectra from a diamond sample with Si and Na contamination before (cyan) and after (red) acid cleaning. The main panel shows the full energy range survey scans, while insets depict higher resolution peak scans at the C 1*s*, O 1*s*, Si 2*p*, and Na 2*p* transitions. (b) Normalized NEXAFS carbon K-edge spectra and a close-up of the pre-edge region of the same sample before and after *in situ* annealing at 530 °C, showing the removal of pre-edge states attributed to adventitious carbon. Dashed line shows the spectrum after re-exposure to atmosphere. (c) Single-quantum relaxation and Hahn echo coherence, measured from the same NV with a contaminated stripline in which the ALD layer has been scratched, compared with a new stripline. 236
A.1 (continued) 237
A.2 **Graphitization of diamond during annealing.** (a) Normalized XPS spectra of the same sample after a 1200 °C anneal with different ramp rates. Material at the surface is converted to sp^2 carbon during annealing (red and green) and manifests as a peak at lower binding energy compared to the spectrum after the subsequent triacid clean (blue), which consists primarily of an sp^3 carbon peak. (b) The Raman spectrum of the 1200 °C annealed surface shows a glassy carbon peak, but no clear evidence of graphite peak at 1580 cm^{-1} [105]. 239
A.3 **Pitting of diamond at higher oxygen annealing temperatures.** (a–c) AFM images of a scaife-polished standard grade sample annealed at successively higher temperatures for temperature calibration of oxygen furnace. Micro-pits (black circles about 20 nm in diameter) are visible after the oxygen anneal at 470 °C. (d) Depth measurements of the six NV centers presented in the main text after different annealing steps. . . 242
A.3 (continued) 243
A.5 **Coherence times of NV centers in pitted diamonds.** (a-c) AFM images and (d-f) NV coherence times $T_{2,\mathrm{Echo}}$ (dark) and $T_{2,\mathrm{XY8}}$ (light) from three additional samples with rougher surface morphologies. The improvement in coherence time after oxygen annealing is less pronounced than that of Sample A. 245
A.4 **Diamond surface damage.** (a-f) Representative AFM scans showing (a) smooth surface morphology and rough surfaces resulting from (b) contamination or surface damage during an oxygen anneal of a contaminated surface, (c) RIE etching after improper polishing, (d) RIE etching of a Na and Cl contaminated surface, (e) an oxygen anneal with uncontrolled gas purity, and (f) micromasking during an oxygen etch. (g-i) SEM images of large scale morphology from a variety of damaged samples after reactive ion etching. (j) Carbon K-edge NEXAFS shows a comparison between a rough surface (purple, sample shown in (c)) and a smooth surface (red) that have been both triacid-cleaned with the full process as described in the main text. (k) High resolution carbon 1*s* XPS spectra from the two surfaces. The rough surface shows a large non-diamond sp^2 carbon peak at lower binding energy. 246
A.4 (continued) 247

A.6 **Dynamical decoupling data.** Coherence time as a function of number of dynamical decoupling pulses, N, for all six NV centers presented in the main text for triacid-cleaned (blue) and oxygen-annealed (red) surfaces. The fit parameters are shown in Table A.1. 249
A.7 **Single and double quantum relaxation.** (a) Energy level diagram of the ground state electronic spin of the NV center, indicating single- and double-quantum relaxation channels, whose rates are denoted by Ω and γ, respectively. (b) SQ and (c) DQ relaxation measurement sequences. The NV is prepared in the $m_S = 0$ ($m_S = -1$) state and the relaxation to $m_S = -1$ ($m_S = +1$) is measured. (d,e) SQ and DQ transition rates as a function of DQ transition frequency ω_{DQ} for two different NV centers. Dashed lines indicate the broadband spectra for Ω and $1/f$ spectra for γ. (f) Comparison of the noise spectral density from single- and double-quantum measurements. The two spectra are plotted on the same scale using the effective electric field noise $S_{E_\perp}$. We found that at high frequencies, magnetic field noise (solid circles) is the dominant source of decoherence for oxygen-annealed surfaces, compared to the electric field noise (open circles). Dashed and dotted lines show an extrapolation with $1/f$ and $1/f^2$ scaling, respectively. 253
A.7 (continued) 254
A.8 **Change in DEER signal with annealing.** (a) Pulse sequence for measuring DEER coupling: a DEER sequence is erleaved with a Hahn echo sequence to mitigate effects from slow system drift. The DEER driving frequency is $\omega_{\mathrm{DEER}} \approx 920$ MHz, corresponding to dark spins with $g = 2$. (b) Hahn echo and DEER decay curves taken at $B_z \approx 330$ G. Collapse and revival arising from hyperfine coupling with a nearby ^{13}C can be observed. (c) Normalized signal, where the ^{13}C modulation is no longer pronounced. (d-e) Spin echo coherence time and DEER coupling for several NV centers in Sample A and Sample C before and after oxygen annealing. Green (red) numbers indicate the average improvement (worsening) in the decoherence rate $1/T_2$, and the average reduction (increase) in the DEER coupling after oxygen annealing. . . 257
A.8 (continued) 258
A.9 **UPS measurements of diamond surfaces.** (a) UPS spectra from triacid-cleaned sample (blue) and oxygen-annealed sample (red) as a function of binding energy relative to the Fermi level. The Fermi level is calibrated with a reference tantalum foil (inset). The spectral width, ω, is calculated as the energy difference between the secondary electron cut-off and valence band maximum, indicated by the dashed rectangles. (b,c) Zoom-in of the secondary electron cut-off and the valence band maximum for the triacid-cleaned sample and the oxygen-annealed sample, respectively. 260
A.10 **LEED of diamond surfaces.** (a) LEED of an oxygen-annealed surface, as shown in Fig. 2.12c. The 1×1 reconstruction is consistent with an ether-terminated surface. (b) LEED after *in situ* annealing at 1000 °C showing 2×1 reconstruction peaks that appear for the same surface after the surface heteroatoms are removed. (c) XPS survey data showing that the O 1*s* peak indeed disappears after annealing at 1000 °C. . 261

A.11 **Additional XPS of annealed and acid cleaned surfaces.** (a, b) Comparison of high-resolution XPS spectra at carbon 1*s* and oxygen 1*s* peaks from triacid-cleaned and oxygen-annealed surfaces. The linewidths are narrower for the oxygen-annealed surface. (c) Histogram of the oxygen 1*s* atomic percentage from the XPS signal, obtained from a large number of triacid-cleaned and oxygen-annealed surfaces. 263

B.1 **NEXAFS through annealing. a**, Oxygen edge NEXAFS for diamond sample with initial acid cleaned surface (green), after 500 °C annealing (blue), 650 °C annealing (purple) and 800 °C annealing (orange). **b**, Carbon edge NEXAFS of the same annealing sequence on the same sample. Red box indicates location of dangling bond peak, shown in detail in **c**. **c**, Detailed view of dangling bond peak showing removal at higher annealing temperatures. **d**, Detailed view of dangling bond peak for several samples with initially prepared acid cleaned surfaces (green) and oxygen annealed surfaces (blue), showing absence of the peak for oxygen annealed surfaces. Oxygen annealing procedure and suppression of DEER signal are described in [308]. 273

B.2 **Coherence times before and after annealing.** Coherence times of NV centers in after annealing, plotted as a function of pre-annealing coherence times. Dashed line has a slope of one. 274

B.3 **Spectral decomposition through annealing.** Spectral decomposition for sample of NV centers in before (blue) and after (orange) 650 °C vacuum anneal. Depths of NV centers are **a** 10.25 nm, **b** 9.72 nm, **c** 10.42 nm 276

B.4 **Surface spin model. a**, The trench structure of (100)-6×6 diamond surface. Surface termination is O/H/OH type, as in [184], and step carbon atoms are saturated by OH. The red and pink balls are hydrogen and oxygen atoms, respectively. The grey balls are carbon atoms, the darker color and smaller size indicate deeper position away from the surface. For the sake of clarity, only the first five layers are presented in the structure plots. **b**, Illustration of the formation of a surface spin at the step edge. The yellow lobe represents the surface spin. **c**, A plausible structure model of a surface spin on the trench of the diamond (100) surface. **d**, The energy level plot of the modeled surface spin. The valence and conduction bands are depicted as blue and red regions, respectively. The orange and white arrows represent spin up and spin down channels, respectively. The spin-polarization energy is high for the dangling bond. We note that the single particle Kohn-Sham levels do not directly refer to the ionization energies of the dangling bond. The surface states are located at 0.3 eV below the conduction band minimum. The valence band maximum positions are aligned to zero. 277

B.5 **Coherently coupled surface spin. a**, Raw DEER (blue) and echo (red) data from an NV center that is coherently coupled to a surface spin. **b**, The raw DEER signal divided by the echo signal. 279

B.6 **DEER frequency sweep** 281

B.7 **DEER Rabi measurement. a** We perform a microwave pulse of varying length on the surface spins during the DEER sequence and **b** fit the normalized signal to a decaying exponential envelope to extract a coherence decay time. 282
B.8 **Measured T1 of surface spins using correlation sequence.** Relaxation time T_1 for surface spins measured by two different NV centers **a** and **b**, using the correlation sequence described in [347]. 283
B.9 **Measured T1 of surface spins by bath correlation measurement.** Relaxation time T_1 for surface spins measured by three different NV centers, depicted in **a**, **b**, and **c**, using the sequence described in [233]. **a** and **b** are from and **c** is from 284
B.10 **Depth scaling in the presence of finite surface spin T_1 time. a**, Calculated decay timescale $T_{2,\mathrm{DEER}}$ with decay profile calculated using Eq. B.45 and fit to $\exp(-(\tau/T_{2,\mathrm{DEER}})^n)$, assuming a finite surface spin T_1 time of 30 μs (black dashed line) and a density $0.005/\mathrm{nm}^2$. **b**, Fitted exponent n. Once $T_{2,\mathrm{DEER}}$ becomes longer than the surface spin T_1 relaxation time, n decreases from the infinite-T_1 limit of $n = 2$ toward the Markovian limit of $n = 1$. The calculated increase of n for shallower NV centers is opposite of the observed trend vs depth in Fig. 2c of the Main Text, and suggests that the depth trend in Fig. 2c is not explained by the effects of finite relaxation time. 296
B.11 **Simulations with incoherent interactions.** Example DEER curves for simulations allowing both flip-flops and spin lattice relaxation between surface spins. Each color represents a different randomly sampled surface spin configuration. Fitting these curves with a stretched exponential produces values of $1 < n < 2$. Some curves additionally show coherent oscillations if the coupling rate to the nearest spin exceeds the rate of incoherent decay. 300
B.12 **Additional NV center measurements a**, $\log S(\tau)^{-1}$ for nine additional NV centers. Inset: pulse sequence used to measure NV centers in (a). Blue lines are fits to the hopping model in the Main Text, and dotted and dashed lines show slopes of 2 and 2/3, respectively. Y axis offset is arbitrary. **b**, DEER XY-4 data for four additional NV centers, plotted as in (a). Inset: DEER XY-4 pulse sequence. **c**, Surface spin densities and depths extracted from NV centers in (a) and (b). Depth_{NMR} is the NV center depth extracted from fitting the proton NMR signal, while Depth_{DEER} and $\mathrm{Depth}_{DEERXY4}$ are the depths extracted from the hopping model in the Main Text. Error bars are one standard error. 301
B.13 **Fits to a bi-exponential for four NV centers a**, Data for each of the four NV centers. The orange lines are best bi-exponential fits based on MCMC analysis. **b**, The posterior distribution function (PDF) of n vs coupling, shown for each NV. **c**, The exponent stretching factors are found by fitting the PDF of n to two Gaussians. . . 302

B.14 **Stability of stretching factors.** Mean and standard error of the two stretching factors (high n and low n) of equation (B.62) as a function of the cutoff value of the coherence for the four NV centers in Fig. B.13. For two NV centers, $C(\tau)$ did not dip below 0.1 during the measurement period and for one NV center, $C(\tau)$ did not dip below 0.2 during the measurement period. However, extracted exponents remained stable for all NV centers regardless of the exact $C(\tau)$ cutoff value. 304

B.15 **Stationary Surface spin fraction. a**, Simulation of the fraction of NV centers that exhibit strong coupling in DEER as a function of depth, if 20% of spins on the surface are placed randomly relative to the NV center and then do not hop. **b**, Simulation of the fraction of NV centers that exhibit strong coupling in their DEER signal as a function of the fraction of spins that are stationary on the surface, given a density of $\sigma = 0.005/\mathrm{nm}^2$, and depths drawn from the distribution of depths measured across all samples. Orange dashed line corresponds to the observed fraction of 3 strongly coupled DEER signals out of 191 NV centers. 307

C.1 **Device fabrication on diamond substrate.** (**A**) Device schematic: Monolayer graphene (grey chain) was graphite contacted and encapsulated with hexagonal boron nitride (hBN). Few-layer graphene (FLG) was used as topgate. (B-H) Micrographs of device fabrication, with 40 μm scalebar in (B)-(G) and 500 μm in (H). (**B**) Exfoliated graphene. White dashed line indicates monolayer region. (**C**) Complete stack on diamond substrate with shallow implanted ($40 - 60$ nm deep) NV centers. (**D**) Initial contacts and wire for delivering reference noise (left-most electrode). (**E**) Device after etch to define geometry. (**F**) Edge contacts constructed through etching and subsequent thermal evaporation. (**G**) Device with etch mask for disconnecting topgate from edge contacts. The left device is the source of data for Figure 2D-E in the main text (Device C2). Note that ripples visible in the image are entirely contained in the top gate graphene and are not expected to affect the transport properties of the channel graphene, due to the thick ($\sim$ 90 nm) hBN dielectric. (**H**) Entire (2×2 mm^2) single crystal diamond, with wire bonded device. 309

C.2 **Device fabrication on Si/SiO_2 substrate.** (**A**) Device schematic: Monolayer graphene (grey chain) was encapsulated with hexagonal boron nitride (hBN). Silicon substrate was used as a global backgate. (B)-(F) Micrographs of device fabrication, with 20 μm scalebar. (**B**) Exfoliated graphene. (**C**) Complete stack on substrate. (**D**) Initial contacts. (**E**) Edge contacts constructed through etching and subsequent thermal evaporation. (**F**) Device after geometry-defining etch. The left-most device is the source of data for 4.8C-E, 3C-D and 4A in the main text (Device A1). 311

C.3 **Calculated mobility of clean device.** Mobility vs. typical range of contact resistivities. 314

C.4 **Measurement circuit.** Circuit diagram for the measurement of noise (red box) and AC differential conductivity (yellow box). 315

C.5 Circuit diagram of wire bonded device, showing main sources of parasitic reactance. 316

C.6 (**A**) Reflection spectrum in the biased (blue) and unbiased (orange) case. (**B**) Relative difference in reflection. The gate is used to keep the DC conductance equal (3.1 mS) in the two cases, and as expected, the DC reflection is approximately equal. At higher frequencies, however, the reflection coefficients differ significantly, indicating that the conductance varies with frequency. 317
C.7 (**A-B**) Real (blue) and imaginary (orange) parts of the reflection coefficient at $\omega = 2\pi\cdot$ 0.2 GHz (A) and $2\pi\cdot$ 1.2 GHz (B), as a function of the conductance (swept through electrostatic gating at zero bias). Using $L = 11$ nH and $C = 0.24$ pF, we extract $r_{\text{ext}}(0.2\text{ GHz}) = -0.011+0.085\text{i}$, $t^2_{\text{ext}}(0.2\text{ GHz}) = 0.66+0.29\text{i}$, $r_{\text{ext}}(1.2\text{ GHz}) = 0.041 - 0.048\text{i}$, and $t^2_{\text{ext}}(1.2\text{ GHz}) = -0.43 - 0.17\text{i}$. (**C**) Total fit error (summed over all ω) as a function of parasitic capacitance and inductance. The error is minimized at $L \sim 11$ nH and $C \sim 0.24$ pF. 318
C.8 **Noise calibration.** In A-C, blue and orange dots represent data at $f = 0.2$ GHz and $f = 1.2$ GHz, respectively. (**A**) Measured noise S_{rec} vs. differential conductance G', at base temperature $T_{\text{C}} = 10$ K (bright dots) and an elevated temperature $T_{\text{H}} = 50$ K (dark dots). The noise is minimized when $Z(G')$ is closest to matching 50 Ω, because at such low temperatures, the noise is dominated by background noise reflected off the sample. As expected, the matching value of G' is above 12 mS (below $\sim$ 80 Ω) at low frequencies, but shifts to $\sim$ 6 mS ($\sim$ 150 Ω) at $f =$1.2 GHz, due to the emerging parasitic reactance. (**B**) Background noise S_0 calculated according to eqn. *C*.6. (**C**) Total gain A calculated according to eqn. *C*.5. Sub-unity transmission and losses in the cables bring A below the 68 dB amplifier gain. (**D-F**) Same as (A)-(C), except as a function of frequency, $f = \omega/2\pi$. Purple and yellow curves show measurements at fixed $G' = 3$ mS. Green curve in (F) accounts for the frequency-dependence of $G'(\omega; j, n)$ for the particular driven case, $j = 0.56$ mA/μm, n $= 2\times10^{12}$ cm^{-2}. This is achieved using the technique outlined in the text. 319
C.9 **Linear relationship between gain and reflection.** Gain $A(\omega, G')$ plotted against the reflection, $|r(\omega, G')|^2$ at $\omega = 2\pi\cdot$ 0.2 GHz (blue) and $\omega = 2\pi\cdot$ 1.2 GHz (orange). The different points are obtained by sweeping the charge density n (and thus also G') at zero bias. As expected, the two quantities are linearly related. The gain in the biased case $A(\omega, G'(\omega; j, n))$ can now be found by measuring the reflection $|r(\omega, G'(\omega; j, n))|^2$ while applying current, and inserting it into the fit. 321
C.10 **NV measurement setup.** The three laser beams used for spin-to-charge readout are combined before the galvonometric mirrors located at one focal point of a 4f system. Lasers are switched by acousto-optic modulators, except for the 637 nm high-powered ionization laser, which is a directly driven diode laser. The objective and sample are located inside a Janis ST-500 cryostat, which is used to keep the sample at ∼70K by a combination of flowing liquid helium and a resistive heater in a PID loop. 323

C.11 **Spin-to-charge readout.** (**A**) Pulse sequence for measuring relaxation rate of NV centers. A 532 nm pulse preferentially prepares the NV center in the NV^- charge state and $m_s = 0$ spin state. The NV center spin is allowed to relax for a time τ before a strong yellow pulse shelves the $m_s = \pm 1$ population in the singlet state. An intense pulse of 637 nm light ionizes any population in the triplet state, while the singlet is protected. The resulting charge state is read out by resonant excitation of the NV^- zero phonon line, and from this, the spin state before the yellow pulse is inferred. (**B**) Photon distribution from NV is fit as a 70%-30% mix of two Poisson distributions with different parameters, λ, corresponding to counts from NV^- and NV^0. (**C**) Post-selected photon distributions. The photon distributions for the two charge states are distinguishable, permitting single-shot charge state readout. 324

C.12 **Noise versus drift velocity** (**A**) Measured noise power spectral density (averaged over 0.1-0.3 GHz) as a function of electronic drift velocity in clean device A1, at bath temperatures 10 K and 80 K (blue and red, respectively). We observe equivalent noise temperatures in excess of 15,000 K. (**B**) Zoomed-in version of (A) to highlight smooth transition into the excess noise regime. Lines are guides to the eye. 327

C.13 **Johnson noise in a disordered device.** Measured noise temperature (blue circles) as a function of input power for disordered device B1. The data agrees well with a fit based on disorder-assisted phonon cooling (black curve), and confirms that the dominant noise source is thermal Johnson-Nyquist noise. 328

C.14 **Dependence of noise on device length**. (**A**) Measured noise power spectral density from devices of different lengths, at $v_D = 3.3 v_s$ and $n = 2 \times 10^{12}$ cm^{-2}. The noise power initially increases superlinearly with device length (inset), but appears to saturate in longer devices. (**B**) Current noise versus carrier density at constant current density $j = 0.6$ mA/μm (circles) and $j = 0.2$ mA/μm (squares). As shown in the main text, the cross-over density decreases with device length. 329

C.15 **Global electronic transport and noise under current inversion**. (**A**) Absolute value of current density versus absolute applied field at $n = 2 \times 10^{12}$ cm^{-2} and $T = 10$ K, for positive (orange) and negative (blue) fields. The $I-V$ curve is observed to be highly symmetric. (**B**) Global noise power spectral density as a function of (absolute) current density. Changing the sign of the current has almost no effect on the measured noise power. Lines are guides to the eye. 330

C.16 **Global conductivity for different charge densities and temperatures.** (**A**) The normalized real part of the conductivity spectrum for $v_D = 0.125 v_F$ at different doping levels. The curves are normalized to have the same vertical spread, and are offset to avoid overlap. The general shape of the conductivity spectrum, as well as the extracted time scales (**B**) are unchanged by varying the charge density. (**C**) The normalized real part of the conductivity spectrum measured at bath temperatures of 300 K (blue) and 10 K (red), at $v_D = 0.125 v_F$ and $n = 2.2 \times 10^{12}$ cm^{-2}. We again observe no clear frequency shifts, but the effect is much (~ 4 times) weaker at room temperature than at 10 K. 331

C.17 **Noise measured at different applied magnetic fields.** Relaxation rates of an NV center at $B = 0$ (red) and $B = 363$ Gauss (blue), for positive and negative bias ($|j| = 0.2$ mA/μm) at $n = 0.92 \times 10^{12}\text{cm}^{-2}$. 332
C.18 **Lattice heating during NV measurements.** Scans of the optical line of an NV center located below device C2. The NV center zero phonon line is broadened by approximately the same amount when a high bias is applied (blue) as when the bath temperature is increased by 10 K at zero bias (green), suggesting that the increase in temperature near the NV during device operation is approximately 10 K. $\delta\lambda$ is approximate and is inferred from cavity piezo voltage and laser manufacturer's specifications (New Focus Velocity 6300). Center wavelength corresponds to ~ 637.4 nm. 334
C.19 **Doping dependence of local magnetic noise.** Locally probed magnetic noise as a function of graphene charge density. Light and dark blue points represent positive and negative source-drain current, respectively. The bias power was kept constant at 1.4 ± 0.1 mW. 335
C.20 **NV center orientation.** (**A**) NV center orientation with respect to diamond surface. (**B**) Projection of the four possible NV axes onto the device plane. Our device is closely aligned along two of the projections, giving rise to two distinctive groupings of NV centers: those with *xy*-projections that are perpendicular to current flow (group I, blue) and those with *xy*-projections parallel to current flow (group II, red). (**C**) DC field measurements. Group I NVs measure a significant current-induced magnetic field, while group II NVs do not. (**D**) Relaxation rates of NVs in group I (blue) and II (red). The noise sensed by nearby NVs from different orientation groups is similar, despite measuring very different DC magnetic fields. $|j| = 0.2$ mA/μm, $n = 0.92 \times 10^{12}$ cm^{-2}. 336
C.21 **DC and AC current measurements.** (**A**) DC current response of two NVs located a similar distance from the source electrode. While one of the NVs shows the expected linear local field dependence on global current (green), the other shows non-linear behavior at high drives (blue). (**B**) Local noise measurements for same NVs as in (**A**). Noise measurements taken at $|j| = 0.2$ mA/μm, $n = 0.92 \times 10^{12}$ cm^{-2}. 337
C.22 **Spatial dependence.** Normalized local emission rate of most amplified mode ($\Delta\gamma_q n_q(x) \propto n_q(x)$, purple), and integrated over phonon modes (yellow), for the parameters used in 4.9D in the main text ($j = 0.18\text{mA}/\mu\text{m}$, $n = 0.92 \times 10^{12}\text{cm}^{-2}$, $\Gamma^{\text{amp}}_{\text{max}} = 10.9$ GHz). Due to the dominance of the most amplified modes, the two curves are very similar. The purple curve has a slightly sharper upturn due to the higher amplification rate. 341

C.23 **Onset of Cerenkov emission.** (**A**) Cartoon showing Cerenkov criterion for graphene. When $v_D > v_s$, the electronic population becomes inverted with respect to phonon-induced transitions. As a result, the phonon emission rate (red arrow) becomes greater than the absorption rate (yellow arrow). (**B**) Net emission rate $\Delta\gamma_q$ vs. phonon wavevector q at various electronic drift velocities $v_D = v_D\hat{x}$, $n = 2 \times 10^{12}\text{cm}^{-2}$ and zero electronic temperature. Once the drift velocity exceeds the speed of sound ($v_s = 21\text{km/s} = 0.021v_F$), we find regions of phononic phase space where $\Delta\gamma_q > 0$ (red), indicating that stimulated emission dominates over absorption. This effect is strongest for the phonon modes moving along the current ($q||\hat{x}$). The circle sector in which the amplification criterion is satisfied becomes wider as the drift velocity increases, and eventually saturates as a semi-circle. (**C**) Line cut along $q_y = 0$ for electronic temperatures $T_e = 0$ K and 350 K at $v_D = 5v_s\hat{x}$. 343

C.24 **Phonon decay rate.** Phonon decay rate (calculated from eqns. *C*.15 and *C*.16) versus phonon wavevector q and energy $v_s q$. 346

C.25 **Including angular spread of phonon emission.** Blue: Measured AC differential conductivity spectrum at 0.8V bias and $n = 2 \times 10^{12}\text{cm}^{-12}$ (identical data shifted to show multiple fits). Black curves: Fits by averaging the phonon emission angle up to varying θ_{max}. We find best agreement at $\theta_{max} = 60°$. 351

C.26 **Non-monotonic charge density dependence of phonon amplification**. (**A**) The net emission rate $\Delta\gamma_q$ at constant current density $j = 0.6\text{mA}/\mu\text{m}$, for various k_F ($k_0 = 165\text{meV}/(v_F\hbar)$). The corresponding charge densities are $n = 2.1, 4.5$ and $8.0 \times 10^{12}\text{cm}^{-2}$, including the effect of the non-zero v_D on n. $\Delta\gamma_q$ becomes zero near $2k_F$. (**B**) The integrand of expression *C*.35, which is expected to be strongly related to the measured noise. The blue curve has the biggest area and thus corresponds to the highest expected noise, for device length $L = 2.5\mu$m. (**C**) Same as (B), but for $L = 7\mu$m. The longer device allows for more filtering, causing the noise to be maximized at a lower k_F (red curve). 354

For Jenelle

Acknowledgments

The list of people who in some way contributed to this thesis could fill a book on its own. This is partly because Harvard has such a wonderfully vibrant and supportive physics community, and partly because the Lukin lab is very, very large.

I am extremely grateful to Misha Lukin for taking me into his lab when I literally showed up at his door one winter, having left my program in Santa Barbara to solve a two body problem. His generosity during this time in my life is hard to overstate, and it is largely because of him that my partner and I are looking for post-pandemic wedding dates. Besides being an incredibly generous person, Misha is also a talented physicist with an almost spooky intuition. He always has some idea about what perplexing results mean and more often than not he is right. Misha has an unrivaled creativity that is grounded in a wide knowledge of physics in many different sub-fields, and I am extremely lucky to have had the chance to learn from him. I am also grateful for the time the rest of my committee has taken to shepherd me through graduate school. Philip Kim was always available for meetings about 2D material related physics even though I was not his student, and his lab's generosity with equipment has been invaluable for all of the 2D materials groups at Harvard. Amir Yacoby has provided valuable input on our condensed matter experiments, as there are few people who understand both NV center and solid state physics as well as him. Although not on my comittee, Hongkun Park also deserves a special mention, as we have always worked closely with Professor Park and his lab members, and he has been very generous in sharing equipment and expertise. Eugene Demler has provided significant theoretical support for many of the projects presented here, and his expertise has been extremely helpful as we attempted to understand our data.

Of course, Misha also deserves thanks for the incredible community he has fostered in his lab. Walking into the coffee room and jumping into a discussion of some technical problem or basic physics question with a group of peers was typical almost daily. It was a stimulating atmosphere that I miss more and more every day due to the ongoing COVID-19 pandemic. All of Misha's students and post docs were incredibly generous with their time, uncommonly intelligent, and always excited to chat about physics. I have never heard of another collection of so many smart people who got along so well. I don't understand how it has worked so well for so long, especially as the group has grown in size, but somehow the Lukin group has maintained a consistently high level of productivity and cohesiveness throughout my time there.

Misha's choices of post docs undoubtedly guide the group dynamics, and I am privileged to have worked alongside some very talented people, many of whom are now "big professors" at their

own institutions. While all of the postdocs in the lab have been invaluable, I would like to extend a particular thanks to the post docs that I worked closely with, especially Javier Sanchez-Yamagishi, Nathalie de Leon, and Kristiaan de Greeve, who I co-authored papers with. Nathalie "adopted" me when I had just joined and had no real project to work on, and we ended up working together for many years after she left to start a position at Princeton. Javier taught me everything I know about 2D materials and cryogenics, and was my most important instructor in the subtleties of experimental physics. My time with Javier was the most productive, exciting, and fun period of my graduate school years. We had a really stellar team in B00. Kristiaan might know more about physics than anyone I have ever met, and he is a ruthless skeptic. I learned to challenge the conclusions of scientific work from him, but I hope he never reviews one of my papers. I am also thankful for the assistance I received from all of the other post docs in the Lukin group who I worked with to varying degrees, including Hannes Bernien, Leigh Martin, Nabeel Aslam, Dennis Sukachdev, Ahmed Omran, Helena Knowles, Crystal Senko, Alexei Bylinskii, Renate Landing, and Jeff Thompson. I am also very thankful for the recent contributions of Sasha Zibrov Jr. who has carried through with a lot of the device fabrication and measurements during this time of COVID restrictions.

Like the post docs in the Lukin lab, the students are also top notch. I would like to extend a special thanks to the senior graduate students who acted as mentors when I arrived at Harvard, especially Arthur Safira, Shimon Kolkowitz, Ruffin Evans, Alp Sipahigil, and Dominick Wild, who made the Lukin lab a welcoming place and were also wonderful friends. I worked closely with Trond Andersen for much of my PhD, and I think I am no alone in regarding him as a genius. I cannot count the number of times I have struggled with a problem, only to have him solve it before I have finished explaining. Javier, Trond, and myself formed a subgroup around sensing 2D materials with NV centers, and these years were the most enjoyable of my time at Harvard. I also worked closely with Elana Urbach, especially over the last two years, and found her an invaluable sounding board for ideas and stupid questions. Besides being a talented scientist, Elana is also one of the strongest community members we have in the Lukin lab, and, along with the rest of the Critical Support Team, deserves more thanks than I can give for keeping things more or less running during the pandemic. I am also thankful for many conversations with Dolev Bluvstein, which eventually led to the realizations of Ch. 3. Dolev has already made wide ranging contributions to the Lukin group in many different subjects, his interests know no bounds and his excitement is infectious. I also want to especially thank Andrey Sushko, and Giovanni Scurri for assisting with experiments in the COVID era, none of Ch. 5 would have been possible without them. I am also thankful for all of the other students in the lab for their help, fruitful discussions, and generally for being awesome people. I will probably miss some people, but here it goes: thank you Christian Nguyen, Mihir Bhaskar, Mike Goldman, Aaron Kabcenell, Emma Rosenfeld, Can Knaut, Frankie Fung, Alex Keesling, David Levonian, Tamara Sumarac, Tamara Dordevic, Harry Levine, Nathan Leitao, Erick Knall, Xiaoling Liu, Bart Machielse, Paloma Ocola, Kristine Rezai, Aditya Venkatramani, Janos Perczel, Leo Zhu, Joonhee Choi, Soonwon Choi, Oksana Makarova, Sephr Ebadi Po Samutpraphoot, DaLi Schaefer, Pavel Stroganov, and Eric Peterson, for all your contributions, inside and outside of lab.

Something that I have always thought was unique about Harvard, or at least Misha's lab, was the

lack of barriers between theorists and experimentalists. I was fortunate to be able to work with many talented theorists, especially Joaquin Rodriguez-Nieva and Kartiek Agarwal, on some of the work presented here. It was also great fun to hear about all of the theoretical work that other Lukin group members were involved in, and I am thankful for all of the exposure to so many things I still do not understand.

I also want to thank the many classmates and friends who made my time here enjoyable, whether that was having a coffee in Harvard Square or driving eight hours to kayak on the Ottawa river. It is my experiences with all of the friends I have made during graduate school that I will cherish the most. It would be a lengthy exercise to list everyone here, but I trust that you know who you are.

I am also extremely thankful for the contributions of the various physics department staff members, including Steve Sandstone, Stan Cotreau, and Andy DiMambro of the machine shop, Jim MacArthur of the electronics shop, Silke Exner and Adam Ackerman of finances, and Lisa Cacciabaudo and Carol Davis of administration. The department just wouldn't function without them. Misha's lab in particular wouldn't function without the many talented administrators it has had, especially Clare Ploucha and Sammantha Dakoulas, who have really gone above and beyond to make the Lukin lab run smoothly.

Finally, I am thankful for my family for their support, even when things were difficult, and for my fiancé Jenelle, without whom none of this would have been possible. I mean that both because I came to Harvard to be with her after we started graduate school on separate coasts, and because I don't think I would have made it through my PhD alone. Graduate school takes a long time, and during our time at Harvard the world has changed dramatically. I am thankful that there is one constant in my life, and that we have been able to whether these storms together. There is a quote from Richard Feynman that "physics is not the most important thing, love is." I am thankful that I didn't have to choose.

I call our world Flatland, not because we call it so, but to make its nature clearer to you, my happy readers, who are privileged to live in Space.

Edwin A. Abbot, first sentence of *Flatland: a Romance in Many Dimensions*

1

Introduction and Background

1.1 Prologue

Flatland: a Romance in Many Dimensions was published in 1884 by Edwin Abbot. His satirical critique of Victorian class structure has had an enduring legacy, less because of its clever jabs at social hierarchy than because of its imaginative exploration of life constrained to different numbers of dimensions. Generations of math and physics students have, just as the two dimensional Square of Abbot's book, tried to wrap their heads around the existence of additional spatial dimensions, such as those predicted by string theory, beyond the three that we are equipped to experience. Just as interesting, however, are the worlds of lower dimension than our own, such as the "flatland" of graphene or the "pointland" of an atom.

Reducing the dimensionality of a physical system does not just constrain it to a simpler projection of the 3D world, it leads to different, and sometimes unexpected, physics. The quantum hall effect, which won Klaus von Klitzing the 1985 Nobel Prize in Physics and is now a part of the redefinition of the kilogram, is the prototypical example of unique 2D physics, but there are many others. Dipolar interactions in two dimensions become externally tunable. Two dimensions is the marginal case for Andersen localization, which is still not well understood in this limit. Electrons in 2D materials can interact more strongly than in their 3D counterparts due to reduced screening. The density of states, scattering probabilities, and band structures are all modified. Many 2D materials exhibit strong interactions with light, or host excitons with much longer lifetimes than those of bulk materials. The physics, as well as the technological applications of such materials, have merited significant interest from the scientific community.

While quasi-2D electronic systems have been a subject of intense research for decades, it was not until the isolation and measurement of graphene at the turn of the century that the physics of 2D materials became a full-fledged industry. Now there are dozens of 2D materials, each with unique properties, that can be peeled, stacked, and twisted to create heterostructures with emergent physical

properties. The possibilities are almost limitless, and the physics is more surprising every year.

In this frontier of materials research, where devices are literally one atom thick, quantum mechanics plays a central role. Local measurements, such as those discussed in this thesis, provide valuable information to supplement more traditional techniques. In this thesis, we explore one local measurement tool in particular: the Nitrogen Vacancy (NV) center, a defect in the diamond lattice that behaves like a single trapped atom. Using the techniques of atomic physics and quantum information, this defect is transformed into a nanoscale sensor of electric and magnetic fields with unmatched spatial resolution, a large sensing bandwidth, and which operates under a wide range of conditions. Using NV center containing diamond as a substrate for 2D heterostructures, we incorporate these spatially resolved measurements while retaining the ability to perform global transport measurements. We use this approach, combining global and local probes, to study two kinds of two dimensional systems: graphene, the original 2D material, and the diamond surface, which, as a boundary, is also a two-dimensional object. While we have made only preliminary progress here, we have already discovered many phenomena for which spatially resolved measurements are invaluable and lead to surprising results. It is my hope that future studies of these systems will be able to take advantage of this two-pronged approach to better elucidate the strange physics of Flatland.

1.2 Overview of this thesis

This thesis describes a series of experiments that make use of NV centers in diamond as quantum sensors. It is divided into five chapters: an introduction followed by four chapters describing different experiments. Each of these four experimental chapters has an associated appendix which contains supplementary information to the main results presented in the chapter. These chapters begin with some background remarks, followed in most cases by a published manuscript, and end with some concluding remarks to tie the results of that section to the broader research landscape. All of

these chapters, in some way, explore the interactions between a point sensor and a two dimensional system.

In Chapter One, I provide background material on the two major subjects of this thesis: the NV center in diamond and the 2D material graphene. This section includes an overview of NV center formation, structure, and sensing modalities followed by calculations of graphene's band structure and response to a magnetic field. The goal of this chapter is to provide sufficient context for the non-expert to understand the chapters that follow.

In Chapter Two, we combine surface sensitive X-ray spectroscopy techniques with measurements of shallow NV centers to investigate the effects of different surface terminations on NV center coherence. This is a central problem for sensing applications as shallow NV centers are more sensitive magnetometers, but they are also plagued by surface noise that limits this sensitivity.

In Chapter Three, we investigate a particular kind of defect using NV centers: the ubiquitous $g = 2$ "dark" spins that are present on most diamond surfaces. By carefully studying the characteristic decoherence profile caused by these spins, we are able to study their dynamics in detail and introduce a framework by which similar systems can be understood.

In Chapter Four, we move on from diamond surfaces to 2D material heterostructures fabricated on top of the diamond surface. We combine global conductivity and noise measurements with local NV center relaxometry to study a new effect in graphene: an electron-phonon Cerenkov-like instability that results in exponential growth of acoustic phonons across a biased sample.

Finally in Chapter Five, we use NV centers to study the intrinsic magnetic properties of graphene. While transport based evidence of orbital magnetism requires an extremely high magnetic field, we are able to observe the effects of graphene's unique Berry phase of π at low fields using NV centers to measure the doping dependant diamagnetic response of a single sheet of graphene. This is a particularly interesting regime where the NV center is closer to the device than the magnetic length, and experiments are still ongoing.

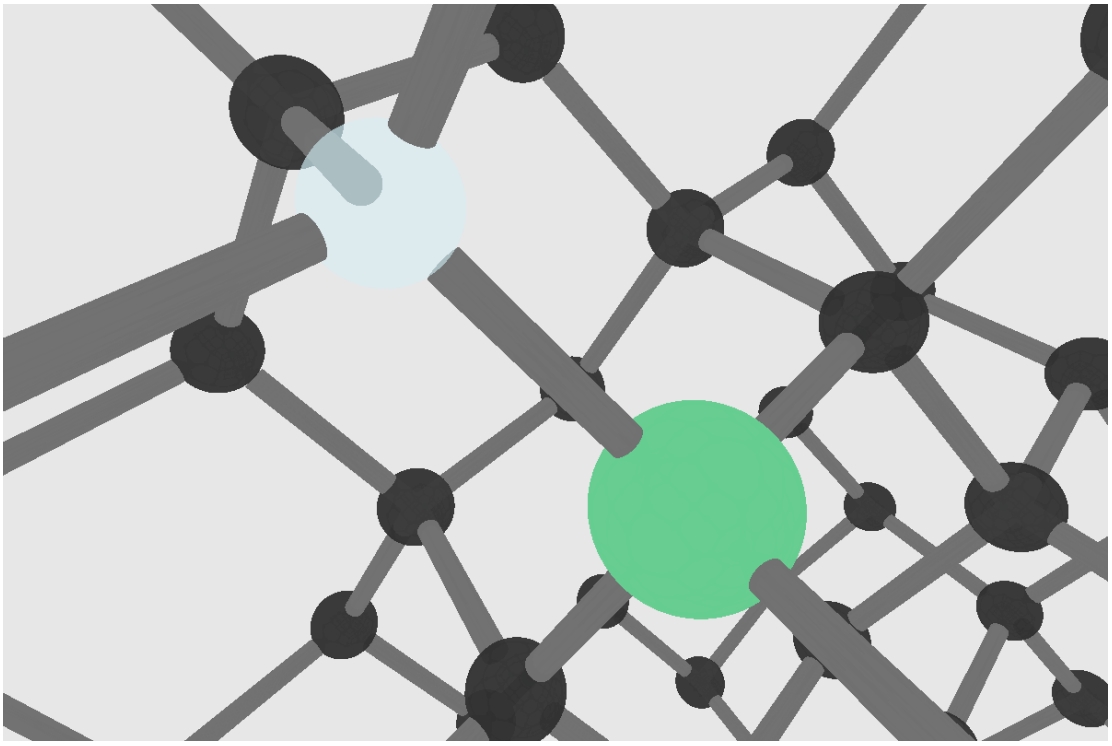


Figure 1.1: Depiction of the positioning of the NV center defect (green and clear spheres) in the carbon (black spheres) lattice of diamond. The quantization axis is the bond connecting the nitrogen and vacancy.

The nitrogen vacancy (NV) center in diamond is a defect in diamond lattice that gives rise to a localized mid-gap electronic state. Held in place by the surrounding carbon atoms, the NV center behaves in many ways like a trapped atom, with laser addressable optical transitions between various orbital and spin states, but unlike other atomic physics systems the trapping is provided for free by the carbon atoms of the diamond lattice. This provides a unique opportunity for integrating technologies based on atoms into small devices. Of particular interest are applications in the rapidly maturing field of quantum technologies. NV centers have been proposed (and demonstrated) as in-

tegral parts of a number of useful hybrid quantum technologies, including single photon sources [17], spin-to-optical interfaces [296,359], and lasers [175]. While solid state qubits like the NV center promise many advantages over their trapped atom counterparts, the solid state environment presents its own challenges. In particular, the local strain and charge environment introduces a large inhomogeneous linewidth distribution of optical transitions [309], instability in spectral lines [69], and, in the case of the NV center, a very small fraction of optical cycles result in coherent photons [183,291]. Despite these challenges, researchers have made tremendous progress on the quantum information front, particularly in the demonstration of photon based NV-NV entanglement [31], a necessary prerequisite for many quantum communication protocols, as well as tests of fundamental physics such as the Bell inequality [149]. While there is still much interest in quantum information processing with NV centers, some work has shifted in recent years to related interstitial defects such as the silicon [327] and germanium [35] vacancies, which, due to their different symmetries, possess more favorable optical qualities.

The other major use of NV centers is as nanoscale sensors, and this will be the primary focus of this thesis. While many defects possess optical transitions between various states, NV centers are somewhat unique in their properties under non-resonant excitation. In particular, there exists a spin-dependent transition to a long-lived metastable state that permits determination of the spin state with off resonant light, and this same pathway provides a mechanism for spin initialization. This remains true at room temperature and above, making spin based sensing schemes with NV centers robust tools that do not require expensive lasers or cryogenics. Diamond is also a favorable host, as it is a very "clean" material, with only one stable spinful isotope (^{13}C, at 1.1% natural abundance) which can be purified away to negligible concentrations [251]. NV centers then exist in an environment that is relatively free of magnetic noise, and hence posses extremely long spin de-

phasing times (T_2^*) and coherence times (T_2)[20]. Finally, the ability to localize NV centers very close[1] to the diamond surface (and hence, sensing targets placed on the diamond surface) provides nearly unparalleled spatial resolution and sensitivity. Sensing protocols based on NV centers have found numerous uses in biology, nuclear magnetic resonance[311], condensed matter physics[56] and earth science[101], to name a few. The opening chapter of this thesis will provide a review of NV center structure and physics, as well as numerous common sensing techniques that are relevant to the remaining chapters.

1.3.1 Diamond properties and NV center formation

Diamond is a material of many amazing properties. It has found many industrial and laboratory applications due to its exceptional thermal conductivity, high hardness, incomprehensibility, large optical transparency window, and low chemical reactivity. The diamond lattice is a face centered cubic (FCC) lattice with a two atom basis. That is, one unit cell of diamond consists of two FCC unit cells, the second offset from the other 1/4 of the way along the diagonal. Each carbon is bonded to its four nearest neighbors by strong sp^3 covalent bonds, with are ultimately the origin diamond's hardness and incompressibility. Unlike other carbon allotropes, such as graphene, all of the orbitals of diamond are involved in bonding and are not available for conduction. Indeed, diamond is a wide band gap semiconductor with a a band gap of 5.5 eV. This results in a transparent material, which, combined with diamond's large refractive index ($n \approx 2.4$) and dispersion creates the stunning visual effects of cut diamond gemstones. Defects within the band gap are tightly localized, and may have optically addressable transitions that still lie below the conduction band edge. Indeed many such defects are known to exist in diamond, and some have proven to be useful for quantum technologies

[1] With good control of diamond surface chemistry, stable NV centers within 3 – 5 nm[226,308] of the diamond surface with good coherence times are routinely produced. It should be noted that many studies cite ion implantation simulation estimates (SRIM) to determine NV depth, but without an independent measurement of NV depth these numbers may be misleading.

[2].

Many people are surprised to learn that diamonds are relatively easy to produce artificially. Diamonds were first produced in the laboratory using high pressure and high temperatures (HPHT) in the 1950s[49]. Similar methods are still used to produce small diamonds for industrial use, such as in abrasives. Large ($\approx$ 1 cm), high quality diamonds are now grown through chemical vapor deposition (CVD), where methane gas is radicalized with microwave radiation and is induced to grow layers of carbon on a substrate material (a smaller diamond seed crystal). At moderate temperatures and pressures, diamond, rather than graphite, is grown. This process is very slow, but both growth rate and impurity content can be controlled and large crystals produced.

The primary reason for preferring CVD diamonds for quantum technology research is the repeatably and uniformly low defect concentrations achievable. Defects in diamond are responsible for the wide range of colors found in natural diamonds. Nitrogen is commonly encountered in natural diamonds, and at high concentrations it gives some diamonds a yellow color. While some natural diamonds have very low concentrations of nitrogen and naturally resolvable NV centers, such as the "Magic Russian" diamond that much early NV center work was performed with[3], such samples are hard to come by. Another advantage of using CVD grown diamonds is that if isotopically purified precursors are used, the resulting diamonds will also be primarily spinless ^{12}C (up to 99.999%)[351].

[2] See, for example, Ref. [393], the bulk of which is devoted to cataloging observed optical transitions in diamond

[3] And which still exists in some small pieces in the Lukin lab!

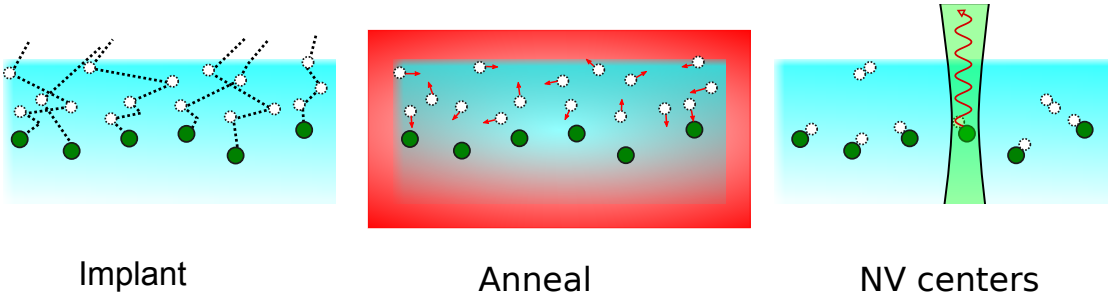


Figure 1.2: NV center formation. Nitrogen ions are implanted with a chosen density and energy (depth), leaving vacancies as they tear through the lattice. Annealing makes the vacancies mobile, and some will naturally find a nitrogen to partner with, forming the NV center complex.

Most diamonds will host some number of NV centers naturally, but it is preferable to control the density and locations of NV centers. Synthetic diamonds can be grown with < 0.03 ppb nitrogen concentration and an NV:N ratio of $\approx 1:100$, making natural NV centers rare. NV centers are then created as shown in Fig. 1.2. Nitrogen ions are accelerated to a pre-determined energy and are directed at the sample, leading to a controlled density of nitrogen atoms at an approximately uniform depth. The implantation process also creates lattice vacancies as the nitrogen ions crash through the lattice. Samples are then annealed in vacuum at 800° C, which is higher than the temperature at which vacancies become mobile[363]. Some number of mobile vacancies settle adjacent to an implanted nitrogen, creating an NV center. This process can be used to produce individually resolvable NV centers at low density, or ensemble samples that contain many NV centers in an optical spot. Typical conversion efficiencies are $> 10\%$ for high energy implantations, but are $< 1\%$ for shallowly implanted nitrogen[276]. However, this can be increased through electron irradiation to create more vacancies before annealing[317,54] or annealing at slightly higher temperatures[61]. The remaining nitrogen atoms form other defects[84] (P1 centers, N_2V, V_2, etc.) which can produce undesirable noise[79,257], and these noise sources can become especially problematic in high density ensemble samples, leading to increased decoherence. It is also possible to incorporate nitrogen into the dia-

mond lattice during growth, which is known as delta doping. Nitrogen is introduced into the CVD chamber during growth and nitrogen atoms are incorporated into the lattice. Vacancies are created by electron irradiation and the diamonds are annealed to make the vacancies mobile[268]. This is a desirable method for producing NV centers with a uniform depth, but few labs have growth facilities on site whereas already grown synthetic diamond can be purchased commercially.

1.3.2 NV center structure

Many of the useful properties of the NV center can be deduced from its atomic structure and symmetry. Group theory makes this possible. We start by considering the symmetry operations that leave the NV center unchanged, and use these to construct linear combinations of atomic orbitals that satisfy the symmetry constraints. Filling these orbitals with electrons provides gives the energy eigenstates, and further symmetry considerations determine the allowed transitions between them.

The NV center complex consists of a substitutional nitrogen atom (^{14}N and ^{15}N are both commonly used), an adjacent vacant lattice site, and, in the case of the negatively charged NV center that is of primary interest for sensing applications, an extra electron donated from somewhere in the lattice (likely from another nitrogen[196]). Six electrons make up this defect: the nitrogen atom contributes two, each carbon dangling bond surrounding the vacancy contributes one, and the "extra" electron contributes one more. These electrons do not just sit at particular lattice sites, however. The single electron orbitals need to have the proper symmetries, as set by the crystal field. We can determine these how these orbitals should look from group theory.

The introduction of a defect into a crystal lattice breaks the translational symmetry of the lattice so that only reflections and rotations of the original lattice symmetry group may be inherited by the defect (e.g. the defect symmetry group is a subgroup of the full lattice symmetry group). While diamond point group is O_h, the NV center possesses C_{3V} symmetry. This naming convention indicates that there are three rotations about the central axis ("C" axis) that leave the NV center unchanged.

	Group operation					
Representation	e	C_1	C_2	σ_1	σ_2	σ_3
A_1	1	1	1	1	1	1
A_2	1	1	1	−1	−1	−1
E	$\begin{pmatrix} 1 & 0 \\ 0 & 1 \end{pmatrix}$	$\begin{pmatrix} -1/2 & -\sqrt{3}/2 \\ \sqrt{3}/2 & -1/2 \end{pmatrix}$	$\begin{pmatrix} -1/2 & \sqrt{3}/2 \\ -\sqrt{3}/2 & -1/2 \end{pmatrix}$	$\begin{pmatrix} -1 & 0 \\ 0 & 1 \end{pmatrix}$	$\begin{pmatrix} 1/2 & -\sqrt{3}/2 \\ -\sqrt{3}/2 & -1/2 \end{pmatrix}$	$\begin{pmatrix} 1/2 & \sqrt{3}/2 \\ \sqrt{3}/2 & -1/2 \end{pmatrix}$

Table 1.1: Irreducible representations of the C_{3V} group.

The "v" stands for vertical plane. There are also three vertical planes through which reflections can be made that leave the center unchanged. There are therefore six symmetry operations in this group: three rotations (including the identity) and three reflections. These six operations (together with a rule for combining them) form a group. Groups are closed under the group multiplication operation, so applying any number of these operations to a system with C_{3V} symmetry results in the same system with one of the operations applied (for example, applying C_1 then C_2 is the same as applying e). There are many ways that one could represent such operations mathematically, and since the operations are not necessarily commutative (rotate $\rightarrow$ reflect $\neq$ reflect $\rightarrow$ rotate, for example) matrices are the usual choice. But which matrices? This choice, called a *representation*, is not unique. We will concern ourselves with some special representations of these groups which cannot be built up from smaller matrices. These are the *irreducible representations* (IRs) of the group.

For C_{3V}, the irreducible representations are listed in Table 1.1. One can check that multiplying the members of a representation together gives the same multiplication rules as applying the symmetry operations to our NV center. One might be tempted to find more irreducible representations, but a theorem from group theory[356] guarantees that the number of irreducible representations is equal to the number of classes of symmetry operations. The identity, rotations, and reflections all constitute different classes, so there should be only three irreducible representations.

One of the very nice things about group theory is that one rarely needs to use the explicit forms of the IRs. Instead, the *character* of each member of the representation contains much of the necessary information. The character is just a single number: the trace of the matrix. The characters for

	Group operation					
Representation	e	C_1	C_2	σ_1	σ_2	σ_3
A_1	1	1	1	1	1	1
A_2	1	1	1	−1	−1	−1
E	2	−1	−1	0	0	0

Table 1.2: Character table of the C_{3V} group.

the members of the IRs of C_{3V} are listed in Table 1.2. Notice that 1) for one-dimensional representations, the character is just the representation itself 2) the character of the identity is the dimension of the representation and 3) the character of each class within a given representation is the same (for example, all rotations in the E representation have character −1).

We can already say something interesting about the electronic states of the NV center. The operations of the point group can be written as unitary matrices, $g_i \in G$, which act on the Hilbert space. The irreducible representations, Γ_k define distinct sets of states where applying the symmetry operations of that IR mixes the states belonging to that IR, but one cannot form states that belong to another IR by applying this transformation. That is

$$g_i^{\Gamma_k} |\Gamma_k, j\rangle = \sum_\alpha g_\alpha^{\Gamma_k} |\Gamma_k, \alpha\rangle \ , \tag{1.1}$$

where $g_i^{\Gamma_k}$ denotes the operator for group operation i in the IR Γ_k.

Since the Hamiltonian of the NV center must have the same symmetry as its point group, the IRs of the group operations commute the Hamiltonian [307]

$$[g_i^{\Gamma_k}, H] = 0 \, . \tag{1.2}$$

If $|\Gamma_k, j\rangle$ is an eigenfunction of H with eigenvalue E_k, then so is $g_i^{\Gamma_k} |\Gamma_k, j\rangle = \sum_\alpha g_\alpha^{\Gamma_k} |\Gamma_k, \alpha\rangle$. This means that in general the degeneracy an eigenstate of the Hamiltonian with energy E_k is the same as the order of the group Γ_k (unless there is an accidental degeneracy). Hence the A-transforming states of the NV center are non-degenerate, but the E-transforming states have degeneracy of two.

With the IRs in hand, the single electron orbitals can be constructed. They must be built up out of the sp^3 dangling bonds that make the NV center. There are three of these from the carbon atoms surrounding the vacancy and one from the nitrogen, denoted σ_1, σ_2, σ_3, and σ_N, respectively. We can see how they are combined to make the single electron orbitals by projecting the dangling bonds onto the irreducible representations of the group[93]:

$$\varphi_r = \frac{l_r}{h} \sum_e \chi_e^r R_e \sigma_i \,, \tag{1.3}$$

where φ_r is the single electron orbital of representation r, l_r is the dimension of r, h is the number of elements in the group, χ_e^r is the character of the operation R_e. We find that the single electron orbitals are[239]

$$a_C = \frac{1}{3}(\sigma_1 + \sigma_2 + \sigma_3) \,, \tag{1.4}$$

$$a_N = \sigma_N \,, \tag{1.5}$$

$$e_x = \frac{1}{\sqrt{6}}(2\sigma_1 - \sigma_2 - \sigma_3) \,, \tag{1.6}$$

$$e_y = \sqrt{2}(\sigma_2 - \sigma_3) \,, \tag{1.7}$$

where (a_C, a_N) transform as A_1 and (e_x, e_y) transform as E. The relative energies of these states cannot be determined from group theory, but modeling the ionic interaction[117] suggests that the lowest lying states are linear combinations of a_C and a_N ($a_1 = \alpha a_C + \beta a_N, a_2 = \alpha a_N + \beta a_C$), followed by the degenerate e_x and e_y states.

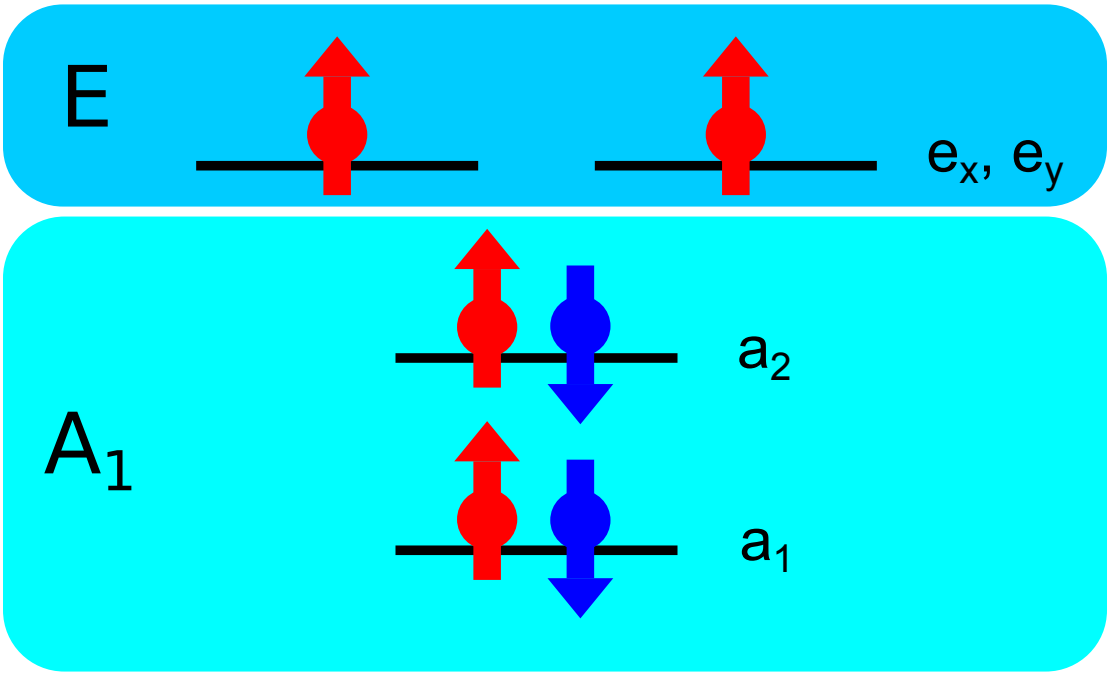


Figure 1.3: The NV level structure. Single electron orbitals are determined by symmetry considerations and filled with the six electrons that make up the NV^- color center. Labels on the left indicate the IR of the single electron orbitals and labels on the right indicate the linear combination of dangling bonds.

With the single electron orbitals identified, we can fill them with electrons following the Pauli exclusion principle and Hund's rules[217]. This leads to the electronic structure shown in Fig. 1.3, where the lower lying A_1 states are completely filled and the e_x and e_y orbitals contain one electron each. The total wavefunction must also be antisymmetric, which implies that the ground state is a singlet of $e_x e_y$ orbitals but is a spin triplet. This is one reason for the long spin coherence times in NV centers. Since it is an orbital singlet in the ground state, it is relatively insensitive to lattice distortions (e.g. phonons) and electric fields which might otherwise cause dephasing and relaxation of the spin quibt.

Group theory can also tell us about the accessible optical transitions of the NV center. While selection rules for atoms are often formulated in terms of the Wigner-Eckhart theorem[307], group

theory gives a general prescription for calculating transitions. The matrix element theorem states that the inner product of two states is different from zero only if the two states contain the same irreducible representation[55]. Specifically for an electric dipole allowed transition between states ψ_1 and ψ_2, where ψ_1 belongs to an IR Γ_1 and ψ_2 belongs to Γ_2. Then we need to determine if

$$\langle \psi_2 | \, \hat{d} \, | \psi_1 \rangle \neq 0 \,, \tag{1.8}$$

where $\hat{d}$ is the electric dipole operator, which belongs to some IR Γ_d (which IR exactly depends on the symmetry group of the system). The matrix element theorem states that this is true only if $\Gamma_d \bigotimes \Gamma_1$ can be decomposed into a set of IRs containing Γ_2. Block diagonalizing a big matrix to look for a certain irreducible representation would be an arduous task, but character tables make it straightforward to determine if one IR is contained in such a direct product product. The characters of a direct product between two IRs in a group are the products of their characters, and these can be decomposed into the direct sum of characters of other IRs in the group. This is often possible by inspection. In free space, an atom has full rotational symmetry. All rotations about any axis are symmetry operations. The spherical harmonics, Y_ℓ^m are the irreducible representations of this group (SO(3)), and the allowed values of angular momentum are the dimensionality. The usual selection rules can be found with the matrix element theorem. The inversion operator, for example, has a character in each IR (labeled by ℓ) given by $\chi_P^\ell = (-1)^\ell (2\ell + 1)$, so the spherical harmonics have definite parity which alternates sign for each ℓ. The electric dipole operator has odd parity[55], so two spherical harmonics must have opposite parity in order to be connected by a dipole allowed transition. Furthermore, since the electric dipole operator has p symmetry (three-dimensional IR), its direct product with an arbitrary Y_ℓ^m will be $3 \times (2\ell + 1)$ dimensional, which decomposes into $\Gamma_d \bigotimes Y_\ell^m = Y_{\ell+1}^m \bigoplus Y_\ell^m \bigoplus Y_{\ell-1}^m$. This, along with the parity rule, gives the familiar selection rule $\Delta\ell = \pm 1$. Determining selection rules in a crystal field of reduced symmetry is similar: find the IR

of the dipole operator, take its direct product with a state that belongs to some IR, and see which IRs are contained in the direct product. These are the allowed transitions.

For the C_{3V} symmetry group, (x, y) are partners of the E irreducible representation. Since a_1 and a_2 are both filled there is no transition linking them. Then we can take $A_1 \bigotimes E = E$, so the allowed dipole transitions are to have an a_2 electron in the orbital belonging to A_1 jump into one of the orbitals belonging to E (which orbital depends on the polarization of the light, but in the current situation they are degenerate).

To find the full states of the NV center, including spin, one takes the direct product of the IR of all six electrons (or equivalently, two holes) with its spin and with all the other electrons, or

$$\Gamma_{\text{Total}} = \prod_n \Gamma_n \bigotimes D_{1/2} \,, \tag{1.9}$$

where Γ_n is the IR of electron n and $D_{1/2}$ is the representation of a spin-$1/2$ particle. Reducing this product into its IRs gives the states listed in Fig. 1.4. The notation is similar to the spectroscopist's notation for the hydrogen atom, e.g. ${}^{2S+1}G$, where S is the total spin projection of the particle (singlet or triplet in this case) and G is the IR. With the states known, it is possible to calculate their ordering by introducing interactions, the results of which have been published elsewhere[239].

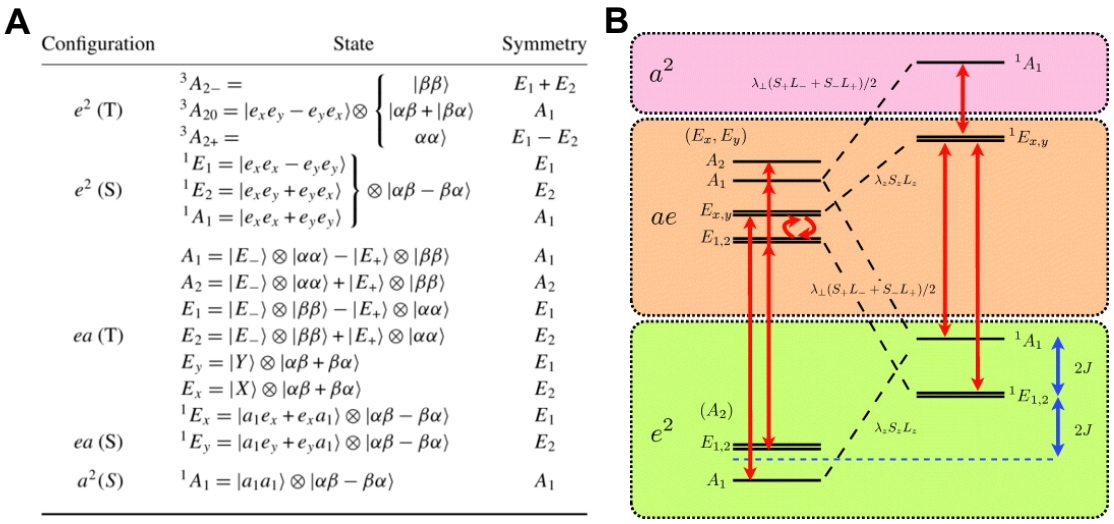


Figure 1.4: Eigenstates and transitions of the NV$^-$ center. (A) Symmetries of the wavefunctions of the NV center as described by two holes. The left hand column indicates the orbitals of the two holes, with the singlet (S) or triplet (T) character in parentheses. The center column lists the spin and orbital parts of the wavefunction, and the right column the overall symmetry. α, β refer to spin up and spin down, respectively. $E_\pm = |a_1 E_\pm - e_\pm a_1\rangle$, with $e_\pm = \mp(e_x \pm ie_y)$. $|X\rangle = \frac{1}{2}(|E_-\rangle - |E_+\rangle)$ and $|Y\rangle = \frac{i}{2}(|E_-\rangle + |E_+\rangle)$. (B) Energy level diagram for the electronic states of the NV center. States on the left are triplets while those on the right are singlets. Red arrows indicate allowed transitions, while dashed arrows are spin orbit induced transitions. J is the exchange energy of the Coulomb interaction. Figures taken with permission from Ref.[239].

The energy level diagram presented in Fig. 1.4B are fare more detailed than what we will work with in this thesis, but there are a few things to notice. First, the primary optical transition is between states transforming as A_2 and states transforming as E. The E states have a very different orbital structure than the A_1 states, (see Eqs. (1.4)-(1.7)). The E states have a different electronic density than the A_1 state, meaning there is a lattice distortion upon excitation. When the NV relaxes to the ground state a lattice vibration is often produced, resulting in a large phonon sideband and only a small amount of coherent light[167]. Next, there exist spin-orbit induced transitions between the triplet states in the left column and the singlets on the right. Unlike the dipole allowed transitions, spin-orbit induced transitions can flip the electron spin. The transition to the metastable singlet states is also favored by states with $m_s = 1$[287,125], which provides a convenient means of spin

pumping into $m_s = 0$ in the ground state by optical excitation. Furthermore, the singlet states are also known experimentally to be metastable, having relatively long lifetimes ($\approx$ 100s ns[3]) compared to the excited state lifetime($\approx$ 10 ns[260]). This results in a fluorescence difference between spin states, permitting all-optical readout of the spin of the NV center.

Group theory has also proven invaluable in the search for other defects in diamond tailored for particular purposes. For example, the NV center lacks inversion symmetry and hence has a non-vanishing permanent electric dipole moment in the excited state. The silicon vacancy center, consisting of an interstitial silicon atom caught mid way between two "half-vacancies," has D_{3d} (the same as the NV center, but with inversion). The ground and excited states have similar electron densities, resulting in a strong zero phonon line. Inversion symmetry also means that the electronic states have no permanent electric dipole moment, hence the SiV is relatively insensitive to spectral diffusion caused by transient occupation of charge traps in the lattice[327]. This makes the transitions more stable and thus more suitable for quantum information applications that require identical photons. Many of the properties of the NV center that make it a useful magnetometer, however, are absent in this system.

1.3.3 Sensing techniques

The Hamiltonian of the ground state spin of the NV center, excluding the host nitrogen, is given by[91]

$$\frac{\mathscr{H}}{\hbar} = (\Delta + E_{\parallel} d_{\parallel}) S_z^2 + \gamma_e \vec{B} \cdot \vec{S} - \frac{d_{\perp} E_{\perp}}{2} (S_+^2 + S_-^2) \,, \tag{1.10}$$

where $\hbar$ is Plank's constant, S_i are the spin-1 Pauli matricies, $S^{\pm}$ are the spin raising and lowering operators, $\Delta/2\pi$ is the zero field splitting of 2.87 GHz, $\gamma_e/2\pi = 2.8$ MHz/Gauss is the electron gyromagnetic ratio, and $d_{\parallel}/2\pi = 0.35$ Hz·cm/V and $d_{\parallel}/2\pi = 17$ Hz·cm/V are the electric field

coupling constants. B_i are the magnetic field components defined with respect to the NV quantization axis (taken to be along $\hat{z}$), which is defined physically by the line between the nitrogen and vacancy of the defect. $E_{\parallel}$ and $E_{\perp}$ are the components of the electric field parallel and perpendicular to the NV axis, respectively. Sensing protocols with NV centers are all, in one way or another, attempts to measure the shifting values of the eigenstates of $\mathscr{H}$, and with this information to infer the electric or magnetic field that caused this shift.

The electric field response of the NV center is, under most conditions, very weak compared to the response to a magnetic field. This is due to the orbital singlet character of the ground state discussed in Sec. 1.3.2, which to first order should have no electric field response. Indeed, the observed sensitivity to electric fields is due to mixing with the excited state[92] and so is greatly suppressed. We will primarily consider magnetic fields in the introduction to sensing protocols, finishing with a note about electric field sensing.

Ground state spin manipulation

The NV center can be pumped into the $m_s = 0$ spin state through optical excitation, but to manipulate the spin further microwave fields are required. These can be introduced to the sample with a suitable waveguide fabricated onto the diamond surface, a glass slide, or even a wire suspended above the sample.

Consider the Hamiltonian of Eq. (1.10), but with a moderate external magnetic field applied along $\hat{z}$ and no applied electric field. The Hamiltonian is then

$$\frac{\mathscr{H}}{\hbar} = \Delta S_z^2 + \gamma_e B_z \tag{1.11}$$

$$= |1\rangle\langle 1|\left(\Delta + \gamma_e B_z\right) + |-1\rangle\langle -1|\left(\Delta - \gamma_e B_z\right), \tag{1.12}$$

where $|\pm 1\rangle$ represents the $m_s = \pm 1$ spin state. If we apply a microwave field, the magnetic part

of the wave can drive transitions between the $|0\rangle \leftrightarrow |\pm 1\rangle$ (it does not couple $|+1\rangle$ to $|-1\rangle$ due to selection rules[307]). The Hamiltonian with the microwave term is

$$\begin{aligned}\frac{\mathscr{H}_{\mathrm{MW}}}{\hbar} = |1\rangle\langle 1|\left(\Delta + \gamma_e B_z\right) + |-1\rangle\langle -1|\left(\Delta - \gamma_e B_z\right) \\ + \frac{g_e \mu_B \mathscr{B}}{\hbar} e^{-i\omega t}\left(|0\rangle\langle 1| + |0\rangle\langle -1| + |1\rangle\langle 0| + |-1\rangle\langle 0|\right) \\ + \frac{g_e \mu_B \mathscr{B}^*}{\hbar} e^{i\omega t}\left(|0\rangle\langle 1| + |0\rangle\langle -1| + |1\rangle\langle 0| + |-1\rangle\langle 0|\right), \quad (1.13)\end{aligned}$$

where $\mathscr{B}$ is the amplitude of the magnetic part of the microwave field at frequency ω, g_e is the electron g factor, and μ_B is the Bohr magneton, which come from the matrix element that couples the spin-1 states in a magentic dipole allowed transition. We will denote the quantity $\frac{g_e \mu_B \mathscr{B}}{\hbar} = \Omega$, which is the Rabi frequency. Now we consider a general state $|\psi(t)\rangle = c_0(t)|0\rangle + c_1(t)|1\rangle + c_{-1}(t)|-1\rangle$. Substituting this into the Schrodinger equation using the Hamiltonian of Eq. (1.13), we obtain the following set of differential equations for the $c_i(t)$:

$$i\dot{c}_0 = (\Omega e^{-i\omega t} + \Omega^* e^{i\omega t})(c_1 + c_{-1}), \quad (1.14)$$

$$i\dot{c}_1 = (\Delta + \gamma_e B_z)c_1 + (\Omega e^{-i\omega t} + \Omega^* e^{i\omega t})c_0, \quad (1.15)$$

$$i\dot{c}_{-1} = (\Delta - \gamma_e B_z)c_{-1} + (\Omega e^{-i\omega t} + \Omega^* e^{i\omega t})c_0. \quad (1.16)$$

Now we transform into a frame that rotates at the frequency of the drive field through a unitary transformation $U = \exp\left[-i\omega t(|1\rangle\langle 1| + |-1\rangle\langle -1|)\right]$. We can incorporate this transformation into Equations (1.14) to (1.16) by making the substitution $c_{\pm 1}(t) = \tilde{c}_{\pm 1}(t)e^{-i\omega t}$. The resulting equations are

$$i\dot{c}_0 = (\Omega^* + \Omega e^{-i2\omega t})(\tilde{c}_1 + \tilde{c}_{-1}) \,, \tag{1.17}$$

$$i\dot{\tilde{c}}_1 = (\Delta + \gamma_e B_z - \omega)\tilde{c}_1 + (\Omega + \Omega^* e^{-i2\omega t})c_0 \,, \tag{1.18}$$

$$i\dot{\tilde{c}}_{-1} = (\Delta - \gamma_e B_z - \omega)\tilde{c}_{-1} + (\Omega + \Omega^* e^{i2\omega t})c_0 \,. \tag{1.19}$$

The only terms with explicit time dependence now rotate at a frequency 2ω. We take the rotating wave approximation (RWA) and disregard these terms to focus on the slow dynamics. This is permissible if we are interested in the dynamics of the states on timescales that are slower than the $\sim$ GHz timescales of ω. The system of differential equations is then

$$i\dot{c}_0 = \Omega^*(\tilde{c}_1 + \tilde{c}_{-1}) \,, \tag{1.20}$$

$$i\dot{\tilde{c}}_1 = (\Delta + \gamma_e B_z - \omega)\tilde{c}_1 + \Omega c_0 \,, \tag{1.21}$$

$$i\dot{\tilde{c}}_{-1} = (\Delta - \gamma_e B_z - \omega)\tilde{c}_{-1} + \Omega c_0 \,. \tag{1.22}$$

Now there are several different cases. First suppose that $\omega = \Delta + \gamma_e B_z$ so that the driving field is on resonance with one transition but is far detuned from the other. Intuitively, the dynamics should be dominated by the c_0 and $\tilde{c}_1$ terms, since the off resonant field should very rarely cause transitions to $|-1\rangle$. We can use adiabatic elimination to set $\dot{\tilde{c}}_{-1} = 0$, which, upon substitution, yields

$$\ddot{c}_0 = -|\Omega|^2 c_0 + i\frac{|\Omega|^2}{\Delta - \gamma_e B_z - \omega}\dot{c}_0 \,, \tag{1.23}$$

which we recognize as the equation for a damped harmonic oscillator. In experiments, B_z is large enough to completely split the degenerate transitions, so the the detuning, $\delta = \Delta - \gamma_e B_z - \omega \gg \Omega$.

So long as we are not interested in the very long time dynamics, we can disregard the damping term caused by the $m_s = -1$ state. If we start in the initial state $|\psi\rangle = |0\rangle$, the states will evolve as

$$c_0(t) = \cos \Omega t \tag{1.24}$$

$$\tilde{c}_1 = i\frac{\Omega}{|\Omega|} \sin \Omega t \,, \tag{1.25}$$

that is, the states will oscillate between each other at a frequency Ω. These are called *Rabi oscillations* and are depicted in Fig. 1.5.

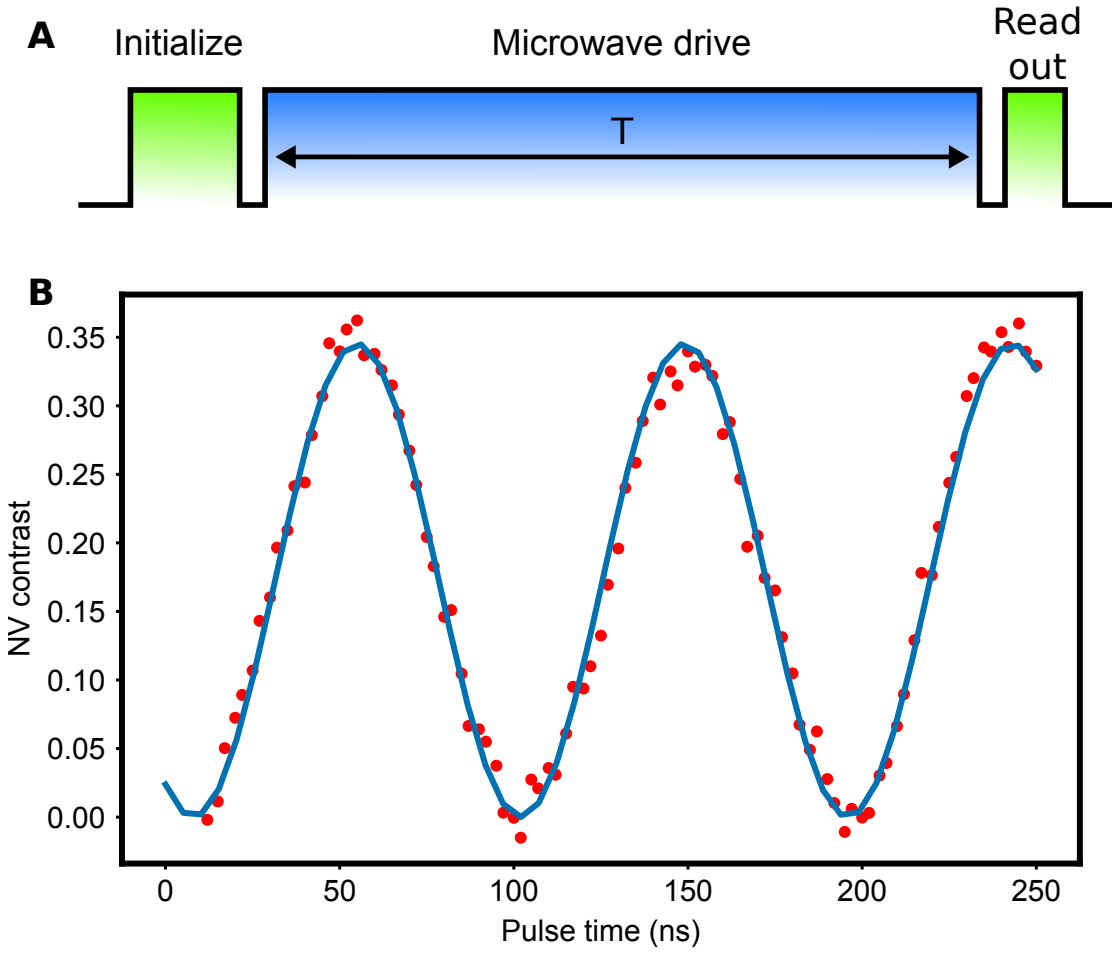


Figure 1.5: Rabi oscillations of an NV center under a microwave drive. (A) Pulse sequence, consisting of an intitalization step that pumps the NV center spin into $m_s = 0$, a microwave drive of variable duration, and optical readout of the NV center spin state. (B) Rabi oscillations from an NV center (red points) with a sinusoidal fit (blue line). The curve does not start exactly at zero due to effects of the microwave switch.

By choosing the duration of the microwave field, the spin can be coherently rotated from one state to another. A π pulse, for example, is a pulse that rotates the state 180°. The microwave field is turned on for $\Omega t = \frac{\pi}{2}$, and takes $|0\rangle \rightarrow i\,|1\rangle$. More generally, with phase control of the microwave field, an arbitrary state $|\psi\rangle = \cos\frac{\theta}{2}\,|0\rangle + e^{i\varphi}\sin\frac{\theta}{2}\,|1\rangle$ can be constructed. It is useful to visualize such a state as a point on the *Bloch sphere*, where the north pole is the state $|0\rangle$, the south pole is

$|1\rangle$, θ is the polar angle, and φ is the azimuthal angle. Arbitrary superpositions then have a unique representation on the Bloch sphere, as depicted in Fig. 1.6.

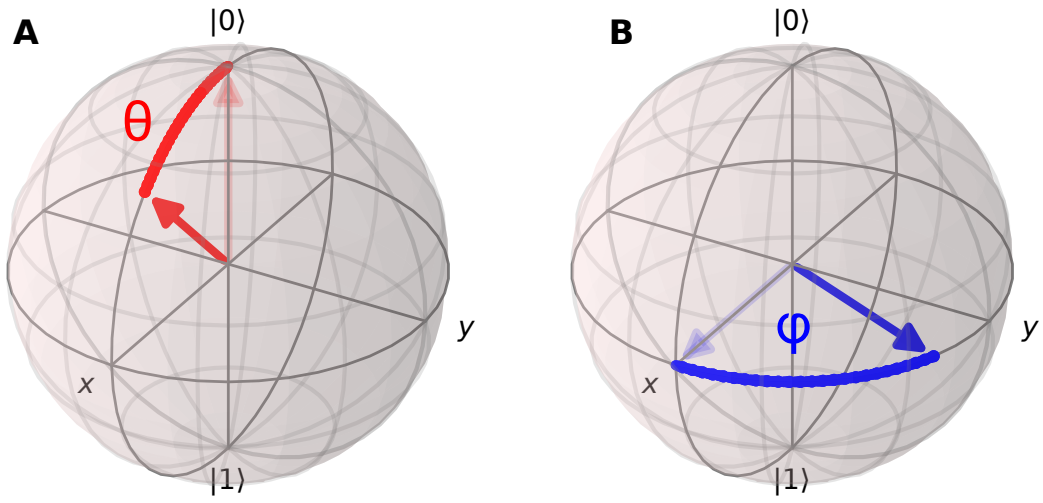


Figure 1.6: State representation on the Bloch sphere. (A) A rotation of θ about the y axis and (B) a rotation of φ about the z axis.

Now suppose that $B_z = 0$ so the $m_s = \pm 1$ states are degenerate. Then if $\omega = \Delta$ (the field is on resonance), we find

$$\ddot{c}_0 = -2\,|\Omega|^2\, c_0\,, \tag{1.26}$$

That is, the oscillations between $|0\rangle$ and $|\pm 1\rangle$ are $\sqrt{2}$ times faster than for the non-degenerate case.

What is the physical intuition behind how a microwave field drives these oscillations? First consider what happens whith a DC field. Consider an electron prepared in the $+1/2$ S_z eignstate. If a field is then applied along $\hat{x}$, the electron is no longer in an eigenstate of the Hamiltonian $H = \gamma_e \hbar S_x B_x$ and hence will undergo oscillations between $m_s = +1/2$ and $m_s = -1/2$ with a frequency $\gamma_e B_x$. So we could make our electron rotate between states by applying a large DC magnetic field,

but we would need nearly a Tesla to achieve a Rabi frequency of 2 MHz, which in practice cannot be switched on and off quickly. In the microwave case, we instead have a Hamiltonian of the form

$$\frac{H}{\hbar} = \gamma_e B_z S_z + \Omega \cos \omega t S_x \,. \tag{1.27}$$

That is, there is still a field applied off axis, but it is small and it oscillates in time. The B_z field is left on. The microwave field causes the spin to rotate slightly from the pole, at which point it precesses at the frequency $\gamma_e B_z$. If the driving field is on resonance so that $\omega = \gamma_e B_z$, then every time the electron precesses around the Bloch sphere the driving field pushes the spin farther from the pole, so that in addition to rapidly rotating azimuthally, there is a slow polar rotation. In a frame rotating at the precession frequency $\gamma_e B_z$, an observer would only see the polar rotation. Hence we are able to use a small oscillating field to accomplish what would have otherwise required a large static field.

Finally, for the case of the two level system, the system of differential equations can be solved for arbitrary detunings. Assuming $c_0(t = 0) = 1$,

$$|c_0(t, \delta)| = 1 - \frac{|\Omega|^2}{|\Omega|^2 + \delta^2} \sin^2 \left(\sqrt{|\Omega|^2 + \delta^2}\, t \right) \,. \tag{1.28}$$

In Fig. 1.7, we plot Eq. 1.28 for a fixed time corresponding to an on resonance π pulse, which gives the population change as one sweeps the drive frequency through resonance, which is one of the DC magnetometry techniques discussed in the next section.

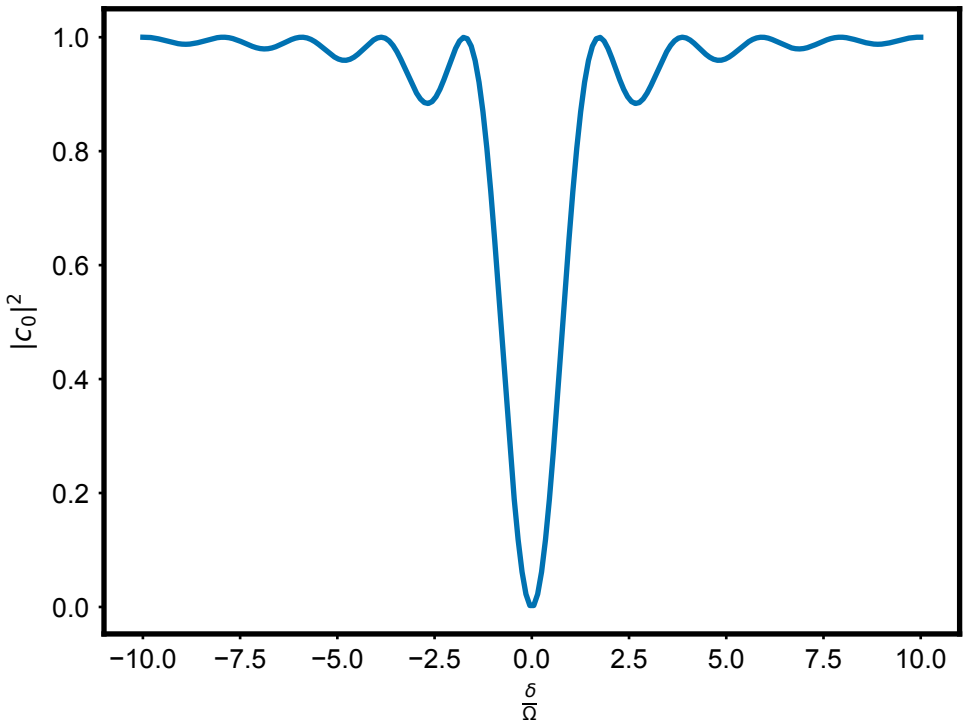


Figure 1.7: π pulse detuning. Detuning dependence for a π pulse applied to a two level system with initial condition $c(t = 0) = 0$

DC MAGNETOMETRY

Perhaps the simplest NV sensing protocol is DC magnetometry, which can be done in a continuous wave (CW) or pulsed manner.

For an NV center under no strain and in zero magnetic field, the $m_s = \pm 1$ spin states are degenerate and are separated from the $m_s = 0$ spin state by the zero field splitting Δ. Optical excitation results in spin pumping through the intersystem crossing, moving a large spin population to the $m_s = 0$ spin state. If microwaves are now applied at the zero field splitting, some popula-

tion is transferred to the $m_s = \pm 1$ states, which preferentially decays into the long lived metastable singlet state, resulting in a decrease in fluorescence. This is optically detected magnetic resonance (ODMR), which is shown in Fig. 1.8.

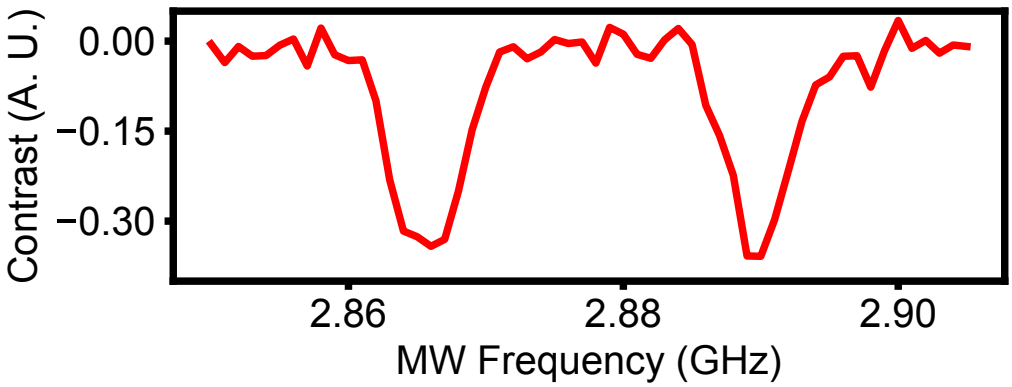


Figure 1.8: NV center ODMR. Optically detected magnetic resonance of an NV center, showing the two spin transitions split by an external magnetic field.

Consider the Hamiltonian for an NV center placed in an external magnetic field, B_z along the NV axis. The field breaks the degeneracy of the $m_s = \pm 1$, splitting them by an amount $2\gamma_e B_z$. Now if the microwave frequency is swept across the zero field splitting, two dips in fluorescence are observed: one corresponding to a resonance with the $m_s = +1$ transition and one corresponding to $m_s = -1$. By measuring the splitting between the $m_s = \pm 1$ states, the z projection of the magnetic field is inferred.

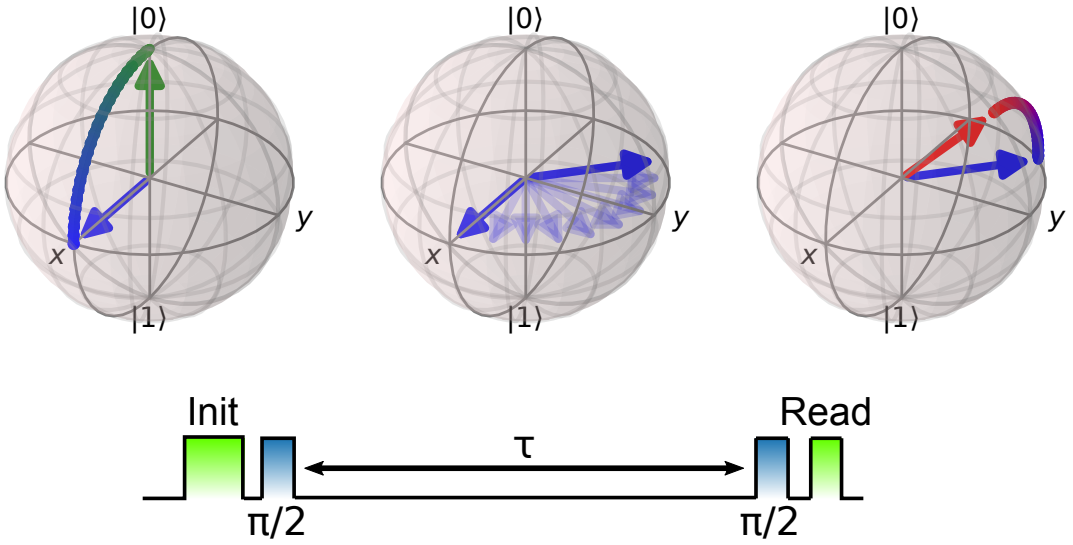


Figure 1.9: Bloch sphere depiction of a Ramsey pulse sequence. A $\pi/2$ pulse sends the spin vector to the equator, where it precesses under the influence of the Hamiltonian to acquire a phase. Following this, another $\pi/2$ pulse around the same axis converts the phase into a spin population that can then be read out..

Another way to measure this splitting is through a Ramsey pulse sequence[350], whose Bloch sphere representation is depicted in Fig. 1.9. For pulsed sequences, a constant external magnetic field is generally applied to split the spin states so that, for example, $m_s = 0$ and $m_s = -1$ may be used as a qubit basis $|0\rangle, |1\rangle$ and the third state is disregarded. The NV center is prepared in the $m_s = 0$ state by optical pumping, after which a $\frac{\pi}{2}$ pulse is applied (typically with a small detuning, δ) to place the NV center in a coherent superposition state

$$|\psi_0\rangle = |0\rangle \xrightarrow{\pi/2} \frac{1}{\sqrt{2}}(|0\rangle + |1\rangle) , \tag{1.29}$$

which evolves for some time under the influence of an unknown DC magnetic field. In the rotating frame, this corresponds to evolution under the Hamiltonian

$$\frac{\mathcal{H}_1}{\hbar} = \delta S_z , \tag{1.30}$$

where δ is the detuning from the "true" resonance $\gamma_e B_z$[4]. After some evolution time τ, the NV center spin state is

$$|\psi(\tau)\rangle = \frac{1}{\sqrt{2}}\left(|0\rangle + e^{-i\delta\tau}|1\rangle\right) , \tag{1.31}$$

Another $\frac{\pi}{2}$ pulse converts the phase into a population difference, giving

$$|\psi(\tau)\rangle \xrightarrow{\pi/2} |\psi_f\rangle = \frac{1}{2}\left((1 - e^{-i\delta})|0\rangle + (1 + e^{-i\delta\tau})|1\rangle\right) . \tag{1.32}$$

Finally, projective measurement of the spin yields

$$\left|\langle 0|\psi_f\rangle\right|^2 = \frac{1}{2}(1 - \cos\delta\tau) . \tag{1.33}$$

In experiments, the form of Eq. (1.33) is actually

$$\left|\langle 0|\psi_f\rangle\right|^2 = \frac{e^{-\tau/T_2^*}}{2}(1 - \cos\delta\tau) , \tag{1.34}$$

where T_2^* is the spin dephasing time. This time sets a limit on how accurately a DC field can be measured. To see this, note that the Fourier transform of e^{-at} is given by

$$\int_0^\infty e^{at}e^{i\omega t}dt = \frac{a + i\omega}{a^2 + \omega^2} . \tag{1.35}$$

In the case of (1.34), the real part is

$$F(\omega) = \frac{1}{T_2^*\left((T_2^*)^2 + \omega^2\right)} , \tag{1.36}$$

[4]In a Ramsey sequence, we measure the difference between the known, fixed frequency of the drive and the exact frequency of the resonance. Since we know exactly what the driving frequency is, after the detuning is determined the "actual" position of the resonance is established.

which is a Lorentzian with linewidth $1/T_2^*$. The uncertainty in the measurement is given by the linewidth of the Fourier transform. This is illustrated for several different dephasing times in Fig. 1.10. Another way to see this is to imagine two sine waves with only slightly different frequencies. It will take many cycles before there is a noticeable difference between the two, but if the spin has dephased by then it will be impossible to tell.

When low microwave powers are used for ODMR, the linewidth of the resonance is also set by T_2^*, and the pulsed and CW techniques are equivalent.

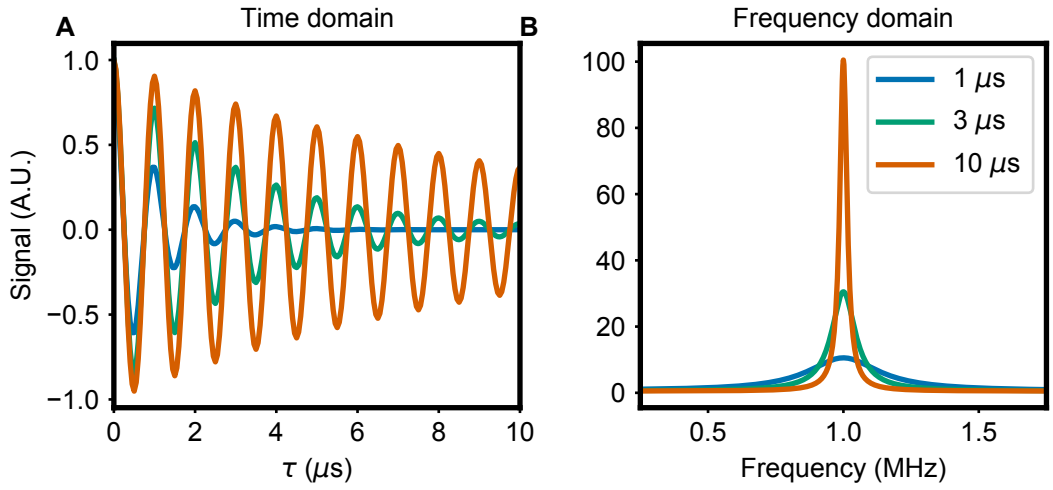


Figure 1.10: Spin dephasing and sensitivity. (A) Simulated NV center fluorescence signals in a DC field of $\gamma_e B_z$ = 1 MHz, but with differing decay envelopes characterized by the exponential decay constant $\frac{1}{T_2^*}$ (B) Fourier transforms of simulated signals in (A), showing increased broadening for shorter values of T_2^*.

AC magnetometry

Many interesting magnetic signals are oscillatory, such as the precession of nuclear spins in a magnetic field, or can be made periodic by changing some parameter. In these situations, techniques built on the spin echo [140] are more appropriate.

Now we assume that microwave pulses are resonant with the splitting induced by a static field, and there exists some small oscillatory field that we would like to sense. The Hamiltonian in the rotating frame is simply

$$\frac{\mathscr{H}_1}{\hbar} = \gamma_e B_z(t)\,. \tag{1.37}$$

A spin echo consists of the pulses shown in Fig,. 1.11. The result of this sequence depends on the form of the periodic signal and how it is timed with the pulse sequence.

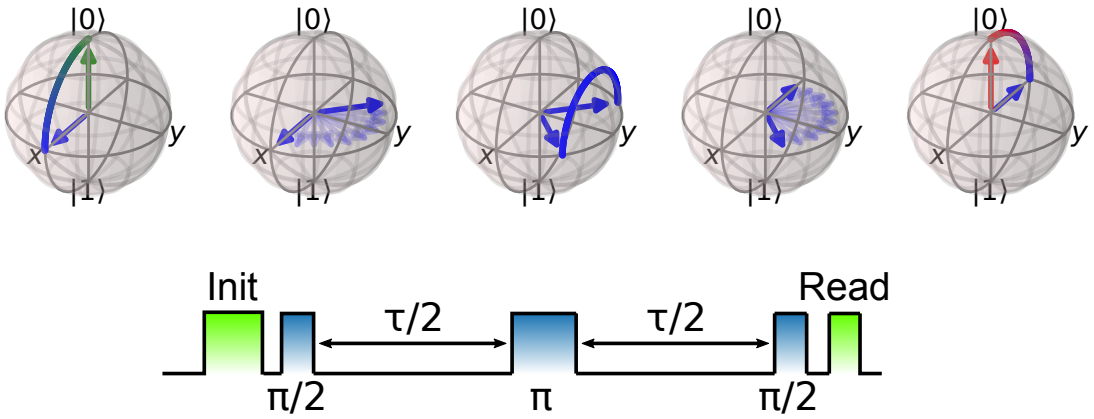


Figure 1.11: Bloch sphere representation of the spin echo. As in the Ramsey sequence, the spin state is tilted onto the equator of the Bloch sphere and allowed to precess, but midway through the free precession interval a π pulse reverses the dynamics. The precession is refocused, except for parts of the Hamiltonian that give different (preferably opposite) phase accumulations in the first and second half of the sequence.

The simplest case is where $B_z(t)$ has the same form in each experiment, that is, it is repeated in the same way at the same time during the pulse sequence. Initializing in the $m_s = 0$ spin state and applying the pulses as in Sec. 1.3.3, the spin population is

$$P = \left|\langle 0|\psi_f\rangle\right|^2 = \frac{1}{2}\left(1 + \cos\gamma_e \Delta B(\tau)\right)\,, \tag{1.38}$$

where

$$\Delta B(\tau) = \int_{\tau/2}^{\tau} B_z(t)dt - \int_0^{\tau/2} B_z(t)dt\,. \tag{1.39}$$

Hence if B_z is a constant function, the resulting phase accumulation is zero. For a simple periodic function, maximum signal is obtained when the field has the same period as the pulse sequence (τ) and is in phase. This is because the direction of phase accumulation switches sign after the π pulse, and so if the field also switches sign at this time the phase accumulation is maximal.

It is also possible to apply the final $\frac{\pi}{2}$ pulse around an axis perpendicular to the initial two pulses, in which case the spin signal becomes

$$P = \frac{1}{2}\left(1 + \sin\gamma_e \Delta B(\tau)\right)\,. \tag{1.40}$$

This is known as sine magnetometry to distinguish it from cosine magnetometry as described by eq. (1.38). For small signals, sine magnetometry may be preferred due to the linear expansion of $\sin x$ for small x. Interestingly, the sensitivity of the two techniques is identical due to the increase in spin projection noise along the equator of the Bloch Sphere (see Sec. 1.3.8).

The AC signal need not be phase locked to the pulse sequence. Indeed, this is most often the case for common AC sensing schemes, such as NMR. In this case, in each repetition of the sequence, the signal has the same frequency, but its phase is random with probability distribution $\varphi(\delta) = \frac{1}{2\pi}$. If we assume that the periodic signal is sinusoidal, e.g. $B_z(t) = B_0 \sin(\omega t + \delta)$, then averaging over this probability distribution gives

$$\langle P \rangle = \int_{-\pi}^{\pi} \varphi(\delta) \cos^2\left(\frac{2\gamma_e B_0}{\omega} \cos\left(\frac{\omega\tau}{2} + \delta\right) \sin^2\left(\frac{\omega\tau}{4}\right)\right) d\delta\,, \tag{1.41}$$

$$= \frac{1}{2\pi} \int_{-\pi}^{\pi} \cos^2\left(\frac{2\gamma_e B_0}{\omega} \cos(\alpha) \sin^2\left(\frac{\omega\tau}{4}\right)\right) d\alpha\,, \tag{1.42}$$

$$= \frac{1}{2}\left(1 + J_0\left(\frac{4\gamma_e B_0}{\omega} \sin^2\left(\frac{\omega\tau}{4}\right)\right)\right)\,, \tag{1.43}$$

where $J_0(x)$ is the Bessel Function of the first kind. The simulated signal is plotted in Fig. 1.12(A). This situation is frequently encountered in experiment. For example, a spin-1/2 ^{13}C nuclear spin located near a target NV center will result in coherence oscillations as depicted in Fig. 1.12(B). The behavior of these oscillaions can be very complex when multiple ^{13}C nuclei with different coupling strengths are involved[65]. These oscillations can be understood as follows: while the periodic field sensed by the NV center has a random phase at $\tau = 0$, after a full precession interval ($\omega\tau = 2\pi$), $\Delta B = 0$ for all initial phases, and so there is no ensemble spread in detected magnetic fields. This is true even if there are many sources of magnetic field with different couplings to the NV center, so long as they are independent and precess at the same frequency.

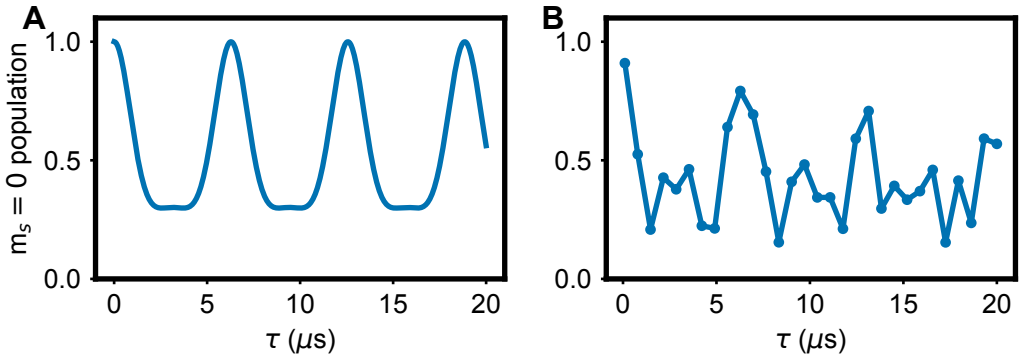


Figure 1.12: Coherence oscillations and revivals. (A) Simulated NV center spin signal for a periodic magnetic field with random phase. (B) Spin Echo signal from an NV center in a diamond with a natural abundance of 13C, displaying oscillations in the coherence at $\gamma_N B_{app}$ due to a nearby 13C atom.

NV centers are more sensitive to AC fields than to DC because spin echo measurements are limited by the spin coherence time, T_2, rather than T_2^*, and this is typically much longer[240]. Shot-to-shot variations in the magnetic field cause dephasing in Ramsey measurements, and these variations can come from slowly varying sources. Indeed, the primary limit of T_2^* for NV centers in diamond with natural isotopic abundance is the bath of ^{13}C spins that provide a randomized, time varying magnetic field at the sensor site[251,237]. The Spin Echo sequence cancels out such slowly varying fields, even if there is shot-to-shot variation. In the Bloch sphere picture, the spin state precesses clockwise and counter-clockwise by the same amount during each measurement, even if the applied field is different for different iterations of the measurement. This means that coherence decay occurs as a result of higher frequency noise that is not canceled by the equal free precession intervals. Some of this high frequency noise can be canceled by the application of additional π pulses, which may extend T_2, depending on the form of the noise bath.

1.3.4 Spectral noise formulation

Multi-pulse sequences are best understood in the spectral noise formulation [194,128,23,100]. Consider a pulse sequence in which a $\pi/2$ pulse is applied, a series of other π pulses are applied with some free precession intervals interleaved, and finaly a $\pi/2$ pulse is applied and the spin state read out. The phase accumulated during this process, φ, can be written as

$$\varphi = \gamma_e \int_0^T f(t)B(t)dt\,, \tag{1.44}$$

where $B(t)$ is the magnetic field at time t and $f(t)$ is a function that takes on values of ± 1 (steps) depending on the number of π pulses applied. Taking the average over many measurements, the NV center signal is given by

$$\begin{aligned} C(\tau) =& \frac{1}{2}\left(1 + \langle \cos\varphi \rangle\right)\,, & (1.45)\\ =& \frac{1}{2}\left(1 + \exp(-\left\langle \varphi^2 \right\rangle/2)\right)\,, & (1.46)\\ =& \frac{1}{2}\left(1 + \exp(-\chi(\tau))\right)\,, & (1.47) \end{aligned}$$

where we have used the fact that, if φ is Gaussian distributed, then $\langle \cos\varphi \rangle = \exp(-\left\langle \varphi^2 \right\rangle/2)$. It is generally true that $B(t)$ is Gaussian distributed for a particular t, but see Ch. 3 for an interesting example where this is not the case.

We then calculate $\chi(\tau)$

$$\begin{aligned} \chi(\tau) =& \frac{1}{2}\gamma_e^2 \left\langle \int f(t)B(t)dt \int f(t')B(t')dt' \right\rangle\,, & (1.48)\\ =& \frac{1}{2}\gamma_e^2 \left\langle \int\int \tilde{f}(\omega_1)\exp(2\pi i\omega_1 t)d\omega_1 B(t)dt \int\int \tilde{f}(\omega_2)\exp(2\pi i\omega_2 t')d\omega_2 B(t')dt' \right\rangle\,. & (1.49) \end{aligned}$$

Expanding $B(t')$, we can write

$$B(t') = \int \exp(2\pi i\omega_3 t')\tilde{B}(\omega_3)d\omega_3 \,, \tag{1.50}$$

$$= \int \exp(2\pi i\omega_3 t') \int \exp(-2\pi i\omega 3t'')B(t'')dt''d\omega_3 \,. \tag{1.51}$$

Inserting this back into eq. (1.48), we can rearrange terms to write

$$\chi(\tau) = \frac{1}{2}\gamma_e^2 \int\int\int \tilde{f}(\omega_1)\tilde{f}(\omega_2)S_B(\omega_3)d\omega_1 d\omega_2 d\omega_3 \int \exp(-2\pi i(\omega_1+\omega_3)t)dt \int \exp(2\pi i(\omega_3-\omega_2)t')dt' \,, \tag{1.52}$$

where $S_B(\omega) = \int \exp(2\pi i\omega t)\left\langle B(t)B(0)\right\rangle dt$ is the magnetic field noise spectral density, by the Weiner-Khinchin theorem.

The above finally simplifies to

$$\chi(\tau) = (\gamma_e)^2 \int \frac{d\omega}{2\pi} S_B(\omega)\frac{F(\omega\tau)}{\omega^2} \,, \tag{1.53}$$

where $F(\omega\tau) = \frac{\omega^2}{2}\tilde{f}(\omega)\tilde{f}^*(\omega)$ is the filter function associated with the pulse sequence. The filter function is aptly named as it selects out certain frequencies from the noise spectrum that influence the coherence. The filter functions for some common pulse sequences are listed in Table 1.3. In general, pulse sequences with a larger number of pulses become more strongly peaked around a central frequency, resulting in a weak influence from noise at frequencies far from the central frequency and a strong signal at the central frequency. This property makes these sequences useful for NMR, where the nuclear spins to be sensed precess at a known frequency, or at least close to a known frequency and the time spacing can be swept. The nuclear spin signal can thus be sensed while all other noise sources at other frequencies are filtered out.

Sequence	Ramsey	Echo	CPMG (n even)	PDD (n odd)
$\mathbf{F}(\mathbf{x})$	$2\sin^2\left(\frac{x}{2}\right)$	$8\sin^4\left(\frac{x}{4}\right)$	$2\sin^2\left(\frac{nx}{4}\right)\left(1-\sec\left(\frac{x}{4}\right)\right)^2$	$2\sin^2\left(\frac{(n+1)x}{4}\right)\tan^2\left(\frac{x}{4}\right)$

Table 1.3: Filter functions for commonly used pulse sequences. n is the number of π pulses.

By using different pulse sequences, it is possible to sample different parts of the noise spectrum, and by inverting the coherence decay one can map out the noisy environment of the NV center. This technique, called spectral decomposition [298,246], is a useful characterization technique for NV centers as well as other qubits. For quantum information applications, this is because mitigation of environmental noise starts with a good understanding of the properties of the noise bath, but the noise bath itself may be of interest. Some phenomena create characteristic noise spectra, or, as Rolf Landauer famously wrote, "the noise is the signal" [209]. We will make use of noise measurement techniques in Ch. 2 and Ch. 4.

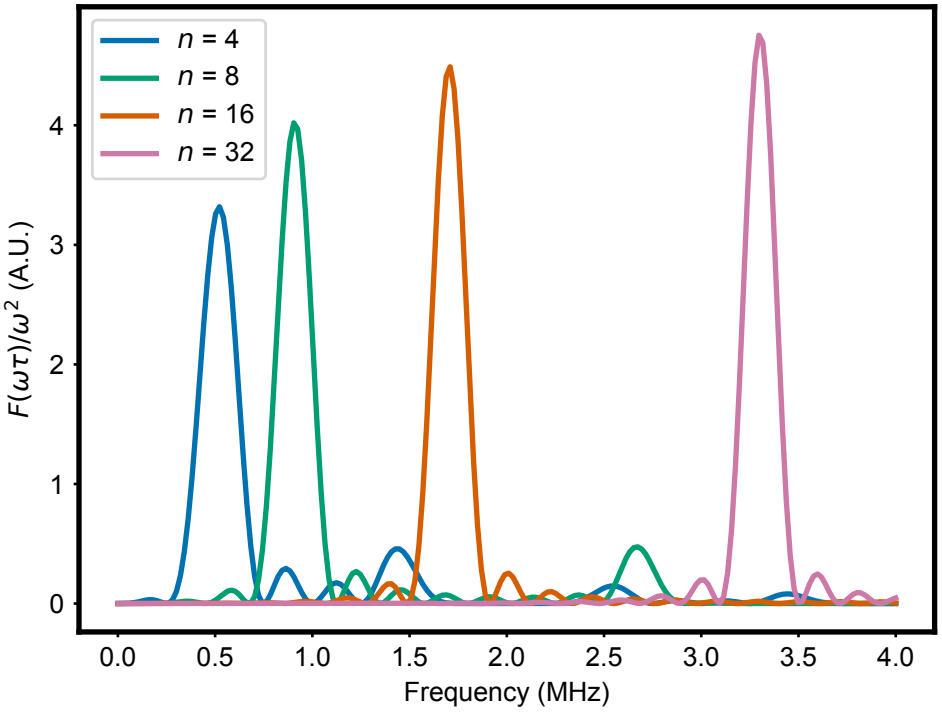


Figure 1.13: Filter function plots for different pulse numbers. Filter functions (divided by ω^2) for CPMG sequences with increasing pulse number n. For a fixed total time, increasing n pushes the filter function to higher frequencies and it becomes more sharply peaked.

Noise generating processes with with some finite correlation time (e.g. a "stationary" process with an exponentially decaying autocorrelation function) produce a noise bath with a Loretnzian power spectral density:

$$S(\omega) = \frac{1}{\pi} \frac{b^2 \tau_c}{1 + \omega^2 \tau_c^2}, \tag{1.54}$$

where τ_c is the correlation time of the noise bath and b is an amplitude parameter. Many naturally occurring processes are well described by this model, including noise from the nuclear spin envi-

ronment of solid state systems [100], two level fluctuators that limit coherence of superconducting qubits [313], and charge traps in semiconductors that are responsible for generation-recombination noise [250]. The form of the coherence decay is influenced directly by the parameters of this noise spectrum. For the FID, we have

$$C(\tau) = \exp - \left(b^2 \tau_c \tau + b^2 \tau_c^2 (e^{-\tau/\tau_c} - 1) \right) , \tag{1.55}$$

$$\approx \exp \left(-b^2 \tau_c \tau \right) , \tag{1.56}$$

where in the last line we have taken $\tau \gg \tau_c$. The stretching factor of the exponent and the decay timescale thus provide insight into the dynamics of the bath–in particular, the decay rate $(1/T_2^*)$ is proportional to the correlation time of the bath[5]. Similarly, in the opposite limit ($\tau \ll \tau_c$), a Ramsey sequence gives a τ^2 dependence that is independent of the bath noise spectrum parameter τ_c; it is a universal decay signature, regardless of environmental factors. Higher pulse number sequences are sensitive only to higher frequency noise components, which do not exist in this example, so there is no coherence decay. This is due to the reversal of the kinetics and refocusing of the Bloch vector in Echo type sequences, which cancel out dephasing due to sufficiently slowly varying noise. By increasing the number of pulses, higher and higher frequency components are canceled, and the coherence time can be extended. For the noise spectrum given by Eq. (1.54) in the limit of a long bath correlation time ($\tau_c > \tau, T_2^*$), coherence time scales with the number of pulses to the 2/3 power [100,350,329]. This has been demonstrated to be the case for bulk NV centers [24,23], suggesting that the electronic spin bath of the host diamond (primarily substitutional nitrogen atoms) is indeed the coherence limiting noise source. For shallow NV centers this is not generally true [298], which

[5] Another interesting phenomenon that is apparent in this example and that is of great interst in NMR is that of motional narrowing, where T_2^* is extended by very short τ_c [83]

hints at a more complicated environment near the surface, a topic we will explore in Ch. 2.

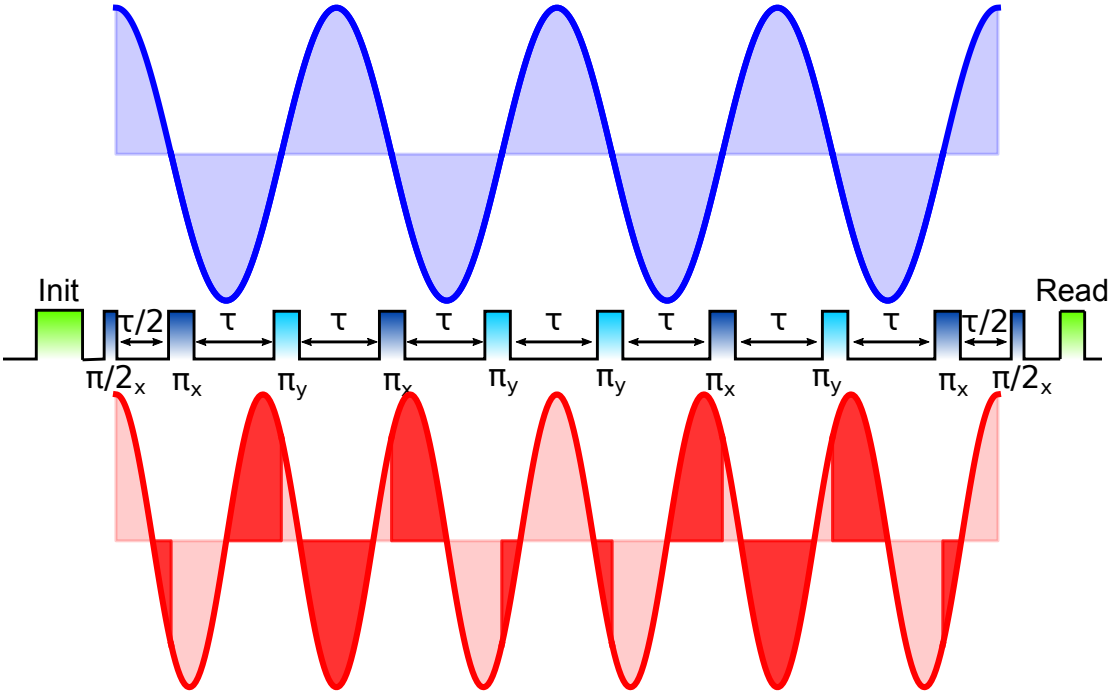


Figure 1.14: Pulse sequence frequency filtering. Intuitive explanation of filtering in CMPG sequences. A signal with a frequency commensurate with the pulse sequence (blue curve) contributes phase of the same sign for the entire sequence (light blue shading). A signal with a different frequency (red curve) contributes positive (light red) and negative (dark red) phases, and so contributes less to the phase accumulation of the NV center. Central pulse sequence is symmetric XY8.

Using Eq. 1.53, it is possible to reconstruct a noise source with sufficient points along the NV center decoherence curve[23]. This is generally accomplished by taking measurements with CPMG pulse sequences of varying pulse numbers. For large numbers of pulses, the filter function in Eq. 1.53 becomes sharply peaked (see Fig. 1.13)[36]. In this limit, the filter function samples the noise spectrum at a single frequency. We can then write

$$-\ln C(\tau) \approx \frac{1}{\pi}\tau S(\omega)\,, \tag{1.57}$$

from which $S(\omega)$ can be reconstructed directly from the decoherence curve.

While the spectral noise formulation is a powerful tool for understanding and mitigating incoherent contributions to the NV center coherence, it does not capture coherent dynamics between the NV center and its environment. These dynamics are ubiqutious when considering interactions between the NV center nuclear spins, are naturally understood in the framework of Nuclear Magnetic Resonance (NMR). Indeed, one of the primary technological aspirations for NV centers is to use them as nanoscale NMR sensors that can sense small quantities of materials[341,124] or elucidate the structure of target molecules[226,316]. In several chapters of this thesis, we use NMR measurements of protons, on the diamond surface to determine the depths of NV centers as depicted in Fig. 1.15[279].

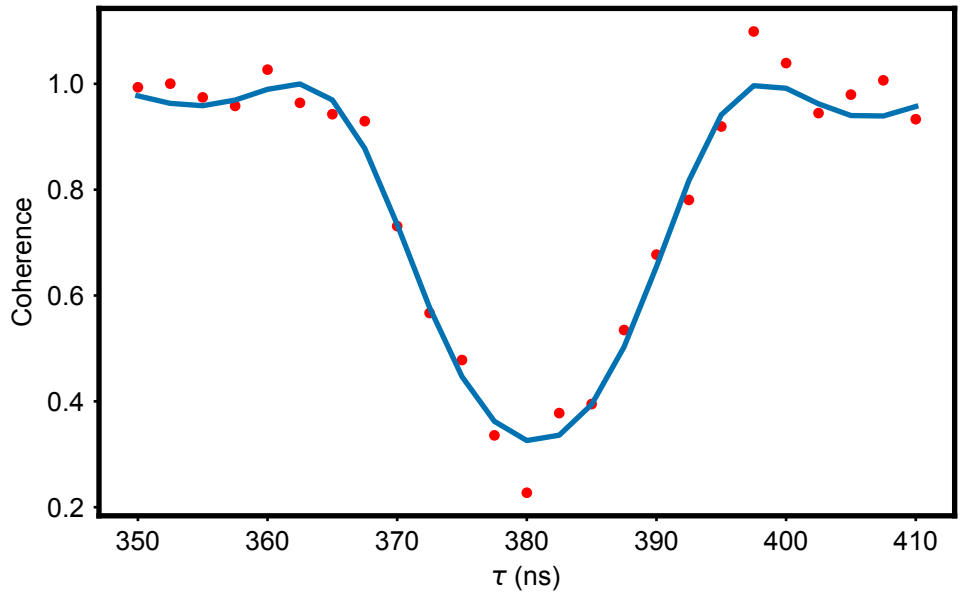


Figure 1.15: NMR signal from protons. Typical NMR signal for a shallow (5 nm) deep NV center. τ is the time between π pulses in a 43 pulse XY-8 sequence. Red points are data, blue is a fit from Ref.[279].

1.3.5 Spin lock

Spin locking is a technique that is used for sensing purposes as well as for polarization transfer [144,310]. For sensing it can be thought of as the continuum limit of dynamical decoupling, and it bridges the frequency gap between the previously discussed sensing techniques and T_1 relaxometry, which will be discussed in the following section. In a spin lock sequence, the NV center spin is tilted onto the equator of the Bloch sphere and a strong drive is applied 90° out of phase with the initial pulse. This results in rapid precession around a new axis. During the "lock" part of the sequence, the NV center is in the dressed state basis

$$|\pm\rangle = \frac{1}{\sqrt{2}} \left(|m_s = 0\rangle \pm |m_s = 1\rangle \right) , \tag{1.58}$$

and the splitting between the two dressed states is given by the microwave drive strength, Ω [225]. If this energy splitting is tuned on resonance with another transition, such as that of ^{13}C spins in the diamond, the two systems become coupled and undergo joint dynamics. By returning the NV center to the $\{|m_s = 0\rangle , |m_s = 1\rangle\}$ basis with a final $\pi/2$ pulse, these dynamics can be observed. The decay of NV coherence during a spin lock, called T_1^ρ, provides information about the incoherent environment of the qubit since it is sensitive to noise at the dressed state splitting Ω. While Ω can theoretically take on arbitrarily large values, it is limited to $\sim$ 10s MHz by experimental considerations such as heating from a strong microwave drive.

1.3.6 T_1 relaxometry

A final distinctive form of sensing that may be employed using NV centers is the measurement of increased spin lattice relaxation rates ($1/T_1$) near certain materials, which is sometimes called "relaxometry" [197]. This is an incoherent (e.g. noise) sensing technique, but it is simple to employ and works at generally higher frequencies than T_2 sensing techniques. The NV center is simply prepared

in a definite spin state (usually $m_s = 0$ through optical pumping) and the spin state is read out some time later. The decay rate from a spin polarized to a mixed state is thus measured.

In bulk diamond, NV center T_1 times are very long (several milliseconds), even at room temperature [173]. As has been previously discussed, the nuclear spin environment of diamond is relatively clean, and direct flips with nuclear spins are anyways suppressed due to the large difference in g factors. T_1 relaxation of NV centers is primarily a phonon driven process, however, due to the orbital nature of the NV center ground state wavefunctions (e.g. orbital singlets, see Sec. 1.3.2), phonons have a weak effect on the ground state spin. Additionally, due to the low phonon occupation at the ground state spin splitting energy, the spin flip is dominated by multiphonon processes with higher energy phonon modes. At moderate and low temperatures, spin relaxation seems to occur due to the occupation of localized modes a the defect center site (an Orbach process [288]), with relaxation rate scaling with temperature as

$$\frac{1}{T_1} \propto \frac{1}{e^{\Delta/k_B T} - 1}, \tag{1.59}$$

where Δ is an activation energy measured to be $\approx$70 meV [173]. Experiments have shown that this transitions to a T^5 scaling at higher temperatures ($>$ 300 K) [173], indicative of a dominant two phonon Raman process [373]. At very low temperatures ($\lesssim$ 30 K), the local spin environment (e.g. nitrogen impurities) can cause T_1 to saturate [173,262] but in clean samples this does not occur. T_1 ultimately places an upper limit on the coherence time (and hence, sensitivity) of NV centers[6]. While a slowly varying noise bath can in principle be decoupled from, truly stochastic processes that cause spin flips cannot. The phonon occupation can be lowered by cooling the diamond to cryogenic

[6] Specifically, $T_2 < 2T_1$ [329]. This is somewhat counterintuitive, but the limiting case occurs only for noise that is primarily transverse. For NV centers it is typically true that $T_2 < T_1$. Furthermore, while it is common practice to think of an NV center spin as a qubit, ignoring the spin-1 nature of the defect, one should be careful in defining what is meant by T_1 in this case as transitions between $m_s = +1$ and $m_s = -1$ can complicate the picture, see Ref. [255].

temperatures. Recent low temperature experiments have pushed NV center T_1 times to nearly 8 hours, limited by the direct single phonon process [15].

If relaxometry were only a probe of phonon occupation of the diamond lattice it would be of limited use for sensing. The NV center spin is additionally sensitive to noise at the $m_s = 0 \leftrightarrow m_s = \pm 1$ transition energy ($\sim$ GHz), which can be varied by application of an external magnetic field. Many systems of interest produce noise in this frequency range, which will affect the relaxation rate of a nearby NV center.

Since this is an incoherent decay rate, it can be calculated using Fermi's Golden Rule[7]:

$$\Gamma_{i\to f} = \frac{1}{T_1} = \frac{2\pi}{\hbar} |\langle f|V|i\rangle|^2 \, \delta(E_f - E_i) \,, \tag{1.60}$$

where $|f\rangle(|i\rangle)$ and $E_f(E_i)$ are the final (initial) state and energy of the final (initial) state, respectively and V is the perturbation that connects these two states [307]. Transitions between $m_s = 0$ and $m_s = \pm 1$ are caused by magnetic fields [255], so we have

$$V = g_e \mu_B \vec{B} \cdot \vec{S} \,, \tag{1.61}$$

where $g_e = 2$ is the electron g-factor, μ_B is the Bohr magneton, $\vec{B}$ is the magnetic field vector and $\vec{S}$ is the vector of Pauli matricies. To evaluate this expression, we need to consider the initial and final

[7] This derivation closely follows that given by Henkel in reference [148] for atoms in traps, but the physics is the same for an NV center near a source of magnetic field noise.

states of both the spin and the field, and sum over all of these states. For the field states, we have

$$\sum_{f,i} p(i) \left| \langle f|\vec{B}|i\rangle \right|^2 \delta(E_f - E_i - \hbar\omega) \tag{1.62}$$

$$= \sum_{f,i} p(i) \langle i|B_j|f\rangle \langle f|B_k|i\rangle \delta(E_f - E_i - \hbar\omega) , \tag{1.63}$$

$$= \int_{-\infty}^{\infty} dt e^{i\omega t} \sum_i p(i) \langle i|e^{iE_i t/\hbar} B_j B_k e^{-iE_i t/\hbar}|i\rangle , \tag{1.64}$$

where $B_{j,k}$ are the components (x,y,z) of the magnetic field and i, f denote the initial and final states of the field. In the last line we make use of the completeness relation summing over the final states.

The environmental magnetic field is in principle a function of both space and time. The NV center has fixed coordinates, but the field at its location will change with time. In the interaction picture, we may write

$$B(t) = e^{iH_0 t\hbar} B e^{-iH_0 t/\hbar} , \tag{1.65}$$

where H_0 is the time independent part of the Hamiltonian with eigenenergies (eigenstates) given by $E_i, E_f (|i\rangle , |f\rangle)$. Substituting this into Eq. (1.62) yields

$$\int_{-\infty}^{\infty} dt e^{i\omega t} \sum_i p(i) \langle i|e^{iH_0 t/\hbar} B_j e^{-iH_0 t/\hbar} B_k|i\rangle = \int_{-\infty}^{\infty} dt e^{i\omega t} \sum_i p(i) \langle i|B_j(t) B_k(0)|i\rangle . \tag{1.66}$$

This is simply the definition of the magnetic field power spectral density (along various directions), $S_{j,k}(\omega)$. To find the spin relaxation rate, we sum over the different directions

$$\Gamma_{I\to F} = \frac{2\pi}{\hbar}(g_e \mu_B)^2 \sum_{j,k=x,y,z} S_{j,k}(\omega) \langle I \left| S_j \right| F\rangle \langle F|S_k|I\rangle , \tag{1.67}$$

where I, F now denote the initial and final states of the spin. This summation must be done carefully for a realistic experiment because NV centers in (100) cut diamond make a 54.7° angle with

the surface. The general result is extremely useful, however: the relaxation rate of an NV center is a measurement of the magnetic field power spectral density at the spin transition frequency! Near a metal, this magnetic noise comes from thermal fluctuations of electrons (Johnson noise) and hence the spin relaxation rate can be used to probe a material's conductivity (see Ref. [5] and Appendix C). This insight has been leveraged to probe ballistic electrons in high quality silver films [197] and as a method to non-invasively map conductivity on the nanoscale [11]. It is a unique conductivity measurement, as in addition to being local in real space, NV center relaxometry probes the *transverse* conductivity at a particular momentum, given by $k \sim 1/d_{\mathrm{NV}}$ (see Ch. 4). This property of NV centers to filter out different electron momenta at different depths has been proposed as a method to investigate various electron transport regimes in conductors, including exotic hydrodynamic electron flow in graphene [5]. In Ch. 4, we use this method to explore the spatial dependence of a large population of phonons that cause electronic noise through scattering.

1.3.7 Electric fields

While the majority research on NV centers as sensors has focused on measuring magnetic signals, they can in principle be used to sense electric fields as well. The sensitivity to electric fields is considerably lower, at least in the ground state. From eq. (1.10), we can see that while magnetic fields split the spin states by 2.8 MHz/Gauss, electric fields cause a splitting of 17 Hz·cm/V at most. This small response to electric fields is again due to the symmetry of the NV center ground state, which is an orbital singlet with no electric dipole moment. In fact, the only reason that the NV center ground state displays any electric field response is due to a small admixture of excited state character in the ground state wavefunction [91]. This mixing comes from spin-orbit coupling ($\lambda_\perp$), and so the ground state dipole moment, d_{gs}, is approximately

$$d_{gs} \propto \frac{\lambda_\perp}{\Delta E} d_{es}\,, \tag{1.68}$$

where d_{es} is the excited state dipole moment and ΔE is the energy of the optical transition between the ground and excited states (1.95 eV). The excited state dipole moment is thought to be several MHz·cm/V, which is comprable to trapped atoms[91].

In addition to having a relatively weak response to electric fields, the way in which electric field enters the Hamiltonian in Eq. (1.10) means that the eigenstates are more complicated than for magnetic fields alone. In particular, in the presence of significant electric fields, the eigenenergies depend strongly on the orientation of the magnetic field. Using second order perturbation theory, the energy splitting between the $m_s = 0$ and $m_s = \pm 1$ states can be shown to be[92]

$$\hbar\omega_{\pm} = d_{\parallel}E_z \pm \left(F(\vec{B},\vec{E}) - F(\vec{B},0)\right) , \tag{1.69}$$

where

$$F\left(\vec{B} = (B_{\perp}, B_z), \vec{E} = (E_{\perp}, E_z)\right) = \left[(\mu_B g_e B_z)^2 + (d_{\perp}E_{\perp})^2 - \frac{\mu_B^2 g_e^2}{\Delta} B_{\perp} d_{\perp} E_{\perp} \cos\left(2\varphi_B + \varphi_E\right) + \frac{\mu_B^4 g_e^4}{4\Delta^2} B_{\perp}^4\right]^{1/2} , \tag{1.70}$$

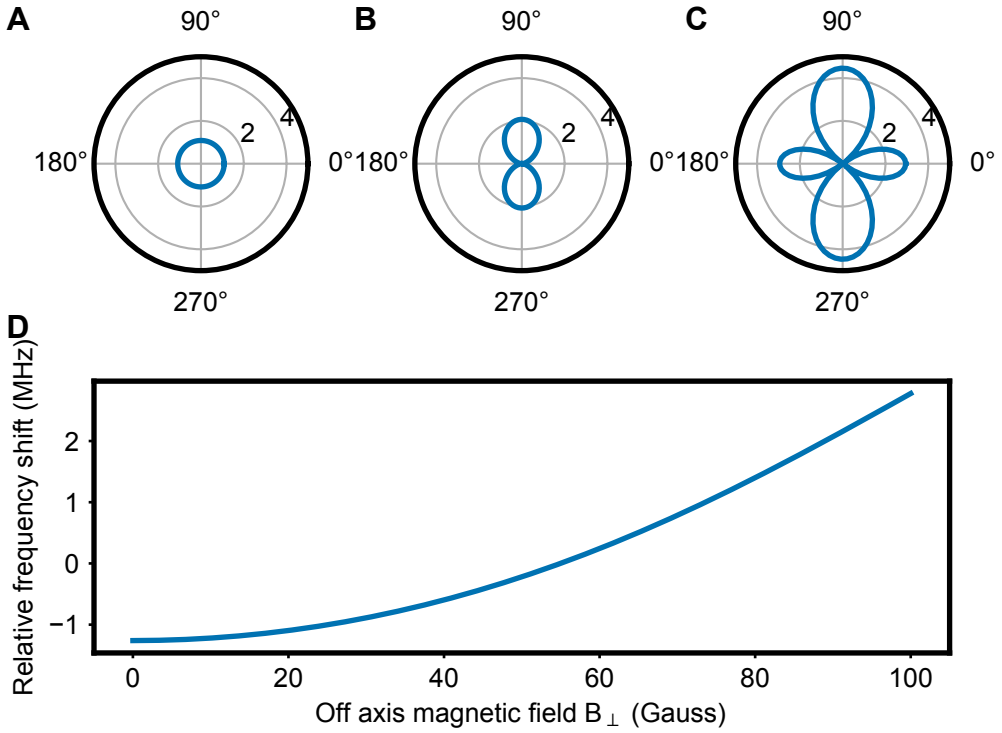


Figure 1.16: NV center electric field sensitivity. (A)-(C): Simulated electric field induced frequency shift for $m_s = -1$, plotted in polar coordinates as a function of φ_B. $E_\perp = 500$ kV/cm, $B_z = 10$ Gauss. $|B_\perp|$ has values of 0 Gauss (A), 50 Gauss (B), and 100 Gauss (C). Radial scale is in MHz. (D) Relative frequency change for $E_\perp = 500$ kV/cm for different strengths of $|B_\perp|$. $B_z = 10$ Gauss.

The angles $\tan\varphi_E = \frac{E_y}{E_x}$ and $\tan\varphi_B = \frac{B_y}{B_x}$ introduce a complicated four-fold dependence to the electric field sensitivity, as varying the magnetic field angle in the presence of a constant electric field will also change the splitting (see Fig. 1.16A-C). While E_z gives a constant offset to both eigenenergies, the sensor can be made more sensitive to $E_\perp$ by applying a large off axis magnetic field (that is, making $B_\perp \gg B_z$), which helps to mitigate the normally low sensitivity to electric fields (see Fig. 1.16D). By carefully controlling the magnetic field alignment and using AC sensing techniques, experiments have demonstrated an electric field sensitivity of ≈ 200 V cm^{-1}Hz^{-1} [92]. This

corresponds to the field produced by a single electron 150 nm away[64], but it is still orders of magnitude less sensitive than competing devices, such as single electron transistors[87]. A more promising approach to external electric field sensing uses the optical transition to the excited state, which as was already mentioned is very sensitive to electric fields[42]. This measurement method is complicated by the need for cryogenic temperatures, broadening of the optical transition in prepared diamond[368], and spectral diffusion of the optical transition due to charge hopping in the local environment[328,381].

Strain sensing, that is, using the NV center to measure its own local lattice distortion, is essentially an electric field sensing technique. While in Eq. (1.69) and Eq. (1.70) we have considered the case of zero strain, in reality all NV centers experience some distortion in the lattice around them. This distortion is felt as an additional electric field term ($\vec{\sigma}$), which is often simply added to the externally applied electric field to obtain a total field: $\vec{\Pi} = \vec{\sigma} + \vec{E}$[8]. This sensitivity to strain has been used to drive spin transitions mechanically[215], as well as to image pressure and magnetic field simultaneously in high-pressure diamond anvil cells[159]. Since temperature also results in expansion and contraction of the lattice, NV centers have been used to measure temperature in this way, most notably inside of living cells[204,66].

[8] While this treatment is common in the literature, it assumes that all in-plane stress is the same, which is not necessarily true. More generally, strain needs to be treated as a tensor, and there are four susceptibility parameters rather than just two. See Ref.[27]

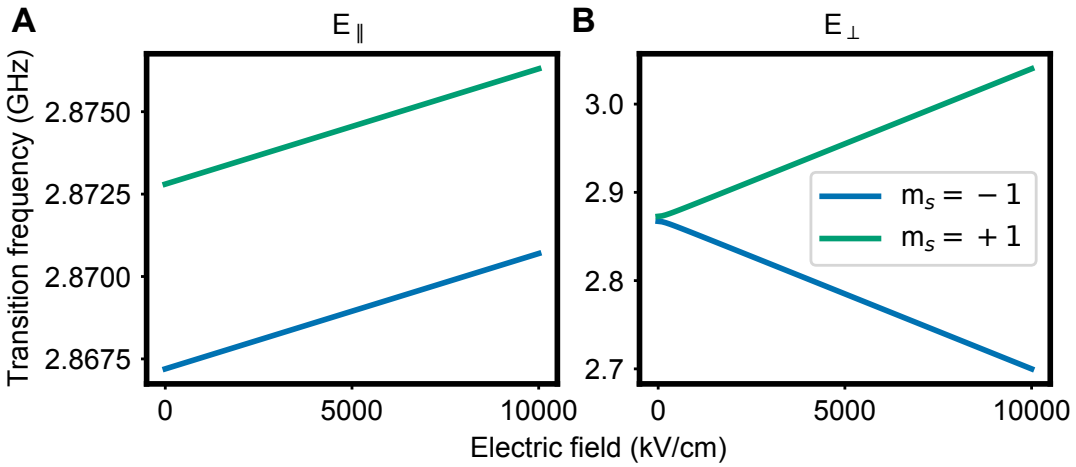


Figure 1.17: Response of $m_s = \pm 1$ splittings under electric fields. A field can be applied parallel ($E_\parallel$, (A)) or perpendicular ($E_\perp$, (B)) to the NV quantization axis. B_z = 1 Gauss to avoid overlap of the two frequencies in (A). Note the different scales of the y axes.

While the electric field sensing prospects of NV centers are somewhat limited, the way in which the transition frequencies respond to electric fields compared to magnetic fields often possible to differentiate between the two in order to determine the origin of an unknown signal. For example, in Fig. 1.17, it is apparent that, unlike magnetic fields, electric fields along the NV axis ($E_\parallel$) shift the $m_s = \pm 1$ states in the same way. This makes it possible to construct pulse sequences using a superposition of $m_s = \pm 1$ spin states that is sensitive only to electric fields ($|\pm\rangle = |-1\rangle \pm |+1\rangle$). Comparing the decoherence of qubits defined in the $\{|\pm\rangle\}$ basis to decohernce in the conventional $\{|0\rangle, |\pm 1\rangle\}$ can shed light on whether the dominant decohernce mechanism comes from electric or magnetic field noise[44].

Similarly, since electric fields drive transitions between $|+1\rangle \leftrightarrow |-1\rangle$ (see the $S_\pm^2$ terms in Eq. (1.10)), by measuring the relaxation rates between $m_s = +1$ and $m_s = -1$ (so called "double quantum" relaxaometry) it is possible to tease out the electric and magnetic field contributions to the T_1 decay[255,120]. We will make use of this technique in Ch. 2 to analyze the relative electric and

magnetic field contributions to the decoherence of near surface NV centers.

Finally, it is also possible to differentiate electric from magnetic field effects by comparing measurements in the $\{|0\rangle, |+1\rangle\}$ basis with the $\{|0\rangle, |-1\rangle\}$ basis. Again, for a magnetic field aligned axially along the NV center quantization axis, $E_{\parallel}$ causes a frequency shift in the same direction for both qubit states, while B_z will cause them to move oppositely. This phenomenon is shown in Fig. 1.17. In Ch. 5, we will employ this method to understand the origins of signals at different locations in a graphene field effect transistor.

1.3.8 Sensitivity

Even if an NV center's spin state can be read out in a single experimental sequence (called "single shot" readout), enough measurements will still need to be accrued to overcome spin projection noise before a signal is detected. This presents a natural way to define the sensitivity of a quantum projection noise limited sensor: the sensitivity is the field at which the size of the signal is equal to its uncertainty, or the signal-to-noise ratio (SNR) is 1. Since we measure in the S_z basis, this means

$$\delta \langle S_z \rangle = \sqrt{\langle S_z^2 \rangle - \langle S_z \rangle^2}, \tag{1.71}$$

where $\langle X \rangle$ denotes the average of a set of N measurement outcomes of the observable X. A Ramsey magnetometry sequence has an expectation value of

$$\langle S_z \rangle = \hbar \cos\left(\gamma_e B \tau\right), \tag{1.72}$$

where τ is the total measurement time. Since $\langle S_z^2 \rangle = 1$, Eq. (1.71) simplifies to

$$\delta \cos \gamma_e B\tau = \sqrt{1 - \cos^2 \gamma_e B\tau}\,, \tag{1.73}$$

$$= \sin \gamma_e B\tau\,. \tag{1.74}$$

but $\delta \cos \gamma_e B\tau = -\sin\left(\gamma_e B\tau\right) \gamma_e \tau \delta B$, so

$$\delta B = \frac{1}{\gamma_e \tau}\,. \tag{1.75}$$

This is actually the same result that is obtained for sine magnetometry, since the cosine term in Eq. (1.73) is replaced with a sine and again the trigonometric terms cancel.

For N independent and uncorrelated measurements of the sensor, the variance of the mean shrinks. This means that the standard deviation of the spin signal is reduced by $\frac{1}{\sqrt{N}}$, or, for N measurements of length τ for a total measurement time T, we should reduce Eq. (1.75) by a factor of $\sqrt{\frac{\tau}{T}}$, so that the minimum field is given by

$$\delta B = \frac{1}{\gamma_E} \frac{1}{\sqrt{T\tau}}\,. \tag{1.76}$$

Sensitivity, η is related to the minimum detectable field by[350]

$$\eta = \delta B \sqrt{T}\,, \tag{1.77}$$

so the sensivitity for a single NV center is

$$\eta = \frac{1}{\gamma_e} \frac{1}{\sqrt{\tau}}\,. \tag{1.78}$$

Since the time for an individual measurement is limited by the decay of the spin coherence, $\tau_{\max} = T_2$ for a spin echo sequence or $\tau_{\max} = T_2^*$ for a Ramsey sequence. Hence a great deal of work has gone into improving this parameter in near surface NV centers, which are most useful for sensing (see Ch. 2).

There are other ways to improve the sensitivity. The most straightforward way is to increase the number of NV centers (N_{NVs}) that are independently measured. The variance of the mean field again shrinks by N_{NVs}, so the sensitivity is improved by $\frac{1}{\sqrt{N_{\text{NVs}}}}$:

$$\eta = \frac{1}{\gamma_e} \frac{1}{\sqrt{\tau N_{\text{NVs}}}}, \tag{1.79}$$

which is known as the standard quantum limit (SQL).

Ensemble diamonds, in which many NV centers occupy a single diffraction limited spot, are often used for sensing for this purpose. The high density of NV centers comes at a cost, however: more NV centers means more nitrogen must be implanted, and this leads to more defects such as P1 centers and multivacancy clusters. These additional defects lead to increased environmental noise and a reduction in coherence, so techniques to obtain high densities of NV centers without introducing significant environmental spins are of great interest. Electron irradiating diamond before annealing, for example, can increase the conversion efficiency of $N \rightarrow NV$ for a given dose of nitrogen. For high enough NV densities, interactions between NV centers will limit the ensemble coherence time[203,68]. Additionally, since there are four orientations of NV centers in an ensemble diamond, there is significant background from the orientations not being used for sensing, but there has been some promising work on growing NV centers with a preferential orientation as well[247,277]. The different orientations do allow for vector reconstruction of the magnetic field, which is a somewhat unique feature of NV center sensing[214].

The expression in Eq. (1.79) is not a fundamental limit to sensitivity. The $\frac{1}{N_{\text{NVs}}}$ arises from a col-

lection of uncorrelated measurements, but it is possible to engineer correlations between sensors that break the standard quantum limit. For a collection of N_{NVs} NV centers that have been appropriately entangled, the sensitivity instead saturates at the so-called Heisenberg limit

$$\eta = \frac{1}{\gamma_e} \frac{1}{\sqrt{\tau N_{\mathrm{NVs}}}} \,. \tag{1.80}$$

While there are many proposed schemes for achieving a Heisenberg limited sensitivity[68], all are hindered by the difficulty of entangling NV centers as it is challenging to engineer interactions between multiple centers.

Typical experiments operate far from the projection noise limit as NV center spin state readout is generally not single-shot. Below we review some common readout techniques and compare them to the single-shot case to get a sense of real-world sensitivity.

1.3.9 Readout techniques

There exists a vast number of readout techniques for the NV center spin, a review of which can be found in Ref. [156]. Here we present a brief review of some of the more commonly employed strategies.

In order to gauge the effectiveness of different schemes, one can compare each to the spin projection noise limit and calculate the factor, σ_R, by which the projection noise limit is exceeded. Since the spin projection noise is the square root of a variance, a technique that provides $\sigma_R = 2$ will take $4\times$ as much averaging to reach the same sensitivity as a technique in which the readouts are single-shot.

Resonant readout

The NV center is essentially an atom with reduced symmetry, and so its state may be determined by probing the optical transitions between a ground and excited state using a laser tuned to the transition frequency. In particular, at low temperatures ($\approx 8K$), the E_x and A_1 excited state transitions are frequency resolvable[296]. For low strain diamonds, spin mixing in the excited state is suppressed so the E_x transition keeps the spin in the $m_s = 0$ manifold, while A_1 transitions keep the spin in $m_s = \pm 1$ for a large number of optical cycles[348]. By tuning a laser to the E_x transition and collecting photons, the spin state is determined to be $m_s = 0$ if a large number of photons are collected and $m_s = \pm 1$ otherwise. Due to the high refractive index of diamond and the finite probability of a spin flip in the excited state, fabricated nanostructures are employed to collect sufficient photons to make a spin state assignment with high fidelity[296,149]. Spin state readout fidelities $> 93\%$ are thus achieved in a single shot, and the spin state can also be initialized with 99.7% probability through optical pumping[296].

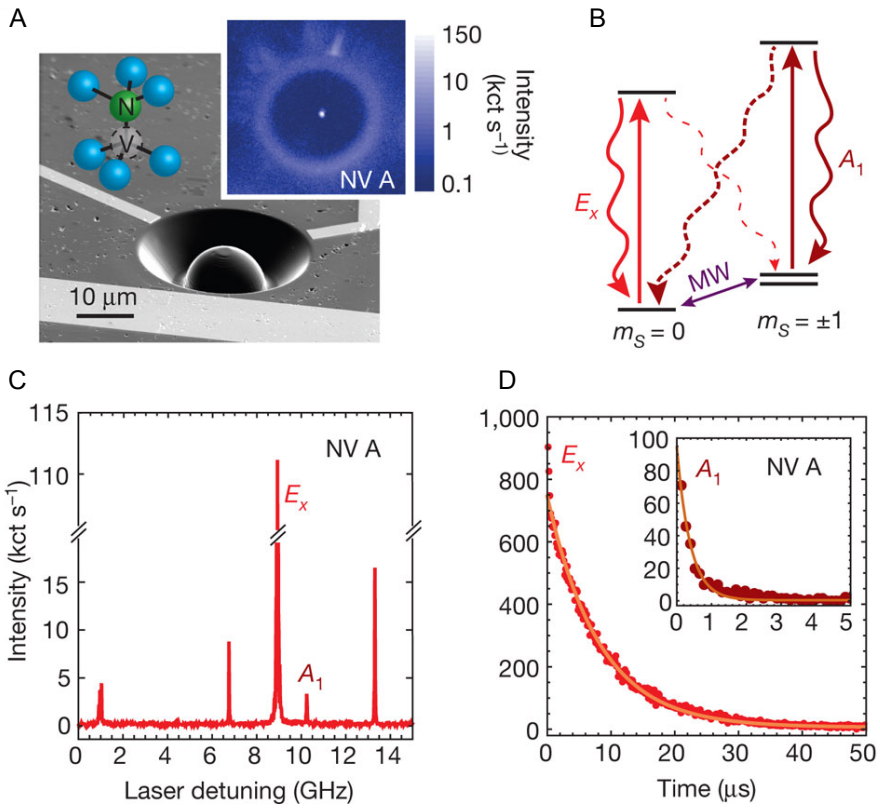


Figure 1.18: Resonant readout of NV centers. (A) SEM of nanostructured solid immersion lens used to increase collection efficiency in resonant readout experiment. (B) Simplified level structure showing the E_x and A_1 transitions used for spin pumping and readout. (C) Photoluminescence spectrum of an NV center taken while scanning the excitation laser frequency, relative to 470.443 THz. (D) Count rates from the E_x transition and A_1 transition (inset) as a function of readout duration. The decay is due to mixing between the excited states that results in non-cyclicity of the transitions. Figure taken with permission from Ref.[295].

While spin selective resonant readout is both accurate and efficient, it is not possible for many sensing applications. It cannot be used at elevated temperatures due to the significant broadening of the zero phonon line by lattice vibrations[112]. The need for a nanostructured diamond to increase collection efficiency is not compatible with all sensing environments. Perhaps most importantly, engineering NV centers with stable spin resolvable optical transitions is challenging. When an NV center is ionized by readout or initialization, the nearby charge environment changes as electrons are

moved between donors and acceptors. Upon recombination, the electric field environment of the NV center is subtly different, but since the excited state has a large dipole moment, the transition energy is now shifted randomly [69]. This spectral diffusion of the zero phonon line between measurements has made techniques reliant on coherent photons extremely difficult and has fueled the search for other diamond defects that do not posses such sensitivity to electric fields in the excited state [327]. In the more disordered environment typically found in implanted diamonds, nanostructured diamonds, or near surface NV centers, the optical linewidth may be extremely large ($\sim$ GHz) even for a single measurement due to enhanced electric field noise, which precludes resonant readout as a viable strategy. Some progress has been made in diamond fabrication to reduce this disorder [304], though it remains an outstanding issue for quantum technologies based on NV centers.

Off-resonant readout

Perhaps the primary reason for the popularity of NV centers as sensors in a variety of fields is that it is possible to initialize and read out the spin state with off-resonant light even under ambient conditions. This is by far the most commonly used readout method due to its simple implementation and broad range of operating conditions.

When the NV center is excited by off resonant light with energy higher than the excited state transition of 1.95 eV, the NV center is excited into a vibrationally excited state of the electronic excited state and undergoes rapid decay to the vibrational ground state [166,365]. While at low temperatures the electronic excited states are well separated and distinct, for temperatures $T > 22$ K they are rapidly mixed by phonons [297,126] and the averaged excited state can be treated as a ^3E spin triplet, orbital singlet system. Both the excitation process and orbital averaging are essentially spin conserving, however. As is depicted in Fig. 1.19, when the electron finally decays back to the ground state, it can either decay directly from the triplet excited state to the triplet ground state or it can nonradiatevly decay to a metastable singlet state (lifetime $\approx$ 300 ns [4]) before returning to the ground state

triplet. Amazingly, the branching ratio into the singlet manifold is $\approx 10\times$ higher for states with $m_s = \pm 1$ [125,156]. The fact that the singlet transition is non-radiative, in addition to the difference in lifetimes between the triplet excited state and the singlet means that over a set period of time, more photons will be emitted by an NV center with $m_s = 0$ than $m_s = \pm 1$. Perhaps more astonishingly, the intersystem crossing allows the spin to flip. Due primarily to the differing intersystem crossing rates of the $m_s = 0$ and $m_s = \pm 1$ states [294], with sufficient excitation cycles, spins are pumped into $m_s = 0$ with high probability. The fidelity of this spin pumping process has been estimated to be anywhere between 80% [294] and 90% [321]. This means that the NV center spin can be prepared and read out with a single, off resonant laser. Typically a 532 nm frequency doubled Nd:YAG laser is used since this is a higher energy than the excited state transition and such lasers are readily available. Many other wavelengths can in principle be used, so long as consideration is given to the ionization dynamics of NV^- and NV^0 [14].

While off resonant readout is technically straightforward, it is inefficient. A typical optimal readout time for an NV center is $\approx$ 300 ns (e.g. the singlet state lifetime), during which time $\approx$ 0.01 photons are collected, depending on the collection efficiency of the setup. This means that measurements are dominated by shot noise rather than projection noise, and many more measurement repetitions are required to even differentiate between the two spin states. If, during a read out window, α_0 photons are collected for an NV center with spin state $m_s = 0$ and α_1 photons are collected for an NV center with spin state $m_s = \pm 1$, then we can define a contrast, C as [350]

$$C = \frac{\alpha_0 - \alpha_1}{\alpha_0 + \alpha_1}. \tag{1.81}$$

The uncertainty in excess of the spin projection noise is then

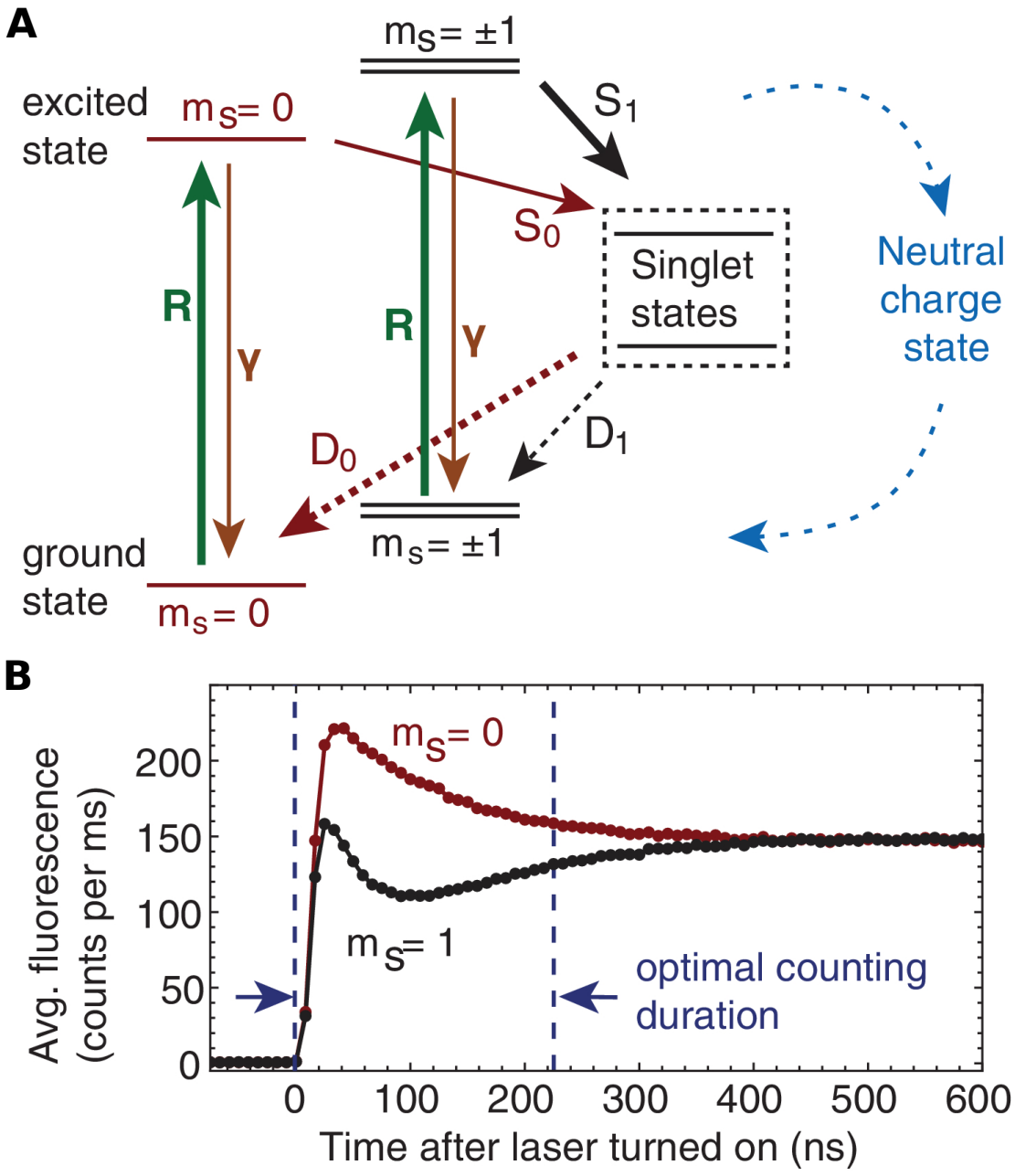
$$\sigma_R = \sqrt{1 + \frac{1}{C^2 \varepsilon}}, \tag{1.82}$$

where ε is the average number of photons collected per readout (e.g. $\varepsilon = (\alpha_0 + \alpha_1)/2$). For single NV center measurements, the contrast is typically $0.3 - 0.4$. This is limited by the branching ratios and lifetimes of the system rather than setup performance (although a high background will degrade the contrast, as is the case for ensembles). The collection efficiency can vary significantly between experiments, with ε ranging from about 0.01 for single NV centers in planar samples measured with an air objective to 0.3 for nanostructured diamond [321,2529]. Nanofabrication of diamond is extremely difficult due to diamond's hardness, chemical inertness, and anisotropic etching properties [380,158], and it is even more difficult to fabricate such structures and maintain good optical and spin properties of NV centers [291,304]. Even with the improved collection efficiency provided

[9] Due to the very high refractive index of diamond ($n = 2.4$) many emitted photons are internally reflected instead of exiting the diamond and being collected by the objective. Nanostructures utilize this high refractive index to guide emitted photons through a beam or pillar so that significantly more photons reach the collection objective.

Figure 1.19 *(following page)*: Off-resonand NV center spin readout. (A) Simplified level diagram showing relevant states and transitions for off-resonant readout and spin pumping. Both of these are enabled by the fact that the decay rate out of $m_s = \pm 1$ into the metastable singlet states (S_1) is greater than that of $m_s = 0$ (S_0). D_0 and D_1 are similar. (B) Photon count rate as a function of readout window time, showing the differing count rate from the two spin states that permits optical spin state readout. Figure taken with permission from Ref. [139].

Figure 1.19: (continued)



by nanostructures, $\sigma_R \approx 10$ [321]. Since most sensing sequences are relatively short ($\approx 100\,\mu$s sensing times), it is possible to perform sufficient measurements to overcome the excess SNR relatively rapidly, and this readout method remains among the most commonly used due to its simplicity.

Spin to charge conversion

There are actually two kinds of NV center: the neutrally charged NV^0 defect and the negatviely charged NV^-, which possesses an extra electron. Ionization and recombination of these defects can occur under sufficiently strong laser illumination, however, this process is thought to primarily occur once the NV center is already in its excited state. This, coupled with the different absorption spectra of the two defects, means that it is possible both to measure a defect's charge state and to selectively change it.

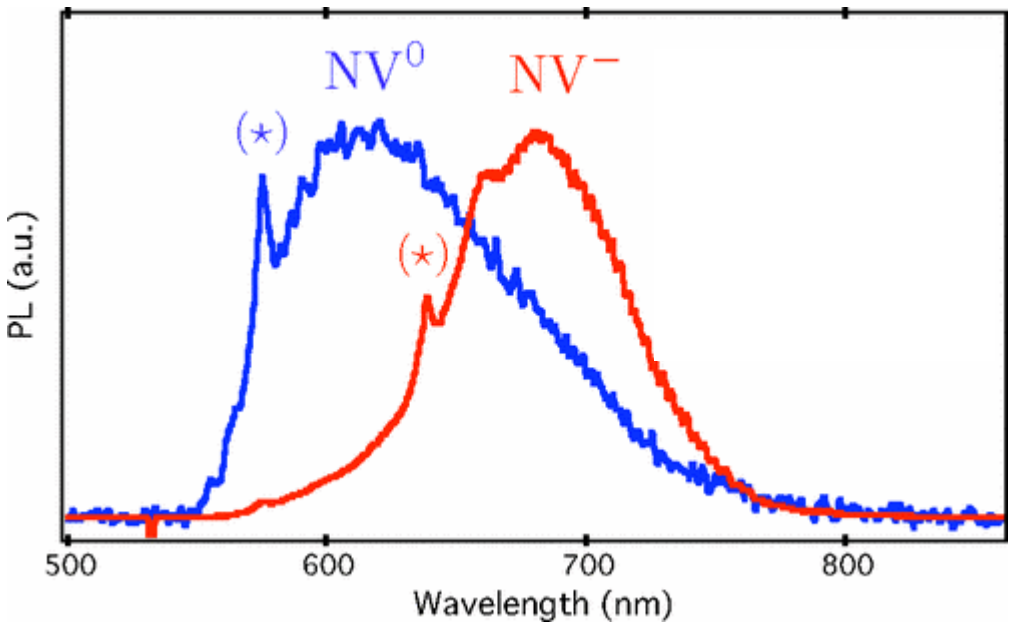


Figure 1.20: Emission spectra of the two charge states of the NV center. Since NV^0 has a higher energy zero phonon line than NV^-, it is possible to selectively excite NV^-. Figure taken with permission from Ref. [299].

The zero phonon line of NV^- is at $\lambda^- = 637$ nm, while for NV^0 it is at $\lambda^0 = 575$ nm[234]. The 532 nm laser that is typically used for spin polarization and readout can excite both defects, and once excited ionization and recombination can occur. The equilibrium charge state ratios under green illumination have been measured to be approximately $30 : 70$ NV^0:NV^-. By contrast, any wavelength $\lambda^0 < \lambda < \lambda^-$ will be able to excite NV^-, but not NV^0. Such a laser can be used to determine the charge state, since NV^0 will not emit photons under illumination. It can also be used to deterministically change NV^- to NV^0, since recombination occurs once the defect is already in the excited state. Since ionization/recombination is a two photon process, it has a quadratic power dependence, while count rate is linearly dependent on power. It is thus possible to select a power and measurement time for which charge state readout fidelity is high, but recombination probability is low. This can be accomplished with 589 nm light, as in Ref.[321], or, at low temperatures, using a tunable laser set to the resonant transition (ZPL) of a particular NV center[170]. Readout of the charge state can be done with extremely high fidelity > 97%[321].

The central breakthrough of Ref.[321] is that it is possible to map the spin state onto the charge state, which can then be read out in a single shot. This is accomplished by using the metastable singlet states to shelve, or protect, the NV^- center from recombination during an intense laser pulse. Since $m_s = \pm 1$ preferentially decays into the singlet state, subsequent charge state readout determines that the spin state was $m_s = \pm 1$ if NV^- is measured and $m_s = 0$ otherwise. This method can be used to reach excess SNR values of $\sigma_R = 2.76$, limited by the imperfect mapping of the spin state onto a charge state due to the branching ratio of excited $m_s = \pm 1$:$m_s = 0$ into the singlet state. The pulse sequence is illustrated in Fig. 1.21, using a laser resonant with the NV center ZPL at cryogenic ($\approx$ 70 K). At these intermediate temperatures, the ZPL absorption is enhanced, but it is still broader than the typical linewidth accounting for spectral diffusion so the laser frequency does not need to be swept.

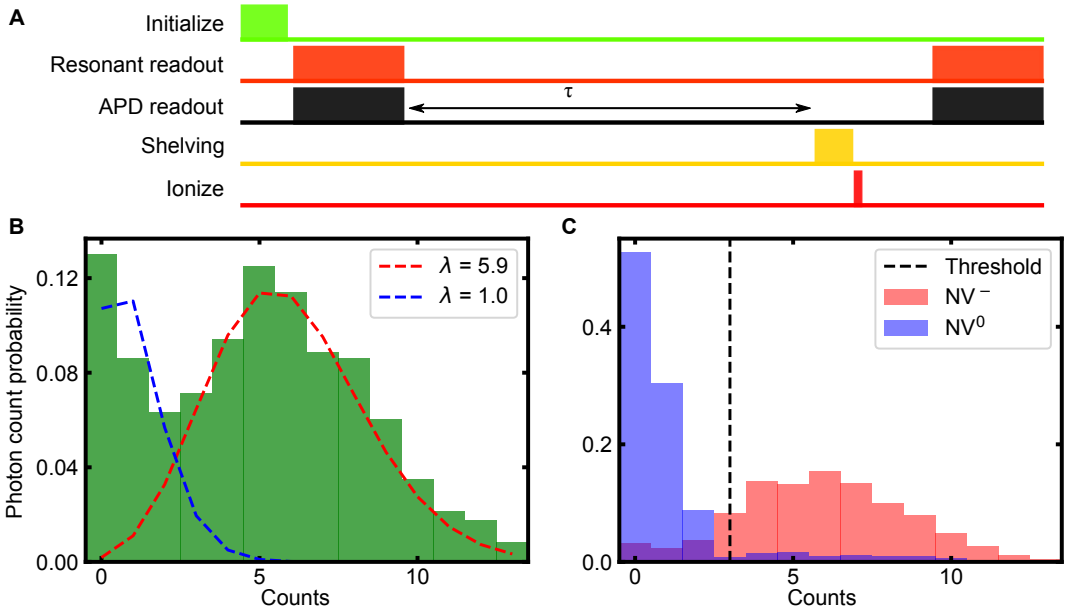


Figure 1.21: Spin to charge mapping. (A) Pulse sequence for a T_1 measurement using spin to charge conversion with resonant charge state readout. (B) Photon count distribution for readouts with the resonant 637 nm laser without any charge state initialization, showing a Poisson mixture distribution. The Poisson parameters for NV^0 and NV^- are given by λ^0 and λ^-, respectively. (C) Separated photon count distributions for NV^0 and NV^- under resonant excitation, separated using optimal thresholding during the initial charge state check readout.

Additional improvement can be achieved by increasing the probability of beginning an experiment in the correct (NV^-) charge state. Since 30% of initialization attempts with green light result in an unusable charge state, either fast electronics must be used to repeatedly attempt to initialize the NV center until the correct charge state is measured, or experiments that fail a charge state check must be eliminated in post selection for maximum readout fidelity[321]. Recently, it was discovered that simultaneous illumination with green and intense infrared light can shift the steady state ratios of NV^- and NV^0 to favor NV^- such that the correct charge state is initialized 90% of the time[154,243]. We have also observed a benefit of charge state initialization with this protocol, and even without tuning NV^- initialization fidelities exceeding 80% were achieved (see Fig. 1.22). This technique can also be applied in tandem with fast feedback electronics to achieve $>$ 99% charge

state initialization fidelity, but with less overhead[155]. Off resonant readout also benefits from such techniques, as the poor initialization fidelity of NV centers under a green laser alone essentially contributes background. In shallow NV centers, fast inter-conversion between NV^- and NV^0 is also thought to be responsible for observed low contrast under traditional readout since it scrambles spin state information during optical pumping and readout[392]. Stabilization of the charge state thus has positive impacts across many readout techniques.

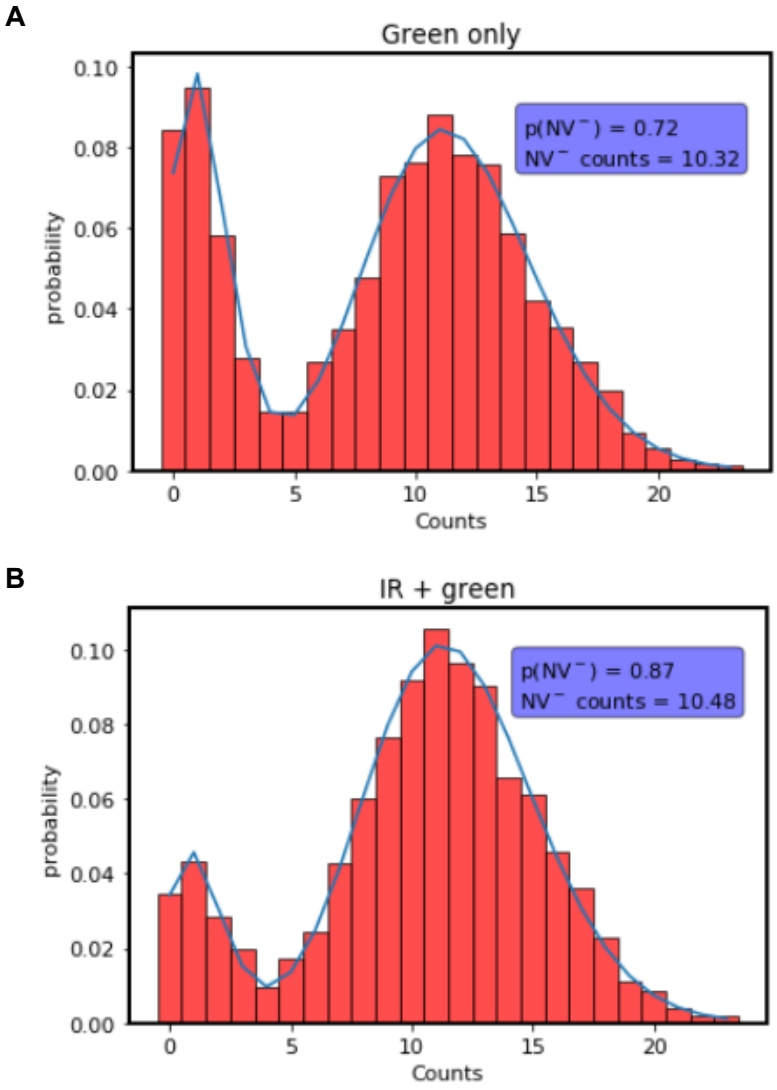


Figure 1.22: Photon count distributions for (A) 532 nm initialization only and (B) multicolor 532 nm + 850 nm initialization. The initialization probabilities are calculated by fitting the distributions to a Poisson mixture model, using the known NV^0 dark count rate.

Another technique for spin to charge conversion (SCC) attempts to ionize the NV center out of the singlet state rather than using this state for shelving[154]. The singlet state has a small absorption cross section in the infrared region, with a zero phonon line at 1042 nm[4]. With a very intense laser pulse at this wavelength, it is possible to excite the NV^- electron to the conduction band and

convert it to NV^0. In the technique developed in Ref. [321], the ionization pulse can be applied only once before charge state readout. This means that the spin to charge conversion efficiency is limited by the intersystem crossing rate of the $m_s = \pm 1$ states, which is only about 50% for an optical cycle [125]. Ionizing from the singlet state can be repeated many times before charge state readout, since it is not destructive to the unshelved states. In principle this technique could offer enhanced spin to charge conversion since it is limited by the 10:1 branching ratio of the different spin states, but the low absorption cross section of the singlet needs to be overcome [154].

Spin to charge conversion is relatively straightforward to implement in NV center experiments at the expense of some additional lasers. Nanostructures are not required, it works under ambient conditions and at cryogenic temperatures, and it has been demonstrated in shallow NV centers[10]. Without nanostructures, the readout window required for non destructive charge state determination can be lengthy, however, and this must be taken into account when calculating the sensitivity enhancement[11]. For short measurement sequences, the sensitivity enhancement without improved collection may be minimal. Additionally, the intense ionization pulse may harm sensing targets that are sensitive to high optical powers, though this step is of short duration (20 ns), so heating is minimal.

Nuclear spin repetitive readout

The final NV center readout technique that will be addressed was developed in Ref. [176]. Following a sensing sequence, the NV center electronic spin state is mapped onto an ancillary nuclear spin. The nuclear spin state is then repeatedly mapped back to the NV center, and the electronic spin state is read out by conventional means. Since the mapping of the nuclear spin state to the electronic

[10] This procedure has been used in the Lukin lab on other projects, but they were unpublished.

[11] In particular, the measurement time that enters into Eq. (1.76) is not $N\tau$, but $N(\tau + t_{\text{init}} + t_{\text{readout}})$. Thus a technique with a long t_{readout} like SCC is more appropriate for a measurement with a long τ, such as T_1 relaxometry.

spin, and subsequent optical readout, can be accomplished as a quantum non demolition measurement[259], sufficient statistics can be collected to overcome shot noise and determine the spin of the nucleus.

Nuclear spins make excellent quantum memories due to their $\approx 10^3\times$ lower gyromagnetic ratio compared to electrons[237]. Physically, this is because of the much larger mass of protons compared to electrons ($\approx 10^4$ ratio), since classically $\gamma \propto \frac{q}{m}$. In diamond, stochastically located ^{13}C atoms can be used as a quantum memory, but a more scalable approach is to use the host nitrogen of the NV center. This can be a spin-1 ^{14}N or the rarer spin $1/2$ ^{15}N. For laboratory created NV centers, this isotope can be chosen during ion implantation or delta doping. We will consider the ^{15}N example here as this was used in Ref.[226], but similar considerations apply to ^{14}N NV centers.

The ground state interaction between the NV center electronic spin and host nitrogen is given by Eq. 1.83. The parallel hyperfine interaction ($A_\parallel$) splits the $m_s = 1$ electronic state, since the electron feels an additional field from the nuclear spin in $m_N = \pm 1/2$ [12]. The perpendicular hyperfine interaction, $A_\perp$, permits flip-flop transitions between the electronic and nuclear spins. The hyperfine splitting of the electronic states permits nuclear spin dependent RF pulses: by applying a pulse at ω_+, the NV center spin is only rotated if the nuclear spin state is $m_N = +1/2$ etc. The $A_\perp$ term presents a challenge to nuclear memory schemes since it permits unwanted spin flips between the nuclear spin and the electronic spin, however in the ground state this issue can be mostly disregarded. Due to the large zero field splitting of the electron spin, even at low fields the states connected by an electron-nuclear flip-flop are far apart in energy ($\Delta \gg A_\perp$), and so the so-called "secular approximation" of NMR is approprate and we can disregard the off diagonal terms. This approximation would of course fail for $\Delta - \gamma_e B_z \sim A_\perp$. Additionally, the hyperfine coupling between the electron and nuclear spin is much larger in the excited state (60 MHz[113]) and the zero

[12] Of course both the $m_s = \pm 1$ electronic states feel this field from the nuclear spin, but we will assume these states have been split by an external field so that the qubit basis $\{m_s = 0, m_s = 1\}$ is being used for the remainder of this section

field splitting in the excited state is smaller ($\Delta_{ES} = 1420$ MHz[171]). There is a level anticrossing in the excited state (ESLAC) at $\approx$ 500 Gauss, and near this level anticrossing the secular approximation fails and spin flips between the electron and nuclear spin cannot be disregarded[13]. In order to isolate the nuclear spin from back action due to optical pumping cycles of the electron spin, it is preferable to apply a very large field along the NV axis to shift the excited state far from the level anticrossing and suppress spin flips[259]. The probability of a nuclear spin flip is what ultimately sets the limit on the number of readout cycles, and hence the sensitivity.

The repetitive readout protocol relies on the fact that, with a sufficiently weak RF pulse ($\Omega < A_{\parallel}$) and sufficiently long dephasing time ($1/T_2^* > \Omega$), a $C_n NOT_e$ gate may be performed by addressing only one of the hyperfine split electron spin transitions. A π pulse on this transition results in a rotation between $m_s = 0 \leftrightarrow m_s = \pm 1$ conditioned on the state of the nuclear spin. Applying an additional π pulse to the nuclear spin allows for a $C_e NOT_n$ gate as well. A SWAP gate can then be constructed using a sequence of CNOT gates: $C_e NOT_n$-$C_n NOT_e$-$C_e NOT_n$[226]. The sequence for repetitive readout based sensing is then depicted in Fig. 1.23. The NV center electron spin is polarized and a sensing sequence is performed. Before optical readout, a SWAP gate is performed with the nuclear spin, mapping the state $\alpha|0\rangle + \beta|1\rangle \rightarrow |0\rangle \otimes (\alpha|\uparrow\rangle + \beta|\downarrow\rangle)$. To read out the nuclear spin, a $C_n NOT_e$ gate (e.g. hyperfine resolved π pulse) is applied, giving the state $\alpha|0,\uparrow\rangle + \beta|1,\downarrow\rangle$. The electronic spin is then read out optically and reset into $|0\rangle$. While this readout collapses the nuclear superposition, additional $C_n NOT_e$ readout sequences can be applied to determine which state the nuclear spin collapsed to. With enough repetitions, the state of the nuclear spin, and hence the original state of the electron spin, can be determined with high fidelity. For 500 repetitive readouts, $\sigma_R = 5$ can be achieved[226], however with higher magnetic fields and more readout cycles, single shot readout of the nuclear spin is possible[259,13].

[13] Since the electron spin is polarized by optical excitation but can flip with the nuclear spin near the ESLAC, this also provides a convenient method for optically induced dynamic nuclear polarization [191]

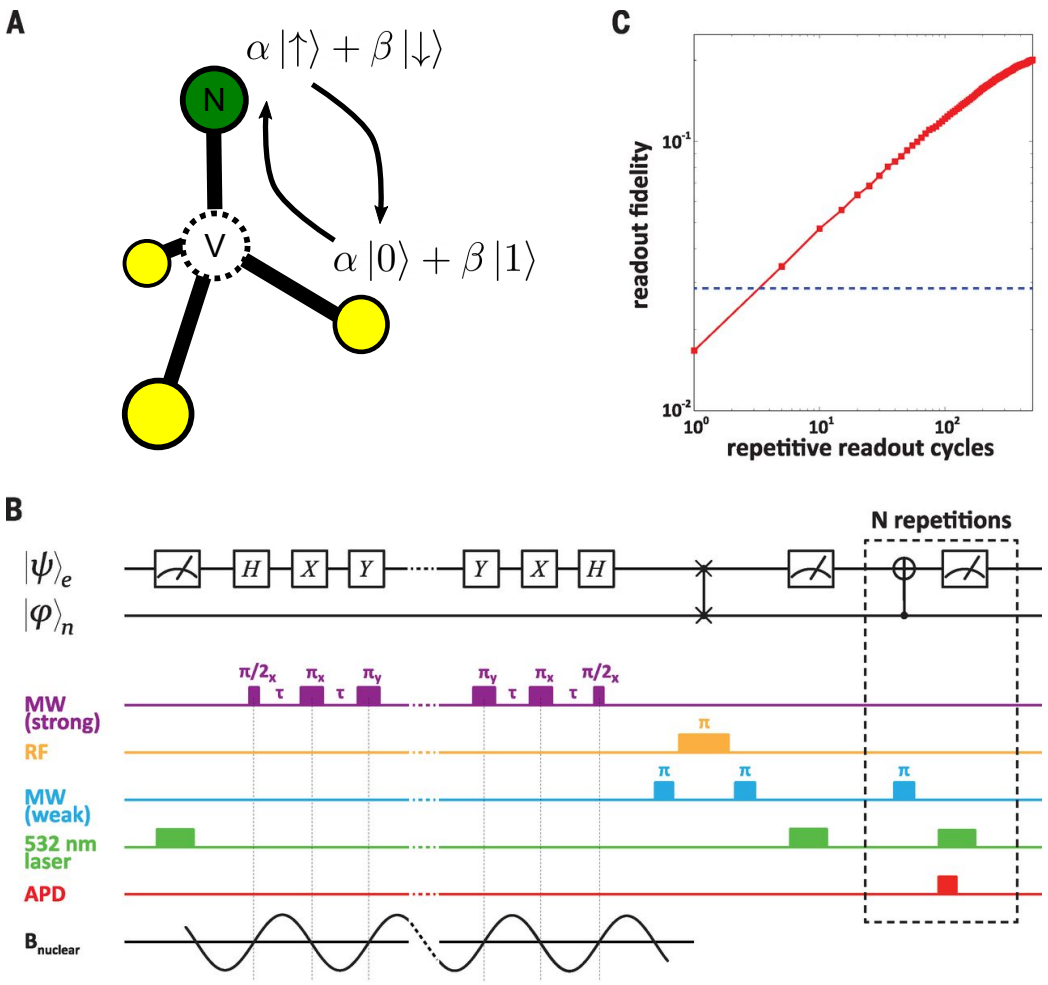


Figure 1.23: Nuclear spin repetitive readout. (A) Illustration of the concept behind repetitive readout of a nuclear spin memory, where the electronic spin state is mapped to the nuclear spin and the nuclear spin state is read out repeatedly. (B) Pulse sequence for sensing with nuclear spin enhanced readout. (C) Readout fidelity of the nuclear spin as a function of repetitions. Figures (B) and (C) taken with permission from from Ref.[226].

Control of the nuclear spin can be difficult to realize in some situations. It requires very strong microwave driving to achieve nuclear rotations on a reasonable ($\approx 10s\,\mu s$) timescale. A very high magnetic field is required, and this field must be carefully aligned with the NV center quantization

axis. This is challenging with permanent magnets, especially in a cryogenic environment, and vector magnets add significant cost and complication. Additionally, repetitive readout adds $\approx 1\mu$s per cycle to the total measurement time, and hence the improvement for shorter sensing sequences (such as T_2^* limited DC magnetometry) is not as large as for lengthy sequences[226].

1.3.10 Nuclear spin

Species	$\mathbf{A}_\parallel$	$\mathbf{A}_\perp$	$\boldsymbol{\gamma}_\mathbf{N}$	**Q**
^{14}N	-2.14 MHz	-2.70 MHz	3.077 MHz/T	-5.01 MHz
^{15}N	3.03 MHz	3.65 MHz	-4.316 MHz/T	0

Table 1.4: Nonzero values of the hyperfine coupling tensor ($\mathbf{A}$), nuclear spin gyromagneitc ratio (γ_N) and quadrupolar coupling (Q) for the two common nitrogen species. Values are taken from Ref. [102].

In writing Eq. (1.10), we have omitted the terms pertaining to the nuclear spin of the NV center. More completely, we should include the nuclear hyperfine term ($\mathscr{H}_{\text{HF}}$), nuclear Zeeman term ($\mathscr{H}_{\text{NZ}}$), and, in the case of ^{14}N, the nuclear quadrupolar term ($\mathscr{H}_{\text{NQ}}$), which are given by

$$\frac{\mathscr{H}_{\text{HF}}}{\hbar} = A_\parallel S_z I_z + \frac{A_\perp}{2}\left(S_+ I_- + S_- I_+\right), \tag{1.83}$$

$$\frac{\mathscr{H}_{\text{NZ}}}{\hbar} = \gamma_N \vec{B}\cdot\vec{I}, \tag{1.84}$$

$$\frac{\mathscr{H}_{\text{NQ}}}{\hbar} = Q I_z^2, \tag{1.85}$$

where $\vec{I}$ is the vector of nuclear spin matricies $\{I_x, I_y, I_z\}$, $A_\parallel$ and $A_\perp$ are the longitudinal and transverse hyperfine couplings, γ_N is the nuclear spin gyromagnetic ratio, and Q is the nuclear spin quadrupolar coupling. Numerical values for these terms are provided in Table 1.4 for the two most commonly found isotopes of nitrogen.

The nuclear spin of the NV center introduces complexity to sensing techniques, but it is also a valuable resource that can be leveraged as a long lived quantum memory (see, for example, Sec. 1.3.9). Here we will briefly cover some of the properties of the NV center electronic spin-nuclear spin system that are important for sensing applications.

1.3.11 Hyperfine splitting

The simplest contribution that the nuclear spin makes to the NV center electronic states is a splitting of the electronic state based on the state of the nuclear spin. The electron spin senses the tiny magnetic field due to the nuclear spin, which shifts it up or down in energy. More concretely, for small magnetic fields we may disregard the flip-flop term in Eq. (1.83) and the nuclear Zeeman term of Eq. (1.84), and in the Hamiltonian becomes

$$\frac{\mathscr{H}}{\hbar} = \Delta S_z^2 + \gamma_e B_z S_z + A_{\parallel} S_z I_z \,, \tag{1.86}$$

which, for a spin-1/2 ^{15}N NV center, has eigenenergies given by $\{\hbar\Delta \pm \gamma_e B_z + \frac{A_\parallel}{2}, \hbar\Delta \pm \gamma_e B_z - \frac{A_\parallel}{2}\}$. For ^{14}N nitrogen vacancy centers, the hyperfine interaction splits each electronic state into a triplet, as shown in Fig. 1.24.

One result of this splitting is that, for pulsed measurements, a strong drive is required ($\Omega_{\text{drive}} > A_{\parallel}$) to ensure that both hyperfine states are rotated (green curves in Fig. 1.24). In some pulse sequences, this splitting must still be taken into account. In a Ramsey sequence, for example, we begin with the NV center electron spin polarized and perform a $\frac{\pi}{2}_x$ pulse, resulting in the state[14]

$$\rho_0 = \frac{1}{2} - \mathcal{S}_y \,. \tag{1.93}$$

The relevant terms of the Hamiltonian in the rotating frame are

$$\frac{\mathscr{H}_{\text{RWA}}}{\hbar} = \delta(\frac{1}{2} + \mathcal{S}_z) + A_{\parallel}\mathcal{S}_z I_z \,. \tag{1.94}$$

The 1/2 contributes an energy offset which we ignore. Since the first and second term of Eq. (1.94) commute, we can apply the time evolution from each separately

[14] In this section and the one that follows, we will perform some calculations using the Product Operator Formalism from NMR, and to simplify calculations we will introduce the spin-1/2 Cartesian operators $\mathcal{S}_i = 1/2\sigma_i$, where σ_i are the Pauli matrices. This is done for normalization purposes so that

$$[S_x, S_y] = iS_z \,, \tag{1.87}$$
$$[S_y, S_z] = iS_x \,, \tag{1.88}$$
$$[S_z, S_x] = iS_y \,. \tag{1.89}$$

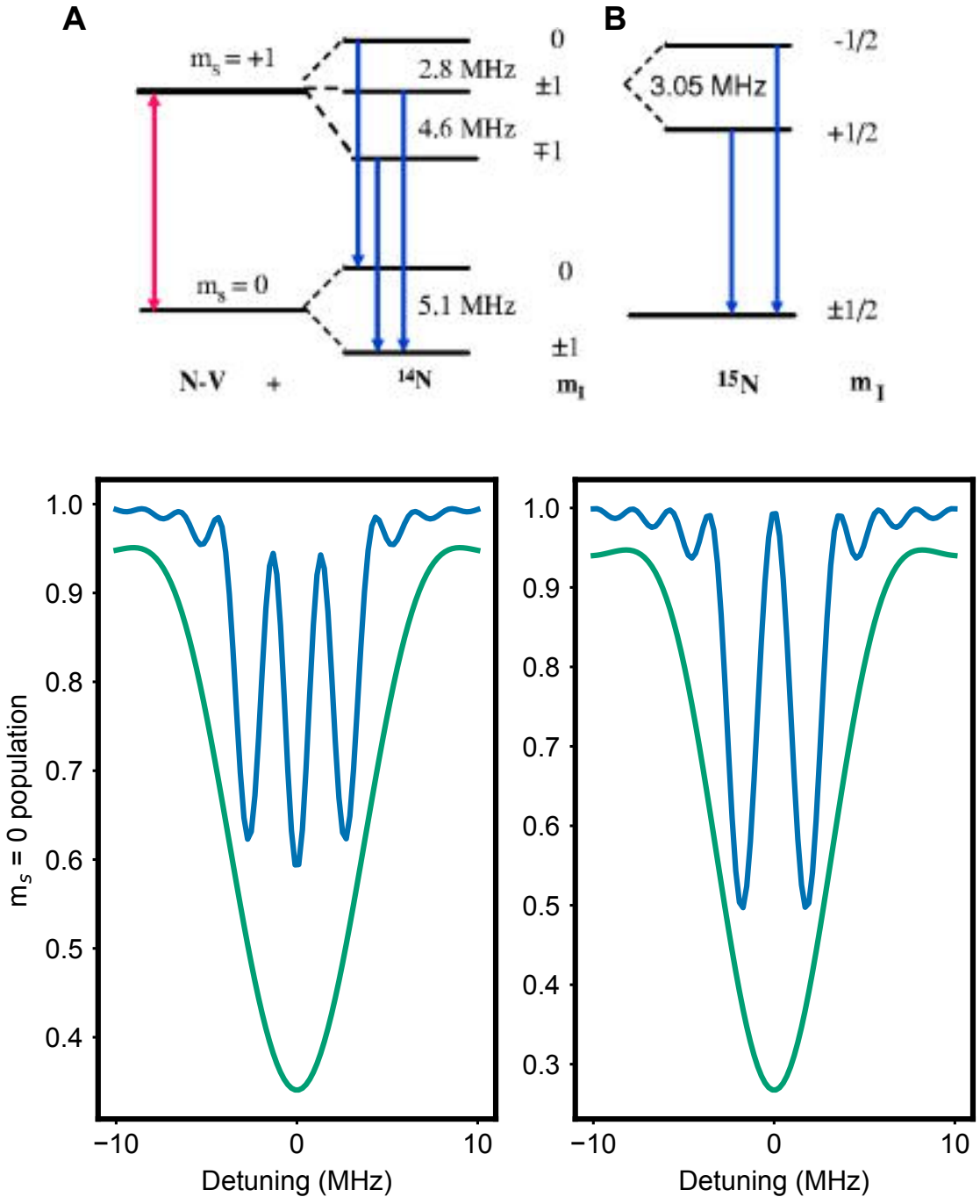
The spin-1 subspace of a single NV center transition can be written in terms of these operators as

$$S_z = \frac{1}{2} + \mathcal{S}_z(1/2) = \mathcal{S}^{\alpha}(1/2) \,, \tag{1.90}$$
$$S_y = 2\mathcal{S}_y(1/2) \,, \tag{1.91}$$
$$S_x = 2\mathcal{S}_x(1/2) \,. \tag{1.92}$$

Nuclear spin operators should be assumed to be the rotation generators for the given angular momentum (1/2 for ^{15}N and 1 for ^{14}N. For more information on the Product Operator Formalism, see Ref. [333] and Ref. [318].

Figure 1.24 *(following page)*: Hyperfine spectrum of the NV center. (A) Hyperfine transitions (top) and simulated ESR spectrum (bottom) for an NV center with a ^{14}N host nitrogen. (B) Same as (A), but for a ^{15}N host. Blue curves are simulations for a 2 MHz Rabi frequency, while green are for a 6.7 MHz Rabi frequency which displays power broadening over the hyperfine structure. Level diagram taken with permission from Ref.[286].

Figure 1.24: (continued)



$$\rho_0 \xrightarrow{\delta \mathcal{S}_z} \frac{1}{2} - \mathcal{S}_y \cos \delta t + \mathcal{S}_x \sin \delta t \,, \tag{1.95}$$

$$\xrightarrow{2\mathcal{S}_z I_z A_\parallel/2} \frac{1}{2} - \mathcal{S}_y \cos \delta t \cos \frac{A_\parallel}{2} t + 2\mathcal{S}_x I_z \cos \delta t \sin \frac{A_\parallel}{2} t + \mathcal{S}_x \sin \delta t \cos \frac{A_\parallel}{2} t + 2\mathcal{S}_y I_z \sin \delta t \sin \frac{A_\parallel}{2} t \,. \tag{1.96}$$

After some time, a final $\frac{\pi}{2}_x$ pulse sends $\mathcal{S}_y \rightarrow -\mathcal{S}_z$, at which point we measure the $m_s = 0$ population $\langle S_z \rangle = 1/2 + \langle \mathcal{S}_z \rangle$:

$$\begin{aligned} \langle \mathcal{S}_z \rangle =& \frac{1}{2} - \cos \delta t \cos \frac{A_\parallel}{2} t \\ =& \frac{1}{2} - \frac{1}{2} \left(\cos \left(\delta + \frac{A_\parallel}{2} \right) t + \cos \left(\delta - \frac{A_\parallel}{2} \right) t \right) \,, \end{aligned} \tag{1.97}$$

which means that the Ramsey measurement should contain two frequency components, oscillating at $\delta \pm \frac{A_\parallel}{2}$. A similar result is obtained for the case of ^{14}N, but the Product Operator Formalism applied to spins $> 1/2$ is more complicated. The spin-1 operators must be decomposed into an invariant term and a doublet that behaves similarly to the spin-1/2 case[333]. The result is that there are three frequency components: δ, $\delta + A_\parallel$, and $\delta - A_\parallel$. These frequencies can be clearly seen in Fig. 1.25. Since the purpose of a Ramsey sequence is to measure δ, the nuclear spin only complicates Ramsey measurements in that it results in multiple frequency components.

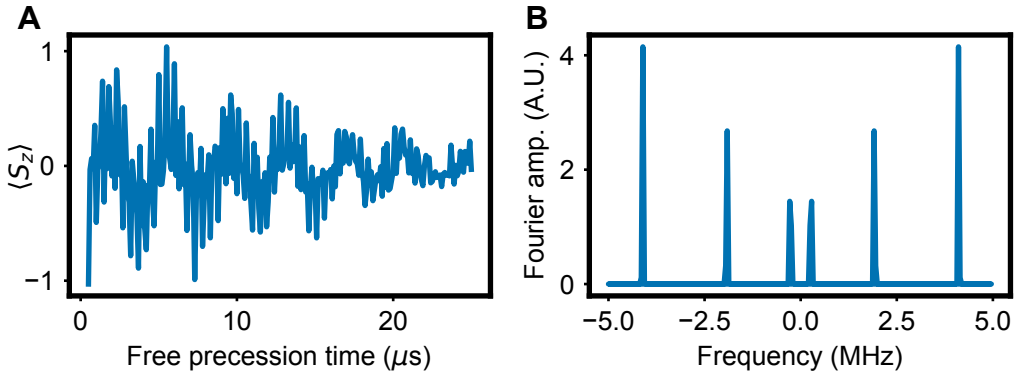


Figure 1.25: Hyperfine oscillations in a Ramsey measurement. (A) Ramsey dataset from a ^{14}N NV center, displaying modulation from the nuclear spin. (B) Fourier transform of (A), in which the three distinct frequencies are visible.

For spin echo type measurements, these oscillations are not encountered as the π pulse in the middle of the sequence ensures that all of the terms in Eq. (1.97) are canceled when equal time is spent in the first and second half of the sequence. To see this, we apply a π_x pulse to Eq. (1.96), which has the effect of sending $\mathcal{S}_y \rightarrow -\mathcal{S}_y$, and then allow the result to evolve under the same Hamiltonian for an equal time t. The result, after some algebra, is

$$\rho_f = \frac{1}{2} + \mathcal{S}_y \,. \tag{1.98}$$

which, after a final $\frac{\pi}{2}_x$ pulse, gives

$$\langle \mathcal{S}_z \rangle = 1 \,, \tag{1.99}$$

e.g. everything is refocused and there is no signal (except for possible coherence decay).

1.3.12 Field alignment and ESEEM

Another effect of the nuclear spin in magnetometry sequences is electron spin echo envelope modulation, or ESEEM [302]. This occurs primarily for ^{15}N nuclei when the externally applied magnetic

field is not aligned along the NV center quantization axis, as this effect is suppressed by the large quadrupolar splitting of ^{14}N. In a spin echo measurement, this causes precession of the nuclear spin along a tilted axis, which the NV center senses as a periodic change in precession frequency. More concretely, assuming a magnetic field that is fairly strong in the $\hat{z}$ direction, but has a small misalignment along $\hat{x}$, or $\vec{B} = (\delta B_x, 0, B_z)$, the Hamiltonian is

$$\frac{\mathscr{H}}{\hbar} = (\Delta + \omega_z)\,\mathcal{S}^{\alpha} + 2\omega_x \mathcal{S}_x + A_{\parallel}\mathcal{S}^{\alpha} I_z + 2A_{\perp}\left(\mathcal{S}_x I_x + \mathcal{S}_y I_y\right) + \omega_N I_z \tag{1.100}$$

Where we have written $\omega_z = \gamma_e B_z$, $\omega_x = \gamma_e \delta B_x$ and $\omega_N = \gamma_N B_z$. We have also dropped the nuclear zeman term along $\hat{x}$ because it is very small. Now we start trying to diagonalize $\mathscr{H}$. First we will eliminate the $\mathcal{S}_x$ term due to field misalignment using the unitary $U_1 = \exp -i\theta\mathcal{S}_y$, where $\tan\theta = \frac{-2\omega_x}{\Delta+\omega_z}$. This leads to

$$\begin{aligned} H_1 = U_1^{\dagger} H U_1 = \bar{\omega}\mathcal{S}_z + A_{\parallel}\left(\left(\frac{1}{2} + \mathcal{S}_z\right) I_z \cos\theta + \mathcal{S}_x I_z \sin\theta\right) \\ +2A_{\perp}\left(\mathcal{S}_x I_x \cos\theta - \mathcal{S}_z I_x \sin\theta + \mathcal{S}_y I_y\right) + \omega_N I_z\,, \end{aligned} \tag{1.101}$$

where $\bar{\omega} = \sqrt{(\Delta + \omega_z)^2 + 4\omega_x^2}$, and we have disregarded a constant energy term.

When we move into the rotating frame, terms that don't commute with S_z will rotate rapidly and we will disregard them. So the only other transformation we need to make before we take the RWA is the $\mathcal{S}_z I_x$ term, which still does not commute with the terms $\left(\frac{\cos\theta}{2} + \omega_N\right) I_z$ or with $\mathcal{S}_z I_z \cos\theta$. This motivates a second transformation $H_1 \xrightarrow{\xi I_y + \eta 2\mathcal{S}_z I_y} H_2$. This is a somewhat lengthy calculation, but it can be found in Ref. [164]. For a Hamniltonian of the form $H = A\mathcal{S}_z I_z + B\mathcal{S}_z I_x + C I_z$, the parameters are

$$\xi = -\frac{1}{2}\left(\tan^{-1}\frac{B}{A-2C}+\tan^{-1}\frac{B}{A+2C}\right), \tag{1.102}$$

$$\eta = \frac{1}{2}\left(\tan^{-1}\frac{B}{A-2C}-\tan^{-1}\frac{B}{A+2C}\right). \tag{1.103}$$

The Hamiltonian is now diagonalized in the $\mathcal{S}_z I_z$ basis as

$$H = -\frac{1}{2}\left(\omega_\alpha+\omega_\beta\right) I_z + \left(\omega_\beta-\omega_\alpha\right)\mathcal{S}_z I_z\,, \tag{1.104}$$

where

$$\omega_\alpha = \left(\left(C+\frac{A}{2}\right)^2+\left(\frac{B}{2}\right)^2\right)^{1/2}, \tag{1.105}$$

$$\omega_\beta = \left(\left(C-\frac{A}{2}\right)^2+\left(\frac{B}{2}\right)^2\right)^{1/2}. \tag{1.106}$$

It is somewhat more convenient to rewrite the Hamiltonian as

$$H = \frac{\omega^+}{2} I_z + \frac{\omega^-}{2}\mathcal{S}_z I_z\,. \tag{1.107}$$

Now we transform the density matrix, let it evolve under the diagonal Hamiltonian, and transform back into the Cartesian basis where we measure. The initial density matrix after spin initialization is given by

$$\rho_0 = \mathcal{S}^\alpha \otimes \frac{1}{2} I, \tag{1.108}$$

$$= \left(\frac{1}{2} + \mathcal{S}_z\right) \otimes \frac{1}{2} I, \tag{1.109}$$

where I is the 2x2 identity. We will drop the initial $\frac{1}{2}$ for simplicity, as it just carries through as a constant and we are most interested in the time dependent behavior of the spin sates. A $\frac{\pi}{2}_x$ pulse sends $\mathcal{S}_z \rightarrow -\mathcal{S}_y$. The U_1 rotation has no effect on this state, so we begin with the second transformation:

$$\rho_0 \xrightarrow{\xi I_y + \eta 2 \mathcal{S}_z I_y} -\cos\eta \mathcal{S}_y + \sin\eta \mathcal{S}_x I_y = \tilde{\rho}_0 \tag{1.110}$$

We have already seen that during a Spin Echo sequence, the $\mathcal{S}_y$ term is completely refocused, so we will omit it for the time evolution calculations. We let the $\mathcal{S}_x I_y$ term evolve under evolve under the I_z term in H for a time $\tau/2$:

$$\sin\eta \mathcal{S}_x I_y \xrightarrow{\frac{\omega^+ I_z \tau}{4}} \sin\eta \left(\mathcal{S}_x I_y \cos\left(\frac{\omega^+ \tau}{4}\right) - \frac{1}{2} \mathcal{S}_x I_x \sin\left(\frac{\omega^+ \tau}{4}\right)\right) = \tilde{\rho}_1 . \tag{1.111}$$

Then we evolve under the $S_z I_z$ term for a time $\tau/2$.

$$\tilde{\rho}_1 \xrightarrow{2\mathcal{S}_z I_z \frac{\omega^- \tau}{8}} \sin\eta \cos\left(\omega^+ \frac{\tau}{4}\right) \cos\left(\omega^- \frac{\tau}{8}\right) \mathcal{S}_x I_y - \frac{1}{2} \sin\eta \sin\left(\omega^+ \frac{\tau}{4}\right) \cos\left(\omega^- \frac{\tau}{8}\right) \mathcal{S}_x I_x \tag{1.112}$$

A π_x pulse sends $\mathcal{S}_y \rightarrow -\mathcal{S}_y$, and we evolve again. This refocuses the $\mathcal{S}_y$ derived terms that we have been ignoring, but does nothing to $\tilde{\rho_1}$. We can just double the evolution time of these states, so

$\tau/2 \to \tau$. The final density matrix in the eigenbasis is

$$\tilde{\rho_f} = \cos\eta\mathcal{S}_y + \sin\eta\cos\left(\omega^+\frac{\tau}{2}\right)\cos\left(\omega^-\frac{\tau}{4}\right)\mathcal{S}_xI_y - \frac{1}{2}\sin\eta\sin\left(\omega^+\frac{\tau}{2}\right)\cos\left(\omega^-\frac{\tau}{4}\right)\mathcal{S}_xI_x \quad (1.113)$$

Where we have included the unchanged $\mathcal{S}_y$ term again. Next we will convert back to the Cartesian basis, apply a final $\pi_x/2$ pulse, and measure $\langle\mathcal{S}_z\rangle$. This final $\pi/2$ pulse just converts $\mathcal{S}_y \to \mathcal{S}_z$, so the only nonzero terms in the average will be proportional to $\mathcal{S}_y$ after the transformation back to the Cartesian basis. These terms are

$$\rho_f \xrightarrow{-\xi I_y - \eta 2\mathcal{S}_z I_y} \cos^2\eta\mathcal{S}_y - \frac{1}{2}\sin^2\eta\cos\left(\omega^+\frac{\tau}{2}\right)\cos\left(\omega^-\frac{\tau}{4}\right)\mathcal{S}_y\,. \quad (1.114)$$

Applying the final $\pi/2$ pulse and taking $\langle\mathcal{S}_z\rangle$, we have the ESEEM signal

$$\langle\mathcal{S}_z\rangle = \cos^2\eta - \frac{1}{2}\sin^2\eta\cos\left(\omega^+\frac{\tau}{2}\right)\cos\left(\omega^-\frac{\tau}{4}\right)\,. \quad (1.115)$$

At low fields, $\omega^+ \approx 2A_\parallel$, so in a spin echo experiment there will be oscillations at the hyperfine coupling frequency. The strength of these oscillations is determined by $\sin\eta$. Remembering the definition of η in Eq. (1.103), we see that the oscillatory term will vanish if $\sin\theta \to 0$, which will happen if $\delta B_x = 0$. Hence the existence of these oscillations is an indication that the magnetic field is not aligned, and the field can be aligned by eliminating them.

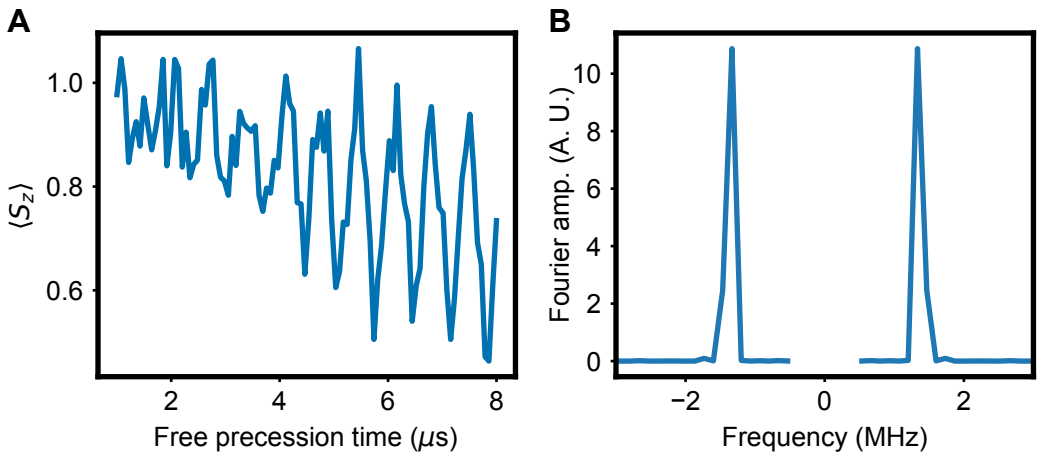


Figure 1.26: ESEEM oscillations. (A) Spin echo experiment performed on a ^{15}N NV center with a slight external field misalignment, displaying ESEEM. (B) Fourier transform of (A).

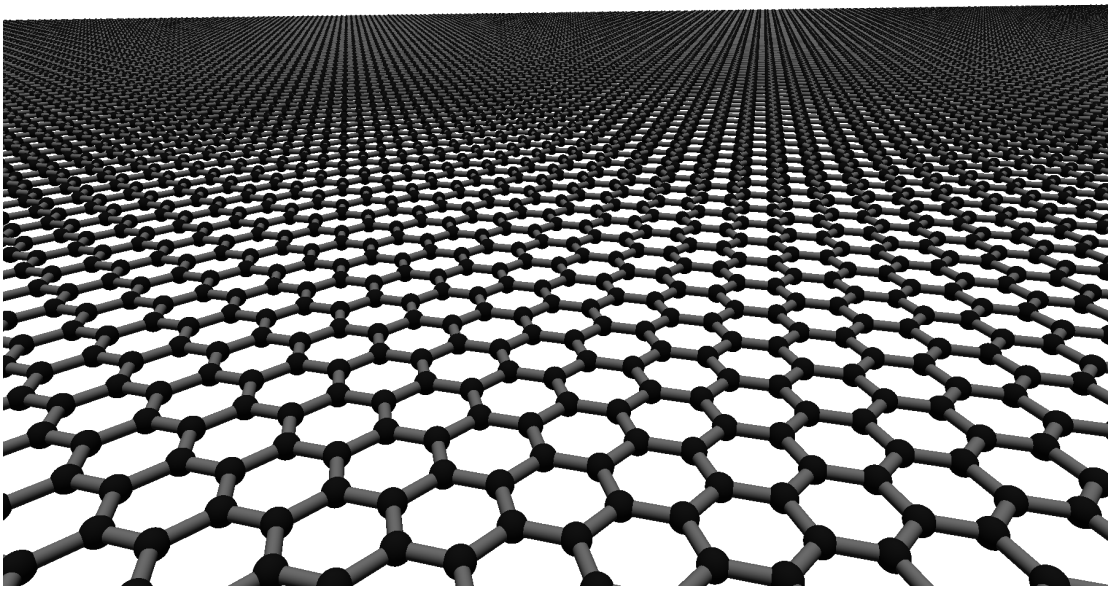


Figure 1.27: The honeycomb lattice of graphene.

Graphene is a remarkable material. In some ways it is the 2-dimensional analogue of diamond, composed of sp^2 carbon bonds in a honeycomb lattice rather than diamonds sp^3 hybridization. While graphene retains some of the strength of diamond in the in-plane direction, it is a very different material in most other respects. Graphene is flexible where diamond is brittle. While diamond is an insulator, graphene is a conductor thanks to the delocalized nature of its non-bonding p_z orbitals. While many future engineering applications may take advantage of graphene's exceptional strength and flexibility, physicists are more interested in its unique electronic characteristics. Electrons in graphene behave differently from those in normal semiconductors, even in other two dimensional

semiconductors, due to the linear, gapless dispersion of the honeycomb lattice.

While techniques for the isolation of mesoscopic graphene flakes were not developed until the turn of the century[264], graphene has been studied theoretically for decades. One of the first calculations that hinted at the surprising electronic properties of graphene was carried out by McClure[241] to explain the large diamagnetic response of graphite. By the time graphene was isolated in 2004, the hexagonal honeycomb lattice had been extensively studied and was thought to host massles Dirac Fermions. The methods developed by Geim and Novoselov in their seminal paper finally allowed graphene to be isolated and studied, and led to the pair sharing a Nobel prize in 2010. As it turned out, graphene was just the beginning. There is now an entire branch of physics concerned with exfoliatable 2D materials that can be stacked into heterostructures[265].

1.4.1 Graphene electronic structure

Graphene electronic orbitals are the result of sp^2 hybridization. σ bonds are formed between carbon atoms, with a nearest neighbor distance of $a = 0.142\,\text{nm}$[58]. The bands resulting from these bonds are completely filled, but the remaining p_z orbital forms a half filled π band through covalent bonding with its neighbors. It is this orbital that gives graphene its electronic properties.

The electronic band structure of graphene can be calculated with the tight binding method, where the atomic orbitals that contribute to conduction are assumed to be tightly localized to their atoms but with some probability of tunneling to neighboring atoms[12]. More specifically, if each of the atoms i on the lattice has electronic wavefunctions given by $\varphi_i(\vec{r})$ and $\vec{v}$ is a lattice vector, then there exist couplings

$$\langle \varphi(\vec{r} - \vec{v}) | H | \varphi \vec{r} \rangle = -t\,, \tag{1.116}$$

where t is the hopping parameter.

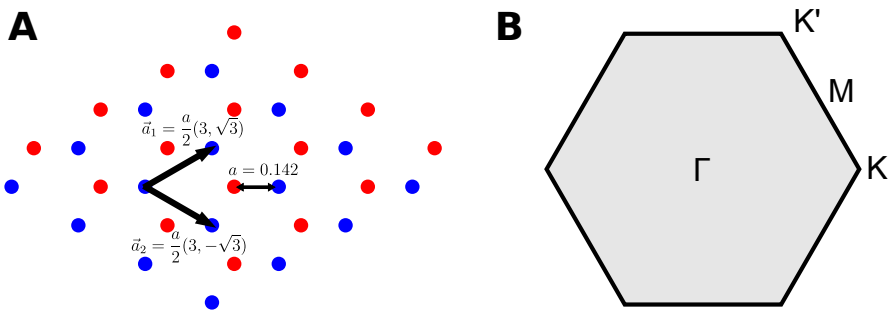


Figure 1.28: The graphene lattice. (A) Hexagonal lattice of graphene, composed of two triangular Bravais lattices (blue and red points). (B) Brillouin zone of the hexagonal lattice. For graphene, the K and K' points are equivalent because of sublattice symmetry.

The hexagonal lattice of graphene is not a Bravais lattice itself, but consists of two triangular sub-lattices (which we will call the A and B sublattice). The two vectors defining a sub-lattice are given by

$$\vec{a_1} = \frac{a}{2}\left(3, \sqrt{3}\right) \tag{1.117}$$

$$\vec{a_2} = \frac{a}{2}\left(3, -\sqrt{3}\right) , \tag{1.118}$$

where a is the carbon-carbon nearest neighbor distance of 0.142 nm. The A and B sublattices are connected by the nearest neighbor vectors

$$\vec{\delta}_1 = \frac{a}{2}\left(1, \sqrt{3}\right) \tag{1.119}$$

$$\vec{\delta}_2 = \frac{a}{2}\left(1, -\sqrt{3}\right) \tag{1.120}$$

$$\vec{\delta}_3 = a\left(-1, 0\right) , \tag{1.121}$$

as is illustrated in Fig. 1.33.

The electronic structure of graphene is simple to obtain in the second quantization treatment

of the tight binding method[58]. We define the operators $\hat{a}^\dagger(\vec{R}), \hat{a}(\vec{R}), \hat{b}(\vec{R}), \hat{b}^\dagger(\vec{R})$, where $\hat{a}^\dagger(\vec{R})$ ($\hat{a}(\vec{R})$) creates (destroys) an electron on the A lattice site ($\vec{R}$), and similarly for the B lattice. These operators satisfy the usual creation and annhilation operator anticommutation relations

$$\{\hat{a}(\vec{R}), \hat{a}^\dagger(\vec{R'})\} = \{\hat{b}(\vec{R}), \hat{b}^\dagger(\vec{R'})\} = \delta_{\vec{R},\vec{R'}} \tag{1.122}$$

$$\{\hat{a}(\vec{R}), \hat{a}(\vec{R'})\} = \{\hat{b}(\vec{R}), \hat{b}(\vec{R'})\} = 0 \tag{1.123}$$

$$\{\hat{a}(\vec{R}), \hat{b}(\vec{R'})\} = \{\hat{a}(\vec{R}), \hat{b}^\dagger(\vec{R'})\} = 0\,. \tag{1.124}$$

Using these conventions, the hopping term of the Hamiltonian can be written as

$$\mathscr{H} = -t \sum_{\vec{R},\vec{\delta}_i} \hat{a}^\dagger(\vec{R}) \hat{b}(\vec{R} + \vec{\delta}_{AB}) + h.c. \tag{1.125}$$

where the sum over $\vec{\delta}_i$ is a sum over each of the nearest neighbor vectors in Eq. 1.119-Eq. 1.121 and $+h.c.$ means "Hermetian conjugate." This Hamiltonian describes the intuitive physical picture of an electron being destroyed on a location on the A sublattice and created on a neighboring B lattice location (hopping), which has an energy cost t.

In order to diagonalize this Hamiltonian, we write the creation and annihilation operators in momentum space as

$$\hat{a}(\vec{R}) = \frac{1}{\sqrt{N}} \sum_{\vec{k}} \exp i\vec{k} \cdot \vec{R} \hat{a}(\vec{k}) \tag{1.126}$$

$$\hat{b}(\vec{R}) = \frac{1}{\sqrt{N}} \sum_{\vec{k}} \exp i\vec{k} \cdot \vec{R} \hat{b}(\vec{k})\,, \tag{1.127}$$

where N is the number of atoms in the crystal and the sums are taken over all k vectors in the Bril-

louin zone. The momentum space Hamiltonian then takes the form

$$\mathscr{H}_{\mathrm{k,q}} = \frac{-t}{N} \sum_{\vec{R},\vec{\delta}_{AB}} \sum_{\vec{k},\vec{q}} \exp i\vec{k}\cdot\vec{R} \exp -i\vec{q}\cdot(\vec{R}+\vec{\delta})\hat{a}(\vec{k})\hat{b}^{\dagger}(\vec{q}) + h.c.] \,, \tag{1.128}$$

$$= \frac{-t}{N} \sum_{\vec{R},\vec{\delta}_{AB}} \sum_{\vec{k},\vec{q}} \exp -i\vec{q}\cdot\vec{\delta} \exp i(\vec{k}-\vec{q})\cdot\vec{R}\hat{a}(\vec{k})\hat{b}^{\dagger}(\vec{q}) + h.c. \,, \tag{1.129}$$

$$= -t \sum_{k,\delta} \exp -i\vec{k}\cdot\vec{\delta}\hat{a}(k)\hat{b}^{\dagger}(q) + h.c. \,. \tag{1.130}$$

In going from Eq. (1.129) to Eq. (1.130), we have made use of the identity $\sum_{\vec{R}} \exp i(\vec{k}-\vec{q})\cdot\vec{R} = N\delta_{\vec{k},\vec{q}}$. This Hamiltonian can be written in matrix form as

$$\mathscr{H}_{\mathrm{k,q}} = \sum_{k,q} \begin{pmatrix} \hat{a}^{\dagger}(\vec{k}) & \hat{b}^{\dagger}(\vec{k}) \end{pmatrix} \begin{pmatrix} 0 & -t\sum_{\delta} e^{i\vec{k}\cdot\delta} \,, \\ -t\sum_{\delta} e^{-i\vec{k}\cdot\delta} & 0 \end{pmatrix} \begin{pmatrix} \hat{a}^{\dagger}(\vec{k}) \\ \hat{b}^{\dagger}(\vec{k}) \end{pmatrix} \tag{1.131}$$

$$= \sum_{k} \psi_k^{\dagger} \tilde{H}_k \psi_k \,. \tag{1.132}$$

The matrix $\tilde{H}$ has eigenvalues

$$\varepsilon_{\pm} = \pm t \sqrt{\left(\sum_{\vec{\delta}_i} e^{i\vec{k}\cdot\delta}\right)\left(\sum_{\vec{\delta}_i} e^{-i\vec{k}\cdot\delta}\right)} \tag{1.133}$$

$$= \pm t \sqrt{3 + 2\cos\left(a\sqrt{3}k_y\right) + 4\cos\left(a\frac{\sqrt{3}}{2}k_y\right)\cos\left(a\frac{3}{2}k_x\right)} \,, \tag{1.134}$$

which give the dispersion relation of graphene. Since graphene has one electron per atom, taking spin into account, at equilibrium the lower band is filled and the upper band is empty. The excitations accessible by most experiments take place around $\varepsilon \approx 0$, which occurs at the K and K' points

of the Brillouin zone

$$\vec{K} = \frac{2\pi}{3a}\left(1, \frac{1}{\sqrt{3}}\right) \tag{1.135}$$

$$\vec{K'} = \frac{2\pi}{3a}\left(1, -\frac{1}{\sqrt{3}}\right) . \tag{1.136}$$

At these points, we can expand the dispersion relation for small $\vec{q}$, we obtain

$$E = \frac{3ta}{2}\sqrt{q_x^2 + q_y^2} \tag{1.137}$$

$$= \hbar v_F |q| . \tag{1.138}$$

where v_F is the Fermi velocity, which has a value $v_F \approx 10^6$ m/s.

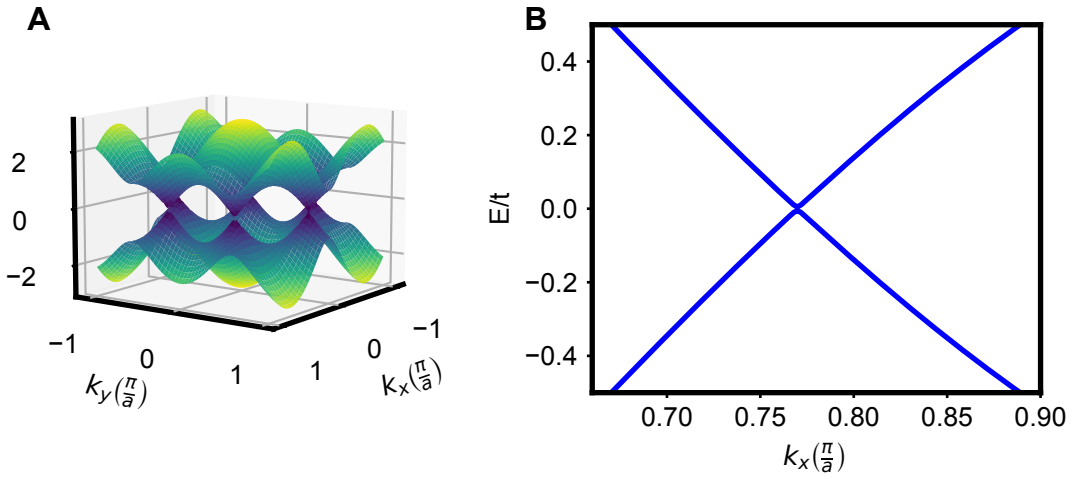


Figure 1.29: Graphene band structure. (A) Band structure of graphene, plotted from Eq. (1.134). (B) Low energy band structure projection near one of the equivalent K points, showing the linear, gapless dispersion of low energy excitations.

Eq. (1.138) is very different from the dispersion relations of most semiconductors, which typically feature quadratic dispersions at the band edges [12]. Instead, excitations in graphene are more like

photons, which have the dispersion relation $E = \hbar ck$, but with a velocity that is 300 times slower. However, the low energy excitations of graphene are not bosons like light, they are electrons and hence obey Fermionic statistics. They are, in fact, massless Dirac Fermions[263]. While electronic conduction in most materials can be approximated with semiclassical equations by invoking an effective electron mass $m^* \propto \frac{1}{\frac{dE}{dK}}$[326], this approach fails in the case of graphene, which must be described by the Dirac equation with the mass term set equal to zero,

$$i\hbar\frac{\partial\Psi}{\partial t} = \hbar F\vec{\sigma}\cdot\vec{q}\Psi\,, \tag{1.139}$$

where $\vec{\sigma}$ is the vector of Pauli matricies, $\{\sigma_x, \sigma_y\}$, and Ψ is the Dirac spinor composed of wavefunctions on the A and B sublattice, $\Psi = \begin{pmatrix}\psi_A\\ \psi_B\end{pmatrix}$. The Dirac equation is a relativistic equation, and indeed relativistic effects can be observed in graphene[182]. Klein tunneling, where back scattering of a relativistic particle is suppressed, was observed in the early days of graphene research[162]. Another important consequence is the effect on the quantum hall effect in graphene and on orbital magnetism, which will be discussed in Sec. 1.4.4.

1.4.2 Sublattice symmetry

Implicit in the tight binding calculation of Section. 1.4.1 is the assumption that the A and B triangular sublattices of graphene are indistinguishable. Indeed, this is an important characteristic of graphene that sets it apart from other 2D materials with a honeycomb crystal lattice, and is ultimately responsible for the massless nature of charge carriers in graphene. To see this, note that sublattice symmetry states that if we swap the atoms on the A and B sublattices, the system should remain the same. That is, the Hamiltonian must be invariant under sublattice inversion. The full

Dirac Hamilonian, including the mass term, is given by

$$\mathscr{H} = v_F \vec{\sigma} \cdot \vec{q} + m v_F^2 \sigma_z \,. \tag{1.140}$$

The only term in this Hamiltonian that is not symmetric under sublattice inversion is σ_z (sending A↔B results in -σ_z), which implies that for systems with sublattice symmetry, such as graphene, the mass term must be 0. For systems without sublattice symmetry, this need not be the case. For example hexagonal boron nitride (hBN) and many transition metal dichalcogonides (TMDCs) share graphene's honeycomb lattice, but have different elements on the two sublattices. hBN is a wide band gap insulator, and many TMDCs such as $MoSe_2$ and WSe_2 are direct band gap semiconductors in the monolayer limit.

It is also possible to break the sublattice symmetry in graphene and create a gap. This can be accomplished by placing graphene on a substrate with an incommensurate lattice, which creates spatial variation in the electrostatic environment of the graphene atoms and leads to sublattice symmetry breaking in certain regions of the sample [163,123].

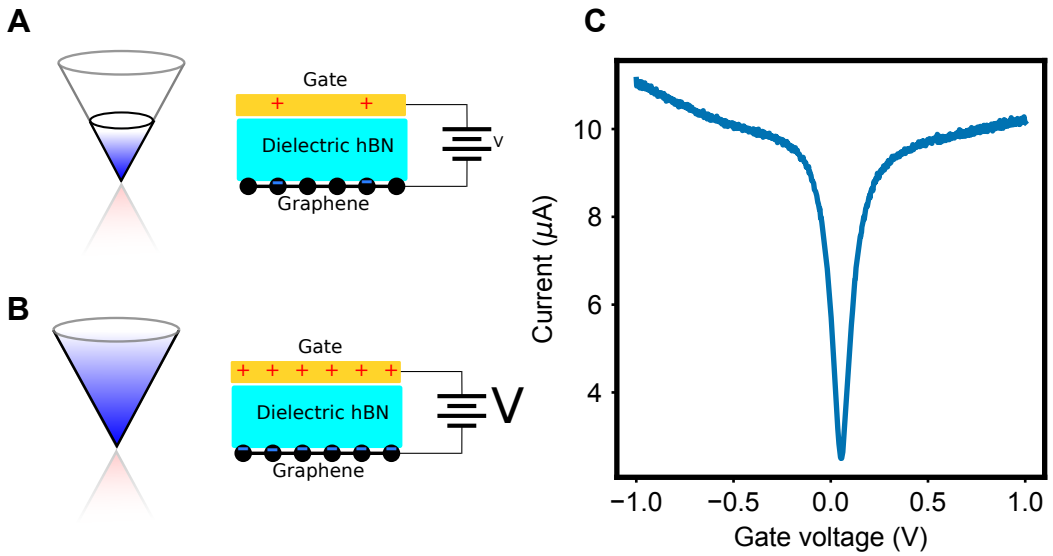


Figure 1.30: Control of the charge density of graphene through the field effect. (A) When a small voltage is applied between the plates of a capacitor made of graphene and a gate, only a few excess electrons are present in the graphene. (B) When a larger voltage is applied, the capacitor equation necessitates that more charge be present on each plate, which increases the charge density and hence the Fermi level of the graphene. (C) Transport through a graphene field effect transistor as the gate voltage is tuned through the Dirac point, showing an increase in resistance there.

If the Fermi energy of graphene were always pinned at 0 (e.g. half filled bands), it would be of limited interest. Due to its two dimensional nature and low intrinsic electron density, it is relatively straightforward to change the number of electrons in graphene by incorporating it into a small capacitor[264]. By applying a voltage between the graphene and a gate (made from some conducting material, including graphite), electrons will flow into (or out of) the graphene sheet according to the capacitor equation $C = QV$, where Q is the total charge, V is the applied voltage, and C is the device capacitance, which can be approximated as

$$C = \frac{\varepsilon A}{d}, \tag{1.141}$$

where ε is the dielectric constant of the environment, A is the area of the plates making up the capacitor, and d is the distance between the plates. Such a device is commonly constructed using a thin layer of hexagonal boron nitride as the gate dielectric, which has $\frac{\varepsilon}{\varepsilon_0} = 3.7$[212].

Using the density of states of graphene, we can write the Fermi energy as a function of applied voltage

$$E_F = \sqrt{\frac{2\pi\varepsilon}{g_s q_e d}} \hbar v_F \sqrt{V} \tag{1.142}$$

where g_s is the degeneracy of the graphene electrons (2 for spin degeneracy and 2 for valley degeneracy).

The ability to electrostatically dope a 2D material provides an important control parameter for experiments and technologies. The conductivity of graphene can be changed in this way, as depicted in Fig. 1.30C. When the gate voltage is swept while applying a small source-drain voltage, the conductivity will show a minimum at the Driac point ($E_F = 0$)[15]. In quantum hall experiments, where traditionally the Fermi energy is fixed and the magentic field is swept, for graphene the field may be held fixed and the Fermi energy altered. Changing the charge density can have other, more far reaching effects, such as on phonon scattering, which will be discussed in Ch. 4.

1.4.4 Graphene magnetism

The eigenfunctions near the K point, written as Dirac spinors[58], take the form

$$\Psi^{\pm} = \frac{1}{\sqrt{2}} \begin{pmatrix} e^{i\theta_q/2} \\ e^{\pm i\theta_q/2}, \end{pmatrix} \tag{1.143}$$

[15] In theory, the Dirac point should occur at a gate voltage of 0, but in real-world devices there is usually a small shift due to intrinsic doping of the graphene from impurities[395] or due to work function mismatches at the contacts[122].

where $\tan\theta_q = \frac{q_x}{q_y}$. In this form, it is clear that graphene electrons have an intersting property: if $\vec{q}$ is rotated completely around the dirac point ($\theta_q = 2\pi$), the wavefunction picks up a phase of π rather than 2π, which is typically the case for electrons. This phase associated with adiabatic evolution through a closed path is called the Berry phase [32], and graphene's peculiar Berry phase of π has consequences for its magnetic properties [382].

The following derivation follows that given in Ref. [383] and gives intuition for how the Berry phase and Landau levels of graphene are interrelated. In the presence of a strong[16] magnetic field perpendicular to the sample, an electron is forced into cyclotron orbits. In order for the wavefunction to be single valued, the orbits should satisfy the Bohr-Sommerfield quantization condition [114]

$$\oint d\vec{r}\cdot\vec{p} = 2\pi(n+\gamma)\hbar\,, \tag{1.144}$$

where n is an integer and γ is the phase mismatch ($0 < \gamma < 1$). The phase mismatch is a fully quantum effect that is not easily calculated, but for single band Bloch electrons it can be shown that $\gamma = \frac{1}{2}$ [114].

The total momentum of an electron in a magnetic field is given by $\vec{p} = \hbar\vec{k} - q_e\vec{A}$, where A is the vector potential [307]. Eq. (1.144) then becomes

$$\pi\left(n+\frac{1}{2}\right) = \oint d\vec{r}\cdot\vec{k} - \frac{e}{\hbar}\oint d\vec{r}\cdot\vec{A} \tag{1.145}$$

$$= -e\vec{B}\cdot\oint d\vec{r}\times\vec{r} - e\iint d\vec{S}\times A\,. \tag{1.146}$$

In Eq. (1.146) we have made use of the fact that $\hbar\vec{k} = \int dt\frac{d\vec{r}}{dt}\times\vec{B}$ [12] and Stokes theorem. The first term of Eq. (1.146) is just $2q_e\left(\pi r^2 B_z\right) = 2q_e\varphi$, where φ is the magnetic flux enclosed by an orbiting

[16] A "strong" magnetic field is one that induces an electron to complete many cyclotron orbits before scattering, e.g. "$\omega_c\tau \gg t$

electron. Similarly, the integral of the second term in Eq. (1.146) is just the magnetic flux, so

$$2\pi\left(n+\frac{1}{2}\right)=q_e\varphi\,. \tag{1.147}$$

A material with a parabolic dispersion would have $E=\frac{\hbar^2k^2}{2m^*}$. By writing the quantization condition of Eq. (1.147) in terms of k, we find that the eigenenergies of the electrons in a magnetic field are

$$E_n=\hbar\omega_c\left(n+\frac{1}{2}\right)\,, \tag{1.148}$$

where $\omega_c=\frac{q_eB}{m^*}$ is called the cyclotron frequency.

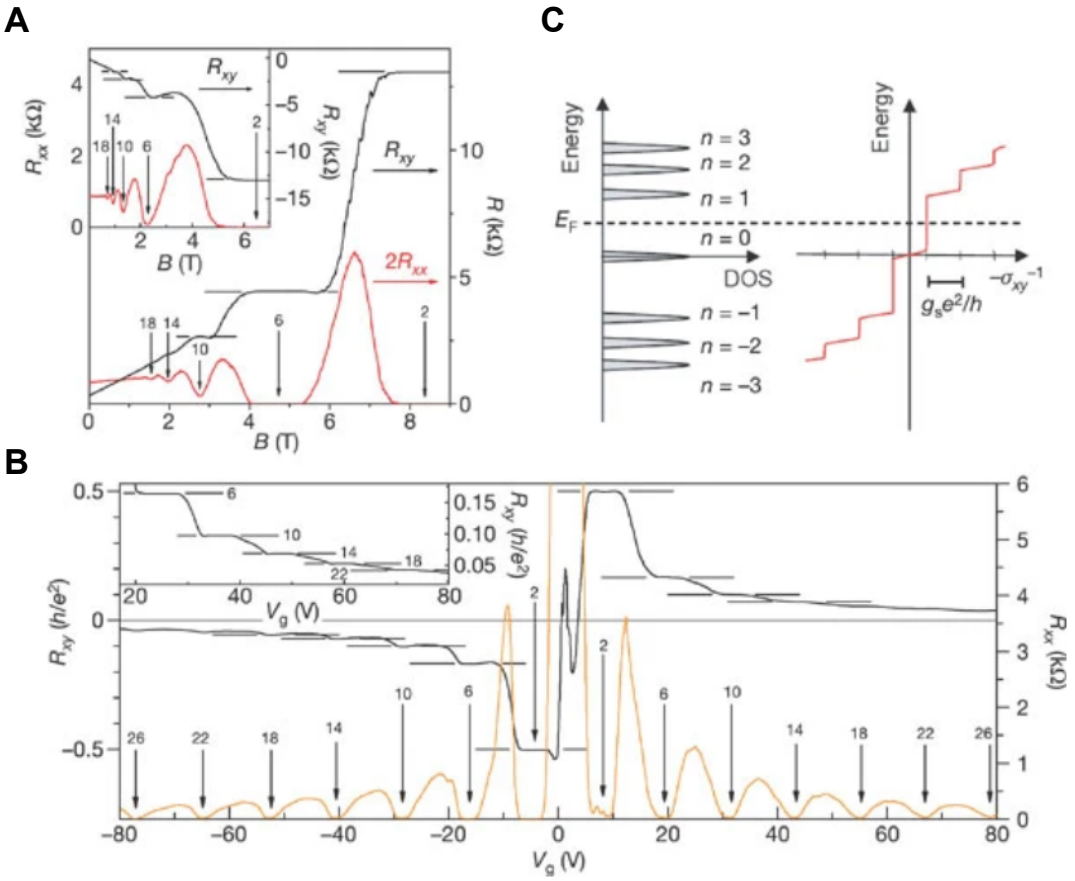


Figure 1.31: Anomalous quantum hall effect in graphene. (A) Hall resistance (black) and magnetoresistance (red) of electrons in graphene as the magnetic field is varied, showing pronounced hall plateaus. Numbers are filling factors. The inset shows the same experiment repeated for hole doped graphene. (B) Hall resistance (black) and magnetoresistance (orange) at 9 T as a function of gate voltage. Unlike in conventional materials, the quantum hall effect can be observed in graphene by varying the Fermi level through electrostatic gating. Inset is zoomed in to the high filling factor region. (C) Diagram showing the Landau level density of states and hall resistance as a function of Fermi energy. Graphene uniquely has a Landau level at $E_F = 0$. Figure taken with permission from Ref.[396].

The quantum hall effect essentially results from the spectrum of this Hamiltonian as the cyclotron frequency is swept through different values of n, which are known as Landau levels. To measure the quantum hall effect, a four terminal device is used so that the resistivity components ρ_{xx} and ρ_{xy} can be measured as a function of magnetic field. When the Fermi energy lies within a Landau

level, the longitudinal resistivity, ρ_{xx}, is finite as there exist unoccupied states that can participate in conduction only a small ∂E away. Between Landau levels, significant energy must be supplied to reach an available state in the next Landau level, and so there are no states available to conduct current[17] The transverse, or Hall, resistivity, by contrast, exhibits plateaus between completely filled Landau levels, with resistivity given by

$$\rho_{xy} = \frac{2\pi\hbar}{q_e^2}\frac{1}{\nu} \tag{1.149}$$

for the νth Landau level. This value of the resistivity is extremely robust, regardless of material makeup and disorder. It can be measured so accurately that it provides the definition of the quantity $\frac{h}{q_e}$, which, together with the Josephson constant, defines the kilogram in terms of fundamental constants[372]. The observation of the quantum hall effect earned Klaus von Klitzing the nobel prize in 1985[371].

While the explanation of the quantum hall effect (and its more complex relatives such as the fractional quantum hall effect[344]) is undoubtedly a triumph of modern physics, it is mentioned here only to compare it to the anomalous behavior of graphene in a magnetic field. While the quantization condition for "normal" electrons is given by Eq. (1.144), for graphene we must include the Berry phase of π in this calculation so that

$$2\pi\left(n+\frac{1}{2}\right) = \oint d\vec{r}\cdot\vec{k} - \frac{e}{\hbar}\oint d\vec{r}\cdot\vec{A} - i\oint \langle\psi|\frac{\partial}{\partial\vec{p}}|\psi\rangle\, dt \tag{1.150}$$

$$= \oint d\vec{r}\cdot\vec{k} - \frac{e}{\hbar}\oint d\vec{r}\cdot\vec{A} + \pi\,. \tag{1.151}$$

Subtracting π from both sides, we see that the zero point energy is canceled by graphene's Berry

[17] The fact that $\rho_{xx} = 0$ between Landau levels might seem to imply perfect conduction, but it in fact implies no dissipation. The longitudinal conductivity, σ_{xx}, is also equal to 0 in this case, since $\sigma_{xx} = \frac{\rho_{xx}}{\rho_{xx}^2+\rho_{xy}^2}$ [326].

phase of π, and hence the Landau levels are shifted such that there now exists an $n = 0$ Landau level at 0 energy. Additionally, while materials with a parabolic dispersion lead to a linear Landau spectrum, the linear dispersion of graphene gives rise to $E_n \propto \sqrt{n}$[18]

This anomalous quantum hall effect was detected experimentally in 2005 [396], but it was predicted in the 1950s by McClure to explain something seemingly unrelated [241]. Graphite exceptionally strong diamagnetism, so much so that chunks of graphite can be levitated on top of strong magnets even at room temperature. It was found that if graphite is treated as many independent sheets of graphene, this strong diamagnetism actually arises from the presence of a Landau level at zero energy. This is due to the large change in free energy that occurs when all of the Bloch state electrons near the Dirac point are compressed into the degenerate Landau level at 0 energy upon application of a large magnetic field. Since the final states have a total energy of 0, this is a particularly large change in the free energy and hence the magnetization, (derivative of some free energy with respect to field) is also very large. This effect is additionally dependent on both temperature and Fermi energy, and should become singular at the Dirac point for very low temperatures. In Ch. 5 we will explore the doping dependent diamagnetic response of graphene using NV centers.

While it may seem an odd candidate for exploring magnetism, there are several other ways to induce magnetism in graphene. Individual vacancies in graphene create a magnetic moment due to the imbalance between the A and B subnlattices [271], which could provide an intersting platform for quantum simulation since these may be created on the lattice scale using high powered TEM [146]. Graphene can also be functionalized with atoms (such as fluorine [220] or hydrogen [127]) or molecules (such as benzoil peroixide [221]) to introduce magnetism. Finally, stacking multiple layers of graphene into twisted Moiré lattices has been shown to induce magnetism [319,283]. While we do not explore this physics in this thesis, the often small sizes of Moiré domains make such physics a natural candi-

[18] This is more appropriately derived by writing out the Dirac Hamiltonian in the presence of a strong magnetic field and explicitly calculating the eigenvalues. The result is the same, but without an explanation of the origin of the shifted Landau levels.

date for study with a local sensor such as the NV center.

1.4.5 Device fabrication

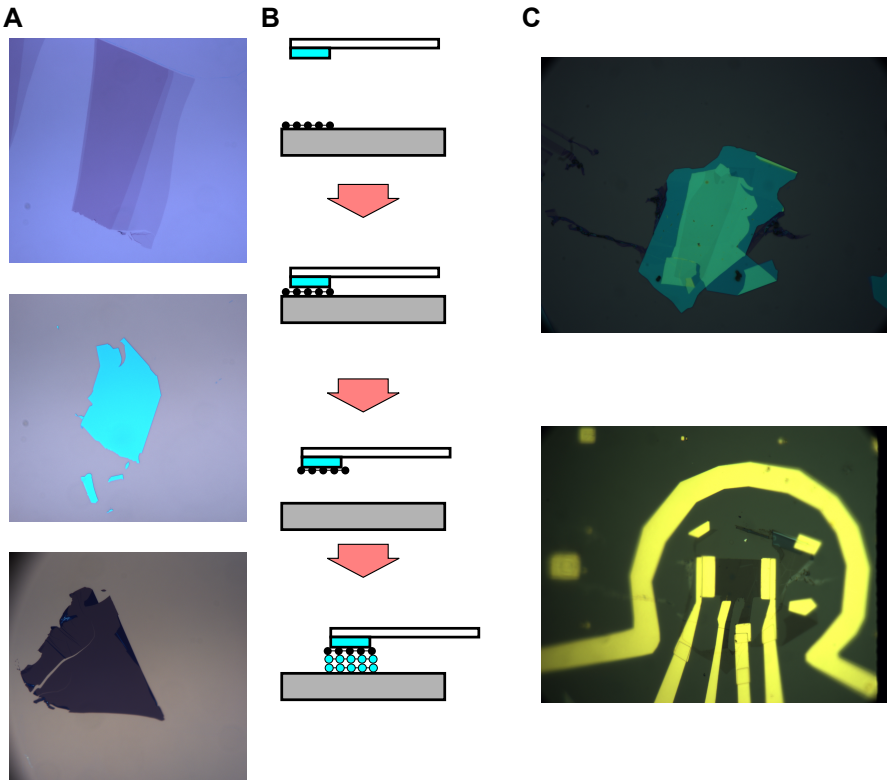


Figure 1.32: Fabrication of 2D heterostructures. Contruction of a 2D material heterostructure. (A) Flakes of different materials are selected by inspection under an optical microscope. (B) A polymer stamp is used to repeatedly pick up and set flakes on top of each other, building a stack from the top down. (C) A finished stack is etched and contacted with standard photolithography techniques.

Graphene is not hard to make. Whenever someone writes with a pencil, some small flakes of graphene are produced[258]. The Nobel prize winning breakthrough of Ref.[264] was determining a way to produce fairly large flakes, and, more importantly, developing a method to find them. Today, while much progress has been made on developing wafers of CVD grown graphene[86], most experiments

requiring high quality devices are performed on small (100s of μm^2) flakes of graphene that have been exfoliated from larger bulk crystals by repeatedly peeling them apart using tape[263]. These flakes are then transferred from the tape to a standard 300 nm thick silicon dioxide on silicon wafer. The thickness is important. Graphene only absorbs about 2% of incident light[256], but interference effects between monolayer graphene and an optimized SiO_2/Si substrate provide good optical contrast ($\approx$ 12%) for monolayer flakes[38]. This means that it is possible not only to see this single atom thick material under a white light microscope, but also to count the number of layers by eye. The layer thickness can be confirmed with Raman spectroscopy[104], but often this is not necessary.

Once a suitable flake as been found with an optical microscope, contacts can be defined by e-beam lithography and metal evaporation, or, for a more high quality device, a heterostructure may be assembled. One of the great breakthroughs of 2D materials research was the discover that other Van der Waals materials can be "stacked" together like Lego© blocks[265]. High quality crystals of hexagonal boron nitride (hBN), for example, can be exfoliated in the same manner as graphene[85,388]. hBN is another Van der Waals material with a honeycomb lattice, like graphene, but due to the lack of sublattice symmetry hBN is a wide bandgap (5.955 eV) insulator rather than a metal[57]. It is also exceptionally clean and flakes can be atomically flat, making it an ideal gate dielectric and encapsulation material to protect graphene from environmental impurities[238]. To construct a stack, a polymer stamp attached to a glass slide is used to pick up a chosen flake, after which the stamp is positioned above the next layer in the stack and the two flakes are pressed together[374]. Continuing in this way, heterostructures consisting of many layers of gates, dielectrics, and active materials can be assembled with atomically perfect interfaces[374]. Once a stack is constructed, it is pressed onto a substrate (such as diamond containing NV centers) and the polymer stamp is dissolved in solvent. This way only the topmost layer is ever exposed to the contaminating effects of the polymer stamp. Patterning of electrodes then proceeds as usual, perhaps with some reactive ion etching to reach buried layers of the stack.

While not especially scalable, constructing heterostructues in this way leads to extremely high quality (e.g. low disorder) devices[238,374] that display unique physics. It also provides a previously inaccessible level of control over device properties: material type, thickness, strain, and relative twist angle can all determine the behavior of the device.

1.4.6 Other 2D materials

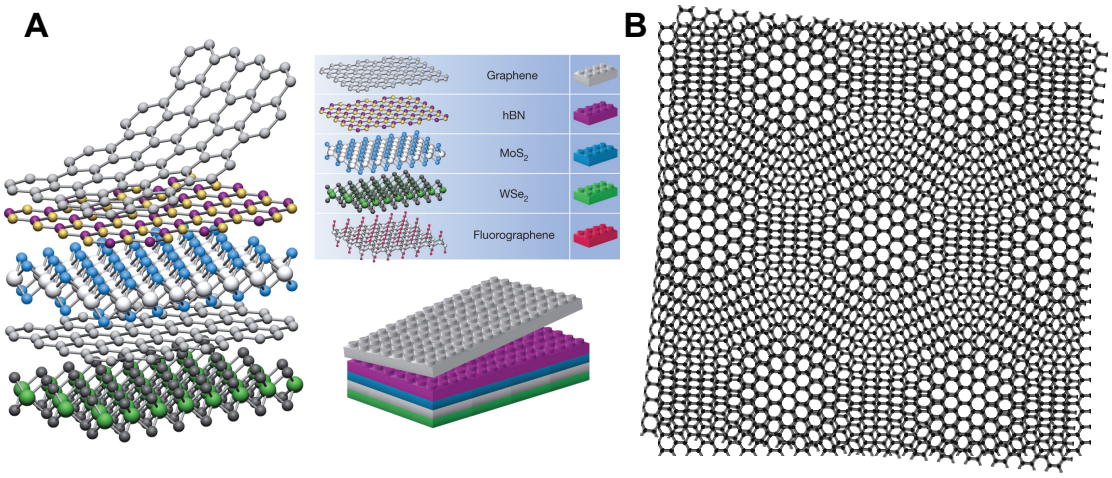


Figure 1.33: Stacking of 2D materials. (A) With the wide variety of different Van der Waals materials available, devices with desirable properties can be constructed layer by layer. Figure taken with permission from Ref.[121]. (B) Relative twist angle is a parameter available in Van der Waals materials that is unique. Rotating two layers with respect to each other results in a long wavelength Moiré potential that can produce interesting effects.

Graphene was the first truly 2D material to be isolated and studied, but today graphene is just one of many 2D materials under investigation[265,121]. Thicker layers of graphite make excellent gates for devices and significantly reduce device disorder[403]. hBN, as previously mentioned, is an insulator that is used as a gate dielectric and to encapsulate other materials to protect them from environmental degradation and electrostatic impurities. A whole family of materials, the transition metal dichalcogonides (TMDCs), have been studied extensively in recent years when it was realized that several

become optically active direct bandgap semiconductors in the monolayer limit and host long lived excitons[335,394]. More recent additions to the 2D materials zoo include two-dimensional magnets such as CrI_3 [161], 2D superconductors such as exfoliated BSCCO [397], and candidate quantum spin liquids such as 1T-TaS_2 [213] and 1T-$TaSe_2$ [303]. Often, these materials are used together in stacks to construct devices with desirable properties, such as stacked TMDCs to make P-N junctions[300,28], or magnetic memories that can be electrically switched [160].

One degree of freedom possessed by all 2D materials that is unique is the lattice mismatch between layers of a stack. This can be an intrinsic mismatch, such as the 1.8% lattice mismatch between aligned hBN and graphene, or it can be intentionally introduced by controlling the rotation angle between materials. In general, a Moiré lattice results, and the additional periodic lattice modifies the band structure [163]. This band engineering can lead to diverse physical phenomena, including the observation of Mott insulating and superconducting phases in bilayer graphene with a "magic" relative twist angle [53], orbital Chern insulators[362,320], periodic confinement of excitons[361,177,8], among other interesting phenomena. Due to twist angle and strain variation, device properties are frustratingly nonuniform in many real world experiments [366], which makes local probes such as scanning nanosquids and NV centers promising platforms for studying Moiré superpotential physics.

God made the bulk; the surface was invented by the devil.

Wolfgang Pauli

2

Origins of diamond surface noise

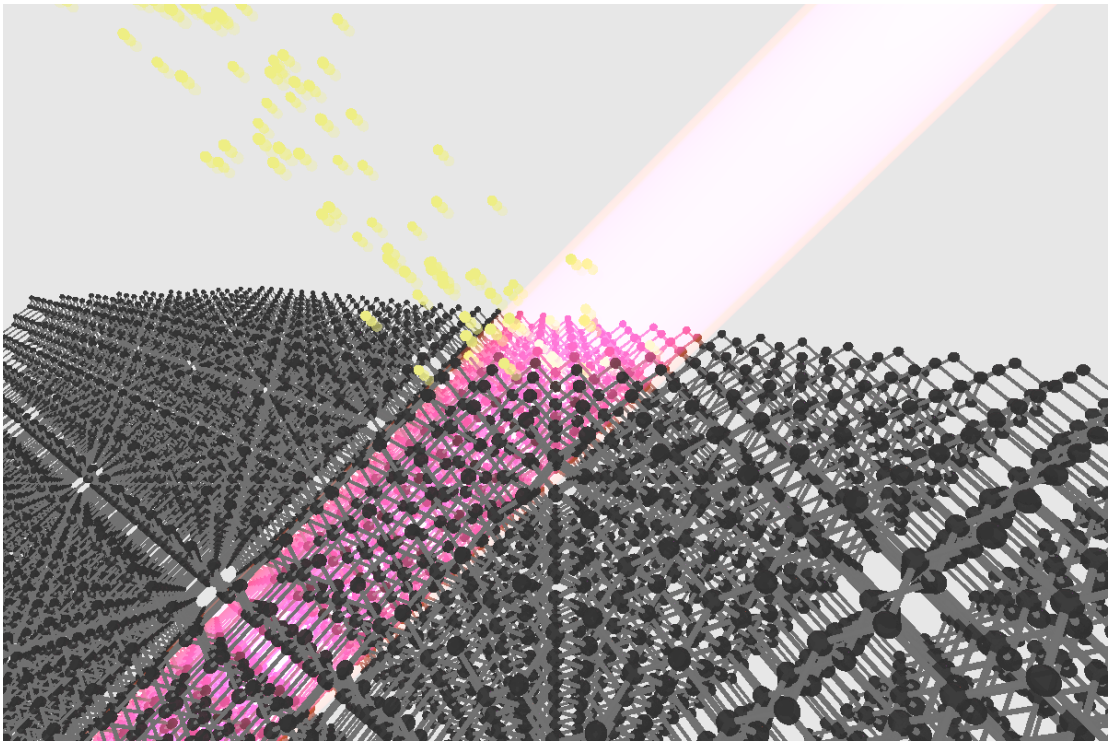


Figure 2.1: Depiction of surface X-ray spectroscopy, where X-rays excite electrons from the atoms of the diamond surface.

2.1 Introduction

In a broad sense there are only two types of targets for NV center sensing: those that exist inside of the diamond and those that are outside of it. Sensing inside of the diamond is generally performed on other types of magnetic defects in the lattice, such as ^{13}C nuclear spins, P1 centers, or other NV centers. While this type of sensing is somewhat limited in scope, the relatively controlled environment of diamond provides an ideal platform for quantum simulation, which can even be accomplished under ambient conditions. Most of the proposed applications of NV centers involve sensing of targets that are external to the lattice. This includes a wide variety of systems, including biomolecules, condensed matter systems, and liquids, to name a few. In all cases, sensing of external

targets necessitates close proximity to the material of interest, which may be accomplished either by placing a target on the surface of a bulk diamond containing shallow NV centers or by scanning a nanostructured diamond containing NV centers over a sample. This proximity is necessary due to the strong distance dependence of the dipolar interaction, which falls off proportional to r^{-3}, where r is the separation between the NV center and the sensing target.

Nanoscale magnetic field sensing with NV centers is a technology that holds great promise, as there are few other sensors that can compete with NV centers on these length scales. The need nanoscale proximity between NV centers and external targets introduces a challenge, however. The primary reason that NV centers make such good sensors is that they possess extremely long coherence times, even at room temperature. As was discussed in Ch. 1, the sensitivity of a quantum sensor depends on this all important parameter. The trouble is that the NV center coherence time is so long because diamond is a magnetically pure material with a low concentration of magnetic impurities that produce decoherence-inducing noise. Once this isolating environment is altered, the high sensitivity of the NV center becomes a hindrance, as it is very sensitive to environmental noise as well as to the desired signal to be sensed. By bringing an NV center within nanometers of the diamond surface, the effects of the disordered surface become apparent rapidly: while bulk NV centers can have $T_2 \approx 1$ ms, for very shallow NV centers this degrades to $< 1\,\mu$s, resulting in a massive decrease in sensitivity. It is then natural to ask where exactly this additional surface noise comes from, and whether or not it can be suppressed (or eliminated completely). Answering these questions is of paramount importance, as the degradation of coherence times for shallow NV centers hinders nearly all NV center based sensing efforts.

In this chapter, I will provide some background on the known properties of diamond surfaces as they relate to NV centers, followed by an exposition of surface spectroscopy methods that will be used in the remainder of the chapter. This surface spectroscopy will be correlated with NV center measurements to determine potential origins of diamond surface noise, and to create a surface

treatment that improves the coherence times of shallow NV centers.

2.1.1 Background

The surface is where the infinite periodicity of the perfect lattice clashes with the messy reality of real world solids. Where we might normally consider real-valued wavevectors when constructing electronic bands, this is not a requirement, and in fact for crystal with a finite boundary states with complex wavevectors exist[12]. The exact character of these surface states depends on how exactly the surface is constructed–what types of atoms and in what orientations they have bonded–and these surface states in turn alter the band structure near the surface. Charge at the surface is usually redistributed due to the break in the periodic lattice here, which results in a bending of the energy bands as one approaches the surface. This process, called band-bending, is depicted in Fig. 2.2.

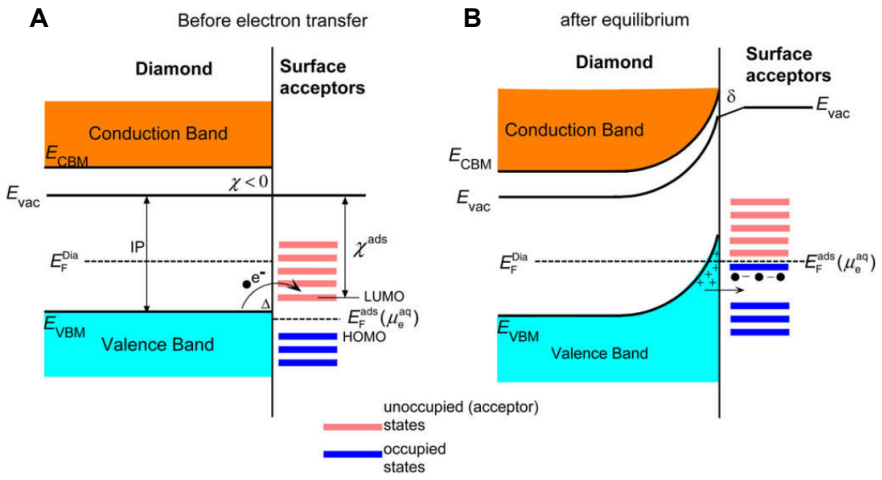


Figure 2.2: Band bending near the diamond surface. (A) Energy levels of diamond before charge redistribution. The presence of acceptor states on the surface alters the charge distribution as electrons move to occupy these low energy states. (B) After charge redistribution, holes accumulate at the surface to balance the electrons that now occupy the surface traps. This has the effect of bending the energy bands upwards on approach to the surface, while the Fermi level remains constant. LUMO: lowest unoccupied molecular orbital, HOMO: highest occupied molecular orbital. Figure taken with permission from Ref.[63].

For NV centers, surface states can have a number of different effects. The previously discussed phenomenon of band bending can either stabilize or destabilize near surface NV centers depending on whether the Fermi level lies above or below the defect energy within the band gap, which can lead to an overall preference for the lower energy (and metrologically useless) NV^0 charge state. Surfaces can also introduce mid gap states that are close in energy to NV^-, which can alter the photoionization dynamics since single photon ionization/recombination processes would then be permitted. From a sensing perspective, surface states can also be problematic as they likely introduce electric and magnetic field noise that severely limits the coherence times of shallow NV centers. Since diamond has a very long screening length, the influence of the surface extends relatively far into the bulk, and even individual defects can strongly perturb the electrostatic environment[71].

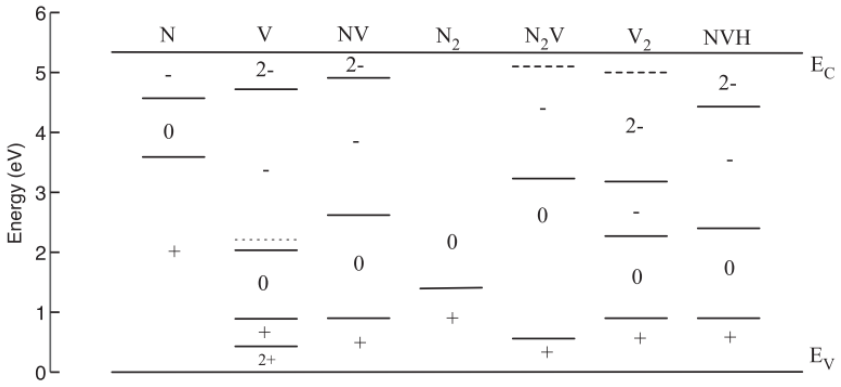


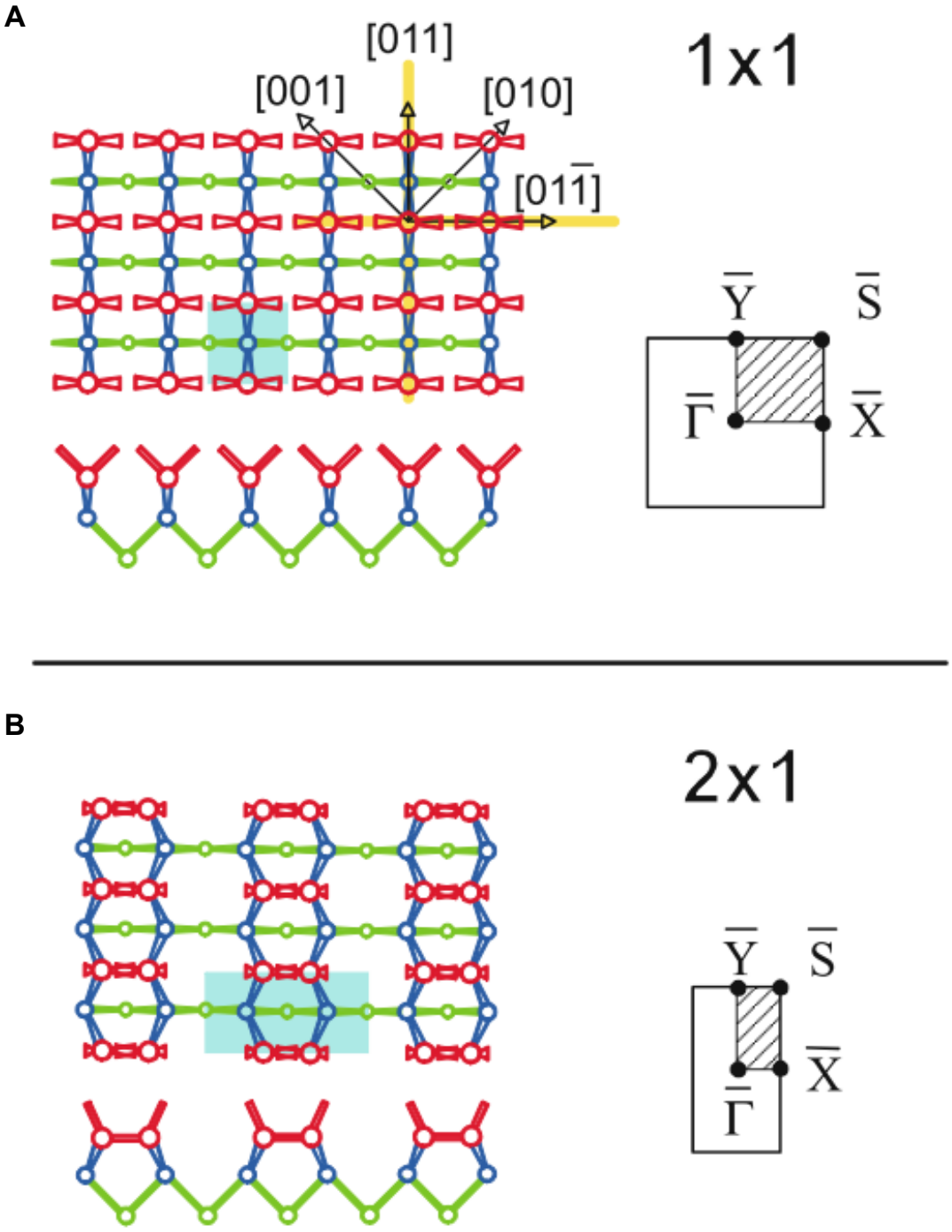
Figure 2.3: Energy levels of defects in the diamond band gap. Energy levels of various defects in diamond relative to the valence (E_V) and conduction E_C bands. Since NV^0 is lower in energy than NV^-, local variations in the Fermi level from nearby defects can make NV^- unstable. Band bending can likewise shift the positions of the defect states so that NV^- lies above the Fermi energy. Figure taken with permission from Ref.[84].

The two most common diamond surfaces are (100) and (111). While other surfaces are possible, these are the slowest growing surfaces and so for the CVD grown diamonds commonly used for NV center experiments, once growth has terminated, all other surfaces have "grown themselves out of existence"[336]. We will concentrate on (100) surfaces here as they are more commonly available, but much work has been done on the properties of (111) surfaces, which in general show different properties from (100) surfaces. A pristine (100) diamond surface has two dangling bonds per atom. These dangling bonds are not a stable configuration, however, and they will pair up to lower the overall energy. This is called *surface reconstruction*, and the geometry of the reconstruction is given indices of the form $m \times n$ to denote the number of unreconstructed cells present in a reconstructed unit cell (along two directions). (100) surfaces undergo a 2×1 reconstruction, as shown in Fig. 2.4, where neighboring pairs of atoms form double bonds. The remaining dangling bonds form bonding (π) and antibonding (π^*) orbitals resulting in a splitting of the surface bands into an occupied π band and an unoccupied π^* band thought to be 2.4 eV above the VBM. The π band is either within the valence band (and hence inactive) or is slightly above it, though this is a topic of some

debate[292,293]. For a (111) surface, the single dangling bonds reconstruct to form Pandey chains. The π orbitals are delocalized along the chain, like in graphene, and so the surface should be metallic in theory, though this has not been observed experimentally[129].

Figure 2.4 *(following page)*: Surface reconstruction of diamond. Models of the last three carbon layers of the (100) diamond surface. (A) Unreconstructed surface, where each of the terminal carbon atoms has two bonds to form. Surface Brillouin zone shown on the right. (B) 2×1 reconstructed surface that corresponds to the clean (100) surface and to the hydrogen terminated surface (hydrogen atoms not shown). Figure taken with permission from Ref.[293]

Figure 2.4: (continued)



The carbon atoms at the surface need not bond only to each other. Indeed, the bare carbon surface reconstruction is difficult to produce except through careful vacuum annealing. There are many possible surface terminations that are possible, though hydrogen and various oxygen groups are the most studded. Hydrogen terminated diamond is typical of CVD grown crystals, or it can be created through exposure to a hydrogen plasma. Hydrogen bonds to the orbitals that form π bonds in the bare surface, modifying bonding/antibonding states and pushing the surface bands apart. This results in the occupied band being pushed even lower into the valence band, and hence the (100) diamond surface is not conducting. An interesting byproduct of hydrogen termination in both (100) and (111) diamond surfaces is a negative electron affinity. This is because the underlying carbon lattice is more electronegative than the terminating hydrogen atoms. Positive partial charge is pulled towards the vacuum side, setting up a dipole moment perpendicular to the surface. When such a surface is exposed to atomosphere, hydrocarbon adsorbates create acceptor states for the surface electrons, resulting in a hole-gas at the surface[229]. This surface transfer doping shifts the Fermi level below the position of NV^- within the band gap, which changes the equilibrium charge state distribution in favor of NV^0 [137]. Hydrogen termination also results in near-surface delocalized states, which should shuttle photoexcited electrons away from NV^- and to the surface, where they would be emitted due to the large negative electron affinity[184]. These effects can extend far into the bulk, again due to the large screening length in diamond, and perhaps due to the long mean free path of conduction band electrons. Experimentally, hydrogen terminated diamonds do not show favorable charge state properties for sensing[147,299].

In contrast to hydrogen termination, oxygen termination tends to increase the electron affinity, which should result in NV^- being a favorable charge state[110]. This is because oxygen has a very large electronegativity. There are, however, multiple ways for the two bonds of oxygen to incorporate into the (100) surface. Oxygen can form double bonds with each carbon atom (C=O, ketone), or it can form a bridge between adjacent carbons (C-O-C, ether). Both of these options should lead

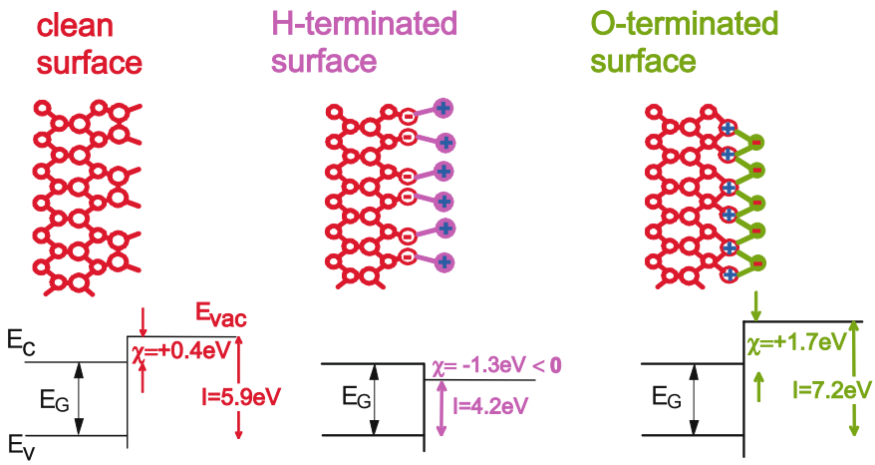


Figure 2.5: Surface electron affinities for different diamond surface terminations. The clean surface has a slightly positive electron affinity, but hydrogen termination makes this negative due to the low electronegativity of hydrogen. Oxygen termination, by contrast, results in a very high electron affinity due to its high electronegativity, surpassed only by Fluorine for common elements. Figure taken with permission from Ref.[293].

to occupied bands below the VBM, and only the ketone-like termination is expected to have unoccupied states within the gap[399]. OH coverage is also possible, though this is less desirable due to a small negative electron affinity[336]. There are also complicated "designer" surface terminations such as a 2×2:H/O/OH reconstruction studied in[184] that should result in good NV center properties but would be difficult to realize in practice. Diamond surfaces can be oxygen terminated by oxidative wet chemistry (commonly a triacid clean, explained in Appendix A) or by exposure to a "gentle" oxygen plasma. The type of oxygen termination produced by these methods is likely of mixed type. Additionally, termination by oxygen plasma is difficult to do without damaging the diamond, since it is one of the commonly used methods for diamond etching.

A final surface termination that should have desirable properties is fluorine termination, which would result in an even higher electron affinity than oxygen[358]. Electron affinity is only a small part of the charge stability story, however. There seems to have been little work done on this type of surface since the publication of Ref.[73], perhaps due to the predicted existence of unoccupied states

just below the conduction band minimum that could periodically trap photo-excited electrons, leading to blinking [184].

When density functional theory calculations are performed for the diamond surface to determine expected surface states, a uniform and perfectly terminated surface is usually assumed. This is, of course, unlikely in real world samples, which are full of step edges, vacancies, and a jumble of different terminations. Graphitic carbon (sp^2) defects, which can locally pin the Fermi level, are relatively common [292]. Real surfaces are also plagued by layers of adventitious hydrocarbons and water which make studying the intrinsic surface difficult.

Besides affecting the charge state stability of NV centers, surface states (and more localized surface defect states) are theorized to be responsible for the decrease in NV center coherence upon approaching the surface. The rapid decrease in coherence for NV centers within 100 nm of the diamond surface has been well documented [301,254,81,230,187,298], with NV center noise spectroscopy revealing a secondary, nearly white noise bath that is not present for bulk centers [254,298]. For at least some diamonds, electric field noise is a significant driver of decoherence [255,120,187], though magnetic noise is more commonly assumed to dominate. The discovery of stable spin-1/2 "dark" spins on the diamond surface has long been thought to provide a broadband magnetic noise bath, and indeed by driving these spins an increase in NV center coherence time (analogous to motional narrowing) has been demonstrated [44]. The required density to explain the level of measured noise (0.04 spins/nm^2 [254]) is relatively high compared to what we have measured in our own samples (see Ch. 3). Additionally, even for samples where mitigating the decoherence induced by surface spins results in an extension of NV center T_2 as in Ref. [44], the coherence time remains significantly lower than bulk values, indicating that other noise sources become dominant. One such defect is the "primal" sp^2 defect studied in Ref. [338], which can be detected in X-ray spectroscopy and is predicted to give rise to unoccupied mid-gap states that could be transiently filled by photoexcitation. The authors also show that these defects lead to band bending and NV center charge state instability within hundreds

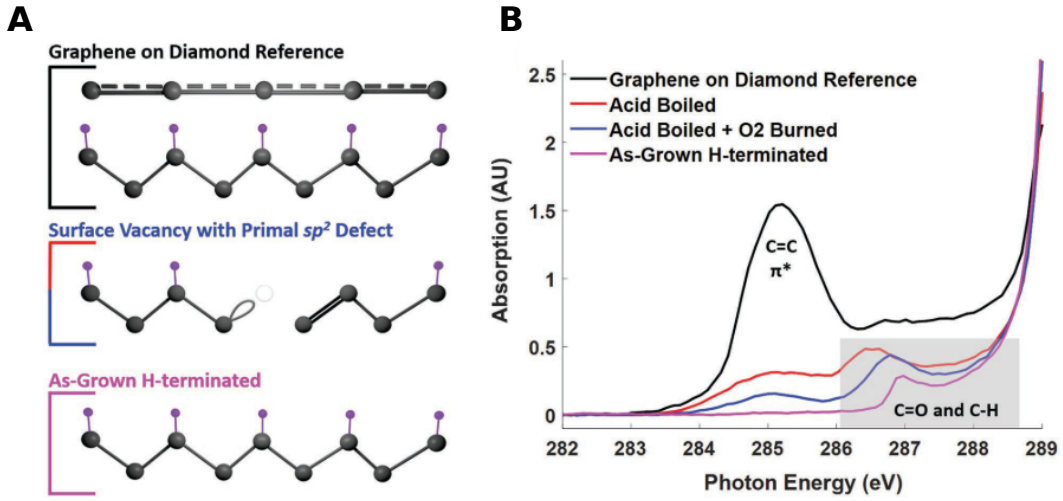


Figure 2.6: sp^2 defects on the diamond surface. (A) first two layers of carbon on (100) diamond, showing an sp^2 defect formed by removal of a terminal carbon atom. (B) NEXAFS spectra near the C1s edge, showing regions associated with sp^2 carbon in three diamond samples (gray box). Graphene was used as a uniform coverage sp^2 reference in this experiment. Figure taken with permission from Ref.[338].

of nanometers of the surface, and that there seems to be some correlation between the density of these defects and NV center optical properties.

Oxygen termination of diamond was originally explored in the context of NV centers as a method of charge state stabilization, due to the aforementioned high electron affinity of oxygen terminated diamond surfaces. It was additionally found in Ref.[227] that careful oxygen annealing can improve the spin properties of NV centers. This same technique appears to lead to a reduction in the number of sp^2 defects on the diamond surface[338].

One final complicating factor for understanding diamond surfaces is that the surface morphology can vary dramatically depending on the initial preparation steps. Some diamonds are used with "as-grown" surfaces, meaning that the crystal faces that remain after CVD growth are still intact when nitrogen is implanted. These surfaces seem to innately have a lower defect density than the alternative diced and polished surfaces[338], but there is significant spatial variability on these surfaces. Diced and polished surfaces can also be etched with a reactive ion etcher (RIE), and all of these steps have

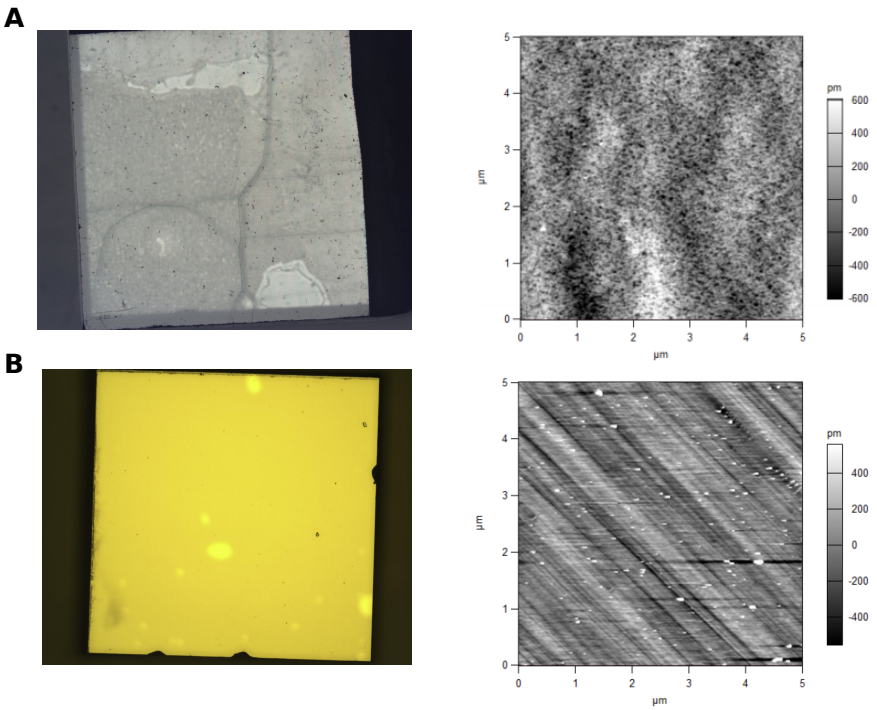


Figure 2.7: As grown and polished surfaces. (A) An as-grown diamond surface displays facets in an optical image (left) but the surface is very smooth on these facets (right). (B) A polished diamond shows scaife marks from the polishing procedure, but these can be smoothed (and the strain removed) by isotropic $ArCl_2$ ion etching.

the potential to leave behind morphological and chemical defects that can affect the local density of states when NV centers are implanted. See Fig. 2.7 for examples.

2.1.2 Measurement overview

In the following experiments, we will correlate NV center measurements with information about the surface gained from a number of surface sensitive spectroscopy techniques. The NV center measurements utilized are introduced in Ch. 1. The following sections provide a brief introduction to the different surface spectroscopy methods that are used in this chapter.

X-ray photoemission spectroscopy (XPS)

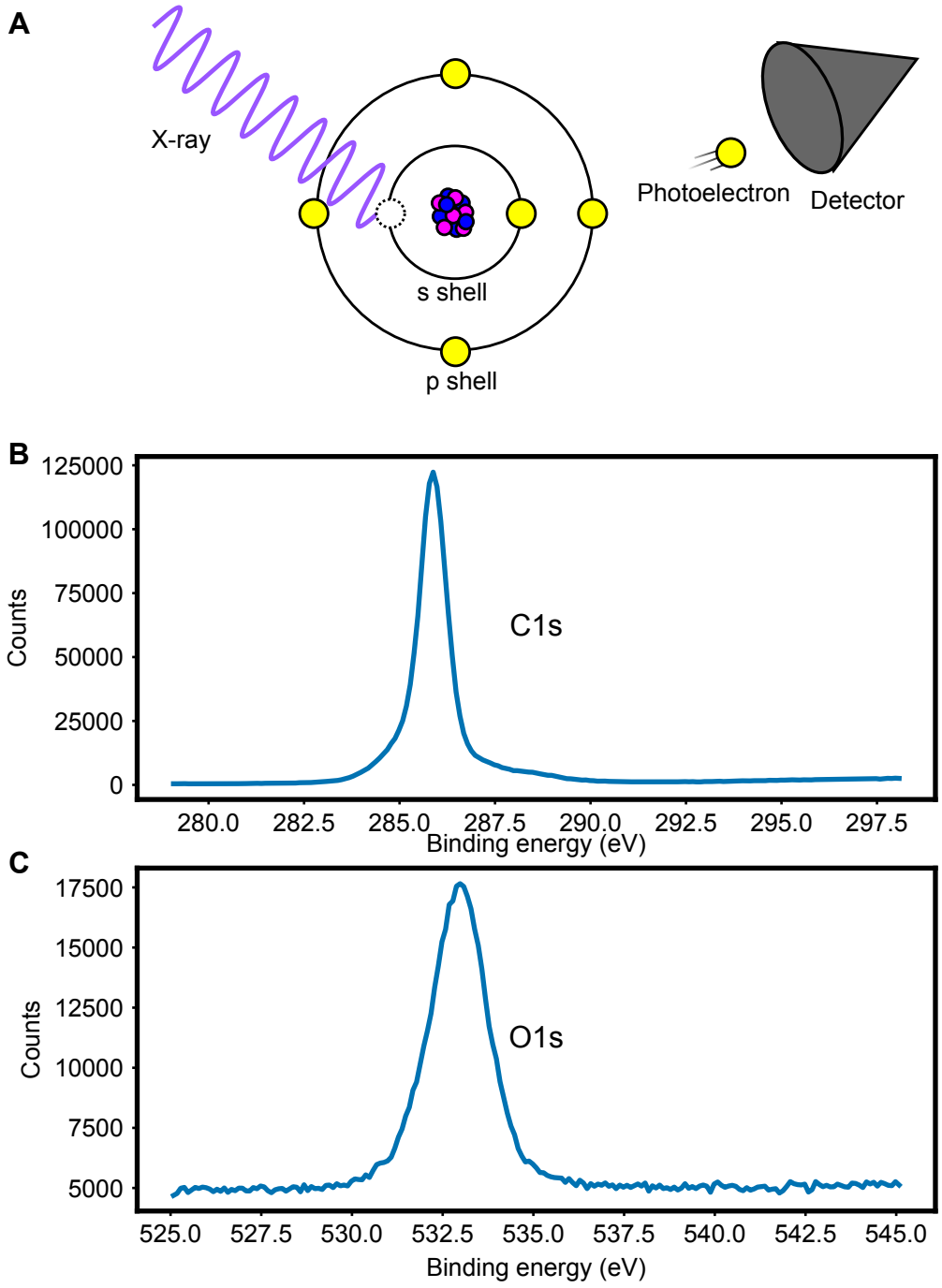
In X-ray photoemission spectroscopy (XPS), a monochromatic beam of X-rays is shone upon a sample and the energy of the incident beam is swept while monitoring the number and energy of electrons that are excited off of the sample and into the vacuum. The X-rays are of a high enough energy (100s eV) to excite core electrons[1], which have a characteristic binding energy for different elements. The presence or absence of emitted core electrons at a particular binding energy is then a probe of the presence or absence of the element whose core electrons have that particular binding energy. That is, XPS can give an elemental fingerprint of a material, and ratios of different elements can be determined by the relative intensity of emitted electrons at that element's characteristic energy. XPS is not sensitive to helium or hydrogen, however. While incident X-rays may excite atoms deep in the sample, emitted electrons are unlikely to make it to the detector unless they are very close to the surface, which makes XPS primarily a surface sensitive technique. In order to probe deeper layers of a sample, XPS is sometimes combined with ion milling. The binding energy of an atom depends on its electrostatic environment, and so in many cases it is also possible to resolve peak shifts

[1] The first shell is called the "K-shell" in X-ray spectroscopy. This absorption threshold is then called the "K-edge."

and broadening due to chemical bonds. The ability to determine both the elemental composition of the surface and they types of chemical bonds have made XPS an extremely important tool. Its development and popularization earned Kai Siegbahn a Nobel Prize in 1981 [325].

Figure 2.8 *(following page)*: XPS schematic. (A) Schematic depicting the XPS measurement, where X-ray photons (purple) ionize core electrons from atoms. The photoelectrons are detected and their energy is measured. (B) Typical XPS spectrum from diamond at the carbon binding energy (C1s). (C) Typical XPS spectrum from diamond at the oxygen binding energy (O1s). The ratio in the two signals can be used to estimate the proportion of the two atomic species.

Figure 2.8: (continued)



Near edge X-ray absorption fine structure absorption spectroscopy (NEXAFS)

NEXAFS is similar to XPS in that high energy (100s eV) X-rays are used to excite core electrons, but rather than measuring the primary electron yield, NEXAFS can monitor fluorescence and secondary (Auger) electrons produced when nearby electrons fall into the hole left by the photoexcited core electron. Auger electrons carry information about the higher lying orbitals that have decayed to fill in the missing core electron. The states that contribute to the NEXAFS signal are much more numerous than for XPS: in NEXAFS a signal can be detected from any final state of the photoexcited electron, rather than just the unbound free primaries as in XPS. This is the "absorption" part of NEXAFS. NEXAFS spectroscopy also probes unoccupied states, which contribute fine structure to the spectrum when electrons of the appropriate energy are excited into unoccupied orbitals instead of exiting the sample. While some bonding information may be inferred from high resolution XPS, it is mostly limited analyzing peak broadening, while NEXAFS spectra contain significant information about local chemical bonds in their detailed fine structure. Of particular note for diamond surfaces, NEXAFS spectroscopy is sensitive to both sp^2 and sp^3 hybridized carbon, and the different types of carbon-carbon bonds are resolvable[338]. Finally, NEXAFS is a polarization sensitive technique, since the excitation probability depends on the overlap between the incident polarization and final state molecular orbital from Fermi's Golden Rule[94]. This polarization dependence is used to determine molecular structure, and provides insight into how well ordered a particular surface is. Like XPS, NEXAFS is a surface sensitive technique, as electrons produced more than a few nanometers below the surface are unlikely to be detected. Unlike XPS, NEXAFS spectroscopy must be performed at a synchrotron that can produce monochromatic X-rays with a narrow linewidth. A good overview of the technique is found in Ref.[343].

Ultraviolet photoemission spectroscopy (UPS)

As the name suggests, in ultraviolet photoemssion spectroscopy, electrons in a sample are excited by photons with ultraviolet wavelengths. These photons are significantly lower energy (10s eV) than those used in the X-ray spectroscopy methods above. Rather than exciting core electrons, ultraviolet photons excite valence electrons. Due to hybridization of these orbitals, UPS spectra posses a certain degree of ambiguity that make them less useful for material identification. UPS is even more surface specifc than XPS and NEXAFS due to the shorter ($2 - 3$ nm) mean free path of photoionized valence electrons. UPS is a convenient way to measure the work function of a material, which is the energy required to remove an electron and send it into the vacuum. Since incident photons are usually produced from a discharge lamp with a fixed wavelength, the work function, W, is given by

$$W = h\nu - (E_{\text{lower}} - E_F) \ , \tag{2.1}$$

where ν is the frequency of the incident photons, E_{lower} is the cutoff energy below which no electrons are collected, and E_F is the Fermi energy, which is the largest binding energy with a measurable signal. The work function provides information about surface atoms, which affect the surface charge distribution, and is related to the electron affinity, $\Delta\chi$, as

$$\Delta\chi = W + E_F \, . \tag{2.2}$$

Low energy electron diffraction (LEED)

Low energy electron diffraction provides structural information about the surface in a manner similar to bulk X-ray diffraction. Just as in X-ray diffraction, the condition for constructive interference

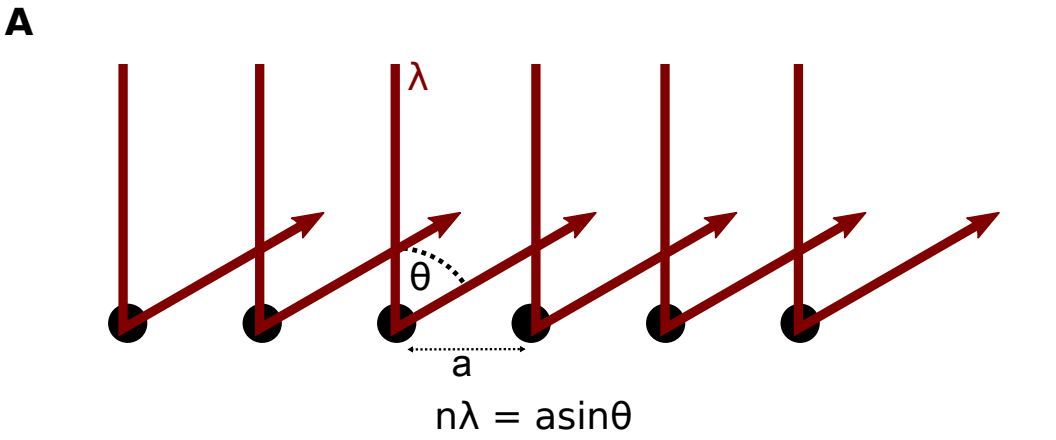
between an incident electron with wavevector $\vec{k}_i$ and a diffracted electron with wavevector $\vec{k}_f$ is [12]

$$\vec{k}_f - \vec{k}_i = \vec{K}\,, \tag{2.3}$$

where $\vec{K}$ is a reciprocal lattice vector. Low energy electrons are used for this technique because they do not penetrate very far into the sample (a few angstroms), so the reciprocal lattice $\vec{K}$ is the 2D lattice of the surface and not of the crystal as a whole. In practice, a collimated beam of low energy ($\approx$ 100 eV) electrons is fired perpendicular to the sample surface so that $\vec{k}_{i,\parallel} = 0$ and the pattern of spots on the screen simply gives the 2D lattice structure in reciprocal space. Since certain surface terminations have characteristic reconstructions, for a well ordered surface the reconstruction type can be determined by LEED.

Figure 2.9 *(following page)*: Depiction of LEED. (A) Principle behind LEED, where diffraction of electrons creates intensity peaks when the difference in path length is an integer multiple of the wavelength. (B) Real space (red) and reciporical space (blue) lattice for a 2D square lattice with equal bond lengths (1×1). (C) Real and reciprocal space lattice for a 2×1 lattice.

Figure 2.9: (continued)



2.2 Origins of diamond surface noise probed by correlating single spin measurements with surface spectroscopy

The following section is a reproduction of the manuscript "Origins of diamond surface noise probed by correlating single spin measurements with surface spectroscopy," by Sorawis Sangtawesin, Bo L. Dwyer *et al* [308].

The nitrogen vacancy (NV) center in diamond exhibits spin-dependent fluorescence and long spin coherence times under ambient conditions, enabling applications in quantum information processing and sensing. NV centers near the surface can have strong interactions with external materials and spins, enabling new forms of nanoscale spectroscopy. However, NV spin coherence degrades within 100 nanometers of the surface, suggesting that diamond surfaces are plagued with ubiquitous defects. Prior work on characterizing near-surface noise has primarily relied on using NV centers themselves as probes; while this has the advantage of exquisite sensitivity, it provides only indirect information about the origin of the noise. Here we demonstrate that surface spectroscopy methods and single spin measurements can be used as complementary diagnostics to understand sources of noise. We find that surface morphology is crucial for realizing reproducible chemical termination, and use these insights to achieve a highly ordered, oxygen-terminated surface with suppressed noise. We observe NV centers within 10 nm of the surface with coherence times extended by an order of magnitude.

NV centers in diamond are a promising platform for quantum information processing and sensing [240,90], and shallow NV centers near the diamond surface are actively explored as highly sensitive sensors with subnanometer resolution [341,232,133,124]. Although it is easy to place NV centers near the surface by low-energy ion implantation [301,298] or delta-doping [254,301], the surface itself can host defects that lead to noise that obscures the sensing target (Fig. 2.10a). We observe that coherence time degrades with proximity to the surface in numerous samples with different surface conditions

(Fig. 2.10b), consistent with prior studies[254,81,230], pointing to the need for new techniques to understand and control diamond surfaces. Gaining precise control over diamond surface chemistry is challenging because diamond is a chemically inert material, and also because it is hard to prepare uniform, flat diamond surfaces. Surface morphology is difficult to control because diamond's hardness makes etching and polishing non-trivial. State-of-the-art diamond polishing can achieve surface roughness below 1 nm, but the resulting surface is highly strained. Plasma etching can remove this strained layer[355,109], but this process is highly anisotropic and therefore small differences in initial conditions can lead to dramatic differences in final morphology and termination[158,380] (see Appendix A6). Therefore, direct characterization of the surface is crucial for establishing that particular protocols reproducibly lead to specific, desired surface terminations.

In this work, we characterize the diamond surface by correlating photoelectron spectroscopy, X-ray absorption, atomic force microscopy (AFM), and electron diffraction with measurements of NV spin decoherence and relaxation to identify and eliminate sources of noise at the surface. We find that surface roughness leads to poor NV coherence, and we observe that surface morphology changes the density of electronic defects observed with photoelectron spectroscopy, even for the same nominal chemical termination, implying that it is critical to maintain precise control over surface purity and morphology at every processing step.

In our procedure, we remove surface and subsurface damage resulting from polishing and reactive ion etching (RIE) before ion implantation, perform high-temperature annealing to remove implantation damage, and use oxygen annealing followed by wet oxidation to terminate the surface (Fig. 2.10c, see also Appendix A1.1). In order to ensure high purity throughout processing, samples are cleaned in a refluxing mixture of concentrated perchloric, nitric, and sulfuric acids (triacid clean) before RIE and all annealing steps. Starting with scaife-polished substrates with RMS roughness of less than 1 nm, we can typically achieve final oxygen-terminated surfaces with RMS roughness $\sim$ 100 pm, as measured by AFM (Fig. 2.10d). We show detailed examples in Appendix A6 of con-

tamination and irreversible surface roughening when this procedure is not followed. Using this surface processing, we extend the coherence times of NV centers within nanometers of the surface by around one order of magnitude (Fig. 2.10b).

To study the effects of different oxygen terminations on spin coherence, we prepare samples containing shallow NV centers using low-energy ion implantation followed by high-temperature annealing at 800 °C and triacid cleaning, and focus on detailed comparison before and after oxygen annealing. This procedure, excluding the final oxygen annealing step, is widely used for preparing shallow NV centers [341,232,254,347,227,279]. We isolate the impact of the oxygen annealing step by studying the same NV centers near the surface through multiple processing cycles with and without this step.

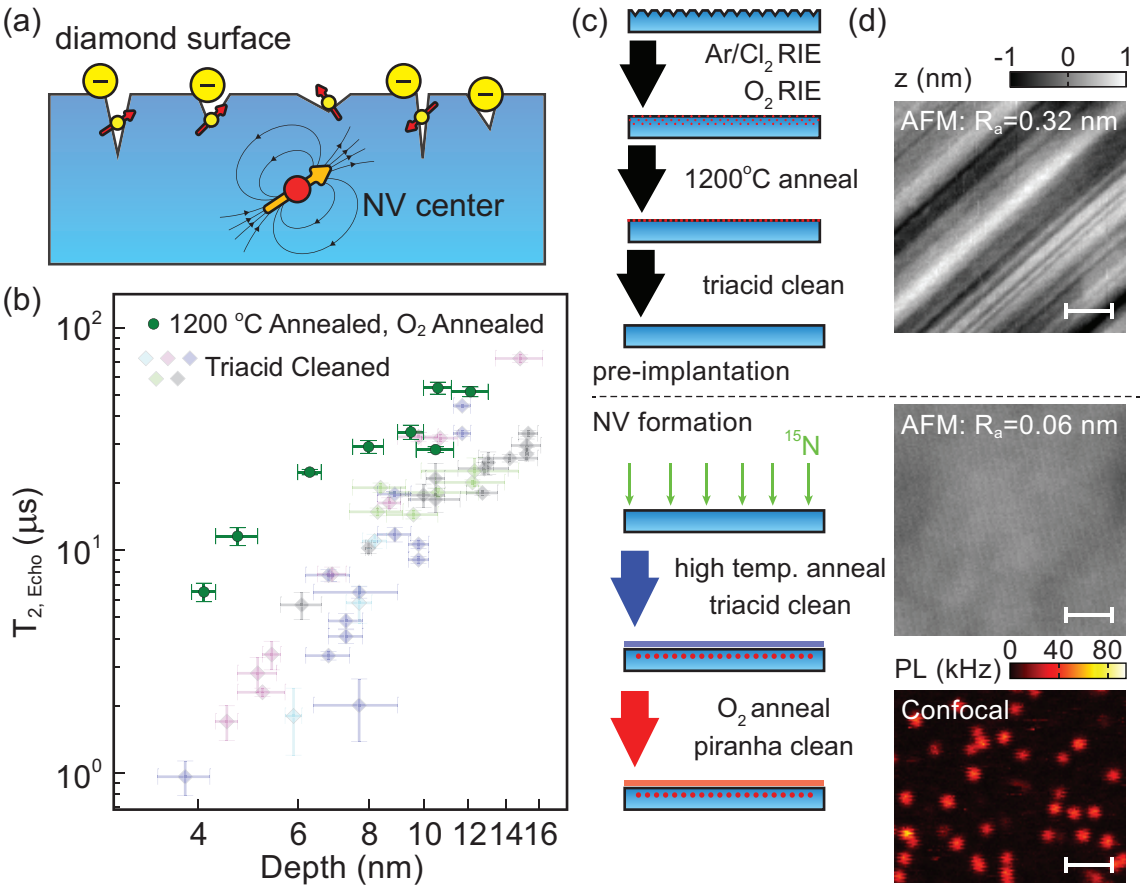


Figure 2.10: Creation of shallow NV centers with long coherence times (a) Schematic showing an NV center near the diamond surface. The surface can host defects that produce electric and magnetic field noise. (b) Hahn echo coherence time, $T_{2,\mathrm{Echo}}$, as a function of NV depth, measured across six samples with different surface conditions. Although the triacid-cleaned surfaces have different origins and processing histories (see Appendix A1), the relationship between $T_{2,\mathrm{Echo}}$ and depth is similar across all samples, and the high-temperature and oxygen-annealed sample exhibits significantly improved coherence times at the same depths. (c) Surface processing steps before implantation to remove surface polish damage and subsurface RIE damage, and after implantation to form NV centers and create a well-ordered oxygen surface termination. The high-temperature annealing step can be performed at 800 °C or 1200 °C. (d) AFM images of initial scaife-polished diamond (top) and the final surface after oxygen annealing (middle). Scale bar is 100 nm. (bottom) Confocal image showing individually resolvable NV centers. Scale bar is 1 μm.

We performed single spin measurements on shallow NV centers that are implanted into an electronic grade diamond sample with natural abundance ^{13}C, before and after oxygen annealing. Six NV centers were randomly selected from a confocal scan. Their depths were measured using proton

NMR signal from the microscope immersion oil[279] (see Appendix A2.4), and the direct comparison of their properties under the two surfaces is shown in Fig. 2.11. We measured the coherence time, $T_{2,\mathrm{Echo}}$, using a Hahn echo sequence for each NV center. We then studied the spectrum of the local noise environment using XY4 and XY8 dynamical decoupling sequences[80,298]. Additionally, we studied the high frequency spectral properties of the noise using single- and double-quantum relaxation measurements for both surfaces[255].

Figure 2.11a shows a comparison of a Hahn echo decay of the same NV center before and after oxygen annealing. The measurements were performed at $B_z = 1900$ G in order to average out the free precession of the 1.1 % natural abundance of ^{13}C in the sample. We observe a significant increase in $T_{2,\mathrm{Echo}}$ under the oxygen-annealed surface compared to the triacid cleaned surface on all NV centers (Fig. 2.11c), indicating that noise at the surface is suppressed upon oxygen annealing. However, $T_{2,\mathrm{Echo}}$ still decreases as the NV centers approach the surface, indicating that surface noise remains the dominant source of decoherence. Figure 2.11b shows an example of the measured coherence time, T_2, as a function of the number of π-pulses, N. We observe a clear improvement in T_2 under the oxygen-annealed surface by up to a factor of four compared to the triacid-cleaned surface for all N (see Appendix A8). For a slowly fluctuating bath, such as ^{13}C nuclear spins or dilute P1 center electron spins, T_2 is expected to scale as $N^{2/3}$ (Fig. 2.11b dashed lines)[80]. We fit the data to the scaling N^s and obtain $s = 0.2 - 0.7$ across all NV centers, and in some cases, we observe that T_2 saturates for $N < 40$ (Fig. 2.11b and Appendix A8). This range of values that deviate from the expected $N^{2/3}$ scaling indicates that the noise at the surface is broadband, and spectral decomposition reveals a noise spectrum spanning 10 kHz to 1 MHz (see Appendix A9).

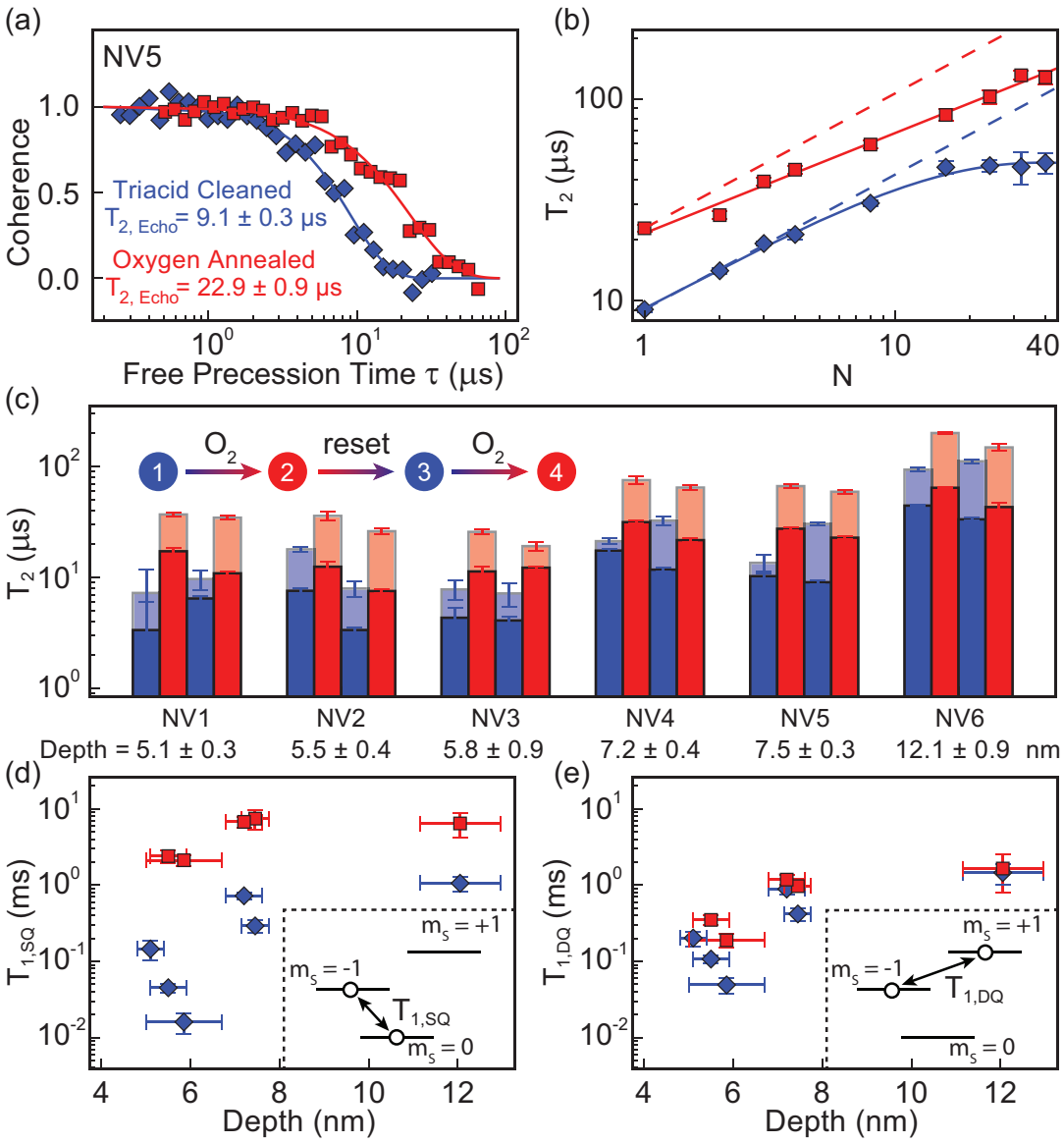
Because the surface morphology remains smooth through oxygen annealing (Fig. 2.10d), the termination is reversible. We demonstrate this reversibility by performing a "surface reset" via 800 °C vacuum annealing and triacid cleaning (Fig. 2.11c, inset). For direct comparison between different surfaces, we measure the coherence time with Hahn echo, $T_{2,\mathrm{Echo}}$, and XY8, $T_{2,\mathrm{XY8}}$, sequences from the same NV centers across different surface terminations. After the surface reset, coherence times are reduced to values comparable to those prior to oxygen annealing. Finally, these coherence times can be restored by repeating the oxygen annealing, showing that we have reproducible control over surface termination.

We note that we achieve the longest coherence times by annealing at 1200 °C after annealing at 800 °C (Fig. 2.10b). The higher temperature removes divacancies and multivacancy centers that form after ion implantation, which can contribute magnetic noise [363,70,81,384]. However, we also observe that the NV center charge state is not stable after 1200 °C annealing without subsequent oxygen annealing. Therefore, to isolate the role of the oxygen termination, we have performed these experiments with only an 800 °C post-implantation anneal.

We probe the separate contributions of electric and magnetic noise by measuring relaxation rates between different levels in the NV ground state (Fig. 2.11d,e). The single-quantum (SQ) transition can be driven by magnetic noise, while the double-quantum (DQ) transition is magnetically forbidden and can thus be used to probe electric field noise. Comparison of the measured SQ and DQ spin relaxation times allows for the extraction of SQ and DQ transition rates, which are a reflection of the relative contributions of electric and magnetic noise [255]. Figure 2.11d shows the measured SQ and DQ spin relaxation times, $T_{1,\mathrm{SQ}}$ and $T_{1,\mathrm{DQ}}$, measured at $B_z = 40$ G for the two different surface terminations. We observe an improvement in $T_{1,\mathrm{SQ}}$ of 1-2 orders of magnitude after oxygen annealing (Fig. 2.11d), indicating that the high frequency magnetic field noise is strongly suppressed, consistent with T_2 measurements that probe the magnetic field noise at lower frequencies. In comparison, $T_{1,\mathrm{DQ}}$ exhibits a small improvement (less than a factor of three) after oxygen annealing

Figure 2.11 ***(following page)*****: Comparison of NV centers under the triacid-cleaned (red squares) and oxygen-annealed (blue diamonds) surfaces** (a) Hahn echo decay curves from the same NV center. The Hahn echo coherence time, $T_{2,\mathrm{Echo}}$, is improved after oxygen annealing. (b) Coherence time, T_2, as a function of number of the dynamical decoupling pulses, N. Dashed lines depict the scaling expected for slowly fluctuating noise, $T_2 \propto N^{2/3}$. (c) Measured $T_{2,\mathrm{Echo}}$ ($N = 1$, opaque) and $T_{2,\mathrm{XY8}}$, ($N = 8$, transparent) for six NV centers through four steps of surface termination and reset (inset), showing that the oxygen annealing is reversible and reproducible. (d,e) Single- and double-quantum spin relaxation times, $T_{1,\mathrm{SQ}}$ and $T_{1,\mathrm{DQ}}$, as a function of NV depth (transitions indicated in insets). $T_{1,\mathrm{SQ}}$ shows a more pronounced improvement with oxygen annealing compared to $T_{1,\mathrm{DQ}}$, indicating that magnetic noise is more strongly suppressed than electric field noise.

Figure 2.11: (continued)



(Fig. 2.11e). Dynamical decoupling, SQ, and DQ relaxation measurements are sensitive to different frequency regimes, but the DQ transition rate is expected to scale inversely with frequency as $1/f^n$ where $n \leq 2$, allowing for extrapolation to other frequencies[255]. Spectral comparison of the dynamical decoupling data and DQ relaxation data indicates that the electric field noise is not the dominant source that limits the coherence of NV centers at high frequencies under either surface termination prepared with our methods (see Appendix A9).

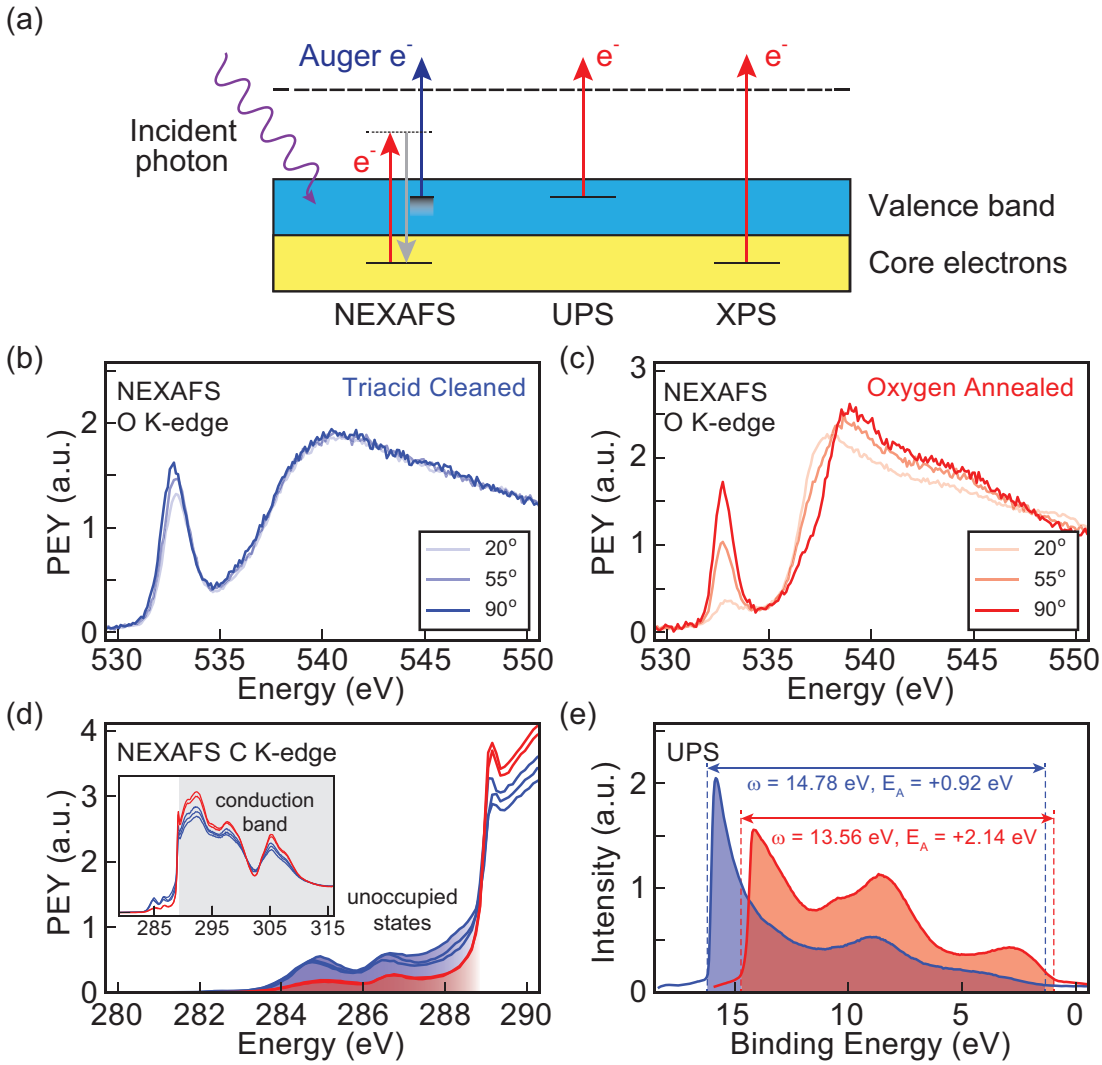
NV-based measurements indirectly suggest that the triacid-cleaned and oxygen-annealed surfaces host different electric and magnetic defects, and therefore have different electronic structure. To directly characterize the structure and chemical composition of the two different oxygen-terminated surfaces, we employ a variety of surface-sensitive spectroscopy techniques (Fig. 2.12a). Near-edge X-ray absorption fine structure spectroscopy (NEXAFS) probes the density of unoccupied states near the surface, ultraviolet photoelectron spectroscopy (UPS) gives information about the Fermi energy and electron affinity, and X-ray photoelectron spectroscopy (XPS) yields information about the chemical state of the surface termination.

The NEXAFS spectra at the oxygen K-edge for the two surfaces are qualitatively similar (Fig. 2.12b,c). Both exhibit a sharp π^* peak at 532.5 eV and a broad σ^* shoulder at around 540 eV, indicating similar chemical states. Varying the angle of incidence of the linearly-polarized X-rays changes the relative polarization with respect to the surface normal. As this angle is varied, the signal changes dramatically for the oxygen-annealed surface (Fig. 2.12c), while the triacid-cleaned surface shows no variation (Fig. 2.12b). Strong polarization dependence arises from distinct and well-resolved bond orientations[343], indicating that the oxygen-annealed surface is highly ordered at the atomic scale, while the oxygen groups in the triacid-cleaned surface are disordered (Fig. 2.13c).

The NEXAFS spectra at the carbon K-edge (Fig. 2.12d) show a characteristic exciton peak at 289.2 eV and a second absolute band gap at 302.2 eV[324]. At energies below the exciton peak at the conduction band edge, both surfaces exhibit two peaks, one at 285 eV that is assigned to sp^2 carbon, and one at 286.5 eV associated with oxygen termination[324]. However, the triacid-cleaned surface has an average of 2.4 times higher density of unoccupied states below the conduction band edge, indicated by the area under the pre-edge region. These energetically deep unoccupied states at the surface can potentially act as electronic traps that host unpaired electrons, which can contribute both magnetic and electric field noise[338]. Furthermore, a morphologically rough surface after the same surface preparation and oxygen annealing exhibits a much larger density of unoccupied states

Figure 2.12 ***(following page):*** **Surface spectroscopy comparison between triacid-cleaned (blue) and oxygen-annealed (red) surfaces** (a) Schematic showing surface-sensitive spectroscopy techniques used to probe the diamond surface. (b,c) Polarization dependence of NEXAFS spectra at the oxygen K-edge. The polarization angle is defined relative to the surface normal. The y-axis for all NEXAFS spectra is the partial electron yield (PEY), normalized and baseline subtracted (see Appendix A2.2). The oxygen-annealed surface spectrum exhibits strong polarization dependence, indicating that oxygen groups at the surface are well-ordered. (d) NEXAFS spectra at the carbon K-edge from three triacid-cleaned samples (blue curves) and two oxygen-annealed samples (red curves). Triacid-cleaned surfaces show a higher density of unoccupied states (shaded regions). The full energy range is shown in the inset. (e) UPS spectra with excitation energy $h\nu = 21.2$ eV of the triacid-cleaned (blue) and oxygen-annealed (red) surfaces. The spectral width, ω, is indicated by the shaded regions. The oxygen-annealed surface exhibits a higher positive electron affinity, E_A, ($+2.14$ eV) than the triacid-cleaned surface ($+0.92$ eV).

Figure 2.12: (continued)



than the smooth surface (see Appendix A6). Using UPS, we observe that the oxygen-annealed surface exhibits a positive electron affinity of +2.14 eV, compared to +0.92 eV for the triacid-cleaned surface (Fig. 2.12e, see also Appendix A10), indicating that the two surfaces possess drastically different electronic structure. To the best of our knowledge, this electron affinity is the largest reported for oxygen-terminated diamond[230].

Combining the data from surface spectroscopy and NV measurements, we conclude that disorder at the surface can lead to unoccupied defect states near the conduction band edge of diamond, which in turn lead to rapid decoherence of NV centers near the surface. These defect states give rise to broadband magnetic noise that cannot be circumvented by simple dynamical decoupling. It is therefore important for future applications in nanoscale sensing to devise methods to eliminate disorder and defect states at the diamond surface.

We now turn our attention to the chemical identification of the well-ordered, oxygen-annealed surface. XPS (Fig. 2.13a) reveals that the only detectable atoms are carbon and oxygen. The oxygen peak comprises 6 %–7 % of the signal, corresponding to approximately monolayer surface coverage (see Appendix A12). High-resolution XPS was used to probe the structure of the carbon and oxygen 1*s* peaks in detail (Fig. 2.13a, inset). The carbon 1*s* spectrum shows a dominant peak at 285 eV, which we assign to diamond sp^3 carbon. Two satellite peaks at higher binding energies of +1.2 eV and +2.4 eV correspond to carbon singly- and doubly-bonded to oxygen, respectively[193]. The peak at lower binding energy of −0.8 eV is assigned to sp^2 carbon. The oxygen 1*s* spectrum shows a major peak at 532.3 eV and two satellite peaks at lower binding energies of −1.0 eV and −2.8 eV with a relative ratio of 11:2:1. These peaks have been previously assigned to ether, alcohol, and ketone, respectively[21]. Low-energy electron diffraction (LEED) indicates that the surface is 1×1 reconstructed (Fig. 2.13b). Combining the XPS and LEED data, we assign the surface as predominantly ether-terminated ($\sim$ 80 %), with a minority mixture of alcohol and ketone groups (Fig. 2.13c). Additionally, our measured electron affinity is consistent with density functional theory calculations of

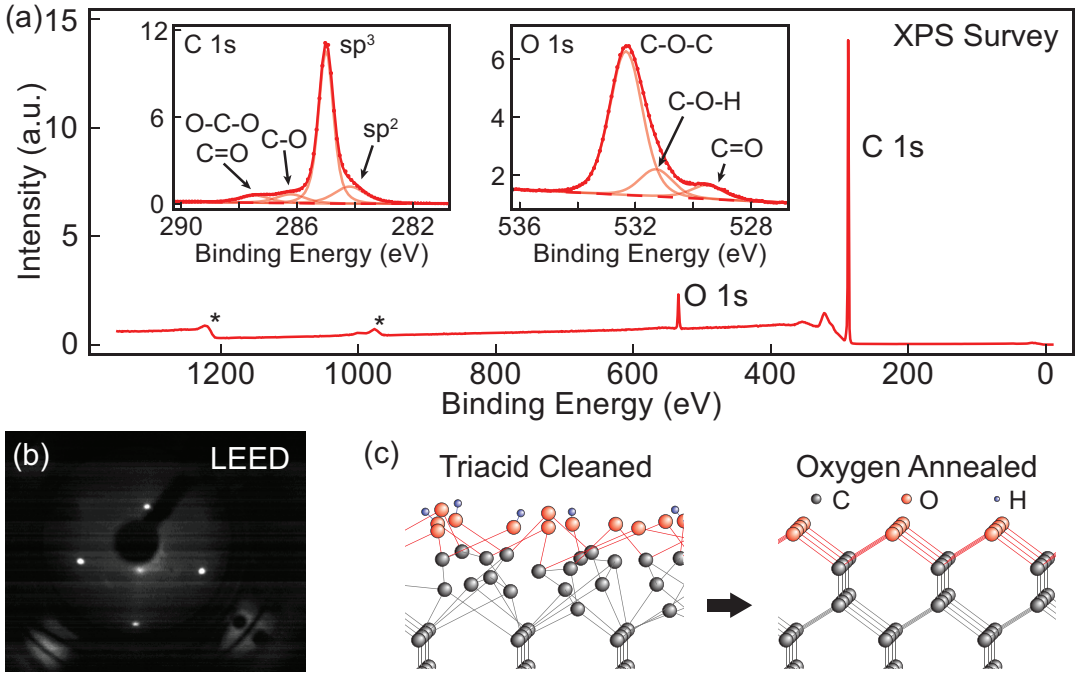


Figure 2.13: Detailed characterization of the oxygen-annealed surface (a) XPS survey scan showing dominant carbon and oxygen peaks. Peaks marked with (∗) are Auger peaks associated with carbon and oxygen. (left inset) High-resolution XPS carbon 1*s* spectrum showing a dominant diamond sp^3 peak with three side peaks assigned to sp^2 carbon, and carbon singly- and doubly-bonded to oxygen. (right inset) High-resolution XPS oxygen 1*s* spectrum showing a dominant ether (C-O-C) peak and two satellite peaks assigned to alcohol (C-O-H) and ketone (C=O). (b) LEED pattern showing a 1×1 reconstruction of the oxygen-annealed surface, consistent with ether termination. (c) Ball and stick diagrams illustrating the surface termination before and after oxygen annealing. The disordered, acid-cleaned surface hosts a mixture of groups, which transform into a highly-ordered, predominantly ether-terminated surface upon oxygen annealing.

an ether-terminated surface[336]. We note that all of the surface spectroscopy techniques are unable to directly detect hydrogen, and we thus cannot exclude that the mixed surface includes residual hydrogen, although the large positive electron affinity rules out significant hydrogen incorporation[230].

While the coherence of shallow NV centers is significantly improved by the techniques presented here, these coherence times remain far from typical bulk values[20]. The present work suggests a number of promising avenues for future study. The sp^2 peak observed in NEXAFS and XPS is a deep electronic trap, and is a natural target for improvement[338]. It was also recently demonstrated that

NV center coherence can be improved by implanting nitrogen through a boron-doped layer[81]. Combining such strategies with our surface preparation could yield even longer spin coherence. Finally, it is unknown what contribution adventitious carbon contamination makes to magnetic and electric field noise. Our ongoing work includes preparing and interrogating surfaces in ultrahigh vacuum conditions to disentangle the contributions of chemical surface termination and exogenous contamination.

Our approach of combining surface spectroscopy with single spin measurements can be applied to the future development of novel surface terminations. We have shown that surface morphology and electronic structure measurements can help to evaluate which surfaces are likely to lead to further improvements in NV coherence, which can provide useful benchmarking for rapid exploration of new surface chemistry. More broadly, the strategy of correlating surface spectroscopy with qubit measurements can be applied to a variety of quantum platforms that also exhibit deleterious effects from surfaces and interfaces, such as superconducting qubits[119], trapped ions[151], and shallow donors[270].

2.3 Discussion

The work presented in the previous section is a small step forward in our understanding of the diamond surface. The eventual goal of such studies is the production of shallow NV centers with properties more akin to those in the bulk: good optical stability, long coherence times, and high NV^- equilibrium distributions. Our oxygen termination procedure addresses some of these requirements, at least in part. NV centers under oxygen terminated surfaces have more typical ionization dynamics[392] and better contrast between spin states[338], in addition to the improved coherence times detailed here. The improvement in coherence times, while significant, is not as high as was reported in Ref.[227], which may indicate some sample dependence. While oxygen annealing pro-

duces longer coherencec times, they are still very far from bulk values. The methods introduced here provide a structured pathway to improvement of surface properties.

For example, besides the higher degree of order in oxygen annealed samples, NEXAFs data shows that samples which have undergone this procedure have a lower surface coverage of sp^2 carbon that can act as an electronic trap [338]. This surface defect is likely a major source of noise at the surface, and its identification here with X-ray spectroscopy enables rapid testing of different surface treatments that may be able to further passivate these defects.

It remains possible that there are other surface effects that influence NV center coherence that can not be easily modified. Ref. [298] suggests that "surface-modified phonons" could be responsible for some portion of the observed noise spectrum. This is supported by some work showing that T_1 of shallow NV centers has significant temperature dependence [301], though in our own samples we have observed a saturation of T_1 at low temperatures that depends on implantation energy (Fig. 2.14). If shallow NV center decohernce is truly phononic in origin, surface chemistry techniques should have little effect on NV center coherence. The observation that oxygen annealing at least can improve coherence times casts doubt on this theory.

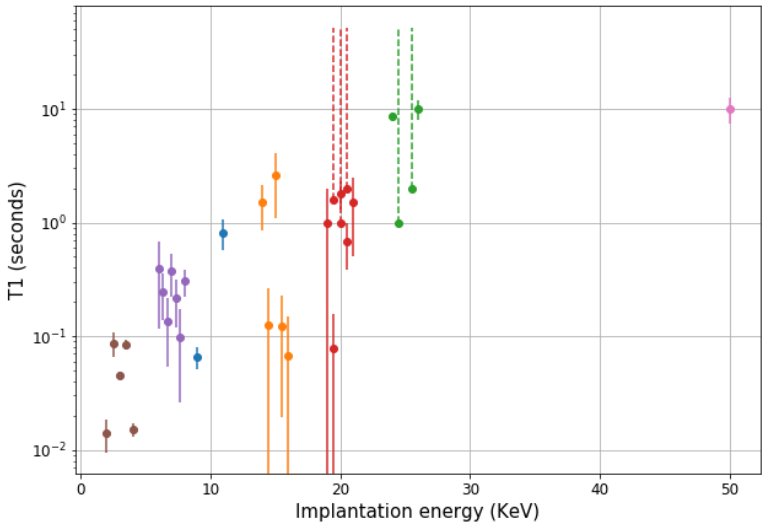


Figure 2.14: T_1 for different implantation energies. Measurements of NV center T_1 relaxation times at 70 K as a function of implantation energy. Straggle is introduced along the x axis to separate points from the same sample, so the energy of each point is approximate.

The combination of surface spectroscopy with qubit measurements has applications beyond NV centers, as many other quantum systems are thought to be limited by surface noise. Qubits based on trapped ions suffer from heating due to currents and electronic states on the trap surfaces [151]. Superconducting qubit coherence is thought to be limited by two level fluctuators on the surface of the qubit [119], but the identification and passivisation of these surface states has not received significant attention [2]. Applying materials science principles to superconducting qubit design has already yielded some exciting results when materials that are less susceptible to the formation of surface states are used [282].

As a final point, we note that NV centers in nanostructured diamonds suffer from many of the

[2] One of the most important discoveries in the superconducting qubit world over the past few years was the recognition that coherence could be extended by reducing the surface/volume ratio of a qubit by placing it in a 3D cavity [269]. In contrast, the coherence times of normal transmon qubits have not improved significantly since 2012 [282]

same noise sources as shallow NV centers, since they are both likely to be close to the surface and because there are simply more surfaces in a nanostructure. Surface treatments can in principle help mitigate some of these issues, but this is complicated by the multiple crystal faces present in a nanostructure and the possibility of subsurface defects, such as multivacancy complexes [169], introduced by reactive ion etching that may be impossible to passivate or anneal out.

The advantage of the resonance method is that it enables one to select out of the total magnetic susceptibility, a particular contribution of interest - one that may, for example, be relatively very weak.

Charles P. Slichter

3

Dynamics of surface defects

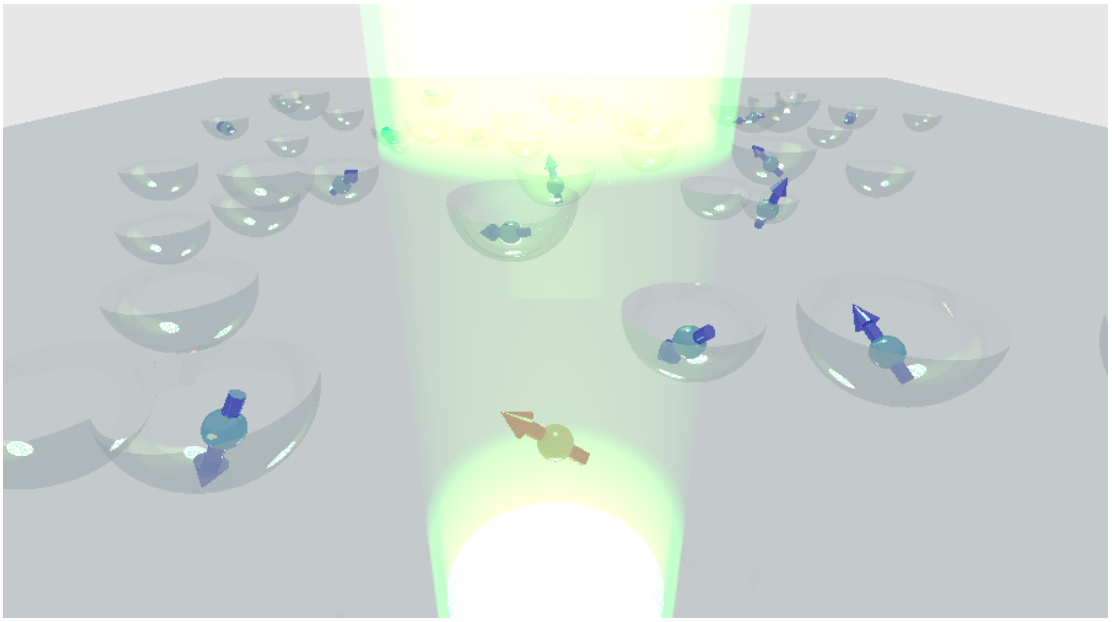


Figure 3.1: Artistic rendition of surface spins temprarily occupying traps on the diamond surface.

In the previous chapter, we inferred the existence of many defects at the diamond surface that likely contribute to NV center decoherence. In this chapter, we will turn our focus to one particular surface defect, the spin-1/2 "dark" spins that are commonly encountered on diamond samples. We will explore surface treatments that are designed to control the surface spin density and use this to investigate the effects of this particular family of spins on NV center decoherence. By investigating the character of the decoherence caused by these spins, we are additionally able to learn about their dynamics.

3.1 Background

Surface spins have long been implicated as potential sources of magnetic noise. Just like the bulk spins that cause decoherence of deep NV centers, a bath of spins on the surface creates a magnetic field that the NV center senses, but due to spin flips the value of the total field changes with time.

There are two important parameters needed to link such a bath to NV center decoherence: the density of the spins, which sets the noise amplitude, and the surface spin relaxation time, T_1, which sets the frequency spectrum of the noise bath. T_1 is also at least partially set by the density. The rate of flip-flops from dipolar coupling between surface spins can be estimated by calculating the flip-flop rate for nearest neighbor spins for a given density

$$\Gamma_{\text{dip}} = \frac{\pi}{2}\left(\frac{\mu_0 \hbar \gamma_e^2}{4\pi r_{\text{NN}}^3}\right)^2 \left(\frac{3\cos^2\theta - 1}{2}\right)^2 \tag{3.1}$$

$$\sim \left(\frac{2\mu_0 \hbar \gamma_e^2}{\pi}\right)^2 \sigma^3 , \tag{3.2}$$

where r_{NN} is the distance between nearest neighbor spins and θ is the angle between these spins. This does not tell the whole story, however, since environmental fluctuations (from neighboring spins or other sources) can significantly reduce the chances of a spin finding a resonant partner. In the presence of disorder of strength γ, the flip-flop rate is reduced to

$$\Gamma_{\text{FF}} = \frac{\Gamma_{\text{dip}}}{\gamma} . \tag{3.3}$$

This, of course, assumes that dipolar interactions are the primary cause of surface spin flips. They could, in principle, be limited by other sources of surface noise or by phonons, for example, in which case $\frac{1}{T_1} > \Gamma_{\text{FF}}$ In any case, as long as the interactions between spins are not too strong, the noise bath will be a Lorentzian with $\tau_c = 2\pi/T_1$. The strength (b in Eq. (1.54)) will show a characteristic d^{-2} scaling if the noise generating spins indeed lie on a 2D surface[254].

The decrease in coherence times of NV centers in nanodiamonds is particularly dramatic, and a bath of surface spins with areal density of $\approx$ 10 spins·nm^{-2} was proposed as the culprit[357]. When shallow NV centers were produced in single crystal diamond, similar problems were encoun-

tered[267][1]. Again, a bath of surface spins with density $0.1 - 10$ spins·nm^{-2} was invoked. The broadening of the NV center ESR lines was used to estimate the noise bath correlation time of $0.1 - 100$ ns. In Ref.[254], a bath of surface spins is introduced to account for the noise bath encountered by near surface NV centers. The authors find that a density of 0.04 spins·nm^{-2} would be needed to account for the noise amplitude, but the bath should have a correlation time $\approx$ 5 MHz if the surface spin T_1 is set by dipole-dipole coupling. This is larger than the 200 KHz correlation time that is experimentally measured through spectral decomposition. Similar densities of 0.04-0.1 spins·nm^{-2} were estimated from T_1 measurements of shallow NV centers[301]. These lower densities reflect the improved properties of NV centers in CVD grown single crystal diamonds.

One of the earliest experiments to directly probe surface spins was published in Ref.[136]. The authors used the technique of "Double electron-electron resonance" (DEER)[211] to observe effects of a second species of spin on the NV center coherence. It is not clear in this work if the spins being measured are intrinsic to the diamond surface, however, as they are only observed in silane treated diamonds and not in triacid cleaned samples. A concrete link between the DEER signal and NV center decoherence was demonstrated shortly afterwards, but again for a spins in a material applied to the diamond surface[233]. If the bath correlation of intrinsic surface spins is really in the ~nanoseconds range, then they would not be detectable by DEER anyways, as the technique requires relatively long target spin T_1 times. It was surprising, then, when surface spins were detected via DEER on the surface of an untreated diamond sample[133]. Using a magnetic tip, Grinolds *et al.* were able to image the spin bath at the surface and extract a density of 0.5 spins·nm^{-2}. While it is possible that the magnetic field gradient used for imaging could have extended the surface spin T_1 by limiting spin diffusion, it is hard to reconcile the short timescales of the noise bath with the surface spin T_1 in this experiment, which must be several μs. The density of surface spins in this sample was also

[1] The depths of the NV centers measured in this reference are likely not accurate, as they are estimated from simulations rather than proton NMR. A 1 nm deep NV center would be extremely shallow, even by modern standards.

rather high compared with subsequent estimates, which may have been due to lattice damage caused by reactive ion etching of the samples. Subsequent investigations in samples with high nitrogen implantation densities have yielded larger surface spin signals as well[352].

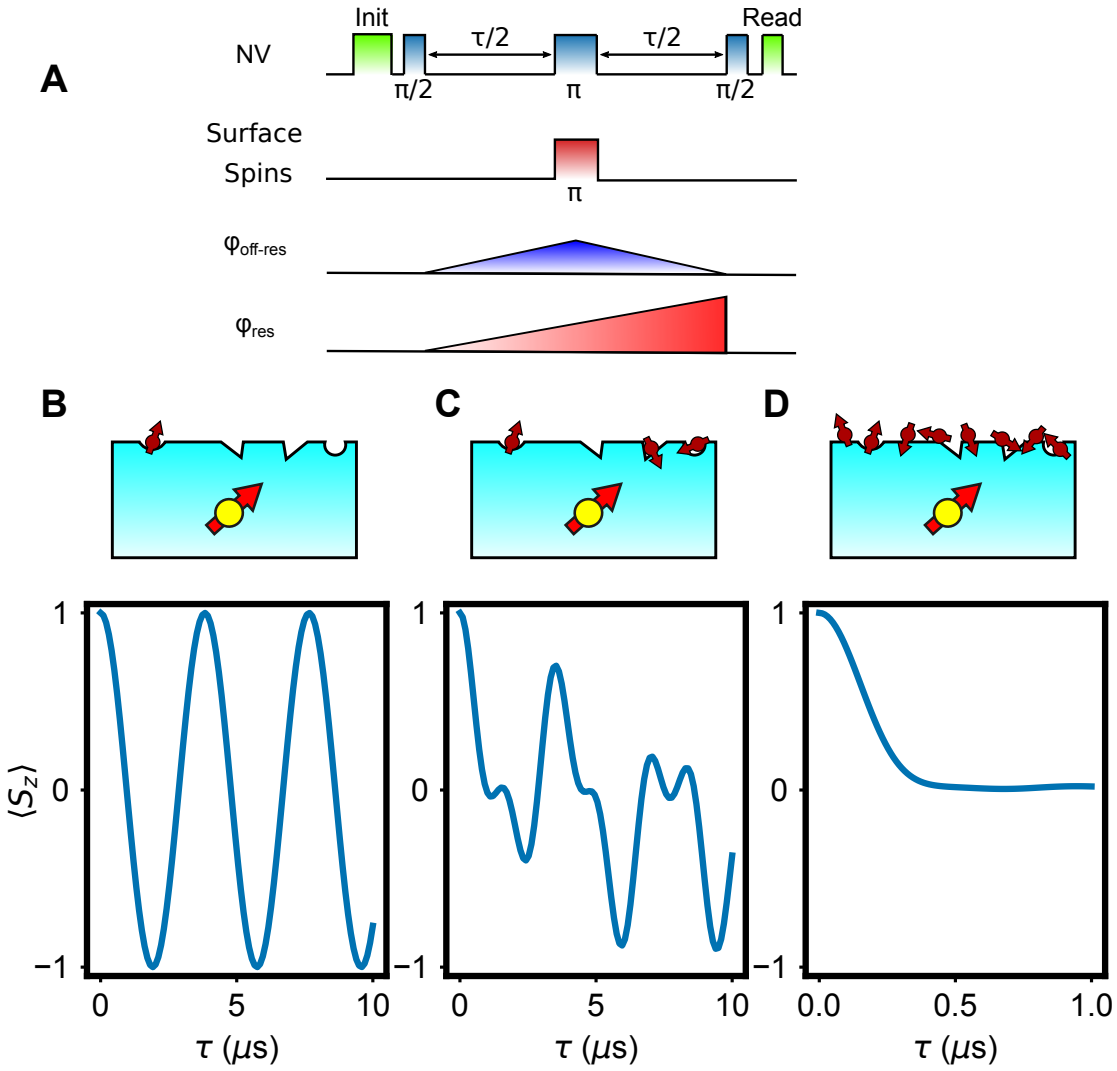


Figure 3.2: Double electron-electron resonance. (A) Pulse sequence for DEER, where a π pulse is applied to a target spin speices concurrent with the NV center π pulse in a spin echo. All off resonant phase precession is refocused, but the target spins are flipped and so phase accumulation continues. (B) For a single nearby target spin, coherent oscillations are observed at the coupling freuqency between the NV center and the surface spin. (C) For a few nearby spins, multiple couplings are resolvable in the DEER signal. (D) For a dense bath of spins, all traces of oscilaltion are eliminated and instead an incoherent, Gaussian decay is expected. Note that the time axis in (D) is reduced by a factor of 10.

In diamonds with a very low density of surface spins, it is possible to observe coherent oscillations in the DEER signal, which is indicative of coupling to a single (or few) electron spins. In Ref.[347], such samples were used to measure the properties of some of these coherently coupled surface spins. Using correlation spectroscopy techniques, Sushkov *et al.* found, somewhat astonishingly, that these surface spins had not only very long T_1 times ($\approx 30\,\mu$s), but also T_2 times of a few microseconds. This was long enough to enable the authors to use the surface spins as intermediaries to sense single proton spins on the diamond surface and relay this signal back to the NV center. This work has spurred some discussion of using surface spins as so-called "quantum reporters" of other targets[227], but to my knowledge there have been no repetitions of the feat described in Ref.[347]. The concept, however, that these surface defects that were long thought to inhibit sensing efforts might be a useful tool, is an intriguing one.

The extent to which surface spins, or at least those that can be detected with DEER, are responsible for shallow NV center decoherence is not exactly clear. In the carefully prepared single crystal diamond samples that are typically used for external sensing, the density of DEER surface spins is often too low to account for the observed decoherence. Furthermore, the long T_1 times of these spins are incompatible with the bath correlation times measured by NV center noise spectroscopy. They certainly do contribute significant noise in some samples, however, as it has been shown that driving the surface spins with a strong microwave tone can extend the coherence times of shallow NV centers in an effect analogous to motional narrowing[44,179]. These experiments still observe saturation of T_2 with microwave drive power, which suggests that the bath of driveable surface spins is not the only thing limiting coherence. It is possible that there is some other spin species that has too fast of a relaxation time to be measured through DEER, or other defects observed in the NEXAFS data of Ch. 2 may play an important role.

Another mystery that arises from the low density of surface spins is that there seems to be little variation in the DEER coupling rates for different NV centers with similar depths. For a low density

of surface spins, statistical variation in the number of spins near an NV center means that different NV centers should sense different signals, particularly as the inter-spin surface spin spacing becomes comparable to the depth of the NV center[44]. In our own samples, even when the surface spin density is low enough to occasionally observe coherent coupling to a few spins, these NV centers are the exception rather than the rule. This statistical inconsistency was one of the major inspirations for the work in this chapter, as it is difficult to reconcile with a low density of surface spins at fixed (but random) spatial locations.

Finally, although surface spins are thought to be a ubiquitous feature of diamond surfaces, their very existence is surprising. These spins seem to exist on diamond surfaces with many different treatments, have no fine structure, and have been verified to have a gyromagnetic ratio $g = 2$. All of this would point to unpaired electrons in dangling bonds, perhaps of the carbon atoms themselves. This is supported by X-ray spectroscopy data (see Appendix B) in which a peak associated with sp^3 dangling bonds is observed. These spins are, however, known to be at the surface from numerous studies[133,347][2]. That unsatisfied dangling bonds could exist in such an unprotected environment, under ambient conditions, is a phenomenon that demands explanation. We will explore one theoretical possibility in Appendix B.

While surface spins have mostly been studied to understand their contribution to NV center decoherence, there have also been many theoretical efforts to harness them. This includes the work on "reporter" based sensing schemes[347] in addition to a few other ideas. A 2D lattice of surface spins that can be manipulated by an NV center could be a promising platform for quantum simulation, especially if the defect lattice could be engineered[52]. Spin simulators in two dimensions are especially interesting because localization and thermalization dynamics are different from their 3D counterparts[216,67]. In two dimensions, the dipolar spin coupling can be easily tuned by varying the direction of the external field, and, with appropriate patterning, 2D frustrated lattices could be

[2] Whether they are actually *on* the surface is another matter entirely.

produced and studied[52].

It is also possible to perform quantum state transfer through a spin chain, which could in principle be used to couple two NV centers[47,38,9,7]. The potential usefulness of a 2D network of spins on the diamond surface has also led to some efforts to produce one in a more controlled fashion by introducing spin labels to the diamond surface[31,2].

3.2 Measurement techniques

The primary measurement technique used in this chapter is double electron-electron resonance (DEER). DEER is similar to a spin echo pulse sequence, but with an additional π pulse applied at a second frequency. The sequence is depicted in Fig. 3.2. After an initial $\frac{\pi}{2}$ pulse, the NV center spin precesses around the Bloch sphere, acquiring a phase given by $\Delta\varphi = \gamma_e B\tau/2$. If B is produced by a surface spin in the quasi static regime (T_1 longer than the sequence time), B is just a constant. The NV center π pulse and subsequent evolution would normally cancel out this phase accumulated from a DC field, but applying a π pulse to the surface spins at the same time as the NV center π pulse inverts the sign of the surface spin field, so the phase accumulation continues instead of reversing and being canceled. Even though the spin echo is an AC field sensing technique, the NV center senses a DC field from the spin bath. The technique is very sensitive since it takes advantage of the longer T_2 time of the NV center rather than T_2^*, and it is frequency selective.

There are different possible results of a DEER echo experiment depending on the density of surface spins. If there is only one spin that the NV is coupled to, each repetition of the DEER sequence achieves the same phase accumulation since $|B|$ is always the same (the initial sign does not matter). This means that the DEER signal will be a cosine at the dipolar coupling rate between the NV center and the single spin. For a few spins, there are multiple possible values of $|B|$, which correspond to the different permutations of spin states of the different surface spins (which are assumed to be

different distances from the NV center, and hence contribute different ammounts to the total field). Since each DEER sequence samples a different $|B|$ from this set, the signal will consist of cosines of a handful of different frequencies. In the limit of many spins, the distribution of possible magnetic fields becomes normally distributed, and $\langle \cos \varphi \rangle \rightarrow e^{-\frac{\langle \varphi^2 \rangle}{2}}$. That is, the signal sensed by the NV center loses all oscillatory character and becomes an exponential decay. The rate of this decay can be used to infer the density of surface spins, although it is somewhat dependent on the microscopic model used.

The extra π pulse applied to the surface spins (from here referred to as the DEER pulse) does not flip the surface spins if it is not on resonance. DEER is thus a frequency selective technique and can be used to perform spectroscopy (DEER ESR) on other spins and to learn about their interactions from dipolar broadening of the transition. The DEER π pulse time can also be varied, which, for a fixed free precession time, leads to Rabi oscillations of the DEER signal, even in the case of a dense bath of spins.

3.3 Probing spin dynamics on diamond surfaces using a single quantum sensor

The following section is a reproduction of the manuscript "Probing spin dynamics on diamond surfaces using a single quantum sensor," by Bo L. Dwyer, Lila V. H. Rodgers, and Elana K. Urbach *et al*[95].

Understanding the dynamics of a quantum bit's environment is essential for the realization of practical systems for quantum information processing and metrology. We use single nitrogen-vacancy (NV) centers in diamond to study the dynamics of a disordered spin ensemble at the diamond surface. Specifically, we tune the density of "dark" surface spins to interrogate their contribution to the decoherence of shallow NV center spin qubits. When

the average surface spin spacing exceeds the NV center depth, we find that the surface spin contribution to the NV center free induction decay can be described by a stretched exponential with variable power n. We show that these observations are consistent with a model in which the spatial positions of the surface spins are fixed for each measurement, but some of them reconfigure between measurements. In particular, we observe a depth-dependent critical time associated with a dynamical transition from Gaussian ($n = 2$) decay to $n = 2/3$, and show that this transition arises from the competition between the small decay contributions of many distant spins and strong coupling to a few proximal spins at the surface. These observations demonstrate the potential of a local sensor for understanding complex systems and elucidate pathways for improving and controlling spin qubits at the surface.

Understanding and controlling the environment of quantum bits is a central challenge in solid-state quantum science and engineering. Nitrogen-vacancy (NV) color centers in diamond have emerged as a promising platform for numerous applications in quantum sensing and information processing[240,52,312]. While bulk NV centers constitute spin qubits with exceptional coherence properties, even under ambient conditions, several applications require shallow NV centers to be placed within nanometers of the diamond surface. In particular, these shallow NV centers can be used for nanoscale sensing applications, enabling detection of individual electron spins[136,134], molecules[226], or nuclei[347]. However, shallow NV centers exhibit increased decoherence due to surface defects[254,298,308], including ubiquitous "dark" unpaired electron spins on the diamond surface[136,134]. Prior studies have demonstrated that these dark spins themselves can have long spin relaxation and coherence times, making them potentially useful as "quantum reporters" in sensing applications[347,134]. While these surface spins have been observed and studied for several years[136,233,134,347,308,44], their origin and properties are not well-understood, limiting the potential applications of shallow NV centers to harness them as a resource for sensing and simulation.

Motivated by these considerations, in this work, we systematically investigate the quantum dy-

namics of over 100 individual shallow NV centers proximal to the diamond surface, using surface treatments to adjust the density of surface spins. We find that the surface spin contribution to the coherence decay, measured across many NV centers in numerous samples, provides insight into the nature of these defects. Moreover, this large dataset permits us to observe a dynamical crossover from Gaussian ($n = 2$) decay to stretched exponential decay ($n < 1$) that is indicative of a dilute two-dimensional spin bath, averaged over many spatial configurations. We show that the crossover time is a generic feature of disordered ensembles, which has broad relevance for other solid-state qubit platforms.

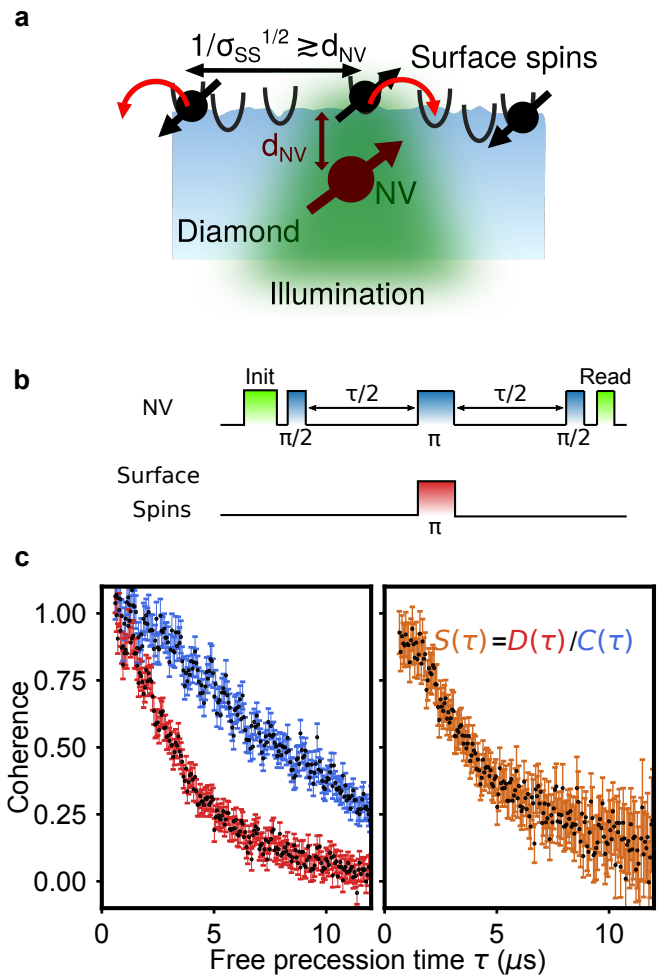


Figure 3.3: Double electron-electron resonance of diamond surface spins. **a**, Cartoon of experiment, depicting a near surface NV center (dark red arrow) with nearby traps (black wells) that are transiently occupied by spin 1/2 defects (black arrows). A 532 nm laser is used to polarize and readout the NV center. **b**, Pulse sequence for DEER, where simultaneous microwave π pulses are applied to the NV center (blue block) and surface spins (red block) midway through the free precession interval τ. Green blocks indicate NV center spin initialization and readout. **c**, Spin echo, $C(\tau)$ (blue) and DEER, $D(\tau)$ (red) curves for a representative NV center with coherence oscillations caused by slight magnetic field misalignment (left panel). In order to investigate the DEER signal, $S(\tau)$ (orange) without the influence of decoherence from other sources, $D(\tau)$ is divided by the coherence curve $C(\tau)$ (right panel). Error bars in **c** are the standard error of the mean due to photon shot noise, propagated point-by-point for the right panel.

Our experiments use NV centers produced by ion implantation [226,308] located at depths d_{NV} = 5-20 nm from the surface, under a number of different surface conditions (Appendix B2). We use

proton NMR measurements to accurately determine the implanted NV depth [278]. The surface-spin-NV interaction is studied using double electron-electron resonance (DEER) on a large, random selection of individual NV centers in each sample [249]. The DEER pulse sequence, illustrated in Fig. 3.3b, is similar to that of a spin echo, except that microwave π pulses are applied to both the NV center spin and the surface spins midway through the free evolution time [134]. This allows for selective interrogation of the flipped spins, while the signal due to non-flipped spins is cancelled to first order by virtue of the echo.

Fig. 3.3c shows an example DEER dataset. In order to remove effects that limit NV center spin coherence in the absence of surface spins, we normalize the DEER decay signal by the coherence signal obtained through a spin echo with no π pulse applied to the surface spins [308]. Since the surface spin contribution to decoherence is not canceled by the echo, the resulting decay is equivalent to the free induction decay (FID) caused by the surface spins alone. This normalization technique has the additional benefit of removing oscillations caused by the periodic entanglement with the ^{13}C nuclear spin bath [65] or slight misalignment between the NV center quantization axis and the externally applied magnetic field [302]. The full data processing and fitting procedures are described in the supplementary materials (Appendix B3).

We fit the resulting FID to an exponential decay of the form $S(\tau) = e^{-(\Gamma_{\mathrm{DEER}}\tau)^n}$, where τ is the total free evolution time, Γ_{DEER} is the DEER decay rate, and n is the exponential stretching factor. The fitted decay rates for 105 NV centers in nine diamond samples are plotted in Fig. 3.4a. For samples with similar processing histories (left plot), the couplings for a given depth cluster together, while samples with different surface preparations (right plot) show different offsets, which we interpret as arising from different densities (σ) of surface spins (Appendix B2).

To demonstrate control over the surface spin density, we anneal one diamond sample at 650 °C in vacuum and measure the same NV centers before and after this procedure (Appendix B4). In Fig. 3.4b, we plot Γ_{DEER} for the same NV centers before and after this annealing procedure and find

that, indeed, the DEER signal is significantly reduced following annealing, suggesting a reduction in the density of surface spins. We also characterize NV center coherence before and after annealing and observe that changes in coherence are minimal (Appendix B4). We note that even carefully prepared diamond surfaces host numerous other electronic traps that can be inferred from X-ray spectroscopy methods[308], and that in our samples these other traps are likely dominant sources of electric and magnetic field noise at the surface.

Previous work has treated the surface spin bath as a dense, 2D ensemble of spins with positions fixed but spin states that are initialized randomly between sequences[347,134,188,44]. The DEER decay rate can then be computed as

$$\Gamma_{\mathrm{DEER}} = \left(\frac{\mu_0}{4\pi}\right) \frac{\sqrt{3\pi\sigma}\gamma_e^2\hbar}{8d_{\mathrm{NV}}^2}, \tag{3.4}$$

where μ_0 is the permeability of free space, γ_e is the electron gyromagnetic ratio in units of radians/second, and $\hbar$ is the reduced Planck's constant. This decay arises from an ensemble average over many realizations of spin state configurations, with fixed locations, in which there is no dominant proximal spin. The resulting distribution of total magnetic field amplitudes sensed by the NV center is then normally distributed, which is a requirement for the derivation of equation (3.4) and also leads to $n = 2$ in the exponential decay[83](Appendix B6).

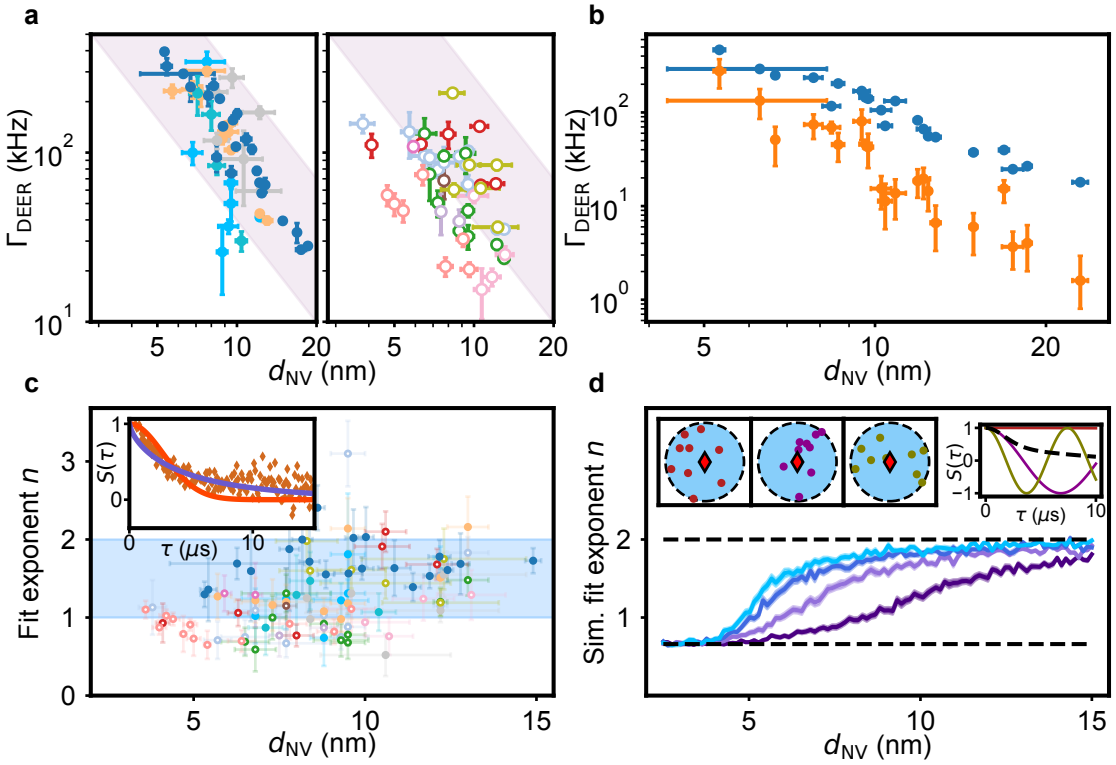


Figure 3.4: DEER coupling rates and stretching factors. **a**, Fitted DEER couplings as a function of depth for numerous NV centers. All samples in the left plot have nominally identical surface preparations (activated or reset surface, SI), while samples in the right plot represent different surface preparations described in Appendix B. Shaded region indicates expected couplings for surface spin densities of $0.001 - 0.05$ nm^{-2}, according to Eq. (3.4). **b**, DEER coupling vs depth for the same NV centers in before (blue) and after (orange) annealing at $650\ ^\circ$C. **c**, Fitted exponent as a function of depth for samples in **a**. Filled markers are samples with similar surfaces. Shaded region indicates exponents between 1 and 2. Inset: example DEER coupling curve from (orange points) fit with a fixed $n = 2$ (red) and with n as a free parameter (purple). $n = 0.7$ is a better fit. **d**, Fits of exponent vs depth for simulated data. Colors indicate different simulation spin densities of 0.008 nm^{-2} (light blue), 0.006 nm^{-2} (dark blue), 0.004 nm^{-2} (light purple), and 0.002 nm^{-2} (dark purple). Shaded regions are confidence intervals for fits of simulated data. Dashed lines indicate limiting values of $n = 2$ and $n = 2/3$. (Inset) Simulation of representative spin configurations (dots) relative to an NV center that is 5 nm deep (red diamond). Simulation radius is 25 nm. DEER signals for the representative configurations are shown in the last panel. Dashed line is an average of $10,000$ iterations. All error bars are 68% confidence intervals of the fits.

Using this model to extract surface spin densities, we find that much of our data fall well outside the regime where the assumptions of equation (3.4) are valid. The lower limit of the shaded region in Fig. 3.4a is plotted from equation (3.4) for a surface spin density of 0.001 nm^{-2}, or an

average nearest neighbor spin-spin separation of $\approx$ 15 nm (Appendix B6), greater than the depth of the majority of NV centers measured here. For such a low density of spatially fixed surface spins, equation (3.4) should not be valid because the NV center primarily senses the field from the few nearest surface spins and hence the distribution of total magnetic field amplitudes is no longer Gaussian. Additionally, different NV centers should statistically sample different surface spin configurations, leading to a large variation in Γ_{DEER} among NV centers[44]. Instead, we observe that Γ_{DEER} is fairly consistent at similar depths, and in particular does not exhibit increased variance for shallower depths, which is expected due to the increased likelihood of finding a few dark spins that are markedly closer to the NV center than the others. In the extremely dilute limit, the NV center would primarily sense the field from a single surface spin, which results in strong coherent oscillations rather than an exponential decay. While some of these strongly coupled surface spins have been observed previously[34,7,134] and were found in some of our nine samples (Appendix B2), these events are relatively rare, occurring in $< 2\%$ of measured NV centers.

In Fig. 3.4c, we examine the fitted exponent across all of the samples depicted in Fig. 3.4a. For the majority of the shallow NV centers we investigated, a Gaussian decay profile provides a poor fit to the data, as is demonstrated in Fig. 3.4c (inset). Furthermore, we observe that shallower NV centers exhibit lower fitted exponents (Pearson's correlation coefficient 0.4, $p < 1.5 \times 10^{-5}$), and that many NV centers exhibit $n < 1$. The exponential stretching factor n is related to the form of the noise generated by the environment spins[83]. In particular, a Gaussian ($n = 2$) decay occurs for a quasi-static bath, while a smaller exponent may arise from a finite bath correlation time. For a white noise bath, this exponent saturates at $n = 1$, so the observation of $n < 1$ for many NV centers is surprising. Additionally, measurements of the surface spin T_1 times for a select number of NV centers in this sample (Appendix B5) find surface spin T_1 times are generally $> 30\ \mu$s, which is long compared to the spin echo decay time of the shallow NV centers, and so the quasi-static assumption is justified. We also note that although a short surface spin T_1 time can reduce the value of n from

2 towards 1, the stretching factor as a function of depth should display a trend opposite to that of Fig. 3.4c (Appendix B7).

Finally, for a few NV centers, we sample the coherence decay with much finer time steps to interrogate the shape of the decay in more detail. In Fig. 3.5a, we plot the logarithm of the inverse DEER signal, $\log\left\{S(\tau)^{-1}\right\}$, as a function of free precession time on a log-log plot so that the stretching factor is given by the slope of the line. Instead of a single slope, we observe a transition in the stretching factor at some critical time, which increases with increasing NV center depth.

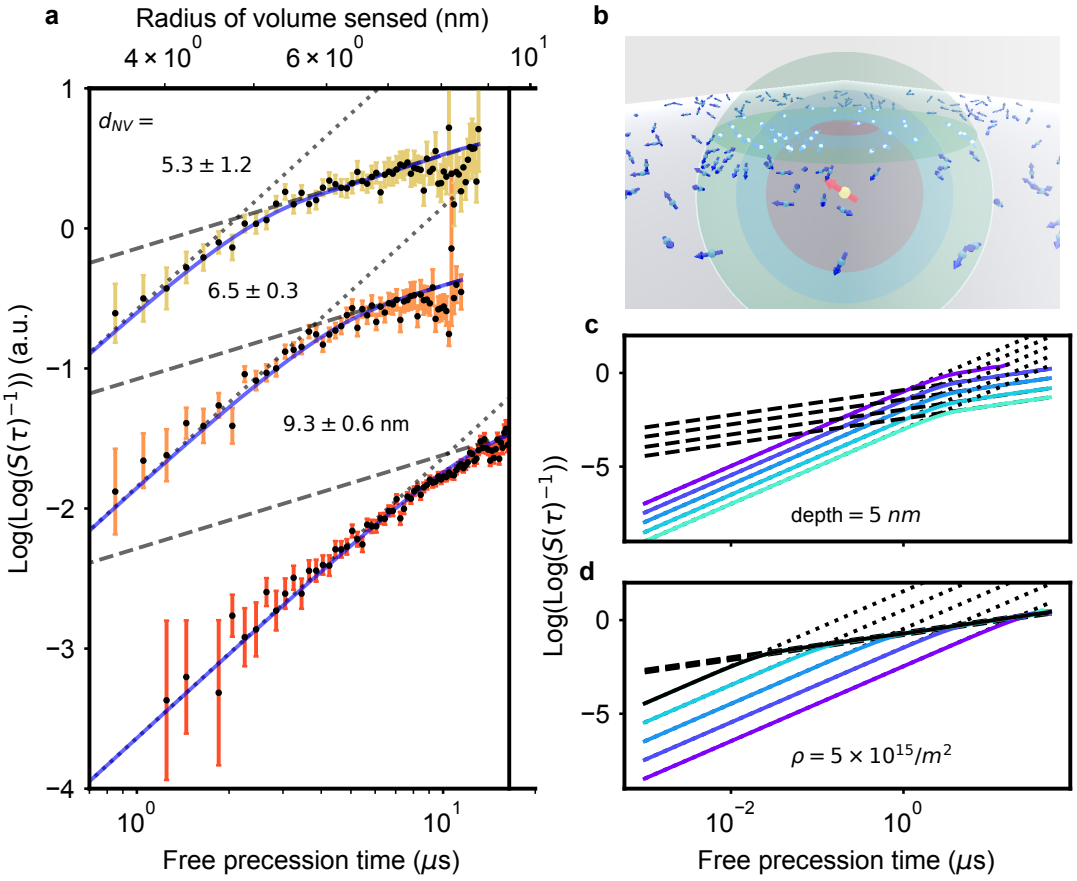


Figure 3.5: Temporal transition of the stretching factor. **a**, DEER echo signal from shallow NV centers in with three different depths extracted from the proton NMR signal. Error bars are the standard error of the mean due to photon shot noise. The purple line is a fit with the analytical result for configurational averaging (SI). Dashed line is $n = 2$, dotted line is $n = \frac{2}{3}$. Curves are offset for clarity. **b**, Diagram depicting the expanding strong dipolar coupling volume of the NV center as the duration of the echo sequence increases. The form of the signal detected by the NV center changes as the volume intersects with the 2D plane of the surface spins. **c**, Simulations of the DEER echo signal detected from a 5 nm deep NV center near a surface with a logarithmically spaced density of 10^{-4} nm^{-2} (blue) to 10^{-2} nm^{-2} (purple) where surface spins undergo configurational averaging. The dashed lines correspond to $n = 2$, and the dotted lines correspond to $n = \frac{2}{3}$. **d**, Simulation of the DEER echo signal detected from NV centers with log spaced depths from 1 nm (blue) to 10 nm (purple) with configurational averaging of the surface spins. The density of simulated surface spins is 0.005 nm^{-2}. The solid black line is the analytic solution for a 1 nm deep NV center (SI).

In order to explain our observations showing the lack of statistical variation among NV centers, the lack of coherent coupling to surface spins, the observed anomalously small decay exponents,

and the transition in decay exponents with time, we consider a model wherein most of the surface spins do not have permanently fixed locations, but can occasionally "hop" between unoccupied sites such that the position is stationary for one experimental sequence and may change between sequences, as depicted in Fig. 3.3a. The NV center then effectively senses a surface spin ensemble averaged over many positional configurations. For a dilute bath, such an averaging drastically changes the form of the decay due to strong fluctuations of the dipolar coupling strength stemming from the shot-to-shot fluctuations in the spin positions [194,89]. In particular, the stretched exponents arise naturally from sampling different configurations of the spin bath, each with its own characteristic decay time [89,339]. Other electronic defects in diamond are known to change occupation under the intense illumination of the 532 nm laser used for NV center polarization and readout [328,381], and so it is conceivable that optical initialization and readout are responsible for inducing reconfiguration. The required averaging in our experiments would make it difficult to determine the frequency of reconfiguration or to observe an effect from illumination power, as, due to the large number of experimental repetitions typical of NV center experiments ($\sim 10^6$ repetitions), even a small probability of hopping results in sampling many spatial spin distributions.

In order to quantitatively investigate our model, we performed Monte Carlo simulations of the DEER signal resulting from configurational averaging of a low density of surface spins, as shown in Fig. 3.4d (insets). By fitting the resulting FID of a large number (10^5) of averages to an exponential decay with a variable exponent n, the depth dependence of n is readily apparent and is in qualitative agreement with the trend observed in Fig. 3.4c. The fitted values of n approach 2 for large depths ($d_{\mathrm{NV}} > 1/(2\sqrt{\sigma})$), but gradually transition to a value of $2/3$ as the depth is decreased below the average surface spin separation.

By integrating over the possible configurations of surface spins [206], we can obtain an analytic expression for the DEER signal measured by an NV center external to the spin bath (Appendix B6). For short times such that $\frac{\mu_0}{4\pi}\gamma_e^2\hbar\tau \ll d_{\mathrm{NV}}^3$, we recover equation (3.4) and $n = 2$, even though the

spins are assumed to be non-stationary in this case. In the opposite limit, $\frac{\mu_0}{4\pi}\gamma_e^2\hbar\tau \gg d_{\mathrm{NV}}^3$, we find instead

$$\langle S(\tau)\rangle_c = \exp\left(-\frac{9\sqrt{\pi}\Gamma(\frac{11}{6})\sigma}{5}\left(\frac{\mu_0\gamma^2\hbar}{8\pi}\right)^{2/3}\tau^{2/3}\right), \tag{3.5}$$

where $\Gamma(x)$ is the Gamma function. The stretching factor $n = 2/3$ for a 2D bath of spins has been predicted previously [103,141], and its appearance here implies that for long times the entire system, including the sensor, behaves as if it is two dimensional.

In our finely sampled data in Fig. 3.5a, we find that the data are well-fit by our analytical model, which captures the transition regions that move to later times for increasing depths. Because the location of this transition is sensitive to depth alone, it is possible to extract a depth for each NV center from these measurements independent of the surface spin density. These extracted depths are in good agreement with those measured by proton NMR, which additionally indicates that the spins we address are indeed at the diamond surface (Appendix Fig. B.12). Further model comparison and additional datasets can be found in the Appendix (Appendix B8-B9).

In Fig. 3.5c and Fig. 3.5d, we examine the simulated behavior of n in more detail by plotting $\log\left\{S(\tau)^{-1}\right\}$. We note a change in the stretching factor from $n = 2$ to $n = 2/3$ at a depth-dependent critical time, similar to what is observed in the data in Fig. 3.5a. The shift of this transition to earlier times for shallower NV centers indicates that the intermediate values of n measured in Fig. 3.4c and simulated in Fig. 3.4d are not the result of a continuously varying exponent, but rather of averaging different numbers of points that lie in either the $n = 2$ or $n = 2/3$ regions of the decay and fitting to a single exponent.

In some cases, re-positioning of surface spins can be detected more directly. In Fig. 3.6a, we show DEER traces from the same NV center measured minutes apart, showing both a coherent coupling signal that dips below 0 (red), and a weak incoherent coupling signal observed a short time later

(orange). By binning into smaller numbers of averages for a fixed free precession interval of 2 μs, it is possible to see the switching behavior in real time in Fig. 3.6b. We interpret these results as indicating the presence or absence of a particularly stable proximal spin, and hence as evidence that the occupation of such traps can change. While our model does not rule out the existence of some number of stable, spatially fixed spins, based on the percentage of measured NV centers in our samples that display coherent oscillations, we estimate an upper bound on the number of stationary surface spins of $\approx 10\%$ of the total spins detectable by DEER (Appendix B10).

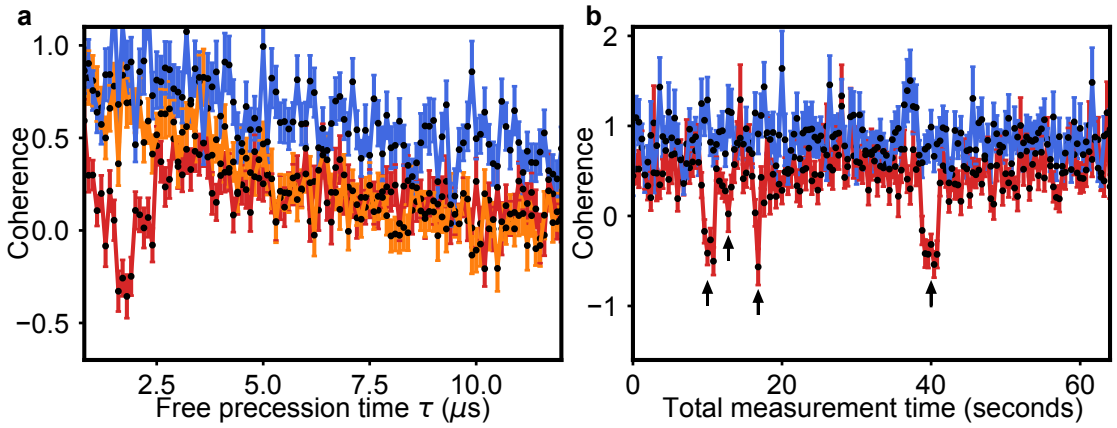


Figure 3.6: Transient strong coupling of surface spins. **a**, Coherence (blue), coherently coupled DEER signal (red), and incoherent bath signal (orange) from the same NV center measured at different times. **b**, Time series for NV center in **a**, with a fixed free precession interval of 2 μs. The DEER signal drops below 0 for short intervals, indicating transient coherent coupling to a nearby dark spin (black arrows). Error bars are the standard error of the mean due to photon shot noise.

The time-dependent behavior of the exponent n can be understood by considering the dipolar coupling between an NV center and the sheet of surface spins at a distance d_{NV} away. Initially, the NV center senses a small contribution from all of the spins, which results in a Gaussian ($n = 2$) decay. Once the phase accumulated from the nearest spin reaches a large enough value ($\frac{\mu_0}{4\pi}\frac{\gamma_e^2\hbar}{d_{\mathrm{NV}}^3}\tau \sim 2\pi$), further time evolution contributes only an oscillatory phase while more distant spins still contribute a summation of many small phases. This process can be considered with a simple geometric picture. The quantity $(\frac{1}{2\pi}\frac{\mu_0}{4\pi}\gamma_e^2\hbar\tau)^{1/3} \approx (52\ \mathrm{MHz}\cdot\mathrm{nm}^3\tau)^{1/3}$ defines the radius of a sphere,

centered on the NV center, that increases with the free evolution time. Spins within this sphere contribute significant phase ($\gtrsim \pi$) to the NV center. Initially, there are no surface spins within this sphere. The sphere of strong coupling will increase in size until it intersects the surface when $(52\,\mathrm{MHz}\cdot\mathrm{nm}^3\tau)^{1/3} \approx d_{\mathrm{NV}}$, at which time spins begin to interact strongly with the NV center. As is depicted in Fig. 3.5b, the number of strongly interacting spins grows with the cross-sectional area that intersects the surface plane, which grows like $\tau^{2/3}$. It is only once the volume of strong interactions grows to include the plane in which the spins dwell that the dimensionality of the bath impacts the NV center coherence, and the NV center decay reflects this dimensionality for long times. In a sense the NV center becomes a member of the 2D bath for sufficiently long interaction times, which is supported by the absence of any dependence on d_{NV} in the long-time limit given by equation (3.5).

The inferred dynamics of the surface spins has immediate consequences for surface-spin-based sensing of external targets and for using surface spins as a model system to explore many-body interactions in two dimensions. In particular, the stability of these spins needs to be taken into account and may need to be enhanced. Samples prepared with different processing might host more stable surface spins [347], and it is possible that diamond surface treatments could be used to stabilize, rather than eliminate, these defects. Lacking this, other, potentially more stable systems, such as spinful defects in 2D materials [221,390], could be transferred onto the diamond surface and interrogated by NV centers. A more accurate determination of reconfiguration probability and mechanism could be made with single-shot readout of the NV center through resonant excitation [296,170] or mapping the electronic spin state to the host nitrogen spin [226]. Furthermore, techniques such as nano-MRI [134,131] or MRFM [305] could enable a more systematic survey of surface spin properties. Dilute spin ensembles in other materials can be studied with scanning NV center experiments [231,272] where the distance to the sample can be tuned continuously. More generally, the techniques for understanding surface environment dynamics presented here may be broadly applicable in other quantum systems.

Specifically, the dynamics of proximal probes can carry significant information: the minimum impurity separation, the dimensionality of the environment, and the scales of finite dimensions are all reflected in the behavior of the decay, constituting a promising tool for studying the disordered environment of quantum systems.

3.4 Discussion

While the statistical arguments and characteristic shape of the coherence decay observed in the previous section certainly suggest that a spatially static bath of surface spins is unlikely, they are far from a direct observation of spin "hopping." More direct determination of this phenomenon may prove difficult, especially if it is indeed facilitated by laser excitation.

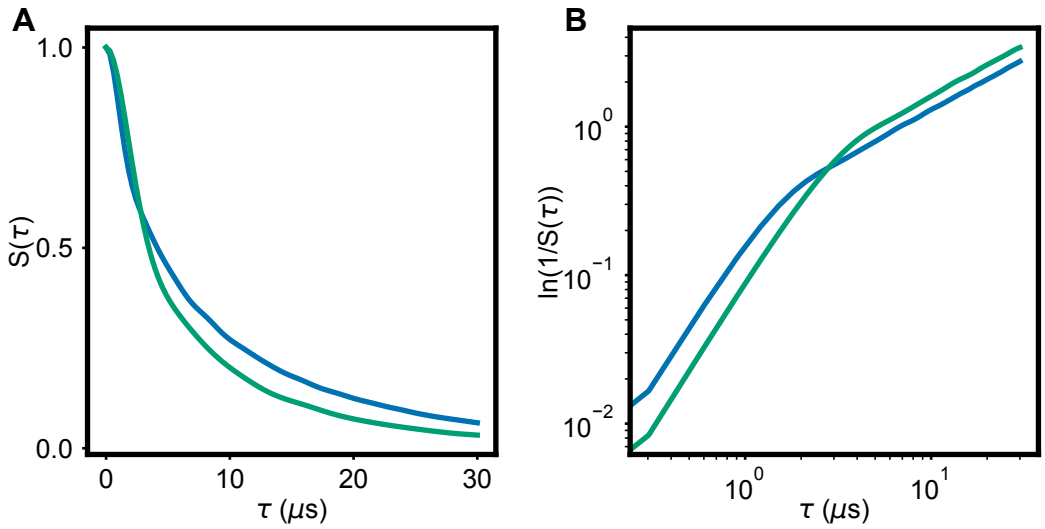


Figure 3.7: Mid sequence scrambling of surface spins.(A) Simulated DEER decay curves for the case of fixed positions for each free precession interval (blue) and for different positions for the two free precession intervals (green), as could be the case for a mid sequence scrambling pulse. (B) Same simulation as in (A), but with $\ln S(\tau)^{-1}$ plotted on a log-log plot so that the stretching factor is given by the slope.

One possibility is that longer wavelength light may also be able to excite reconfiguration of surface spins, but without affecting the NV center. If this were the case, it would be possible to induce reconfiguration mid sequence, which would result in a different decoherence profile (Fig. 3.7). The difference from the usual configurational averaging prediction is not dramatic, however. If it so happens that light with a wavelength shorter than the NV center zero phonon line is required, a similar effect could be obtained using a "donut" beam, wich could excite nearby traps without repolariz-

ing the NV center at the center, as long as the electronic mean free path on the surface is sufficiently long. It might also be possible to observe a motional narrowing effect by rapidly photoexciting the surface spins during an NV center sequence. However, the best tool to study these spins would likely be one that does not rely on photoexcitation, such as scanning SQUIDs or MRFM. While we have proposed photoexcitation as a probable mechanism for rearrangement, this has not in fact been demonstrated. It is also possible that thermal excitations are the culprit–some charge traps have been observed to change occupation in the dark[43].

The dynamical nature of these defects complicates proposals to use them as tools for sensing and simulation. For sensing, at least, it is important that the reporter spin maintains a constant relative position between itself and the NV center that is used to interrogate it. While such stable spins have been observed, their rarity means that such tools are inherently stochastic and are ill suited for general sensing work where co-localization is already a difficult task. For simulation, dynamic, random redistribution of the simulation components would severely limit the sorts of systems that could be studied. Since all of the spin-spin couplings could change for each repetition, performing state transfer through a spin bus would also likely be impossible. This does not mean that all of these proposals are in vain, but perhaps they would be better realized in a more stable spin environment. Attaching molecules with protected electronic spins to the diamond surface, or using defects in Van der Waals materials, are two possible avenues for realizing controlled and stable spin networks.

In addition to investigating the dynamics of the surface spins, we have provided a possible microscopic model for how they could arise in sterically protected step edges of the diamond surface. X-ray spectroscopy data, coupled with the NV center DEER measurements, provides some evidence that the DEER spins are indeed sp^3 dangling bonds, but more study is needed. In particular, the diamonds used for the NEXAFS study and DEER study were not the same, and different furnaces were used for the annealing procedures which may have had different calibrations. Even if all of these details were worked out, correlation between the NEXAFS data and the NV center measure-

ments does not necessarily mean that the dangling bond peak in NEXAFS is the *cause* of the DEER signal.

Finally, the analysis of the decoherence profile applied in this chapter is a very general technique that can be applied to any number of disordered quantum ensembles. Indeed, while preparing this manuscript, we became aware of a related work[78] exploring the same concept in a different system. In their manuscript, Davis *et al.* investigate the decohernce profile of a quasi-2D layer of P1 centers that, unlike the surface spins investigated here, have fairly strong interactions. They find analogous results, but for a system with a fast bath correlation (e.g. $n = 1/3$ instead of $n = 2/3$ in the long time limit).

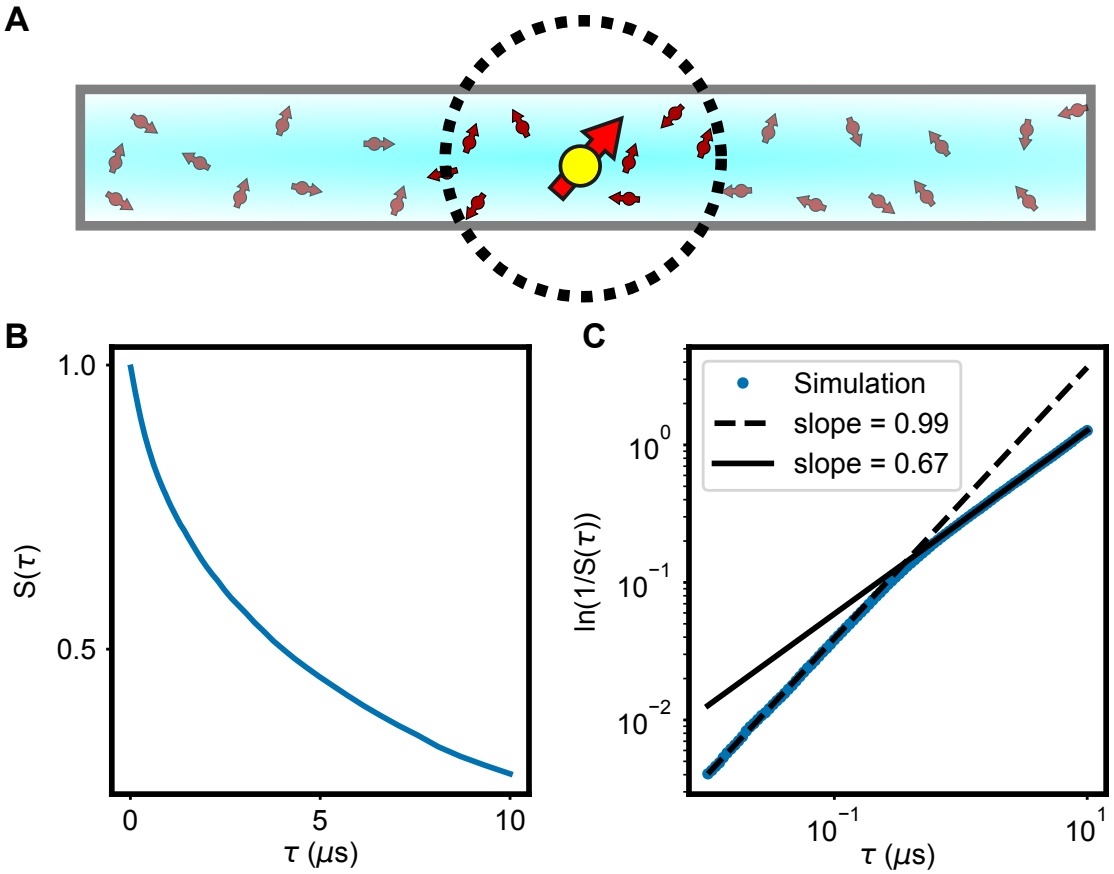


Figure 3.8: Simulation of 3D to 2D crossover behavior in the case of a central spin sensing a spin bath in a slab of finite thickness. (A) Schematic of a central spin (yellow and red arrow) in a slab of bath spins (red). Once the sphere of strong coupling breaks out of the slab, counting proceeds as a 3D volume intersecting a surface. (B) Calcualted DEER signals for the slab geometry. (C) Same simulation as in (B), but with $\ln S(\tau)^{-1}$ plotted on a log-log plot so that the stretching factor is given by the slope. The initial slope is for 3D spin counting ($n = 1$) but when the dipolar coupling volume breeches the slab it continues as 2D ($n = 2/3$). In principle at the very earliest times, no spins are counted and $n = 2$, which is the regime explored in the previous section.

These results are also not limited to NV centers. The same behavior could, in principle, be observed in the free induction decay of a bulk crystal. It is, however, the shortest spin-spin spacing that sets the transition time in a bulk measurement, however, so the time at which the exponent changes scale would be very short. Part of the advantage of an external probe is that this length scale can be varied by simply moving the probe farther away. The behavior of systems with different interaction

strengths, such as Rydberg atoms r^{-6}, or systems with more complex dimensionalities, such as a slab of spins with finite thickness, are also easy to predict with our geometric model (see Fig. 3.8). These techniques will hopefully find widespread use in may different quantum systems.

The noise is the signal.

Rolf Landauer

4

Global and local probes of an electron-phonon Cerenkov instability in graphene

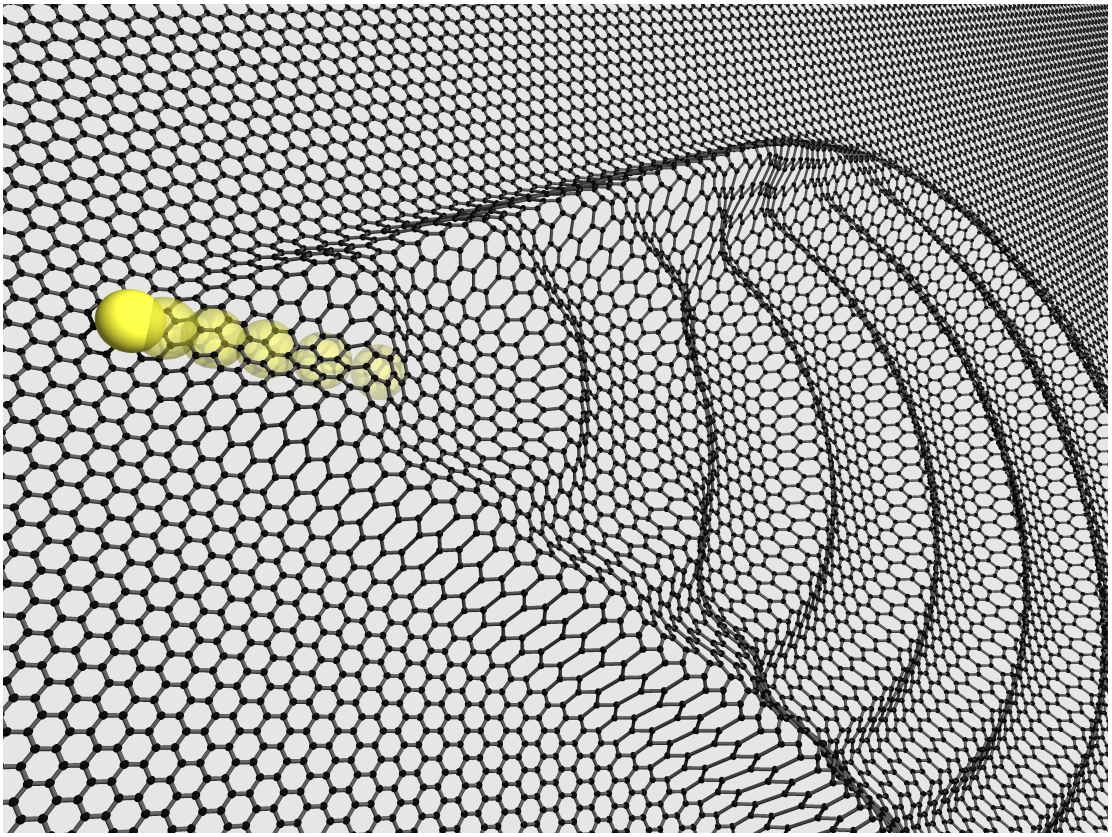


Figure 4.1: Artistic rendition of the electron-phonon Cerenkov effect in graphene.

In this chapter, we move away from sensing intrinsic diamond properties and instead turn our focus to the exploration of external materials. We combine global transport-based noise measurements of graphene with the unique nanoscale noise sensing capabilities of the NV center to explore a striking phenomenon in highly biased graphene. This chapter begins with a discussion of the types of noise common in electronic systems, which will be contrasted with the observed noise in our graphene devices. Previous experiments quantifying noise in graphene are reviewed, followed by a brief explanation of the techniques that will be used throughout this chapter. After this, we present the experiments published in Ref. [9], followed by a discussion of their relevance and future applications. Throughout this chapter we will use the notation $S_x(\omega)$ to refer to the noise spectrum of a

measurable quantity x, with V for voltage and I for current.

4.1 Background

All measurements are subject to noise of some sort. Usually, as experimentalists, we would like to eliminate as much noise as possible in order to perform measurements with a high degree of precision. It may seem surprising, then, that noise itself can contain useful information, and is itself the target of experiments. We have already seen some examples of this in Ch. 2 and Ch. 3, where the measured noise spectrum includes information about spins in a qubit's environment. In fact, noise measurements have a long and important history. It was, after all, the observation of a type of noise, Brownian motion in 1827, and it subsequent explanation by Einstein[98] that unequivocally proved the particulate nature of matter. Noise continues to be a useful tool for studying physical systems, in a large part due to the fluctuation dissipation theorem.

4.1.1 The fluctuation dissipation theorem

The linear response of a system can be expressed in terms of the system's thermal fluctuations. This is the statement of the fluctuation-dissipation theorem, one of the capstones of statistical physics. More concretely, for a linear[1] system with a response function $\chi(t)$, in thermal equilibrium at a temperature T, the fluctuation-dissipation theorem states that

$$S_f(\omega) = \coth\left(\frac{\hbar\omega}{k_B T}\right) \mathrm{Im}[\chi(\omega)]\,, \tag{4.1}$$

where $S_f(\omega)$ is the noise spectral density at a frequency and Im denotes taking the imaginary part of χ. k_B is Boltzmann's constant. Eq. (4.1) is the full quantum mechanical version of the theorem,

[1] By linear, we mean that the response of the system is linear in the perturbation. That is, for some observable $x(t)$ and a perturbation $f(t)$, we should be able to write $\langle x(t)\rangle = x_0 + \int_{-\infty}^{t} \chi(t-\tau) f(\tau) d\tau$, where χ is the response function that describes how the observable responds to the perturbation.

which shows the influence of vacuum fluctuations in the regime $k_B T \ll \hbar\omega$. Although this distinction is important in some cases[314], we can usually take the high temperature limit to find the more familiar classical version of Eq. (4.1):

$$S_f(\omega) = \frac{k_B T}{\omega} \mathrm{Im}[\chi(\omega)] \,. \tag{4.2}$$

While this relation may at first seem surprising, the physical intuition behind it is straightforward. Considering the Brownian motion example, applying a (randomized) force to the particles in a system will add energy and cause them to heat up, and conversely increasing the temperature will cause more random motion of the particles, which should result in more noise. The really remarkable thing is how universal this realtion is.

The fluctuation-dissipation theorem applies to any system that obeys detailed balance, and hence there are many physically relevant χ that can be measured simply by monitoring thermal noise! This includes, for example, the mobility of particles diffusing in a medium (e.g. Brownian motion), dielectric and magnetic susceptibilities, and the conductivity of a metal. It is this last response function that we will concern ourselves with here.

4.1.2 Johnson-Nyquist noise

Johnson-Nyquist noise is the electronic equivalent of Brownian motion, where the random motion of electrons in a conductor cause voltage fluctuations. This type of noise was first observed by Johnson in 1927[178] and later given a straightforward derivation by Nyquist[266]. This broadband noise is given by

$$S_V(\omega) = 4 R k_B T \,, \tag{4.3}$$

where R is the resistance. We recognize Eq. (4.3) as a special case of the fluctuation-dissipation the-

orem with $\mathrm{Im}[\chi(\omega)] = 4\omega R$. This noise exists regardless of the type or composition of the conductor. Since Johnson-Nyquist noise depends only on the resistance of the sample (which can be measured) and the temperature, it has been used extensively as a thermometry technique[378]. In addition to being universal, Johson-Nyquist noise is essentially featureless: it has no dependence on ω, at least for $k_B T \gg \hbar\omega$ and reasonable frequencies. This is because the low-frequency conductivity of metals is not very exciting: it is flat up to the electron scattering time ($\sim$THz). At a constant temperature, fluctuations (Johnson noise) are really a measurement of the response function (conductivity), and so the noise spectrum is also flat.

Graphene is a somewhat unique material in that the electron and phonon temperatures need not coincide. It is possible to heat graphene electrons far out of equilibrium with the lattice by flowing a current, for example, because acoustic phonon scattering is very inefficient[332], as is demonstrated in Fig. 4.2. It is so inefficient, in fact, that the primary cooling pathway between hot electrons and phonons is thought to be defect mediated "supercollision" cooling[33,199]. This introduces a cooling bottleneck, and so even at a low bath temperature, the electrons in graphene can be very hot. This electron temperature is naturally measured through Johnson noise thermometry[72].

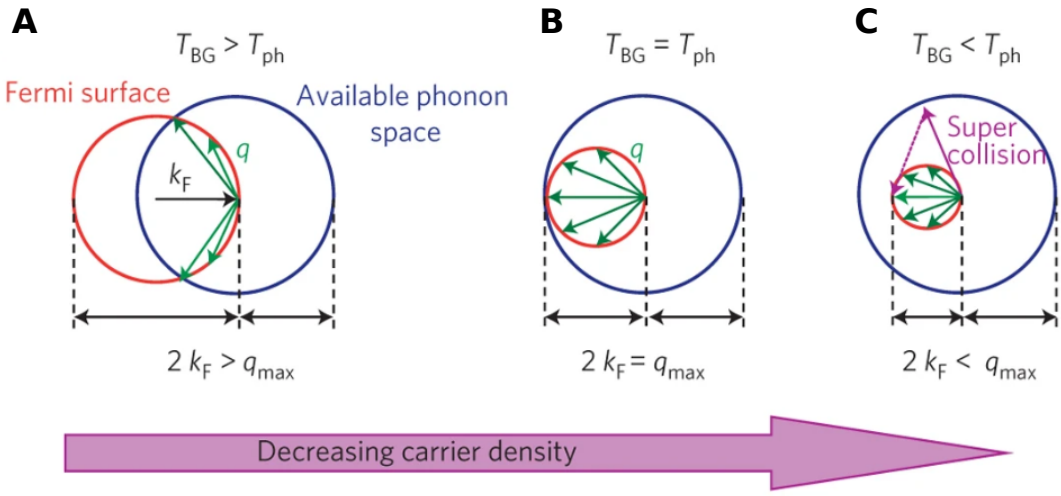


Figure 4.2: Acoustic phonon scattering in graphene. (A) If the Fermi surface of graphene is large enough, it is easy for an electron to scatter to an unoccupied state along the Fermi surface through absorption or emission of a phonon in the available phonon space. (B) Once the Fermi surface shrinks such that $2k_F < q_{\max}$, only a small fraction of the available phonon space can contribute to scattering. (C) A "supercollision" scattering event permits an electron to scatter with a long wavelength phonon since the defect absorbs some momentum. T_{BG} = Bloch-Gr'uniesen temperature, $2\hbar v_s k_F/k_B$, where v_s is the speed of sound. Figure taken with permission from Ref.[33].

1/F NOISE

$1/f$ noise is so named because the noise spectral power density increases for low frequencies according to

$$S(\omega) \propto \frac{1}{\omega^{\alpha}}, \tag{4.4}$$

where $1 \leq \alpha < 2$. This noise typically only occurs at low frequencies ($\lesssim$ 1 GHz), as the rapid decrease with frequency means other noise types (Johnson Noise, for example) dominate at higher frequencies[153]. $1/f$ noise is ubiquitous, afflicting everything from superconducting qubits[50] to graivtional wave detectors[1]. There is no generalized theory of $1/f$ noise[40], but it is thought in some cases to arise from charge traps with a wide distribution of trapping times. By considering many such flickering noise sources, each with its own characteristic time[153], it is possible to reproduce the

$1/f$ scaling as is outlined in Fig. 4.3 [242]. $1/f$ noise has a power dependence as well as a spectral dependence as it tends to increase in magnitude for increasing current. The reason for this is simple: $1/f$ fluctuations are actually fluctuations of the conductance, and so application of a large current results in a large voltage fluctuation through Ohm's law. Since many modern devices operate at much higher frequencies, $1/f$ noise is avoided, but it can be a consideration in high powered electronics due to its correspondingly larger magnitude in high current devices.

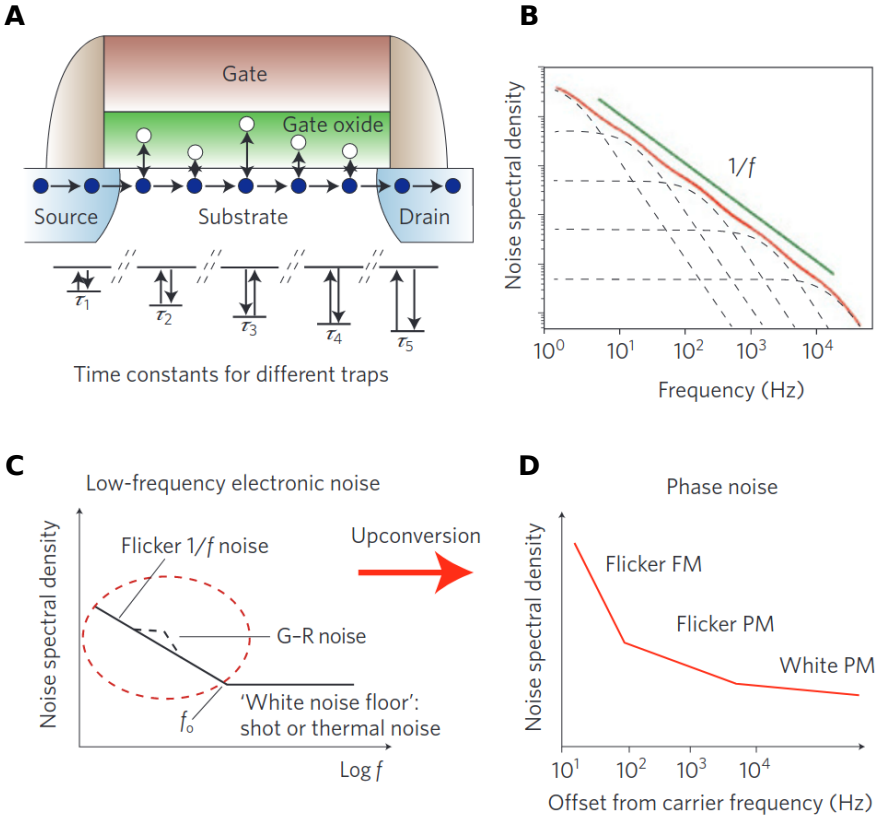


Figure 4.3: Origins of 1/f noise. (A) Traps in the substrate or gate dielectric can cause conductance fluctuations with a distribution of time constants. (B) For a logaraithmically spaced distribution of trapping times, the total noise exhibits a 1/f spectral dependence. (C) Typical noise spectrum in electronic devices, which is dominated at low frequencies by 1/f noise but which transitions to thermal or shot noise once the 1/f noise decreases below the noise floor. Some devices may exhibit an additional G-R "bump" at a characteristic frequency. (D) 1/f noise only occurs at low frequencies, but it upconverts to higher frequencies in real world systems due to nonlinearities and so makes up a significant portion of the noise in modern communications systems. Figure taken with permission from Ref. [19].

$1/f$ noise has been observed in graphene devices on silicon dioxide[33,19], but is greatly suppressed in devices that use hBN as a substrate[185]. This is thought to be due to the much higher number of defects at the graphene/SiO_2 interface compared with hBN, which could provide electronic traps and local changes to the doping profile.

4.1.3 Shot noise

Shot noise is another fundamental noise that arises from the discrete nature of particles. It is a sort of counting noise that quantifies the variation in the number of particles that arrive at a detector in some time t. For fully independent particles, if the mean number of detected particles in a time t is λt, then the number of particles that are detected follows a Poisson distribution

$$p(n) = \frac{(\lambda t)^n}{n!} e^{-t}, \tag{4.5}$$

where $p(n)$ is the probability of detecting n particles. The variance of this distribution, and hence the shot noise, is given by $\sigma^2 = \lambda t$. Shot noise is commonly encountered in optics experiments when few photons are collected (including NV center experiments). Since electrons are also discrete particles that can be counted, current flowing through a conductor should also display shot noise. It turns out that shot noise in conductors is a phenomenon of some subtlety, and explaining when it should occur and why was a major triumph of mesoscopic physics.

Schottky showed that electron shot noise should take on the value[315]

$$S_V(\omega) = 2eI, \tag{4.6}$$

where e is the electric charge of an electron and I is the average current. While this was observed to be the case in vacuum tubes, noise in conductors is usually dominated by Johnson-Nyquist noise.

In order to observe electron shot noise in conductors, experiments had to be conducted at very low temperatures and with a limited number of conduction channels. Even then this effect is difficult to observe: unlike photons, electrons are 1) Fermions and 2) interact strongly with matter and with each other. Since electrons are Fermions, the independence constraint of Poissonian statistics is not exactly satisfied, as electrons cannot occupy the same state (for example, a transmission mode in a conductor) simultaneously. The result is that for perfectly ballistic transport in a thin wire, no shot noise is observed[289]. When otherwise ballistic electrons undergo some scattering, shot noise arises from the probabalistic transmission and reflection of electrons at these scatterers, which partition the conductor. The shot noise in a conductor should actually be given by

$$S = \frac{e^3 V}{\pi\hbar} \sum_n T_i(1 - T_i)\,, \tag{4.7}$$

where T_i are the transmission eigenvalues for each conducting channel. Application of this formula generally results in a value of the shot noise that is less than Eq. (4.6), which is only recovered in the limit of very small T_i. The ratio of the measured noise to the value $2eI$ is known as the Fano Factor, $\mathscr{F}$, and this may be calculated explicitly for many systems. Interestingly, partitioning a wire into many segments, as effectively happens in a disordered conductor, again leads to a suppression of the noise to a value of 1/3 of the Poissonian value[29]. Real macroscopic conductors see even greater suppression, which may be due to inelastic scattering[208,29], but some work has shown that correlations between electrons due to Fermi statistics are sufficient[223,222]. This is a useful result, as it implies that measurements of shot noise provide information about scattering mechanisms[2]. One expects different values of $\mathscr{F}$ depending on whether electrons remain phase coherent ($\mathscr{F} = 1/3$), momentum conserving (electron-electron) collisions dominate ($\mathscr{F} = \sqrt{3}/4$), or there is no scattering

[2] Another way that shot noise can provide information about a system is if the value of e differs from that of a bare electron. Shot noise resulting from transmission across a superconducting/normal barrier, for example, has a Fano factor of 2 because Cooper pairs have charge $2e$[30]. Quasiparticles with fractional electron charge have also been measured in this way[82], and there exist proposals to probe Majoranas[46].

($\mathscr{F} = 0$)[342].

Shot noise has been observed in graphene[88,75] (see Fig. 4.4), which has a predicted Fano factor of $1/3$ near the charge neutrality point[364]. This value is surprising, since it is the same as for a disordered metal, but occurs only in the ballistic regime where no shot noise should be observed for a perfect conductor. It is a peculiar quirk of massless Dirac Fermions, as at the charge neutrality point, transport is thought to occur through evanescent modes extending across short distances[364], and so the similarity to the disordered metal result is purely coincidental. For higher charge densities, the Fano factor is decreased further.

Shot noise and Johnson noise are fundamental types of noise. When no bias is applied to a sample, there is only thermal noise. When a current is flowing, shot noise becomes dominant. This transition is captured by the expression[51]

$$S_V(\omega) = 2eI\mathscr{F} \coth\left(\frac{eV_{\mathrm{sd}}}{2k_BT}\right) . \tag{4.8}$$

The transition between these two regimes in graphene is displayed in Fig. 4.4B.

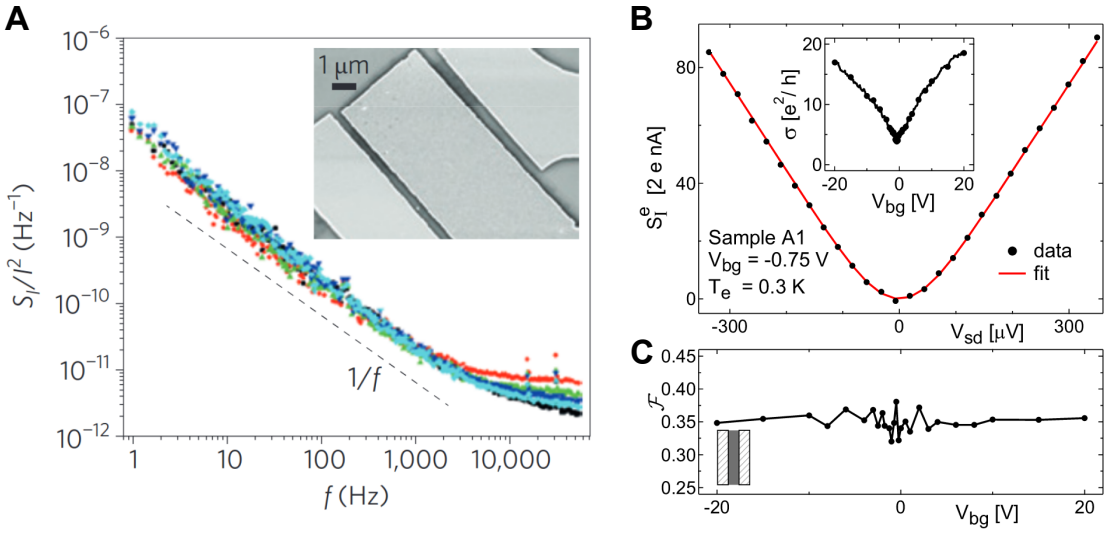


Figure 4.4: Noise in graphene devices. (A) 1/f noise in several graphene devices on SiO_2. Figure taken with permission from Ref.[19]. (B) Crossover from thermal noise to shot noise in a short graphene device. Inset: conductivity of graphene device as a function of gate voltage showing the Dirac peak. Fit is to the expression in Eq. (4.8). (C) Fitted Fano factor of $\approx 1/3$ at different gate voltages. (B) and (C) taken with permission from Ref.[88].

4.1.4 Generation recombination noise

A final common type of noise in electronic systems is generation recombination (GR) noise. This noise occurs due to fluctuations in the numbers of charge carriers in a semiconductor due to transitions between different states, for example different energy bands or mid gap states[250]. This noise has a characteristic timescale associated with the carrier lifetime, and so has a Lorentzian (or multiple Lorentzian) spectrum.

Graphene is a semimetal rather than a semiconductor so there should not traps within the band gap, but traps in the substrate and gate dielectric can locally change the conductivity as charges tunnel into and out of these traps. These sorts of traps are likely the origin of 1/f noise in graphene, but distinctive GR noise with a Lorentzian frequency dependence is only expected to occur at graphene PN junctions, or possibly at metallic contacts, which can slightly dope graphene[59]. While GR noise is not usually observed as a unique noise source in graphene, we mention it here for completeness.

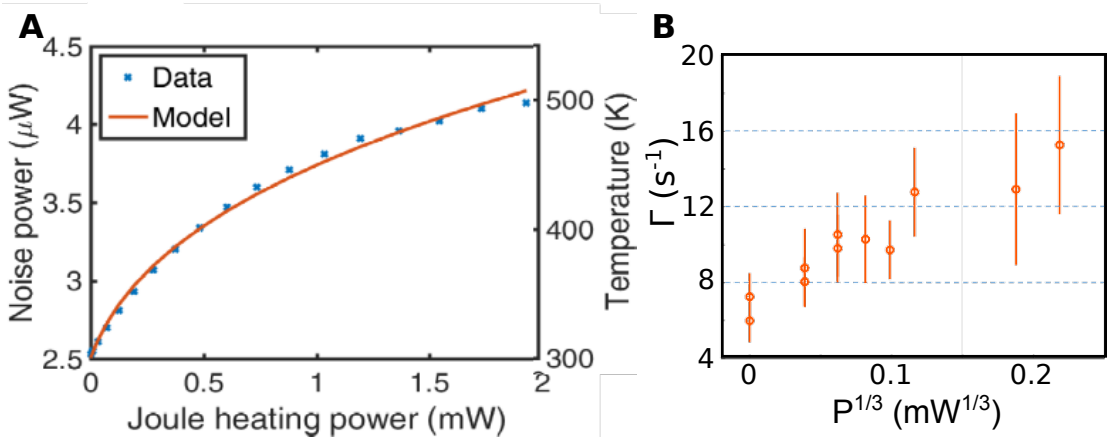


Figure 4.5: Power dependence of noise in graphene. (A) Temperature of electrons in a graphene device as a function of heating power, as measured by Johnson noise thermometry. The fit is to a 1/3 power scaling. (B) NV center relaxation rate as a function of heating power, showing a similar scaling. The power scaling is in agreement with a dominant defect assisted cooling mechanism[33].

All of the types of electronic noise we have discussed so far have characteristic dependencies on applied power. Shot noise is proportional to current, and so $S_V(\omega) \propto \sqrt{P}$. $1/f$ noise typically scales linearly with power. The scaling of Johnson noise with power depends on the cooling pathways (how this power translates into increased temperature), but it is sublinear in power[97,331]. For clean graphene at low doping, $T \propto P^{1/3}$ [33] (Fig. 4.5). For higher dopings where acoustic phonon scattering is more efficient, $T \propto P^{1/4}$ [34]. GR noise also scales with $S_V(\omega) \propto \sqrt{P}$. None of these common noise sources give rise to a signal that is superlinear in the applied power over any integrated frequency range. As we will see, such a power dependence can occur, but it implies there is some sort of instability in the system providing positive feedback.

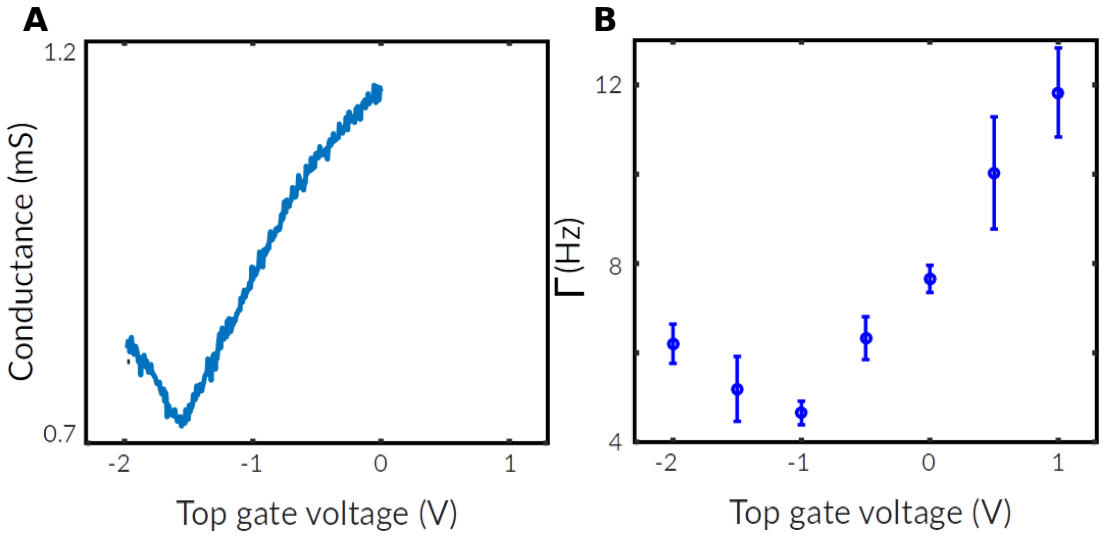


Figure 4.6: Global and local conductivity measurement of graphene. (A) Global conductance of a graphene field effect transistor as a function of gate voltage, measured in transport. (B) Corresponding relaxation rate of a NV center located under the device. A small, constant Joule heating current of 2.7 mW is applied to increase the electron temperature and make the noise signal larger.

In order to investigate noise sources in a biased graphene field effect transistor, we utilized both global and local measurements, some examples of which are shown in Fig. 4.6. In the simplest of these measurements, the graphene is simply connected to a low-noise amplifier and the voltage fluctuations are measured on a spectrum analyzer while a DC current is applied. Note that while we report noise in terms of an equivalent temperature, this does not mean that the electrons in the sample actually reach this temperature. This notation expressed how hot electrons *would* be if this noise were only Johnson noise.

To supplement these noise measurements, the frequency dependent conductivity of the device was also measured. This measurement is performed in a similar manner, but instead of measuring the noise at all frequencies, a small voltage signal is applied to the sample and its reflection and transmission coefficients (and phases) are monitored while the signal frequency is swept. This informa-

tion is used to calculate the real and imaginary parts of the graphene conductivity. This technique is explained in more detail in Appendix C. Because of the fluctuation dissipation theorem, the noise and conductivity are related, though the exact relationship is likely complicated here due to additional noise sources. Generally, if the conductivity drops (resistance rises), one expects to measure a corresponding increase in the noise.

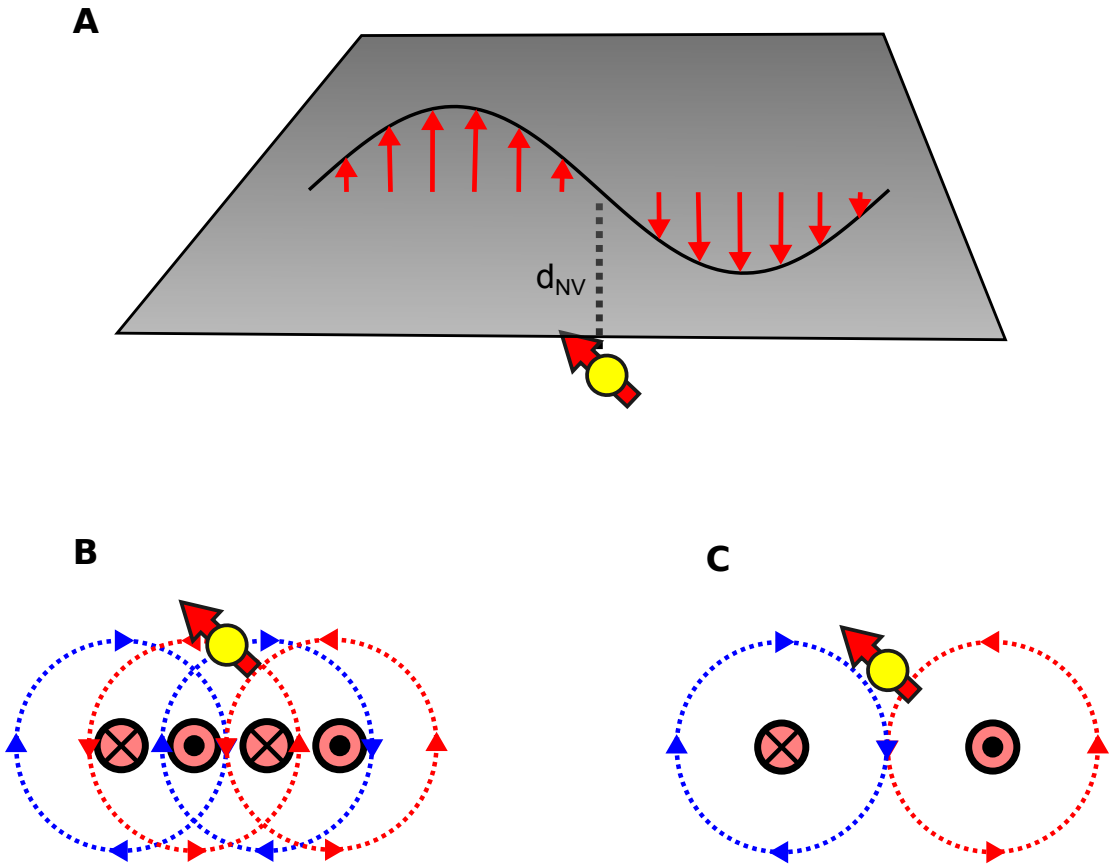


Figure 4.7: Relaxation of NV centers near conductors. (A) The NV center relaxation rate is sensitive to the transverse conductivity of a material, since longitudinal charge fluctuations are suppressed. (B) Fluctuations with a short wavelength (large k) create a magnetic field that averages out at the location of the NV center, while (C) $k \sim 1/d_{NV}$ has the largest contribution to the decay.

Finally, we perform local measurements by measuring the relaxation time of NV centers underneath the device, which provides a spatial map of the magnetic noise at frequencies near the zero

field splitting. Under equilibrium conditions, this noise arises from the thermal motion of electrons, it is a measurement of the local conductivity [197]. By changing the electron density of the device by gating, we can alter the conductivity, which results in a change in the relaxation rate of the NV center since $\Gamma \propto \frac{k_B T}{d_{NV}^2}\sigma$. In the following sections, we measure noise far in excess of what is expected for simple conductivity changes from gating. Although the conductivity of the device is indeed modified by stimulated acoustic phonon emission, the extremely high noise measured is the result of rapid scattering of electrons through stimulated phonon emission, and so is a rough measurement of the local phonon population. Most noise sources are isotropic and hence should have no spatial dependence, but by measuring NV centers under different regions of the sample, we are able to see how the noise changes as electrons flow across the sample, which is a striking characteristic of electron-phonon Cerenkov noise.

4.2 Electron-phonon instability in graphene revealed by global and local noise probes

The following section is a full reproduction of the manuscript "Electron-phonon instability in graphene revealed by global and local noise probes" by T. I. Andersen, B. L. Dwyer, and J. D. Sanchez-Yamagishi *et al* [9].

Understanding and controlling non-equilibrium electronic phenomena is an outstanding challenge in science and engineering. By electrically driving ultra-clean graphene devices out of equilibrium, we observe an instability that is manifested as dramatically enhanced current fluctuations and suppressed conductivity at microwave frequencies. Spatial mapping of the non-equilibrium current fluctuations using nanoscale magnetic field sensors reveals that the fluctuations grow exponentially along the direction of carrier flow. Our observations, including the dependence on density and temperature, are consistently explained by the emergence

of an electron-phonon Cerenkov instability at supersonic drift velocities. These results offer the opportunity for tunable terahertz generation and active phononic devices based on two-dimensional materials.

Non-equilibrium phenomena in driven electronic and optical systems display rich dynamics that can be harnessed for important applications, such as Gunn diodes and lasers. Two-dimensional (2d) materials[265] constitute a new platform for exploring such non-equilibrium phenomena. In particular, modern ultraclean graphene devices exhibit high mobilities[376] and can be driven to high electronic drift velocities where instabilities have been predicted to occur. Examples include hydrodynamic instabilities[244] in electronic fluids[205,72], as well as Dyakonov-Shur instabilities, where plasmons are amplified by driven electrons[96,360]. In addition to the potential use for high-frequency signal generation, understanding non-equilibrium dynamics is vital for many technological applications of graphene, including high-frequency transistors[219], ultra-fast incandescent light sources[190], and flexible transparent interconnects[189]. In practice, such electronic instabilities are difficult to realize due to increased phonon scattering at high drift velocities. While phonon scattering is typically an irreversible loss channel, long-lived phonons can themselves act as a source of instabilities. Specifically, when the electronic drift velocity (v_D) exceeds the sound velocity (v_s), stimulated phonon emission can dominate over absorption (4.8B), resulting in exponential growth of the phonon population known as phonon Cerenkov amplification[280,334]. This phenomenon has long been theoretically explored as a method to produce high-frequency acoustic waves[198,398], with experimental evidence found in bulk systems and semiconductor superlattices via acoustic and optical measurements[165,284,99,322].

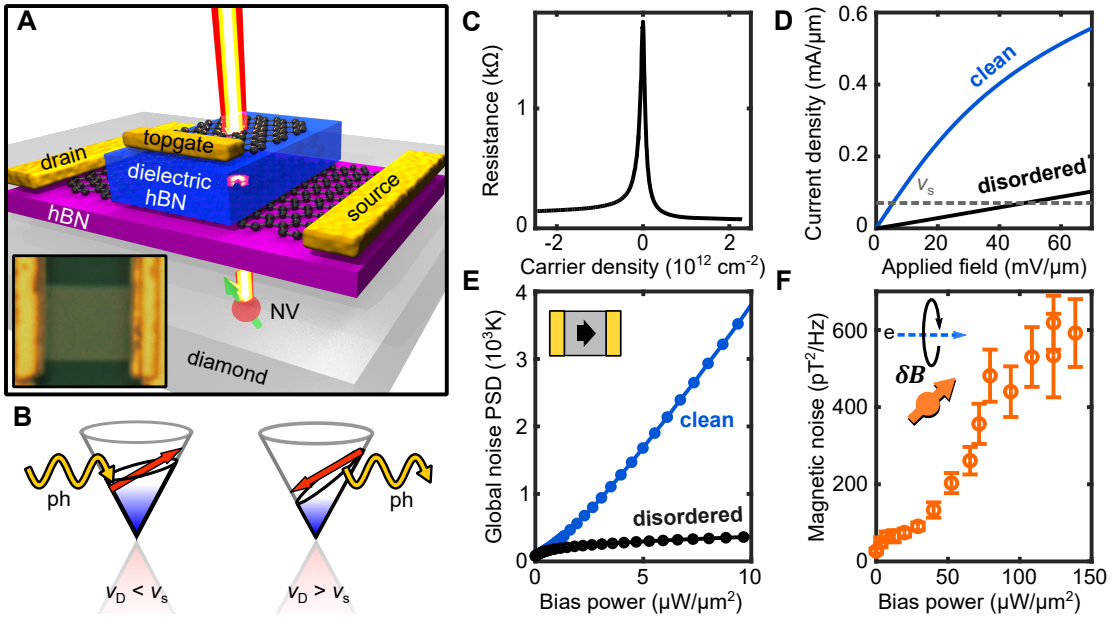


Figure 4.8: Non-equilibrium dynamics in graphene probed both globally and locally. (**A**) Device schematic: hBN-encapsulated graphene device on diamond substrate containing NV centers for nano-magnetometry. Inset: optical image of clean hBN-encapsulated device A1 ($6 \times 5.4\,\mu$m^2). (**B**) Condition for Cerenkov emission of phonons: when $v_D > v_s$, stimulated phonon emission dominates over absorption (right). (**C**) 2-probe resistance versus carrier density of device A1 ($T = 10$ K). (**D**) Current density as a function of applied electric field ($T = 80$ K) in clean device A1 (blue) and disordered device B1 ($7 \times 18\,\mu$m^2, black). The gray dashed line indicates where $v_D = v_s$ for the LA mode. (**E**) Global electronic noise PSD (averaged over $100 - 300$ MHz) as a function of bias power in devices A1 (blue) and B1 (black). Blue curve satisfies $v_D > v_s$ for $P > 0.12\,\mu$W$/\mu$m^2. (**F**) Local magnetic noise (measured by NV nano-magnetometry) versus applied bias power in clean device C1 on diamond substrate.

Our experiments make use of electrically gated graphene devices encapsulated in hexagonal boron nitride (hBN, 4.8A), and are conducted at cryogenic temperatures (T=10 $-$ 80 K). Figure 1C presents the low-bias transport properties of the ultraclean graphene system, with a mobility of $20 - 40$ m^2/Vs at a carrier density of 2×10^{12} cm^{-2}, corresponding to nearly-ballistic transport (Ch. C). Due to the high mobility, carriers can be accelerated by an electric field to high drift velocities ($v_D \gg v_s = 21$ km/s), where a non-linear current response is observed (4.8D, blue). By

contrast, a disordered device shows linear Ohmic behavior (4.8D, black).

We first study the non-equilibrium behavior by measuring the global noise in the source-drain current with a spectrum analyzer (noise power spectral density, PSD, averaged over $0.1 - 0.3$ GHz), while varying the applied bias power, P. The noise observed in disordered devices (black, 4.8E) is in good agreement with increased thermal noise due to Joule heating, and shows a characteristic $P^{1/3}$-dependence (Ch. C)[33]. Different behavior is observed in clean (hBN-encapsulated) devices, where the noise grows superlinearly with drive power and reaches values that are inconsistent with thermal noise. In particular, at higher biases the noise increases to values equivalent to the thermal noise expected for a sample at $10,000$ K (Ch. C). This behavior, observed consistently in 12 devices (Ch. C), stands in stark contrast to that of more disordered (not hBN-encapsulated) devices studied here and elsewhere[33,387], indicating a new noise source in driven graphene devices with low disorder.

To gain insights into the origin of this anomalous noise, we perform spatially-resolved noise measurements by fabricating graphene devices on diamond substrates that contain shallow NV color-center impurities ($40 - 60$ nm depth (Ch. C)[240]. These atom-like spin qubits can be individually measured using confocal microscopy, and can probe nanoscale current noise by measuring the resulting magnetic fields[197,5,56]. The locally probed noise under a driven clean graphene device exhibits similar superlinear behavior as global measurements (4.8F).

We probe the spatial dependence of the anomalous noise by optically addressing single NV centers along the device (4.9A) and measuring their spin relaxation rate (4.9B), which is determined by the local noise at 2.87 GHz[197]. Far from the midpoint of the device, the noise exhibits a clear asymmetry with current direction (4.9C), with nearly an order of magnitude difference when the current is reversed. This is surprising given that the global noise and transport properties are independent of current direction (Ch. C). Using the device gate, we invert the sign of the charge carriers and find that the asymmetric pattern also inverts, indicating that the local noise signal depends on the flow direction of momentum, not charge. 4.9D shows the local noise profile along the source-drain direc-

tion when $v_D = 5.8v_s$. We observe that the noise is small at the carrier entry point, but then grows exponentially as the carriers flow downstream the $L = 17\ \mu$m long device. The noise profile inverts when the current direction is reversed, and flips back when the carrier sign is also switched (4.9E).

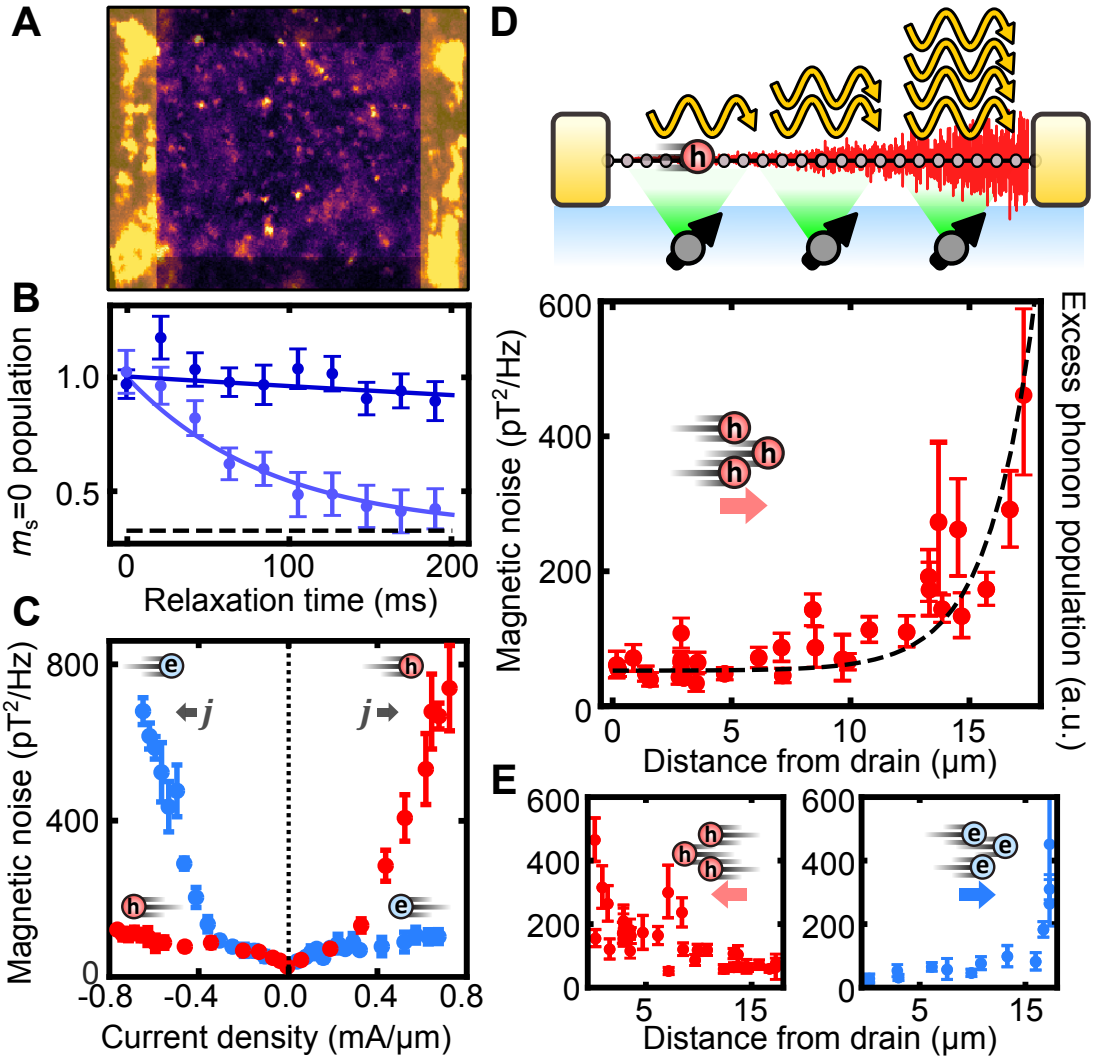


Figure 4.9: Spatially-resolved local noise measurements with NV magnetometry. (**A**) Fluorescence image of NV centers underneath device C2, with false colored contacts and boarders added. (**B**) NV spin relaxation from polarized to thermal state (dashed lines), when DC currents $j = 0$ (dark) and $j = 0.19$ mA/μm (light) are passed through the device. Solid lines are fits. (**C**) Local magnetic noise near drain contact as a function of graphene current density (device C1), in electron- and hole-doped regime (blue and red, respectively). (**D**) Spatial map of the local magnetic noise (device C2) at $j = 0.18\,\mathrm{mA}/\mu\mathrm{m}$ and $n = 0.92 \times 10^{12}\,\mathrm{cm}^{-2}$. The spatial profile is consistent with the exponential growth of phonons due to Cerenkov amplification (cartoon, top). Dashed black curve shows the theoretically predicted excess phonon population (offset to account for background noise). (**E**) The growth direction is reversed by changing the current direction (left) or the charge carrier sign (right).

To explore the underlying dynamics, we measure the spectrum of the global current noise. When driven, the disordered graphene samples show $1/f$ and white thermal noise (black curve, 4.10A), consistent with previous studies [33,19]. Clean devices, on the other hand, exhibit a peaked spectrum with a roll-off at $\sim$ 1.5 GHz. Interestingly, the AC differential conductivity is suppressed at similar frequencies (4.10B). These GHz features are in stark contrast to the equilibrium graphene Drude spectrum, which is featureless up to $\sim$THz [157,16], thus indicating timescales much longer than the typical electronic lifetime. Importantly, the frequencies of these non-equilibrium features are independent of drive voltage, doping and temperature (Ch. C), but are upshifted in a shorter device (4.10C-D).

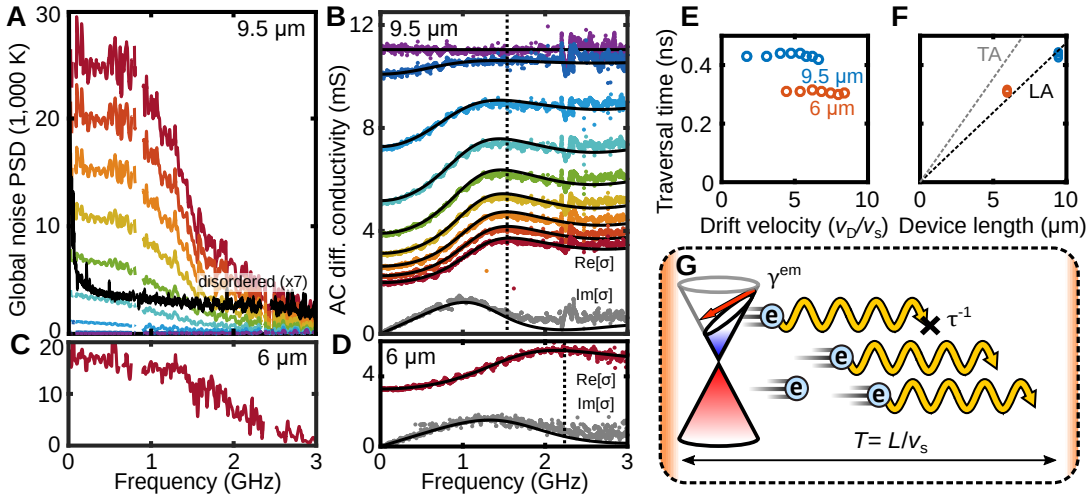


Figure 4.10: Slow dynamics in global electronic measurements. (**A**) Global noise spectra at $n = 2 \times 10^{12}$ cm^{-2}. Colored curves: Clean device A2 ($9.5 \times 11\ \mu$m^2) at bias ranging from 0 to 0.8 V (bottom to top). Black: Disordered device B1 at maximum power applied to device A2 (scaled 7x). (**B**) AC differential conductivity spectra (excitation -20dBm) (Ch. C) with biases 0 to 0.8 V (top to bottom, colors same as A). The real component is suppressed at low frequencies. Grey curve: imaginary component at 0.8 V. Black lines are fits. (**C-D**) Features in noise and conductivity spectra shift to higher frequencies in a shorter (6 μm) device (device A1), under similar electric field as maximum in (A) and (B). (**E-F**) Extracted traversal time from (B) and (D) as a function of drift velocity and device length. Dashed curves correspond to speed of sound in graphene (light gray: TA, dark gray: LA). (**G**) Cartoon of important rates in the driven electron-phonon system. During Cerenkov amplification, the correlation time observed in electronic measurements is limited by the phonon traversal time, $T = L/v_s$.

The observed spectrum, spatial dependence, and scale of the anomalous noise are inconsistent with conventional noise sources (such as $1/f$ or white thermal/shot noise)[145]. Our observations, especially the slow timescales and their independence on electronic parameters, are incompatible with many purely electronic mechanisms for AC signal generation[244,96,248] (Ch. C), and suggest that other, longer-lived excitations play a role. In particular, the timescales match well with the time taken for acoustic phonons to traverse the device. Furthermore, the anomalous effects only occur when the electronic drift velocity is higher than the speed of sound, but onset at energies that are too low to excite optical phonons and plasmons ($2\hbar k_F v_D$, $k_B T < 20$ meV) (Ch. C).

We now show that all our observations are consistently explained as an electron-phonon Cerenkov instability. The key insight is that when the electronic drift velocity exceeds the speed of sound, a cone of forward-moving acoustic phonon modes experience a faster rate of stimulated emission (γ_q^{em}) than absorption (γ_q^{abs})[280,334,198,398]. In order for the emitted phonons to amplify, γ_q^{em} must exceed the loss rate due to absorption and other decay sources. Pristine graphene exhibits long acoustic phonon lifetimes (τ_q)[261], thus an emitted phonon can stimulate the emission of more phonons, leading to exponential growth (4.10G). This process is seeded by a wide spectrum of spontaneously emitted and thermal phonons, and is therefore expected to have limited coherence. Stochastic electronic scattering with the growing phonon population is expected to reduce the conductivity and increase noise.

To model these effects, we analyze the coupled electron-phonon dynamics by including the influence of the phonons on the electronic scattering rate, Γ_e (Ch. C):

$$\partial_t j(r,t) = DE(r,t) - \Gamma_e(\{n_q\}) \cdot j(r,t) \tag{4.9}$$

$$\partial_t n_q = -\frac{(n_q - n_{q,0})}{\tau_q} + \gamma_q^{em}(j)\,(n_q + 1) - \gamma_q^{abs}(j) \cdot n_q - v_s \hat{q} \cdot \nabla n_q. \tag{4.10}$$

Here, $D = 2e^2 v_F k_F/h$ is the Drude weight of graphene, n_q is the phonon occupation at wavevector q, $n_{q,0}$ is the equilibrium phonon occupation when $j = 0$, and τ_q^{-1} is assumed to be dominated by anharmonic interactions. Note that while we describe the phonon population using second quantization, the results can also be obtained through a semi-classical treatment. Using known constants for the electron-phonon coupling and anharmonic decay, we find that phonon amplification ($\Gamma_q^{amp} = \gamma_q^{em} - \gamma_q^{abs} - \tau_q^{-1} > 0$) can be easily achieved for a wide range of parameters (Ch. C). For instance, the parameters used in 4.9D ($v_D = 5.8 v_s$) give a maximum $\gamma_q^{em} - \gamma_q^{abs} = 11$ GHz at $q \sim 2\pi/(25\text{ nm})$, where $\tau_q^{-1} = 0.02$ GHz. The amplification of stochastically emitted phonons is expected to cause large fluctuations in the local electronic scattering rate, thus generating current noise. Due to the Poissonian nature of phonon emission, the fluctuations are expected to scale with the mean emission rate, which is proportional to n_q. We thus plot the spatial profile of the excess phonon population ($\sim e^{\Gamma^{amp} x/v_s} - 1$) associated with $\Gamma^{amp} = 11$ GHz (dashed black curve) along with the noise profile in 4.9D, and find good agreement with our experimental results. Integrating over more modes gives a similar profile, indicating the dominance of the most amplified modes (Ch. C). This amplification behavior is also consistent with our global measurements, where the anomalous noise increases with device length (Ch. C).

The model also predicts that the electron-phonon Cerenkov instability gives rise to a conductivity spectrum of the form:

$$\sigma(\omega) = \frac{\sigma^{Drude}(0)}{1 - \frac{iK}{\omega T}\left(1 - e^{-i\omega T}\right)}, \tag{4.11}$$

where $\sigma^{Drude}(0) = D/\Gamma_e$ is the usual DC Drude conductivity and K is an increasing function of Γ_q^{amp} (Ch. C). Importantly, $\sigma(\omega)$ depends on the the sample traversal time for phonons, $T = L/v_s$. When Cerenkov amplification occurs, the correlation time probed in conductivity measurements is no longer limited by the individual electron and phonon lifetimes but by the traversal time, because the memory of an emission event is amplified until the phonons reach the edge (reflected,

backwards-moving modes are no longer amplified). To account for the variation in T with phonon emission angle, we sum over a cone in phonon phase space in our fits (Ch. C). Our model gives excellent agreement with the observed conductivity spectra (4.10B and D, black lines), and even predicts the slight oscillatory behavior due to the sharp transit time cut-off. The extracted traversal time is independent of drift velocity (4.10E), and the corresponding speed matches that of the longitudinal acoustic mode in graphene (4.10F)[180].

The extension of the correlation time is expected to also cause noise in the same low-frequency range, consistent with our observations (4.10A and C). While the stochastic emission of a phonon normally causes a small drop in current that only lasts for $1/\Gamma_e \sim$ ps, Cerenkov amplification both prolongs and magnifies the effect. Intuitively, the emitted phonon stimulates cascading emission of subsequent phonons, causing the current to continue decreasing until the phonon packet reaches the device edge. This should give strong current correlations $\langle \delta j(t) \delta j(t+\tau) \rangle$ for long τ (up to $T \sim$ 100 ps) and thus noise at low frequencies $\lesssim 1/T$.

Cerenkov amplification is sensitive to the phonon lifetime, and the effect is therefore expected to intensify at lower temperatures due to slower anharmonic decay[195]. Indeed, we observe a strong increase in noise as the temperature is reduced from 300 to 10 K (4.11A), in clear contrast to the decreasing thermal noise observed at low drives ($v_D \lesssim v_s$). This suggests that the amplification process is limited by scattering with thermally occupied modes at similar energies as the amplified mode (~ 7 THz ~ 50 K at $n = 2 \times 10^{12}$ cm^{-2}).

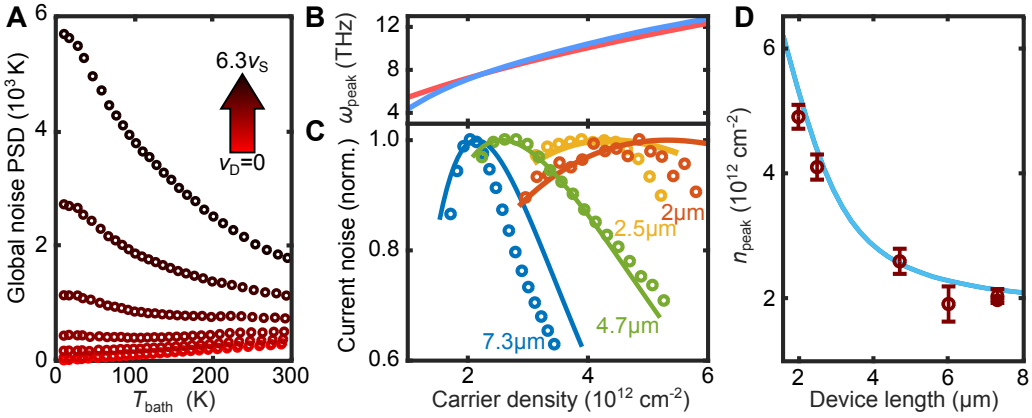


Figure 4.11: Dependence on bath temperature and charge density. (**A**) Global noise PSD as a function of bath temperature at constant drift velocities and carrier density $n = 2\times10^{12}$ cm^{-2}. (**B**) Calculated peak phonon emission frequency, which can be tuned via the graphene carrier density. (Blue: $T_e = 0$ K, red: $T_e = 320$ K). (**C**) Normalized global current noise as a function of carrier density for different device lengths ($j = 0.6$ mA/μm). Solid curves show predicted total phonon emission. (**D**) The charge density at which the noise peaks (n_{peak}) for a wider variety of samples than in (C), with fit (turquoise). Error bars represent sampling spacing of carrier densities.

Another important aspect of Cerenkov amplification in graphene is that the peak emission frequency is tunable via the carrier density, n (4.11B). This peak occurs just below the upper limit $\omega \sim 2v_s k_F$, corresponding to transitions across the entire Fermi surface. The frequency tunability manifests as a non-monotonic dependence of the global current noise on n (4.11C) (Ch. C). Initially, the noise increases with n, because the larger Fermi surface permits emission of more (and higher energy) modes. In other words, increasing n broadens Γ_q^{amp}. However, its maximum value decreases at constant current since $v_D = j/(ne)$, eventually causing a downturn in noise.

The cross-over density, n_{peak}, is determined by the relative importance of the width and maximum of Γ_q^{amp}, which depends on the device length. Analogously to an active filter, the amplification process narrows the excess phonon distribution $n_q(x) \sim e^{\Gamma_q^{\text{amp}} x/v_s}$ as it traverses the device. In longer devices, the noise therefore depends more on the maximum of Γ_q^{amp} than its width, causing a smaller n_{peak}. We observe such a length dependence, shown in 4.11C-D in terms of current noise to facili-

tate comparison with the model. Plotting the predicted total phonon emission along with the data, we find that our model reproduces both the peak shift and narrowing well (Ch. C).

These considerations show that our observations are well explained as an electron-phonon Cerenkov instability in a 2d material. This driven electron-phonon system shows rich non-equilibrium dynamics that merit further exploration, potentially by developing new techniques to directly characterize the phonon spectrum. Prior theoretical work predicts that the amplified phonons in graphene have frequencies as high as 10 THz[398], significantly higher than that observed in other materials[165,284,322]. Moreover, this system can offer purely electrical generation and amplification of phonons in a single μm-scale device, with wide frequency tunability. Future work could explore coupling to a mechanical cavity to develop a phononic laser, as well as out-coupling of the amplified sound waves to far-field THz radiation. Our results represent a promising step towards a new generation of active phononic and photonic devices based on 2d materials.

4.3 Discussion

The electron-phonon Cerenkov effect discussed here is not unique to graphene, but graphene has many favorable properties that facilitate its observation. What is needed is a system with very little scattering so that a high drift velocity can be achieved, and with no other low lying energy bands that very biased electrons can scatter into (such as in the Gunn effect[138]). Graphene devices can be made very clean by hBN encapsulation (our SiO_2 devices did not show enhanced noise). Acoustic phonon scattering in graphene is very weak, at least outside of the Cerenkov regime, and impurities are relatively rare, so electrons have long mean free paths (and hence high drift velocities). Optial phonons in graphene are very high energy ($\approx$ 200 meV) and so they do not efficiently scatter electrons. hBN optical phonons are slightly lower in energy, and so it is likely that remote scattering by hBN phonons eventually limits this effect[385]. Additionally, graphene has no other energy bands

that can be reached at transport energies. The very high speed of sound of graphene is in many ways a hindrance to the observation of this effect, since the Fermi surface must be tilted very steeply for stimulated emission to occur.

Phononic Cernkov emission is an important effect to understand because it limits high bias transport in graphene, leading to velocity saturation even before other types of scattering become dominant. It could also prove to be a useful tool: the amplification of phonons discussed here is exactly analogous to amplified spontaneous emission of light in a laser medium. Just as in a laser, many modes are amplified initially, but, with the introduction of a cavity, it may be possible for one mode to out-compete the others. This behavior is already present in very long devices, since the amplification is exponential in the length, the most amplified mode has the largest gain with distance. Future work could explore phononic cavities that could be used to augment this mode competition and create a true sound laser (or SASER). Another worth-wile avenue of exploration concerns the potential out-coupling of these amplified phonon modes to electromagnetic radiation, perhaps through a plasmonic intermediary. An on chip, tunable source of terahertz electromagnetic radiation could revolutionize modern electronics, as these frequencies are typically difficult to produce even with bulky and expensive equipment.

Finally, a word about NV center relaxometry. While non-isotopic noise sources such as the one studied here are uncommon, the nanoscale sensing capabilities of the NV center are still well suited for noise measurements in condensed matter systems. This is because, in addition to the NV center's ability to map out noise spatially, it can also map out noise in momentum space. An NV center at a depth d_{NV} is most sensitive to transverse fluctuations of electrons at a particular wave vector $k \sim 1/d_{\mathrm{NV}}$ [5]. Transport probes the $k = 0$ conductivity modes of a system, while optical methods measure the conductivity at very small momenta due to the high velocity of light. In order to probe phenomena at nonzero k, the extra momentum must be supplied somehow, usually be a grating or some kind of tip. Despite many interesting phenomena in condensed matter physics having non-

trivial dispersions, they are difficult to probe. Because of this, NV center relaxometry has been suggested as a probe of hydrodynamic electrons[3] [5] and more recently quantum spin liquids[62,186]. The wireless nature of NV center sensors also makes them attractive conductivity probes of materials for which electrical contact is challenging, including many emerging 2D materials[74].

[3] This was actually the original motivation for this experiment, but while heating the electrons to increase the electron-electron scattering rate we discovered an unexpected effect.

A method is even more important than a discovery,
since the right method will lead to new and even more
important discoveries.

Lev Landau

5

Local probe of magnetic susceptibility in 2D materials

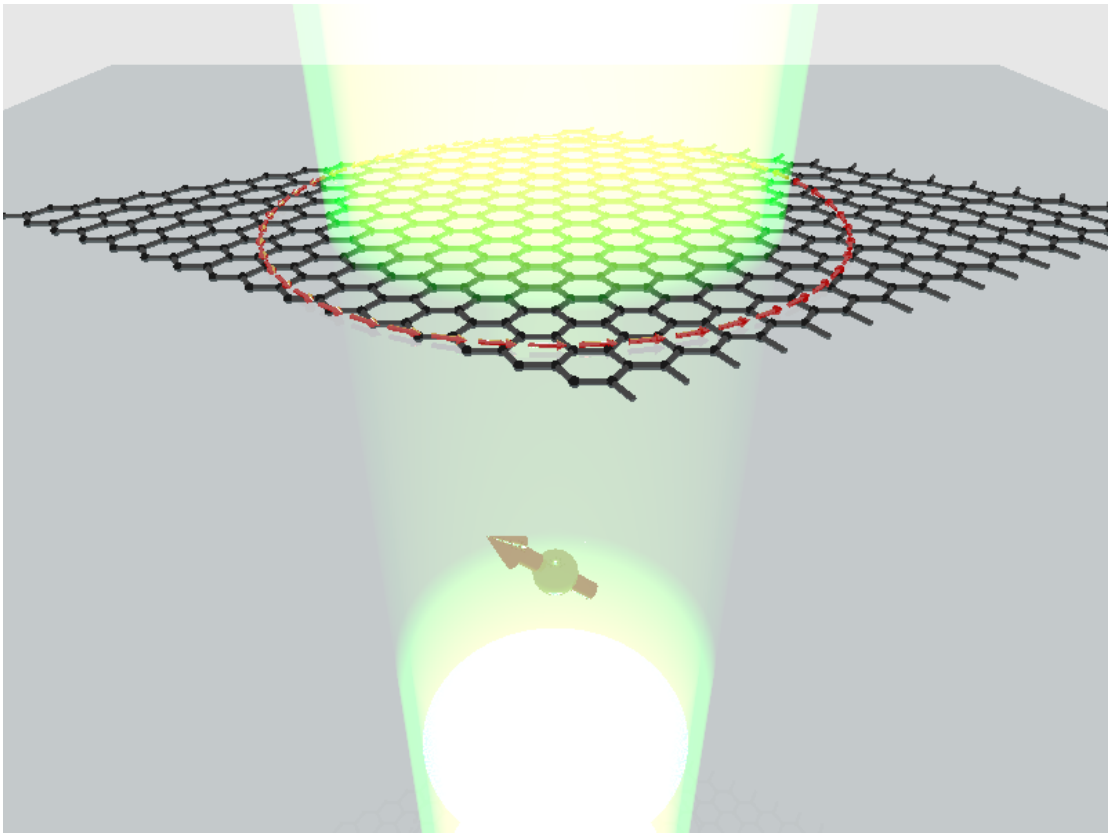


Figure 5.1: Artistic rendition of orbital diamagnetism detection in graphene.

5.1 Introduction

NV centers are desirable magnetometers for a number of reasons. The first is their small size, which, until recently, was really unparalleled. While there existed many other magnetometers, even the smallest was on the $\sim$ μm scale. NV centers can measure fields on the nanometer scale, set primarily by the distance between the NV center and the target. For many phenomena, nanoscale resolution is desired, and hence the large investment in scanning NV center probes over the last decade[401,10,354,152,272,231]. NV centers can also be extremely sensitive probes at these scales–they are capable of measuring individual electron spins[132] and single nuclei[347]. The sensitivity numbers

quoted for NV centers can be somewhat misleading, however. The sensitivity of the magnetometer to DC magentic fields, which is limited by T_2^*, is far inferior to its AC sensitivity, which is limited by the substantially longer T_2. While NMR measurements are a natural fit for AC sensing schemes due to the known precession frequencies of nuclear species, much of the work in condensed matter systems has only used NV centers as DC magnetometers[1] It is sometimes possible to transform DC measurements into AC measurements by modulating some parameter of the system, which is the technique that is explored in this chapter.

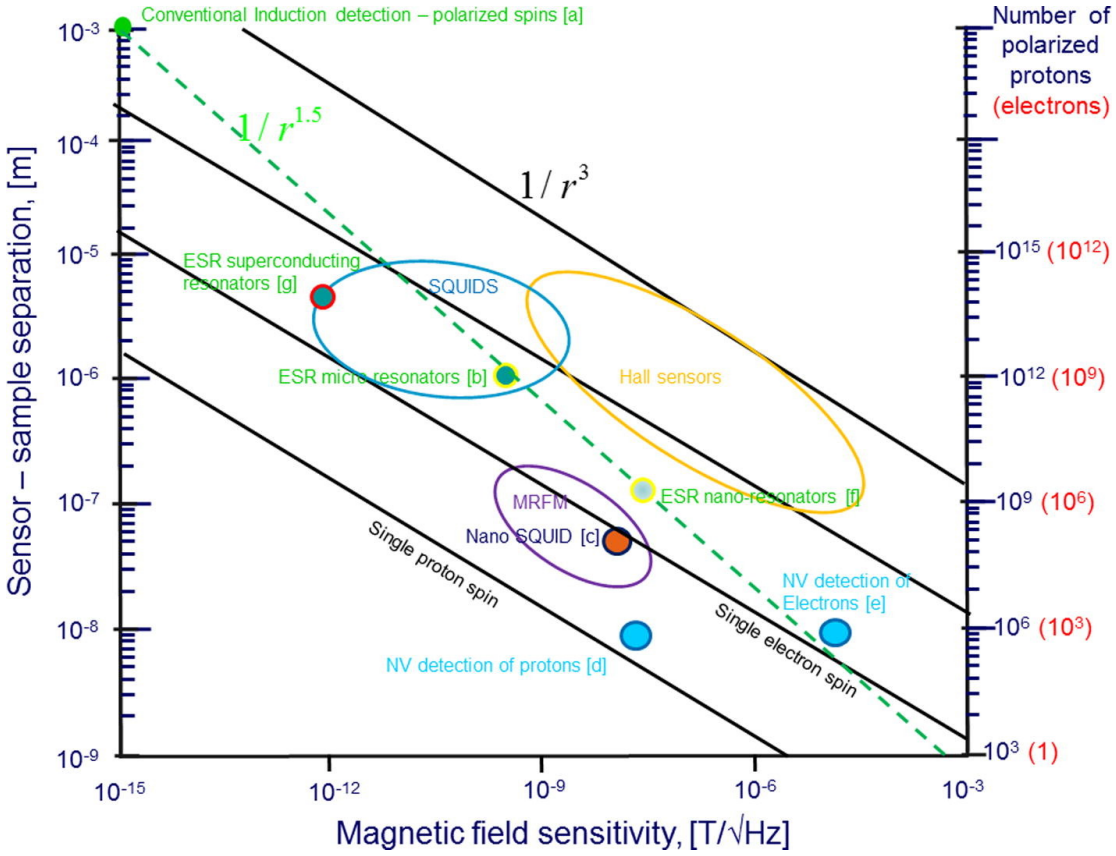


Figure 5.2: Sensitivity and resolution of magnetometers. Sensitivity vs. sample separation for several different magenetometers, including NV centers. Figure taken with permission from Ref.[39].

[1] Some experiments have combined scanning NV center probes with T_1 relaxometry measurements, however[11,273].

The measurement utilized in this chapter is somewhat akin to a lock-in measurement, and as a result has been called a "quantum lock-in" technique[400]. The key idea is to modulate some parameter of the sensing target while a spin echo pulse sequence is applied to the NV center. The phase accumulated by the NV center will be given by

$$\varphi = \gamma_e \left(\int_{\tau/2}^{\tau} B_z(t)dt - \int_0^{\tau/2} B_z(t)dt \right) . \tag{5.1}$$

If $B_z(t)$ has a different value for the two halves of the free precession interval, a net phase will be accumulated. For maximum sensitivity, $B_z(t)$ should have the same period as the pulse sequence and should have opposite magnitudes in each half of the sequence. The best case is a square wave with amplitude B_0, in which case the total phase accumulated is

$$\varphi = \gamma_e B_0 \tau . \tag{5.2}$$

Fields that do not oscillate at the frequency set by the spin echo filter function are canceled, as is the DC offset in the signal. This includes environmental noise that the NV center is sensitive to, and so decoherence is reduced and the measurement can be performed at $\tau = T_2$ for maximum sensitivity. In this way, fields in the $\sim$ nanotesla range can be readily measured, and using a higher number of pulses field changes in the picotesla range can in principle be sensed.

While not all sensing targets are amenable to modulation, 2D materials have many properties that are sensitive to electrostatic doping and displacement field. This includes the previously discussed conductivity of graphene, as well as excitonic properties in TMDCs[174], energy gaps[349], and phase transitions[53]. In the following section, we will use this technique to measure gate dependent orbital magnetism in graphene.

Unlike the other chapters of this thesis, this section has not been published elsewhere and represents work that is ongoing.

5.2 NV centers as local probes of orbital magnetism in 2D materials

Many exotic phenomena in condensed matter physics, including the quantum hall effects, topological states of matter, and magnetoelectric effects, can be understood in terms of the Berry phase of electrons in a solid. One of the first observations of a Berry phase effect was in graphene, whose Berry phase of π shifts a Landau level at zero energy, resulting in an unconventional quantum hall effect and a diverging magnetic susceptibility at the Dirac point. We introduce a novel technique for measuring the susceptibility of 2D materials using nitrogen vacancy centers implanted in a diamond substrate. We use these wireless susceptometers to non-invasively measure the gate dependent magnetic response of graphene and find the predicted sharp increase in signal near the Dirac point. The local nature of our measurements permit us to map this signal at different locations under the device, including under multilayer graphene regions. This technique gives insight into the origins of the quantum hall effect in graphene, and more importantly provides a straightforward method for measuring orbital magnetism and other Berry phase effects in many 2D materials such as topological insulators and twisted structures that exhibit emergent Moiré potentials.

Well before the isolation and measurement of graphene samples, graphene was a material of significant theoretical interest due to its peculiar magnetic properties. It was well known that graphite, uniquely among naturally occurring materials, has a very large diamagnetic susceptability. It is so strong that it is possible to levitate a graphite chunk over a strong magnet, as is shown in Fig. 5.3. In 1956, McClure showed that this strong diamagnetism arises naturally in the case of graphene, and, treating graphite as a consisting of many weakly interacting layers of graphene, was able to explain the observed magnetism in bulk graphite[241].

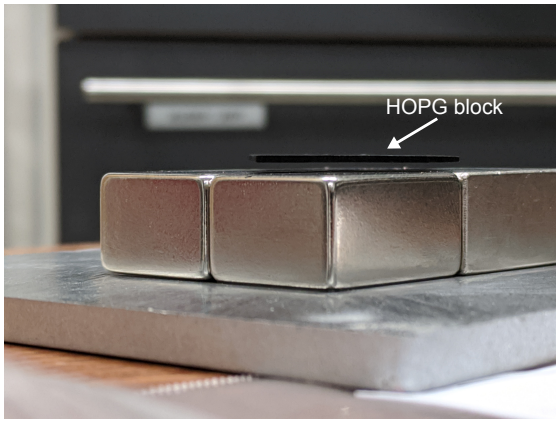


Figure 5.3: Levitation of graphite. Bulk graphite can be levitated over a permanent magnet under ambient conditions. HOPG = higyly oriented pyrolitic graphite, which is a form of graphite where the individual graphite crystals are well aligned with each other.

In modern parlance, charge carriers in graphene are massless Dirac Fermions which have a surprising property in an applied magnetic field: they acquire a Berry phase of π during a cyclotron orbit, in contrast to the 2π phase of most other materials[391,382]. This unique Berry phase shifts the energy position of the Landau Levels (LL) in graphene[396], which results in a distinct LL at zero energy and a divergent diamagnetic susceptabilty at low temperatures[241,200,201]. Thus the levitation of graphite, which can be observed at room temperature with no specialized equipment, is a manifestation of the relativistic quantum mechanics embodied by the charge carriers of graphene.

While McClure's result in many ways began the search for interesting physics in graphene, this phenomena has proven difficult to measure in monolayer flakes due to the small signal from a single flake and the incompatibility of traditional measurements with gated devices. Some work has been done exploring the field dependence of bulk samples[218], but without a field effect transistor and a high quality monolayer sample the predicted gate dependence of the susceptibility could not be observed. It was only very recently that researchers were able to measure this effect in a gated device using a giant magnetorsistance sensor, finding good agreement with theoretical predictions[367].

We present here a new technique for measuring the magnetic susceptibility of 2D materials using

nitrogen vacancy (NV) centers in diamond. By fabricating devices on top of diamond substrates containing NV centers, we measure the local gate dependent change in magnetic field below the device that results from orbital magnetic currents in the material. This technique exhibits several advantages over other approaches, since in addition to its exquisite sensitivity, NV centers are non-invasive, local sensors that provide spatial information about current distributions in the sample. Additionally, NV centers operate over a wide range of temperatures [328,173] and magnetic fields [107]. While we demonstrate the usefulness of this technique for graphene, it has wide applicability to other 2D materials, particularly those in which spatial inhomogeneity make global measurements difficult.

5.3 Experimental results

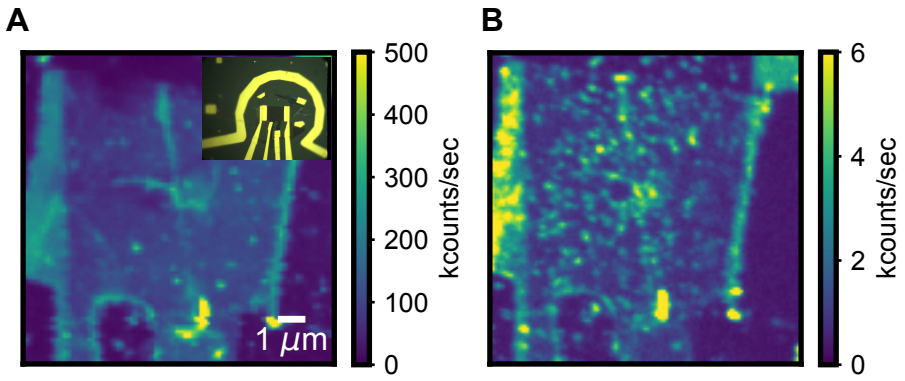


Figure 5.4: Graphene device on diamond. (A) Image taken under 532 nm illumination, which produces background fluorescence that overwhelms the NV center fluorescence. Inset: optical image of the device on diamond. (B) Same as (A) but taken with a low powered laser tuned to the NV center zero phonon line (ZPL), which permits imaging through the device and selectively addressing NV centers that are close together due to the inhomogeneous distribution of ZPLs.

We fabricate graphene field effect transistors on top of diamond containing individually resolvable NV centers $\approx$ 50 nm below the surface. The devices are dual graphite gated to reduce disorder [290], and hexagonal boron nitride is used as a gate dielectric. Fluorescence scans of a device are shown

in Fig. 5.4. We utilize a 637 nm laser resonant with the NV center zero phonon line to image and measure NV centers with minimal background.

NV center measurements are performed in an AC sensing scheme. An NV center is optically initialized in the $m_s = 0$ spin state and a spin echo sequence is performed while a parameter of the device is varied in phase with the sensing sequence. This "quantum lock-in " technique cancels phase contributions from sources that are not modulated at the echo frequency, $f_{\text{sig}} = 1/\tau$. This technique permits much higher sensitivity for NV center measurements than DC magnetometry because it is limited by T_2 rather than T_2^*. For NV centers, T_2 is much longer than T_2^* [26]. Fig. 5.5 shows representative measurements of T_2^* and T_2 in our diamond samples.

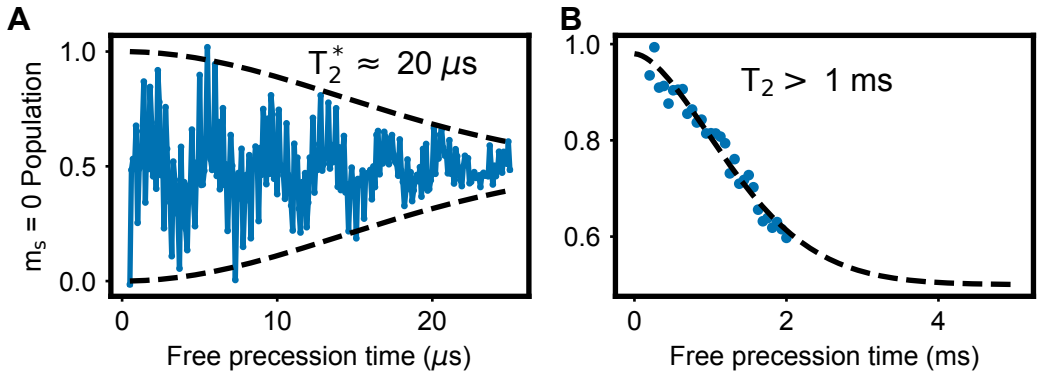


Figure 5.5: NV center decohrence at low temperatures. (A) Representative T_2^* measurement for NV centers in a ^{12}C enriched diamond at 60K. (B) Representative T_2 measurement for NV ceters in the same diamond sample. The longer decoherence time translates to increased sensitivity in an AC sensing scheme.

To test the sensing capabilities of the NV center, we first apply a small sinusoidal voltage to the graphene and measure the NV center phase accumulation for a fixed free precision interval, as depicted in Fig. 5.6A. Repeating this measurement at different gate voltages yields the magnetic field values shown in Fig. 5.6B. Approximating the graphene as an infinite sheet of current, the magnetic

field along the NV center quantization axis, B_z can be written as

$$B_z = \frac{\mu_0 \sigma}{2} \sin \alpha \,, \tag{5.3}$$

where μ_0 is the vacuum permeability, σ is the 2D current density, and α is the angle of the NV center quantization axis with respect to the surface normal ($\approx$ 54.7° for the (100) diamond surfaces used here). The current density extracted from the local measurement agrees well with that obtained from global transport, but the Dirac peak is shifted slightly, which may be a result of local disorder[395].

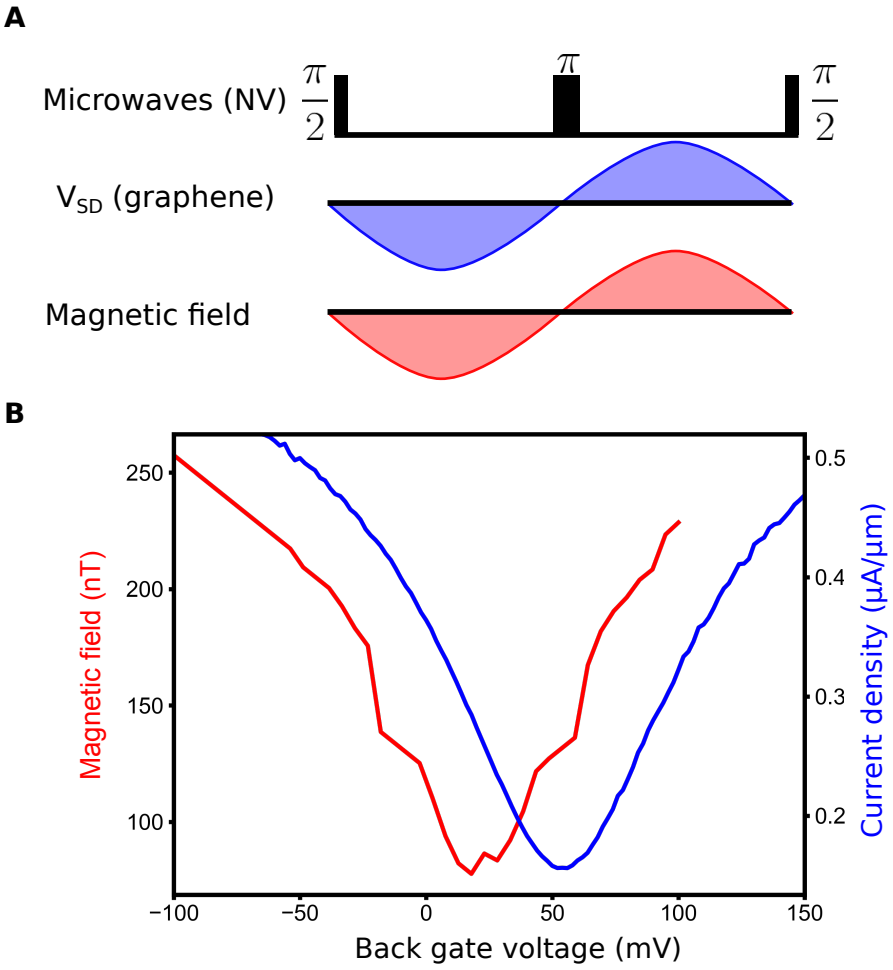


Figure 5.6: Global and local transport of graphene. (A) Quantum lock in sequence for AC sensing graphene currents. V_{SD} is sinusoidally varied (amplitude = 5 mV) in phase with a concurrent spin echo on the NV center. (B) Each gate voltage produces a different current density (blue), which the NV center sense as a change in magnetic field (red). Blue curve is determined from a global transport measurement.

To measure the diamagnetic response of graphene, we ground the graphene and apply a small external field to the sample ($\approx$ 200 Gauss) to separate the spin states of the NV center. We apply an offset voltage, V_{off} to the gate and modulate it with a square wave of amplitude $\delta V = 40$ mV at $f = 1/\tau = 5$ KHz, in phase with the echo sequence. Applying this sequence while sweeping V_{off} through the charge neutrality point yields $\frac{\partial \Delta B}{\partial V} \propto \frac{\partial M}{\partial \mu}$, where ΔB is the change in magnetic

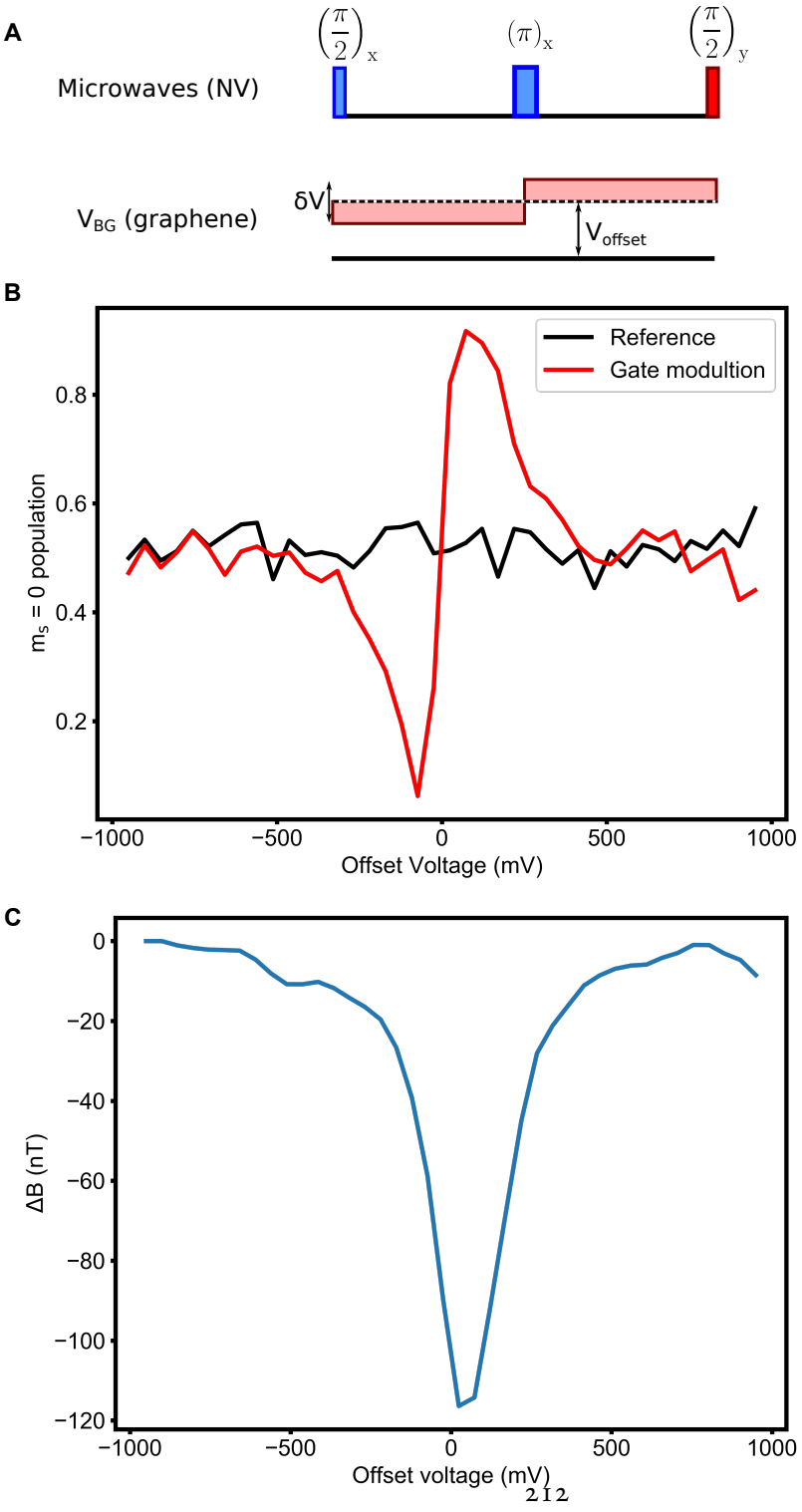
field from the applied value, M is the magnetization of the sample, and μ is the Fermi level of the graphene. We show the result of one such measurement in Fig. 5.7, along with the integrated signal, which is displays the expected peak around the Dirac point.

While the graphene is grounded during these measurements, a small amount of charge must necessarily flow into the graphene when it is gated so that the charge density changes. This is a negligible contribution to the detected signal for a few reasons. Firstly, the current should be out of phase with the voltage modulation by 90°, which means that the signal would be canceled in the two halves of the echo sequence. Second, since the phase accumulated is $\varphi_{NV} \propto \int B(t)dt \propto \int I(t)dt$, the phase is proportional to the total charge that flows into the graphene, independent of the temporal dynamics of the current. Thus we can calculate that the resulting magnetic signal from this flowing charge would be in the femptotelsla, range which is significantly less than the observed signal.

A key advantage of NV centers as susceptometers is that they are local probes and hence the magnetization of the sample can be mapped out. Both transport and the orbital magnetic response of graphene are thought to be limited by local variations in the Dirac point within the sample[395,200], and local probes that are sensitive only to the local material properties should be less sensitive to these extrinsic effects. In Fig. 5.8, we repeat the gate modulation measurement for several NVs located at different points on the sample. Interestingly, all of these NV centers record approximately the same signal. This is unusual because of the expected effects of disorder. Perhaps more surprisingly, the signal seems to have no dependence on the distance between the NV center and the edge of the sample. In the simplest model of orbital magnetism, application of a magnetic field induces cyclotron orbits of the electrons, which set up an opposing magnetic field. However, all of the orbits in the bulk of the sample should cancel, leaving only a contribution from the current flowing along the edge of the sample. Hence NV centers near the edge of the device should experience a larger change in magnetic field, as if the field were produced by a thin wire outlining the sample. Only the NV center nearest to the edge shows any deviation in the measured signal, but this is likely due to electric field effects, as discussed below.

Figure 5.7 *(following page)*: Gate dependent diamagnetism in graphene. (A) Pulse sequence used to detect diamagnetic sheilding from graphene. A square wave of amplitude 40 mV is applied at different offset values while a sine magnetometry pulse sequence is applied to the NV center. The signal detected by the NV center is the derivative of the magnetic field with respect to the gate voltage, which we integrate in (C) to find the change in magnetic field as the gate is swept through the Dirac point.

Figure 5.7: (continued)



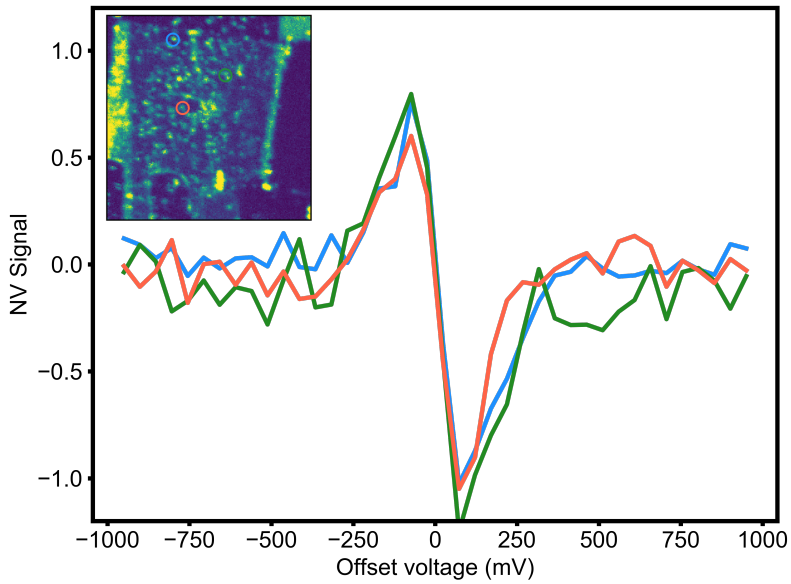


Figure 5.8: Magnetization signal at different locations. Each color curve is taken from an NV center at the corresponding location in the inset.

A useful feature of NV centers is that it is possible to distinguish electric from magnetic field signals by observing the behavior of different qubit states. For a magnetic field aligned closely with the NV center quantization axis, application of a small additional magnetic field causes the eigenenergies of the $m_s = \pm 1$ qubit states to move in opposite directions, as shown in Fig. 5.9. Application of an electric field causes them to shift together in the same direction[92]. By measuring in both the $\{m_s = 0, m_s = +1\}$ and the $\{m_s = 0, m_s = -1\}$ basis, the nature of the field can be determined. For NV centers near the bulk of the device, we find that changing qubit basis also inverts the sign of the signal, as expected for an NV center in a magnetic field. The near edge NV center, on the other hand, shows a signal that does not invert when the qubit basis is changed, indicating that the signal is likely electric in origin. While NV centers are less sensitive to electric fields than to magnetic fields, the extremely large fields produced over short distances in nanoscale field effect transistors can produce fringe fields that produce phase accumulations of a similar magnitude to the magnetic fields we

attempt to measure here.

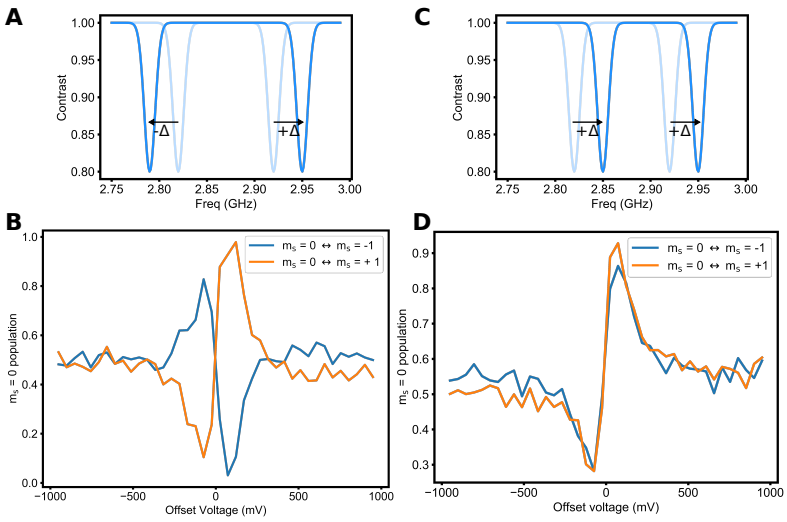


Figure 5.9: Discriminating between electric and magnetic fields. (A) Applying amagnetic field results in opposite frequency shifts for the m_s = +1 and m_s = -1 states. (B) By chaning the measurement qubit basis, we find that the signal inverts, which implies that it is magnetic in nature. (C) Electric fields cause the qubit states to move in the same direction. (D) For an NV center very close to the device edge, we find that the measured signal does not invert upon switching qubit bases, implying that this signal is due to the fringing electric fields of the FET.

While NV centers can in principle be used over a large range of magnetic fields ($0 - 8$ T [106]) and temperatures ($4 - 300$ K), the details of our experiment make varying these parameters challenging. Nevertheless we present a measurement taken at 5 K which can be compared with the previous measurements at 60 K. Interestingly, while the peak in susceptibility is predicted to become singular at low temperatures [241,367], we find significant broadening at low temperatures. Additional temperature dependent measurements are ongoing.

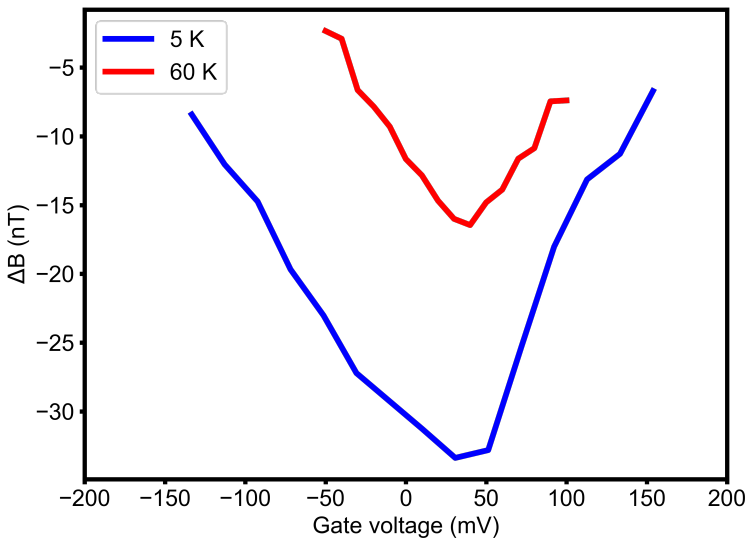


Figure 5.10: Temperature dependence of magnetization peak. NV center measurement taken at different temperatures, showing an increase in the measured field difference and broadening of the signal.

5.4 Methods

NV centers were created by implanting ^{14}N ions in electronic grade diamonds (Eelement Six) with a ^{12}C isotopically purified overgrowth layer to achieve maximum coherence times. Samples were annealed in vacuum with a two step process: first to 800 ° for 8 hours to create NV centers and then ramped to 1200 ° for 2 hours to remove divacancies[77]. The second annealing step reduces environmental noise, as is evidenced by the increase in NV center T_1 after this procedure (Fig. 5.11). Diamonds were then cleaned in a refluxing mixture of 1:1:1 sulfuric:nitric:perchloric acid to remove graphitic carbon on the surface.

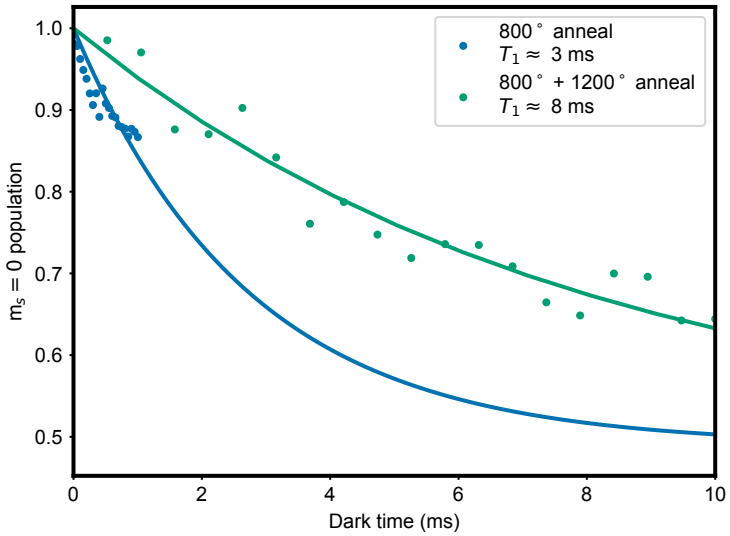


Figure 5.11: High temperature annealing effect on T_1. For samples implanted at high densities, an additional anneal at 1200° C improves spin relaxation time because divacancies are annealed out.

2D material heterostructures were assembled using the dry transfer technique[374,281]. The stacks were annealed on a SiO_2 substrate at 350° C for 15 minutes before being picked up and transferred to the diamond. Contacts were made by E beam lithography, and any etching was done using CHF_3 plasma reactive ion etching.

Measurements were taken in a Montana Cryostation with optical access. An external magnetic field is required to split off the NV center spin transitions so that it may be used as a two level system for sensing. We applied a field normal to the sample using a permanent magnet on a translation stage inside of the cryostat, as depicted in Fig. 5.12, and added a longitudinal component with an external magnet to better align the field with the NV center quantization axis (54.7o to the surface normal) for one of the four possible orientations of NV centers.

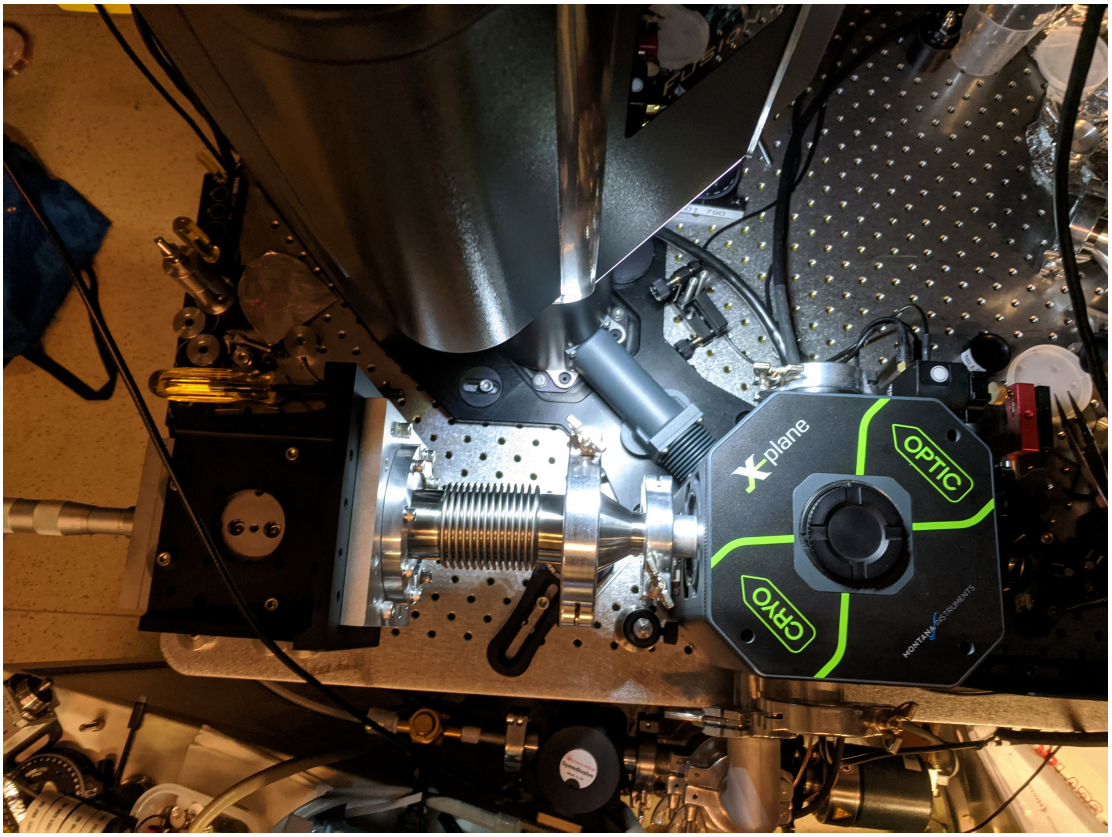


Figure 5.12: Cryostat used for NV center measurements. A magnet is attached to the translation stage inside of the bellows to introduce a magnetic field to the sample.

Pulse sequences were synthesized using two synced Tektronix AFG3022C arbitrary function generators. These were used to send TTL signals to a Minicircuits ZASWA-2-50DR+ high isolation switch and IQ modulation inputs to an SRS SG384 microwave signal generator, which provided the microwave signals used to manipulate the NV center spin. The remaining channel was output to an analog switch and then to one of the device gates. The switch allowed for the sample to be grounded while the NV center was initialized and read out, which reduces photodoping of the sample. The switch was connected to the AFG during pulse sequences so that the gate voltage could be modulated. Additional DC voltage control and transport measurements used Keithley 2400 source

meters.

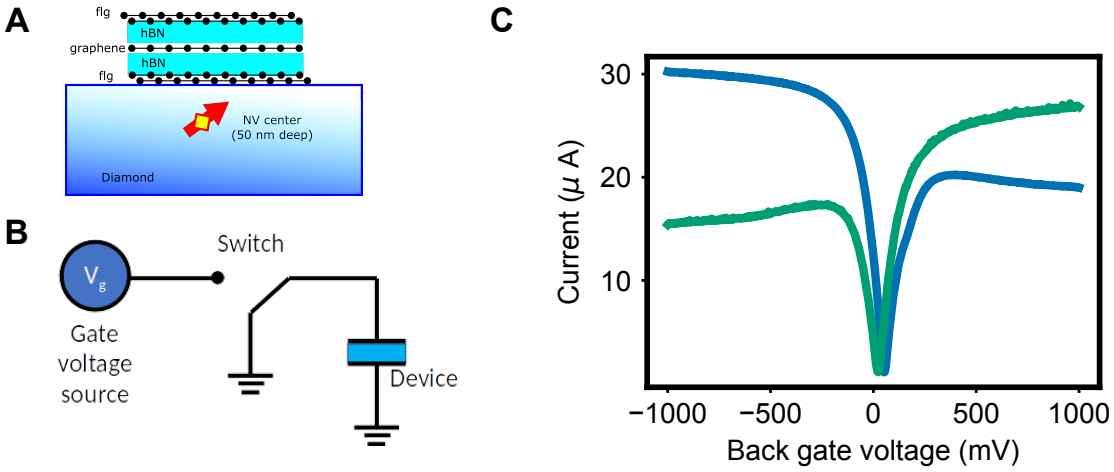


Figure 5.13: Minimizing photodoping. (A) Device structure, with a back gate between the dielectric interface between the bottom hBN and diamond to prevent charge accumulation during photoexcitation. (B) As an additional precaution, the device gate was connected to an analog switch so that it could be grounded whenever a laser was switched on for readout. (C) As a result of these precautions, photodoping was significantly reduced. Global transport measurements during initial cool down (blue) and taken after one month of measurements (green).

The pulse sequence were orchestrated by a pulseblaseter ESR-PRO board, which, in addition to triggering the pulse sequence, controlled NV center initialization and readout. Readout was accomplished using a modified spin-to-charge mapping procedure with a resonant external cavity diode laser (Newfocus Velocity TLB 6704) tuned to the NV center zero phonon line for readout. The resonant laser permitted easy imaging through the device due to the low background it produced. Additionally, due to the broad inhomogenous distribution of NV center zero phonon lines, it was possible to distinguish individual NV centers at different wavelengths even though the sample was implanted densely enough that individual centers were not resolvable under off resonant excitation. These measurements rely on the zero phonon line being thermally broadened to avoid spectral diffusion. For low temperature measurements, the laser frequency must be swept across the range of possible optical transitions during a readout sequence, which was accomplished by modulating the cavity piezo on of the laser.

NV center spin readout was accomplished with a modified spin-to-charge conversion scheme[32,1,9]. Following a measurement period, the NV center was excited using a strong 594 nm laser to shelve the $m_s = 1$ population in the metastable singlet state. Before the singlet has decayed, an intense, short 637 nm pulse is applied with a diode laser ($\approx$ 70 mW), which ionizes any population that is not shelved. Charge state readout is then performed using the resonant laser, and the spin state can be inferred based on the number of counts since they indicate the final charge state.

5.5 Discussion

The unique gate dependent diamagnetism studied here is a manifestation of the Berry phase of the charge carriers in graphene. Typically, such effects require high magnetic fields to observe, such as in the quanum hall effect, but here we have demonstrated their effects in thermodynamic quantities that can be observed without the need for strong magnets. The local nature of the NV center makes it a particularly appealing probe, as this permits a measurement of the scaling of orbital magnetism under different numbers of layers in the same device.

While the gate dependence of the magnetization of graphene is not unexpected, the measurements recounted above show some unexpected behavior that is difficult to reconcile with our understanding of orbital magnetism. In particular, the absence of dependence of the magnetization signal on the distance from the edge is intriguing and begs for an explanation. Typically in these types of experiments, very large magnetic fields are applied so that the electronic wavefunctions are eigenstates of a shifted harmonic oscillator Hamiltonian. Classically they are often thought of as undergoing cyclotron orbits with a small radius, and with a frequency such that many orbits are completed before any scattering occurs. In our samples under a 200 Gauss field, the magnetic length ($\approx$ 200 nm) is much larger than the NV center to sample distance ($\approx$ 70 nm), which is a regime in which the cyclotronic treatment of electrons may not be valid. Further investigation is required to

understand these measurements.

As this experiment was cut short by the outbreak of the COVID-19 pandemic, there are several other measurements we would like to perform to obtain a more comprehensive picture of magnetism in graphene.

First, another possible source of the signal in Fig. 5.7 is the graphite gates on the top and bottom of the sample, since graphite should also show a diamagnetic response that depends on doping. To rule out this contribution, we plan to repeat the differential magnetization measurements but applying voltages of $\pm V$ volts to the top and bottom gates, respectively, which will dope them far from charge neutrality while leaving the graphene neutral. Applying the modulation to the top gate and sweeping the offset, we will then attempt to reproduce Fig. 5.7, but now with the gates doped the evidence that the signal comes from the graphene alone will be more solid.

Second, we plan to use the spatial distribution of NV centers to measure the layer dependence of the magnetization in multilayer graphite. We plan to fabricate a device that has different thicknesses of graphite in a single flake, and by measuring the magnetic field change underneath regions of the sample consisting of monolayer, bilayer, and trilayer graphene, we hope to observe different magnetizations. In particular, the different numbers of layers are expected to display switching between bilayer-like behavior and monolayer + bilayer-like behavior as the number of layers is changed[201].

While we have used gate modulation based quantum lock-in techniques to study diamagnetism in graphene, this is in many ways a proof of principle demonstration of the more general technique. Diamagnetism in graphene, while difficult to measure, was never in doubt, but there exist many other phenomena that are more contentious. Graphene aligned to hBN, for example, is predicted to exhibit diamagnetism at the Van Hove singularities in the superlattice band structure[253] and may also exhibit a special kind of orbital ferromagnetism[320]. Twisted bilayer graphene also possesses Van Hove singularities that appear to give rise to a diamagnetic response at half filling[224]. Graphene is of course not the only 2D material with interesting magnetic properties. Recently discovered

Wigner Crystals in TMDCs[330,402] also likely have magnetic ordering, but it is currently unknown if this is ferromagnetic or antiferromagnetic. Since this crystallization occurs only for particular electronic densities, it can be studied with the same gate modulation technique. Perhaps the greatest field in which NV center based suscptometers could make an impact is that of Moiré lattices of 2D materials, including twisted bilayer graphene, because the twist angle is generally not uniform across the device making local probes desirable. NV centers would be excellent tools to study such systems in the future.

Finally, while we have utilized bulk implanted NV centers in order to achieve good coherence times, gate modulation could also be applied to devices under a scanning NV center setup. NV centers in nanostructured diamond typically achieve coherence times that are inferior to their bulk counterparts due to many of the reasons discussed in Ch. 2. Since nanostructures have more surfaces, and the NV centers they contain are close to multiple surfaces, they are more sensitive to noise. Additionally, the fabrication process itself likely introduces additional defects that can act as charge traps which destabilize the Fermi level and create electric and magnetic field noise. Even with such effects, the T_2 times of NV centers in nanostructured diamond are much longer than their T_2^* times, and so in general a great improvement in sensitivity is expected.

6

Conclusion

It could be said that there are two approaches to the study of condensed matter physics. There is the "bottom up" approach employed by atomic physicists, where a suitable model for a real world crystal is constructed atom by atom. Such experiments, though unparalleled in their control of the constituent particles, are necessarily simplified simulations of a real solid. At the other extreme, transport and related techniques attempt to infer the properties and behavior of the particles in a solid through collective measurements over an entire crystal. Such techniques, though they operate

on "real" materials, are somewhat indirect and can be muddied by real world complications such as material impurities and inhomogeneity. Somewhere in the middle lies the local sensor, which measures the properties of a real and possibly complex material, but is sensitive to mesoscopic numbers of particles. While local measurements are not always warranted, there is clearly demand for the information they provide. Consider how much research relies on the Atomic Force Microscope (AFM) or the electron microscope as a characterization technique. A tool that could provide similar information for electric or magnetic properties would be invaluable.

NV centers join a growing family of local probes, including scanning tunneling microscopes (STMs), scanning superconducting quantum interference devices (SQUIDs) [192], scanning single electron transistors (SETs) [236], that can provide detailed spatial information about materials. The length scale at which these techniques operate has improved rapidly. Scanning SQUIDs, for example, achieved resolutions of a micron a decade ago [192], but today nano-SQUIDs are being produced with 10s of nanometers resolution [369]. This improves our ability to study physics that occurs on small length scales, or that has variable spatial extent. Sometimes the world just looks different on small length scales, as is exemplified by NV center conductivity measurements that show ballistic electrons on short length scales even though the entire sample is diffusive [197].

NV centers are not, in all cases, the preferred method of probing local physics, but they do have certain characteristics that set them apart from competing technologies and are advantageous for studying certain systems. First, NV centers operate over a wide range of temperatures, which makes them promising candidates for biological applications in particular. An entire field of NV center research concerns their use for nanoscale NMR, which promises to characterize minute quantities of substances [13] and may one day be able to elucidate the structure of individual proteins [6]. These techniques will benefit from a solution to the "surface problem" discussed in Chapter 2 of this thesis, as it is necessary to bring NV centers close to these molecules while retaining good coherence properties for maximum sensitivity. Second, NV centers can sense over a wide frequency range using

different techniques, from DC to several GHz, which enables detection of specific signals as well as spectroscopy. Third, and perhaps most importantly, while much effort has been spent on creating scanning NV center systems, experiments incorporating NV centers need not be so difficult. One of the great hurdles to overcome for scanning systems is their prohibitive complexity of operation, which is undoubtedly a major reason they have not seen universal adoption. By fabricating devices on top of diamonds, a local measurement technique can be introduced with a relatively straightforward optical system, without compromising traditional electrical measurements. Some resolution is lost with this method, but, as we have seen in the preceding chapters, there is still interesting physics to study.

For 2D materials specifically, future experiments involving Moiré superlattices could benefit greatly from local probes, including NV centers. In many of these structures, the superlattice has a length scale that is compatible with the NV center sensing resolution ($\sim$10 nm)[163,53]. They are also rarely uniform. When a heterostructure is constructed with a twist angle, the misaligned sublattices are not in an energetically favorable position and can undergo reconstruction[346], concentrating strain at domain boundaries, or there can be variable strain and a nonuniform twist angle throughout the device. For structures where this twist angle is of paramount importance, such as magic angle bilayer graphene, this means only a small portion of the device is actually at the correct twist angle, and it is by luck that the contacted region of the device overlaps with the region of appropriate twisting. This variation in twist angle has already been observed with a local probe[366]. The ability to measure different regions of the device is extremely helpful here. These structures additionally display exotic phenomena that are not well understood, such as emergent magnetism[319] and superconductivity[22], which can be sensed by magnetometers. The coming years will be an exciting time for the physics of 2D materials as the mysteries of Moiré hetrostructures are unraveled, and perhaps NV centers will play a role in deepening our understanding.

A

Supporting material for Chapter 2

A1 Methods

Samples

In this letter, we present NV coherence data from several samples in Fig. 2.10b. Here, we describe the different samples:

- Sample A: The sample used for data in Fig. 2.11. Commercially available electronic grade

diamond (Element Six) with <5 ppb nitrogen and <1 ppb boron.

- Sample B: The sample that was subjected to 1200 °C annealing followed by oxygen annealing, presented in Fig. 2.10b. This sample originated from the same crystal as sample A. The crystal was sliced prior to any processing described in Fig. 2.10c.
- Sample C: Another sample that originated from the same crystal as sample A. The crystal was sliced prior to any processing described in Fig. 2.10c.
- Sample D: An electronic grade sample with ^{12}C-enriched layer that was processed according to Fig. 2.10c.
- Sample E: An electronic grade sample with ^{12}C-enriched layer with rough, as-grown surface that was subsequently processed with Ar/Cl_2 and O_2 RIE.
- Sample F: An electronic grade sample with ^{12}C-enriched layer. The surface is left as-grown.

In addition to these NV samples, surface spectroscopy data is presented from several electronic grade samples. Three triacid-cleaned samples and three oxygen-annealed samples, one of which is morphologically rough, were used for NEXAFS and high-resolution XPS (Fig. 2.12b–d, Fig. 2.13a, inset). A boron doped sample (0.1 ppm boron and <5 ppb nitrogen) was used for UPS spectroscopy (Fig. 2.12e) to prevent charging. Finally, a lower purity sample (<1 ppm nitrogen and <0.5 ppm boron, Element Six "standard grade") was used for oxygen annealing calibration.

A1.1 Sample Preparation

Our method for preparing a high-quality diamond surface prior to ion implantation relies on a multi-step process to remove surface and subsurface damage. Unless indicated otherwise, all samples described above are laser cut and scaife-polished to a RMS roughness of less than 1 nm with a (100)

major face and ⟨110⟩ edges, specified to within 3 °. In order to prepare substrates for implantation, reactive ion etching was performed using an inductively coupled plasma (ICP) with the following parameters: 400 W ICP power, 250 W substrate bias RF power, 25 sccm Ar, 40 sccm Cl_2, 8 mTorr (1 Pa) for 30 minutes followed by 700 W ICP, 100 W substrate bias, 30 sccm O_2, 10 mTorr (1.3 Pa) for 25 minutes (Plasma-Therm Versaline ICP RIE). These two RIE steps etch approximately 2 μm and 4 μm of the subsurface polish damage layer, respectively [109].

In order to remove residual subsurface damage from ICP RIE, 1200 °C vacuum annealing is performed in a Lindberg Blue tube furnace with high purity (>99.5 %) alumina ceramic tubes at pressures between 1×10^{-7} Torr (1×10^{-5} Pa) and 2×10^{-6} Torr (3×10^{-4} Pa) with the following sequence, starting from room temperature:

1. Ramp to 100 °C over 1 hour. Hold for 11 hours.
2. Ramp to 400 °C over 4 hours. Hold for 8 hours.
3. Ramp to 800 °C over 6 hours–12 hours. Hold for 8 hours.
4. Ramp to 1200 °C over 6 hours–12 hours. Hold for 2 hours.
5. Let cool to room temperature.

This annealing results in a <3 nm layer of amorphous carbon at the surface, which is subsequently removed by cleaning the sample in a refluxing 1:1:1 mixture of concentrated sulfuric, nitric, and perchloric acids (triacid clean) for at least one hour. The conversion of material to amorphous carbon and subsequent removal is critical for removing subsurface damage resulting from RIE processing. Annealing at lower pressures (below 1×10^{-7} Torr (1×10^{-5} Pa)) does not result in a thick layer of amorphous carbon, and thus does not remove this damage layer (Fig. A.2).

Sample A was then sent for ^{15}N ion implantation (Innovion) with the recipe: dose = 1×10^9 cm^{-2}, energy = 3 keV, and 0 ° tilt. Other samples were implanted with the same parameters,

except with doses of 3×10^9 cm^{-2} for samples B and F and 5×10^8 cm^{-2} for samples C, D, and E. Following implantation, all samples are triacid cleaned and 800 °C annealed in vacuum using the same recipe as above, with or without the 1200 °C step. Another triacid clean following this vacuum anneal results in the condition referred to as the "triacid cleaned" surface throughout the text.

To create the oxygen-terminated surface, the sample is then annealed at 445 °C–450 °C in a tube furnace (Lindberg Blue Mini-Mite with high-purity quartz process tube) under continuous flow of O_2 at atmospheric pressure for 4 hours. The oxygen flow is regulated with a mass flow controller, and the outlet of the process tube is connected to a bubbler to prevent backflow of gases. The input gases, oxygen (for annealing) and nitrogen (for venting the furnace), are filtered via SAES Sentrol point-of-use purifiers, MC1-203F and MC1-902F, respectively. Following the oxygen anneal, the sample is cleaned in a 1:2 mixture of hydrogen peroxide in concentrated sulfuric acid ("piranha"). The resulting sample condition is referred to as the "oxygen-annealed" surface throughout the text. Finally, Sample B was annealed at 1200 °C and subsequently oxygen annealed to achieve the best spin coherence times, shown in Fig. 2.10b.

XPS is used between each step to verify that the surface is contamination free at the 0.1 % level, which is the sensitivity limit of the instrument. If any heteroatoms other than C and O are found (e.g. Na, Cl, Si), the sample is repeatedly cleaned with either triacid or piranha until the contamination is eliminated. We show examples of XPS spectra from a contaminated sample before and after acid cleaning in Fig. A.1, as well as micromasking and surface roughening that can result from contamination in Fig. A.4.

A2 Process Calibration for Oxygen Annealing

Since diamond etches when heated in an oxygen atmosphere [116], changing the surface termination while avoiding etching requires careful temperature calibration. Our process proceeds as follows:

1. Clean sample in 1:2 hydrogen peroxide in sulfuric acid (piranha). Verify that the sample is contaminant-free in XPS.
2. In the furnace, ramp to the target temperature over 4 hours, and anneal at the target temperature for another 4 hours.
3. Repeat step 1.
4. Examine the sample in AFM to check for morphological changes at the surface.
5. Cycle back to first step and increase target temperature.

Previous studies showed that diamond starts to etch in oxygen around 500 °C [116]. Therefore, we begin with 450 °C for our calibration and choose the final temperature to be the highest temperature that does not produce pitting on the sample. Examples of AFM images taken after annealing at different temperatures are shown in the Fig. A.3.

A2.1 XPS and AFM Characterization

XPS survey scans in Fig. 2.13a and AFM images in Fig. 2.10c were performed at the Imaging and Analysis Center (IAC) at Princeton University. XPS was performed with a Thermo Fisher K-Alpha spectrometer, collecting photoelectrons normal to the surface. AFM was performed interchangeably with either a Bruker Nanoman or a Bruker ICON3 AFM operating in AC tapping mode (AFM tip: Asylum Research AC160TS-R3, resonance frequency 300 kHz). Each diamond was thoroughly cleaned with either triacid or piranha before AFM scans were performed. Large-scale (5 μm$\times$5 μm)

and small-scale (1 μm$\times$1 μm or 0.5 μm$\times$0.5 μm) scans were performed in several distinct areas of the diamonds, away from the edge. In general, for the same sample, no clear variation of the RMS roughness was observed across the interrogated areas.

A2.2 NEXAFS and High-Resolution XPS

In near-edge X-ray absorption fine structure spectroscopy (NEXAFS), monochromatic X-rays excite core electrons, and secondary electron yield is measured as a function of the incident X-ray energy, giving a signal that is proportional to the density of unoccupied states near the surface. In XPS, incident X-rays ionize core electrons, and the measured binding energy is sensitive to the chemical environment of the ionized atom.

Unless indicated otherwise, all NEXAFS data and high-resolution XPS spectra (Fig. 2.13 insets) were acquired at the Australian Synchrotron soft X-ray spectroscopy beamline, using light from an APPLE II undulator generating linearly polarized photons and passed through a plane-grating monochromator. Prior to scanning, the samples were annealed *in situ* at 430 °C to remove adventitious carbon [25].

Carbon K-edge and oxygen K-edge NEXAFS were collected in partial electron yield mode with grid biases of 220 V and 440 V, respectively. The spectra are processed and calibrated by first dividing by the total incident power measured using photoelectrons from clean gold foil in the chamber, subtracting the average pre-edge background (270 eV–275 eV for carbon, 520 eV–525 eV for oxygen), and normalizing to the post-edge electron yield (315 eV–320 eV for carbon, 558 eV–560 eV for oxygen). The energy is calibrated by setting the sharp σ^* exciton peak of the gold foil to 291.65 eV [377].

High-resolution XPS spectra were analyzed using a SPECS Phoibos 150 hemispherical analyzer with the pass energy set to 5 eV, resulting in a linewidth of better than 0.1 eV. An excitation photon energy of 600 eV was used. XPS spectra were fitted using CasaXPS. A linear fit to the pre-edge was

first subtracted from the data to account for the rising secondary electron tail apparent in spectra acquired with a photon energy close to the core level energy. Subsequently, a universal Tougaard background was subtracted and Voigt functions were used to fit the resulting spectra. Each component function was constrained to have the same FWHM as all others within the same spectrum. We find that the carbon signal fit residual is minimized by fitting two side peaks on the high binding energy side rather than one, and that it does not improve by fitting three side peaks. We identify these two peaks as carbon singly- and doubly-bonded to oxygen.

A2.3 Additional XPS, UPS, and LEED Measurements

Additional XPS in Fig. A.10, UPS, and LEED measurements were carried out in a custom UHV spectrometer at Aberystwyth University. X-ray excitation was provided by a VG twin-anode (Mg and Al) source and He I UV radiation was provided by a SPECS UVS 300 source. Photoelectrons were collected at normal emission by a SPECS Phoibos 100 analyzer using a 2D CCD electron detector.

In UPS, ultraviolet photons (21.2 eV) ionize valence electrons, and their binding energy can then be used to determine the Fermi energy and electron affinity. For XPS, the sample was kept at earth potential while for UPS, a bias of -2 V was applied to the sample to enable collection of low energy electrons over a range of sample work functions. The electron analyzer was operated in wide angle mode to sample band edge states averaged in momentum space. Since the apparent binding energy of electron states measured by photoelectron spectroscopy is affected by surface charging and photovoltage generation [379], we calibrate the valence band edge against the Fermi edge of a tantalum standard. Rear-view VG LEED optics were used to record surface electron diffraction patterns. The beam energy was set to 86 eV for the diffraction pattern shown in Fig. 2.13b.

A2.4 NV Measurement Setup

NV measurements were performed on a home-built confocal microscope. NV centers are excited by a 532 nm optically pumped solid state laser (Coherent Sapphire LP 532-300), which is modulated with an acousto-optic modulator (Isomet 1205C-1). The beam is scanned using galvo mirrors (Thorlabs GVS012) and projected into an oil immersion objective (Nikon, Plan Fluor 100×, NA = 1.30) with a telescope in a $4f$ configuration. Laser power at the back of the objective was kept between 60 μW–100 μW, approximately 25 % of the saturation power of a single NV center, in order to avoid irreversible photobleaching. A dichroic beamsplitter (Thorlabs DMLP567) separates the excitation and collection pathways, and fluorescence is measured using a fiber-coupled avalanche photodiode (Excelitas SPCM-AQRH-44-FC). A neodymium magnet is used to introduce a DC magnetic field for Zeeman splitting, and the orientation of the magnetic field was aligned to within 1 ° of the NV axis using a combination of a rotation stage and a goniometer.

Spin manipulation on the NV center was accomplished using microwaves generated by a dual-channel signal generator (R&S SMATE200A). The two channels are independently gated with fast SPDT switches (Mini-Circuits ZASWA-2-50DR+) and combined with a resistive combiner (Mini-Circuits ZFRSC-42-S+) for double-quantum and DEER measurement capabilities. The combined signal is then amplified with a high-power amplifier (Mini-Circuits ZHL-16W-43+) and delivered to the sample via a coplanar stripline. The stripline is fabricated by depositing 10 nm Ti, 1000 nm Cu, and 200 nm Au on a microscope coverslip. Following metallization, the stripline is photolithographically defined and etched with gold etchant and hydrofluoric acid. Finally, a 100 nm layer of Al_2O_3 is deposited on top of the fabricated stripline via atomic layer deposition (ALD) to protect the metal layer. This Al_2O_3 layer is crucial for separating the diamond surface from the metal layer of the stripline, which can contaminate the diamond surface (Fig. A.1). Pulse timing is controlled with a Spincore PulseBlaster ESR-PRO500 with 2 ns timing resolution, and phase control of the

NV microwave pulses is achieved with an arbitrary waveform generator (Agilent 33622A).

To avoid effects of pulse errors during dynamical decoupling, we alternate the phase of each π-pulse using the XY4 protocol for the 4-pulse sequence, the XY8 protocol for the 8-pulse sequence, and repeated XY8 protocol for higher order sequences[375].

The errors in depth and coherence presented in the main text and appendices are calculated for each NV center as follows. Each sequence consists of measuring the NV coherence as a function of inter-pulse duration. We fit the data according to[279] and obtain the depth and uncertainty from the fit. We then average the depths from the different pulse sequences and report the uncertainty to be either the standard deviation, or the largest uncertainty from the fit, whichever is greater. For error bars in coherence presented in the graphs, the reported values and error bars are obtained from the fit to a coherence/relaxation decay curve. Each data point results from measuring NV population as a function of evolution time, such as the data in Fig. 2a.

A3 Effects of Sample Contamination

In this work, we emphasize that prior to any surface processing step, it is critical to start with a morphologically smooth and contamination-free surface, since impurities can cause irreversible surface damage through processing. It is also important to monitor the surface roughness and contamination between each step. To ensure purity between each processing step, we clean the diamonds in triacid or piranha solution and check for contaminants in XPS before proceeding. Figure A.1a shows examples of XPS spectra from the same sample before and after triacid cleaning. While both surfaces show identical survey scans, fine scans can reveal small Si and Na contamination peaks (cyan curves) that are removed after triacid cleaning. Typical sources of Si, Cl, Na, and other contamination include improper drying and handling, used solvent bottles, and device packaging. We have also performed similar contamination checks to develop processes such that annealing and reactive ion

etching steps do not introduce surface contamination.

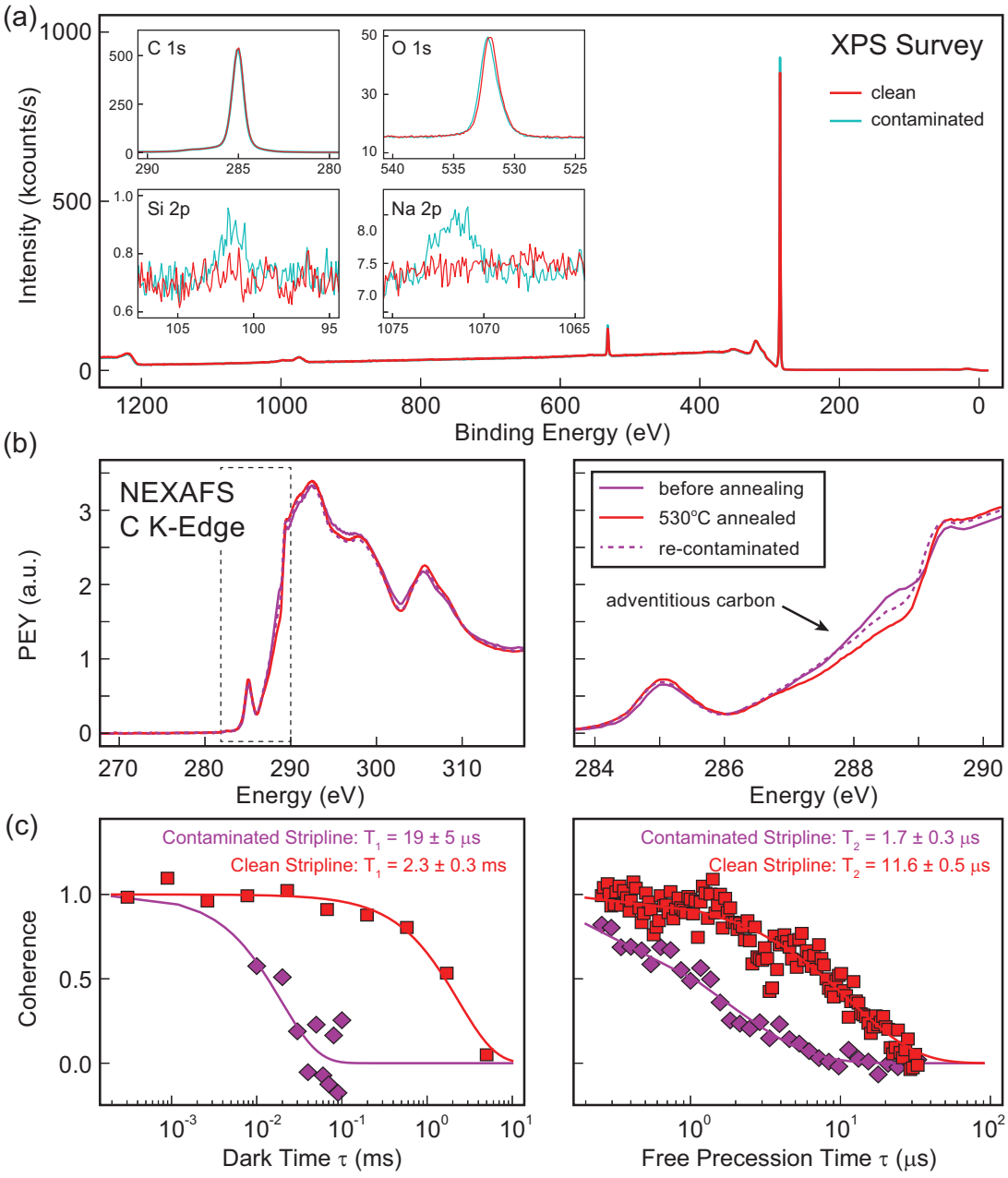
If the surface is contaminated before etching or annealing, micromasking and formation of surface carbides can lead to irreversible surface roughening. For example, silicon-containing polymers used in packaging, gloves, and other containers can leech onto the diamond surface, as verified by XPS. If the diamond is annealed above around 900 °C, this silicon containing contamination layer forms a carbide at the diamond surface, which cannot be removed with triacid cleaning, piranha solution, or any other acid or base that we have explored. This carbide layer then results in surface roughening through subsequent processing, such as oxygen annealing. Similarly, Na and Cl contamination are correlated with surface roughening during reactive ion etching, which we attribute to micromasking. We show in Fig. A.4 examples of surface roughness that can result from surface contamination and damage, and we discuss the consequences for electronic structure and NV coherence in Appendix A6 and Appendix A7.

Another source of surface contamination is adventitious carbon that is ubiquitous on surfaces exposed to atmosphere[25]. For NEXAFS and high-resolution XPS, we performed *in situ* annealing in order to probe the intrinsic electronic structure of the surface, rather than the adventitious carbon. Figure A.1b shows a representative NEXAFS spectrum at the carbon K-edge before and after annealing at 530 °C. After annealing, the density of unoccupied states near the conduction band edge is suppressed, indicating either the removal or rearrangement of carbon-containing groups at the diamond surface. The sample was then removed from vacuum and exposed to atmosphere for a few minutes, and re-inserted into the chamber without further annealing. Upon re-exposure to atmosphere, much of the pre-edge density returned, indicating that this pre-edge feature arises from carbon-containing contamination of the surface.

This particular NEXAFS dataset was acquired at the NIST U7a beamline of the National Synchrotron Light Source (NSLS) at Brookhaven National Laboratory, NY. For data taken at NSLS, the carbon K-edge and oxygen K-edge NEXAFS were collected in a partial electron yield (PEY) mode with an entrance grid bias of 220 V for carbon, and 400 V for oxygen. The incident light from

Figure A.1 *(following page)*: Sample contamination. (a) XPS spectra from a diamond sample with Si and Na contamination before (cyan) and after (red) acid cleaning. The main panel shows the full energy range survey scans, while insets depict higher resolution peak scans at the C 1*s*, O 1*s*, Si 2*p*, and Na 2*p* transitions. (b) Normalized NEXAFS carbon K-edge spectra and a close-up of the pre-edge region of the same sample before and after *in situ* annealing at 530 °C, showing the removal of pre-edge states attributed to adventitious carbon. Dashed line shows the spectrum after re-exposure to atmosphere. (c) Single-quantum relaxation and Hahn echo coherence, measured from the same NV with a contaminated stripline in which the ALD layer has been scratched, compared with a new stripline.

Figure A.1: (continued)



a bending magnet is passed through a toroidal spherical grating monochromator, focused through a monochromator slit, and enters the chamber polarized perpendicular to the plane of incidence. The polarization with respect to the sample can then be controlled by changing the angle of the sample. Spectra are processed and calibrated by first dividing by the total incident intensity, which is measured using photocurrent from a clean gold grid in the chamber, subtracting the average pre-edge background (270 eV–275 eV for carbon, 520 eV–525 eV for oxygen), and normalizing to the post-edge electron yield (340 eV–342 eV for carbon, 568 eV–570 eV for oxygen). The energy calibration is reported relative to amorphous carbon and oxygen standards. A tantalum heater was used for *in situ* annealing in the loadlock at pressures ranging from 3×10^{-7} Torr (4×10^{-5} Pa) to 8×10^{-7} Torr (1×10^{-4} Pa).

Finally, surface contamination after processing can impact the coherence and spin relaxation of shallow NV centers. In particular, contact with metal particles from the coplanar microwave stripline can result in decreased spin relaxation time T_1 and coherence time T_2. Without the protection of the Al_2O_3 ALD layer, shallow NV centers exhibit shorter spin relaxation and coherence times when placed in microscope immersion oil on the metal stripline, as illustrated in Fig. A.1c.

A4 sp^2 Carbon Formation During High Temperature Annealing to Remove Etch Damage Layer

XPS of the carbon 1*s* peak following the 1200 °C anneal (Fig. A.2a) shows a significant sp^2 carbon peak at 284.2 eV, in addition to the diamond sp^3 carbon peak at 285 eV. The double-peak is consistent with an sp^2 carbon layer that is <3 nm thick, and the relative magnitude of this peak can be increased by shortening the ramp time and thus increasing the peak pressure during the vacuum anneal. Typical peak pressures are 2×10^{-6} Torr (4×10^{-5} Pa) to 5×10^{-6} Torr (7×10^{-4} Pa) for the 12 hour and 6 hour ramps, respectively. Triacid cleaning removes the sp^2 carbon layer, as shown by

the blue curve in Fig. A.2a. Raman spectroscopy (Horiba LabRam Evolution, 532 nm excitation) of the surface with the sp^2 carbon layer shows no evidence of graphitic carbon, but instead reveals a side peak associated with glassy or amorphous carbon around 1350 cm^{-1}.

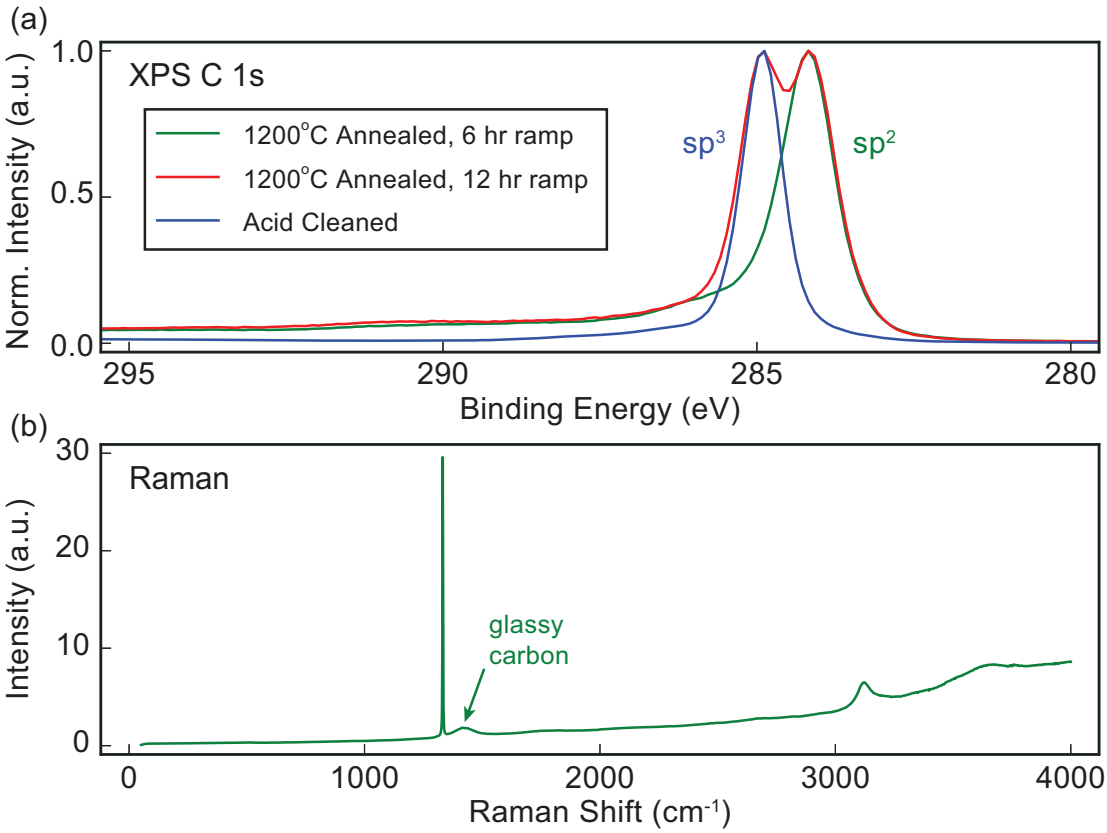


Figure A.2: Graphitization of diamond during annealing. (a) Normalized XPS spectra of the same sample after a 1200 °C anneal with different ramp rates. Material at the surface is converted to sp^2 carbon during annealing (red and green) and manifests as a peak at lower binding energy compared to the spectrum after the subsequent triacid clean (blue), which consists primarily of an sp^3 carbon peak. (b) The Raman spectrum of the 1200 °C annealed surface shows a glassy carbon peak, but no clear evidence of graphite peak at 1580 cm^{-1} [105].

A5 Process Calibration for Oxygen Annealing

At low temperatures, oxygen annealing is not effective at changing the diamond surface chemistry, and at temperatures between 450 °C and 500 °C, oxygen annealing can lead to irreversible surface

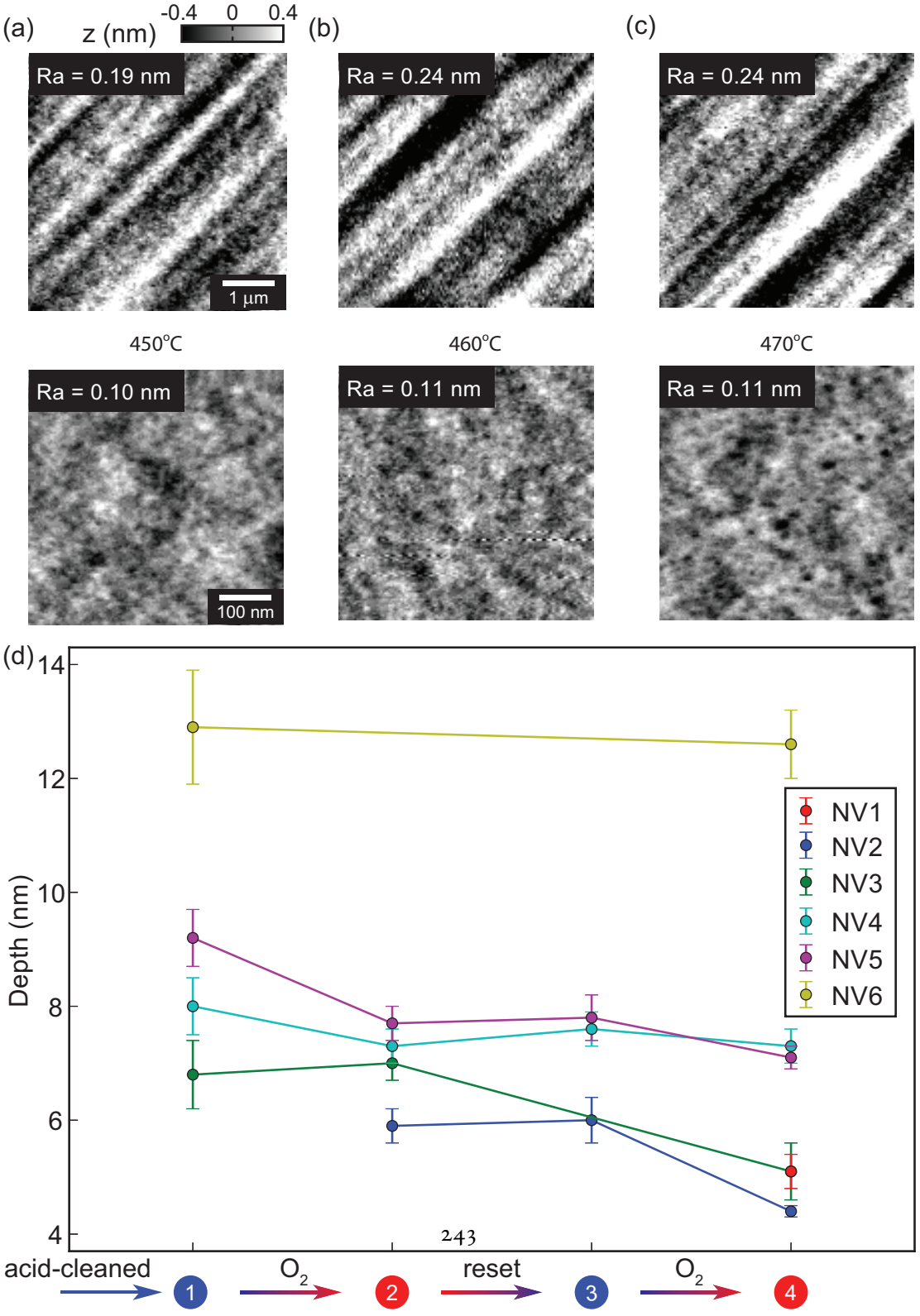
roughening. In order to precisely calibrate the oxygen annealing temperature, we perform detailed AFM characterization to detect the onset of surface roughening. Figure A.3a–c shows AFM images from the oxygen annealing calibration after annealing at 450 °C–470 °C in 10 °C steps. The top (bottom) row shows 5 μm × 5 μm (500 nm × 500 nm) scans. The sample annealed at 470 °C shows micro-pits that are more visible in the 500 nm × 500 nm scan. Therefore, we anneal the NV samples at 445 °C–450 °C to avoid pitting.

Most failures of the oxygen anneal result in high surface roughness and prevalence of micro-pits, as shown in Fig. A.5a and Fig. A.5b. Anecdotally, we also found that after several annealing cycles with the same oxygen tank, the process starts to result in micro-pits, despite the oxygen tank being more than half full. Switching the oxygen tank more frequently results in a smooth surface with no significant change in the optimal temperature after calibration.

To monitor the etching of the diamond surface due to oxygen annealing, we measure the depths of the NV centers at each of the successive annealing steps. The results are shown in Fig. A.3d. While we observe a small decrease in depths (1 nm–2 nm) on NV2, NV3, and NV5, the depths of NV4 and NV6 remain unchanged across the four processing steps. The depth decrease from the subset of NV centers could be attributed to micro-pits that occur after successive oxygen annealing (Fig. A.3c). For the depths presented in the main text, we use the average and standard deviation of all the depth measurements for a given NV center through different processing steps.

Figure A.3 ***(following page)*****: Pitting of diamond at higher oxygen annealing temperatures.** (a–c) AFM images of a scaife-polished standard grade sample annealed at successively higher temperatures for temperature calibration of oxygen furnace. Micro-pits (black circles about 20 nm in diameter) are visible after the oxygen anneal at 470 °C. (d) Depth measurements of the six NV centers presented in the main text after different annealing steps.

Figure A.3: (continued)



A6 Surface Damage from Oxygen Processing and Reactive Ion Etching

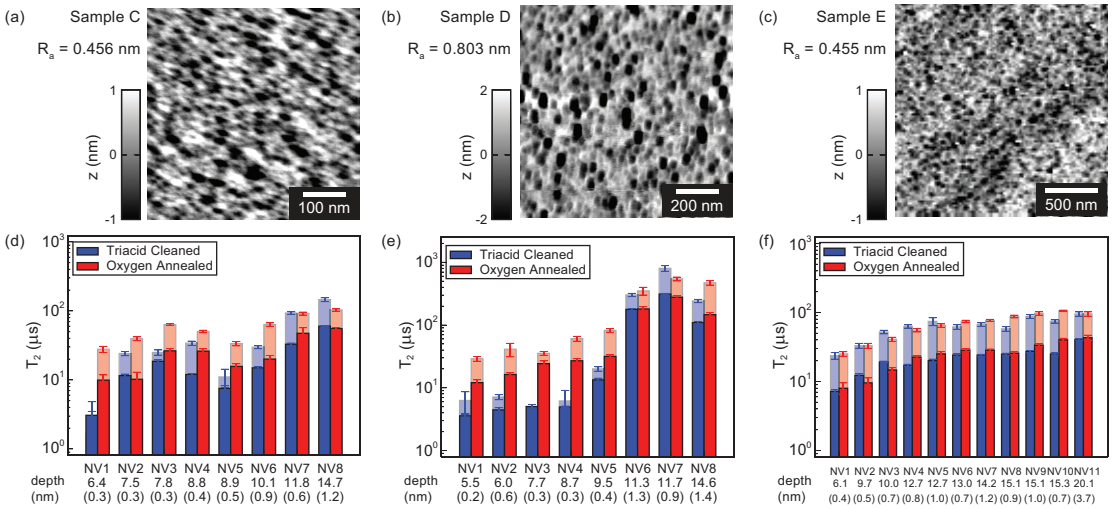
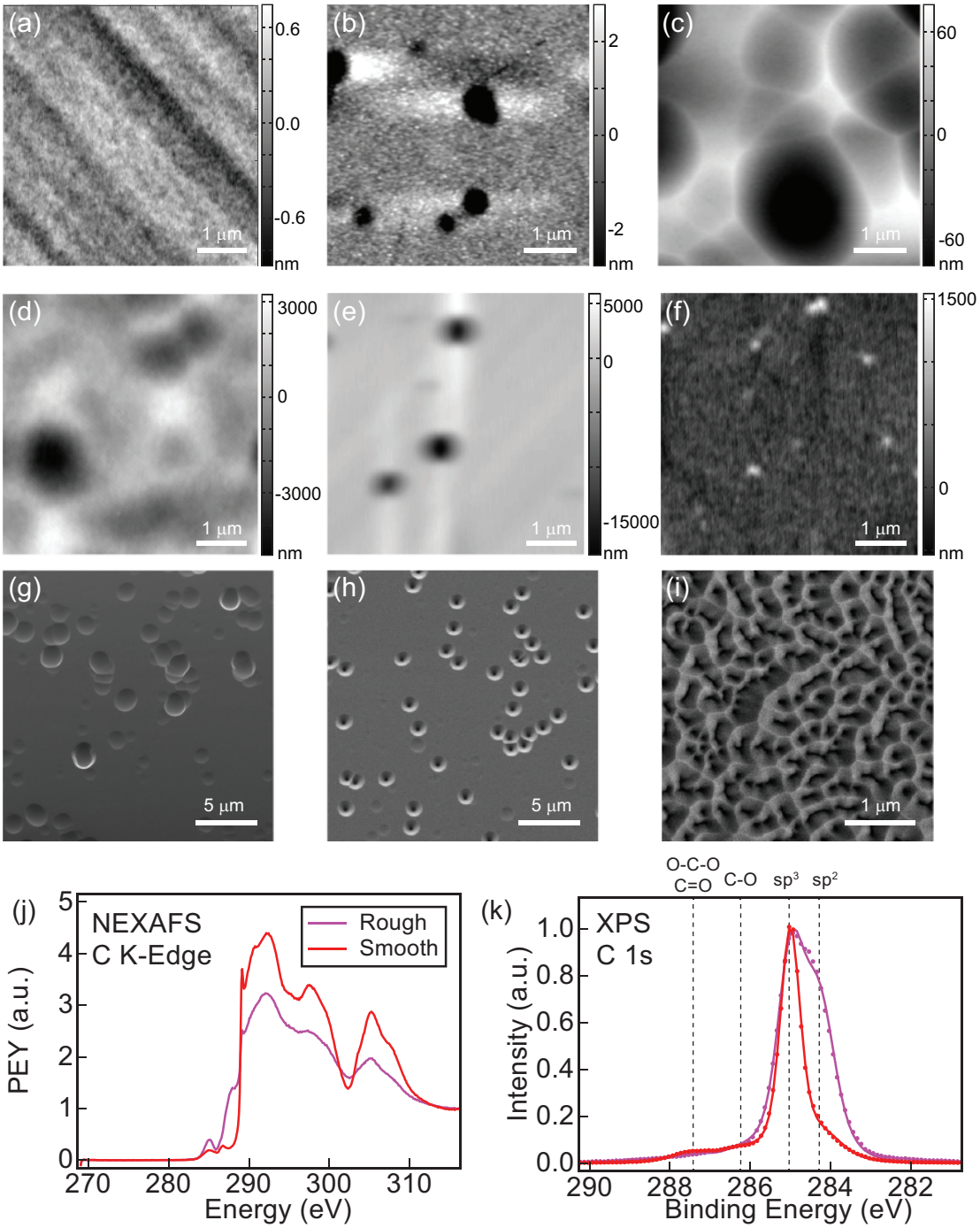


Figure A.5: Coherence times of NV centers in pitted diamonds. (a-c) AFM images and (d-f) NV coherence times $T_{2,\mathrm{Echo}}$ (dark) and $T_{2,\mathrm{XY8}}$ (light) from three additional samples with rougher surface morphologies. The improvement in coherence time after oxygen annealing is less pronounced than that of Sample A.

We show in Fig. A.4b–i AFM and SEM images of various samples with rough surface morphology that result from surface contamination and subsequent processing. This surface roughness leads to drastic differences in the electronic structure at the surface, which is evident in photoelectron spectroscopy. For example, the sample in Fig. A.4c was RIE etched after improper polishing. Figures A.4j,k show the NEXAFS and XPS spectra from this same sample after subsequent oxygen annealing, overlaid with spectra from a smooth diamond for comparison. Figure A.4j shows a larger pre-edge sp^2 carbon peak, a much larger density of unoccupied density of states below the conduction band edge, and a lower contrast second band gap. The carbon 1*s* XPS spectrum for this rough surface (Fig. A.4k) also shows a significantly larger 284 eV "non-diamond" carbon peak. These data show that despite nominally identical processing, the rough surface exhibits very different electronic characteristics compared to a smooth surface, and thus it is important to start with and maintain the smooth surface morphology throughout various processing steps.

Figure A.4 ***(following page):*** **Diamond surface damage.** (a-f) Representative AFM scans showing (a) smooth surface morphology and rough surfaces resulting from (b) contamination or surface damage during an oxygen anneal of a contaminated surface, (c) RIE etching after improper polishing, (d) RIE etching of a Na and Cl contaminated surface, (e) an oxygen anneal with uncontrolled gas purity, and (f) micromasking during an oxygen etch. (g-i) SEM images of large scale morphology from a variety of damaged samples after reactive ion etching. (j) Carbon K-edge NEXAFS shows a comparison between a rough surface (purple, sample shown in (c)) and a smooth surface (red) that have been both triacid-cleaned with the full process as described in the main text. (k) High resolution carbon $1s$ XPS spectra from the two surfaces. The rough surface shows a large non-diamond sp^2 carbon peak at lower binding energy.

Figure A.4: (continued)



A7 Shallow NV Spin Coherence in Rough Samples

In addition to the data in the main text, we also performed oxygen annealing on three additional samples: Samples C, D, and E (Fig. A.5). While we observe improvements in coherence times for Sample C and Sample D after oxygen annealing, the effects are not as pronounced as that of Sample A. Moreover, Sample E shows essentially no improvement.

By examining the surface properties of these samples, we found that the surfaces are morphologically different from Sample A. These samples had all undergone extensive prior processing. Notably, all three samples have higher average roughness and show micropits that we do not observe in Sample A. These results suggest that subtle differences in surface morphology have a significant effect on NV coherence times, even after oxygen annealing.

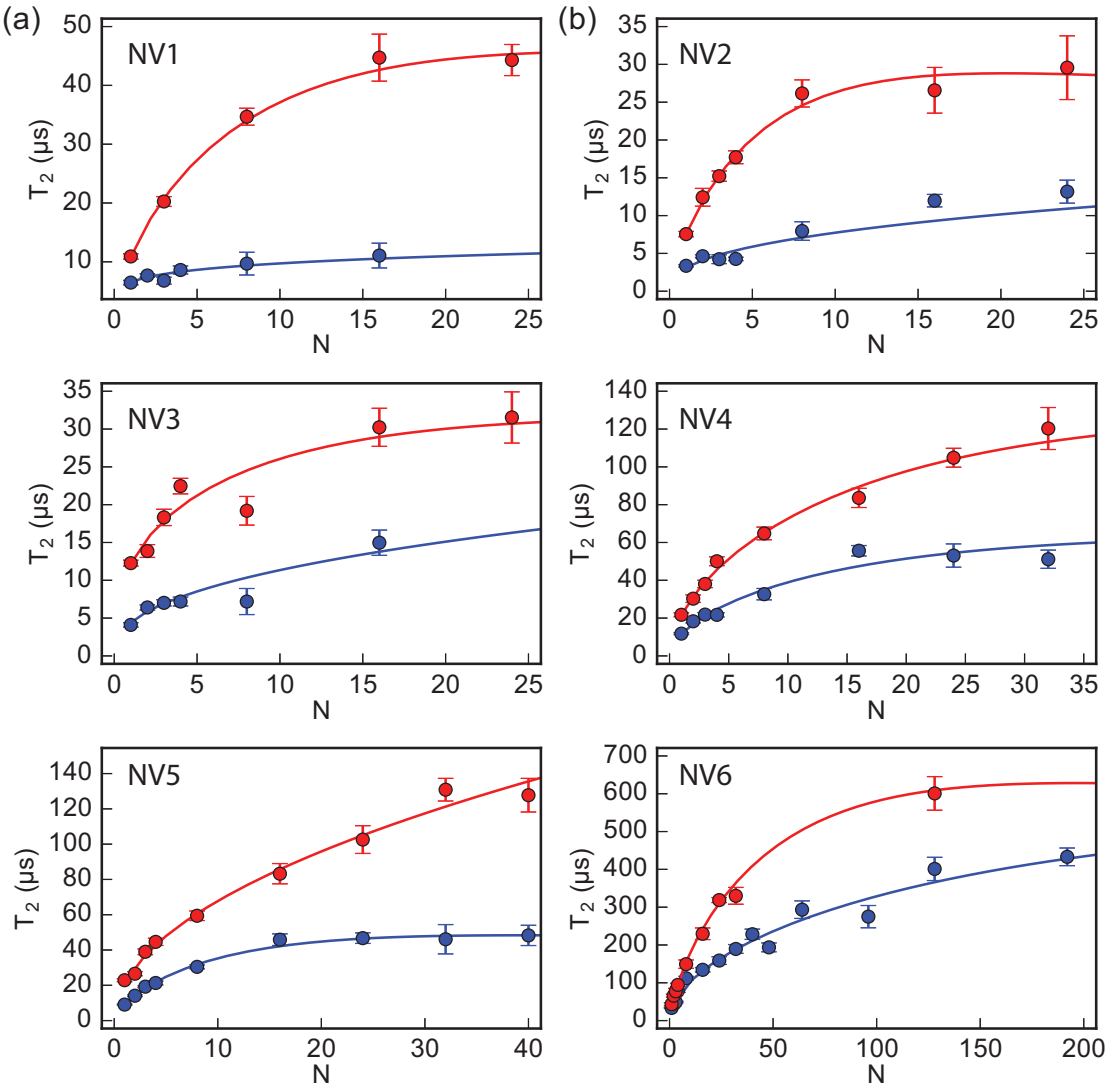


Figure A.6: Dynamical decoupling data. Coherence time as a function of number of dynamical decoupling pulses, N, for all six NV centers presented in the main text for triacid-cleaned (blue) and oxygen-annealed (red) surfaces. The fit parameters are shown in Table A.1.

We show in Fig. 2.11b that shallow NV centers under both triacid-cleaned and oxygen-annealed surfaces show scaling of coherence time with number of pulses that differ from that of a slowly fluctuating spin bath, $T_2 \propto N^{2/3}$. We fit the data to a saturation curve, given by

$$T_2(N) = T_2(1)[N^s_{\text{sat}} + (N^s - N^s_{\text{sat}})e^{N/N_{\text{sat}}}], \tag{A.1}$$

or to a power law, given by

$$T_2(N) = T_2(1)N^s, \tag{A.2}$$

when there is no observable saturation of T_2 [298]. The fitted curves are shown in Fig. A.6 and the fitting parameters for the two surface terminations are shown in Table A.1.

NV	d [nm]	Triacid-cleaned				oxygen-annealed			
		s	$T_2(1)$ [μs]	N_{sat}	$T_{2,\text{sat}}$ [μs]	s	$T_2(1)$ [μs]	N_{sat}	$T_{2,\text{sat}}$ [μs]
1	5.1(3)	0.17(5)	6.6(3)	-	-	0.56(4)	8.8(5)	16(2)	43.0(6.4)
2	5.5(4)	0.39(9)	3.1(4)	-	-	0.66(5)	5.7(4)	10(1)	26.7(4.5)
3	5.8(9)	0.41(6)	4.4(3)	-	-	0.32(8)	11.3(1.3)	22(27)	30.5 (15.4)
4	7.2(4)	0.49(7)	10.4(1.4)	35(27)	60(31)	0.49(4)	19.4(1.5)	41(19)	120(36)
5	7.5(3)	0.60(4)	7.4(4)	20(3)	45.2(7.6)	0.50(2)	21.4(9)	-	-
6	12.1(9)	0.47(2)	31.5(2.1)	388(341)	517(248)	0.66(4)	30.2(3.5)	51(9)	586(133)

Table A.1: Fit parameters for the dynamical decoupling scaling shown in Fig. A.6.

A9 Noise Spectral Density Extracted from NV Center Measurements

A9.1 Dynamical Decoupling Spectral Decomposition

We probe the spectral density of the noise bath from the oxygen-terminated surface using dynamical decoupling. From the coherence decay $C(T)$, where $T = N\tau$ is the total free precession time, the

noise spectrum $S(\omega)$ can be obtained using spectral decomposition Eq. A.3 and Eq. A.4 [255,298].

$$C(T) = \exp[-\chi(T)], \tag{A.3}$$

$$\chi(T) = -\ln C(T) = \frac{1}{\pi}\int_0^\infty S(\omega)\frac{F_N(\omega T)}{\omega^2}d\omega \approx \frac{TS(\omega)}{\pi}, \tag{A.4}$$

where $F_N(\omega T)$ is the N-pulse filter function with a peak maximum at $\omega = \pi N/T$, given by

$$F_N(\omega T) = 8\sin^4\left(\frac{\omega T}{4N}\right)\frac{\sin^2\left(\frac{\omega T}{2}\right)}{\cos^2\left(\frac{\omega T}{2N}\right)}. \tag{A.5}$$

Spectral decomposition reveals a broadband noise spectrum across the frequency range of 0.01 MHz–1 MHz (Fig. A.7f).

A9.2 Double Quantum Relaxometry

To probe the electric field noise, we follow the procedure and notation from Myers *et al.*[255]. We briefly outline their methods here, starting from the NV Hamiltonian, given by

$$H/h = (D + d_{\parallel}\Pi_{\parallel})S_z^2 + \gamma_e \vec{B}\cdot\vec{S} - \frac{d_{\perp}\Pi_{\perp}}{2}(S_+^2 + S_-^2), \tag{A.6}$$

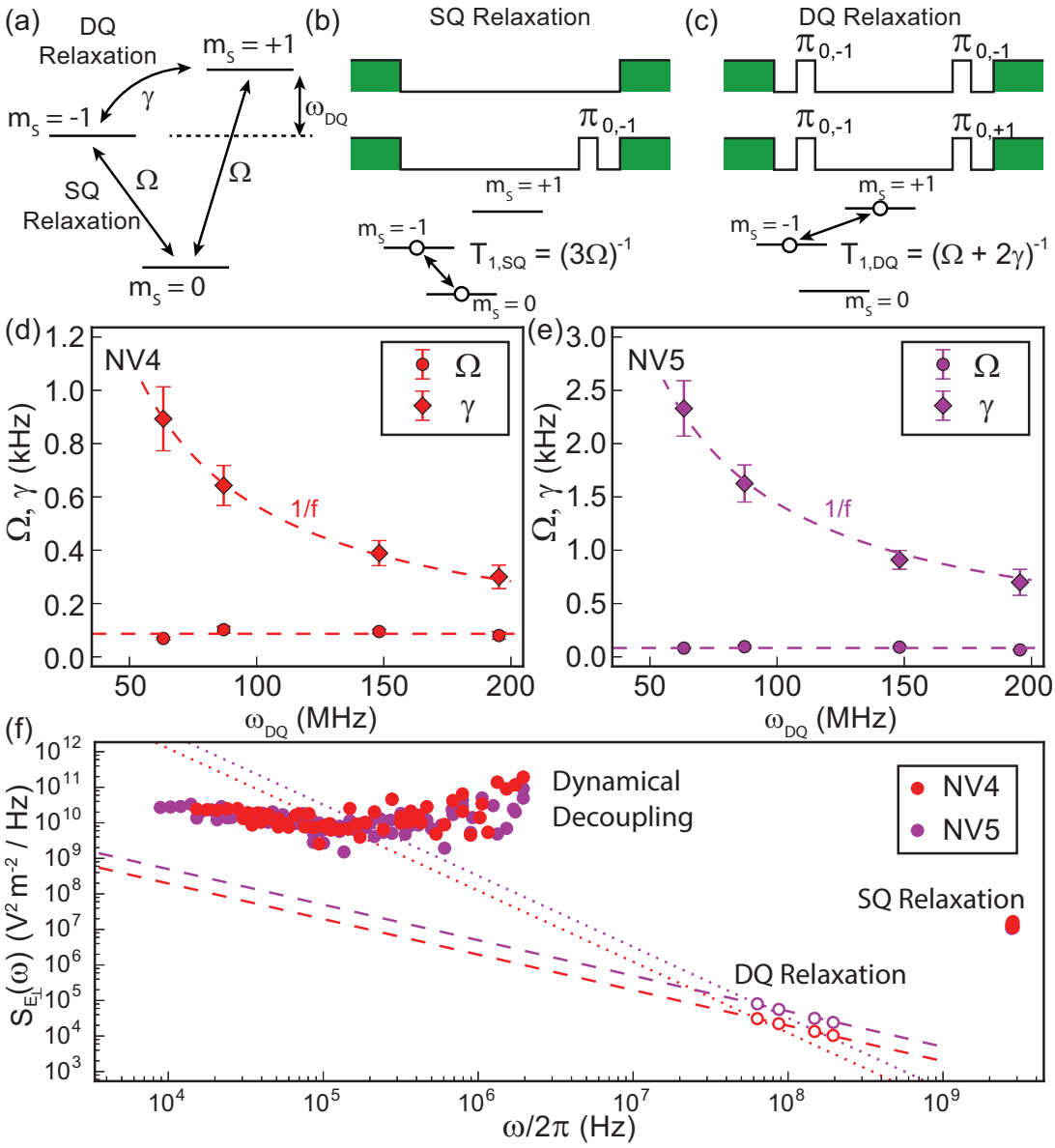
where $D = 2.87$ GHz is the zero-field splitting, $\gamma_e = 2.8$ MHz/G is the electron gyromagnetic ratio, and $d_{\parallel} = 0.35$ Hz $\cdot$ cm/V, $d_{\perp} = 17$ Hz $\cdot$ cm/V are the electric dipole moments. From the Hamiltonian, we can see that while the magnetic field $\vec{B}$ can only drive the single-quantum (SQ) transition ($\Delta m_s = \pm 1$), the electric field component $\Pi_{\perp}$ can result in a double-quantum (DQ) transition ($\Delta m_s = \pm 2$) from the last term in Eq. A.6. Therefore, a full three-level model is required to account for the full spin relaxation resulting from magnetic and electric field noise. The three-level energy diagram is depicted in Fig. A.7a, with the SQ and DQ transition rates denoted by Ω and γ, respectively. The pulse sequences for measuring the relaxation times $T_{1,\mathrm{SQ}}$ and $T_{1,\mathrm{DQ}}$ are shown in Fig. A.7b,c. From SQ and DQ T_1 measurements, we can extract the SQ and DQ transition rates, Ω and γ, from Eq. A.7[255].

$$T_{1,\mathrm{SQ}} = (3\Omega)^{-1}, \qquad T_{1,\mathrm{DQ}} = (\Omega + 2\gamma)^{-1}. \tag{A.7}$$

The electric field noise spectrum, expressed in terms of coupling strength to the NV center, in the units of $\mathrm{Hz}^2/\mathrm{Hz}$, can be obtained directly from the DQ transition rate $S_{\mathrm{DQ}}(\omega_{\mathrm{DQ}}) = \gamma(\omega_{\mathrm{DQ}})$, where ω_{DQ} is the double-quantum transition frequency[255]. Figure A.7d,e shows the noise spectra sampled from NV4 and NV5, consistent with $1/f$ noise. Similarly, the magnetic field noise spectrum, expressed in terms of coupling strength to the NV center, can be obtained from the SQ transition rate $S_{\mathrm{SQ}}(\omega_{\mathrm{SQ}}) = \Omega(\omega_{\mathrm{SQ}})$, where $\omega_{\mathrm{SQ}} = D - \gamma_e B_z = D - \omega_{\mathrm{DQ}}/2$. Unlike S_{DQ}, S_{SQ} is roughly

Figure A.7 ***(following page)*****: Single and double quantum relaxation.** (a) Energy level diagram of the ground state electronic spin of the NV center, indicating single- and double-quantum relaxation channels, whose rates are denoted by Ω and γ, respectively. (b) SQ and (c) DQ relaxation measurement sequences. The NV is prepared in the $m_S = 0$ ($m_S = -1$) state and the relaxation to $m_S = -1$ ($m_S = +1$) is measured. (d,e) SQ and DQ transition rates as a function of DQ transition frequency ω_{DQ} for two different NV centers. Dashed lines indicate the broadband spectra for Ω and $1/f$ spectra for γ. (f) Comparison of the noise spectral density from single- and double-quantum measurements. The two spectra are plotted on the same scale using the effective electric field noise $S_{E_\perp}$. We found that at high frequencies, magnetic field noise (solid circles) is the dominant source of decoherence for oxygen-annealed surfaces, compared to the electric field noise (open circles). Dashed and dotted lines show an extrapolation with $1/f$ and $1/f^2$ scaling, respectively.

Figure A.7: (continued)



constant across this magnetic field range.

A9.3 Comparing Magnetic and Electric Noise Spectra

Several reports have observed that electric field can significantly contribute to the decoherence of shallow NV centers [187,172]. Here we combine decoherence and relaxation measurements to compare the noise spectral density arising from magnetic field and electric field noise. Even though the magnetic field noise spectrum obtained from SQ measurements (dynamical decoupling and SQ relaxation) and the electric field noise spectrum obtained from DQ measurements are of distinct origins, we can place them on the same scale for comparison by considering the effective field $E_\perp$ [255], given by

$$S^{\mathrm{SQ}}_{E_\perp}(\omega) = 2S^{\mathrm{SQ}}_{E_\parallel}(\omega) = 2\frac{S_{\mathrm{SQ}}(\omega)}{d^2_\parallel}, \qquad S^{\mathrm{DQ}}_{E_\perp}(\omega) = \frac{S_{\mathrm{DQ}}(\omega)}{d^2_\perp}, \tag{A.8}$$

where $S^{\mathrm{SQ}}_{E_\parallel}$ is obtained by considering an effective electric field that would cause first-order dephasing and the relationship $\langle E_\perp\rangle^2 = 2\langle E_\parallel\rangle^2$ is obtained by considering the geometry of the NV axis on a (100)-oriented diamond. The combined spectrum is shown in Fig. A.7f.

Because we probe a small frequency range over which our scaling of $1/f$ (dashed lines) differs from what is reported by Myers et. al [255], we also plot the extrapolated noise spectral density with a scaling of $1/f^2$ (dotted lines), which would be expected from a sum of many Lorentzian noise sources with different cutoff frequencies, as a worst case estimate. Based on this extrapolation, and comparing to the amplitude of the magnetic field noise obtained from dynamical decoupling and SQ relaxation, we find that the magnetic field noise is the dominant source of noise for the oxygen-annealed surface for $\omega > 2\pi \times 200$ kHz.

A9.4 Coupling to Dark Surface Spins

Several experiments have reported that the coherence times of the shallow NV centers are limited by magnetic noise arising from "dark" surface spins that are not optically active[227,254,81,301]. To examine this hypothesis, we probe the coupling of our NV centers to dark spins via double electron-electron resonance (DEER) spectroscopy, where a second microwave tone is applied to flip the dark spins during the NV π-pulse in the Hahn echo sequence. To extract the DEER coupling, we model the decoherence of the NV center with two separable sources of decoherence, one arising from the dark spins, and another decoherence rate attributable to everything else. The coherence C as a function of free precession time t can be written as:

$$C_{\mathrm{NV}}(t) = \exp\left[-\left(\frac{t}{T_{2,\mathrm{NV}}}\right)^{N_{\mathrm{NV}}}\right], \tag{A.9}$$

$$C_{\mathrm{DEER}}(t) = \exp\left[-\left(\left(\frac{t}{T_{2,\mathrm{DEER}}}\right)^{N_{\mathrm{DEER}}} + \left(\frac{t}{T_{2,\mathrm{NV}}}\right)^{N_{\mathrm{NV}}}\right)\right], \tag{A.10}$$

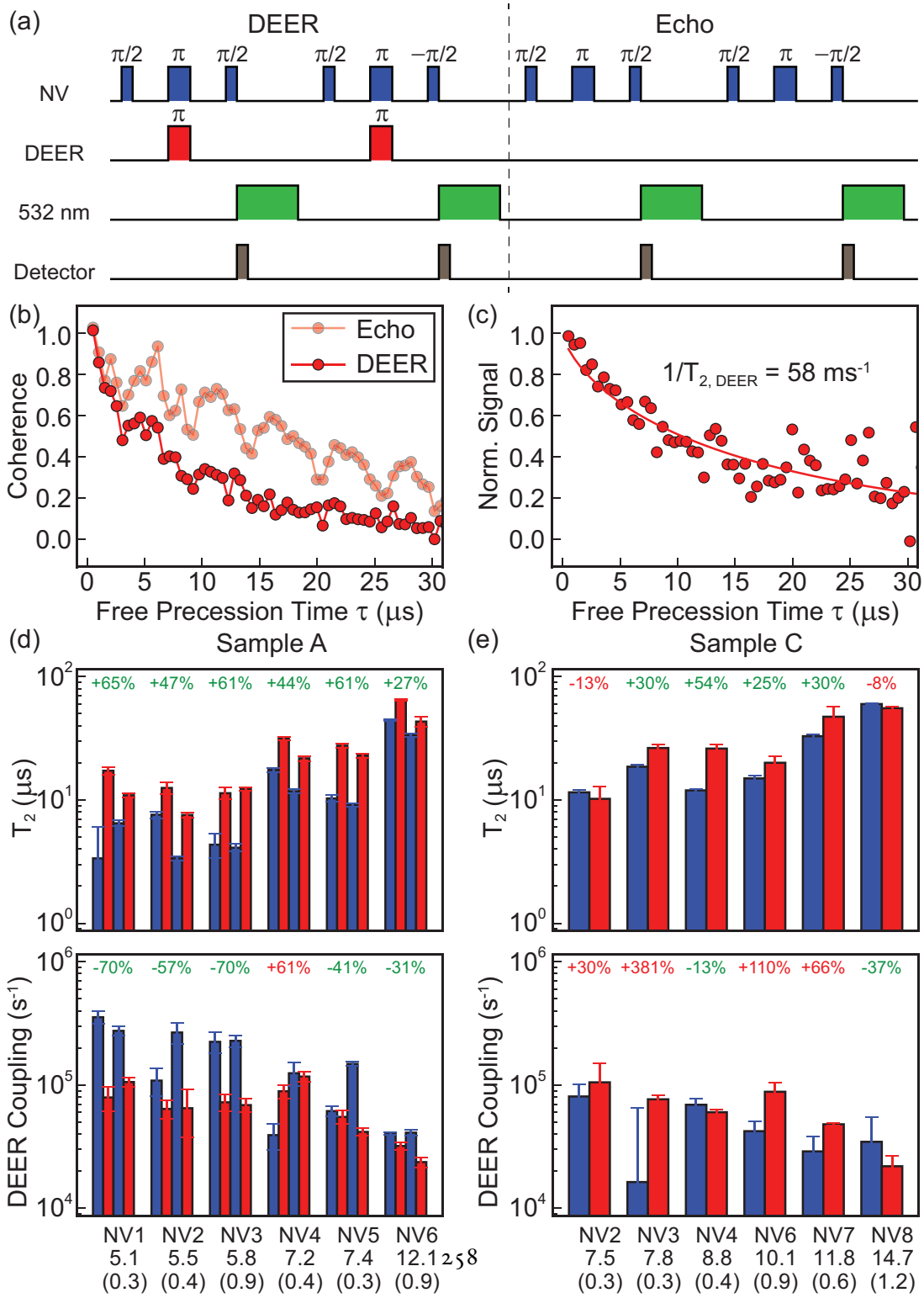
where N_{NV} and N_{DEER} are stretching factors. To directly measure the DEER coupling, we can normalize the DEER decay curve using the Hahn echo decay curve. The resulting decay curve can be used to extract DEER coupling $g_{\mathrm{DEER}} = 1/T_{2,\mathrm{DEER}}$.

$$\frac{C_{\mathrm{DEER}}(t)}{C_{\mathrm{NV}}(t)} = \exp\left[-\left(\frac{t}{T_{2,\mathrm{DEER}}}\right)^{N_{\mathrm{DEER}}}\right] \tag{A.11}$$

Experimentally, we interleave the DEER experiment with the Hahn echo experiment in order to mitigate any long term drift. The pulse sequence and a sample set of data are shown in Fig. A.8a–c. We performed DEER measurements on the same NV centers across several surface processing steps. We observe that for Sample A, whose coherence data is presented in the main text, the oxygen annealing also results in a lower DEER coupling across all the NV centers, and this lower DEER

Figure A.8 ***(following page)*****: Change in DEER signal with annealing.** (a) Pulse sequence for measuring DEER coupling: a DEER sequence is erleaved with a Hahn echo sequence to mitigate effects from slow system drift. The DEER driving frequency is $\omega_{\mathrm{DEER}} \approx 920\,\mathrm{MHz}$, corresponding to dark spins with $g = 2$. (b) Hahn echo and DEER decay curves taken at $B_z \approx 330\,\mathrm{G}$. Collapse and revival arising from hyperfine coupling with a nearby ^{13}C can be observed. (c) Normalized signal, where the ^{13}C modulation is no longer pronounced. (d-e) Spin echo coherence time and DEER coupling for several NV centers in Sample A and Sample C before and after oxygen annealing. Green (red) numbers indicate the average improvement (worsening) in the decoherence rate $1/T_2$, and the average reduction (increase) in the DEER coupling after oxygen annealing.

Figure A.8: (continued)



coupling is reversible and reproducible. In section A7, we show that across several samples with different surface morphology, there are varying degrees of improvement to the coherence times of the NV centers with oxygen annealing, but the oxygen-annealed surface shows consistently better coherence. However, the change in DEER coupling is inconsistent among these samples, suggesting that rough surface morphology can lead to a population of persistent dark spins that are not eliminated by oxygen annealing. Figure A.8d–e shows a comparison of changes in T_2 and DEER coupling between Sample A and Sample C. While the oxygen annealing improves the coherence times in both samples and reduces the DEER coupling in Sample A, the DEER coupling stays the same or increases in Sample C.

We calculate the Pearson's product-moment correlation coefficient between the coherence time improvement and DEER coupling reduction for both samples and we find no significant correlation (correlation coefficients -0.44 and $+0.25$, respectively).

A10 Electron Affinity Measurement

The electron affinity was calculated from the measured spectral width in UPS (Fig. 2.12e, also duplicated in Fig. A.9a). The binding energy scale was calibrated to the core levels and Fermi edge of a tantalum calibration sample (Fig. A.9a, inset). The width of the electron distribution curve, ω, can be measured as the energy difference between the valence band maximum (VBM) and the secondary electron cutoff at high binding energy, as shown in Fig. A.9b,c. The ionization energy, E_i, can then be used to relate the spectral width, ω, to the electron affinity, E_A, by

$$E_i = h\nu - \omega = E_g + E_A, \tag{A.12}$$

where $h\nu = 21.2$ eV is the excitation energy from He I UV source and $E_g = 5.5$ eV is the band gap of the diamond.

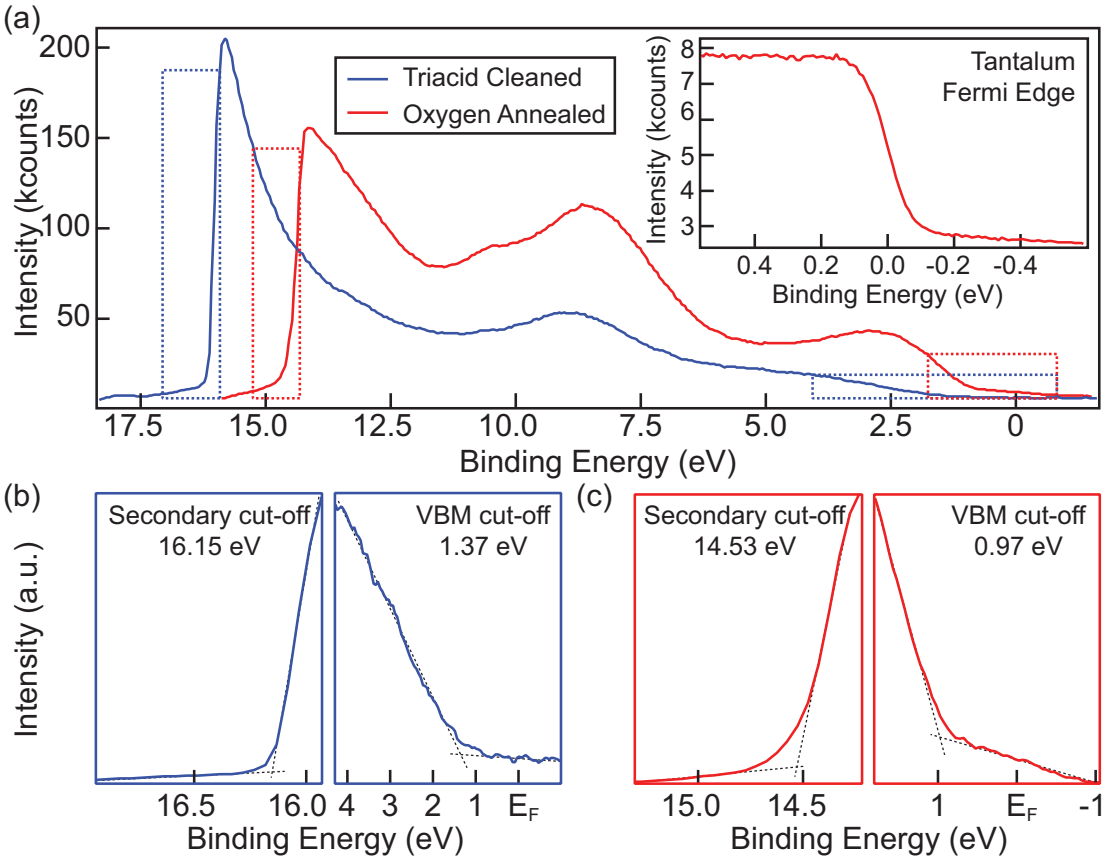


Figure A.9: UPS measurements of diamond surfaces. (a) UPS spectra from triacid-cleaned sample (blue) and oxygen-annealed sample (red) as a function of binding energy relative to the Fermi level. The Fermi level is calibrated with a reference tantalum foil (inset). The spectral width, ω, is calculated as the energy difference between the secondary electron cut-off and valence band maximum, indicated by the dashed rectangles. (b,c) Zoom-in of the secondary electron cut-off and the valence band maximum for the triacid-cleaned sample and the oxygen-annealed sample, respectively.

A11 LEED Pattern of Oxygen-annealed Surface

The LEED pattern for the oxygen-annealed surface (Fig. 2.12c, duplicated in Fig. A.10a) shows that the surface is 1×1 reconstructed, and there is no evidence of 2×1 reconstruction. In order to verify that the absence of 2×1 diffraction peaks does not arise from disorder obscuring the peaks, the sample was annealed at 1000 °C to remove the oxygen termination, as verified by XPS (Fig. A.10c).

A clear sign of 2×1 reconstruction emerges in the diffraction spots (Fig. A.10b), which are absent before annealing (Fig. A.10a).

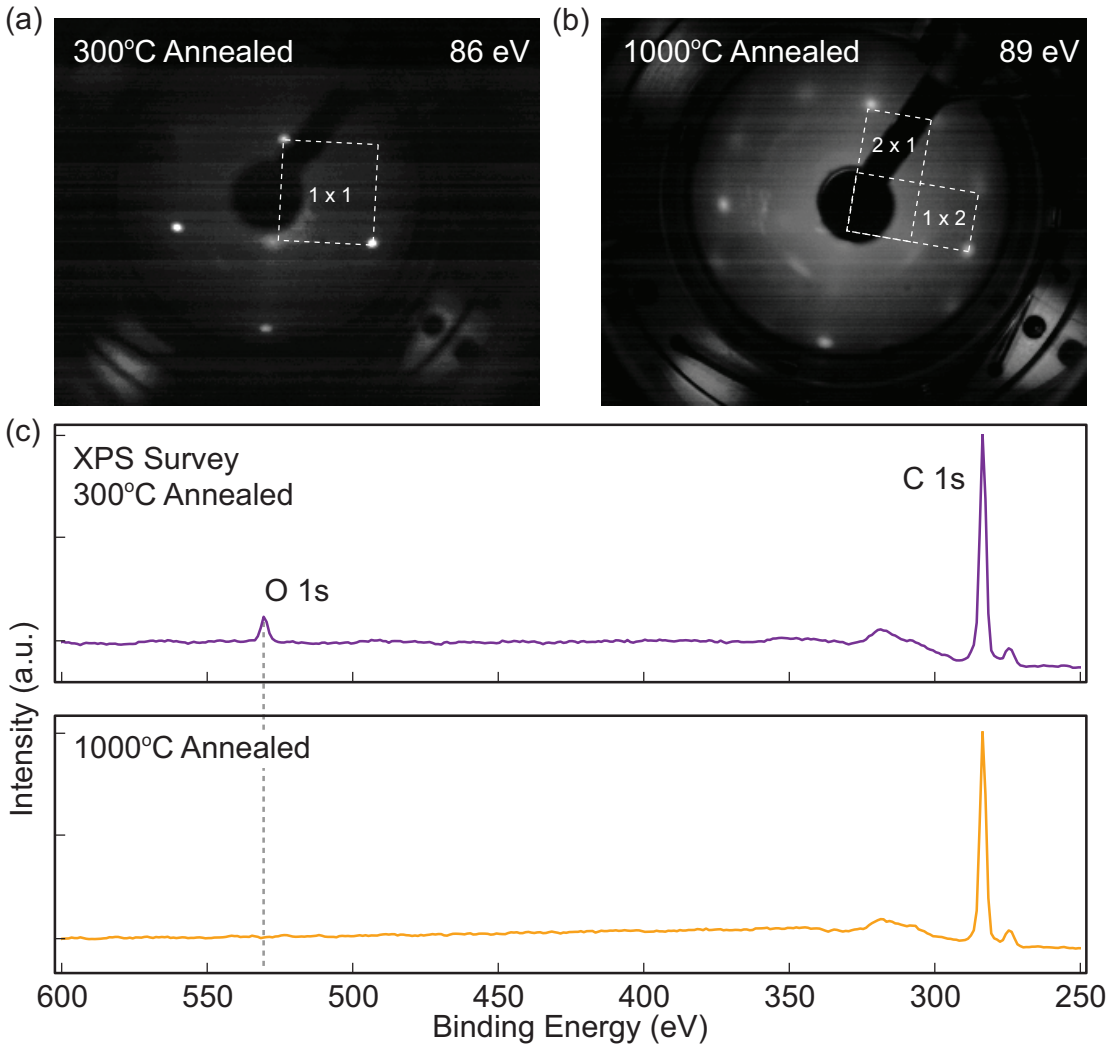


Figure A.10: LEED of diamond surfaces. (a) LEED of an oxygen-annealed surface, as shown in Fig. 2.12c. The 1×1 reconstruction is consistent with an ether-terminated surface. (b) LEED after *in situ* annealing at 1000 °C showing 2×1 reconstruction peaks that appear for the same surface after the surface heteroatoms are removed. (c) XPS survey data showing that the O 1*s* peak indeed disappears after annealing at 1000 °C.

A12 Comparison of XPS Spectra for Triacid-cleaned and Oxygen-annealed Surfaces

High-resolution XPS spectra were measured at the Australian Synchrotron. The carbon 1*s* spectrum (Fig. A.11a) for the triacid-cleaned sample shows a larger peak width compared to the oxygen-annealed surface, individual satellite peaks cannot be resolved, and the sp^2 carbon peak at lower binding energy is more pronounced. There is also some weight to the spectrum at higher binding energies, above 288 eV, possibly indicating the presence of some carboxylic acid groups at the surface[345]. The oxygen 1*s* spectrum (Fig. A.11b) for the triacid-cleaned surface also shows a single dominant peak with some species at lower binding energies, but the peak width is 2.1 eV, compared to 1.3 eV for the oxygen-annealed surface. The broader peak widths are consistent with a highly disordered, heterogeneous surface termination.

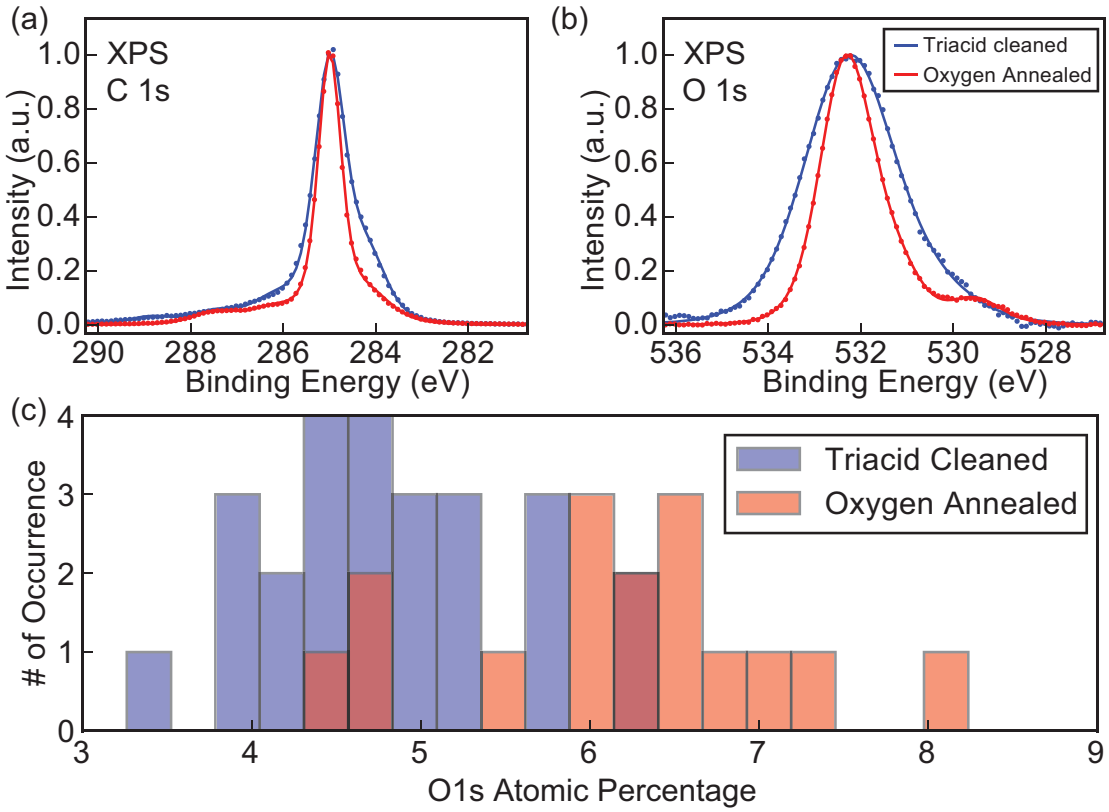


Figure A.11: Additional XPS of annealed and acid cleaned surfaces. (a, b) Comparison of high-resolution XPS spectra at carbon 1*s* and oxygen 1*s* peaks from triacid-cleaned and oxygen-annealed surfaces. The linewidths are narrower for the oxygen-annealed surface. (c) Histogram of the oxygen 1*s* atomic percentage from the XPS signal, obtained from a large number of triacid-cleaned and oxygen-annealed surfaces.

XPS survey scans of many samples across many processing steps were taken at the Princeton IAC. From the survey scans, the atomic composition of the surface can also be estimated by comparing the magnitude of the XPS peaks. Here, we focus on the oxygen 1*s* spectra from triacid-cleaned surfaces and oxygen-annealed surfaces. From the inelastic mean free path of photoelectrons at these energies (2.2 nm for 1487 eV Al Kα)[323], we estimate the contribution of the signal from a monolayer of atoms on the diamond surface to be 7.6 %. Figure A.11c shows a histogram of the measured oxygen 1*s* atomic percentage from multiple XPS spectra, where the oxygen-annealed surfaces show markedly higher oxygen 1*s* percentage compared to the triacid-cleaned surfaces. The values obtained

are consistent with an oxygen monolayer on the surface after oxygen annealing, while the triacid-cleaned surfaces have lower oxygen coverage, indicating incomplete oxygen termination.

B

Supporting material for Chapter 3

B1 Measurement setup

The details of our measurement setup have been published elsewhere[308], but we briefly review them here for completeness. The data for this manuscript were taken on several measurement setups that were constructed in a similar manner but with different components.

NV center measurements were performed on a home-built confocal microscope. NV centers

are excited by a 532 nm frequency doubled Nd:YAG solid state laser which is modulated with an acousto-optic modulator. The beam is scanned using galvo mirrors and projected into an oil immersion objective (Nikon, Plan Fluor 100X,NA = 1.30) with a telescope in a 4f configuration. Laser power at the back of the objective was kept between 60–100 μW, approximately 25% of the saturation power of a single NV center, in order to avoid irreversible photobleaching. A dichroic beamsplitter separates the excitation and collection pathways, and fluorescence is measured using a fiber-coupled avalanche photodiode (Excelitas SPCM-AQRH-44-FC). A neodymium permanent magnet was used to introduce a DC magnetic field for Zeeman splitting, and the orientation of the magnetic field was aligned to within 1° of the NV center axis using a goniometer. Measurements were performed at moderate magnetic fields of $\approx$ 300 Gauss so that the surface spin and NV center transitions were frequency-resolved.

Spin manipulation on the NV center and surface spins was accomplished using microwaves. Two signal generators, which output the NV center and DEER transition frequencies, were separately gated with fast SPDT switches (Mini-Circuits ZASWA-2-50DR+). In one set up, these signals were then amplified by Mini-Circuits ZHL-16W-43+ and ZHL-100W-13+, respectively before being combined with a high-power resistive combiner and delivered to the sample via a coplanar stripline. In another set up, the gated signals were combined with a resistive combiner (Mini-Circuits ZFRSC-42-S+) and amplified with a high-power amplifier (Ophir 5022A) before being delivered to the sample via a coplanar stripline. The stripline was fabricated by depositing 10 nm Ti, 1000 nm Cu, and 200 nm Au on a microscope coverslip. Following metallization, the stripline was photolithographically defined and etched with gold etchant and hydrofluoric acid. Finally, a 100 nm layer of Al_2O_3 was deposited on top of the fabricated stripline via atomic layer deposition (ALD) to protect the metal layer. Pulse timing was controlled with a Spincore PulseBlaster ESR-PRO500 with 2 ns timing resolution. The DEER pulse was either applied simultaneously to the NV center pulse, as depicted in the Main Text Fig. 1, or it was offset from the NV center pulse in order to avoid

saturation of the amplifier in some cases. In the latter case, an identical DEER pulse was applied immediately after the first $\pi/2$ pulse on the NV center as in [233].

B2 Sample processing

All of the samples measured for this work were electronic grade samples (<5 ppb nitrogen, <1 ppb boron) from Element 6. Those with an additional overgrown ^{12}C enriched layer are indicated in Table B.1. Most of the samples had surfaces that were prepared prior to implantation following the procedure outlined in [308]. Briefly, the pre-implantation surface preparation begins with scaife polishing, followed by etching in Ar/Cl_2 followed by O_2 plasma, and then annealing to 1200°C in a vacuum tube furnace to graphitize and remove the first few nanometers of the surface. and did not undergo this surface preparation prior to implantation and were implanted with the "as grown" surface. All samples were implanted with ^{15}N, and annealed to 800°C in a tube-vacuum furnace to form NV centers.

After the activation anneal, NV centers were measured under a variety of different surfaces, as noted in Table B.1. In some cases, DEER coupling was characterized in the same sample after different surface processing steps. The final surface conditions noted in Table B.1 were prepared as follows:

- Activated: NV centers were measured directly after 800°C activation anneal and triacid cleaning (reflux sample in 1:1:1 sulfuric, nitric, and perchloric acids for 2 hrs)
- Oxygen annealed: NV centers were measured after heating the sample to 440-460°C while flowing an atmosphere of oxygen gas over the samples, followed by cleaning in a 2:1 piranha mixture (sulfuric acid and hydrogen peroxide) for 20 min.
- Reset: NV centers were measured after 'resetting' the surface to a state comparable to the

activated surface by reannealing the sample to 800°C in a vacuum tube furnace at around 10^{-6} mbar, and subsequently triacid cleaning the sample.

- 500°C annealed: NV centers were measured after annealing the sample to 500°C in a vacuum tube furnace, followed by triacid cleaning.

Sample	C12 enriched	Pre implant surface prep	Color	Surface condition
		×		activated
				oxygen annealed
				reset
				oxygen annealed
		×		oxygen annealed
	×			activated
		×		reset
	×	×		oxygen annealed
				reset
		×		oxygen annealed
				reset
				500°C annealed
		×		activated
	×	×		activated
	×			oxygen annealed

Table B.1: Diamond samples

B3 Fitting procedures

DEER datasets consist of a bright ($m_s = 0$ projection) and dark ($m_s = -1$ projection) reference (BrightRef and DarkRef, respectively), spin echo signals projected onto $m_s = 0$ and $m_s = -1$ (sig_0 and sig_1, respectively), and DEER projected onto $m_s = 0$ and $m_s = -1$ (deero and deer1, respectively). There are also error bars for each point in each of these categories, given by the variance of the counts, which is $\sqrt{N_{\text{photons}}}$ for the shot-noise limited NV center spin readout employed here. These signals are then averaged to calculate coherence decay points, C_i:

$$C_i = \left(\frac{\text{Sig}_{0\text{i}} - \text{Sig}_{1\text{i}}}{\text{BrightRef}_{\text{i}} - \text{DarkRef}_{\text{i}}} \right) \tag{B.1}$$

and DEER measurement points, D_i, in the same fashion. The error bars for the coherence are then given by

$$\sigma_{Ci}^2 = \left(\frac{1}{\text{BrightRef}_{\text{i}} - \text{DarkRef}_{\text{i}}} \right)^2 (\sigma_{0i}^2 + \sigma_{1i}^2) + \left(\frac{\text{Sig}_{0\text{i}} - \text{Sig}_{1\text{i}}}{(\text{BrightRef}_{\text{i}} - \text{DarkRef}_{\text{i}})^2} \right)^2 (\sigma_{Bi}^2 + \sigma_{Di}^2) \tag{B.2}$$

An equivalent expression can be written down for the DEER signal error bars.

In order to remove the effects of other decoherence mechanisms from the DEER measurement and obtain a free induction decay curve due to the surface spins alone, we divide the DEER signal by the coherence:

$$S_i = \frac{D_i}{C_i} \tag{B.3}$$

and propagate the error bars

$$\sigma_{Si}^2 = \left(\frac{\sigma_{Di}}{C_i}\right)^2 + \left(\frac{\sigma_{Ci} D_i}{(C_i)^2}\right)^2 \tag{B.4}$$

For the data presented in Fig. 1, we then fit to the stretched exponential function

$$f(\tau; a, \Gamma_{\mathrm{DEER}}, n) = a e^{-(\Gamma_{\mathrm{DEER}}\tau)^n} \tag{B.5}$$

in order to obtain DEER decay rates (Γ_{DEER} and stretching factor n). The parameter a is experimentally found to be very close to 1.

The data presented in Fig. 3 undergo further processing to better observe the transition in n with time. Taking the logarithm of $1/f(\tau)$ and plotting on a log-log scale gives a line with a slope given by n and an intercept of $n \log_{10} \Gamma_{\mathrm{DEER}}$.

First a conservative cutoff of $D_i > 0.1$ is introduced to remove sections of data with low signal to noise and to avoid infinities in taking the logarithm. We then calculate

$$g_i = \log_{10} \ln \frac{1}{S_i} \tag{B.6}$$

and the error bars of g_i

$$\sigma_{g_i} = \frac{\sigma_{Si}}{\ln(10) S_i \ln(S_i)} \tag{B.7}$$

For many of the NV centers presented in Fig. 2, the DEER coupling rates are extremely small and in many cases consistent with 0. The processing and fitting procedure defined above was found to give poor results and instead a Markov Chain Monte Carlo procedure was employed to simultaneously fit the coherence and DEER data without division. The coherence was assumed to follow a

function of the form

$$C(\tau) = ae^{-(\tau/T_2)^c} \tag{B.8}$$

While the DEER signal was assumed to follow

$$D(\tau) = e^{-(\Gamma_{\mathrm{DEER}}\tau)^n} \cdot C(\tau) \tag{B.9}$$

The data C_i and D_i were used to calculate likelihood functions for $C(\tau)$ and $D(\tau)$, respectively.

B4 Removal of surface spins through annealing

B4.1 X-ray spectroscopy

To investigate the microscopic origin of surface spins and to develop a procedure for their selective removal, we interrogated diamond surfaces using X-ray spectroscopy. In near-edge X-ray absorption fine structure (NEXAFS) spectroscopy, monochromatic incident X-rays excite core electrons, and the electron yield is measured as a function of X-ray energy, giving a signal that is proportional to the unoccupied density of states near the surface[343]. We performed NEXAFS spectroscopy on diamond samples prepared with the standard surface preparation procedure described in section B2, without implanting NV centers. NEXAFS spectroscopy at the carbon edge reveals a peak at 282.5 eV (Fig. B.1b). Previous studies assign this peak to sp^3 dangling bonds at the diamond surface[45]. The presence of this dangling bond peak in the NEXAFS spectra correlates with the surface spin DEER signal measured via shallow NV centers. Specifically, we observe that the peak at 282.5 eV is present in thermally annealed and acid cleaned samples, while it is absent in samples after oxygen annealing as described in [308]. Quantitatively, oxygen annealing diminishes this peak from a signal to noise ratio of around four to a value below the noise floor (Fig. B.1(d)). Correspondingly, we have

also previously shown that individual NV centers show decreased DEER coupling rates after oxygen annealing, and increased coupling after a thermal surface reset process[308].

The correlation between the 282.5 eV peak in NEXAFS and DEER coupling strengths across samples suggests that dangling bonds at the diamond surface may be responsible for the surface spin signal detected in NV center-based sensing experiments. However, there are a variety of observable changes at the diamond surface upon oxygen annealing[308], and a definitive link requires a process for selectively removing dangling bonds. When the samples are annealed in high vacuum at 650°C for one hour, the dangling bond peak falls below the noise floor (Fig. B.1(c)), but the oxygen edge NEXAFS spectrum is essentially unchanged (Fig. B.1(a)). Thus, annealing at 650°C leads to selective removal of the dangling bond peak. This annealing procedure also leads to a decrease in DEER coupling for the same NV centers, as shown in the Main Text.

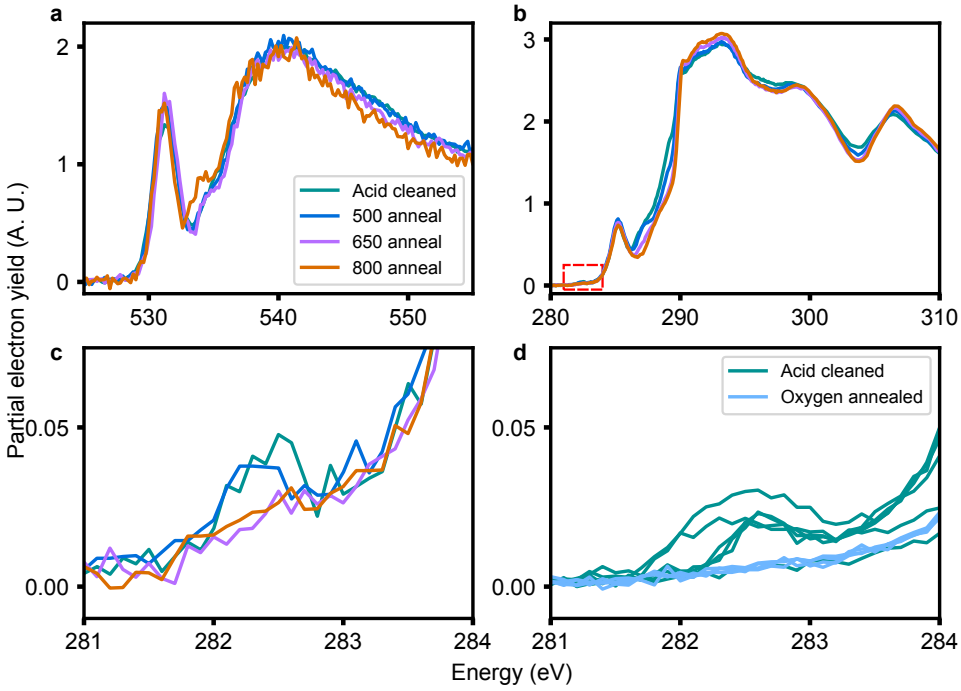


Figure B.1: NEXAFS through annealing. **a**, Oxygen edge NEXAFS for diamond sample with initial acid cleaned surface (green), after 500 °C annealing (blue), 650 °C annealing (purple) and 800 °C annealing (orange). **b**, Carbon edge NEXAFS of the same annealing sequence on the same sample. Red box indicates location of dangling bond peak, shown in detail in **c**. **c**, Detailed view of dangling bond peak showing removal at higher annealing temperatures. **d**, Detailed view of dangling bond peak for several samples with initially prepared acid cleaned surfaces (green) and oxygen annealed surfaces (blue), showing absence of the peak for oxygen annealed surfaces. Oxygen annealing procedure and suppression of DEER signal are described in [308].

B4.2 Annealing procedure

was annealed in a vacuum tube furnace with a base pressure around 10^{-6} mbar. The sample was heated from room temperature to 100°C over 1 hour, held at 100°C for 11 hours, heated to 650 °C over 20 hours, held at 650°C for 2 hours, then cooled to room temperature.

We note that we have tried annealing in different vacuum systems and have sometimes measured a reduction in DEER coupling at inconsistent temperatures. We attribute these discrepancies to dif-

ferences in annealing duration, temperature calibration, or thermal anchoring of sample to heater. Other samples showed a persistent DEER signal that was not reduced by vacuum thermal annealing or oxygen annealing. Many of these samples either did not go through processing to reduce subsurface damage prior to implantation or had rough surface morphologies from iterative processing.

B4.3 Coherence change with annealing

For the NV centers depicted in Main Text figure Fig. 2a, we also measured the spin echo coherence time (T_2) of each NV center before and after annealing. The results are plotted in Fig. B.2. In contrast to oxygen annealing coherence times of these NV centers are not significantly affected by the vacuum annealing procedure[308]. Because the DEER couplings for these NV centers are reduced by annealing, we interpret these results together to imply that the surface spin bath is not primarily responsible for limiting the coherence time of near surface NV centers in this sample.

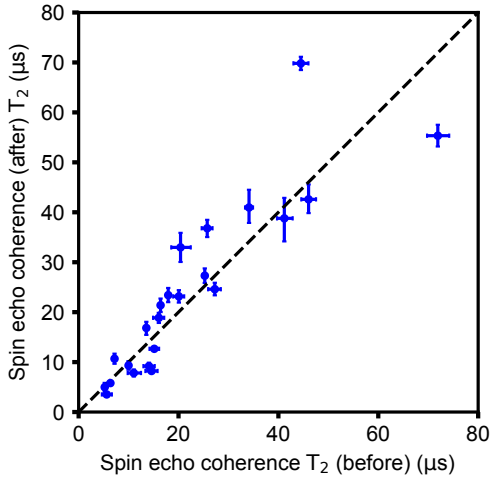


Figure B.2: Coherence times before and after annealing. Coherence times of NV centers in after annealing, plotted as a function of pre-annealing coherence times. Dashed line has a slope of one.

B4.4 Spectral decomposition through annealing

The spectral density of the noise bath, $S(\omega)$ can be probed by dynamical decoupling [308,254,298]. We use the non-symmetric XY8 pulse sequence [375] with multiple repetitions to probe different regions of the noise spectrum.

In general, the coherence decay, $C(T)$, of an NV center is given by

$$C(T) = \exp(-\chi(T)), \tag{B.10}$$

where T is the total free precession time ($T = N\tau$ for N precession intervals of length τ) and $\chi(T)$ is given by

$$\chi(T) = \frac{1}{\pi}\int_0^\infty S(\omega)\frac{F_N(\omega T)}{\omega^2}d\omega \tag{B.11}$$

where $S(\omega)$ is the magnetic noise spectrum and $F_N(\omega T)$ is the N-pulse filter function given by

$$F_N(\omega T) = 8\sin^4\left(\frac{\omega T}{4N}\right)\frac{\sin^2\left(\frac{\omega T}{2}\right)}{\cos^2\left(\frac{\omega T}{2N}\right)}. \tag{B.12}$$

When $F_N(\omega T)$ is sharply peaked, Eq. (B.11) can be approximated as

$$\chi(T) \approx \frac{TS(\omega)}{\pi}. \tag{B.13}$$

We apply this procedure to the decoherence curves of select NV centers in before and after a 650 °C vacuum anneal to investigate the change in the noise spectrum due to annealing, and find that it is not significantly affected by the annealing procedure. These results are presented in Fig. B.3. NV centers in this sample displayed reduced DEER signals after annealing, and so the absence of change in the noise spectrum indicates that the surface spins do not contribute significantly to the surface noise bath in this sample at the frequencies probed.

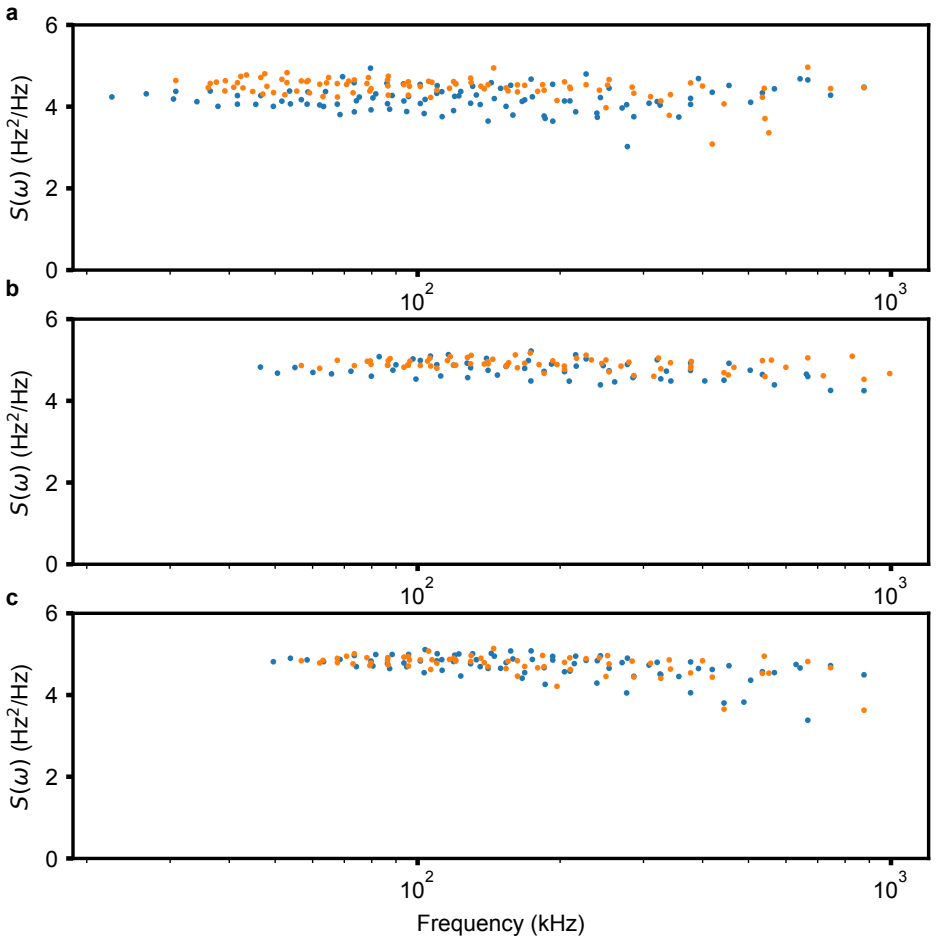


Figure B.3: Spectral decomposition through annealing. Spectral decomposition for sample of NV centers in before (blue) and after (orange) 650 °C vacuum anneal. Depths of NV centers are **a** 10.25 nm, **b** 9.72 nm, **c** 10.42 nm

B4.5 Atomistic model for surface spins on (100) diamond surface

X-ray spectroscopy data indicate that carbon sp^3 dangling bonds are a likely source of surface spins (Section B4.1). This is a surprising result as surface sp^3 dangling bonds (DBs) appear to be chemi-

cally stable in ambient conditions, but are expected to be highly reactive in atmosphere. In order to set up a plausible model, we assume that some structural disorder is left on the surface after oxygenation, so the surface is not atomically smooth.

We propose a model to explain the existence and chemical stability of surface spins on the (100) diamond surface as sp^3 DBs at a (111) step edge. A (111) surface is essential to create a single dangling bond as, in contrast to a (100) surface, each carbon atom under a (111) surface possesses three bonds downward and one bond upward, from which it is possible to form a single sp^3 dangling bond defect with minimal change of the diamond lattice. In this model, all C(*) atoms are saturated with OH and the total spin of these systems is S=1/2. We also propose that the (111) facet, which is naturally generated at a step edge of (100) crystalline diamond surfaces, can sterically protect these spinful defects.

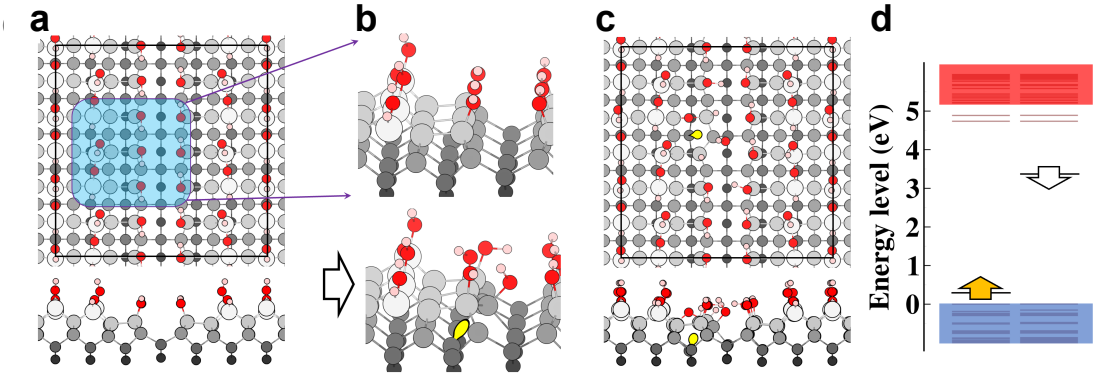


Figure B.4: Surface spin model. **a**, The trench structure of (100)-6×6 diamond surface. Surface termination is O/H/OH type, as in [184], and step carbon atoms are saturated by OH. The red and pink balls are hydrogen and oxygen atoms, respectively. The grey balls are carbon atoms, the darker color and smaller size indicate deeper position away from the surface. For the sake of clarity, only the first five layers are presented in the structure plots. **b**, Illustration of the formation of a surface spin at the step edge. The yellow lobe represents the surface spin. **c**, A plausible structure model of a surface spin on the trench of the diamond (100) surface. **d**, The energy level plot of the modeled surface spin. The valence and conduction bands are depicted as blue and red regions, respectively. The orange and white arrows represent spin up and spin down channels, respectively. The spin-polarization energy is high for the dangling bond. We note that the single particle Kohn-Sham levels do not directly refer to the ionization energies of the dangling bond. The surface states are located at 0.3 eV below the conduction band minimum. The valence band maximum positions are aligned to zero.

It has been previously reported that O/H/OH mixed termination of (100) diamond minimally introduces defect levels to the bandgap [184], so we use this surface as our starting model. In order to mimic the local disorder at the surface, we create two step edges forming a trench configuration [60], as shown in Fig. B.4(a). A previous study [386] indicated that such a trench structure can be energetically more favorable than the flat structure on the diamond (100) surface. We carried out first principles calculations on this surface model using the plane-wave based Vienna *Ab Initio* Simulation Package [202]. The projector augmented-wave [41] method is used to represent the electron-ionic core interactions. For the exchange-correlation functionals, we used spin-polarized gradient-corrected Perdew-Burke-Ernzerhof (PBE) functional [274] for structure optimization and Heyd-Scuseria-Ernzerhof (HSE06) [150] hybrid functional for electronic structure calculations that would be capable of providing correct defect levels and defect-related electronic transition within $\approx$ 0.1 eV to experiments [118]. A cutoff energy of 370 eV resulted in an equilibrium lattice parameter of diamond of 3.570 Å, which agrees with the experimental value of 3.567 Å. We use a 6×6 supercell to simulate the trench models. The thickness of the vacuum layer is more than 10 Å. There are eleven carbon layers, the surface seven layers are allowed to be fully relaxed until the forces are below 0.01 eV/Å and the bottom four layers are fixed at their bulk positions. The k-point sampling is Γ only, which is sufficient to map the Brillouin-zone.

In the starting model, a single carbon sp^3 dangling bond is introduced as the hypothetical source of the S=1/2 spin defect. The carbon atoms at the atomic step are more reactive because they do not possess ideal bonding configuration, and thus may be attacked by a radical such as –OH groups present in the oxygenation process. We simulated this situation as shown in Fig. B.4(b). First principles calculations showed that the surface carbon atom attacked by the –OH group spontaneously breaks a bond with a neighbor carbon atom beneath the surface, creating an sp^3 DB with S=1/2 spin as respectively shown in Fig. B.4(c) and (d). This near-surface carbon sp^3 DB resides in the fourth atomic layer referred to the topmost carbon atom layer which is topographically protected

by the direct interaction with species from the gas phase. As expected, the sp^3 DBs are electrically and optically active; the latter may be achieved by photo-ionization to the negative charge state. The actual photo-ionization energy threshold may depend on the interaction with other defects at the surface or beneath the surface.

B5 Additional surface spin measurements

B5.1 Coherently coupled surface spins

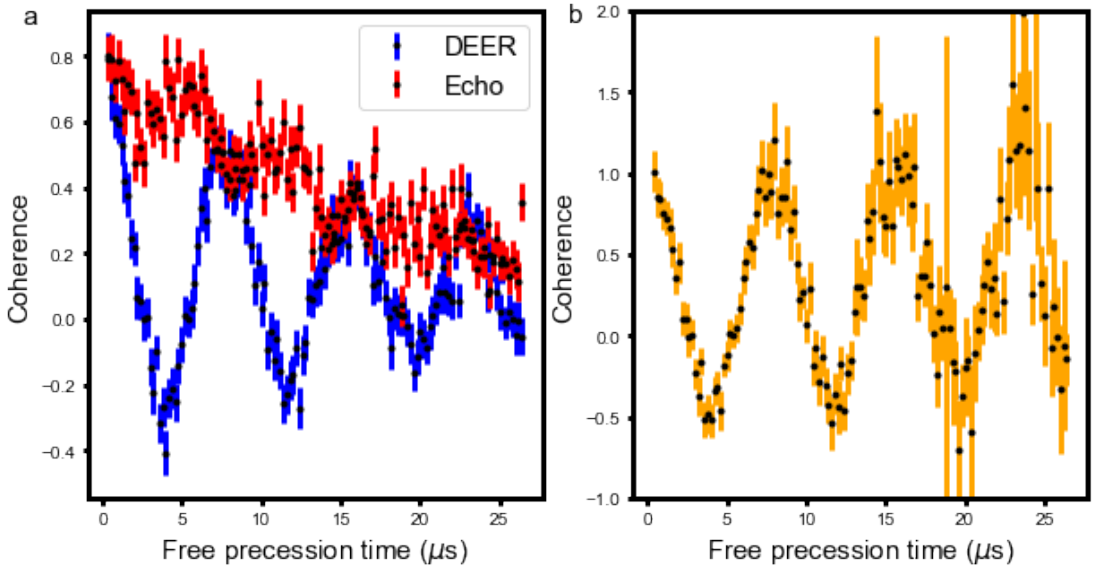


Figure B.5: Coherently coupled surface spin. **a**, Raw DEER (blue) and echo (red) data from an NV center that is coherently coupled to a surface spin. **b**, The raw DEER signal divided by the echo signal.

Over all the samples investigated here, coherently coupled surface spins are rarely observed. One example of this rare occurrence is shown in Fig. B.5. Based on the coupling strength, it is 6-7 nm from the NV center, which is consistent with the 7 nm depth as measured by proton NMR. However, we also note that it cannot be conclusively shown with our methods that this defect exists at the surface.

This particular spin survived multiple acid cleanings and surface treatments and so may be deeper than the bath spins probed in the remainder of this work. There may exist several types of defects with an observable DEER signal, some of which are found below the diamond surface [134].

B5.2 Surface spin linewidth

Another important parameter of the surface spin bath is the linewidth of the DEER transition, as this provides information about the disorder on the surface experienced by the surface spins. We measure the linewidth by performing a DEER pulse sequence while sweeping the frequency of the surface spin π pulse. A typical dataset, with a Lorentzian fit, is shown in Fig. B.6. We note that this value of 35 MHz is slightly larger than the $\approx$ 20 MHz linewidths reported in the literature [44,233,134,347], which may be a result of power broadening. For the following discussions this discrepancy will not be relevant, however.

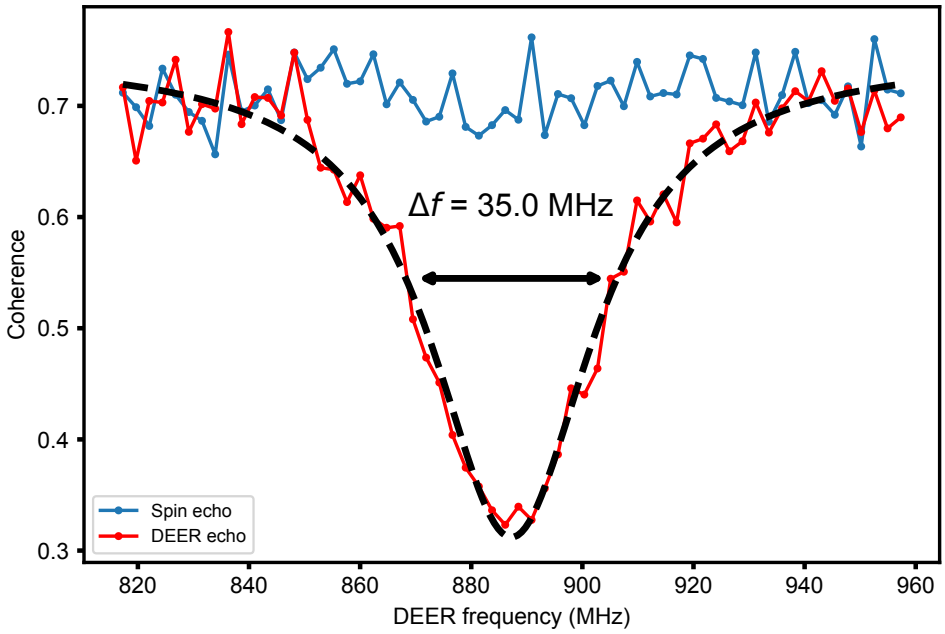


Figure B.6: DEER frequency sweep

B5.3 Surface spin $T_{2,\mathrm{Rabi}}$

As an additional measurement to bound the disorder of the surface spins, we sweep the duration of the microwave pulse performed on the surface spins during the DEER sequence. We fit the resulting curve to a cosine with an exponentially decaying envelope, and find a characteristic decay time of 200 ± 30 ns (see Fig. B.7).

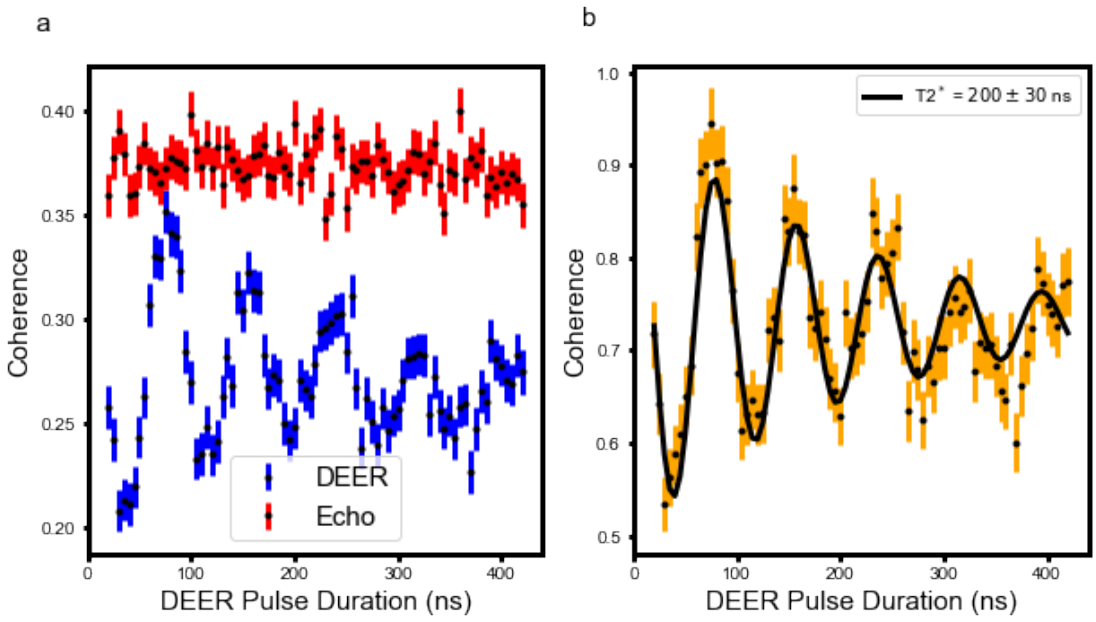


Figure B.7: DEER Rabi measurement. **a** We perform a microwave pulse of varying length on the surface spins during the DEER sequence and **b** fit the normalized signal to a decaying exponential envelope to extract a coherence decay time.

B5.4 Measured surface spin T_1 relaxation times

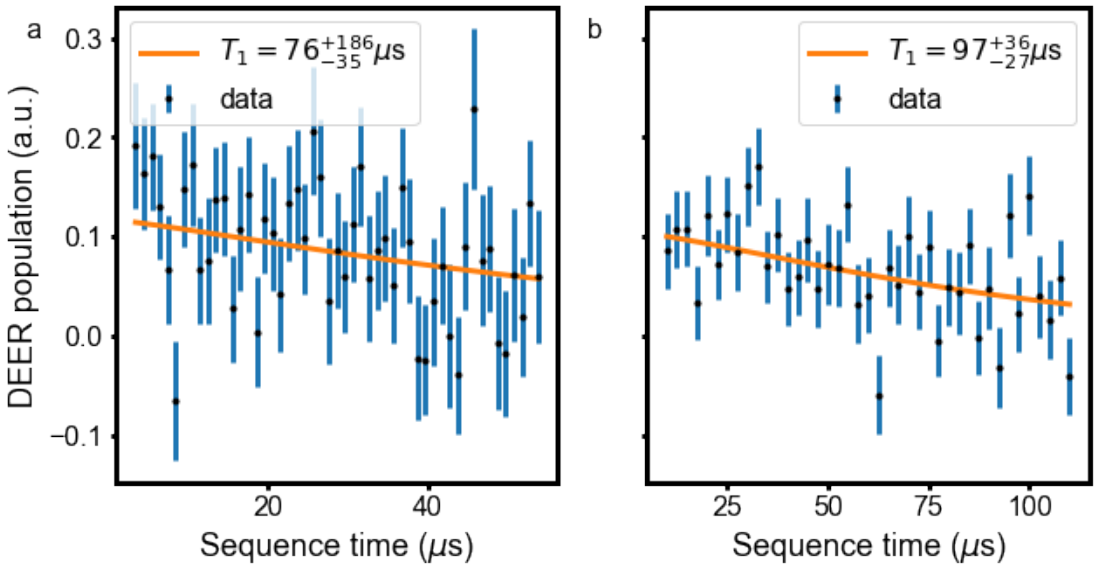


Figure B.8: Measured T1 of surface spins using correlation sequence. Relaxation time T_1 for surface spins measured by two different NV centers **a** and **b**, using the correlation sequence described in [347].

The surface spin T_1 relaxation times were measured on several NV centers in using a correlation spin sequence [347,210]. Results can be seen in Fig. B.8. Additionally, for , a sampling of surface spin T_1 times were measured by sweeping the time of the DEER microwave pulse within the echo sequence [233]. Extracted T_1 times were consistent with those measured in correlation spectroscopy (see Fig. B.9). These T_1 times were significantly longer than the length of the DEER sequences performed in the main text.

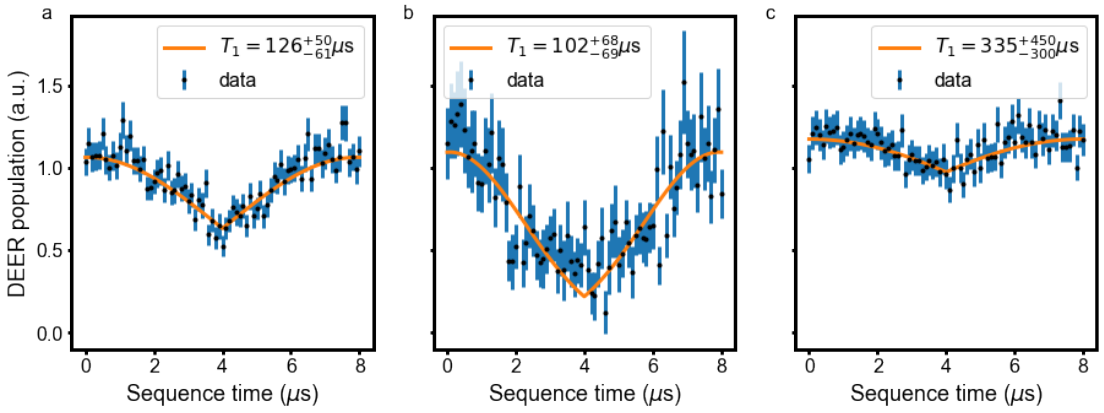


Figure B.9: Measured T1 of surface spins by bath correlation measurement. Relaxation time T_1 for surface spins measured by three different NV centers, depicted in **a**, **b**, and **c**, using the sequence described in [233]. **a** and **b** are from and **c** is from .

B6 Derivation of DEER signal for static and hopping surface spins

B6.1 System description

We consider a single NV center coupled to a 2D spin bath. We assume the 2D spin bath to be located at $z = 0$, in the $\hat{x} - \hat{y}$ plane, and the NV center to be located at $z = -d_{\mathrm{NV}}$. Consistent with a global magnetic field applied along the NV center quantization axis and for [100] diamond, we assume that all spins are oriented in a direction 54.7° from the $\hat{z}$-axis. The Hamiltonian of the system with NV center spin S with resonant frequency ω_s, and surface spins I_i with Larmor frequencies ω_i can be written as

$$\mathbf{H} = \omega_S \mathbf{S}^z + \sum_i \omega_i \mathbf{I}_i^z + \sum_i J_i \mathbf{S}^z \mathbf{I}_i^z \tag{B.14}$$

where we have assumed that the interaction between the NV center and surface spins takes an Ising form, since they have different resonance frequencies. The interaction strengths J_i are assumed to be dipolar interactions, and we will explicitly calculate their distributions below.

In the above equation, we have also neglected the interactions between the surface spins, which may be justified for two reasons: first, local disorder fields experienced by the surface spins that cause their resonance frequencies to vary (see Section B5.2, as well as [134]), and this will suppress spin-exchange processes; second, the Ising interaction component will not change the I^z component of each spin, and thus it will not affect the NV center spin signal. Note that we have also assumed a quasi-static bath for now and neglect the finite T_1 relaxation time of the spins. Spin-exchange processes between bath spins could be approximately treated in a similar fashion as a finite T_1 time. For completeness, we present some results from simulations that include interactions in section B7.3.

We now calculate the DEER signal expected for an NV center in the case of static surface spins and of surface spins undergoing configurational averaging.

B6.2 Derivation of DEER coupling for dense static spins

The combined NV center-surface spin Hamiltonian is given by Eq. (B.14). In the rotating frame [329], this simplifies to

$$\mathbf{H} = \gamma_e \mathbf{S}^z B_z^{\mathrm{DEER}} \tag{B.15}$$

where γ_e is the electron gyromagnetic ratio and B_z^{DEER} is the total z component of the magnetic field due to the surface spins at the location of the NV center. We now calculate the signal measured by an NV center during a DEER spin echo pulse sequence, in the case that other decoherence mechanisms affecting the NV center are negligible.

After spin initialization, the NV center spin starts out in the spin state $|0\rangle$ ($m_s = 0$), and the surface spins have an initial state vector $|I\rangle = |I_1, I_2 ... I_n\rangle$, where $\mathbf{I}_i^z |I_i\rangle = \pm\hbar/2 |I_i\rangle$. The initial spin states are random for each repetition of the experiment. Then we apply a $\pi/2$ pulse to the NV

center to put the system in the superposition state

$$|\psi_{NV}(t=0)\rangle = \frac{1}{\sqrt{2}}\left(|0\rangle + |1\rangle\right) \otimes |I\rangle \tag{B.16}$$

The NV center spin then evolves for a time $\tau/2$ under the influence of the magnetic field produced by the surface spins. This field is given by the summation of all dipole fields from the n spins:

$$B_z^{\mathrm{DEER}}(t) = \frac{\mu_0}{4\pi}\sum_i \frac{3u_z^i(\vec{m^i}\cdot\vec{u^i}) - m_z^i}{|r^i|^3} \tag{B.17}$$

where $\vec{u}$ is a unit vector from the NV center to spin i, r^i is the distance to the ith spin, and $m^i = -\frac{\gamma_e\hbar}{2}\vec{\sigma^i}$, and σ^i is the Pauli matrix for spin i.

After a time $\tau/2$, the NV center spin will be in a state

$$|\psi_{NV}(t=\frac{\tau}{2})\rangle = \frac{1}{\sqrt{2}}\left(|0\rangle \otimes |I\rangle\right) + \frac{1}{\sqrt{2}}\left(|1\rangle \otimes e^{-i\sum_i \varphi_1^i}|I\rangle\right) \tag{B.18}$$

where

$$\varphi_1^i = -\gamma_e^2\hbar\frac{\mu_0}{8\pi\hbar}\frac{1}{|r^i|^3}(3u_z^iu_z^i - 1)I_i\frac{\tau}{2} \tag{B.19}$$

and I_i is either +1 or -1 for each spin, but it is initialized randomly for each experiment.

Next we apply a resonant π pulse to the NV center and surface spins simultaneously, which has the effect of swapping $|0\rangle \leftrightarrow |1\rangle$ and also swapping $|I_i\rangle \rightarrow |-I_i\rangle$. The state is now

$$|\psi_{NV}(t=\frac{\tau}{2})\rangle = \frac{1}{\sqrt{2}}\left(|1\rangle \otimes |-I\rangle\right) + \frac{1}{\sqrt{2}}\left(|0\rangle \otimes e^{-i\sum_i \varphi_1^i}|-I\rangle\right) \tag{B.20}$$

After another free evolution period of $\tau/2$, we have

$$|\psi_{NV}(t=\tau)\rangle = \frac{1}{\sqrt{2}}\left(|1\rangle \otimes e^{-i\sum_i \varphi_2^i}|-I\rangle\right) + \frac{1}{\sqrt{2}}\left(|0\rangle \otimes e^{-i\sum_i \varphi_1^i}|-I\rangle\right) \tag{B.21}$$

where

$$\varphi_2^i = +\gamma_e^2\hbar\frac{\mu_0}{8\pi\hbar}\frac{1}{|r^i|^3}(3u_z^i u_z^i - 1)I_i\frac{\tau}{2} = -\varphi_1^i \tag{B.22}$$

The final $\pi/2$ pulse on the NV center leads to

$$|\psi_{NV}(t=\tau)\rangle = \frac{1}{2}\left(|1\rangle - |0\rangle\right) \otimes e^{-i\sum_i \varphi_2^i}|-I\rangle + \frac{1}{2}\left(|0\rangle + |1\rangle\right) \otimes e^{-i\sum_i \varphi_1^i}|-I\rangle \tag{B.23}$$

Measuring in the $|0\rangle$ basis then gives

$$\left|\langle 0 \mid \psi_{NV}\rangle\right|^2 = \left|-1/2e^{-i\sum_i \varphi_2^i} + 1/2e^{-i\sum_i \varphi_1^i}\right|^2 \tag{B.24}$$

$$= 1/2\left(1 + \cos\sum_i \Delta\varphi^i\right) \tag{B.25}$$

where

$$\Delta\varphi^i = \gamma_e^2\hbar\frac{\mu_0}{8\pi\hbar}\frac{1}{|r^i|^3}(3u_z^i u_z^i - 1)I_i\tau \tag{B.26}$$

If there is only one nearby dark spin coupled to the NV center, we will see full contrast oscillations at the coupling frequency of the surface spin.

The more typical situation is one in which the NV center senses many dark spins. At each experimental repetition, the NV center senses a different total magnetic field depending on the random spin states of the surface spins. The total signal is the average of this Bernoulli random process for many trials. For a large number of trials, this can be approximated by a Gaussian process, e.g.

$\langle \cos \varphi \rangle = e^{-\langle \varphi^2 \rangle / 2}$. This will only be true if the NV center is coupled to sufficiently many spins with comparable coupling strengths, and in the limit of a dilute spin bath the Gaussian approximation will fail because of strong trial-to-trial fluctuations in the strength of dipolar coupling between the NV center and the dark spins, which lead to a distinctly non-Gaussian distribution of acquired phases[194,89].

Computing the average of squares we find

$$\langle \Delta\varphi^2 \rangle = \left(\frac{\tau \gamma_e^2 \mu_0 \hbar}{8\pi} \right)^2 \sum_i \frac{1}{|r^i|^6} (3 u_z^i u_z^i - 1)^2 \tag{B.27}$$

If the surface spins are dense enough that the average spin-spin spacing is much smaller than the NV center depth, d_{NV}, the sum can be approximated as an integral over a continuous density of surface spins, σ. We can write $r = \sqrt{a^2 + d_{\mathrm{NV}}^2}$ and $u_z = \frac{1}{r}(d_{\mathrm{NV}} \cos\theta + a \sin\theta) \cos\alpha$ and calculate

$$\sum_i \frac{1}{|r^i|^6} (3 u_z^i u_z^i - 1)^2 \approx \int_0^{2\pi} \int_0^{\infty} \frac{da d\alpha a}{(d_{\mathrm{NV}}^2 + a^2)^3} \left(\frac{3}{a^2 + d_{\mathrm{NV}}^2} (d_{\mathrm{NV}} \cos\theta + a \sin\theta)^2 \cos^2\alpha - 1 \right)^2 \tag{B.28}$$

$$= \frac{3\pi}{8 d_{\mathrm{NV}}^4} \tag{B.29}$$

for $\theta = 54.7°$, the angle of NV centers in (100) diamond with respect to the surface. Converting the population to the coherence, we finally obtain

$$\langle S(\tau) \rangle = \exp\left(- \left(\frac{\mu_0}{4\pi} \right)^2 \frac{3\pi \gamma_e^4 \hbar^2 \sigma}{64 d_{\mathrm{NV}}^4} \tau^2 \right) \tag{B.30}$$

B6.3 Calculation of NV coherence decay for configurationally averaged surface spins

Based on experimental observations of a small stretched exponent and the absence of strongly coupled spins, we calculate the case where surface spins can change positions between measurements, effectively allowing a configurational averaging when evaluating the coherence decay.

Since configurational averaging can result from random spin hopping, we can make use of the methods in Ref. [103,2] to calculate the coherence decay. The intuition of the calculation is that, since all interactions take the Ising form, we can simply add up the phases. It turns out that the resulting expression, after being written in an exponential form, can be factorized into a product of cosines corresponding to the individual phase accumulations, which can then be integrated over different spatial configurations. We will not reproduce the full details here, but simply note that the same argument should also apply to a spin located at some distance external to the spin bath, and one simply needs to replace the interaction strength by the corresponding one for the external spin.

Thus, we need to calculate the interaction strength between the NV center located at $(0, 0, -d_{\mathrm{NV}})$ and a spin located at position $(r\cos\alpha, r\sin\alpha, 0)$. The quantization axis is assumed to be pointing in $\hat{n} = (\sin\theta, 0, \cos\theta)$, where $\theta = 54.7°$, such that $\cos^2\theta = 1/3$. Taking the inner product, we have that the interaction strength is

$$\frac{\mu_0}{4\pi}\frac{\gamma_e^2\hbar t}{2(r^2+d_{\mathrm{NV}}^2)^{3/2}}\left(\frac{3(r\cos\alpha\sin\theta + d_{\mathrm{NV}}\cos\theta)^2}{r^2+d_{\mathrm{NV}}^2} - 1\right) = \frac{\mu_0}{4\pi}\frac{\gamma_e^2\hbar t(2r^2\cos^2\alpha - r^2 - 2\sqrt{2}rd_{\mathrm{NV}}\cos\alpha)}{2(r^2+d_{\mathrm{NV}}^2)^{5/2}} \tag{B.31}$$

Transcribing the expressions found in Ref. [103] with these interactions, we find that the coherence

decay should satisfy

$$\begin{aligned}\langle S(t)\rangle_c &= \exp\left\{\sigma\int_0^{2\pi}d\alpha\int_0^{\infty}rdr\times[\cos\frac{\mu_0\gamma_e^2\hbar\tau(2r^2\cos^2\alpha-r^2-2\sqrt{2}rd_{\mathrm{NV}}\cos\alpha)}{8\pi(r^2+d_{\mathrm{NV}}^2)^{5/2}}-1]\right\}\\ &= \exp\left\{\sigma d^2\int_0^{2\pi}d\alpha\int_0^{\infty}xdx\times[\cos\frac{\mu_0\gamma_e^2\hbar\tau}{8\pi d_{\mathrm{NV}}^3}\frac{(2x^2\cos^2\alpha-x^2-2\sqrt{2}x\cos\alpha)}{(x^2+1)^{5/2}}-1]\right\},\end{aligned} \tag{B.32}$$

where we have written $x = r/d_{\mathrm{NV}}$.

We would like to note that here $\mu_0\gamma_e^2\hbar\tau/8\pi d_{\mathrm{NV}}^3$ always appears together in the integral, which means that the shape of the curve should be the same regardless of the depth d_{NV}. Changing d only leads to a rescaling of the time at which changes in shape happen. However, note that since there is a d_{NV}^2 in front, the timescale involved in the stretched exponential decay can change.

While the above expression does not appear to be easily integrated, we can take appropriate limits to understand its behavior. First, let us consider the limit where τ is small, such that $\mu_0\gamma_e^2\hbar\tau \ll 8\pi d_{\mathrm{NV}}^3$. In this case, intuitively, the spins far away will not have the time to interact yet, so we are dominated by contributions from small r. In this case, the argument of the cosine in Eq. (B.32) is small, such that we can perform a Taylor expansion to obtain

$$\begin{aligned}\langle S(t)\rangle_c &= \exp\left\{\sigma d_{\mathrm{NV}}^2\int_0^{2\pi}d\alpha\int_0^{\infty}xdx\times[-\frac{1}{2}\left(\frac{\mu_0\gamma_e^2\hbar\tau}{8\pi d_{\mathrm{NV}}^3}\frac{(2x^2\cos^2\alpha-x^2-2\sqrt{2}x\cos\alpha)}{(x^2+1)^{5/2}}\right)^2]\right\}\\ &= \exp\left[-\frac{3\pi\sigma d_{\mathrm{NV}}^2}{16}\left(\frac{\mu_0\gamma_e^2\hbar\tau}{8\pi d_{\mathrm{NV}}^3}\right)^2\right].\end{aligned} \tag{B.33}$$

Thus, at short times, we recover the Gaussian decay in Eq. B.30.

Next, let us consider the limit where τ is large, such that $\mu_0\gamma_e^2\hbar\tau \gg 8\pi d_{\mathrm{NV}}^3$. Intuitively, the time is long enough such that the external spin sees the influence of all spins far away, and the situation will be similar to a 2D spin bath. In this case, we will have contributions from a large range of values

of x. Due to the x factor outside the parenthesis however, coming from the volume element in the Jacobian, the main contribution to the integral will be coming from values of x that are large, and thus we may approximate the fraction as

$$\frac{(2x^2\cos^2\alpha - x^2 - 2\sqrt{2}x\cos\alpha)}{(x^2+1)^{5/2}} \approx \frac{(2x^2\cos^2\alpha - x^2)}{x^5} = \frac{2\cos^2\alpha - 1}{x^3}. \tag{B.34}$$

Explicitly performing the integral in this limit gives

$$\langle S(t)\rangle_c = \exp\left(-\frac{9\sqrt{\pi}\Gamma(\frac{11}{6})\sigma}{5}\left(\frac{\mu_0\gamma_e^2\hbar\tau}{8\pi}\right)^{2/3}\right), \tag{B.35}$$

which reproduces the $\tau^{2/3}$ scaling in this limit. Note also that in this limit, d_{NV} drops out of the problem. The intuition is again that the spin sees everything out to infinity, and the only spatial scale left in the problem is an average distance between the surface spins.

B6.4 Mean nearest neighbor separation

In the main text, an average spin-spin separation, ℓ_{SS}, is calculated from a fitted density of surface spins, σ. From dimensional analysis, these quantities are related by

$$\ell_{SS} \propto \frac{1}{\sqrt{\sigma}} \tag{B.36}$$

, however the constant of proportionality is ambiguous. In the main text, we specifically are referring to the mean value of the distribution of nearest neighbor distances for a randomly distributed layer of spins with density σ. In this case the constant of proportionality is $1/2$, and for completeness we derive this result below.

We can obtain this by considering the probability of finding a neighboring spin a distance r away.

The distribution function, $w(r)dr$ = P(no neighbor < r)×P(neighbor between r and $r + dr$):

$$w(r)dr = \left(1 - \int_0^r w(r')dr'\right) \times (2\pi r dr\sigma) \tag{B.37}$$

Taking the derivative gives

$$\frac{dw(r)}{dr} = 2\pi\sigma\left(1 - \int_0^r w(r')dr'\right) - w(r) \times (2\pi r\sigma) \tag{B.38}$$

Substituting into the first equation we can eliminate the integral

$$\frac{dw(r)}{dr} = \frac{w(r)}{r} - w(r) \times (2\pi r\sigma) \tag{B.39}$$

This differential equation has the solution

$$w(r) = Kr\exp\left\{-\pi r^2\sigma\right\} \tag{B.40}$$

Where K is an integration constant, which from normalization must be $K = 2\pi\sigma$. So the nearest neighbor probability distribution function is

$$w(r) = 2\pi\sigma r\exp\left\{-\pi r^2\sigma\right\} \tag{B.41}$$

We then calculate the first moment of Eq. (B.41):

$$\langle \ell_{SS}\rangle = \int_0^\infty rw(r)dr \tag{B.42}$$

$$= 2\pi\sigma\frac{1}{4\pi\sigma^{3/2}} \tag{B.43}$$

$$= \frac{1}{2\sqrt{\sigma}} \tag{B.44}$$

Eq. (B.44) is the expression used in the calculations of the Main Text.

B7 Effects of finite surface spin T_1 time

Here we calculate the effects of finite surface spin T_1 time on the DEER exponent n in order to investigate whether the observed coherence decay behavior can be accounted for by surface spin relaxation.

In the presence of Gaussian-distributed noise amplitudes (as expected from a continuous density of surface spins), the quasistatic limit $T_1 \gg T_{2,\mathrm{DEER}}$ gives a DEER decay exponent $n = 2$, and the Markovian limit $T_1 \ll T_{2,\mathrm{DEER}}$ gives a DEER decay exponent $n = 1$. Quantitatively, the case of finite-T_1 time is calculated in [233] and is given by

$$\langle S(\tau)\rangle = \exp\left[-(\Gamma_{\mathrm{DEER}}\tau)^2 f(\tau, T_1)\right], \tag{B.45}$$

where

$$f(\tau, T_1) = \frac{2T_1^2}{\tau^2}\left[\frac{\tau}{T_1} - 1 + e^{-\tau/T_1}\right], \tag{B.46}$$

is a dimensionless quantity that describes the effects of finite surface spin T_1 relaxation time. Note that in the limit of $\tau \ll T_1$ one finds $f(\tau, T_1) = 1$.

In Fig. B.10 we fit Eq. B.45 to $\exp(-(\tau/T_{2,\mathrm{DEER}})^n)$. As expected, for shallow NV centers $T_{2,\mathrm{DEER}} \ll T_1$ and so we recover the quasistatic limit $n = 2$, whereas for deeper NV centers $T_{2,\mathrm{DEER}} \gg T_1$ and we recover the Markovian limit $n = 1$. The trend of n vs depth in Fig. B.10(b) is opposite from the trend observed in Fig. 2c of the Main Text, indicating that spin relaxation cannot account for our data.

B7.1 Exponents n under the assumption of a noise spectral density

Here we show that the exponents n from DEER exponential decays of the form $C(\tau) = \exp[-(\tau/T_2)^n]$ will have $n \geq 1$ if the noise spectrum is flat ($n = 1$) or monotonically decreasing as a function of frequency ($n > 1$), assuming the noise spectral density formulation holds. The assumption of a monotonically decreasing noise spectrum is physically reasonable and consistent with experimentally observed noise spectra; accordingly, a likely explanation for the observed DEER exponents $n < 1$ is that the noise spectral density formulation does not hold, in particular because the noise amplitudes are not Gaussian-distributed, as is found in the case of discrete hopping spins.

We now show that $n \geq 1$ for a monotonically decreasing noise spectral density. We show this to be true for a general N-pulse qubit filter function $\frac{F_N(\omega T)}{\omega^2}$, defined to be continuous and non-negative across all frequencies, including Ramsey / DEER measurements with filter function $\frac{4\sin^2(\omega T/2)}{\omega^2}$. Note that during a DEER sequence, if the surface spins are perfectly flipped during the NV center π pulse, then the NV center filter function to the surface spins will be identical to that of Ramsey. The FID can then be described by Eq. (B.10). The noise spectrum $S(\omega) \geq 0$, and for physically relevant noise sources is monotonically decreasing, i.e. $\frac{dS(\omega)}{d\omega} \leq 0 \; \forall \omega$, and with $S(\omega)$ and $\frac{dS(\omega)}{d\omega}$ defined over $\omega \in [0, \infty)$. We rewrite Eq. (B.11) as

$$\chi(T) = \frac{1}{\pi} T \left[\int_0^\infty S\left(\frac{x}{T}\right) \frac{F_N(x)}{x^2} dx \right], \tag{B.47}$$

where $x \equiv \omega T$ is a dimensionless integration variable. In order to probe the exponent n associated with $\chi(T) = (T/T_2)^n$, we apply $(T\frac{d}{dT} - 1)$ to $\chi(T)$ in Eq. (B.47); using the product rule we find

$$\left(T\frac{d}{dT} - 1\right)\chi(T) = \frac{1}{\pi} T^2 \left[\int_0^\infty \frac{dS(x/T)}{dT} \frac{F_N(x)}{x^2} dx \right]. \tag{B.48}$$

Using $\omega(T) = x/T$, we can evaluate

$$\frac{dS(\omega(T))}{dT} = \frac{dS(\omega)}{d\omega}\frac{d\omega(T)}{dT} = \frac{dS(\omega)}{d\omega}\left(\frac{-x}{T^2}\right), \tag{B.49}$$

Eq. B.48 simplifies to

$$T\frac{d\chi(T)}{dT} - \chi(T) = \frac{1}{\pi}\int_0^\infty \left(\frac{-dS(\omega)}{d\omega}\right)\Big|_{\omega=x/T} \frac{F_N(x)}{x}dx \tag{B.50}$$

We can rewrite the left-hand-side of Eq. B.50 by using $dT/T = d\ln T$, and since, by assumption, $\chi(T)$ is positive and differentiable at times $T > 0$, we write

$$T\frac{d\chi(T)}{dT} - \chi(T) = \chi(T)\left(\frac{1}{\chi(T)}\frac{d\chi(T)}{d\ln T} - 1\right) = \chi(T)\left(\frac{d\ln\chi(T)}{d\ln T} - 1\right) \tag{B.51}$$

So, Eq. B.50 can be written as

$$\frac{d\ln\chi(T)}{d\ln T} = 1 + \frac{1}{\chi(T)}\frac{1}{\pi}\int_0^\infty \left(\frac{-dS(\omega)}{d\omega}\right)\Big|_{\omega=x/T} \frac{F_N(x)}{x}dx \tag{B.52}$$

As defined, the right-hand-side is necessarily ≥ 1 for all times T because $\chi(T) > 0\ \forall T$, $F_N(x) \geq 0\ \forall x$ and $\frac{dS(\omega)}{d\omega} \leq 0\ \forall\omega$. Accordingly,

$$\frac{d\ln\chi(T)}{d\ln T} \geq 1 \tag{B.53}$$

for all free precession times $T > 0$. And, if in some region of times T the function $\chi(T)$ has a power-law form $(T/T_2)^n$, then

$$n \geq 1 \tag{B.54}$$

Under these mathematical arguments, we cannot observe $n < 1$ for a monotonically decreasing

noise spectral density, because the integral is shown to be ≥ 0 for all times T. A monotonically increasing noise spectral density would give a negative integral in Eq. B.52 and therefore $n < 1$, but this is physically unreasonable and inconsistent with observed noise spectra.

Further, note Eq. B.53 holds for a general $\chi(T)$, and implies that the slope on a plot of $\ln\chi(T)$ versus $\ln(T)$ will be ≥ 1 for a monotonically decreasing noise spectral density. In the Main Text we plot $\ln\chi(T)$ versus $\ln(T)$ and find slopes less than 1, which implies that the noise spectral density formulation does not hold, in particular because the noise amplitudes are not Gaussian-distributed. The configurational averaging of surface spins results in a non-Gaussian distribution of noise amplitudes (i.e., for some shots there are many surface spins nearby and for some shots there are no surface spins nearby), which violates the requirements for the noise spectral density formulation and explains the exponents $n < 1$ that we observe.

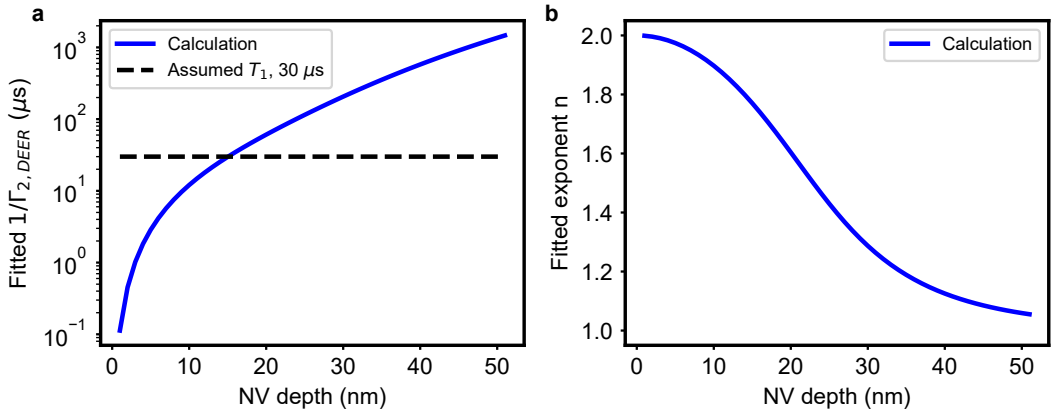


Figure B.10: Depth scaling in the presence of finite surface spin T_1 time. a, Calculated decay timescale $T_{2,\text{DEER}}$ with decay profile calculated using Eq. B.45 and fit to $\exp(-(\tau/T_{2,\text{DEER}})^n)$, assuming a finite surface spin T_1 time of 30 μs (black dashed line) and a density $0.005/\text{nm}^2$. **b**, Fitted exponent n. Once $T_{2,\text{DEER}}$ becomes longer than the surface spin T_1 relaxation time, n decreases from the infinite-T_1 limit of $n = 2$ toward the Markovian limit of $n = 1$. The calculated increase of n for shallower NV centers is opposite of the observed trend vs depth in Fig. 2c of the Main Text, and suggests that the depth trend in Fig. 2c is not explained by the effects of finite relaxation time.

B7.2 Note about filter functions

In the above derivation, it is assumed that the filter function used during a measurement is that of the Ramsey free induction decay (FID) due to the surface spins alone. Experimentally this is not what is measured due to non surface spin contributions to the FID. In the Main Text, we attempt to remedy this by dividing by a spin echo signal. However, depending on the form of the noise spectrum, this filter function may be different from what is desired.

To see this, we write the noise spectrum experienced by the NV center as a sum of two terms:

$$S(\omega) = S(\omega)_{\mathrm{SS}} + S(\omega)_{\mathrm{EE}} \tag{B.55}$$

where $S(\omega)_{\mathrm{SS}}$ is the noise spectrum of the surface spins and $S(\omega)_{\mathrm{EE}}$ is the noise spectrum due to all other noise sources. The spin echo measurement probes the entire noise spectrum $S(\omega)$ with the spin echo filter function. In the spectral noise formalism the signal is given by

$$C(\tau) = \exp \frac{-1}{\pi} \int_0^\infty S(\omega) F^{SE}(\omega\tau) \frac{d\omega}{\omega^2} \tag{B.56}$$

where $F^{SE}(\omega\tau)$ is the spin echo filter function, given by

$$F^{SE}(\omega\tau) = 8 \sin^4 \frac{\omega\tau}{4} . \tag{B.57}$$

The DEER measurement, in contrast, probes $S(\omega)_{\mathrm{SS}}$ with the spin echo filter function, but $S(\omega)_{\mathrm{EE}}$ is probed with the Ramsey filter function, $F^R(\omega)$, given by

$$F^R(\omega\tau) = 2 \sin^2 \frac{\omega\tau}{2} . \tag{B.58}$$

The DEER measurement signal is then given by

$$D(\tau) = \exp \frac{-1}{\pi} \int_0^\infty \left(S(\omega)_{\mathrm{SS}} F^R(\omega\tau) + S(\omega)_{\mathrm{EE}} SF^{SE}(\omega\tau) \right) \frac{d\omega}{\omega^2} \,. \tag{B.59}$$

When we divide these two signals, what we actually measure is not the FID of the surface spins alone, but rather the quantity

$$S(\tau) = \exp \frac{-1}{\pi} \int_0^\infty S(\omega)_{\mathrm{SS}} \left(F^R(\omega\tau) - F^{SE}(\omega\tau) \right) \frac{d\omega}{\omega^2} \,. \tag{B.60}$$

If the surface spins have a long relaxation time ($T_1^{DEER} > T_2^{NV}$), the second term is negligible due to the low weight of the filter function near $\omega = 0$. For fast relaxation times, the stretching factor of the quantity $S(\tau)$ does not go to $2/3$, but rather to 0, and this occurs for $\tau > T_1^{DEER}$. This can be intuitively understood by the following argument: once the free precession interval exceeds T_1^{DEER}, there is no difference between the measurement with and without a π pulse on the surface spins and so the two measurements become nominally identical. Our measurements of surface spin relaxation times (see Section B5.4) indicate that we are not in this regime, but for systems with much shorter relaxation times this additional transition should be observable.

B7.3 Effects of interactions

Spin flips among surface spins can arise from environmental interactions and interactions between the surface spins (e.g. dipolar flip-flops). In order to determine whether flip-flops among static surface spins could reproduce the observed experimental results, we performed Monte Carlo simulations for $\sim$ 100 random fixed spin configurations. Interactions between the spins were assumed to be incoherent due to the large mismatch between the measured disorder of surface spin systems ($1/(2\pi T_2^*) \approx 35$ MHz, see Section B5.2) and the average nearest neighbor dipolar couplings at the inferred spin densities (≈ 100 kHz). In this regime, the probability of a spin exchange between spin

i and j is given by [142]

$$p_{i,j} = \frac{\omega_{i,j}^2}{\gamma}\delta t \tag{B.61}$$

where $\omega_{i,j}$ is the dipolar coupling between spins i and j and γ is the disorder. δt is the time step of the simulation, chosen such that all $p_{i,j} < 1$. Additionally, spins are allowed to relax without spin exchange through spin-lattice relaxation at a rate $1/(2T_1)$. For a simulation, spins were given random coordinates, the all-to-all couplings were calculated, and the spins randomly initialized. At each time step, spins were allowed to flip or flip-flop based on draws from a Bernoulli distribution, and the phases for the entire time evolution were summed. Some results for simulation parameters $d_{\mathrm{NV}} = 5$ nm, $\sigma_{2D} = .005$ nm^{-2}, $T_1 = 50\,\mu$s, and $\gamma = 100$ kHz are shown in Fig. B.11. For these parameters, $\sim$ 20% of configurations lead to the observation of coherent oscillations in the DEER signal (whenever the nearest spin coupling is greater than the incoherent decay rate). No simulations with experimentally relevant parameters have resulted in stretching factor $n < 1$.

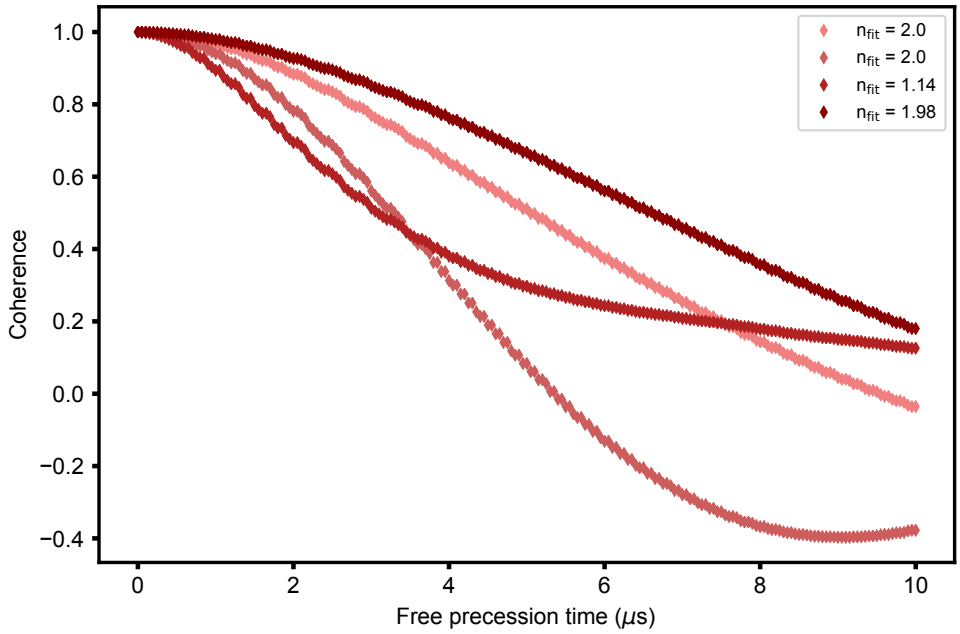
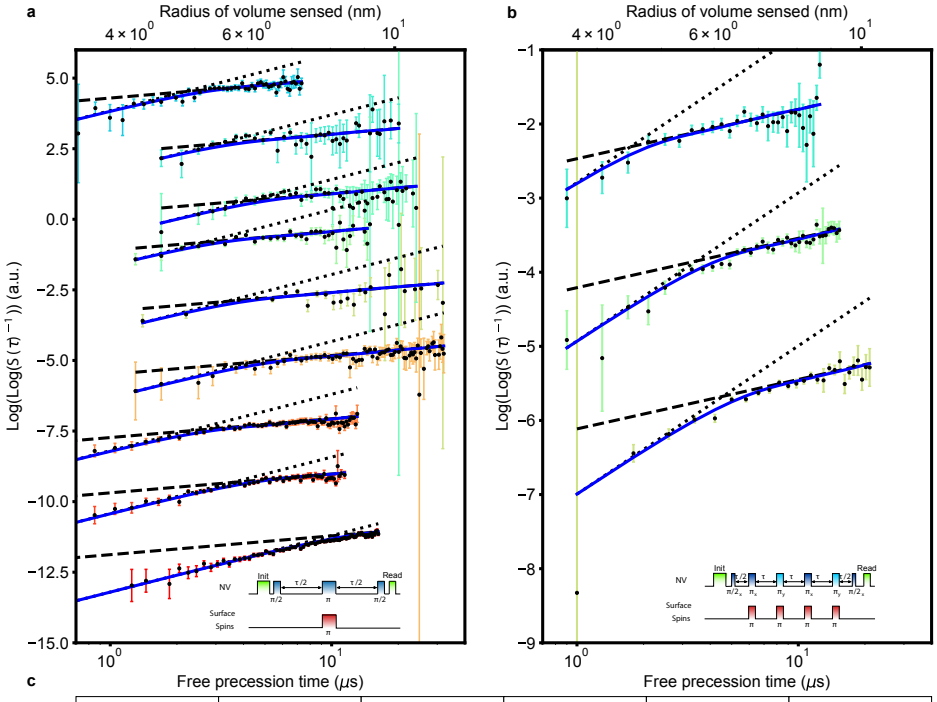


Figure B.11: Simulations with incoherent interactions. Example DEER curves for simulations allowing both flip-flops and spin lattice relaxation between surface spins. Each color represents a different randomly sampled surface spin configuration. Fitting these curves with a stretched exponential produces values of $1 < n < 2$. Some curves additionally show coherent oscillations if the coupling rate to the nearest spin exceeds the rate of incoherent decay.

B8 Exponent transition for additional NV centers

In Fig. B.12, we present additional finely sampled datasets from NV centers of various depths as in Fig. 3a. Again, we plot $\log S(\tau)^{-1}$ on a log-log scale so that the exponent, n, is given by the slope of the line. In addition to the DEER Echo type measurements presented in the Main Text, for some NV centers we performed a dynamical decoupling sequence (XY-4) on the NV center while applying multiple π pulses to the surface spins, which in principle permits a longer interrogation of the surface spin FID before the NV center decoheres. The interpretation of this type of measurement is complicated by the short dephasing time of the surface spins and the longer total rotation time

required for multiple π pulses. The close agreement with $n = 2/3$ at long times is striking nevertheless.



c

	sample	$\text{depth}_{\text{NMR}}$ (nm)	$\text{depth}_{\text{DEEREcho}}$ (nm)	$\text{density}_{\text{DEEREcho}}$ (nm^{-2})	$\text{depth}_{\text{DEERXY 4}}$ (nm)	$\text{density}_{\text{DEERXY 4}}$ (nm^{-2})
1	9	$3.6^{+0.3}_{-0.3}$	$4.7^{+0.3}_{-0.3}$	$0.005^{+0.0009}_{-0.0006}$	-	-
2	3	$3.6^{+0.1}_{-0.1}$	$5.1^{+0.5}_{-0.8}$	$0.001^{+0.0002}_{-0.0001}$	$4.3^{+0.6}_{-1.4}$	$0.001^{+0.0002}_{-0.0001}$
3	3	$4.0^{+0.2}_{-0.2}$	$5.8^{+11.7}_{-0.8}$	$0.000^{+0.0083}_{-0.0001}$	-	-
4	3	$4.2^{+0.2}_{-0.2}$	$4.9^{+0.4}_{-0.3}$	$0.002^{+0.0003}_{-0.0002}$	$5.5^{+0.5}_{-0.6}$	$0.002^{+0.0002}_{-0.0002}$
5	3	$4.4^{+0.2}_{-0.2}$	$5.4^{+7.5}_{-0.6}$	$0.001^{+0.0211}_{-0.0002}$	$6.0^{+0.4}_{-0.6}$	$0.002^{+0.0004}_{-0.0002}$
6	3	$4.9^{+0.2}_{-0.2}$	$5.8^{+9.2}_{-0.7}$	$0.001^{+0.0071}_{-0.0001}$	-	-
7	9	$5.3^{+1.2}_{-1.2}$	$4.7^{+0.3}_{-0.3}$	$0.005^{+0.0009}_{-0.0005}$	-	-
8	9	$6.5^{+0.3}_{-0.3}$	$5.6^{+0.4}_{-0.3}$	$0.005^{+0.0013}_{-0.0007}$	-	-
9	9	$9.3^{+0.6}_{-0.6}$	$7.9^{+0.6}_{-0.4}$	$0.004^{+0.0012}_{-0.0007}$	-	-

Figure B.12: Additional NV center measurements a, $\log S(\tau)^{-1}$ for nine additional NV centers. Inset: pulse sequence used to measure NV centers in (a). Blue lines are fits to the hopping model in the Main Text, and dotted and dashed lines show slopes of 2 and 2/3, respectively. Y axis offset is arbitrary. **b**, DEER XY-4 data for four additional NV centers, plotted as in (a). Inset: DEER XY-4 pulse sequence. **c**, Surface spin densities and depths extracted from NV centers in (a) and (b). Depth_{NMR} is the NV center depth extracted from fitting the proton NMR signal, while Depth_{DEER} and $\text{Depth}_{DEERXY4}$ are the depths extracted from the hopping model in the Main Text. Error bars are one standard error.

B9 Additional model analysis

B9.1 Analysis of two-exponent fits

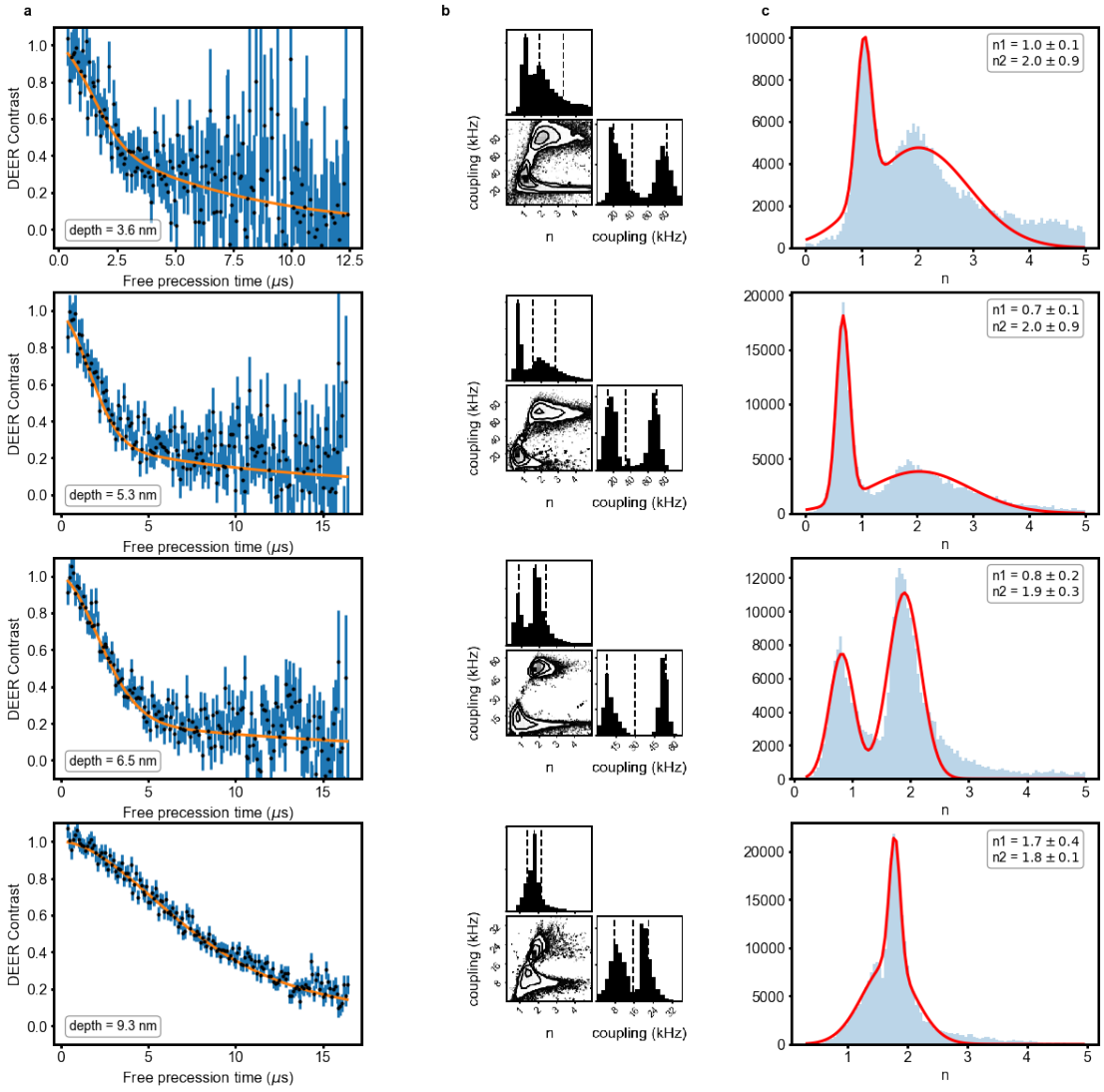


Figure B.13: Fits to a bi-exponential for four NV centers a, Data for each of the four NV centers. The orange lines are best bi-exponential fits based on MCMC analysis. **b**, The posterior distribution function (PDF) of n vs coupling, shown for each NV. **c**, The exponent stretching factors are found by fitting the PDF of n to two Gaussians.

For the shallow NV centers investigated in this work, a single exponential with $n = 2$ fixed leads to a poor fit while permitting n to vary leads to better fits with $n < 2$, in general. Additionally, we claim that for configurationally averaged surface spins, the short and long time behavior of the FID should have different stretching factors. In particular, it should be possible to observe $n = 2$ for short times and $n = 2/3$ for long times in NV centers that are closer to the surface than the average surface spin separation. Here we investigate the veracity and robustness of this claim by fitting the DEER signal of four NV centers from . These are the three NV centers depicted in Fig. 3 of the Main Text, plus one more that is located at a similar depth to the shallowest. We fit these data to a function of the form

$$f(\tau) = a \exp -(\Gamma_1 \tau)_1^n + (1 - a) \exp -(\Gamma_2 \tau)_2^n \,, \tag{B.62}$$

where τ is the free precession time and $a, \Gamma_1, \Gamma_2, n_1, n_2$ are the fit parameters. Here we take a fully Bayesian approach and use Markov Chain Monte Carlo (MCMC) to sample the posterior distribution of these parameters, using a Gaussian likelihood with $\mu = f(\tau)$ and $\sigma(\tau)$ from the actual variance of the data. Priors for the fit parameters are uniform distributions. The resulting posterior distributions of n_1 and n_2 are shown in Fig B.13. We find that the early time exponent, n_2, has a mean value close to two while the late time exponent n_1 is lower. For the deepest NV center, the two distributions are nearly indistinguishable, indicating that the biexponential has collapsed into a single exponential, which is expected for an NV center that is deeper than the average spin-spin separation.

Our data processing procedure, as described in Section B3, necessitates choosing a cutoff value of $C(\tau)$ in time after which data is discarded. This is to prevent the signal to noise ratio of the FID data from becoming too large, which is an unavoidable consequence of dividing the DEER echo by the spin echo coherence. We show in Fig. B.14 that reasonable choices of the cutoff value do not affect

the results of the fit. That is, for these datasets, there is enough coherence left at the cutoff point that the fit parameters are well constrained.

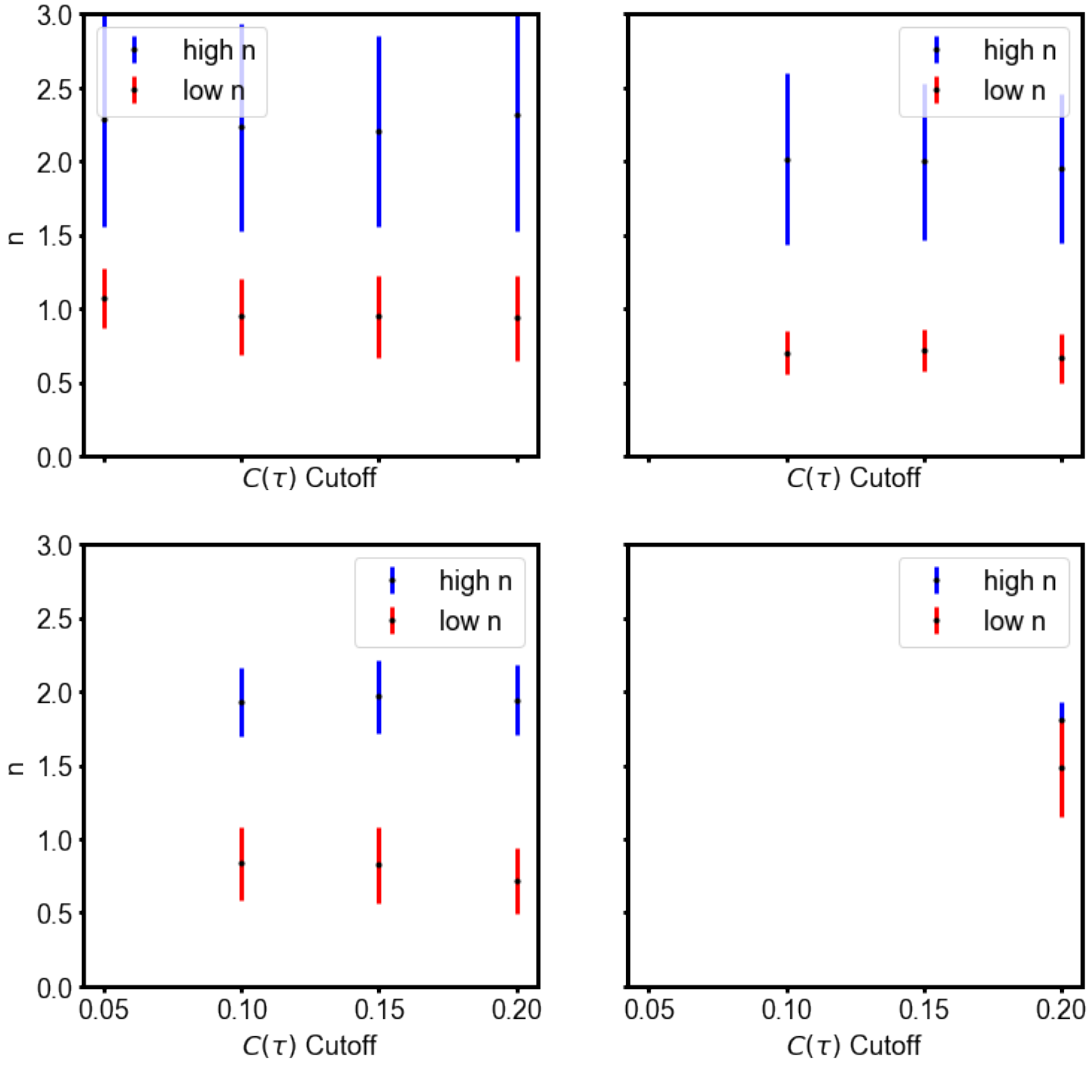


Figure B.14: Stability of stretching factors. Mean and standard error of the two stretching factors (high n and low n) of equation (B.62) as a function of the cutoff value of the coherence for the four NV centers in Fig. B.13. For two NV centers, $C(\tau)$ did not dip below 0.1 during the measurement period and for one NV center, $C(\tau)$ did not dip below 0.2 during the measurement period. However, extracted exponents remained stable for all NV centers regardless of the exact $C(\tau)$ cutoff value.

B9.2 Model comparison

While it is instructive to extract bi-exponential stretching factors observe short and long time behavior, Eq. (B.62) is not the form that the free induction decay is expected to take in either the static spin or configurational averaging picture. To assess the utility of the configurational averaging model, we compare the fit of the Monte Carlo simulated spin hopping model to the single exponential model fit for the four NV centers in Figure B.13 (three of which are also depicted in Fig. 3 of the Main Text) using several standard Bayesian model comparisons [370,130]. For each of these NV centers, we report the Widely Applicable Information Criteria (WAIC) and associated error, σ_{WAIC}, the Leave-One-Out (LOO) cross validation statistic and associated error, σ_{LOO}, and the total model log-likelihood and associated error, $\sigma_{\text{Log}-\text{likelihood}}$, for the two different models. The results are reported in Table B.2, from which it is apparent that the configurational averaging model is preferred over the single exponential predicted from a static bath in all cases, and that this difference is significant for two NV centers. The reason for the low significance of NV1 is likely the lower signal to noise of this measurement, and for NV4 the two models are expected to perform similarly due to the depth of this NV center.

For the single exponential fit, the stretching factor n is constrained to be $n \geq 1$ following the discussion of noise sources in Section B7.1. For the configurational averaging Monte Carlo model, both the depth and the surface spin density are free parameters. In order to remove any ambiguity regarding data cutoffs, the coherence and the DEER signal are fit simultaneously with separate Gaussian likelihoods. This is possible for these NV centers because the host diamond is isotopically purified, and the absence of ^{13}C oscillations greatly simplifies the fitting. The coherence is therefore assumed to take the form of a stretched single exponential.

NV Center	Model	WAIC	σ_{WAIC}	LOO	σ_{LOO}	Log-likelihood	$\sigma_{\mathrm{Log-likelihood}}$
NV1	Hopping	196	12	196	11	1243	13
(3.6 nm)	Static	192	12	192	11	1235	14
NV2	Hopping	253	9	253	9	1429	15
(5.3 nm)	Static	226	2	226	12	1401	17
NV3	Hopping	277	8	277	9	1543	15
(6.5 nm)	Static	244	11	244	12	1497	19
NV4	Hopping	293	20	293	20	1664	18
(9.3 nm)	Static	288	22	288	22	1501	72

Table B.2: Model comparison between static spins (single exponent) and configurational averaging models for four highly sampled NV center datasets.

B10 Fraction of spins that are hopping

Across the nine samples listed in Table B.1 and an additional five samples with similar implantation parameters and surface preparations, we measured DEER signals on 191 unique NV centers and observed only three spins that exhibited obvious coherent oscillations, as defined by a DEER contrast (DEER echo divided by coherence) that dipped below -0.1. This ratio allows us to place a bound on the number of spins that could still be stationary while the remaining spins hop. If we assume typical extracted densities of $\sigma = 0.005/\mathrm{nm}^2$, then given that the typical NV center depths in our samples are on average less than 10 nm, we expect that less than 20% of surface spins are stationary (see Fig. B.15).

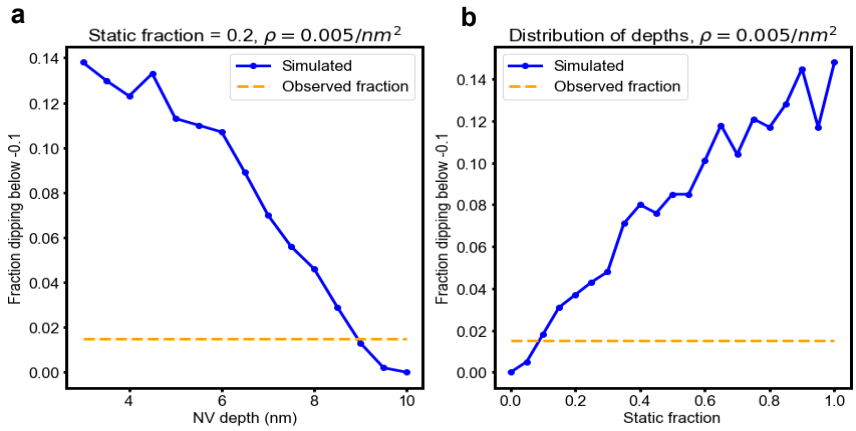


Figure B.15: Stationary Surface spin fraction. **a**, Simulation of the fraction of NV centers that exhibit strong coupling in DEER as a function of depth, if 20% of spins on the surface are placed randomly relative to the NV center and then do not hop. **b**, Simulation of the fraction of NV centers that exhibit strong coupling in their DEER signal as a function of the fraction of spins that are stationary on the surface, given a density of $\sigma = 0.005/\text{nm}^2$, and depths drawn from the distribution of depths measured across all samples. Orange dashed line corresponds to the observed fraction of 3 strongly coupled DEER signals out of 191 NV centers.

C

Supporting material for Chapter 4

C1 Device fabrication

We here outline the fabrication processes used to make devices on diamond and Si/SiO_2 substrates.

C1.1 Devices on diamond substrate

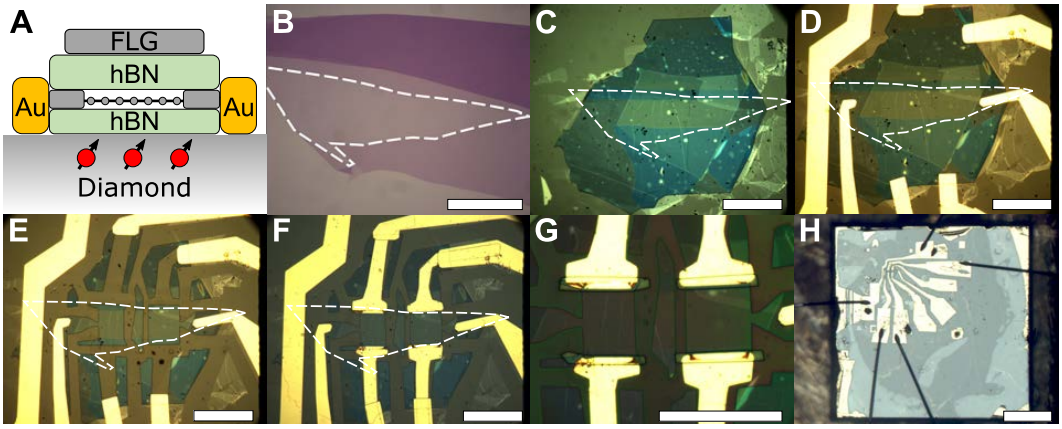


Figure C.1: Device fabrication on diamond substrate. (**A**) Device schematic: Monolayer graphene (grey chain) was graphite contacted and encapsulated with hexagonal boron nitride (hBN). Few-layer graphene (FLG) was used as topgate. (B-H) Micrographs of device fabrication, with 40 μm scalebar in (B)-(G) and 500 μm in (H). (**B**) Exfoliated graphene. White dashed line indicates monolayer region. (**C**) Complete stack on diamond substrate with shallow implanted ($40 - 60$ nm deep) NV centers. (**D**) Initial contacts and wire for delivering reference noise (left-most electrode). (**E**) Device after etch to define geometry. (**F**) Edge contacts constructed through etching and subsequent thermal evaporation. (**G**) Device with etch mask for disconnecting topgate from edge contacts. The left device is the source of data for Figure 2D-E in the main text (Device C2). Note that ripples visible in the image are entirely contained in the top gate graphene and are not expected to affect the transport properties of the channel graphene, due to the thick ($\sim$ 90 nm) hBN dielectric. (**H**) Entire (2×2 mm^2) single crystal diamond, with wire bonded device.

First, we exfoliated flakes of hexagonal boron nitride (hBN) and graphene onto a Si/SiO_2 substrate (Fig. C.1B), and used optical microscopy as well as atomic force microscopy (AFM) to pick clean flakes of the desired thicknesses. We then used the hot polycarbonate (PC) assembly technique[285] ($T_{\text{engage}} \sim 100\,^{\circ}$C) to assemble the flakes into stacks (Fig. C.1A). These consisted of fully hBN-encapsulated single layer graphene flakes, with two graphite contacts, and a few-layer graphene topgate. The top graphene was 3-5 layers thick to ensure uniform doping while still allowing us to optically address the NV centers through the stack. The top hBN flake was relatively thick ($\sim$ 90 nm) to minimize the doping effect of the source-drain voltage, while the bottom layer was thinner ($\leq$ 20 nm) to minimize the graphene-NV distance. The graphite contacts were used

to ensure that the contact interface was under the topgate electrode. Upon assembling the stack, we transferred it onto a Si/SiO_2 substrate ($T_{transfer} \sim 180\ ^\circ C$) and vacuum annealed at 350 °C for 2 minutes. Next, the stack was picked up again and transferred onto the diamond substrate (Fig. *C*.1C). The vacuum annealing was not done on the diamond substrate, since we consistently observed that this caused a strong background fluorescence signal.

We then used e-beam lithography (JEOL JSM-7000F) and thermal evaporation (10 nm Cr + 100 nm Au) to construct bonding pads and contacts (Fig. *C*.1D). During lithography steps, Aquasave was deposited on top of the PMMA layer to prevent charging effects. We also fabricated a thick wire surrounding the stack for delivering reference microwave noise to the NV centers. Next, we defined the geometry of the device (Fig. *C*.1E) using a reactive ion etch ($CHF_3,\ Ar,\ O_2$), carefully choosing the cleanest region of the stack based on AFM images. Using a new PMMA etch mask, we gently O_2-etched the two edges of the device that were to be contacted, in order to make sure the graphite contacts were well exposed. We then evaporated 2 nm Cr and 120 nm Au to create edge contacts (Fig. *C*.1F). This procedure is further described in Ref. [376]. Finally, another gentle O_2 etch was used to create two $\sim$ 200 nm cuts in the topgate graphene (Fig. *C*.1G) in order to disconnect it from the source-drain contacts. The complete, wire bonded device on diamond is shown in Fig. C.1H.

C1.2 Devices on Si/SiO_2 substrate

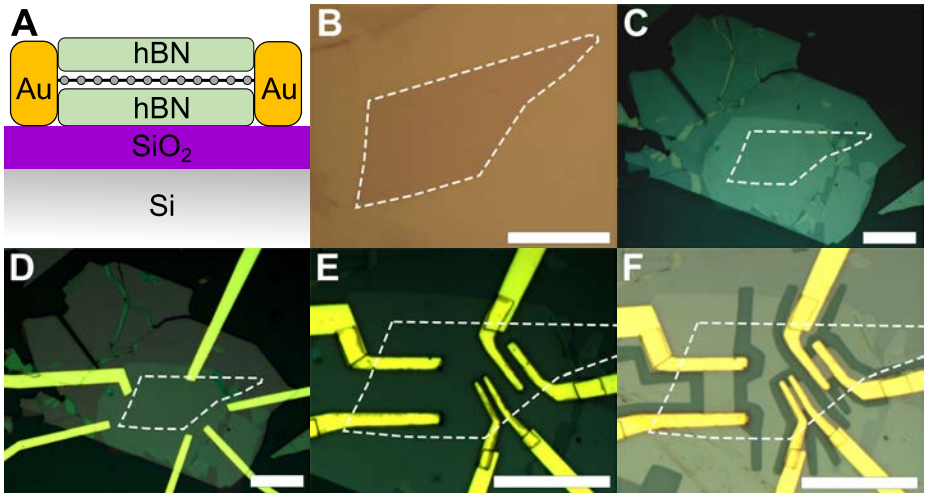


Figure C.2: Device fabrication on Si/SiO_2 substrate. (**A**) Device schematic: Monolayer graphene (grey chain) was encapsulated with hexagonal boron nitride (hBN). Silicon substrate was used as a global backgate. (B)-(F) Micrographs of device fabrication, with 20 μm scalebar. (**B**) Exfoliated graphene. (**C**) Complete stack on substrate. (**D**) Initial contacts. (**E**) Edge contacts constructed through etching and subsequent thermal evaporation. (**F**) Device after geometry-defining etch. The left-most device is the source of data for 4.8C-E, 3C-D and 4A in the main text (Device A1).

In fabricating devices on Si/SiO_2-substrates, we used the same exfoliation and stacking technique as outlined in the previous section. However, these samples were gated using a global backgate through the 1 μm thick SiO_2 (Fig. C.2A), and therefore did not need a topgate and graphite contacts. Thus, the stacks simply consisted of an hBN-encapsulated graphene channel. The remaining fabrication process (Fig. C.2B-F) was identical to the procedure on diamond substrate, except without the reference noise wire and the final topgate etch step.

Table C.1 ***(following page)*****: (following page) Device overview.** Here, we give a brief overview of the numerous samples measured. The key observation is that the anomalous noise signal is found in all the 12 clean (fully encapsulated) devices with lengths $\geq 2\mu\mathrm{m}$. The disordered (partially or not encapsulated) devices, on the other hand, never exhibit this signal. The devices that are extensively discussed in the main text appear in bold. **Unclear: Higher noise temperature than expected from thermal model, but the other signatures are missing: The spectrum is white, and the noise depends sub-linearly on power. We propose that this is due to shot noise, commonly observed in short devices.*

Table C.1: (continued)

Device name	hBN-encapsulation	Substrate	$L \times W(\mu m^2)$	Abnormal noise
A1	Fully	SiO_2	6×5.4	Yes
A2	Fully	SiO_2	9.5×11	Yes
A3	Fully	SiO_2	2.5×11	Yes
A4	Fully	SiO_2	2.0×3.3	Yes
A5	Fully	SiO_2	4.7×2.3	Yes
A6	Fully	SiO_2	7.3×5.3	Yes
A7	Fully	SiO_2	7.3×5.3	Yes
A8	Fully	SiO_2	45×15	Yes
A9	Fully	SiO_2	1.3×5.0	Unclear*
A10	Fully	SiO_2	1.0×5.0	Unclear*
B1	Bottom Only	SiO_2	7×18	No
B2	None	SiO_2	10×15	No
B3	None	SiO_2	12×19	No
B4	Top Only	SiO_2	10×15	No
B5	Top Only	SiO_2	12×19	No
C1	Fully	Diamond	6×22	Yes
C2	Fully	Diamond	17×20	Yes
C3	Fully	Diamond	20×23	Yes
C4	Fully	Diamond	6×8.4	Yes

C2 AC conductivity and noise measurements

C2.1 Electronic high frequency measurement setup

High-frequency noise and conductivity measurements were performed in a Janis ST-400 cryostat equipped with coax lines. To improve high-frequency signal transmission, we used a PCB with co-planar waveguides that were connected to the device with short wire bonds. The DC bias was applied through an external bias tee (Minicircuits ZBT-4R2GW+) that directed AC signals to either an amplifier (Fairview SLNA-030-34-14-SMA) and spectrum analyzer (Keysight N9322C) for noise measurements, or to a network analyzer (Keysight N5222A) for AC conductivity measurements.

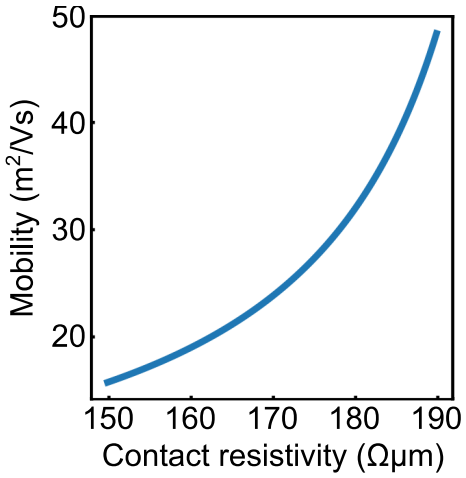


Figure C.3: Calculated mobility of clean device. Mobility vs. typical range of contact resistivities.

C2.2 AC conductivity calibration

For the sake of clarifying terminology, we would first like to note that the (intensive) conductivity spectrum $\sigma(\omega) = L/W \cdot G'(\omega)$ was found by first determining the (extensive) differential conductance $G'(\omega)$ and then multiplying by the aspect ratio L/W. Moreover, we always refer to the

differential conductance $G'(\omega) = dI(\omega)/dV(\omega)$, not the chord conductance $G = I/V$.

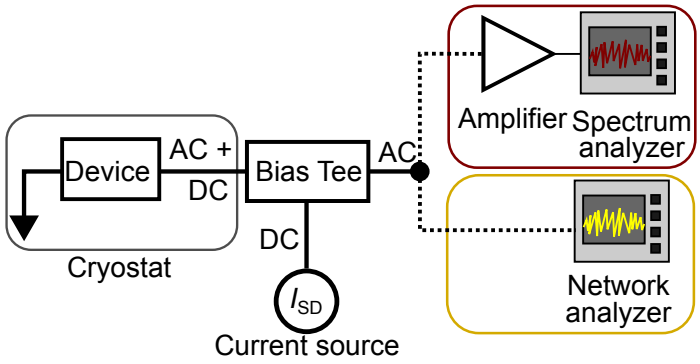


Figure C.4: Measurement circuit. Circuit diagram for the measurement of noise (red box) and AC differential conductivity (yellow box).

In order to determine the AC conductance spectrum, we used a bias tee to measure the reflection coefficient $r = |r|e^{i\varphi}$ with a network analyzer, while simultaneously DC-biasing the sample. The reflection coefficient depends on not only the impedance matching to the sample, but also the external cabling leading up to it:

$$|r|e^{i\varphi} = r_{\text{ext}}(\omega) + t_{\text{ext}}^2(\omega) \cdot \frac{50\Omega - Z(\omega, G')}{50\Omega + Z(\omega, G')} \tag{C.1}$$

where $r_{\text{ext}}(\omega)$ is the reflection from external components between the network analyzer and the sample (e.g. connectors, cables), and $t_{\text{ext}}(\omega)$ is the transmission through these. We note that r_{ext} and t_{ext} are completely independent of the sample conductance, and one would observe $r = r_{\text{ext}} - t_{\text{ext}}^2$ if the cable was open instead of connected to the sample. $Z(\omega, G')$ is the complex impedance of the sample, which depends on its differential conductance, but also on parasitic reactance. The latter comes predominantly from two sources:

1) Capacitance from the $\sim$ 75 x 75μm^2 source bonding pad on 1μm SiO_2 dielectric ($C \sim 0.2$pF)

2) Inductance from $\sim$ 10mm wirebond ($L \sim 10$nH)

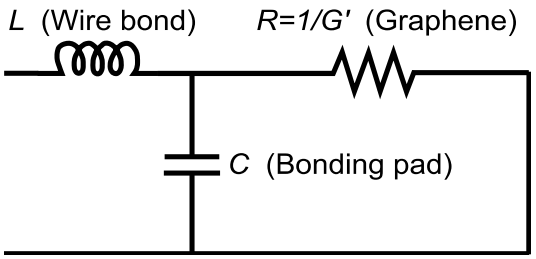


Figure C.5: Circuit diagram of wire bonded device, showing main sources of parasitic reactance.

We thus use the circuit model shown in Fig. *C*.5, which gives the impedance:

$$Z(\omega, G') = i\omega L + \frac{1}{G'(\omega) + i\omega C} \tag{C.2}$$

In what follows, we assume that the parasitic L and C do not change with the graphene doping or the current flowing through the sample. A key observation then is that the reflection coefficient $r(\omega, G')$ depends on only one graphene property, namely the differential conductance $G'(\omega)$. The latter depends on both the graphene current density (j) and doping (n), but if two pairs of parameters (j_A, n_A) and (j_B, n_B) give the same $G'_A(\omega) = G'_B(\omega)$ at a given ω, then their reflection coefficients must also be the same at that ω.

An important result in the main text is that the AC differential conductivity of clean graphene devices becomes frequency-dependent in the GHz-range when a strong DC bias is applied. This can be seen clearly in the raw reflection measurements shown in Fig. *C*.6. We have here chosen to compare a biased measurement ($j_A = 0.56$ mA/μm, $n_A = 2 \times 10^{12}$ cm^{-2}) to an unbiased one ($j_B = 0.0$ mA/μm, $n_B = 0.24 \times 10^{12}$ cm^{-2}), that have the same DC conductance $G'_A(0) = G'_B(0) = 3.1$ mS. As expected, we therefore also find that these two pairs have the same DC reflection $r_A(0) = r_B(0)$. However, at higher frequencies, one finds $r_A(\omega > 0) \neq r_B(\omega > 0)$, which indicates that $G'_A(\omega > 0) \neq G'_B(\omega > 0)$. Since it is theoretically expected and previously experimentally established that the unbiased $G'_B(\omega)$ is frequency-independent at the low frequencies

considered here [157,16], we conclude that the the biased $G'_A(\omega)$ develops a frequency dependence.

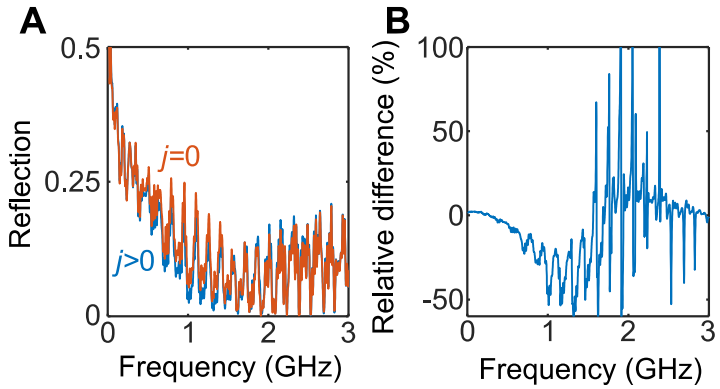


Figure C.6: (**A**) Reflection spectrum in the biased (blue) and unbiased (orange) case. (**B**) Relative difference in reflection. The gate is used to keep the DC conductance equal (3.1 mS) in the two cases, and as expected, the DC reflection is approximately equal. At higher frequencies, however, the reflection coefficients differ significantly, indicating that the conductance varies with frequency.

In order to determine $G'(\omega)$ at non-zero bias, one must determine C, L, $r_{\text{ext}}(\omega)$ and $t_{\text{ext}}(\omega)$. This was done by measuring $|r|e^{i\varphi}$ at zero bias, while sweeping G' using the electrostatic gate. We note that since no DC bias was applied during this calibration step, it was assumed that the graphene conductance G' was frequency-independent through the entire frequency range used here (< 3 GHz). In other words, we could simply measure the DC conductance $G'(0)$, and use $G'(\omega) = G'(0)$. We stress that this only applies to the conductance of the graphene itself, not the total impedance, which also contains the frequency-dependent reactance due to parasitic capacitance and inductance.

Using eqn. *C*.1, we fit both the real and imaginary parts of $r(\omega, G')$ (examples in Fig. *C*.7A-B), and find $C = 0.24\ (0.22)$ pF and $L = 11\ (16)$ nH for device A2 (A1) (Fig. *C*.7C), in excellent agreement with the expected parasitic reactance components.

The extracted parameters were used to determine the frequency-dependent conductance $G'(\omega; j, n)$ in the biased case, using the measured $r(\omega; j, n)$. Finally, we filtered out a small spurious periodic signal whose period was found to vary with cable length l according to l/c. The resulting

spectra are plotted in Figure 3B and 3D in the main text.

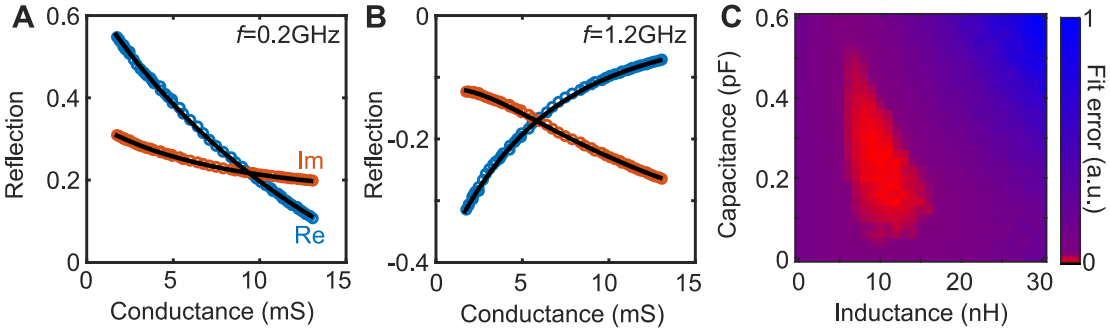


Figure C.7: (**A-B**) Real (blue) and imaginary (orange) parts of the reflection coefficient at $\omega = 2\pi \cdot 0.2$ GHz (A) and $2\pi \cdot 1.2$ GHz (B), as a function of the conductance (swept through electrostatic gating at zero bias). Using $L = 11$ nH and $C = 0.24$ pF, we extract $r_{\text{ext}}(0.2\text{ GHz}) = -0.011 + 0.085\text{i}$, $t^2_{\text{ext}}(0.2\text{ GHz}) = 0.66 + 0.29\text{i}$, $r_{\text{ext}}(1.2\text{ GHz}) = 0.041 - 0.048\text{i}$, and $t^2_{\text{ext}}(1.2\text{ GHz}) = -0.43 - 0.17\text{i}$. (**C**) Total fit error (summed over all ω) as a function of parasitic capacitance and inductance. The error is minimized at $L \sim 11$ nH and $C \sim 0.24$ pF.

C2.3 Noise measurement and calibration

In the main text, we report global noise in terms of noise power spectral density in units of Kelvin. This quantifies the noise power dissipated in the device per unit bandwidth, and corresponds to the equivalent electron temperature necessary to generate the same noise signal from thermal (Johnson-Nyquist) noise alone. For example, 300 K corresponds to -174 dBm/Hz of noise power per unit bandwidth. We emphasize that the anomalous noise signal we measure in clean devices is not due to Johnson-Nyquist noise (see discussion in section C5.2).

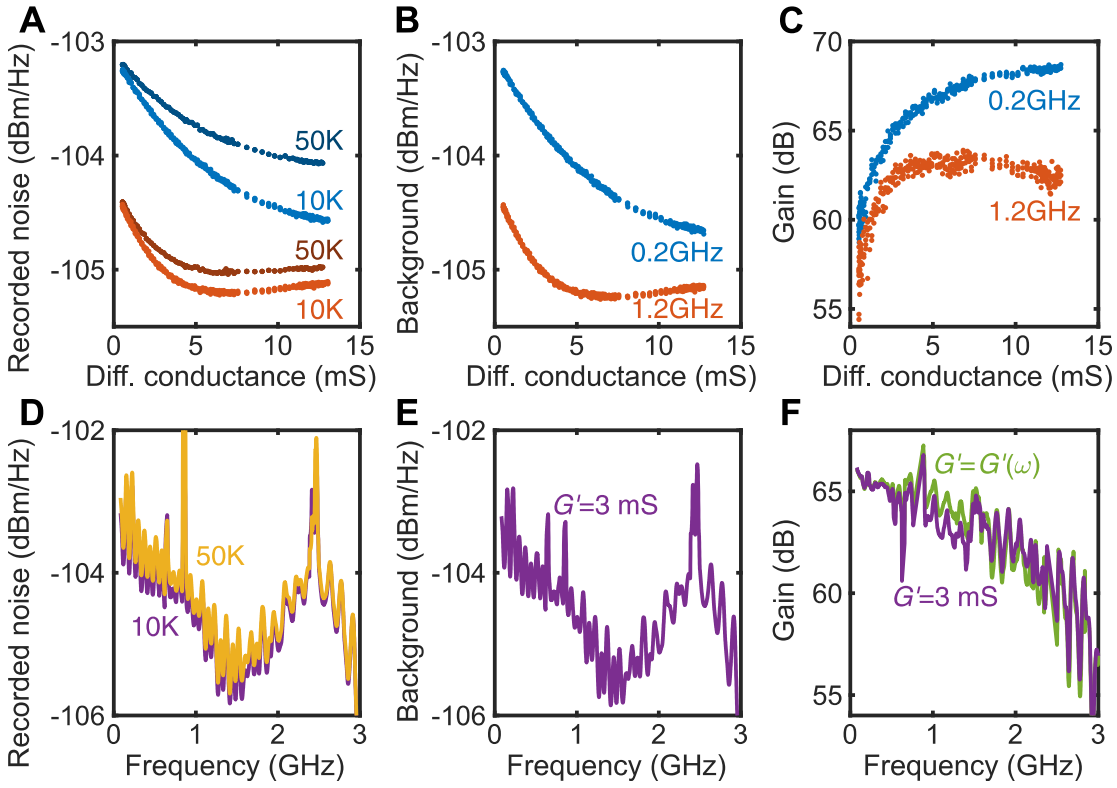


Figure C.8: Noise calibration. In A-C, blue and orange dots represent data at $f = 0.2$ GHz and $f = 1.2$ GHz, respectively. (**A**) Measured noise S_{rec} vs. differential conductance G', at base temperature $T_{\text{C}} = 10$ K (bright dots) and an elevated temperature $T_{\text{H}} = 50$ K (dark dots). The noise is minimized when $Z(G')$ is closest to matching 50 Ω, because at such low temperatures, the noise is dominated by background noise reflected off the sample. As expected, the matching value of G' is above 12 mS (below $\sim$ 80 Ω) at low frequencies, but shifts to $\sim$ 6 mS ($\sim$ 150 Ω) at f =1.2 GHz, due to the emerging parasitic reactance. (**B**) Background noise S_0 calculated according to eqn. $C.6$. (**C**) Total gain A calculated according to eqn. $C.5$. Sub-unity transmission and losses in the cables bring A below the 68 dB amplifier gain. (**D-F**) Same as (A)-(C), except as a function of frequency, $f = \omega/2\pi$. Purple and yellow curves show measurements at fixed $G' = 3$ mS. Green curve in (F) accounts for the frequency-dependence of $G'(\omega; j, n)$ for the particular driven case, $j = 0.56$ mA/μm, n $= 2 \times 10^{12}$ cm^{-2}. This is achieved using the technique outlined in the text.

To measure the noise from our graphene sample, we amplified the current fluctuations with two low-noise 34 dB amplifiers in series (Fairview SLNA-030-34-14-SMA) and recorded the spectrum with a spectrum analyzer. The recorded noise $S_{\text{rec}}(\omega)$ is a transformed version of the device noise

$S_{\mathrm{dev}}(\omega)$, due to both background noise $S_0(\omega, G')$ and the gain function $A(\omega, G')$ of the total setup:

$$S_{\mathrm{rec}}(\omega; j, n) = S_0(\omega, G'(\omega; j, n)) + A(\omega, G'(\omega; j, n)) \cdot S_{\mathrm{act}}(\omega; j, n) \tag{C.3}$$

Both S_0 and A depend on the sample conductance spectrum $G'(\omega; j, n)$, which depends on the current and charge densities, j and n. The background S_0 has a weak G'-dependence because part of the external background noise is reflected off the sample before reaching the spectrum analyzer. Indeed, we observe a higher background signal when the conductance G' is further away from the impedance-matched value. The gain A depends on G' more strongly, because the impedance matching determines the transmission of the signal from the sample to the 50 Ω cable. In addition, A also depends on external factors, such as amplifier gain and cable attenuation (represented by $A_{\mathrm{ext}}(\omega)$ below):

$$A(\omega, G') = A_{\mathrm{ext}}(\omega) \cdot \left(1 - \left|\frac{50\Omega - Z(\omega, G')}{50\Omega + Z(\omega, G')}\right|^2\right) \tag{C.4}$$

Here, Z is the (complex) impedance of the sample, which depends on the differential conductance G' of the sample, as well as parasitic reactive components.

In order to characterize $S_0(\omega, G')$ and $A(\omega, G')$, we need two known (preferably white) noise signals from the sample. Thus, we used a heating stage to record the Johnson noise $k_B T$ from the graphene at an elevated temperature T_{H} and at the base temperature T_{C}, while sweeping the gate through a wide range of G' (Fig. *C*.8A and *C*.8D). To minimize heating effects on $S_0(\omega)$ (by heating up other noisy components), or on $A(\omega, G')$ (through temperature-induced changes in parasitic reactive components), we used a local heater that only heats the silicon substrate supporting the graphene device, keeping the rest of the cryostat cold. We could then find $S_0(\omega, G')$ and $A(\omega, G')$

from:

$$A(\omega, G') = \frac{S^{\mathrm{H}}_{\mathrm{rec}}(\omega, G') - S^{\mathrm{C}}_{\mathrm{rec}}(\omega, G')}{k_B(T_{\mathrm{H}} - T_{\mathrm{C}})} \tag{C.5}$$

$$S_0(\omega, G') = \frac{S^{\mathrm{C}}_{\mathrm{rec}}(\omega, G')T_{\mathrm{H}} - S^{\mathrm{H}}_{\mathrm{rec}}(\omega, G')T_{\mathrm{C}}}{T_{\mathrm{H}} - T_{\mathrm{C}}} \tag{C.6}$$

where $S^{\mathrm{H(C)}}_{\mathrm{rec}}(\omega, G')$ is the noise recorded at $T_{\mathrm{H(C)}}$. We remind that no bias was applied during these calibration measurements, so the conductance spectrum was flat and could be easily determined from DC measurements. The procedure to find $S_0(\omega, G')$ and $A(\omega, G')$ is shown as a function of G' in Fig. *C*.8B-C, and as a function of ω in Fig. *C*.8E-F.

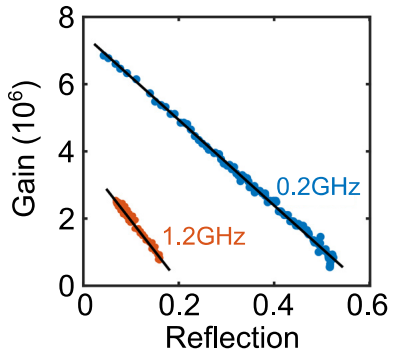


Figure C.9: Linear relationship between gain and reflection. Gain $A(\omega, G')$ plotted against the reflection, $|r(\omega, G')|^2$ at $\omega = 2\pi \cdot 0.2$ GHz (blue) and $\omega = 2\pi \cdot 1.2$ GHz (orange). The different points are obtained by sweeping the charge density n (and thus also G') at zero bias. As expected, the two quantities are linearly related. The gain in the biased case $A(\omega, G'(\omega; j, n))$ can now be found by measuring the reflection $|r(\omega, G'(\omega; j, n))|^2$ while applying current, and inserting it into the fit.

As shown in Fig. *C*.8F, we finally corrected for the effect of the frequency-dependent G' on the gain (the effect on S_0 is much smaller $\sim 0.1\%$). This was done by also measuring the reflection coefficient (plotted against initial gain calibration in Fig. *C*.9), and utilizing the near-linear relationship

between reflection and transmission:

$$A(\omega, G') \sim A_{\text{ext}} \left(1 - \frac{|r(\omega, G')|^2}{|t_{\text{ext}(\omega)}|^4}\right) \tag{C.7}$$

where r is the measured reflection coefficient with the network analyzer, and t_{ext} is the transmission through external cabling (section C2.2). Reflections from external components were here ignored, since reflections predominantly come from the sample. A key point is that while the gain $A(\omega, G')$ must be measured at $j = 0$, the reflection $|r(\omega, G')|^2$ can be measured while applying a non-zero current. Thus, we can measure $|r(\omega, G'(\omega; j, n))|^2$ and translate it to $A(\omega, G'(\omega; j, n))$, using the fits of $A(\omega, G')$ vs. $|r(\omega, G')|^2$ at each ω (Fig. *C*.9). The corrected gain profile $A(\omega, G'(\omega; j, n))$ at a particular (non-zero) current density $j = 0.56$ mA/μm and $n = 2 \times 10^{12}$ cm^{-2} is shown in Fig. *C*.8F (green curve).

After these calibration steps, we finally applied a current j through the device and measured the noise $S_{\text{rec}}(\omega; j, n)$. We could then use the determined $S_0(\omega, G')$ and $A(\omega, G'(\omega; j, n))$ to determine the device noise, $S_{\text{dev}}(\omega; j, n)$ from eqn. *C*.3. Telecom signals at $f = 800$ MHz were removed, as well as regions where the linear relationship in eqn. *C*.7 broke down due to strong external reflections.

C3 Local noise measurements with diamond NV magnetometry

C3.1 NV measurement setup

For local noise measurements, the graphene devices were fabricated on single crystal E-grade diamonds with a (100) major face (Element Six). Prior to device fabrication, the substrates were plasma etched, implanted, and annealed as in Reference [308], but without the oxygen annealing step. This process resulted in a very smooth surface (<200 pm RMS roughness). ^{15}N ions were implanted at 20 keV, which corresponds to an approximate depth of 40-60 nm (calculated by Stopping and Range

of Ions in Matter simulation).

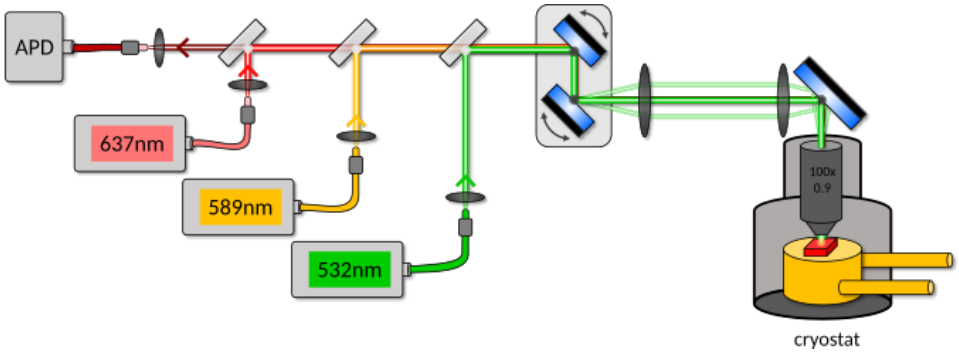


Figure C.10: NV measurement setup. The three laser beams used for spin-to-charge readout are combined before the galvonometric mirrors located at one focal point of a 4f system. Lasers are switched by acousto-optic modulators, except for the 637 nm high-powered ionization laser, which is a directly driven diode laser. The objective and sample are located inside a Janis ST-500 cryostat, which is used to keep the sample at ∼70K by a combination of flowing liquid helium and a resistive heater in a PID loop.

NV center measurements were performed in a Janis ST-500 flow cryostat. Cryogenic temperatures allowed for resonant excitation of the NV center at low powers to reduce background. A scanning mirror-based confocal microscope was used to address, track and read out the NV centers during measurements. The full initialization and readout sequence required lasers of wavelengths 532 nm, 594 nm, and 637 nm that were separately switched with acousto-optic modulators. One of the 637 nm lasers (NewFocus Velocity TLB6704) was an external cavity diode laser that was tuned to each NV zero phonon line. The other red laser was a high-powered diode laser that was used to apply short >70 mW pulses to ionize NV centers. Photons emitted in the phonon side-band were collected with a fiber-coupled SPCM (Excelitas Technologies). Timings were orchestrated by a SpinCore PulseBlaster ESRPro with 2.5 ns timing resolution. The cryostat was equipped with coax lines, both for driving microwave pulses to manipulate the NV center, and to perform high-frequency measurements of the graphene device as described in the previous sections. Microwave signals for NV center manipulations were generated on an SRS SG384 signal generator and am-

plified with a Minicircuits ZHL-16W-43+ amplifier. For microwave noise references, phase noise was introduced by applying 200 MHz bandwidth white noise to the IQ modulation input on the SRS. Non-zero magnetic field measurements were achieved by positioning large rare earth magnets outside the cryostat, approximately aligned with one of the NV axes.

C3.2 Spin-to-charge readout

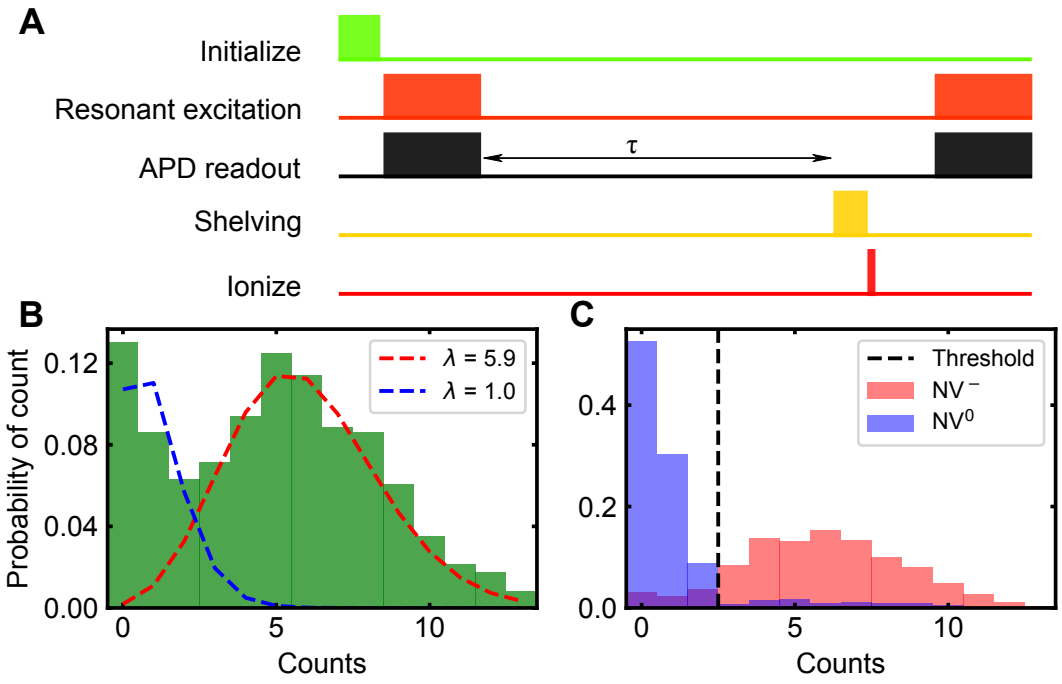


Figure C.11: Spin-to-charge readout. (**A**) Pulse sequence for measuring relaxation rate of NV centers. A 532 nm pulse preferentially prepares the NV center in the NV^- charge state and $m_s = 0$ spin state. The NV center spin is allowed to relax for a time τ before a strong yellow pulse shelves the $m_s = \pm 1$ population in the singlet state. An intense pulse of 637 nm light ionizes any population in the triplet state, while the singlet is protected. The resulting charge state is read out by resonant excitation of the NV^- zero phonon line, and from this, the spin state before the yellow pulse is inferred. (**B**) Photon distribution from NV is fit as a 70%-30% mix of two Poisson distributions with different parameters, λ, corresponding to counts from NV^- and NV^0. (**C**) Post-selected photon distributions. The photon distributions for the two charge states are distinguishable, permitting single-shot charge state readout.

Due to the often slow NV decay rates, we read out our NV center spins using a modified spin-to-charge mapping (Fig. *C*.11A) to reduce our readout noise to only 6.3 times the projection noise limit[321]. The NV centers were first initialized into the $m_s = 0$ spin state by shining a 1 mW pulse of 532 nm light for 25 μs[143]. This also preferentially prepared the NV center in the NV^- charge state with ~70% fidelity[14], as shown in Fig. *C*.11B. To improve this further, we performed post-selection based on an initial charge state readout, using a low-power pulse from an external cavity diode laser tuned to the NV^- zero phonon line near 637 nm. Extremely low power (~nW) was used to avoid ionizing the NV center while determining its initial charge state. The NV was then allowed to relax for a variable amount of time (τ) in the dark, before the spin state was mapped onto a charge state. Spin-to-charge conversion was achieved by applying a strong (5 mW) pulse of 589 nm light for 40 ns to preferentially shelve any $m_s = \pm 1$ population in the metastable singlet state, and then using a 20 ns pulse of ~70 mW 637 nm light to efficiently ionize any population in the triplet state. The protected population in the singlet then relaxed back to the triplet manifold by an intersystem crossing so that only the $m_s = \pm 1$ population remained in the NV^- charge state. The final charge state was then read out using the resonant laser, and the number of collected photons was used to assign a charge state. With an optimal threshold for photon counts, the single-shot charge state readout fidelity was 80%-99% depending on the NV center (Fig. *C*.11C), and the technique was limited primarily by spin-to-charge mapping efficiency.

C4 Basic device transport characterization

C4.1 Device mobility calculation

In the main text, we report a mobility of 20-40 m^2/Vs for device A1 (depicted in inset of 4.8A). This device measures $L \times W = 6 \times 5.4\,\mu m^2$ and we calculate the mobility at $n = 2 \times 10^{12}\ cm^{-2}$ as $\mu = \frac{L}{Wne}\frac{1}{R-R_c}$, where R is the 2-probe device resistance (4.8C in the main text), and R_c is the

contact resistance. Since we do not measure the contact resistance directly, we plot the mobility as a function of the contact resistivity (Fig. C.3) over a range of typical values for Cr+Au edge contacts[376].

C5 Additional noise and conductivity measurements

C5.1 Noise power vs. drift velocity

In 4.8E in the main text, we show the noise power as a function of bias power P for a limited range of P, to facilitate comparison between clean and disordered devices and highlight their contrasting behavior. Here, we show the dependence of global noise on electronic drift velocity for the full range of bias drives (Fig. *C*.12A). As expected, no anomalous noise is observed below $v_D = v_s$ (Fig. *C*.12B). We note that no sharp transition is expected at $v_D = v_s$, since at this point, only one phonon mode satisfies the Cerenkov criterion, and with a negligible amplification rate. Thus, one should instead observe a smooth transition into the excess noise regime, as the number of amplified modes and the amplification rate increase.

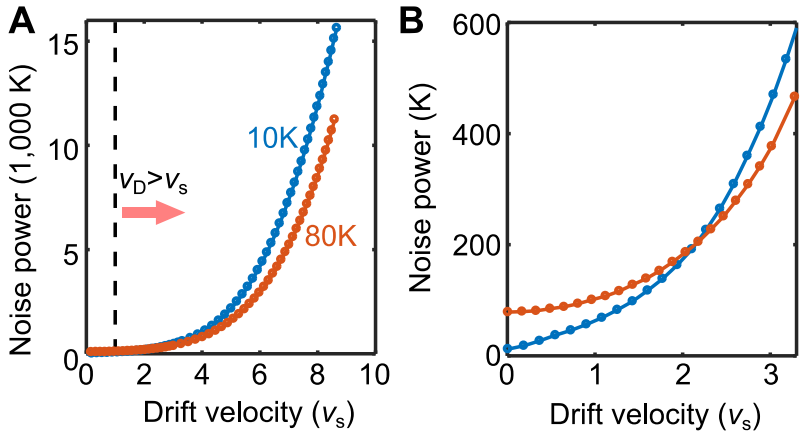


Figure C.12: Noise versus drift velocity (**A**) Measured noise power spectral density (averaged over 0.1-0.3 GHz) as a function of electronic drift velocity in clean device A1, at bath temperatures 10 K and 80 K (blue and red, respectively). We observe equivalent noise temperatures in excess of 15,000 K. (**B**) Zoomed-in version of (A) to highlight smooth transition into the excess noise regime. Lines are guides to the eye.

C5.2 Disordered device noise

To model the thermal noise observed in a disordered device, we need to consider the balance between Joule heating P and phonon cooling. The rate of the latter is typically given by $\Sigma(T_e^\delta - T_{ph}^\delta)$, where Σ is a cooling constant and T_e and T_{ph} are the electron and phonon temperatures, respectively[33]. Solving for the electronic temperature, one finds:

$$T_e = \left(T_{bath}^\delta + P/\Sigma\right)^{1/\delta} \tag{C.8}$$

where we have assumed that the phonon temperature remains close to the base temperature T_{bath}, as normally observed.

In samples with high impurity density, phonon cooling is usually dominated by "supercollision" scattering, in which electrons scatter with phonons with the assistance of defects[331]. In that case, one finds $\delta = 3$ and $\Sigma = 9.62\frac{g^2 \mathrm{DoS}^2(E_F)k_B^3}{\hbar k_F \ell}$, where $g = D/\sqrt{2\rho v_s^2}$ is the electron-phonon coupling

and ℓ is the mean-free path. Fitting our data with expression C.8, we reach good agreement (Fig. C.13) and find $\delta = 3.04$. We also extract the deformation potential from the fitted value of Σ, and find $D = 39$ eV ($E_F = 165$ meV). This is consistent with a previous study on disorder-assisted cooling in graphene ($D = 70$ eV)[33] and the typically reported range of $\sim 10 - 30$ eV[85]. (We note that we use the more accepted value of $D = 20$ eV for all other fits pertaining to Cerenkov emission in clean devices.) This confirms that the dominant noise in our driven disordered devices is thermal Johnson-Nyquist noise.

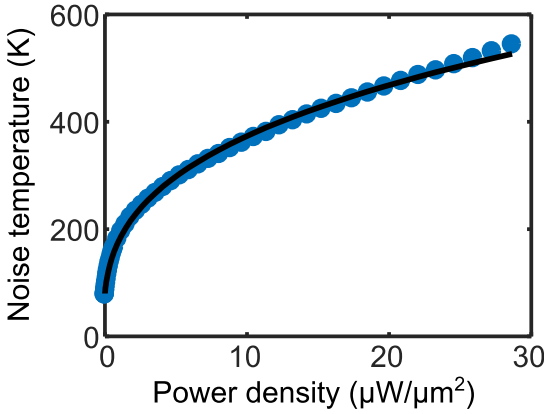


Figure C.13: Johnson noise in a disordered device. Measured noise temperature (blue circles) as a function of input power for disordered device B1. The data agrees well with a fit based on disorder-assisted phonon cooling (black curve), and confirms that the dominant noise source is thermal Johnson-Nyquist noise.

C5.3 Length dependence in global noise measurements

Local (NV) noise measurements indicate that the noise grows across the device in the direction of carrier flow. By measuring devices of different lengths, we find a similar trend in the global noise. At a constant electronic drift velocity ($v_D = 3.3v_s$) and charge density ($n = 2 \times 10^{12}$ cm^{-2}), the noise initially grows superlinearly with device length (Fig. C.14A, inset). Our longest device does not appear to follow the initial length dependence, hinting at the role of saturation effects that prevent unbounded exponential growth of the phonon population (Fig. C.14A).

We here also show the charge density dependence (4.11C in the main text) before normalization (Fig. C.14B). In addition to the data shown in the main text, we have also included measurements of our longest ($L = 45\mu$m) device (purple squares), which broke down before we could reach the current density used for the main text figure. As expected from our theory (main text and section C7.6), this longer device shows a cross-over at an even lower charge density than the other devices. As in the main text, we show the density dependence in terms of current noise $\delta^2 I$, which is similar to noise power, but divided by the differential resistance. This was done in the main text to allow for comparison with the model, but we note that the non-monotonic dependence is also observed when plotted in terms of noise power.

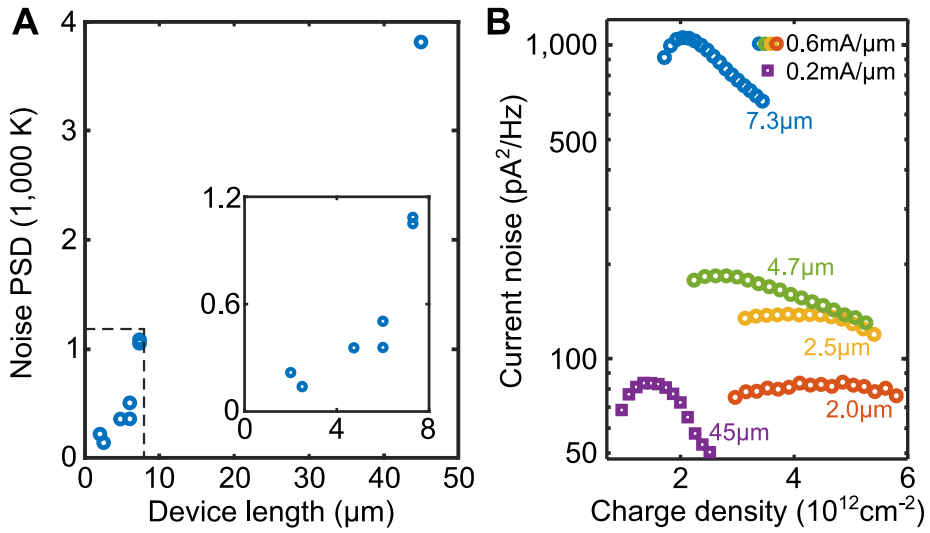


Figure C.14: Dependence of noise on device length. (**A**) Measured noise power spectral density from devices of different lengths, at $v_D = 3.3v_s$ and $n = 2 \times 10^{12}$ cm^{-2}. The noise power initially increases superlinearly with device length (inset), but appears to saturate in longer devices. (**B**) Current noise versus carrier density at constant current density $j = 0.6$ mA/μm (circles) and $j = 0.2$ mA/μm (squares). As shown in the main text, the cross-over density decreases with device length.

C5.4 Global noise independent of carrier flow direction

In the main text, we demonstrate that the local noise measured far from the middle of the device exhibits strong asymmetry with respect to carrier flow direction (main text, 4.9C). Here, we show that no such asymmetry is observed in *I-V* transport or global noise measurements (Fig. C.15A and B, respectively).

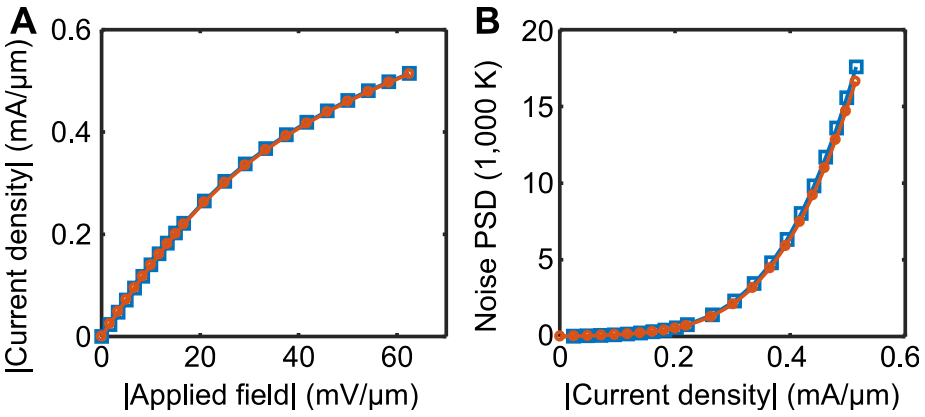


Figure C.15: Global electronic transport and noise under current inversion. (**A**) Absolute value of current density versus absolute applied field at $n = 2 \times 10^{12}$ cm^{-2} and $T = 10$ K, for positive (orange) and negative (blue) fields. The $I - V$ curve is observed to be highly symmetric. (**B**) Global noise power spectral density as a function of (absolute) current density. Changing the sign of the current has almost no effect on the measured noise power. Lines are guides to the eye.

C5.5 Independence of conductivity time scales on charge density and temperature

As shown in the main text, the time scale extracted from conductivity measurements is independent of drift velocity. We here show that the time scale does not depend on charge density (Fig. C.16A-B) and sample temperature (Fig. C.16C) either. Fig. C.16A shows normalized AC conductivity spectra measured at charge densities ranging from $n = 1.3$ to 2.2×10^{12}cm^{-2}, with the extracted time scales displayed in Fig. C.16B. Evidently, no dependence on charge density is observed. We also compare

the conductivity spectra obtained at 10 K and room temperature (Fig. C.16C), and again observe no clear change in the time scale. The independence on these parameters is consistent with our model, since the time scale is expected to be determined by the phonon traversal time $t_{\mathrm{T}} = L/v_{\mathrm{s}}$. We emphasize that this is only the case for the time scale; the magnitude of both the conductivity and noise features depend strongly on drift velocity, charge density and bath temperature.

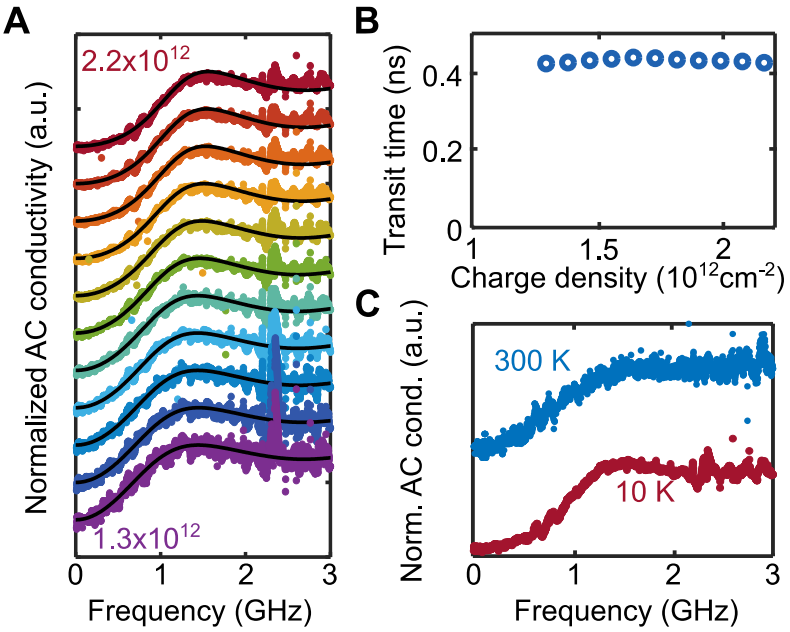


Figure C.16: Global conductivity for different charge densities and temperatures. (**A**) The normalized real part of the conductivity spectrum for $v_{\mathrm{D}} = 0.125 v_{\mathrm{F}}$ at different doping levels. The curves are normalized to have the same vertical spread, and are offset to avoid overlap. The general shape of the conductivity spectrum, as well as the extracted time scales (**B**) are unchanged by varying the charge density. (**C**) The normalized real part of the conductivity spectrum measured at bath temperatures of 300 K (blue) and 10 K (red), at $v_{\mathrm{D}} = 0.125 v_{\mathrm{F}}$ and $n = 2.2 \times 10^{12}$ cm^{-2}. We again observe no clear frequency shifts, but the effect is much (~ 4 times) weaker at room temperature than at 10 K.

C6 Additional NV center measurements

C6.1 NV relaxation rate near a conductor

Near a conductor, the spin relaxation rate of the NV center is enhanced due to magnetic field fluctuations resonant with the $m_s = 0$ to $m_s = \pm 1$ transitions (2.87 GHz), caused by current fluctuations in the conductor [197,148,5]. More formally, if we consider a 2d conductor in the xy-plane and an NV center located at $-d_{\mathrm{NV}}\hat{z}$, Fermi's Golden Rule can be used to calculate the decay rate:

$$\Gamma^0_{0\to 1} = \frac{1}{\hbar^2}\sum_{a,b} \langle 0|\mu_a|1\rangle \langle 1|\mu_b|0\rangle S_B^{a,b}\left(\omega, -d_{\mathrm{NV}}\hat{z}\right), \tag{C.9}$$

where $\mu_{a,b}$ are the magnetic dipole transition elements and $S_B^{a,b}(\omega,\mathbf{r}) = \int_{-\infty}^{\infty} dt e^{-i\omega t}\langle B_a(r,t)B_b(r,0)\rangle$ is the magnetic noise spectrum tensor [148], which scales with the current fluctuations due to the Biot-Savart Law [5].

C6.2 Local noise spectroscopy

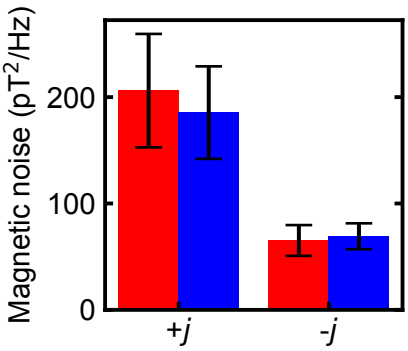


Figure C.17: Noise measured at different applied magnetic fields. Relaxation rates of an NV center at $B = 0$ (red) and $B = 363$ Gauss (blue), for positive and negative bias ($|j| = 0.2$ mA/μm) at $n = 0.92 \times 10^{12}\mathrm{cm}^{-2}$.

Spectroscopy of the local noise can be performed by varying the spin flip transition frequency of the NV center. We tuned the level-splitting of the two transitions to $\omega = 2.87 \pm 1.01$ GHz by applying an external magnetic field of 363 Gauss, and found no significant change in the relaxation rate of NV centers (Fig. C.17). We note that when measuring the decay into both the m_s =+1 and m_s =-1 states, cancellation effects can occur since the two transition frequencies are changed by equal and opposite amounts. In the worst case, $\Gamma(\omega)$ decreases linearly, and the relaxation rates of the two transitions change from Γ_0 to $\Gamma_0 \pm \partial\Gamma$. It can then be shown that the measured relaxation rate Γ_{meas} out of the initial $m_s = 0$ state should increase, with a relative change given by $\partial\Gamma_{\text{meas}}/\Gamma_{\text{meas}} = \partial\Gamma^2/(6\Gamma_0^2)$. Considering the $< 10\%$ change observed here, we conclude that the local noise varies by $< \sqrt{6 \cdot 10\%} \sim 80\%$ over 1 GHz. The difference from the much sharper frequency dependence observed in globally measured spectra is expected: the global measurements are sensitive to phonon-mediated electronic correlations across the entire device, and should thus show a roll-off corresponding to the (inverse) sample traversal time ($v_s/L \sim$ GHz). The NV, on the other hand, is primarily sensitive to correlations that occur within its $\sim 50 \times 50$ nm^2 sampling area. Thus, the NV centers are expected to observe a significantly higher frequency cut-off ($v_s/d_{\text{NV}} > 100$GHz) and very weak spectral dependence around 2.87 GHz.

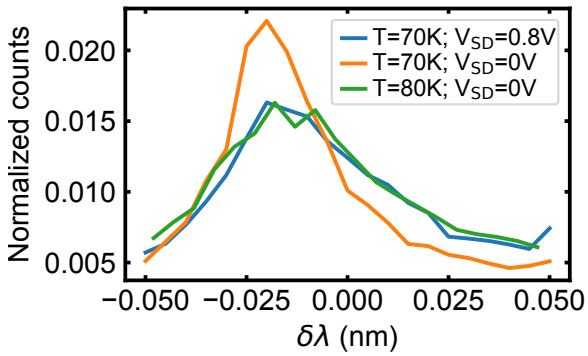


Figure C.18: Lattice heating during NV measurements. Scans of the optical line of an NV center located below device C2. The NV center zero phonon line is broadened by approximately the same amount when a high bias is applied (blue) as when the bath temperature is increased by 10 K at zero bias (green), suggesting that the increase in temperature near the NV during device operation is approximately 10 K. $\delta\lambda$ is approximate and is inferred from cavity piezo voltage and laser manufacturer's specifications (New Focus Velocity 6300). Center wavelength corresponds to ~ 637.4 nm.

When large source-drain voltages are applied to the device, a significant amount of power is dissipated ($\sim$5 mW). Since the relaxation rate of an NV center is temperature-dependent, it is important to consider the temperature change of the diamond lattice from this power dissipation. This can be done by measuring the linewidth of the NV zero-phonon line, which is very sensitive to temperature and scales with T^5 [111]. We measure the fluorescence of an NV center as a function of excitation wavelength and find a slight change in linewidth for the highest applied biases (Fig. C.18). By heating the cryostat from 70 to 80 K, we achieve a similar level of broadening at zero bias. This shows that the bias-induced increase in the diamond temperature near the NV is very small ($\sim$ 10 K), consistent with the high thermal conductivity of diamond. Since the spin relaxation rate is proportional to T in the regime considered here[262], and the intrinsic spin relaxation rate was measured to be very low (<0.2 Hz), this slight temperature increase should have a negligible effect compared to the high levels of noise from the graphene. Moreover, the clear gate dependence observed at con-

stant power (section C6.4) further shows that the increased spin relaxation rate is due to noise from the graphene. Nevertheless, to keep the diamond temperature as constant as possible, we lowered the cryostat base temperature by 10 K while measuring at the highest biases.

C6.4 Local doping dependence

By focusing on a single NV center and measuring its relaxation rate while sweeping the topgate voltage, we map out the charge density dependence of the Cerenkov noise on the nanoscale (Fig. *C*.19). As with the current dependence, the anomalous noise is only observed when the charge carrier sign is such that the NV center is downstream with respect to the carrier flow. These measurements were done at constant power, so the drift velocity increases with doping level, leading to an abrupt increase in noise once the Cerenkov condition is satisfied.

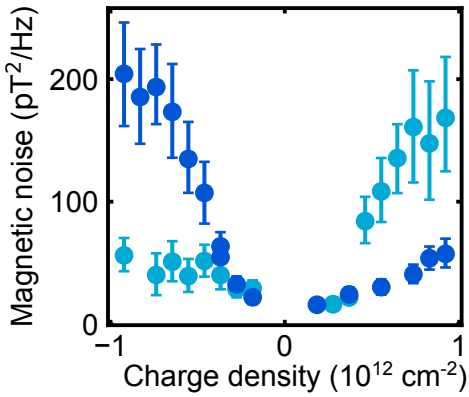


Figure C.19: Doping dependence of local magnetic noise. Locally probed magnetic noise as a function of graphene charge density. Light and dark blue points represent positive and negative source-drain current, respectively. The bias power was kept constant at 1.4 ± 0.1 mW.

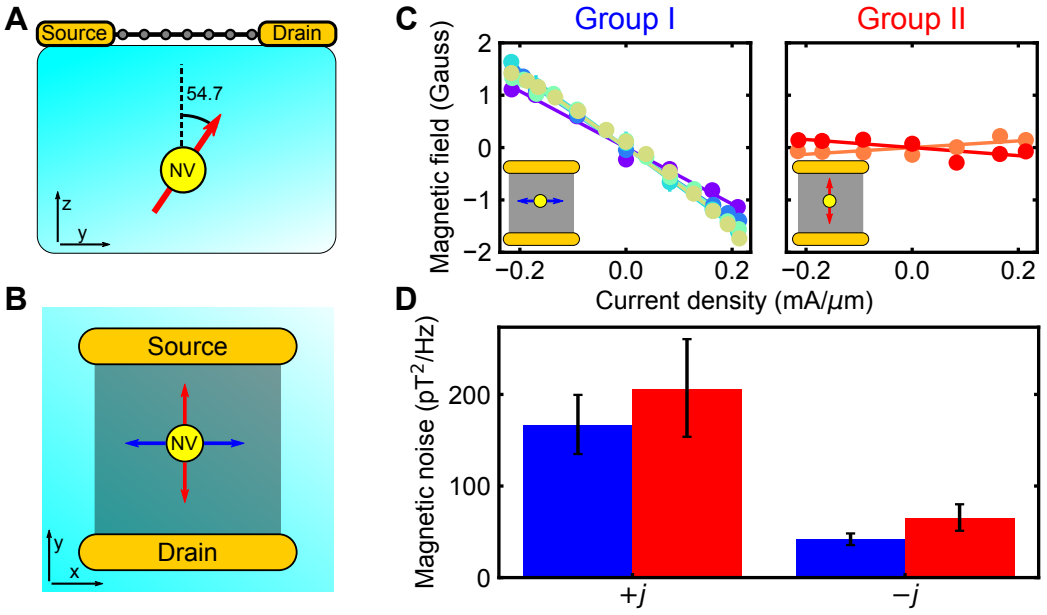


Figure C.20: NV center orientation. (**A**) NV center orientation with respect to diamond surface. (**B**) Projection of the four possible NV axes onto the device plane. Our device is closely aligned along two of the projections, giving rise to two distinctive groupings of NV centers: those with xy-projections that are perpendicular to current flow (group I, blue) and those with xy-projections parallel to current flow (group II, red). (**C**) DC field measurements. Group I NVs measure a significant current-induced magnetic field, while group II NVs do not. (**D**) Relaxation rates of NVs in group I (blue) and II (red). The noise sensed by nearby NVs from different orientation groups is similar, despite measuring very different DC magnetic fields. $|j| = 0.2$ mA/μm, $n = 0.92 \times 10^{12}$ cm^{-2}.

Our diamond samples were all cut such that the devices are fabricated on the (100) surface. The diamond crystal structure entails that each NV axis (the vector connecting nitrogen and vacancy sites) points in one out of four directions. The four possible NV axes all make the same angle $\sim 54.7°$ with the surface normal vector (Fig. *C*.20A), but have four different projections onto the xy-plane (Fig. *C*.20B). We align our devices to be parallel with the xy-projection of two axes (red, group II), and perpendicular to the other two (blue, group I) (Fig. *C*.20B). The NV centers can be used to sense DC currents by measuring the Zeeman splitting of the $m_s = \pm 1$ states, $2\gamma_e B_{||}(I)$, where

$B_{||}$ is the projected field onto the NV-axis[240]. Thus, aligning our devices in this way enables us to determine the NV groupings by measuring the DC current response. When flowing a source-drain current through the device, the magnetic field projection onto group I is large, but nearly zero for group II, as shown in Fig. *C*.20C. We also note that the consistency of the field measured by group I NVs suggests that the current is very uniform. In section C6.6, we comment on a few NVs that showed discrepancy.

Spin relaxation, on the other hand, is determined by the *perpendicular* component of the noise on the NV axis, which should in principle allow for observing effects of anisotropic noise. However, we do not observe a significant difference in relaxation rates under driven graphene for nearby NVs in different orientation groups (Fig. *C*.20D), suggesting that the induced noise is relatively isotropic.

C6.6 DC MEASUREMENTS OF LOCAL CURRENT DISTRIBUTION

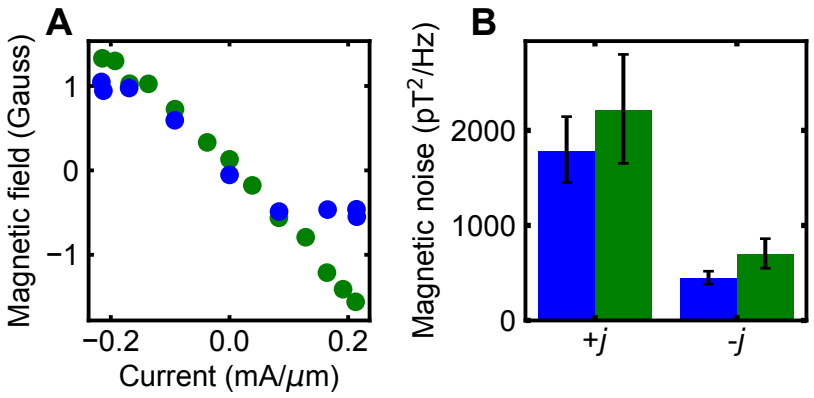


Figure C.21: DC and AC current measurements. (**A**) DC current response of two NVs located a similar distance from the source electrode. While one of the NVs shows the expected linear local field dependence on global current (green), the other shows non-linear behavior at high drives (blue). (**B**) Local noise measurements for same NVs as in (**A**). Noise measurements taken at $|j| = 0.2$ mA/μm, $n = 0.92 \times 10^{12}$ cm^{-2}.

Our devices are not implanted at a high density, which precludes vector reconstruction of the DC current distribution at all points, but the NV density is high enough to measure general trends.

Overall, we observe that the DC magnetic field shift of the NV centers is uniform and consistent with the applied global current density (Fig. *C*.20C). However, we observe some small departures at discrete locations that are likely due to local disorder. Current imaging in graphene samples has shown that edges, folds, and defects can cause the current density to vary across the sample[353]. At these locations in our samples, the field sensed by the NV is not linear in the applied current: at some threshold current density, the slope of the current-field curve changes (Fig. C.21A, blue). We emphasize that this non-linear behavior is not expected to be related to the anomalous noise effects described in the main text, since it is only observed in a few discrete locations. This is further supported in Fig. C.21B, where we show that two NVs at similar distances from the source electrode both show the asymmetric noise behavior, despite their different DC current profiles. As expected, the outlier NV that measures a lower local current than the global average also measures slightly less noise. Along with variations in NV depth, such discrete discrepancies in local current may have caused some of the departures from the overall trends observed in 4.9D-E in the main text.

C7 Theory

We here present the theoretical model used to describe the electron-phonon dynamics observed in our experiment, inspired by Refs.[280,334,198,398]. In section C7.1, we motivate and introduce a modified Drude model that evolves the coupled electronic current and phonon population in both space and time. Two important components of this model are the rates of (net) phonon emission and decay, which we discuss in sections C7.2 and C7.3, respectively. In section C7.4, we use the model to demonstrate the importance of the phonon traversal time on electronic response, and derive a new expression for the AC conductivity spectrum during Cerenkov amplification. In section C7.5, we explain the connection between global noise and phonon fluctuations, and then proceed to theoretically predict the dependence of global noise on charge density (section C7.6). Finally, we consider

the local current fluctuations, and show that these depend predominantly on the *local* phonon population (section C7.7).

C7.1 Coupled electron-phonon dynamics

The dynamics of our system could in principle be modeled by a complete Boltzmann treatment of both electronic and phononic degrees of freedom. However, at the high electronic temperatures reached in our experiments, rapid e-e collisions ensure that the electronic system reaches local equilibrium at much shorter timescales (< 1ps) than those probed here. Therefore, a full Boltzmann framework is not necessary, and we can instead represent the electronic system by the three variables governing its equilibrium distribution. These include the electronic temperature T_e, charge density n, and drift velocity v_D. The electrostatic gate keeps the charge density spatially uniform, and we shall assume that the effects of variations in electronic temperature are negligible as well. Indeed, the temperature profile has been found to be relatively uniform in the high-bias regime [108,135], and temperature-induced changes in chemical potential are suppressed in the degenerate regime ($\mu \gg k_B T_e$). Moreover, we show in section C7.2 that the net phonon emission rate is only weakly dependent on electronic temperature. In order to connect our theory to measured quantities, we will often refer to the current density $j = nev_D$ instead of the drift velocity. We do not make the same equilibrium assumption about the phononic system, and will treat each phonon mode separately.

Our model then takes the form of a modified Drude formula, which explicitly accounts for the dependence of the electronic scattering rate Γ_e on the phonon population $\{n_q\}$:

$$\partial_t j(r,t) = DE(r,t) - \Gamma_e(\{n_q\}) \cdot j(r,t) \tag{C.10}$$

$$\partial_t n_q = -\frac{\left(n_q - n_{q,0}\right)}{\tau_q} + \gamma_q^{\text{em}}(j)\left(n_q + 1\right) - \gamma_q^{\text{abs}}(j) \cdot n_q - v_s \hat{q} \cdot \nabla n_q$$

$$= \overbrace{\left(\gamma_q^{\mathrm{em}}(j) - \gamma_q^{\mathrm{abs}}(j) - \tau_q^{-1}\right)}^{\equiv \Gamma_q^{\mathrm{amp}}(j)} \cdot n_q + n_{q,0}\tau_q^{-1} + \gamma_q^{\mathrm{em}}(j) - v_s \hat{q} \cdot \nabla n_q \tag{C.11}$$

where $D = 2e^2 v_F k_F / h$ is the Drude weight of graphene, $E(r,t)$ is the electric field, τ_q^{-1} is the (q-dependent) phonon decay rate, v_s is the speed of sound, and $n_{q,0}$ is the phonon population at $j = 0$. γ_q^{em} and γ_q^{abs} are the stimulated emission and absorption rates per phonon (calculated in section C7.2). In the derivations shown here, the only assumptions made about the electronic scattering rate Γ_e are 1) that it depends on the phonon population n_q, and 2) that we can use an average electronic lifetime to write equations for the current. Both of these assumptions are well supported in the literature [168,180,340], and can simply be thought of as a phonon-dependent resistance. Although not used explicitly here, the specific form of $\Gamma_e(\{n_q\})$ can be found in Refs. [168,180,340].

In our experiment, we apply a DC voltage across the device (in addition to a weak AC excitation in conductivity measurements), and we will define $\hat{x}$ to point along the applied field. Since the electric field is uniform in the transverse ($\hat{y}$) direction, the steady state current $\langle j \rangle = \langle j \rangle \hat{x}$ and phonon occupation $\langle n_q \rangle$ are too. (Here, and in what follows, we use $\langle\rangle$ to refer to temporal averages). Moreover, the high energy cost of local charge buildup entails that $\langle j \rangle$ is divergence-free and thus independent of x as well. We emphasize therefore that $\langle j \rangle$ is an entirely global property of the sample.

The phonon occupation, on the other hand, will change along the sample due to the convective term in eqn. *C*.11. We find the steady state spatial profile $\langle n_q(x) \rangle$:

$$\langle n_q(x) \rangle = n_{q,0} e^{\langle \Gamma_q^{\mathrm{amp}} \rangle x / v_q} + \frac{1}{\langle \Gamma_q^{\mathrm{amp}} \rangle \tau_q} \left(n_{q,0} + \tau_q \langle \gamma_q^{\mathrm{em}} \rangle \right) \left(e^{\langle \Gamma_q^{\mathrm{amp}} \rangle x / v_q} - 1 \right) \tag{C.12}$$

where $v_q = v_s \hat{q} \cdot \hat{x}$. Clearly, the phonon population increases exponentially through the sample for wavevectors q that have $\Gamma_q^{\mathrm{amp}} > 0$. This is the expression plotted in 4.9D in the main text. Since we expect the measured local current noise to be due to local fluctuations in phonon emission (section

C7.7), which is a Poissonian process, it should scale with the (local) mean emission rate. The latter is proportional to n_q, so the current noise profile should be representative of the spatial distribution of phonons. Seeing as the most amplified modes dominate strongly in long samples like the one shown in 4.9D ($L = 17\mu$m), we plot $n_q(x)$ for the most amplified mode. Including background effects (thermal noise and intrinsic NV decay), we find that the current noise should be of the form $\langle \delta I^2 \rangle(x) = A + Be^{\Gamma_{\max}^{\text{amp}} x/v_s}$. In Fig. *C*.22, we show that integrating over all modes gives a similar result, due to the dominance of the most amplified modes.

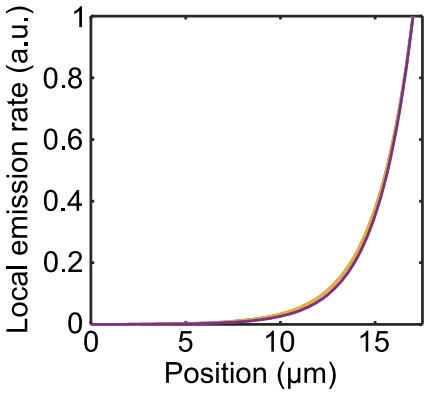


Figure C.22: Spatial dependence. Normalized local emission rate of most amplified mode ($\Delta\gamma_q n_q(x) \propto n_q(x)$, purple), and integrated over phonon modes (yellow), for the parameters used in 4.9D in the main text ($j = 0.18\text{mA}/\mu\text{m}$, $n = 0.92 \times 10^{12}\text{cm}^{-2}$, $\Gamma_{\max}^{\text{amp}} = 10.9$ GHz). Due to the dominance of the most amplified modes, the two curves are very similar. The purple curve has a slightly sharper upturn due to the higher amplification rate.

Finally, we note that eqn. *C*.12 breaks down for $\hat{q}$ with large transverse components, due to the finite width of our samples. The treatment of these modes is discussed further in the end of section C7.4.

C7.2 Phonon emission rate

In order to determine the net emission rate $\Delta\gamma_q = \gamma_q^{\text{em}} - \gamma_q^{\text{abs}}$ of a phonon mode with wavevector q, we sum over all electronic transitions accompanying the emission/absorption event:

$$\Delta\gamma_q = \gamma_q^{\text{em}} - \gamma_q^{\text{abs}} =$$

$$\frac{2\pi N}{\hbar}\sum_{k,k'}|C_{k,k',q}|^2\left(f_k(1-f_{k'})-f_{k'}(1-f_k)\right)\cdot\delta_{k-k',q}\cdot\delta(E_k-E_{k'}-\hbar v_{\text{s}}|q|) \tag{C.13}$$

where the first term represents an electron moving from k to k' while emitting a phonon, and the second represents an electron moving from k' to k while absorbing a phonon. Here, v_{s} is the speed of sound, $N = 4$ is the number of valley/spin flavors, $E_k = \hbar v_{\text{F}}|k|$ is the electron energy, $f_k = (e^{\beta(\hbar(v_{\text{F}}|k|-k\cdot v_{\text{D}})-\mu)}+1)^{-1}$ is the drifting Fermi-Dirac distribution with drift velocity v_{D}, and $|C_{k,k',q}|^2$ is the deformation potential coupling matrix element [180,168,340]:

$$|C_{k,k',q}|^2 = \frac{D^2\hbar q}{2\rho A v_{\text{s}}}\cos^2(\theta_{k,k'}/2) \tag{C.14}$$

Here, D is the deformation potential, ρ is the (2D) mass density, A is the sample area, and $\theta_{k,k'}$ is the angle between k and k'.

At zero drift velocity, f_k is simply a (decreasing) function of E_k, and one therefore finds that every term in eqn. *C*.13 is negative. At higher v_{D}, however, the Fermi surface becomes tilted (Fig. *C*.23A), causing higher-energy states on one side of the Dirac cone to have higher occupation than lower-energy states on the other side. In order to achieve positive terms in eqn. *C*.13, the Fermi surface must become steeper than the phonon-assisted transitions (red arrow), which gives the Cerenkov criterion, $v_{\text{D}} > v_{\text{s}}$. We here emphasize that this phenomenon is very different from the effects of

high electronic temperatures. While the latter allows for the probabilistic occupation of higher-energy states, the mean occupation is still a decreasing function of energy, causing $\Delta\gamma$ to remain negative.

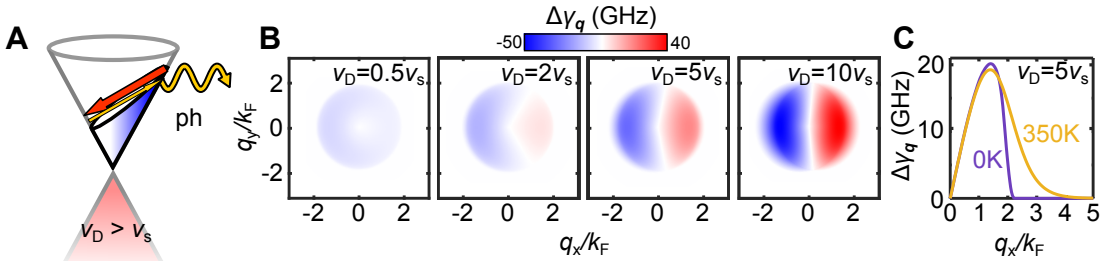


Figure C.23: Onset of Cerenkov emission. (**A**) Cartoon showing Cerenkov criterion for graphene. When $v_D > v_s$, the electronic population becomes inverted with respect to phonon-induced transitions. As a result, the phonon emission rate (red arrow) becomes greater than the absorption rate (yellow arrow). (**B**) Net emission rate $\Delta\gamma_q$ vs. phonon wavevector q at various electronic drift velocities $v_D = v_D\hat{x}$, $n = 2\times10^{12}\mathrm{cm}^{-2}$ and zero electronic temperature. Once the drift velocity exceeds the speed of sound ($v_s = 21\mathrm{km/s} = 0.021\mathrm{v_F}$), we find regions of phononic phase space where $\Delta\gamma_q > 0$ (red), indicating that stimulated emission dominates over absorption. This effect is strongest for the phonon modes moving along the current ($q||\hat{x}$). The circle sector in which the amplification criterion is satisfied becomes wider as the drift velocity increases, and eventually saturates as a semi-circle. (**C**) Line cut along $q_y = 0$ for electronic temperatures $T_e = 0$ K and 350 K at $v_D = 5v_s\hat{x}$.

Fig. *C*.23B shows the numerically calculated net emission rate at various electronic drift velocities, using deformation potential $D = 20$ eV. When the drift velocity exceeds the speed of sound, stimulated emission dominates over absorption ($\Delta\gamma > 0$) for a cone in phonon phase space moving along with the carrier flow. We find that the highest net emission rate exceeds 5 GHz already at $v_D = 2v_s$, and increases all the way up to 40 GHz at $v_D = 10v_s$. The net emission rates greatly exceeds the rate of phonon decay (section C7.3), as such $\Gamma_q^{amp} > 0$ and phonon Cerenkov amplification is predicted to occur.

At zero temperature, phonon amplification occurs for modes with wavevectors up to $2k_F$, cor-

responding to electronic transitions across the entire Fermi surface. As expected, this upper bound is found to be less sharp at higher temperatures (Fig. *C*.23C). However, the region near the peak (which dominates after nonlinear amplification) is relatively insensitive to electronic temperature, since absorption and stimulated emission change by a similar amount.

Finally, we note that a different coupling rate may result from considerations of a gauge potential coupling[235]. However, we expect this to only modify the scale of the coupling rate, and to result in even higher emission rates. In particular, it should not change the qualitative behavior of net stimulated emission when $v_D > v_s$.

C7.3 Phonon decay rate

As explained in Refs.[261,195,306], the acoustic phonon decay rate τ_q^{-1} in graphene becomes very slow at low temperatures, especially for the small phonon energies relevant in our experiment ($\sim$ THz). Indeed, this is one of the main reasons graphene has such an exceptional thermal conductivity[18]. Here, we discuss the three types of decay pathways considered in Ref.[261] for the relevant phonon modes, in order to demonstrate that Cerenkov amplification can easily occur ($\Delta\gamma_q > \tau_q^{-1}$) at the drift velocities reached in our experiment. Since the decay rate is found to be very small compared to $\Delta\gamma$, we emphasize that our fits depend only very weakly on the exact numerical value of the decay rate.

First, we shall consider point-defect scattering, given by $\gamma^{PD} = S_0\omega^3/(v_s^2)\cdot\sum_i p_i(1 - M_i/\overline{M})^2$[337], where S_0 is the atomic cross-sectional area and $\bar{M}$ is the average atomic mass. p_i and M_i are the percentage and atomic mass of defect type i. Considering the contribution from the 1% natural abundance of ^{13}C, one finds $\gamma^{PD} \sim 1.5$MHz at $\omega = 5$ THz, which is clearly much smaller than $\Delta\gamma$. Due to the low impurity content in our exfoliated graphene samples, we do not expect significantly larger contributions from other defect types.

We then proceed to consider anharmonic decay, where our mode of interest interacts with two

other modes, with wavevectors q' and q'', and energies ω' and ω''. These processes can be divided into two types, based on the hierarchy of the three phonon energies: I) $\omega'' > \omega, \omega'$, and II) $\omega > \omega', \omega''$. Following Ref.[261], the rate of the two processes are given by:

$$\gamma_q^{\mathrm{I}} = \frac{2\pi}{\hbar} \sum_b \sum_{s',s''} \sum_{q',q''} |C_{\omega,\omega',\omega''}|^2 \left[n(\omega') - n(\omega'') \right] \delta(\omega'' - \omega - \omega) \delta_{q'',q'+q'+b} \tag{C.15}$$

$$\gamma_q^{\mathrm{II}} = \frac{2\pi}{\hbar} \sum_b \sum_{s',s''} \sum_{q',q''} |C_{\omega,\omega',\omega''}|^2 \left[n(\omega') + n(\omega'') + 1 \right] \delta(\omega - \omega' - \omega'') \delta_{q,q'+q''+b} \tag{C.16}$$

where b is a lattice vector. Non-zero b correspond to Umklapp scattering, where total phonon momentum is not conserved. At the low temperatures and small q considered here, normal processes ($b = 0$) are expected to dominate strongly, so we consider only these. While these do not reduce thermal conductivity (since they conserve momentum), they are still expected to affect Cerenkov amplification, since they can scatter phonon modes out of the amplified region of phononic phase space. s' and s'' represent the branches that our mode interacts with; as shown in Ref.[261], the small-q LA modes considered here are expected to predominantly interact with TA and LA modes in our hBN-encapsulated devices. $n(\omega)$ is the phonon distribution function. Since only a small part of the total phonon phase space experiences Cerenkov amplification, we here assume that the amplified modes mainly interact with non-amplified modes that remain close to thermal equilibrium. We therefore set $n(\omega)$ to be the Bose-Einstein distribution $n(\omega) = \left(e^{\beta\hbar\omega} - 1\right)^{-1}$ at bath temperature ($\beta = (k_{\mathrm{B}} T_{\mathrm{bath}})^{-1}$). Finally, $|C_{\omega,\omega',\omega''}|^2$ is the coupling matrix element:

$$|C_{\omega,\omega',\omega''}|^2 = \frac{2\gamma_{\mathrm{G}}^2 \omega\omega'\omega''\hbar}{3\rho v_{\mathrm{s}}^2 A} \tag{C.17}$$

where γ_{G} is the Gruneisen parameter. γ_{G} is in principle mode-dependent, but we have here replaced

it with an average value ($\gamma_G = 2$), as often done in the literature. As before, ρ is the (2D) mass density, and A is the device area, which we note is canceled out when turning the sum over wavevectors into an integral.

We plot $\gamma_q^{\mathrm{I}} + \gamma_q^{\mathrm{II}}$ for a relevant range of phonon wavevectors in Figure C.24, and find that these decay rates are faster than γ^{PD}, but still much slower than typical values of $\Delta\gamma$.

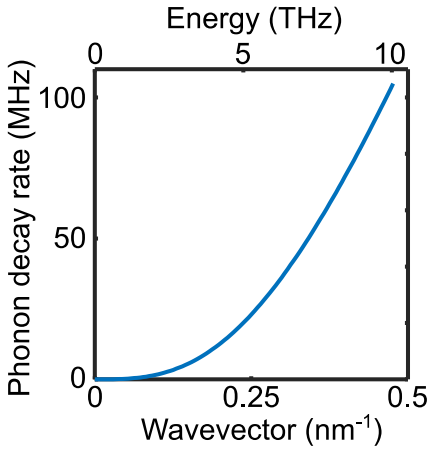


Figure C.24: Phonon decay rate. Phonon decay rate (calculated from eqns. C.15 and C.16) versus phonon wavevector q and energy $v_s q$.

The third decay pathway that we shall discuss is scattering off the rough device edges. Indeed, we assume that the phonons decay when they have traversed the sample and reach the sample edge. This is not only due to the absorption at the edge, but also because the reflected (backwards-moving) modes are no longer in the amplified region of phonon phase space, and are thus quickly absorbed by the electronic system. Phonon amplification is strongest for modes moving at small angles with the source-drain axis, and the emission of these is expected to impact the current most strongly due to the large momentum transfer in the direction of current. Nevertheless, in section C7.4, we discuss the treatment of modes that move at large enough angles to hit the side edges before traversing the whole device.

C7.4 AC conductivity

In order to find the AC conductivity, we consider the current response to a voltage $V(t) = V_0 + \delta V e^{i\omega t}$.

Since we are now concerned with only the field-induced (not stochastic) fluctuations, we can apply our argument about $\langle j \rangle$ and $\langle n_q \rangle$ (section C7.1) to the fluctuations δj and δn_q as well. In other words, we have the simplifications $\delta j(r,t) = \delta j(t)\hat{x}$ and $\delta n_q(r,t) = \delta n_q(x,t)$, and can thus treat this as a 1D problem.

Since n_q (and thus the scattering rate $\Gamma_e(\{n_q\})$) can vary with x, the electric field $E = \left(E_0(x) + \delta E(x) e^{i\omega t}\right)\hat{x}$ can too. Analogously to a series of resistors, the applied potential difference is divided unequally across the resistors if they do not have the same resistance. Fortunately, this does not affect us for now, because we can only measure the *global* AC conductivity anyway:

$$\sigma = \frac{\delta j}{\delta V / L} = \frac{\delta j}{\frac{1}{L}\int_0^L \delta E(x) dx} = \frac{1}{\frac{1}{L}\int_0^L \sigma^{-1}(x) dx} \tag{C.18}$$

where L is the length of the device. This is nothing but the spatially averaged conductivity (in reciprocal), and is completely equivalent to adding resistors in series. In order to make any sensible comparison with experiment, we should therefore integrate equation *C*.10 over x:

$$\partial_t j = \frac{DV(t)}{L} - \overbrace{\frac{1}{L}\int_0^L \Gamma_e\left(\{n_q(r,t)\}\right) dx}^{\overline{\Gamma_e}} \cdot j(t) \tag{C.19}$$

Here, and in what follows, barred quantities are spatially averaged, while brackets $\langle\rangle$ are used for temporal averages.

The oscillating parts of n_q and j then evolve according to:

$$i\omega\delta j(\omega) = \frac{D\delta V(\omega)}{L} - \overline{\langle\Gamma_e\rangle}\delta j(\omega) - \sum_q \overline{\left(\frac{\partial\Gamma_e}{\partial n_q}\cdot\delta n_q(x,\omega)\right)\langle j\rangle} \tag{C.20}$$

$$\begin{aligned} i\omega\delta n_q(x,\omega) = &\overbrace{\left(\langle\gamma_q^{em}\rangle - \langle\gamma_q^{abs}\rangle - \langle\tau_q^{-1}\rangle\right)}^{\langle\Gamma_q^{amp}\rangle}\cdot\delta n_q(x,\omega) + \\ &\frac{\partial\Gamma_q^{amp}}{\partial j}\cdot\delta j(\omega)\langle n_q(x)\rangle + \overbrace{\frac{\partial\gamma_q^{em}}{\partial j}\delta j(\omega)}^{\text{Spont. emission}} - v_s\hat{q}\cdot\hat{x}\partial_x\delta n_q(x,\omega) \end{aligned} \tag{C.21}$$

Since both absorption and stimulated emission of phonons are linear processes, we shall assume that Γ_e is linear in n_q, and can therefore write:

$$\overline{\left(\frac{\partial\Gamma_e}{\partial n_q}\cdot\delta n_q(x,\omega)\right)} = \frac{\partial\Gamma_e}{\partial n_q}\cdot\overline{\delta n_q(x,\omega)} \tag{C.22}$$

Moreover, we note that although we use Γ_q^{amp}, our treatment also applies to the non-amplifying case ($\Gamma_q^{amp} < 0$). For now, we shall focus on phonon modes that move in parallel with the current ($q||\hat{x}$). We will discuss the inclusion of larger-angle modes in the end of this section.

We can immediately solve for $\delta n_q(x,\omega)$ in terms of $\delta j(\omega)$:

$$\delta n_q(x,\omega) = v_s^{-1}\delta j(\omega)\int_0^x\left(\frac{\partial\Gamma_q^{amp}}{\partial j}\cdot\langle n_q(x')\rangle + \frac{\partial\gamma_q^{em}}{\partial j}\right)e^{\left(\langle\Gamma_q^{amp}\rangle - i\omega\right)(x-x')/v_s}dx' =$$

$$\left[\frac{C}{i\omega}e^{\langle\Gamma_q^{amp}\rangle x/v_s} + \frac{i\omega B - \langle\Gamma_q^{amp}\rangle C}{i\omega\left(\langle\Gamma_q^{amp}\rangle - i\omega\right)}e^{\left(\langle\Gamma_q^{amp}\rangle - i\omega\right)x/v_s} + \frac{C-B}{\langle\Gamma_q^{amp}\rangle - i\omega}\right]\delta j(\omega) \tag{C.23}$$

where

$$B = \frac{\partial\Gamma_q^{amp}}{\partial j}\cdot n_{q,0} + \frac{\partial\gamma_q^{em}}{\partial j} \tag{C.24}$$

$$C = \frac{\partial \Gamma_q^{\text{amp}}}{\partial j} \cdot \left(n_{q,0} + \frac{n_{q,0}}{\langle \Gamma_q^{\text{amp}} \rangle \tau_q} + \frac{\langle \gamma_q^{\text{em}} \rangle}{\langle \Gamma_q^{\text{amp}} \rangle} \right) \tag{C.25}$$

Before we can plug this back into the equation for δj, we need to calculate the spatial average:

$$\overline{\delta n_q(\omega)} = \frac{1}{L} \int_0^L \delta n_q(x, \omega) dx =$$

$$\overbrace{\left[\frac{C}{i\omega t_{\text{T}} \langle \Gamma_q^{\text{amp}} \rangle} \left(e^{\langle \Gamma_q^{\text{amp}} \rangle t_{\text{T}}} - 1 \right) + \frac{i\omega B - \langle \Gamma_q^{\text{amp}} \rangle C}{i\omega t_{\text{T}} \left(\langle \Gamma_q^{\text{amp}} \rangle - i\omega \right)^2} \left(e^{\left(\langle \Gamma_q^{\text{amp}} \rangle - i\omega \right) t_{\text{T}}} - 1 \right) + \frac{C - B}{\langle \Gamma_q^{\text{amp}} \rangle - i\omega} \right]}^{\tilde{\chi}(q,\omega)} \delta j(\omega) \tag{C.26}$$

where $t_{\text{T}} = L/v_{\text{s}}$ is the sample transit time. We have here introduced the phonon-current response function $\tilde{\chi}(q, \omega)$, defined through $\overline{\delta n_q(\omega)} = \tilde{\chi}(q, \omega) \delta j(\omega)$. Inserting this expression back into our expression for $\delta j(\omega)$, we find:

$$\sigma(\omega) = \frac{L \delta j(\omega)}{\delta V(\omega)} = \frac{D}{i\omega + \langle \Gamma_{\text{e}} \rangle + \sum_q \frac{\partial \Gamma_{\text{e}}}{\partial n_q} \tilde{\chi}(q, \omega) \langle j \rangle} \tag{C.27}$$

As expected, we retrieve the original Drude result if the phonons do not respond to the current ($\tilde{\chi}(q, \omega) = 0$), or the scattering rate does not depend on the phonon occupation ($\frac{\partial \Gamma_{\text{e}}}{\partial n_q} = 0$). We note that so far, no mathematical approximations have been made.

Expression *C.27* has a clear intuitive motivation. A fluctuation $\delta j(\omega)$ will not only decay due to $\langle \Gamma_{\text{e}} \rangle$, but also cause a change in phonon population δn_q, which changes the scattering rate $\delta \Gamma_{\text{e}}(\omega)$:

$$\delta \Gamma_{\text{e}}(\omega) = \frac{\partial \overline{\langle \Gamma_{\text{e}} \rangle}}{\partial j} \delta j(\omega) = \sum_q \frac{\partial \langle \Gamma_{\text{e}} \rangle}{\partial n_q} \frac{\partial \overline{n_q}}{\partial j} \delta j(\omega) = \sum_q \frac{\partial \langle \Gamma_{\text{e}} \rangle}{n_q} \tilde{\chi}(q, \omega) \delta j(\omega) \tag{C.28}$$

Let's now consider the low-frequency regime ($\omega \ll \Gamma_{\text{e}} \sim$ THz), in the case where certain

phonon modes are amplified strongly ($e^{\Gamma^{\text{amp}} t_{\text{T}}} \gg 1$). For these modes, the response function $\tilde{\chi}(q,\omega)$ simplifies to:

$$\tilde{\chi}(q,\omega) = \frac{C}{i\omega t_{\text{T}} \langle \Gamma_q^{\text{amp}} \rangle} e^{\langle \Gamma_q^{\text{amp}} \rangle t_{\text{T}}} \left(1 - e^{-i\omega t_{\text{T}}}\right) \tag{C.29}$$

Since the strongly amplified modes will have the dominant impact on the AC conductivity, we can apply the above simplifications to all the terms in the sum over q in eqn. *C*.27. We then find:

$$\boxed{\sigma^{\text{Cerenkov}}(\omega) = \frac{D}{\langle \Gamma_{\text{e}} \rangle + \sum_q \frac{\partial \Gamma_{\text{e}}}{\partial n_q} \langle j \rangle \frac{C}{i\omega t_{\text{T}} \langle \Gamma_q^{\text{amp}} \rangle} e^{\langle \Gamma_q^{\text{amp}} \rangle t_{\text{T}}} \left(1 - e^{-i\omega t_{\text{T}}}\right)} = \frac{\sigma^{\text{Drude}}(0)}{1 + \frac{K}{i\omega t_{\text{T}}} \left(1 - e^{-i\omega t_{\text{T}}}\right)}} \tag{C.30}$$

where $\sigma^{\text{Drude}}(0) = D/\langle \Gamma_{\text{e}} \rangle$ is the regular DC Drude conductivity. Since the contributions from all the amplified phonon modes show the same ω-dependence, we could conveniently factor out the sum over q and define a single dimensionless parameter K:

$$K \equiv \sum_q \frac{\partial \Gamma_{\text{e}}}{\partial n_q} \frac{\langle j \rangle C e^{\langle \Gamma_q^{\text{amp}} \rangle t_{\text{T}}}}{\langle \Gamma_q^{\text{amp}} \rangle \langle \Gamma_{\text{e}} \rangle} \tag{C.31}$$

As mentioned above, expression *C*.30 was derived for phonon modes moving in the x-direction. Other phonon modes moving at an angle θ with the x-axis have different traversal times $t_{\text{T}}(\theta) = L/(v_{\text{s}} \cos\theta)$, and are thus expected to dampen the oscillations in $\sigma(\omega)$. Indeed, we find that expression *C*.30 - although capturing the qualitative features of our data - overestimates the amplitude of the oscillations (top curve in Fig. *C*.25). To account for the spread in emission angles in 2D, we include more phonon modes in the second term of the denominator in eqn. *C*.30.

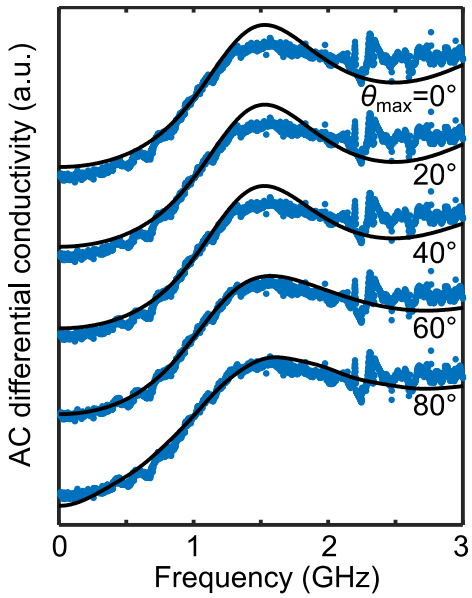


Figure C.25: Including angular spread of phonon emission. Blue: Measured AC differential conductivity spectrum at 0.8V bias and $n = 2 \times 10^{12}\mathrm{cm}^{-12}$ (identical data shifted to show multiple fits). Black curves: Fits by averaging the phonon emission angle up to varying $\theta_{\max}$. We find best agreement at $\theta_{\max} = 60°$.

The contribution of phonon modes at different angles depends not only on the θ-dependent K, but also on reflections from the side edges of our finite-sized devices. The latter depends on the specularity of the graphene edges. As a first approximation, we average over θ with equal weights up to a maximum angle $\theta_{\max}$, and already find improving agreement with the data (Fig. C.25). We find that $\theta_{\max} \sim 60°$ accounts for the spread in t_{T} well, and therefore use this value for fitting the data in the main text. Since this angle is slightly larger than $\tan^{-1}(L/W)$, it suggests that edge-reflection plays a small, but not insignificant role. We note that the reported extracted traversal time is the shortest $t_{\mathrm{T}}(\theta)$ in the average ($\min(t_{\mathrm{T}}(\theta)) = t_{\mathrm{T}}(\theta = 0)$), so that $t_{\mathrm{T}} = L/v_{\mathrm{s}}$ still holds.

In order to derive a more exact angular distribution, one could include the side edge reflection in the model, as well as other θ-dependent effects, including: 1) For a given $|q|$, the amplification rate Γ_{e} is maximized for $\theta = 0$ and decreases monotonically with increasing angle. 2) Modes with larger

θ take longer to traverse the sample, and are thus amplified for a longer time. 3) Phonons with large θ are expected to impact the current less than those moving in parallel with the current, since the large-angle modes remove less longitudinal momentum from the electronic population.

C7.5 Connection between global noise and phonon fluctuations

In order to relate the global noise to phonon fluctuations, we return to eqn. *C*.20, but now without an oscillating field, since only a DC field is applied in noise measurements:

$$i\omega\delta j(\omega) = -\overline{\langle\Gamma_e\rangle}\delta j(\omega) - \sum_q \overline{\left(\frac{\partial\Gamma_e}{\partial n_q}\cdot\delta n_q(x,\omega)\right)}\langle j\rangle \tag{C.32}$$

Note that we still operate with the spatially averaged phonon population $\overline{\delta n_q}$, since the global measurements are only sensitive to the uniform component of current fluctuations (other components do not contribute a net current).

Solving for the current fluctuations at low frequencies $\omega \ll \Gamma_e \sim$ THz and assuming that the phonon modes are independent, we then find:

$$\langle\delta^2 j(\omega)\rangle = \langle\overline{\Gamma_e}\rangle^{-2}\sum_q\left(\frac{\partial\Gamma_e}{\partial n_q}\right)^2\langle\overline{\delta n_q(\omega)}^2\rangle\langle j\rangle^2, \tag{C.33}$$

We here observe that the current fluctuations mimic the behavior of $\overline{\delta n_q}$ at low frequencies, which can be intuitively thought of as the current response to slow variations in the total device resistance. The phonon fluctuations are here given by:

$$\langle\overline{\delta n_q(\omega)}^2\rangle = \int_0^L\int_0^L\langle\delta n(x_1,\omega)\delta n(x_2,\omega)\rangle dx_1 dx_2 \tag{C.34}$$

Since an emitted phonon can keep stimulating emission of subsequent phonons as it moves

through the sample, we expect $\langle \overline{\delta n(t)} \cdot \overline{\delta n(t+\tau)} \rangle > 0$ for τ up to the traversal time t_T, causing roll-offs in both $\langle \overline{\delta n_q(\omega)}^2 \rangle$ and $\langle \delta^2 j(\omega) \rangle$ at low frequencies ($\lesssim 1/t_T$). We expect that the total phonon fluctuations (integrated over space and modes) to scale with the total emission rate, due to the Poissonian nature of phonon emission.

C7.6 Dependence of global noise on charge density

In order to understand the charge density dependence of phonon amplification, we need to consider the q-distribution of phonon emission (Fig. *C*.26A). At low q, the net emission rate $\Delta\gamma_q = \gamma_q^{em} - \gamma_q^{abs}$ increases with q, both because the electron-phonon coupling constant is linear in q, and because larger q permits more accompanying electronic transitions for phonon emission. However, the emission rate starts decreasing again when q approaches the maximum momentum transfer $2k_F(1 + v_D/v_F) \sim 2k_F$, corresponding to electronic transitions across the entire (shifted) Fermi surface.

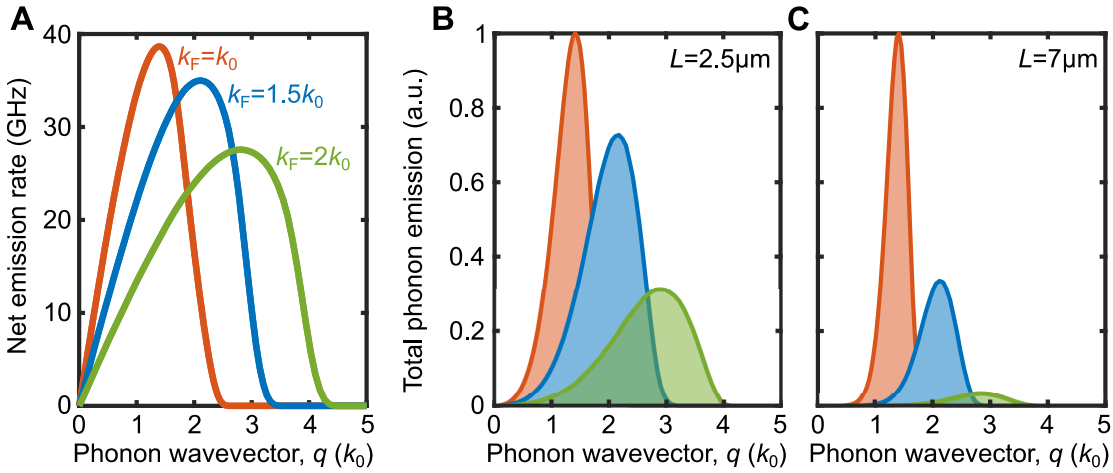


Figure C.26: Non-monotonic charge density dependence of phonon amplification. (**A**) The net emission rate $\Delta\gamma_q$ at constant current density $j = 0.6\text{mA}/\mu\text{m}$, for various k_F ($k_0 = 165\text{meV}/(v_\text{F}\hbar)$). The corresponding charge densities are $n = 2.1, 4.5$ and $8.0 \times 10^{12}\text{cm}^{-2}$, including the effect of the non-zero v_D on n. $\Delta\gamma_q$ becomes zero near $2k_\text{F}$. (**B**) The integrand of expression $C.35$, which is expected to be strongly related to the measured noise. The blue curve has the biggest area and thus corresponds to the highest expected noise, for device length $L = 2.5\mu\text{m}$. (**C**) Same as (B), but for $L = 7\mu\text{m}$. The longer device allows for more filtering, causing the noise to be maximized at a lower k_F (red curve).

When the charge density n is increased through electrostatic gating (red to blue to green curve in Fig. $C.26$A), this upper bound is shifted according to $k_\text{F} = \sqrt{\pi n}\cdot(1-(v_\text{D}/v_\text{F})^2)^{3/4}$. This causes a blue-shift of the amplified phonon population, and increases the number of amplified modes. At the same time, however, the amplitude of $\Delta\gamma_q$ decreases, because the drift velocity $v_\text{D} = j/(ne)$ decreases with n at constant current density. In other words, increasing n causes the emission spectrum to become wider, but smaller in magnitude. We shall see that the competition between these two effects cause a non-monotonic dependence on charge density.

As argued in the main text, the measured noise is expected to be due to the stochastic emission of phonons, and should scale with the total phonon emission rate due to the Poissonian nature. We

thus integrate the phonon generation rate over both space and phonon modes:

$$\int \int_0^L \Delta\gamma_q n_q(x) dx \cdot q dq \tag{C.35}$$

where the spatial profile $n_q(x)$ is given in eqn. *C*.12. We here integrate along the x-axis in q-space and account for the cone shaped emission pattern by weighting by q. This is the quantity plotted in Figure 4C in the main text.

We plot the integrand of the q-integral in eqn. *C*.35 in Fig. *C*.26B for $L = 2.5\,\mu$m, and observe that the area is maximized at an intermediate doping level (blue curve), as argued in the main text. At this cross-over point, one achieves an optimal balance between the width and height of the gain profile for this particular device length. We turn to a longer ($7\,\mu$m) sample in Fig. *C*.26C, and observe a more sharply peaked phonon spectrum. Intuitively, the longer device allows for more nonlinear amplification, which acts as an active filter centered at the most amplified phonon mode. This filtering effect skews the competition between the width and height of the gain profile. Since the most amplified modes strongly dominate in the longer device, it is more favorable to have a few modes with high amplification rate (red curve) than many weakly amplified modes (blue and green curves). Thus, the integrated phonon emission is maximized at a lower doping level in longer devices. Another consequence of this filtering effect is that the cross-over behavior is predicted to be sharper in longer devices. As shown in 4.11C in the main text, we find that our model agrees very well with the data, with regards to both the shifts and broadening of the cross-over peaks.

Since the cut-off at $q = 2k_F$ is less sharp at higher temperatures, it is expected that the non-monotonic behavior will have some dependence on the electronic temperature. The latter is expected to be elevated above the lattice temperature due to Joule heating. Using no other fit parameters, we find best agreement with our data at an electronic temperature of 320 K. In order to evaluate whether this value is reasonable, we compare with an upper bound corresponding to the

case where cooling only occurs through electronic conduction to the contacts. Using the thermal conductivity given by Wiedemann-Franz law and relevant bias voltages of $0.2 - 0.3$ V, we find temperatures of 340-500 K. Since in reality phonons also contribute to cooling, we expect that the electronic temperature should be somewhat lower than this. We thus consider the value used here to be reasonable. We finally note that the electronic temperature is expected to show some variation with charge density, which may explain the discrepancy between our model and the data at high charge densities.

C7.7 Local noise

The NV center measures magnetic noise due to local current fluctuations, which are intuitively expected to be determined by the local phonon fluctuations. However, if one considers the 1D case, where the current has to be constant along the whole device, one quickly finds this not to be the case. This comes from the fact that we can no longer integrate eqn. *C*.10 over the device length to remove local fluctuations in the electric field. A change in the resistance in one part of the device will thus affect the electric field in other parts of the device, due to the division of the bias potential along the device. Here, we show that this non-local effect is negligible in two dimensions, and that the local current fluctuations are indeed determined by the local phonon fluctuations.

We do this by dividing the sample into small squares of size corresponding to the NV sensing area, and then think of the sample as a grid of $N \times N$ resistors with resistance $R(x, y, t) \propto \Gamma_e(\{n_q(x, y, t)\})$. We here remind that Γ_e is the electronic scattering rate. The NV sampling dimension is approximately given by its depth $d_{\mathrm{NV}} \sim 50$nm, so the number of resistors $N^2 = A_{\mathrm{sample}}/A_{\mathrm{NV}} \sim 10^5$ is very large. We now switch to discretized subscripts instead of x and y to represent position, and consider an NV center located just below position (m, n) in the grid. The

current moving right above the NV center is then given by:

$$j_{mn} = \frac{j_{\text{tot}} R_m}{R_{mn}} \propto \frac{R_m}{R_{mn} R_{\text{tot}}} \tag{C.36}$$

$$R_{\text{tot}} = \sum_i R_i = \sum_i \left(\sum_j R_{ij}^{-1} \right)^{-1} \tag{C.37}$$

where the first subscript is the position along the current (x), and the second is in the transverse direction (y). When only one subscript i is used, it refers to the total cross-sectional resistance at $x = i$ ($R_i = 1/\sum_j R_{ij}^{-1}$). We see that all resistors affect the total current j_{tot}, but only resistors on the same transverse plane as the NV affect the portion of j_{tot} that goes through the NV sensing area. The local current fluctuations probed by the NV are then given by the sum:

$$\delta j_{mn} = \langle j_{mn} \rangle \left(-\frac{\delta R_{\text{tot}}}{\langle R_{\text{tot}} \rangle} + \frac{\delta R_m}{\langle R_m \rangle} - \frac{\delta R_{mn}}{\langle R_{mn} \rangle} \right) \tag{C.38}$$

There are thus three candidates for which resistors we have to consider, corresponding to the three terms above: 1) All of them, 2) The ones on the same transverse plane as the NV, or 3) Only the resistor at the NV location, R_{mn}. In order to determine which effect is larger, we for now assume that all resistors have the same rms fluctuations δR_{rms} and mean resistance R, so: $\langle R_{\text{tot}} \rangle = \langle R_{mn} \rangle =$

$N\langle R_m\rangle = R$. We then have:

$$
\begin{aligned}
&1)\ \frac{\partial R_{\text{tot}}}{\langle R_{\text{tot}}\rangle} = \frac{1}{R}\sum_{ij}\frac{\partial R_i}{\partial R_{ij}}\partial R = \frac{1}{R}\sum_{ij}\frac{R_i^2}{R_{ij}^2}\partial R = \sum_{ij}\frac{\partial R_{ij}}{N^2 R} \rightarrow \left(\frac{\partial R_{\text{tot}}}{\langle R_{\text{tot}}\rangle}\right)_{\text{rms}} = \frac{1}{N}\frac{\partial R_{\text{rms}}}{\langle R\rangle} \\
&2)\ \frac{\partial R_m}{\langle R_m\rangle} = \frac{N}{R}\sum_j \frac{\partial R_m}{\partial R_{mj}}\partial R_{mj} = \frac{1}{R_m}\sum_j \frac{R_m^2}{R_{mj}^2}\partial R_{mj} = \sum_j \frac{\partial R_{mj}}{NR} \rightarrow \left(\frac{\partial R_m}{\langle R_m\rangle}\right)_{\text{rms}} = \frac{1}{\sqrt{N}}\frac{\partial R_{\text{rms}}}{\langle R\rangle} \\
&3)\ \frac{\partial R_{mn}}{\langle R_{mn}\rangle} = \frac{\partial R_{mn}}{R} \rightarrow \left(\frac{\partial R_{mn}}{\langle R_{mn}\rangle}\right)_{\text{rms}} = \frac{\partial R_{\text{rms}}}{\langle R\rangle}
\end{aligned}
\tag{C.39}
$$

Assuming the phonon fluctuations at each site are independent, we find that the rms values of the three terms scale as $1/N$, $1/\sqrt{N}$ and 1, respectively. It is the parallel connections that prevent ∂R_{tot} and ∂R_m from simply scaling with the square root of the number of resistors involved. We thus only have to consider the phonon fluctuations right above the NV center to determine the local current fluctuations. We here stress that this is only the case for fluctuations; the mean local current depends on the total phonon population (all resistors in the grid).

This justifies our argument that the spatial current noise profile (4.9D in the main text) is representative of the *local* phonon fluctuations. Moreover, it is now clear that the NV center is only sensitive to correlations within its sampling area. This means that the locally measured fluctuations should have a frequency cut-off given by the inverse transit time of the NV sampling area ($v_s/d_{\text{NV}} \sim$ THz), not the total device, consistent with our observations in section C6.2.

C8 Alternative mechanisms

We include here an accounting of other known processes that may occur in highly biased graphene and comment on their inconsistency with our observations. By contrast, as shown in the main text,

the electron-phonon Cerenkov instability agrees very well with all of our observations.

C8.1 Optical phonon scattering

When biased to very large drift velocities, electrons in graphene can relax by emitting optical phonons, eventually leading to current saturation[245,76,275]. In particular, this behavior is often observed in devices fabricated directly on SiO_2, where the optical phonon energy is only $\sim$50 meV. The anomalous noise and conductivity features investigated in the main text are only observed in fully hBN-encapsulated devices, where the relevant low-lying optical phonon mode is in the hBN itself[385]. This mode has a higher energy of $\sim$ 100 meV, which is only accessible at biases far beyond the onset of the anomalous behavior. In particular, we observe that the AC conductivity spectrum has developed clear low-frequency features and that the noise is superlinear in power when the available excitations ($k_B T$, $2\hbar k_F v_D$) are less than 20 meV. This is clearly too low for substantial optical phonon emission.

Besides being outside the parameter range required to excite optical phonons, it is not expected that optical phonon scattering will lead to the observed strong noise signal and its growth across the sample. Indeed, noise measurements in disordered samples on SiO_2 clearly show that the noise signal is simply dominated by thermal (white) noise when the graphene sample is biased strongly enough to access optical phonons[48]. Furthermore, the velocity extracted from 4.10 matches well with the acoustic phonon velocity, while optical phonons have orders of magnitude lower group velocities. Lastly, due to the high energy of optical phonons, it is not expected that their effects should be as dependent on lattice temperature as we observe in the 10-300 K range (4.11A).

C8.2 Plasmonic effects

A plasmonic analogue to phonon Cerenkov amplification in graphene has also been proposed [181]. While plasmons in graphene have far too high velocities (∼10 times higher than the drift velocities in our experiment) to match well with our observations [228], losses could allow for accessing lower-velocity modes below the dispersion. However, we operate in a parameter regime that is far from that required to achieve this. As analyzed in Ref. [181], intra-band transitions are only accessed by very high initial electronic excitations of ∼2000 meV above the Fermi energy, which is two orders of magnitude higher than the excitations reached in our experiment at the onset of the anomalous observations ($k_B T$, $2\hbar k_F v_D$<20 meV).

Another plasmonic effect of interest is the Dyakonov-Shur (DS) instability [96]. We also exclude this mechanism based on many considerations: 1) This mechanism relies on carefully chosen boundary conditions not satisfied in our experiment. 2) The DS instability requires much longer electronic mean free paths than what we observe when applying high bias. 3) Since DS plasmon amplification occurs at the sample edge and the plasmons are damped in the channel, the signal is expected to be higher in shorter samples. In clear contrast, we observe that the signal increases with device length (section SC5.3). 4) The DS instability is expected to cause oscillations at much higher frequencies (∼THz) than what is observed in our experiment.

Moreover, there is another critical difference between phonons and plasmons: while the speed of sound does not depend on electronic parameters, the plasmon velocity is highly dependent on charge density [228]. Thus, if plasmonic emission were driving the instability, the timescale (device traversal time) observed in noise and AC conductivity measurements should change with gating. As explained in the manuscript and shown in Fig. C.16, we show that this is not the case. Based on these arguments, we conclude that plasmons are not connected with our observations.

C8.3 Hydrodynamic instabilities

When electron-electron interactions are the dominant scattering mechanism in the device, graphene enters the hydrodynamic regime and may exhibit instabilities such as vortex shedding and pre-turbulent flow[244]. We discount such hydrodynamic instabilities as an explanation for our observations for the following reasons: 1) The rate of electron-phonon scattering in driven graphene-hBN heterostructures is too high to realize long-range hydrodynamic instabilities. This was recently discussed in Ref.[115]. 2) The frequency of vortex shedding in pre-turbulent oscillations should be highly dependent on drift velocity, in contrast to our observations in 4.10, where the observed timescales are independent of electronic parameters. 3) The extent to which hydrodynamic instabilities occur increases with the Reynolds number, $\mathrm{Re} = v_D L/\eta$, where η is the kinematic viscosity. The Reynolds number is expected to decrease monotonically with increasing carrier density n for two reasons: The kinematic viscosity of the electron fluid increases with n, and at constant current density, the drift velocity decreases with n. Thus, we do not expect hydrodynamic instabilities to show the non-monotonic doping dependence observed in 4.11C.

D

Supporting material for Chapter 5

D1 Theoretical treatment

A simple way to understand the emergence of graphene's large diamagnetic response is to calculate the energy difference between free electrons and electrons that have collapsed into the zeroth Lan-

dau Level. In the absence of magnetic fields, an electron in graphene has energy given by

$$\varepsilon = \hbar v_{\mathrm{F}} k \,, \tag{D.1}$$

were v_{F} is the Fermi velocity of graphene ($\approx c/300$) and k is the momentum of an electron. This defines the linear dispersion of low-energy graphene electrons at the K point. The density of states graphene electrons is given by

$$g(\varepsilon) = \frac{2}{\pi(\hbar v_{\mathrm{F}})^2} |\varepsilon| \,. \tag{D.2}$$

In a strong magnetic field, the formerly free electrons coalesce into degenerate Landau Levels. The energy of the Nth LL is given by

$$E(N) = \mathrm{sgn(N)} \sqrt{2\mathrm{e}\hbar \mathrm{v}_{\mathrm{F}}^2 \mathrm{B}|\mathrm{N}|} \,, \tag{D.3}$$

where B is the applied magnetic field and e is the charge of the electron. The $\sqrt{N}$ dependence of the LL energy spectrum in graphene contrasts with the linear in N spectrum of normal electrons. Each LL is degenerate, with degeneracy given by

$$D(B) = \frac{2eB}{\pi\hbar} \,. \tag{D.4}$$

Using Equations (D.1) to (D.4), we can calculate the energy change of the free electrons as they move into the 0th LL, where all electrons have $\varepsilon = 0$. The initial total energy energy of the electrons (and holes) near the Dirac point is given by

$$U_0 = \int_{-\lambda}^{\lambda} \varepsilon g(\varepsilon) f(\varepsilon) d\varepsilon \,, \tag{D.5}$$

where $f(\varepsilon)$ is the Fermi distribution function and the limits $\pm\lambda$ are the minimum and maximum

energies of the free electron states that will fill the 0th LL, as opposed to a higher N. This is easily obtained from the LL energy: the states that become the Nth LL come from states that were originally between $E(N+1/2)$ and $E(N-1/2)$. If we are only considering the 0th LL, this means that

$$\lambda(B) = v_{\mathrm{F}}\sqrt{e\hbar B}\,. \tag{D.6}$$

Since the final energy of these electrons is just $U_f = 0$, we have that $\Delta U = U_0$. The susceptibility is found by taking

$$\begin{aligned}
\frac{\chi}{\mu_0} =& \frac{1}{B}\frac{\partial U_0}{\partial B}\,, && \text{(D.7)}\\
=& \frac{1}{B}\frac{\partial}{\partial B}\left(\int_{-\lambda(B)}^{\lambda(B)} \varepsilon g(\varepsilon) f(\varepsilon) d\varepsilon\right)\,, && \text{(D.8)}\\
=& \frac{1}{B}\lambda(B) g(\lambda(B))\frac{d\lambda}{dB}\left(f(\lambda(B)) - f(-\lambda(B))\right)\,. && \text{(D.9)}
\end{aligned}$$

If we are interested in relatively low magnetic fields (so that $\frac{\lambda}{kT} \ll 1$), we can expand the Fermi functions to find that they simplify to

$$\left(f(\lambda(B)) - f(-\lambda(B))\right) \approx -\frac{\lambda}{2kT}\mathrm{sech}^2\left(\frac{\mu}{2\mathrm{kT}}\right)\,. \tag{D.10}$$

So that the susceptibility is given by

$$\chi(\mu) = -\frac{\mu_0 v_{\mathrm{F}}^2 e^2}{4\pi kT}\mathrm{sech}^2\left(\frac{\mu}{2\mathrm{kT}}\right)\,, \tag{D.11}$$

which is the result obtained by McClure[241].

This result provides good physical intuition for why diamagnetism is so much stronger in

graphene than in other materials: there is a particularly large energy change for electrons (and holes) when a magnetic field is applied, since the final states have 0 energy. For a Fermi energy at the Dirac point, the filled states rise in energy as a field is applied, so the energy change is negative and hence the system is diamagnetic. The other reason that the diamagnetism is so strong is that graphene electrons, having an extremely small effective mass, move very fast (at v_F)[241].

This calculation is simplified for two reasons. First, in using the total energy of the electrons in place of the thermodynamic free energy, we have neglected any contributions from entropy, which increases upon the application of a magnetic field. This is taken into account in Ref.[241] and it is found that the value of the susceptibility is smaller by about a factor of three when calculated using the Helmholtz free energy. The second reason is that it neglects contributions from the other Landau levels. These can be taken into account as in Ref.[367] or Ref.[218]. Briefly, in the zero temperature limit, the total energy is calculated by taking an integral over the density of states up to the Fermi energy. For the degenerate Landau levels, the density of states is given by

$$g(\varepsilon) = \frac{2eB}{\pi\hbar} \sum_{N=-\infty}^{\infty} \delta\left(\varepsilon - \mathrm{sgn(N)}\sqrt{2e\hbar v_F^2 B|N|}\right) , \tag{D.12}$$

where δ is the Dirac delta function. There are several ways to evaluate this sum, which are given in the above references as well as in the famous book by Landau[207].

To take both finite temperature and higher N LLs into account, we should consider the Grand potential[37], given by

$$\Omega = \frac{1}{\beta} \sum_i \ln\left(1 + \exp\beta(\mu - \varepsilon_i)\right) , \tag{D.13}$$

$$= \frac{1}{\beta} \sum_i f(\mu - \varepsilon_i) , \tag{D.14}$$

where ε_i is the energy of particle i, $\beta = (k_B T)^{-1}$, μ is the chemical potential, and the sum is over all particles in the system. When a magnetic field is applied, we can rewrite Eq. (D.19) as a summation over all of the LL indices, multiplied by the degeneracy. We have to be careful about the states with $\varepsilon < 0$, however, since it is more convenient to set the Dirac Point to be $E = 0$. We can deal with these by treating them as being relative to a negative chemical potential, so that the Grand potential, including degeneracy given by Eq. (D.4), is

$$\Omega = \frac{4eB}{\pi\hbar\beta}\left(\sum_{N=0}^{\infty} f(\mu - a\sqrt{|N|}) + \sum_{N=1}^{\infty} f(a\sqrt{|N|} - \mu)\right), \tag{D.15}$$

where $a = \sqrt{2e\hbar v_F^2 B}$. Now we evaluate the sum using the Poisson summation formula, given by

$$\sum_{j=-\infty}^{\infty} \delta(x - j) = \sum_{k=-\infty}^{\infty} \exp(2\pi i k x), \tag{D.16}$$

where $\delta(x)$ is the Dirac Delta function.

To evaluate the first sum, we multiply both sides by $f(\mu - a\sqrt{|x|})$ and integrate from 0 to ∞

$$\frac{1}{2}f(\mu) + 2\sum_{n=1}^{\infty} f(\mu - a\sqrt{|n|}) = \frac{1}{a^2}\int_0^{\infty} f(\mu - x)2x dx + \frac{2}{a^2}\sum_{k=1}^{\infty}\int_0^{\infty} \cos\left(\frac{2\pi k x^2}{a^2}\right) f(\mu - x)2x dx. \tag{D.17}$$

Where we have made a substitution to eliminate the square root of x in f. Now we follow the same perscription for the negative energy terms, but instead integrate from $-\infty$ to 0:

$$\frac{1}{2}f(\mu) + 2\sum_{n=1}^{\infty} f(a\sqrt{|n|} - \mu) = \frac{1}{a^2}\int_{-\infty}^{0} f(x - \mu)2x dx + \frac{2}{a^2}\sum_{k=1}^{\infty}\int_{-\infty}^{0} \cos\left(\frac{2\pi k x^2}{a^2}\right) f(x - \mu)2x dx. \tag{D.18}$$

It is worth noting at this point that some of these terms will not contribute to the magnetization,

and we will drop them. In particular, the $k = 0$ terms have no field dependence, so we write the Grand Potential as

$$\Omega - \Omega_0 = \left(\frac{2}{\hbar^2 v_F^2 \pi \beta}\right)\left(\sum_{k=1}^{\infty}\int_0^{\infty}\cos\left(\frac{2\pi k x^2}{a^2}\right) f(\mu - x) 2x dx + \sum_{k=1}^{\infty}\int_{-\infty}^{0}\cos\left(\frac{2\pi k x^2}{a^2}\right) f(x - \mu) 2x dx\right), \tag{D.19}$$

which can be numerically integrated. To obtain the magnetization, we take the derivative with respect to the magnetic field.

In the limit of zero temperature, Eq. (D.19) can be simplified significantly, though the integrals must still be evaluated numerically. The results of the calculation done in this limit are presented in Ref. [367]. See Ref. [367] also for a discussion of how disorder enters into the calculation.

References

[1] Abbott, B., Abbott, R., Adhikari, R., Ajith, P., Allen, B., Allen, G., Amin, R., Anderson, S., Anderson, W., Arain, M., et al. (2009). Ligo: the laser interferometer gravitational-wave observatory. *Reports on Progress in Physics*, 72(7), 076901.

[2] Abragam, A. (1961). *The principles of nuclear magnetism*. Oxford university press.

[3] Acosta, V. M. (2011). Optical Magnetometry with Nitrogen-Vacancy Centers in Diamond. *PhD Thesis*, (pp. 118).

[4] Acosta, V. M., Jarmola, A., Bauch, E., & Budker, D. (2010). Optical properties of the nitrogen-vacancy singlet levels in diamond. *Physical Review B - Condensed Matter and Materials Physics*, 82(20), 2–5.

[5] Agarwal, K., Schmidt, R., Halperin, B., Oganesyan, V., Zaránd, G., Lukin, M. D., & Demler, E. (2017). Magnetic noise spectroscopy as a probe of local electronic correlations in two-dimensional systems. *Physical Review B*, 95(15).

[6] Ajoy, A., Bissbort, U., Lukin, M. D., Walsworth, R. L., & Cappellaro, P. (2015). Atomic-scale nuclear spin imaging using quantum-assisted sensors in diamond. *Physical Review X*, 5(1), 011001.

[7] Ajoy, A. & Cappellaro, P. (2013). Quantum simulation via filtered hamiltonian engineering: Application to perfect quantum transport in spin networks. *Physical review letters*, 110(22), 220503.

[8] Alexeev, E. M., Ruiz-Tijerina, D. A., Danovich, M., Hamer, M. J., Terry, D. J., Nayak, P. K., Ahn, S., Pak, S., Lee, J., Sohn, J. I., et al. (2019). Resonantly hybridized excitons in moiré superlattices in van der waals heterostructures. *Nature*, 567(7746), 81–86.

[9] Andersen, T. I., Dwyer, B. L., Sanchez-Yamagishi, J. D., Rodriguez-Nieva, J. F., Agarwal, K., Watanabe, K., Taniguchi, T., Demler, E. A., Kim, P., Park, H., et al. (2019). Electron-phonon instability in graphene revealed by global and local noise probes. *Science*, 364(6436), 154–157.

[10] Appel, P., Neu, E., Ganzhorn, M., Barfuss, A., Batzer, M., Gratz, M., Tschöpe, A., & Maletinsky, P. (2016). Fabrication of all diamond scanning probes for nanoscale magnetometry. *Review of Scientific Instruments*, 87(6), 063703.

[11] Ariyaratne, A., Bluvstein, D., Myers, B. A., & Jayich, A. C. B. (2018). Nanoscale electrical conductivity imaging using a nitrogen-vacancy center in diamond. *Nature communications*, 9(1), 1–7.

[12] Ashcroft, N. W., Mermin, N. D., et al. (1976). Solid state physics [by] neil w. ashcroft [and] n. david mermin.

[13] Aslam, N., Pfender, M., Neumann, P., Reuter, R., Zappe, A., De Oliveira, F. F., Denisenko, A., Sumiya, H., Onoda, S., Isoya, J., & Wrachtrup, J. (2017). Nanoscale nuclear magnetic resonance with chemical resolution. *Science*, 357(6346), 67–71.

[14] Aslam, N., Waldherr, G., Neumann, P., Jelezko, F., & Wrachtrup, J. (2013). Photo-induced ionization dynamics of the nitrogen vacancy defect in diamond investigated by single-shot charge state detection. *New Journal of Physics*, 15(1), 013064.

[15] Astner, T., Gugler, J., Angerer, A., Wald, S., Putz, S., Mauser, N. J., Trupke, M., Sumiya, H., Onoda, S., Isoya, J., et al. (2018). Solid-state electron spin lifetime limited by phononic vacuum modes. *Nature materials*, 17(4), 313–317.

[16] Awan, S., Lombardo, A., Colli, A., Privitera, G., Kulmala, T., Kivioja, J., Koshino, M., & Ferrari, A. (2016). Transport conductivity of graphene at RF and microwave frequencies. *2D Mater.*, 3(1), 015010.

[17] Bahe, J., Zhou, X., Kippenberg, T., Stiebeiner, A., Rauschenbeutel, A., Rabeau, J., & Weinfurter, H. (2009). A single photon source based on nv centers in diamond nanocrystals. *CLEO/Europe - EQEC 2009 - European Conference on Lasers and Electro-Optics and the European Quantum Electronics Conference*, 3433(2002), 85748.

[18] Balandin, A. A. (2011). Thermal properties of graphene and nanostructured carbon materials. *Nat. Mater.*, 10(8), 569–581.

[19] Balandin, A. A. (2013). Low-frequency 1/f noise in graphene devices. *Nat. Nanotechnol.*, 8(8), 549.

[20] Balasubramanian, G., Neumann, P., Twitchen, D., Markham, M., Kolesov, R., Mizuochi, N., Isoya, J., Achard, J., Beck, J., Tissler, J., Jacques, V., Hemmer, P. R., Jelezko, F., & Wrachtrup, J. (2009). Ultralong spin coherence time in isotopically engineered diamond. *Nature Materials*, 8(5), 383–387.

[21] Baldwin, C. G., Downes, J. E., McMahon, C. J., Bradac, C., & Mildren, R. P. (2014). Nanostructuring and oxidation of diamond by two-photon ultraviolet surface excitation: An XPS and NEXAFS study. *Phys. Rev. B*, 89(19), 195422.

[22] Balents, L., Dean, C. R., Efetov, D. K., & Young, A. F. (2020). Superconductivity and strong correlations in moiré flat bands. *Nature Physics*, 16(7), 725–733.

[23] Bar-Gill, N., Pham, L. M., Belthangady, C., Le Sage, D., Cappellaro, P., Maze, J. R., Lukin, M. D., Yacoby, a., & Walsworth, R. (2012). Suppression of spin-bath dynamics for improved coherence of multi-spin-qubit systems. *Nature communications*, 3(May), 858.

[24] Bar-Gill, N., Pham, L. M., Jarmola, A., Budker, D., & Walsworth, R. L. (2013). Solid-state electronic spin coherence time approaching one second. *Nature Communications*, 4.

[25] Barr, T. L. & Seal, S. (1995). Nature of the use of adventitious carbon as a binding energy standard. *Journal of Vacuum Science & Technology A*, 13(3), 1239.

[26] Barry, J. F., Schloss, J. M., Bauch, E., Turner, M. J., Hart, C. A., Pham, L. M., & Walsworth, R. L. (2019). Sensitivity Optimization for NV-Diamond Magnetometry.

[27] Barson, M. S., Peddibhotla, P., Ovartchaiyapong, P., Ganesan, K., Taylor, R. L., Gebert, M., Mielens, Z., Koslowski, B., Simpson, D. A., McGuinness, L. P., et al. (2017). Nanomechanical sensing using spins in diamond. *Nano letters*, 17(3), 1496–1503.

[28] Baugher, B. W., Churchill, H. O., Yang, Y., & Jarillo-Herrero, P. (2014). Optoelectronic devices based on electrically tunable p–n diodes in a monolayer dichalcogenide. *Nature nanotechnology*, 9(4), 262–267.

[29] Beenakker, C. & Büttiker, M. (1992). Suppression of shot noise in metallic diffusive conductors. *Physical Review B*, 46(3), 1889.

[30] Beenakker, C. & Schonenberger, C. (2003). Quantum Shot Noise. *Physics Today*, 56(5), 37–42.

[31] Bernien, H., Hensen, B., Pfaff, W., Koolstra, G., Blok, M. S., Robledo, L., Taminiau, T. H., Markham, M., Twitchen, D. J., Childress, L., & Hanson, R. (2013). Heralded entanglement between solid-state qubits separated by three metres. *Nature*, 497(7447), 86–90.

[32] Berry, M. V. (1984). Quantal phase factors accompanying adiabatic changes. *Proceedings of the Royal Society of London. A. Mathematical and Physical Sciences*, 392(1802), 45–57.

[33] Betz, A., Jhang, S. H., Pallecchi, E., Ferreira, R., Fève, G., Berroir, J.-M., & Plaçais, B. (2013). Supercollision cooling in undoped graphene. *Nat. Phys.*, 9(2), 109.

[34] Betz, A., Vialla, F., Brunel, D., Voisin, C., Picher, M., Cavanna, A., Madouri, A., Fève, G., Berroir, J.-M., Plaçais, B., et al. (2012). Hot electron cooling by acoustic phonons in graphene. *Physical Review Letters*, 109(5), 056805.

[35] Bhaskar, M. K., Sukachev, D. D., Sipahigil, A., Evans, R. E., Burek, M. J., Nguyen, C. T., Rogers, L. J., Siyushev, P., Metsch, M. H., Park, H., Jelezko, F., Lončar, M., & Lukin, M. D. (2017). Quantum Nonlinear Optics with a Germanium-Vacancy Color Center in a Nanoscale Diamond Waveguide. *Physical Review Letters*, 118(22), 1–6.

[36] Biercuk, M. J., Doherty, A. C., & Uys, H. (2010). Dynamical decoupling sequence construction as a filter-design problem. *arXiv.org*, quant-ph.

[37] Biswas, S., Sen, S., & Jana, D. (2013). A complete theory for the magnetism of an ideal gas of electrons. *Physics of Plasmas*, 20(5), 052503.

[38] Blake, P., Hill, E. W., Castro Neto, A. H., Novoselov, K. S., Jiang, D., Yang, R., Booth, T. J., & Geim, A. K. (2007). Making graphene visible. *Applied Physics Letters*, 91(6), 2007–2009.

[39] Blank, A., Twig, Y., & Ishay, Y. (2017). Recent trends in high spin sensitivity magnetic resonance. *Journal of Magnetic Resonance*, 280, 20–29.

[40] Blanter, Y. M. & Büttiker, M. (2000). Shot noise in mesoscopic conductors. *Physics reports*, 336(1-2), 1–166.

[41] Blöchl, P. E. (1994). Projector augmented-wave method. *Physical review B*, 50(24), 17953.

[42] Block, M., Kobrin, B., Jarmola, A., Hsieh, S., Zu, C., Figueroa, N., Acosta, V., Minguzzi, J., Maze, J., Budker, D., et al. (2020). Optically enhanced electric field sensing using nitrogen-vacancy ensembles. *arXiv preprint arXiv:2004.02886*.

[43] Bluvstein, D., Zhang, Z., & Jayich, A. C. (2019a). Identifying and Mitigating Charge Instabilities in Shallow Diamond Nitrogen-Vacancy Centers. *Physical Review Letters*, 122(7), 1–13.

[44] Bluvstein, D., Zhang, Z., McLellan, C. A., Williams, N. R., & Jayich, A. C. B. (2019b). Extending the quantum coherence of a near-surface qubit by coherently driving the paramagnetic surface environment. *Physical review letters*, 123(14), 146804.

[45] Bobrov, K., Comtet, G., Dujardin, G., & Hellner, L. (2001). Electronic structure of partially hydrogenated si (100)-(2$\times$ 1) surfaces prepared by thermal and nonthermal desorption. *Physical review letters*, 86(12), 2633.

[46] Bolech, C. & Demler, E. (2007). Observing majorana bound states in p-wave superconductors using noise measurements in tunneling experiments. *Physical review letters*, 98(23), 237002.

[47] Bose, S. (2003). Quantum communication through an unmodulated spin chain. *Physical review letters*, 91(20), 207901.

[48] Brunel, D., Berthou, S., Parret, R., Vialla, F., Morfin, P., Wilmart, Q., et al. (2015). Onset of optical-phonon cooling in multilayer graphene revealed by RF noise and black-body radiation thermometries. *J. Phys. Condens. Matter*, 27(16), 164208.

[49] Bundy, F., Hall, H. T., Strong, H., & Wentorfjun, R. (1955). Man-made diamonds. *nature*, 176(4471), 51–55.

[50] Burnett, J., Faoro, L., Wisby, I., Gurtovoi, V., Chernykh, A., Mikhailov, G., Tulin, V., Shaikhaidarov, R., Antonov, V., Meeson, P., et al. (2014). Evidence for interacting two-level systems from the 1/f noise of a superconducting resonator. *Nature communications*, 5(1), 1–6.

[51] Büttiker, M. (1992). Scattering theory of current and intensity noise correlations in conductors and wave guides. *Physical Review B*, 46(19), 12485.

[52] Cai, J., Retzker, A., Jelezko, F., & Plenio, M. B. (2013). A large-scale quantum simulator on a diamond surface at room temperature. *Nature Physics*, 9(3), 168–173.

[53] Cao, Y., Fatemi, V., Demir, A., Fang, S., Tomarken, S. L., Luo, J. Y., Sanchez-Yamagishi, J. D., Watanabe, K., Taniguchi, T., Kaxiras, E., Ashoori, R. C., & Jarillo-Herrero, P. (2018). Correlated Insulator Behaviour at Half-Filling in Magic Angle Graphene Superlattices. (pp. 1–38).

[54] Capelli, M., Heffernan, A., Ohshima, T., Abe, H., Jeske, J., Hope, A., Greentree, A., Reineck, P., & Gibson, B. (2019). Increased nitrogen-vacancy centre creation yield in diamond through electron beam irradiation at high temperature. *Carbon*, 143, 714–719.

[55] Cardona, M. & Peter, Y. Y. (2005). *Fundamentals of semiconductors*. Springer.

[56] Casola, F., Van Der Sar, T., & Yacoby, A. (2018). Probing condensed matter physics with magnetometry based on nitrogen-vacancy centres in diamond. *Nature Reviews Materials*, 3.

[57] Cassabois, G., Valvin, P., & Gil, B. (2016). Hexagonal boron nitride is an indirect bandgap semiconductor. *Nature photonics*, 10(4), 262–266.

[58] Castro Neto, A. H., Peres, N. M. R., Novoselov, K. S., Geim, A. K., & Guinea, F. (2009). The electronic properties of graphene. *Reviews of Modern Physics*, 81(1), 109–162.

[59] Cayssol, J., Huard, B., & Goldhaber-Gordon, D. (2009). Contact resistance and shot noise in graphene transistors. *Physical Review B*, 79(7), 075428.

[60] Chadi, D. (1987). Stabilities of single-layer and bilayer steps on si (001) surfaces. *Physical Review Letters*, 59(15), 1691.

[61] Chakravarthi, S., Moore, C., Opsvig, A., Pederson, C., Hunt, E., Ivanov, A., Christen, I., Dunham, S., & Fu, K.-M. C. (2020). Window into nv center kinetics via repeated annealing and spatial tracking of thousands of individual nv centers. *Physical Review Materials*, 4(2), 023402.

[62] Chatterjee, S., Rodriguez-Nieva, J. F., & Demler, E. (2019). Diagnosing phases of magnetic insulators via noise magnetometry with spin qubits. *Physical Review B*, 99(10), 104425.

[63] Chen, W., Qi, D., Gao, X., & Wee, A. T. S. (2009). Surface transfer doping of semiconductors. *Progress in Surface Science*, 84(9-10), 279–321.

[64] Chen, X. D., Li, S., Shen, A., Dong, Y., Dong, C. H., Guo, G. C., & Sun, F. W. (2017). Near-Infrared-Enhanced Charge-State Conversion for Low-Power Optical Nanoscopy with Nitrogen-Vacancy Centers in Diamond. *Physical Review Applied*, 7(1), 1–9.

[65] Childress, L., Gurudev Dutt, M. V., Taylor, J. M., Zibrov, A. S., Jelezko, F., Wrachtrup, J., Hemmer, P. R., & Lukin, M. D. (2006). Coherent dynamics of coupled electron and nuclear spin qubits in diamond. *Science*, 314(5797), 281–285.

[66] Choi, J., Zhou, H., Landig, R., Wu, H.-Y., Yu, X., Von Stetina, S. E., Kucsko, G., Mango, S. E., Needleman, D. J., Samuel, A. D., et al. (2020). Probing and manipulating embryogenesis via nanoscale thermometry and temperature control. *Proceedings of the National Academy of Sciences*, 117(26), 14636–14641.

[67] Choi, J.-y., Hild, S., Zeiher, J., Schauß, P., Rubio-Abadal, A., Yefsah, T., Khemani, V., Huse, D. A., Bloch, I., & Gross, C. (2016). Exploring the many-body localization transition in two dimensions. *Science*, 352(6293), 1547–1552.

[68] Choi, S., Yao, N. Y., & Lukin, M. D. (2017). Quantum metrology based on strongly correlated matter. *arXiv preprint arXiv:1801.00042*.

[69] Chu, Y., De Leon, N. P., Shields, B. J., Hausmann, B., Evans, R., Togan, E., Burek, M. J., Markham, M., Stacey, A., Zibrov, A. S., Yacoby, A., Twitchen, D. J., Loncar, M., Park, H., Maletinsky, P., & Lukin, M. D. (2014a). Coherent optical transitions in implanted nitrogen vacancy centers. *Nano Letters*, 14(4), 1982–1986.

[70] Chu, Y., de Leon, N. P., Shields, B. J., Hausmann, B., Evans, R., Togan, E., Burek, M. J., Markham, M., Stacey, A., Zibrov, A. S., Yacoby, A., Twitchen, D. J., Loncar, M., Park, H., Maletinsky, P., & Lukin, M. D. (2014b). Coherent Optical Transitions in Implanted Nitrogen Vacancy Centers. *Nano Lett.*, 14(4), 1982.

[71] Collins, A. T. (2002). The Fermi level in diamond. *Journal of Physics Condensed Matter*, 14(14), 3743–3750.

[72] Crossno, J., Shi, J. K., Wang, K., Liu, X., Harzheim, A., Lucas, A., et al. (2016). Observation of the Dirac fluid and the breakdown of the Wiedemann-Franz law in graphene. *Science*, 351(6277), 1058–1061.

[73] Cui, S. & Hu, E. L. (2013). Increased negatively charged nitrogen-vacancy centers in fluorinated diamond. *Applied Physics Letters*, 103(5), 051603.

[74] Cui, X., Shih, E.-M., Jauregui, L. A., Chae, S. H., Kim, Y. D., Li, B., Seo, D., Pistunova, K., Yin, J., Park, J.-H., et al. (2017). Low-temperature ohmic contact to monolayer mos2 by van der waals bonded co/h-bn electrodes. *Nano letters*, 17(8), 4781–4786.

[75] Danneau, R., Wu, F., Craciun, M., Russo, S., Tomi, M., Salmilehto, J., Morpurgo, A., & Hakonen, P. J. (2008). Shot noise in ballistic graphene. *Phys. Rev. Lett.*, 100(19), 196802.

[76] DaSilva, A. M., Zou, K., Jain, J., & Zhu, J. (2010). Mechanism for current saturation and energy dissipation in graphene transistors. *Phys. Rev. Lett.*, 104(23), 236601.

[77] Davies, G. (1981). The Jahn-Teller effect and vibronic coupling at deep levels in diamond. *Reports on Progress in Physics*, 44(7), 787–830.

[78] Davis, E. J., Ye, B., Machado, F., Meynell, S. A., Mittiga, T., Schenken, W., Joos, M., Kobrin, B., Lyu, Y., Bluvstein, D., et al. (2021). Probing many-body noise in a strongly interacting two-dimensional dipolar spin system. *arXiv preprint arXiv:2103.12742*.

[79] de Lange, G., Wang, Z. H., Ristè, D., Dobrovitski, V. V., & Hanson, R. (2010a). Universal dynamical decoupling of a single solid-state spin from a spin bath. *Science (New York, N.Y.)*, 330(6000), 60–3.

[80] de Lange, G., Wang, Z. H., Ristè, D., Dobrovitski, V. V., & Hanson, R. (2010b). Universal Dynamical Decoupling of a Single Solid-State Spin from a Spin Bath. *Science*, 330(6000), 60.

[81] de Oliveira, F. F., Antonov, D., Wang, Y., Neumann, P., Momenzadeh, S. A., Häußermann, T., Pasquarelli, A., Denisenko, A., & Wrachtrup, J. (2017). Tailoring spin defects in diamond by lattice charging. *Nat. Commun.*, 8, 15409.

[82] De-Picciotto, R., Reznikov, M., Heiblum, M., Umansky, V., Bunin, G., & Mahalu, D. (1998). Direct observation of a fractional charge. *Physica B: Condensed Matter*, 249, 395–400.

[83] de Sousa, R. (2009). *Electron Spin as a Spectrometer of Nuclear-Spin Noise and Other Fluctuations*, (pp. 183–220). Springer Berlin Heidelberg: Berlin, Heidelberg.

[84] Deák, P., Aradi, B., Kaviani, M., Frauenheim, T., & Gali, A. (2014). Formation of NV centers in diamond: A theoretical study based on calculated transitions and migration of nitrogen and vacancy related defects. *Physical Review B - Condensed Matter and Materials Physics*, 89(7), 1–12.

[85] Dean, C. R., Young, A. F., Meric, I., Lee, C., Wang, L., Sorgenfrei, S., Watanabe, K., Taniguchi, T., Kim, P., Shepard, K. L., et al. (2010). Boron nitride substrates for high-quality graphene electronics. *Nature nanotechnology*, 5(10), 722–726.

[86] Deng, B., Liu, Z., & Peng, H. (2019). Toward mass production of cvd graphene films. *Advanced Materials*, 31(9), 1800996.

[87] Devoret, M. H. & Schoelkopf, R. J. (2000). Amplifying quantum signals with the single-electron transistor. *Nature*, 406(6799), 1039–1046.

[88] DiCarlo, L., Williams, J., Zhang, Y., McClure, D., & Marcus, C. (2008). Shot noise in graphene. *Phys. Rev. Lett.*, 100(15), 156801.

[89] Dobrovitski, V., Feiguin, A., Awschalom, D., & Hanson, R. (2008). Decoherence dynamics of a single spin versus spin ensemble. *Physical Review B*, 77(24), 245212.

[90] Dobrovitski, V. V., Fuchs, G. D., Falk, A. L., Santori, C., & Awschalom, D. D. (2013). Quantum control over single spins in diamond. *Annu. Rev. Condens. Matter Phys.*, 4(1), 23.

[91] Doherty, M. W., Dolde, F., Fedder, H., Jelezko, F., Wrachtrup, J., Manson, N. B., & Hollenberg, L. C. (2012). Theory of the ground-state spin of the NV - center in diamond. *Physical Review B - Condensed Matter and Materials Physics*, 85(20), 1–21.

[92] Dolde, F., Fedder, H., Doherty, M. W., Nöbauer, T., Rempp, F., Balasubramanian, G., Wolf, T., Reinhard, F., Hollenberg, L. C., Jelezko, F., & Wrachtrup, J. (2011). Electric-field sensing using single diamond spins. *Nature Physics*, 7(6), 459–463.

[93] Dresselhaus, M. S., Dresselhaus, G., & Jorio, A. (2007). *Group theory: application to the physics of condensed matter*. Springer Science & Business Media.

[94] Duncan, D. (2018). Synchrotron-based spectroscopy in on-surface polymerization of covalent networks. In K. Wandelt (Ed.), *Encyclopedia of Interfacial Chemistry* (pp. 436–445). Oxford: Elsevier.

[95] Dwyer, B. L., Rodgers, L. V., Urbach, E. K., Bluvstein, D., Sangtawesin, S., Zhou, H., Nassab, Y., Fitzpatrick, M., Yuan, Z., De Greve, K., et al. (2021). Probing spin dynamics on diamond surfaces using a single quantum sensor. *arXiv preprint arXiv:2103.12757*.

[96] Dyakonov, M. & Shur, M. (1993). Shallow water analogy for a ballistic field effect transistor: New mechanism of plasma wave generation by DC current. *Phys. Rev. Lett.*, 71(15), 2465.

[97] Efetov, D. K. & Kim, P. (2010). Controlling electron-phonon interactions in graphene at ultrahigh carrier densities. *Physical Review Letters*, 105(25), 2–5.

[98] Einstein, A. (1905). Ueber die von der molekularkinetischen theorie der warme geforderte bewegung von in ruhenden fliussigkeiten suspendierten teilchen. *Ann. der Phys.[41 17, 549-560*.

[99] Eizenberg, M. & Fisher, B. (1978). X-ray Brillouin scattering and electrical measurements of acoustoelectric gain and lattice attenuation in semidegenerate n-GaAs. *J. Appl. Phys.*, 49(10), 5260–5269.

[100] Fanciulli, M. (2009). *Electron spin resonance and related phenomena in low-dimensional structures*, volume 115. Springer Science & Business Media.

[101] Farchi, E., Ebert, Y., Farfurnik, D., Haim, G., Shaar, R., & Bar-Gill, N. (2017). Quantitative Vectorial Magnetic Imaging of Multi-Domain Rock Forming Minerals Using Nitrogen-Vacancy Centers in Diamond. *Spin*, 7(3), 1–8.

[102] Felton, S., Edmonds, A., Newton, M., Martineau, P., Fisher, D., Twitchen, D., & Baker, J. (2009). Hyperfine interaction in the ground state of the negatively charged nitrogen vacancy center in diamond. *Physical Review B*, 79(7), 075203.

[103] Fel'dman, E. B. & Lacelle, S. (1996). Configurational averaging of dipolar interactions in magnetically diluted spin networks. *The Journal of chemical physics*, 104(5), 2000–2009.

[104] Ferrari, A. C., Meyer, J. C., Scardaci, V., Casiraghi, C., Lazzeri, M., Mauri, F., Piscanec, S., Jiang, D., Novoselov, K. S., Roth, S., & Geim, A. K. (2006). Raman Spectrum of Graphene and Graphene Layers. 187401(NOVEMBER), 1–4.

[105] Ferrari, A. C. & Robertson, J. (2004). Raman spectroscopy of amorphous, nanostructured, diamond–like carbon, and nanodiamond. *Philosophical Transactions of the Royal Society of London A*, 362(1824), 2477.

[106] Fortman, B., Mugica-Sanchez, L., Tischler, N., Selco, C., Hang, Y., Holczer, K., & Takahashi, S. (2021). Electron-electron double resonance detected nmr spectroscopy using ensemble nv centers at 230 ghz and 8.3 tesla.

[107] Fortman, B., Pena, J., Holczer, K., & Takahashi, S. (2020). Demonstration of nv-detected esr spectroscopy at 115 ghz and 4.2 tesla. *arXiv preprint arXiv:2002.11845*.

[108] Freitag, M., Chiu, H.-Y., Steiner, M., Perebeinos, V., & Avouris, P. (2010). Thermal infrared emission from biased graphene. *Nat. Nanotechnol.*, 5(7), 497.

[109] Friel, I., Clewes, S. L., Dhillon, H. K., Perkins, N., Twitchen, D. J., & Scarsbrook, G. A. (2009). Control of surface and bulk crystalline quality in single crystal diamond grown by chemical vapour deposition. *Diamond Relat. Mater.*, 18, 808.

[110] Fu, K. M., Santori, C., Barclay, P. E., & Beausoleil, R. G. (2010). Conversion of neutral nitrogen-vacancy centers to negatively charged nitrogen-vacancy centers through selective oxidation. *Applied Physics Letters*, 96(12), 1–4.

[111] Fu, K. M. C., Santori, C., Barclay, P. E., Rogers, L. J., Manson, N. B., & Beausoleil, R. G. (2009). Observation of the dynamic Jahn-Teller effect in the excited states of nitrogen-vacancy centers in diamond. *Physical Review Letters*, 103(25), 1–4.

[112] Fu, L. & Kane, C. (2009). Probing Neutral Majorana Fermion Edge Modes with Charge Transport. *Physical Review Letters*, 102(21), 216403.

[113] Fuchs, G., Dobrovitski, V., Hanson, R., Batra, a., Weis, C., Schenkel, T., & Awschalom, D. (2008). Excited-State Spectroscopy Using Single Spin Manipulation in Diamond. *Physical Review Letters*, 101(11), 117601.

[114] Fuchs, J., Piéchon, F., Goerbig, M., & Montambaux, G. (2010). Topological berry phase and semiclassical quantization of cyclotron orbits for two dimensional electrons in coupled band models. *The European Physical Journal B*, 77(3), 351–362.

[115] Gabbana, A., Mendoza, M., Succi, S., & Tripiccione, R. (2018). Numerical evidence of electron hydrodynamic whirlpools in graphene samples. *Computers & Fluids*, 172, 644–650.

[116] Gaebel, T., Bradac, C., Chen, J., Say, J. M., Brown, L., Hemmer, P., & Rabeau, J. R. (2012). Size-reduction of nanodiamonds via air oxidation. *Diamond Relat. Mater.*, 21, 28.

[117] Gali, A., Fyta, M., & Kaxiras, E. (2008). Ab initio supercell calculations on nitrogen-vacancy center in diamond: Electronic structure and hyperfine tensors. *Physical Review B - Condensed Matter and Materials Physics*, 77(15), 1–12.

[118] Gali, A., Janzén, E., Deák, P., Kresse, G., & Kaxiras, E. (2009). Theory of spin-conserving excitation of the n- v- center in diamond. *Physical review letters*, 103(18), 186404.

[119] Gao, J., Daal, M., Vayonakis, A., Kumar, S., Zmuidzinas, J., Sadoulet, B., Mazin, B. A., Day, P. K., & Leduc, H. G. (2008). Experimental evidence for a surface distribution of two-level systems in superconducting lithographed microwave resonators. *Appl. Phys. Lett.*, 92(15), 152505.

[120] Gardill, A., Cambria, M. C., & Kolkowitz, S. (2020). Fast relaxation on qutrit transitions of nitrogen-vacancy centers in nanodiamonds. *Physical Review Applied*, 13(3), 034010.

[121] Geim, a. K. & Grigorieva, I. V. (2013). Van der Waals heterostructures. *Nature*, 499(7459), 419–25.

[122] Giovannetti, G., Khomyakov, P. A., Brocks, G., Karpan, V. v., van den Brink, J., & Kelly, P. J. (2008). Doping graphene with metal contacts. *Physical review letters*, 101(2), 026803.

[123] Giovannetti, G., Khomyakov, P. A., Brocks, G., Kelly, P. J., & Van Den Brink, J. (2007). Substrate-induced band gap in graphene on hexagonal boron nitride: Ab initio density functional calculations. *Physical Review B*, 76(7), 073103.

[124] Glenn, D. R., Bucher, D. B., Lee, J., Lukin, M. D., Park, H., & Walsworth, R. L. (2018). High-resolution magnetic resonance spectroscopy using a solid-state spin sensor. *Nature*, 555(7696), 351–354.

[125] Goldman, M. L., Doherty, M. W., Sipahigil, A., Yao, N. Y., Bennett, S. D., Manson, N. B., Kubanek, A., & Lukin, M. D. (2015a). State-selective intersystem crossing in nitrogen-vacancy centers. *Physical Review B - Condensed Matter and Materials Physics*, 91(16), 1–11.

[126] Goldman, M. L., Sipahigil, A., Doherty, M., Yao, N. Y., Bennett, S., Markham, M., Twitchen, D., Manson, N., Kubanek, A., & Lukin, M. D. (2015b). Phonon-induced population dynamics and intersystem crossing in nitrogen-vacancy centers. *Physical review letters*, 114(14), 145502.

[127] González-Herrero, H., Gómez-Rodríguez, J. M., Mallet, P., Moaied, M., Palacios, J. J., Salgado, C., Ugeda, M. M., Veuillen, J.-Y., Yndurain, F., & Brihuega, I. (2016). Atomic-scale control of graphene magnetism by using hydrogen atoms. *Science*, 352(6284), 437–441.

[128] Gordon, G., Erez, N., & Kurizki, G. (2007). Universal dynamical decoherence control of noisy single-and multi-qubit systems. *Journal of Physics B: Atomic, Molecular and Optical Physics*, 40(9), S75.

[129] Graupner, R., Hollering, M., Ziegler, A., Ristein, J., Ley, L., & Stampfl, A. (1997). Dispersions of surface states on diamond (100) and (111). *Physical Review B*, 55(16), 10841.

[130] Gregory, P. (2005). *Bayesian logical data analysis for the physical sciences: a comparative approach with mathematica® support*. Cambridge University Press.

[131] Grinolds, M., Maletinsky, P., Hong, S., Lukin, M., Walsworth, R., & Yacoby, A. (2011). Quantum control of proximal spins using nanoscale magnetic resonance imaging. *Nature Physics*, 7(9), 687–692.

[132] Grinolds, M. S., Hong, S., Maletinsky, P., Luan, L., Lukin, M. D., Walsworth, R. L., & Yacoby, a. (2013). Nanoscale magnetic imaging of a single electron spin under ambient conditions. *Nature Physics*, 9(4), 215–219.

[133] Grinolds, M. S., Warner, M., De Greve, K., Dovzhenko, Y., Thiel, L., Walsworth, R. L., Hong, S., Maletinsky, P., & Yacoby, A. (2014a). Subnanometre resolution in three-dimensional magnetic resonance imaging of individual dark spins. *Nature Nanotech.*, 9(4), 279.

[134] Grinolds, M. S., Warner, M., De Greve, K., Dovzhenko, Y., Thiel, L., Walsworth, R. L., Hong, S., Maletinsky, P., & Yacoby, a. (2014b). Subnanometre resolution in three-dimensional magnetic resonance imaging of individual dark spins. *Nature Nanotechnology*, 9(April), 1–6.

[135] Grosse, K. L., Bae, M.-H., Lian, F., Pop, E., & King, W. P. (2011). Nanoscale Joule heating, Peltier cooling and current crowding at graphene–metal contacts. *Nat. Nanotechnol.*, 6(5), 287.

[136] Grotz, B., Beck, J., Neumann, P., Naydenov, B., Reuter, R., Reinhard, F., Jelezko, F., Wrachtrup, J., Schweinfurth, D., Sarkar, B., & Hemmer, P. (2011). Sensing external spins with nitrogen-vacancy diamond. *New Journal of Physics*, 13(5), 055004.

[137] Grotz, B., Hauf, M. V., Dankerl, M., Naydenov, B., Pezzagna, S., Meijer, J., Jelezko, F., Wrachtrup, J., Stutzmann, M., Reinhard, F., & Garrido, J. A. (2012). Charge state manipulation of qubits in diamond. *Nature communications*, 3, 729.

[138] Gunn, J. B. (1963). Microwave oscillations of current in iii–v semiconductors. *Solid State Commun.*, 1(4), 88–91.

[139] Gupta, A., Hacquebard, L., & Childress, L. (2016). Efficient signal processing for time-resolved fluorescence detection of nitrogen-vacancy spins in diamond. *JOSA B*, 33(3), B28–B34.

[140] Hahn, E. L. (1950). Spin echoes. *Physical review*, 80(4), 580.

[141] Hahn, W. & Dobrovitski, V. (2019). Long-lived coherence in driven spin systems: from two-to infinite spatial dimensions. *arXiv preprint arXiv:1911.06272*.

[142] Hall, L. T., Kehayias, P., Simpson, D. A., Jarmola, A., Stacey, A., Budker, D., & Hollenberg, L. C. L. (2016). Detection of nanoscale electron spin resonance spectra demonstrated using nitrogen-vacancy centre probes in diamond. *Nature Communications*, 7(1), 10211.

[143] Harrison, J., Sellars, M. J., & Manson, N. B. (2006). Measurement of the optically induced spin polarisation of N-V centres in diamond. *Diamond and Related Materials*, 15(4-8), 586–588.

[144] Hartmann, S. & Hahn, E. (1962). Nuclear double resonance in the rotating frame. *Physical Review*, 128(5), 2042.

[145] Hartnagel, H. L., Katilius, R., & Matulionis, A. (2001). *Microwave noise in semiconductor devices*.

[146] Hashimoto, A., Suenaga, K., Gloter, A., Urita, K., & Iijima, S. (2004). Direct evidence for atomic defects in graphene layers. *nature*, 430(7002), 870–873.

[147] Hauf, M. V., Grotz, B., Naydenov, B., Dankerl, M., Pezzagna, S., Meijer, J., Jelezko, F., Wrachtrup, J., Stutzmann, M., Reinhard, F., & Garrido, J. a. (2011). Chemical control of the charge state of nitrogen-vacancy centers in diamond. *Physical Review B*, 83(8), 081304.

[148] Henkel, C., Krüger, P., Folman, R., & Schmiedmayer, J. (2003). Fundamental limits for coherent manipulation on atom chips. *Applied Physics B: Lasers and Optics*, 76(2), 173–182.

[149] Hensen, B., Bernien, H., Dreaú, A. E., Reiserer, A., Kalb, N., Blok, M. S., Ruitenberg, J., Vermeulen, R. F., Schouten, R. N., Abellán, C., Amaya, W., Pruneri, V., Mitchell, M. W., Markham, M., Twitchen, D. J., Elkouss, D., Wehner, S., Taminiau, T. H., & Hanson, R. (2015). Loophole-free Bell inequality violation using electron spins separated by 1.3 kilometres. *Nature*, 526(7575), 682–686.

[150] Heyd, J., Scuseria, G. E., & Ernzerhof, M. (2006). Hybrid functionals based on a screened coulomb potential. *The Journal of chemical physics*, 124(219906).

[151] Hite, D. A., Colombe, Y., Wilson, A. C., Allcock, D. T. C., Leibfried, D., Wineland, D. J., & Pappas, D. P. (2013). Surface science for improved ion traps. *MRS Bulletin*, 38(10), 826.

[152] Hong, S., Grinolds, M. S., Pham, L. M., Le Sage, D., Luan, L., Walsworth, R. L., & Yacoby, A. (2013). Nanoscale magnetometry with nv centers in diamond. *MRS bulletin*, 38(2), 155–161.

[153] Hooge, F. N. (1994). 1/f noise sources. *IEEE Transactions on electron devices*, 41(11), 1926–1935.

[154] Hopper, D. A., Grote, R. R., Exarhos, A. L., & Bassett, L. C. (2016). Near-Infrared-Assisted Charge Control and Spin Readout of the Nitrogen-Vacancy Center in Diamond. 0.

[155] Hopper, D. A., Lauigan, J. D., Huang, T.-Y., & Bassett, L. C. (2020). Real-time charge initialization of diamond nitrogen-vacancy centers for enhanced spin readout. *Physical Review Applied*, 13(2), 024016.

[156] Hopper, D. A., Shulevitz, H. J., & Bassett, L. C. (2018). Spin readout techniques of the nitrogen-vacancy center in diamond. *Micromachines*, 9(9), 1–30.

[157] Horng, J., Chen, C.-F., Geng, B., Girit, C., Zhang, Y., Hao, Z., Bechtel, H. A., Martin, M., Zettl, A., Crommie, M. F., et al. (2011). Drude conductivity of Dirac fermions in graphene. *Phys. Rev. B*, 83(16), 165113.

[158] Howe, J. Y., Jones, L. E., & Coffey, D. W. (2000). The evolution of microstructure of cvd diamond by oxidation. *Carbon (New York, NY)*, 38(6), 931–933.

[159] Hsieh, S., Bhattacharyya, P., Zu, C., Mittiga, T., Smart, T., Machado, F., Kobrin, B., Höhn, T., Rui, N., Kamrani, M., et al. (2019). Imaging stress and magnetism at high pressures using a nanoscale quantum sensor. *Science*, 366(6471), 1349–1354.

[160] Huang, B., Clark, G., Klein, D. R., MacNeill, D., Navarro-Moratalla, E., Seyler, K. L., Wilson, N., McGuire, M. A., Cobden, D. H., Xiao, D., et al. (2018). Electrical control of 2d magnetism in bilayer cri 3. *Nature nanotechnology*, 13(7), 544–548.

[161] Huang, B., Clark, G., Navarro-Moratalla, E., Klein, D. R., Cheng, R., Seyler, K. L., Zhong, D., Schmidgall, E., McGuire, M. A., Cobden, D. H., Yao, W., Xiao, D., Jarillo-Herrero, P., & Xu, X. (2017). Layer-dependent Ferromagnetism in a van der Waals Crystal down to the Monolayer Limit. *Nature Publishing Group*, submitted(7657), 270–273.

[162] Huard, B., Sulpizio, J., Stander, N., Todd, K., Yang, B., & Goldhaber-Gordon, D. (2007). Transport measurements across a tunable potential barrier in graphene. *Physical review letters*, 98(23), 236803.

[163] Hunt, B., Sanchez-Yamagishi, J. D., Young, A. F., Yankowitz, M., LeRoy, B. J., Watanabe, K., Taniguchi, T., Moon, P., Koshino, M., Jarillo-Herrero, P., et al. (2013). Massive dirac fermions and hofstadter butterfly in a van der waals heterostructure. *Science*, 340(6139), 1427–1430.

[164] Hustedt, E., Schweiger, A., & Ernst, R. (1992). Stimulated soft electron spin echo envelope modulation spectroscopy. *The Journal of chemical physics*, 96(7), 4954–4962.

[165] Hutson, A. R., McFee, J. H., & White, D. L. (1961). Ultrasonic amplification in CdS. *Phys. Rev. Lett.*, 7, 237–239.

[166] Huxter, V. M., Oliver, T. a. a., Budker, D., & Fleming, G. R. (2012). Vibrational and electronic ultrafast relaxation of the nitrogen-vacancy centers in diamond. *ArXiv*, (pp. 1–3).

[167] Huxter, V. M., Oliver, T. A. A., Budker, D., & Fleming, G. R. (2013). Vibrational and electronic dynamics of nitrogen–vacancy centres in diamond revealed by two-dimensional ultrafast spectroscopy. *Nature Physics*, 9(10), 1–4.

[168] Hwang, E. H. & Sarma, S. D. (2008). Acoustic phonon scattering limited carrier mobility in two-dimensional extrinsic graphene. *Phys. Rev. B*, 77(11).

[169] Iakoubovskii, K. & Stesmans, A. (2004). Vacancy clusters in diamond studied by electron spin resonance. *physica status solidi (a)*, 201(11), 2509–2515.

[170] Irber, D. M., Poggiali, F., Kong, F., Kieschnick, M., Lühmann, T., Kwiatkowski, D., Meijer, J., Du, J., Shi, F., & Reinhard, F. (2020). Robust all-optical single-shot readout of nv centers in diamond. *arXiv preprint arXiv:2006.02938*.

[171] Jacques, V., Neumann, P., Beck, J., Markham, M., Twitchen, D., Meijer, J., Kaiser, F., Balasubramanian, G., Jelezko, F., & Wrachtrup, J. (2009). Dynamic polarization of single nuclear spins by optical pumping of nitrogen-vacancy color centers in diamond at room temperature. *Physical review letters*, 102(5), 057403.

[172] Jamonneau, P., Lesik, M., Tetienne, J. P., Alvizu, I., Mayer, L., Dréau, A., Kosen, S., Roch, J.-F., Pezzagna, S., Meijer, J., Teraji, T., Kubo, Y., Bertet, P., Maze, J. R., & Jacques, V. (2016). Competition between electric field and magnetic field noise in the decoherence of a single spin in diamond. *Phys. Rev. B*, 93(2), 024305.

[173] Jarmola, A., Acosta, V. M., Jensen, K., Chemerisov, S., & Budker, D. (2012). Temperature- and magnetic-field-dependent longitudinal spin relaxation in nitrogen-vacancy ensembles in diamond. *Physical Review Letters*, 108(19), 1–5.

[174] Jauregui, L. A., Joe, A. Y., Pistunova, K., Wild, D. S., High, A. A., Zhou, Y., Scuri, G., De Greve, K., Sushko, A., Yu, C.-H., et al. (2019). Electrical control of interlayer exciton dynamics in atomically thin heterostructures. *Science*, 366(6467), 870–875.

[175] Jeske, J., Lau, D. W., Vidal, X., McGuinness, L. P., Reineck, P., Johnson, B. C., Doherty, M. W., McCallum, J. C., Onoda, S., Jelezko, F., Ohshima, T., Volz, T., Cole, J. H., Gibson, B. C., & Greentree, A. D. (2017). Stimulated emission from nitrogen-vacancy centres in diamond. *Nature Communications*, 8.

[176] Jiang, L., Hodges, J. S., Maze, J. R., Maurer, P., Taylor, J. M., Cory, D. G., Hemmer, P. R., Walsworth, R. L., Yacoby, a., Zibrov, a. S., & Lukin, M. D. (2009). Repetitive readout of a single electronic spin via quantum logic with nuclear spin ancillae. *Science (New York, N.Y.)*, 326(5950), 267–72.

[177] Jin, C., Regan, E. C., Yan, A., Utama, M. I. B., Wang, D., Zhao, S., Qin, Y., Yang, S., Zheng, Z., Shi, S., et al. (2019). Observation of moiré excitons in wse 2/ws 2 heterostructure superlattices. *Nature*, 567(7746), 76–80.

[178] Johnson, J. B. (1927). Thermal agitation of electricity in conductors. *Nature*, 119(2984), 50–51.

[179] Joos, M., Bluvstein, D., Lyu, Y., Weld, D. M., & Jayich, A. B. (2021). Protecting qubit coherence by spectrally engineered driving of the spin environment. *arXiv preprint arXiv:2101.09654*.

[180] Kaasbjerg, K., Thygesen, K. S., & Jacobsen, K. W. (2012). Unraveling the acoustic electron-phonon interaction in graphene. *Phys. Rev. B*, 85(16), 165440.

[181] Kaminer, I., Katan, Y. T., Buljan, H., Shen, Y., Ilic, O., López, J. J., et al. (2016). Efficient plasmonic emission by the quantum čerenkov effect from hot carriers in graphene. *Nat. Commun.*, 7, ncomms11880.

[182] Katsnelson, M. & Novoselov, K. (2007). Graphene: New bridge between condensed matter physics and quantum electrodynamics. *Solid State Communications*, 143(1-2), 3–13.

[183] Kaupp, H., Deutsch, C., Chang, H. C., Reichel, J., Hänsch, T. W., & Hunger, D. (2013). Scaling laws of the cavity enhancement for nitrogen-vacancy centers in diamond. *Physical Review A - Atomic, Molecular, and Optical Physics*, 88(5), 1–8.

[184] Kaviani, M., Deák, P., Aradi, B., Frauenheim, T., Chou, J.-P., & Gali, A. (2014). Proper surface termination for luminescent near-surface nv centers in diamond. *Nano letters*, 14(8), 4772–4777.

[185] Kayyalha, M. & Chen, Y. P. (2015). Observation of reduced 1/f noise in graphene field effect transistors on boron nitride substrates. *Applied Physics Letters*, 107(11), 113101.

[186] Khoo, J. Y., Pientka, F., & Sodemann, I. (2021). The universal shear conductivity of fermi liquids and spinon fermi surface states and its detection via spin qubit noise magnetometry. *arXiv preprint arXiv:2103.05095*.

[187] Kim, M., Mamin, H. J., Sherwood, M. H., Ohno, K., Awschalom, D. D., & Rugar, D. (2015a). Decoherence of Near-Surface Nitrogen-Vacancy Centers Due to Electric Field Noise. *Phys. Rev. Lett.*, 115(8), 087602.

[188] Kim, M., Mamin, H. J., Sherwood, M. H., Ohno, K., Awschalom, D. D., & Rugar, D. (2015b). Decoherence of Near-Surface Nitrogen-Vacancy Centers Due to Electric Field Noise. *Physical Review Letters*, 115(8), 1–5.

[189] Kim, R.-H., Bae, M.-H., Kim, D. G., Cheng, H., Kim, B. H., Kim, D.-H., Li, M., Wu, J., Du, F., Kim, H.-S., et al. (2011). Stretchable, transparent graphene interconnects for arrays of microscale inorganic light emitting diodes on rubber substrates. *Nano Lett.*, 11(9), 3881–3886.

[190] Kim, Y. D., Gao, Y., Shiue, R.-J., Wang, L., Aslan, O. B., Bae, M.-H., et al. (2018). Ultrafast graphene light emitters. *Nano Lett.*, 18(2), 934–940.

[191] King, J. P., Jeong, K., Vassiliou, C. C., Shin, C. S., Page, R. H., Avalos, C. E., Wang, H.-J., & Pines, A. (2015). Room-temperature in situ nuclear spin hyperpolarization from optically pumped nitrogen vacancy centres in diamond. *Nature communications*, 6(1), 1–5.

[192] Kirtley, J., Ketchen, M., Stawiasz, K., Sun, J., Gallagher, W., Blanton, S., & Wind, S. (1995). High-resolution scanning squid microscope. *Applied Physics Letters*, 66(9), 1138–1140.

[193] Kitagawa, F., Mizuno, J., Shoji, S., Shinohara, H., Ohara, O., Takahashi, Y., Nakahara, A., & Otsuka, K. (2011). XPS and NEXAFS studies of VUV/O3-treated aromatic polyurea and its application to microchip electrophoresis. *IET Nanobiotechnol.*, 5(4), 136.

[194] Klauder, J. & Anderson, P. (1962). Spectral diffusion decay in spin resonance experiments. *Physical Review*, 125(3), 912.

[195] Klemens, P. & Pedraza, D. (1994). Thermal conductivity of graphite in the basal plane. *Carbon*, 32(4), 735–741.

[196] Kok, P. & Lovett, B. W. (2006). Pieter Kok and Brendon W. Lovett. *Nature*, 444(November), 2006.

[197] Kolkowitz, S., Safira, A., High, A. A., Devlin, R. C., Choi, S., Unterreithmeier, Q. P., Patterson, D., Zibrov, A. S., Manucharyan, V. E., Park, H., & Lukin, M. D. (2015). Probing Johnson noise and ballistic transport in normal metals with a single-spin qubit. *Science (New York, N.Y.)*, 347(6226), 1129–32.

[198] Komirenko, S. M., Kim, K. W., Demidenko, A. A., Kochelap, V. A., & Stroscio, M. A. (2000). Generation and amplification of sub-THz coherent acoustic phonons under the drift of two-dimensional electrons. *Phys. Rev. B*, 62, 7459–7469.

[199] Kong, J. F., Levitov, L., Halbertal, D., & Zeldov, E. (2018). Resonant electron-lattice cooling in graphene. *Physical Review B*, 97(24), 245416.

[200] Koshino, M. & Ando, T. (2007a). Diamagnetism in disordered graphene. *Physical Review B - Condensed Matter and Materials Physics*, 75(23), 1–8.

[201] Koshino, M. & Ando, T. (2007b). Orbital diamagnetism in multilayer graphenes: Systematic study with the effective mass approximation. *Physical Review B - Condensed Matter and Materials Physics*, 76(8), 2–12.

[202] Kresse, G. & Furthmüller, J. (1996). Efficient iterative schemes for ab initio total-energy calculations using a plane-wave basis set. *Physical review B*, 54(16), 11169.

[203] Kucsko, G., Choi, S., Choi, J., Maurer, P. C., Zhou, H., Landig, R., Sumiya, H., Onoda, S., Isoya, J., Jelezko, F., et al. (2018). Critical thermalization of a disordered dipolar spin system in diamond. *Physical review letters*, 121(2), 023601.

[204] Kucsko, G., Maurer, P. C., Yao, N. Y., Kubo, M., Noh, H. J., Lo, P. K., Park, H., & Lukin, M. D. (2013). Nanometre-scale thermometry in a living cell. *Nature*, 500(7460), 54–58.

[205] Kumar, R. K., Bandurin, D., Pellegrino, F., Cao, Y., Principi, A., Guo, H., et al. (2017). Superballistic flow of viscous electron fluid through graphene constrictions. *Nat. Phys.*, 13(12), 1182.

[206] Lacelle, S. & Tremblay, L. (1993). What is a typical dipolar coupling constant in a solid? *The Journal of chemical physics*, 98(5), 3642–3649.

[207] Landau, L. (1980). Em lifshitz statistical physics. *Course of theoretical physics*, 5, 396–400.

[208] Landauer, R. (1993). Solid-state shot noise. *Physical Review B*, 47(24), 16427.

[209] Landauer, R. (1998). The noise is the signal. *Nature*, 392(6677), 658–659.

[210] Laraoui, A., Dolde, F., Burk, C., Reinhard, F., Wrachtrup, J., & Meriles, C. A. (2013). High-resolution correlation spectroscopy of 13 c spins near a nitrogen-vacancy centre in diamond. *Nature communications*, 4(1), 1–7.

[211] Larsen, R. G. & Singel, D. J. (1993). Double electron–electron resonance spin–echo modulation: Spectroscopic measurement of electron spin pair separations in orientationally disordered solids. *The Journal of chemical physics*, 98(7), 5134–5146.

[212] Laturia, A., Van de Put, M. L., & Vandenberghe, W. G. (2018). Dielectric properties of hexagonal boron nitride and transition metal dichalcogenides: from monolayer to bulk. *npj 2D Materials and Applications*, 2(1), 1–7.

[213] Law, K. T. & Lee, P. A. (2017). 1t-tas2 as a quantum spin liquid. *Proceedings of the National Academy of Sciences*, 114(27), 6996–7000.

[214] Le Sage, D., Arai, K., Glenn, D. R., DeVience, S. J., Pham, L. M., Rahn-Lee, L., Lukin, M. D., Yacoby, a., Komeili, a., & Walsworth, R. L. (2013). Optical magnetic imaging of living cells. *Nature*, 496(7446), 486–9.

[215] Lee, K. W., Lee, D., Ovartchaiyapong, P., Minguzzi, J., Maze, J. R., & Jayich, A. C. B. (2016). Strain coupling of a mechanical resonator to a single quantum emitter in diamond. *Physical Review Applied*, 6(3), 034005.

[216] Lee, P. A. & Fisher, D. S. (1981). Anderson localization in two dimensions. *Physical Review Letters*, 47(12), 882.

[217] Lenef, A. & Rand, S. C. (1996). Electronic structure of the N-V center in diamond: Theory. *Physical Review B*, 53(20), 13441–13455.

[218] Li, Z., Chen, L., Meng, S., Guo, L., Huang, J., Liu, Y., Wang, W., & Chen, X. (2015). Field and temperature dependence of intrinsic diamagnetism in graphene: Theory and experiment. *Physical Review B - Condensed Matter and Materials Physics*, 91(9), 1–5.

[219] Lin, Y.-M., Dimitrakopoulos, C., Jenkins, K. A., Farmer, D. B., Chiu, H.-Y., Grill, A., & Avouris, P. (2010). 100-GHz transistors from wafer-scale epitaxial graphene. *Science*, 327(5966), 662–662.

[220] Liu, H., Hou, Z., Hu, C., Yang, Y., & Zhu, Z. (2012). Electronic and magnetic properties of fluorinated graphene with different coverage of fluorine. *The Journal of Physical Chemistry C*, 116(34), 18193–18201.

[221] Liu, H., Ryu, S., Chen, Z., Steigerwald, M. L., Nuckolls, C., & Brus, L. E. (2009). Photochemical reactivity of graphene. *Journal of the American Chemical Society*, 131(47), 17099–17101.

[222] Liu, R., Eastman, P., & Yamamoto, Y. (1997). Inhibition of elastic and inelastic scattering by the pauli exclusion principle: Supperssion mechanism for mesoscopic partition noise. *Solid state communications*, 102(11), 785–789.

[223] Liu, R. & Yamamoto, Y. (1995). Conductance dependent suppression of current partition noise in mesoscopic electron branching circuits. *Physica B: Condensed Matter*, 210(1), 37–42.

[224] Liu, Y.-W., Qiao, J.-B., Yan, C., Zhang, Y., Li, S.-Y., & He, L. (2019). Magnetism near half-filling of a van hove singularity in twisted graphene bilayer. *Physical Review B*, 99(20), 201408.

[225] London, P., Scheuer, J., Cai, J.-M., Schwarz, I., Retzker, A., Plenio, M. B., Katagiri, M., Teraji, T., Koizumi, S., Isoya, J., et al. (2013). Detecting and polarizing nuclear spins with double resonance on a single electron spin. *Physical review letters*, 111(6), 067601.

[226] Lovchinsky, I., Sushkov, A. O., Urbach, E., de Leon, N. P., Choi, S., De Greve, K., Evans, R., Gertner, R., Bersin, E., Müller, C., McGuinness, L., Jelezko, F., Walsworth, R. L., Park, H., & Lukin, M. D. (2016a). Nuclear magnetic resonance detection and spectroscopy of single proteins using quantum logic. *Science (New York, N.Y.)*, 351(6275), 836–841.

[227] Lovchinsky, I., Sushkov, A. O., Urbach, E., de Leon, N. P., Choi, S., De Greve, K., Evans, R., Gertner, R., Bersin, E., Müller, C., McGuinness, L., Jelezko, F., Walsworth, R. L., Park, H., & Lukin, M. D. (2016b). Nuclear magnetic resonance detection and spectroscopy of single proteins using quantum logic. *Science*, 351(6275), 836.

[228] Lundeberg, M. B., Gao, Y., Asgari, R., Tan, C., Van Duppen, B., Autore, M., et al. (2017). Tuning quantum nonlocal effects in graphene plasmonics. *Science*, (pp. aan2735).

[229] Maier, F., Riedel, M., Mantel, B., Ristein, J., & Ley, L. (2000). Origin of Surface Conductivity in Diamond. *Physical Review Letters*, 85(16), 3472–3475.

[230] Maier, F., Ristein, J., & Ley, L. (2001). Electron affinity of plasma-hydrogenated and chemically oxidized diamond (100) surfaces. *Phys. Rev. B*, 64(16), 165411.

[231] Maletinsky, P., Hong, S., Grinolds, M. S., Hausmann, B., Lukin, M. D., Walsworth, R. L., Loncar, M., & Yacoby, A. (2012). A robust scanning diamond sensor for nanoscale imaging with single nitrogen-vacancy centres. *Nature nanotechnology*, 7(5), 320–324.

[232] Mamin, H. J., Kim, M., Sherwood, M. H., Rettner, C. T., Ohno, K., Awschalom, D. D., & Rugar, D. (2013). Nanoscale Nuclear Magnetic Resonance with a Nitrogen-Vacancy Spin Sensor. *Science*, 339(6119), 557.

[233] Mamin, H. J., Sherwood, M. H., & Rugar, D. (2012). Detecting external electron spins using nitrogen-vacancy centers. *Physical Review B*, 86(19), 195422.

[234] Manson, N. B., Beha, K., Batalov, A., Rogers, L. J., Doherty, M. W., Bratschitsch, R., & Leitenstorfer, A. (2013). Assignment of the nv 0 575-nm zero-phonon line in diamond to a 2 e-2 a 2 transition. *Physical Review B*, 87(15), 155209.

[235] Mariani, E. & von Oppen, F. (2010). Temperature-dependent resistivity of suspended graphene. *Phys. Rev. B*, 82(19).

[236] Martin, J., Akerman, N., Ulbricht, G., Lohmann, T., Smet, J. v., Von Klitzing, K., & Yacoby, A. (2008). Observation of electron–hole puddles in graphene using a scanning single-electron transistor. *Nature physics*, 4(2), 144–148.

[237] Maurer, P. C., Kucsko, G., Latta, C., Jiang, L., Yao, N. Y., Bennett, S. D., Pastawski, F., Hunger, D., Chisholm, N., Markham, M., Twitchen, D. J., Cirac, J. I., & Lukin, M. D. (2012). Room-temperature quantum bit memory exceeding one second. *Science (New York, N.Y.)*, 336(6086), 1283–6.

[238] Mayorov, A. S., Gorbachev, R. V., Morozov, S. V., Britnell, L., Jalil, R., Ponomarenko, L. A., Blake, P., Novoselov, K. S., Watanabe, K., Taniguchi, T., et al. (2011). Micrometer-scale ballistic transport in encapsulated graphene at room temperature. *Nano letters*, 11(6), 2396–2399.

[239] Maze, J. R., Gali, A., Togan, E., Chu, Y., Trifonov, A., Kaxiras, E., & Lukin, M. D. (2011). Properties of nitrogen-vacancy centers in diamond: The group theoretic approach. *New Journal of Physics*, 13.

[240] Maze, J. R., Stanwix, P. L., Hodges, J. S., Hong, S., Taylor, J. M., Cappellaro, P., Jiang, L., Dutt, M. G., Togan, E., Zibrov, A., et al. (2008). Nanoscale magnetic sensing with an individual electronic spin in diamond. *Nature*, 455(7213), 644–647.

[241] McClure, J. W. (1956). Diamangetism of graphite. *Physical Review*, 104(3).

[242] McWhorter, A. (1957). Semiconductor surface physics. *Univerisity of Pennsylvania Press, Philadelphia, PA*, 207.

[243] Meirzada, I., Hovav, Y., Wolf, S. A., & Bar-Gill, N. (2018). Negative charge enhancement of near-surface nitrogen vacancy centers by multicolor excitation. *Physical Review B*, 98(24), 1–8.

[244] Mendoza, M., Herrmann, H., & Succi, S. (2011). Preturbulent regimes in graphene flow. *Phys. Rev. Lett.*, 106(15), 156601.

[245] Meric, I., Han, M. Y., Young, A. F., Ozyilmaz, B., Kim, P., & Shepard, K. L. (2008). Current saturation in zero-bandgap, top-gated graphene field-effect transistors. *Nat. Nanotechnol.*, 3(11), 654.

[246] Meyer, J. C., Chuvilin, A., Algara-Siller, G., Biskupek, J., & Kaiser, U. (2009). Selective sputtering and atomic resolution imaging of atomically thin boron nitride membranes. *Nano Letters*, 9(7), 2683–2689.

[247] Michl, J., Teraji, T., Zaiser, S., Jakobi, I., Waldherr, G., Dolde, F., Neumann, P., Doherty, M. W., Manson, N. B., Isoya, J., et al. (2014). Perfect alignment and preferential orientation of nitrogen-vacancy centers during chemical vapor deposition diamond growth on (111) surfaces. *Applied Physics Letters*, 104(10), 102407.

[248] Mikhailov, S. A. (2013). Graphene-based voltage-tunable coherent terahertz emitter. *Phys. Rev. B*, 87(11), 115405.

[249] Milov, A., Salikhov, K., & Shirov, M. (1981). Application of the double resonance method to electron spin echo in a study of the spatial distribution of paramagnetic centers in solids. *Sov. Phys. Solid State*, 23, 565–569.

[250] Mitin, V., Reggiani, L., & Varani, L. (2002). Generation-Recombination Noise in Semiconductors. *Noise and Fluctuations Control in Electronic Devices*, (pp. 1–19).

[251] Mizuochi, N., Neumann, P., Rempp, F., Beck, J., Jacques, V., Siyushev, P., Nakamura, K., Twitchen, D., Watanabe, H., Yamasaki, S., et al. (2009). Coherence of single spins coupled to a nuclear spin bath of varying density. *Physical review B*, 80(4), 041201.

[252] Momenzadeh, S. A., Stohr, R. J., De Oliveira, F. F., Brunner, A., Denisenko, A., Yang, S., Reinhard, F., & Wrachtrup, J. (2015). Nanoengineered diamond waveguide as a robust bright platform for nanomagnetometry using shallow nitrogen vacancy centers. *Nano letters*, 15(1), 165–169.

[253] Moriya, R., Kinoshita, K., Crosse, J., Watanabe, K., Taniguchi, T., Masubuchi, S., Moon, P., Koshino, M., & Machida, T. (2020). Emergence of orbital angular moment at van hove singularity in graphene/h-bn moiré superlattice. *Nature communications*, 11(1), 1–6.

[254] Myers, B., Das, A., Dartiailh, M., Ohno, K., Awschalom, D., & Bleszynski Jayich, A. (2014). Probing Surface Noise with Depth-Calibrated Spins in Diamond. *Physical Review Letters*, 113(2), 027602.

[255] Myers, B. A., Ariyaratne, A., & Jayich, A. C. (2017). Double-Quantum Spin-Relaxation Limits to Coherence of Near-Surface Nitrogen-Vacancy Centers. *Physical Review Letters*, 118(19), 1–7.

[256] Nair, R. R., Blake, P., Grigorenko, a. N., Novoselov, K. S., Booth, T. J., Stauber, T., Peres, N. M. R., & Geim, a. K. (2008). Fine Structure Constant Defines Visual Transperency of Graphene. *Science*, 320(June), 2008.

[257] Naydenov, B., Reinhard, F., Lämmle, A., Richter, V., Kalish, R., D'Haenens-Johansson, U. F., Newton, M., Jelezko, F., & Wrachtrup, J. (2010). Increasing the coherence time of single electron spins in diamond by high temperature annealing. *Applied Physics Letters*, 97(24), 10–13.

[258] Neto, A. H. C. (2009). The electronic properties of graphene. 81(March).

[259] Neumann, P., Beck, J., Steiner, M., Rempp, F., Fedder, H., Hemmer, P. R., Wrachtrup, J., & Jelezko, F. (2010). Single-shot readout of a single nuclear spin. *Science*, 329(5991), 542–544.

[260] Neumann, P., Kolesov, R., Jacques, V., Beck, J., Tisler, J., Batalov, A., Rogers, L., Manson, N. B., Balasubramanian, G., Jelezko, F., & Wrachtrup, J. (2009). Excited-state spectroscopy of single NV defects in diamond using optically detected magnetic resonance. *New Journal of Physics*, 11.

[261] Nika, D. L., Pokatilov, E. P., Askerov, A. S., & Balandin, A. A. (2009). Phonon thermal conduction in graphene: Role of Umklapp and edge roughness scattering. *Phys. Rev. B*, 79(15), 155413.

[262] Norambuena, A., Muñoz, E., Dinani, H. T., Jarmola, A., Maletinsky, P., Budker, D., & Maze, J. R. (2018). Spin-lattice relaxation of individual solid-state spins. *Physical Review B*, 97(9), 1–13.

[263] Novoselov, K. S., Geim, A. K., Morozov, S. V., Jiang, D., Katsnelson, M. I., Grigorieva, I., Dubonos, S., Firsov, & AA (2005). Two-dimensional gas of massless dirac fermions in graphene. *Nature*, 438(7065), 197–200.

[264] Novoselov, K. S., Geim, A. K., Morozov, S. V., Jiang, D., Zhang, Y., Dubonos, S. V., Grigorieva, I. V., & Firsov, A. A. (2004). Electric field effect in atomically thin carbon films. *science*, 306(5696), 666–669.

[265] Novoselov, K. S., Mishchenko, A., Carvalho, A., Neto, A. H. C., & Road, O. (2016). 2D materials and van der Waals heterostructures. *Science*, 353(6298), aac9439.

[266] Nyquist, H. (1928). Thermal agitation of electric charge in conductors. *Phys. Rev.*, 32(1), 110.

[267] Ofori-Okai, B. K., Pezzagna, S., Chang, K., Loretz, M., Schirhagl, R., Tao, Y., Moores, B. A., Groot-Berning, K., Meijer, J., & Degen, C. L. (2012). Spin properties of very shallow nitrogen vacancy defects in diamond. *Physical Review B*, 86(8), 081406.

[268] Ohno, K., Joseph Heremans, F., Bassett, L. C., Myers, B. A., Toyli, D. M., Bleszynski Jayich, A. C., Palmstrøm, C. J., & Awschalom, D. D. (2012). Engineering shallow spins in diamond with nitrogen delta-doping. *Applied Physics Letters*, 101(8).

[269] Paik, H., Schuster, D., Bishop, L. S., Kirchmair, G., Catelani, G., Sears, A., Johnson, B., Reagor, M., Frunzio, L., Glazman, L., et al. (2011). Observation of high coherence in josephson junction qubits measured in a three-dimensional circuit qed architecture. *Physical Review Letters*, 107(24), 240501.

[270] Paik, S. Y., Lee, S. Y., Baker, W. J., McCamey, D. R., & Boehme, C. (2010). T_1 and T_2 spin relaxation time limitations of phosphorous donor electrons near crystalline silicon to silicon dioxide interface defects. *Phys. Rev. B*, 81(7), 075214.

[271] Palacios, J. J., Fernández-Rossier, J., & Brey, L. (2008). Vacancy-induced magnetism in graphene and graphene ribbons. *Physical Review B*, 77(19), 195428.

[272] Pelliccione, M., Jenkins, A., Ovartchaiyapong, P., Reetz, C., Emmanouilidou, E., Ni, N., & Bleszynski Jayich, A. C. (2016). Scanned probe imaging of nanoscale magnetism at cryogenic temperatures with a single-spin quantum sensor. *Nature Nanotechnology*, 11(8), 700–705.

[273] Pelliccione, M., Myers, B. A., Pascal, L., Das, A., & Jayich, A. B. (2014). Two-dimensional nanoscale imaging of gadolinium spins via scanning probe relaxometry with a single spin in diamond. *Physical Review Applied*, 2(5), 054014.

[274] Perdew, J. P., Burke, K., & Wang, Y. (1996). Generalized gradient approximation for the exchange-correlation hole of a many-electron system. *Physical Review B*, 54(23), 16533.

[275] Perebeinos, V. & Avouris, P. (2010). Inelastic scattering and current saturation in graphene. *Phys. Rev. B.*, 81(19), 195442.

[276] Pezzagna, S., Naydenov, B., Jelezko, F., Wrachtrup, J., & Meijer, J. (2010). Creation efficiency of nitrogen-vacancy centres in diamond. *New Journal of Physics*, 12(6), 065017.

[277] Pham, L. M., Bar-Gill, N., Le Sage, D., Belthangady, C., Stacey, A., Markham, M., Twitchen, D., Lukin, M. D., & Walsworth, R. L. (2012). Enhanced metrology using preferential orientation of nitrogen-vacancy centers in diamond. *Physical Review B*, 86(12), 121202.

[278] Pham, L. M., Devience, S. J., Casola, F., Lovchinsky, I., Sushkov, A. O., Bersin, E., Lee, J., Urbach, E., Cappellaro, P., Park, H., Yacoby, A., Lukin, M., & Walsworth, R. L. (2016a). NMR technique for determining the depth of shallow nitrogen-vacancy centers in diamond. *Physical Review B*, 93(4), 1–12.

[279] Pham, L. M., DeVience, S. J., Casola, F., Lovchinsky, I., Sushkov, A. O., Bersin, E., Lee, J., Urbach, E., Cappellaro, P., Park, H., Yacoby, A., Lukin, M. D., & Walsworth, R. L. (2016b). NMR technique for determining the depth of shallow nitrogen-vacancy centers in diamond. *Phys. Rev. B*, 93(4), 045425.

[280] Pippard, A. (1963). Acoustic amplification in semiconductors and metals. *Philos. Mag.*, 8(85), 161–165.

[281] Pizzocchero, F., Gammelgaard, L., Jessen, B. S., Caridad, J. M., Wang, L., Hone, J., Bøggild, P., & Booth, T. J. (2016). The hot pick-up technique for batch assembly of van der waals heterostructures. *Nature communications*, 7(1), 1–10.

[282] Place, A. P., Rodgers, L. V., Mundada, P., Smitham, B. M., Fitzpatrick, M., Leng, Z., Premkumar, A., Bryon, J., Sussman, S., Cheng, G., et al. (2020). New material platform for superconducting transmon qubits with coherence times exceeding 0.3 milliseconds. *arXiv preprint arXiv:2003.00024*.

[283] Polshyn, H., Zhu, J., Kumar, M. A., Zhang, Y., Yang, F., Tschirhart, C. L., Serlin, M., Watanabe, K., Taniguchi, T., MacDonald, A. H., et al. (2020). Nonvolatile switching of magnetic order by electric fields in an orbital chern insulator. *arXiv preprint arXiv:2004.11353*.

[284] Pomerantz, M. (1964). Amplification of microwave phonons in germanium. *Phys. Rev. Lett.*, 13(9), 308.

[285] Purdie, D., Pugno, N., Taniguchi, T., Watanabe, K., Ferrari, A., & Lombardo, A. (2018). Cleaning interfaces in layered materials heterostructures. *arXiv preprint*.

[286] Rabeau, J. R., Reichart, P., Tamanyan, G., Jamieson, D. N., Prawer, S., Jelezko, F., Gaebel, T., Popa, I., Domhan, M., & Wrachtrup, J. (2006). Implantation of labelled single nitrogen vacancy centers in diamond using N15. *Applied Physics Letters*, 88(2), 023113.

[287] Redman, D., Brown, S., & Rand, S. C. (1992). Origin of persistent hole burning of N–V centers in diamond. *Journal of the Optical Society of America B*, 9(5), 768.

[288] Redman, D. a., Brown, S., Sands, R. H., & Rand, S. C. (1991). Spin dynamics and electronic states of N-V center in diamond by EPR and Four-Wave_Mixing spectroscopy. *Physical Review Letters*, 64(24), 3420–3423.

[289] Reznikov, M., Heiblum, M., Shtrikman, H., & Mahalu, D. (1995). Temporal correlation of electrons: Suppression of shot noise in a ballistic quantum point contact. *Physical Review Letters*, 75(18), 3340.

[290] Rhodes, D., Chae, S. H., Ribeiro-Palau, R., & Hone, J. (2019). Disorder in van der waals heterostructures of 2d materials. *Nature materials*, 18(6), 541–549.

[291] Riedel, D., Söllner, I., Shields, B. J., Starosielec, S., Appel, P., Neu, E., Maletinsky, P., & Warburton, R. J. (2017). Deterministic enhancement of coherent photon generation from a nitrogen-vacancy center in ultrapure diamond. *Physical Review X*, 7(3), 1–8.

[292] Ristein, J. (2000). Electronic properties of diamond surfaces - blessing or curse for devices? *Diamond and Related Materials*, 9(3), 1129–1137.

[293] Ristein, J. (2006). Diamond surfaces: Familiar and amazing. *Applied Physics A: Materials Science and Processing*, 82(3 SPEC. ISS.), 377–384.

[294] Robledo, L., Bernien, H., Van Der Sar, T., & Hanson, R. (2011a). Spin dynamics in the optical cycle of single nitrogen-vacancy centres in diamond. *New Journal of Physics*, 13(2), 025013.

[295] Robledo, L., Bernien, H., Van Weperen, I., & Hanson, R. (2010). Control and coherence of the optical transition of single nitrogen vacancy centers in diamond. *Physical Review Letters*, 105(17), 1–4.

[296] Robledo, L., Childress, L., Bernien, H., Hensen, B., Alkemade, P. F., & Hanson, R. (2011b). High-fidelity projective read-out of a solid-state spin quantum register. *Nature*, 477(7366), 574–578.

[297] Rogers, L. J., McMurtrie, R. L., Sellars, M. J., & Manson, N. B. (2009). Time-averaging within the excited state of the nitrogen-vacancy centre in diamond. *New Journal of Physics*, 11.

[298] Romach, Y., Muller, C., Unden, T., Rogers, L. J., Isoda, T., Itoh, K. M., Markham, M., Stacey, A., Meijer, J., Pezzagna, S., Naydenov, B., Mcguinness, L. P., Bar-Gill, N., & Jelezko, F. (2015). Spectroscopy of Surface-Induced Noise Using Shallow Spins in Diamond. *Phys. Rev. Lett.*, 114(15), 017601.

[299] Rondin, L., Tetienne, J.-P., Hingant, T., Roch, J.-F., Maletinsky, P., & Jacques, V. (2014). Magnetometry with nitrogen-vacancy defects in diamond. *Reports on progress in physics. Physical Society (Great Britain)*, 77(5), 056503.

[300] Ross, J. S., Klement, P., Jones, A. M., Ghimire, N. J., Yan, J., Mandrus, D., Taniguchi, T., Watanabe, K., Kitamura, K., Yao, W., et al. (2014). Electrically tunable excitonic light-emitting diodes based on monolayer wse 2 p–n junctions. *Nature nanotechnology*, 9(4), 268–272.

[301] Rosskopf, T., Dussaux, A., Ohashi, K., Loretz, M., Schirhagl, R., Watanabe, H., Shikata, S., Itoh, K. M., & Degen, C. L. (2014). Investigation of surface magnetic noise by shallow spins in diamond. *Phys. Rev. Lett.*, 112(14), 147602.

[302] Rowan, L., Hahn, E., & Mims, W. (1965). Electron-spin-echo envelope modulation. *Physical Review*, 137(1A), A61.

[303] Ruan, W., Chen, Y., Tang, S., Hwang, J., Tsai, H.-Z., Lee, R., Wu, M., Ryu, H., Kahn, S., Liou, F., et al. (2020). Imaging spinon density modulations in a 2d quantum spin liquid. *arXiv preprint arXiv:2009.07379*.

[304] Ruf, M., IJspeert, M., Van Dam, S., De Jong, N., Van Den Berg, H., Evers, G., & Hanson, R. (2019). Optically coherent nitrogen-vacancy centers in micrometer-thin etched diamond membranes. *Nano letters*, 19(6), 3987–3992.

[305] Rugar, D., Budakian, R., Mamin, H. J., & Chui, B. W. (2004). Single spin detection by magnetic resonance force microscopy. *Nature*, 430(6997), 329–32.

[306] Saito, R., Mizuno, M., & Dresselhaus, M. S. (2018). Ballistic and diffusive thermal conductivity of graphene. *Phys. Rev. Appl.*, 9(2).

[307] Sakurai, J. J. & Commins, E. D. (1995). Modern quantum mechanics, revised edition.

[308] Sangtawesin, S., Dwyer, B. L., Srinivasan, S., Allred, J. J., Rodgers, L. V., De Greve, K., Stacey, A., Dontschuk, N., O'Donnell, K. M., Hu, D., et al. (2019). Origins of diamond surface noise probed by correlating single-spin measurements with surface spectroscopy. *Physical Review X*, 9(3), 031052.

[309] Santori, C., Fattal, D., Spillane, S. M., Fiorentino, M., Beausoleil, R. G., Greentree, A. D., Olivero, P., Draganski, M., Rabeau, J. R., Reichart, P., Rubanov, S., Jamieson, D. N., & Prawer, S. (2006). Coherent population trapping in diamond N-V centers at zero magnetic field. *Optics InfoBase Conference Papers*, 14(17), 7986–7994.

[310] Scheuer, J., Schwartz, I., Müller, S., Chen, Q., Dhand, I., Plenio, M. B., Naydenov, B., & Jelezko, F. (2017). Robust techniques for polarization and detection of nuclear spin ensembles. *Physical Review B*, 96(17), 174436.

[311] Schirhagl, R., Chang, K., Loretz, M., & Degen, C. L. (2014). Nitrogen-Vacancy Centers in Diamond: Nanoscale Sensors for Physics and Biology. *Annual Review of Physical Chemistry*, 65(1), 83–105.

[312] Schlipf, L., Oeckinghaus, T., Xu, K., Dasari, D. B. R., Zappe, A., De Oliveira, F. F., Kern, B., Azarkh, M., Drescher, M., Ternes, M., et al. (2017). A molecular quantum spin network controlled by a single qubit. *Science advances*, 3(8), e1701116.

[313] Schlör, S., Lisenfeld, J., Müller, C., Bilmes, A., Schneider, A., Pappas, D. P., Ustinov, A. V., & Weides, M. (2019). Correlating decoherence in transmon qubits: Low frequency noise by single fluctuators. *Physical review letters*, 123(19), 190502.

[314] Schoelkopf, R., Burke, P., Kozhevnikov, A., Prober, D., & Rooks, M. (1997). Frequency dependence of shot noise in a diffusive mesoscopic conductor. *Physical review letters*, 78(17), 3370.

[315] Schottky, W. (1918). Über spontane stromschwankungen in verschiedenen elektrizitätsleitern. *Annalen der physik*, 362(23), 541–567.

[316] Schwartz, I., Rosskopf, J., Schmitt, S., Tratzmiller, B., Chen, Q., McGuinness, L. P., Jelezko, F., & Plenio, M. B. (2019). Blueprint for nanoscale nmr. *Scientific reports*, 9(1), 1–11.

[317] Schwartz, J., Aloni, S., Ogletree, D. F., & Schenkel, T. (2012). Effects of low-energy electron irradiation on formation of nitrogen–vacancy centers in single-crystal diamond. *New Journal of Physics*, 14(4), 043024.

[318] Schweiger, A. & Jeschke, G. (2001). *Principles of pulse electron paramagnetic resonance*. Oxford University Press on Demand.

[319] Sharpe, A. L., Fox, E. J., Barnard, A. W., Finney, J., Watanabe, K., Taniguchi, T., Kastner, M., & Goldhaber-Gordon, D. (2019). Emergent ferromagnetism near three-quarters filling in twisted bilayer graphene. *Science*, 365(6453), 605–608.

[320] Sharpe, A. L., Fox, E. J., Barnard, A. W., Finney, J., Watanabe, K., Taniguchi, T., Kastner, M. A., & Goldhaber-Gordon, D. (2021). Evidence of orbital ferromagnetism in twisted bilayer graphene aligned to hexagonal boron nitride. *arXiv preprint arXiv:2102.04039*.

[321] Shields, B. J., Unterreithmeier, Q. P., De Leon, N. P., Park, H., & Lukin, M. D. (2015). Efficient Readout of a Single Spin State in Diamond via Spin-to-Charge Conversion. *Physical Review Letters*, 114(13), 1–5.

[322] Shinokita, K., Reimann, K., Woerner, M., Elsaesser, T., Hey, R., & Flytzanis, C. (2016). Strong Amplification of Coherent Acoustic Phonons by Intraminiband Currents in a Semiconductor Superlattice. *Physical Review Letters*, 116(7), 1–5.

[323] Shinotsuka, H., Tanuma, S., Powell, C. J., & Penn, D. R. (2015). Calculations of electron inelastic mean free paths. X. Data for 41 elemental solids over the 50keV to 200keV range with the relativistic full penn algorithm. *Diamond Relat. Mater.*, 47(9), 871.

[324] Shpilman, Z., Gouzman, I., Minton, T. K., Shen, L., Stacey, A., Orwa, J., Prawer, S., Cowie, B. C. C., & Hoffman, A. (2014). A near edge X-ray absorption fine structure study of oxidized single crystal and polycrystalline diamond surfaces. *Diamond Relat. Mater.*, 45(C), 20.

[325] Siegbahn, K. (1985). Electron spectroscopy for atoms, molecules and condensed matter - an overview. *Journal of Electron Spectroscopy and Related Phenomena*, 36(2), 113–129.

[326] Singleton, J. & Singleton (2001). Band Theory and Electronic Properties of Solids. (pp. 240).

[327] Sipahigil, A., Jahnke, K. D., Rogers, L. J., Teraji, T., Isoya, J., Zibrov, A. S., Jelezko, F., & Lukin, M. D. (2014). Indistinguishable photons from separated silicon-vacancy centers in diamond. *Physical Review Letters*, 113(11), 1–5.

[328] Siyushev, P., Pinto, H., Vörös, M., Gali, A., Jelezko, F., & Wrachtrup, J. (2013). Optically controlled switching of the charge state of a single nitrogen-vacancy center in diamond at cryogenic temperatures. *Phys. Rev. Lett.*, 110, 167402.

[329] Slichter, C. P. (2013). *Principles of magnetic resonance*, volume 1. Springer Science & Business Media.

[330] Smoleński, T., Dolgirev, P., Kuhlenkamp, C., Popert, A., Shimazaki, Y., Back, P., Kroner, M., Watanabe, K., Taniguchi, T., Esterlis, I., et al. (2020). Observation of wigner crystal of electrons in a monolayer semiconductor. *arXiv preprint arXiv:2010.03078*.

[331] Song, C.-L., Wang, Y.-L., Jiang, Y.-P., Wang, L., He, K., Chen, X., Hoffman, J. E., Ma, X.-C., & Xue, Q.-K. (2012). Suppression of Superconductivity by Twin Boundaries in FeSe. *Physical Review Letters*, 109(13), 137004.

[332] Song, J. C. & Levitov, L. S. (2015). Energy flows in graphene: hot carrier dynamics and cooling. *Journal of Physics: Condensed Matter*, 27(16), 164201.

[333] Sørensen, O., Eich, G., Levitt, M. H., Bodenhausen, G., & Ernst, R. (1984). Product operator formalism for the description of nmr pulse experiments. *Progress in nuclear magnetic resonance spectroscopy*, 16, 163–192.

[334] Spector, H. N. (1962). Amplification of acoustic waves through interaction with conduction electrons. *Phys. Rev.*, 127(4), 1084.

[335] Splendiani, A., Sun, L., Zhang, Y., Li, T., Kim, J., Chim, C.-Y., Galli, G., & Wang, F. (2010). Emerging photoluminescence in monolayer mos2. *Nano letters*, 10(4), 1271–1275.

[336] Sque, S. J., Jones, R., & Briddon, P. R. (2006). Structure, electronics, and interaction of hydrogen and oxygen on diamond surfaces. *Phys. Rev. B*, 73(8), 085313.

[337] Srivastava, G. P. (1990). *The Physics of Phonons*. CRC press.

[338] Stacey, A., Dontschuk, N., Chou, J. P., Broadway, D. A., Schenk, A. K., Sear, M. J., Tetienne, J. P., Hoffman, A., Prawer, S., Pakes, C. I., Tadich, A., de Leon, N. P., Gali, A., & Hollenberg, L. C. L. (2019). Evidence for primal sp^2 defects at the diamond surface: Candidates for electron trapping and noise sources. *Advanced Materials Interfaces*, 6(3), 1801449.

[339] Stanwix, P. L., Pham, L. M., Maze, J. R., Le Sage, D., Yeung, T. K., Cappellaro, P., Hemmer, P. R., Yacoby, A., Lukin, M. D., & Walsworth, R. L. (2010). Coherence of nitrogen-vacancy electronic spin ensembles in diamond. *Phys. Rev. B*, 82, 201201.

[340] Stauber, T., Peres, N., & Guinea, F. (2007). Electronic transport in graphene: A semiclassical approach including midgap states. *Phys. Rev. B*, 76(20), 205423.

[341] Staudacher, T., Shi, F., Pezzagna, S., Meijer, J., Du, J., Meriles, C. a., Reinhard, F., & Wrachtrup, J. (2013). Nuclear magnetic resonance spectroscopy on a (5-nanometer)3 sample volume. *Science (New York, N.Y.)*, 339(6119), 561–3.

[342] Steinbach, A. H., Martinis, J. M., & Devoret, M. H. (1996). Observation of hot-electron shot noise in a metallic resistor. *Physical Review Letters*, 76(20), 3806–3809.

[343] Stöhr, J. (1992). *NEXAFS Spectroscopy*, volume 25 of *Springer Series in Surface Sciences*. Berlin, Heidelberg: Springer Berlin Heidelberg.

[344] Stormer, H. L., Tsui, D. C., & Gossard, A. C. (1999). The fractional quantum hall effect. *Reviews of Modern Physics*, 71(2), S298.

[345] Strobel, P., Ristein, J., & Ley, L. (2008). Controlled hydroxylation of diamond for covalent attachment of fullerene molecules. *Diamond Relat. Mater.*, 17(7), 1362.

[346] Sushko, A., De Greve, K., Andersen, T. I., Scuri, G., Zhou, Y., Sung, J., Watanabe, K., Taniguchi, T., Kim, P., Park, H., et al. (2019). High resolution imaging of reconstructed domains and moire patterns in functional van der waals heterostructure devices. *arXiv preprint arXiv:1912.07446*.

[347] Sushkov, A. O., Lovchinsky, I., Chisholm, N., Walsworth, R. L., Park, H., & Lukin, M. D. (2014). Magnetic Resonance Detection of Individual Proton Spins Using Quantum Reporters. *Phys. Rev. Lett.*, 113(19), 197601.

[348] Tamarat, P., Manson, N. B., Harrison, J. P., McMurtrie, R. L., Nizovtsev, A., Santori, C., Beausoleil, R. G., Neumann, P., Gaebel, T., Jelezko, F., Hemmer, P., & Wrachtrup, J. (2008). Spin-flip and spin-conserving optical transitions of the nitrogen-vacancy centre in diamond. *New Journal of Physics*, 10.

[349] Taychatanapat, T. & Jarillo-Herrero, P. (2010). Electronic transport in dual-gated bilayer graphene at large displacement fields. *Physical review letters*, 105(16), 166601.

[350] Taylor, J. M., Cappellaro, P., Childress, L., Jiang, L., Budker, D., Hemmer, P. R., Yacoby, A., Walsworth, R., & Lukin, M. D. (2008). High-sensitivity diamond magnetometer with nanoscale resolution. *Nature Physics*, 4(10), 810–816.

[351] Teraji, T., Yamamoto, T., Watanabe, K., Koide, Y., Isoya, J., Onoda, S., Ohshima, T., Rogers, L. J., Jelezko, F., Neumann, P., et al. (2015). Homoepitaxial diamond film growth: High purity, high crystalline quality, isotopic enrichment, and single color center formation. *physica status solidi (a)*, 212(11), 2365–2384.

[352] Tetienne, J. P., De Gille, R. W., Broadway, D. A., Teraji, T., Lillie, S. E., McCoey, J. M., Dontschuk, N., Hall, L. T., Stacey, A., Simpson, D. A., & Hollenberg, L. C. (2018). Spin properties of dense near-surface ensembles of nitrogen-vacancy centers in diamond. *Physical Review B*, 97(8), 1–11.

[353] Tetienne, J.-P., Dontschuk, N., Broadway, D. A., Stacey, A., Simpson, D. A., & Hollenberg, L. C. (2017). Quantum imaging of current flow in graphene. *Sci. Adv.*, 3(4), e1602429.

[354] Tetienne, J.-P., Hingant, T., Kim, J.-V., Diez, L. H., Adam, J.-P., Garcia, K., Roch, J.-F., Rohart, S., Thiaville, A., Ravelosona, D., et al. (2014). Nanoscale imaging and control of domain-wall hopping with a nitrogen-vacancy center microscope. *Science*, 344(6190), 1366–1369.

[355] Thoms, B. D., Owens, M. S., Butler, J. E., & Spiro, C. (1994). Production and characterization of smooth, hydrogen-terminated diamond C(100). *Appl. Phys. Lett.*, 65(23), 2957.

[356] Tinkham, M. (2003). *Group theory and quantum mechanics*. Courier Corporation.

[357] Tisler, J., Balasubramanian, G., Naydenov, B., Kolesov, R., Grotz, B., Reuter, R., Boudou, J.-P., Curmi, P. A., Sennour, M., Thorel, A., Börsch, M., Aulenbacher, K., Erdmann, R., Hemmer, P. R., Jelezko, F., & Wrachtrup, J. (2009). Fluorescence and Spin Properties of Defects in Single Digit Nanodiamonds. *ACS Nano*, 3(7), 1959–1965.

[358] Tiwari, A. K., Goss, J., Briddon, P., Wright, N. G., Horsfall, A. B., Jones, R., Pinto, H., & Rayson, M. (2011). Calculated electron affinity and stability of halogen-terminated diamond. *Physical Review B*, 84(24), 245305.

[359] Togan, E., Chu, Y., Trifonov, A. S., Jiang, L., Maze, J., Childress, L., Dutt, M. V., Sørensen, A. S., Hemmer, P. R., Zibrov, A. S., & Lukin, M. D. (2010). Quantum entanglement between an optical photon and a solid-state spin qubit. *Nature*, 466(7307), 730–734.

[360] Tomadin, A. & Polini, M. (2013). Theory of the plasma-wave photoresponse of a gated graphene sheet. *Phys. Rev. B*, 88(20), 205426.

[361] Tran, K., Moody, G., Wu, F., Lu, X., Choi, J., Kim, K., Rai, A., Sanchez, D. A., Quan, J., Singh, A., et al. (2019). Evidence for moiré excitons in van der waals heterostructures. *Nature*, 567(7746), 71–75.

[362] Tschirhart, C., Serlin, M., Polshyn, H., Shragai, A., Xia, Z., Zhu, J., Zhang, Y., Watanabe, K., Taniguchi, T., Huber, M., et al. (2020). Imaging orbital ferromagnetism in a moir\'e chern insulator. *arXiv preprint arXiv:2006.08053*.

[363] Twitchen, D. J., Newton, M. E., Baker, J. M., Anthony, T. R., & Banholzer, W. F. (1999). Electron-paramagnetic-resonance measurements on the divacancy defect center $R4/W6$ in diamond. *Phys. Rev. B*, 59(20), 12900.

[364] Tworzydło, J., Trauzettel, B., Titov, M., Rycerz, A., & Beenakker, C. W. (2006). Sub-poissonian shot noise in graphene. *Physical review letters*, 96(24), 246802.

[365] Ulbricht, R., Dong, S., Gali, A., Meng, S., & Loh, Z. H. (2018). Vibrational relaxation dynamics of the nitrogen-vacancy center in diamond. *Physical Review B*, 97(22), 1–6.

[366] Uri, A., Grover, S., Cao, Y., Crosse, J. A., Bagani, K., Rodan-Legrain, D., Myasoedov, Y., Watanabe, K., Taniguchi, T., Moon, P., et al. (2020). Mapping the twist-angle disorder and landau levels in magic-angle graphene. *Nature*, 581(7806), 47–52.

[367] Vallejo, J., Wu, N., Fermon, C., Pannetier-Lecoeur, M., Wakamura, T., Watanabe, K., Taniguchi, T., Pellegrin, T., Bernard, A., Daddinounou, S., et al. (2020). Detection of graphene's divergent orbital diamagnetism at the dirac point. *arXiv preprint arXiv:2012.05357*.

[368] van Dam, S. B., Walsh, M., Degen, M. J., Bersin, E., Mouradian, S. L., Galiullin, A., Ruf, M., IJspeert, M., Taminiau, T. H., Hanson, R., et al. (2019). Optical coherence of diamond nitrogen-vacancy centers formed by ion implantation and annealing. *Physical Review B*, 99(16), 161203.

[369] Vasyukov, D., Anahory, Y., Embon, L., Halbertal, D., Cuppens, J., Neeman, L., Finkler, A., Segev, Y., Myasoedov, Y., Rappaport, M. L., et al. (2013). A scanning superconducting quantum interference device with single electron spin sensitivity. *Nat. Nanotechnol.*, 8(9), 639.

[370] Vehtari, A., Gelman, A., & Gabry, J. (2017). Practical bayesian model evaluation using leave-one-out cross-validation and waic. *Statistics and computing*, 27(5), 1413–1432.

[371] Von Klitzing, K. (1986). The quantized hall effect. *Reviews of Modern Physics*, 58(3), 519.

[372] von Klitzing, K. (2019). Essay: Quantum hall effect and the new international system of units. *Physical review letters*, 122(20), 200001.

[373] Walker, M. (1968). At 5 spin–lattice relaxation rate for non-kramers ions. *Canadian Journal of Physics*, 46(11), 1347–1353.

[374] Wang, L. (2013). One-Dimensional Electrical Contact to. *Science (New York, N.Y.)432*, 342(November), 614–617.

[375] Wang, Z. H., de Lange, G., Ristè, D., Hanson, R., & Dobrovitski, V. V. (2012). Comparison of dynamical decoupling protocols for a nitrogen-vacancy center in diamond. *Phys. Rev. B*, 85(15), 155204.

[376] Wang, Z. H. & Takahashi, S. (2013). Spin decoherence and electron spin bath noise of a nitrogen-vacancy center in diamond. *Physical Review B - Condensed Matter and Materials Physics*, 87(11), 1–6.

[377] Watts, B. & Ade, H. (2008). A simple method for determining linear polarization and energy calibration of focused soft X-ray beams. *Journal of Electron Spectroscopy and Related Phenomena*, 162(2), 49.

[378] White, D., Galleano, R., Actis, A., Brixy, H., De Groot, M., Dubbeldam, J., Reesink, A., Edler, F., Sakurai, H., Shepard, R., et al. (1996). The status of johnson noise thermometry. *Metrologia*, 33(4), 325.

[379] Williams, G. T., Cooil, S. P., Roberts, O. R., Evans, S., Langstaff, D. P., & Evans, D. A. (2014). High temperature photoelectron emission and surface photovoltage in semiconducting diamond. *Appl. Phys. Lett.*, 105(6), 061602.

[380] Wolfer, M., Biener, J., El-dasher, B. S., Biener, M. M., Hamza, A. V., Kriele, A., & Wild, C. (2009). Crystallographic anisotropy of growth and etch rates of CVD diamond. *Diamond Relat. Mater.*, 18(5), 713.

[381] Wolters, J., Sadzak, N., Schell, A. W., Schröder, T., & Benson, O. (2013). Measurement of the ultrafast spectral diffusion of the optical transition of nitrogen vacancy centers in nanosize diamond using correlation interferometry. *Physical review letters*, 110(2), 027401.

[382] Xiao, D., Chang, M.-C., & Niu, Q. (2010). Berry phase effects on electronic properties. *Reviews of modern physics*, 82(3), 1959.

[383] Xue, J. (2013). Berry phase and the unconventional quantum hall effect in graphene. *arXiv preprint arXiv:1309.6714*.

[384] Yamamoto, T., Umeda, T., Watanabe, K., Onoda, S., Markham, M. L., Twitchen, D. J., Naydenov, B., McGuinness, L. P., Teraji, T., Koizumi, S., Dolde, F., Fedder, H., Honert, J., Wrachtrup, J., Ohshima, T., Jelezko, F., & Isoya, J. (2013). Extending spin coherence times of diamond qubits by high-temperature annealing. *Phys. Rev. B*, 88(7), 075206.

[385] Yamoah, M. A., Yang, W., Pop, E., & Goldhaber-Gordon, D. (2017). High-velocity saturation in graphene encapsulated by hexagonal boron nitride. *ACS Nano*, 11(10), 9914–9919.

[386] Yang, H., Xu, L., Fang, Z., Gu, C., & Zhang, S. (2008). Bond-counting rule for carbon and its application to the roughness of diamond (001). *Physical review letters*, 100(2), 026101.

[387] Yang, W., Berthou, S., Lu, X., Wilmart, Q., Denis, A., Rosticher, M., Taniguchi, T., Watanabe, K., Feve, G., Berroir, J.-M., et al. (2018). A graphene Zener-Klein transistor cooled by a hyperbolic substrate. *Nat. Nanotechnol.*, 13(1), 47.

[388] Yankowitz, M., Ma, Q., Jarillo-Herrero, P., & LeRoy, B. J. (2019). van der waals heterostructures combining graphene and hexagonal boron nitride. *Nature Reviews Physics*, 1(2), 112–125.

[389] Yao, N. Y., Jiang, L., Gorshkov, A. V., Gong, Z.-X., Zhai, A., Duan, L.-M., & Lukin, M. D. (2011). Robust quantum state transfer in random unpolarized spin chains. *Physical review letters*, 106(4), 040505.

[390] Yazyev, O. V. & Helm, L. (2007). Defect-induced magnetism in graphene. *Physical Review B*, 75(12), 125408.

[391] Young, A. F., Zhang, Y., & Kim, P. (2014). Experimental manifestation of berry phase in graphene. In *Physics of Graphene* (pp. 3–27). Springer.

[392] Yuan, Z., Fitzpatrick, M., Rodgers, L. V., Sangtawesin, S., Srinivasan, S., & de Leon, N. P. (2020). Charge state dynamics and optically detected electron spin resonance contrast of shallow nitrogen-vacancy centers in diamond. *Physical Review Research*, 2(3), 033263.

[393] Zaitsev, A. M. (2013). *Optical properties of diamond: a data handbook*. Springer Science & Business Media.

[394] Zhang, X., Zou, C.-l., Jiang, L., & Tang, H. X. (2014). Strongly coupled magnons and cavity microwave photons. (pp. 1–5).

[395] Zhang, Y., Brar, V. W., Girit, C., Zettl, A., & Crommie, M. F. (2009). Origin of spatial charge inhomogeneity in graphene. *Nature Physics*, 5(10), 722–726.

[396] Zhang, Y., Tan, Y.-W., Stormer, H. L., & Kim, P. (2005). Experimental observation of the quantum hall effect and berry's phase in graphene. *nature*, 438(7065), 201–204.

[397] Zhao, S. F., Poccia, N., Panetta, M. G., Yu, C., Johnson, J. W., Yoo, H., Zhong, R., Gu, G., Watanabe, K., Taniguchi, T., et al. (2019). Sign-reversing hall effect in atomically thin high-temperature bi 2.1 sr 1.9 cacu 2.0 o 8+ δ superconductors. *Physical review letters*, 122(24), 247001.

[398] Zhao, S.-X., Gao, F., Wang, Y.-N., & Bogaerts, A. (2013). Gas ratio effects on the Si etch rate and profile uniformity in an inductively coupled Ar/CF 4 plasma. *Plasma Sources Science and Technology*, 22(1), 015017.

[399] Zheng, J., Xie, X., Wee, A., & Loh, K. P. (2001). Oxygen-induced surface state on diamond (100). *Diamond and related materials*, 10(3-7), 500–505.

[400] Zhou, B. B., Jerger, P. C., Lee, K.-H., Fukami, M., Mujid, F., Park, J., & Awschalom, D. D. (2020a). Spatiotemporal mapping of a photocurrent vortex in monolayer mos 2 using diamond quantum sensors. *Physical Review X*, 10(1), 011003.

[401] Zhou, T. X., Stöhr, R. J., & Yacoby, A. (2017). Scanning diamond nv center probes compatible with conventional afm technology. *Applied Physics Letters*, 111(16), 163106.

[402] Zhou, Y., Sung, J., Brutschea, E., Esterlis, I., Wang, Y., Scuri, G., Gelly, R. J., Heo, H., Taniguchi, T., Watanabe, K., et al. (2020b). Signatures of bilayer wigner crystals in a transition metal dichalcogenide heterostructure. *arXiv preprint arXiv:2010.03037*.

[403] Zibrov, A. A., Kometter, C., Zhou, H., Spanton, E., Taniguchi, T., Watanabe, K., Zaletel, M., & Young, A. (2017). Tunable interacting composite fermion phases in a half-filled bilayer-graphene landau level. *Nature*, 549(7672), 360–364.



This thesis was typeset using LaTeX, originally developed by Leslie Lamport and based on Donald Knuth's TeX. The body text is set in 11 point Egenolff-Berner Garamond, a revival of Claude Garamont's humanist typeface. The above illustration, "Science Experiment 02", was created by Ben Schlitter and released under CC BY-NC-ND 3.0. A template that can be used to format a PhD thesis with this look and feel has been released under the permissive MIT (X11) license, and can be found online at github.com/suchow/Dissertate or from its author, Jordan Suchow, at suchow@post.harvard.edu.